

nature

IN FOR THE KRILL

Foraging measurements reveal the huge volume of food consumed by baleen whales



Global warming
Climate scientists discuss their fears for the future

Coronavirus
Restricted clinical trials hamper Africa's bid to find COVID treatments

Internal insight
Machine learning offers detailed view of cells and tissue in 3D

Nature.2021.11.06

[Sat, 06 Nov 2021]

- [This Week](#)
- [News in Focus](#)
- [Books & Arts](#)
- [Opinion](#)
- [Work](#)
- [Research](#)
- [Amendments & Corrections](#)

This Week

- **[Glass is the hidden gem in a carbon-neutral future](#)** [03 November 2021]
Editorial • Recycling glass does not degrade it, and manufacturing it can be carbon-free. So why are many countries still burying glass in the ground?
- **[The African Academy of Sciences is in crisis — responsibility must be shared](#)** [03 November 2021]
Editorial • The pan-African science academy is in turmoil. Funders and fellows must jointly own the crisis, and work to stop it happening again.
- **[Scientists: don't feed the doubt machine](#)** [02 November 2021]
World View • From climate to COVID, naivety about how science is hijacked promotes more of the same.
- **[How climate change will make the hottest tropical days even more extreme](#)** [25 October 2021]
Research Highlight • Dryness begets heat, and atmospheric moisture in the tropics is expected to be low on the hottest days in a warmer world.
- **[Enigmatic Falklands 'fox' might have hitched a ride with humans](#)** [29 October 2021]
Research Highlight • Findings suggest that people lived on the islands earlier than thought — and could have imported the canid called the warrah.
- **[All in the mind: what the placebo effect looks like in the brain](#)** [29 October 2021]
Research Highlight • When pain relief is expected, specific circuits in the brainstem become more active.
- **[Marine urban sprawl is gobbling up Earth's coastlines](#)** [26 October 2021]
Research Highlight • Jetties, docks and other artificial structures are fast replacing the natural ecosystems where sea meets land.
- **[The faint little galaxies that could shed light on the early cosmos](#)** [29 October 2021]
Research Highlight • Small galaxies seem to be forming stars the old-fashioned way: in splendid isolation.

- **How ‘sleep misperception’ fools people into thinking they don’t sleep** [29 October 2021]

Research Highlight • Research on slumbering volunteers reveals the surprising stage when we feel most deeply asleep.

- **Baby bats try out their ‘sonar’ just after birth** [27 October 2021]

Research Highlight • Fruit-bat pups can send short echolocation clicks — and sense those of others — from day zero.

- EDITORIAL
- 03 November 2021

Glass is the hidden gem in a carbon-neutral future

Recycling glass does not degrade it, and manufacturing it can be carbon-free. So why are many countries still burying glass in the ground?



Workers sort out glass for recycling following an August 2020 explosion that damaged more than half of Beirut. Credit: Joseph Eid/AFP/Getty

Glass can be recycled infinitely without losing any of its properties. Why, then, are most countries — with the exception of those in Europe — still burying most of their glass as landfill by the tonne? In 2018, the United States alone offloaded almost 7 million tonnes of glass into landfill sites,

accounting for 5.2% of all solid municipal waste, according to the US Environmental Protection Agency.

The push to cut plastics use is accelerating the search for new materials, especially for containers that can hold liquids. But glass is an existing material that could be the star of a net-zero carbon economy.

Worldwide, glass manufacturing produces at least 86 million tonnes of carbon dioxide every year. But most of this can be eliminated when glass is recycled, and existing technologies could turn glass manufacturing into a mostly carbon-free process. What needs to happen is for countries to stop sending glass to landfill sites, and to make glass recycling mandatory.



Chemistry can make plastics sustainable – but isn't the whole solution

Glass is made by heating limestone, sand and soda ash to 1,500 °C. This heat comes from natural gas, and it accounts for between 75% and 85% of the carbon emissions from glass manufacturing. The remaining emissions are a by-product of the chemical reactions between the raw materials. But some of these materials can be replaced with crushed recycled glass, known as cullet. When cullet is melted, no CO₂ is released. And furnaces don't have to burn so fiercely to melt glass as to melt the raw materials, offering further carbon savings. According to the European Container Glass Federation (FEVE), an industry group based in Brussels, 10% more cullet in

a furnace lowers CO₂ emissions by 5% compared with making glass entirely from raw materials.

As with most forms of recycling, some caveats apply. The type of glass used to make windows — known as flat glass — cannot contain impurities, unlike glass used in many other applications. So it's not possible to melt down jam jars to get a window pane. But flat-glass cullet can be used to make more flat glass.

Some questions will need further research. For example, governments will need to know the monetary cost of boosting systems for glass collection and recycling, so that they can allocate appropriate resources. Furthermore, glass is heavier than plastic, so using it as a replacement will probably add to transport costs and emissions, and that, too, needs to be understood.



Concrete needs to lose its colossal carbon footprint

When it comes to glass recycling, Europe is the world's most advanced region by some margin, and has ambitions to be even better. Researchers could study how Europe's recycling scheme came about, its strengths and weaknesses and whether there are lessons for other countries. Three-quarters of glass used for containers such as bottles is collected for recycling across all 27 member states and the United Kingdom. As a result, new glass made in the European Union already contains some 52% recycled material. The

glass-container industry has set itself a target of collecting 90% of all waste container glass in the EU by 2030.

But other countries are not where they need to be. Moreover, data on glass recycling are difficult to find, partly because most countries are not reporting what they are doing. There seems to be no international body that collects glass-recycling data. That needs to change.

That said, national efforts are under way to improve collection and recycling rates. The United States recycles, on average, just 31% of its glass containers, but the Glass Packaging Institute, a trade association based in Arlington, Virginia, is pushing to increase that to 50% by 2030 (to achieve that, 56% of all waste glass must be collected). Similarly, a project run by the Glass Recycling Company in Johannesburg increased the recycling rate across South Africa from 18% in 2005–06 to 42% in 2018–19, including boosting the use of returnable bottles. But elsewhere — in Brazil, China and India, for example — authorities are silent, or, at the very least, are not reporting their plans and ambitions.

More countries need to pass laws to reduce waste and eventually stop sending glass to landfill. That will automatically create greater incentives for glass to be recycled. Europe already mandates that 70% of waste building and construction materials are recycled. The remainder currently ends up being used as aggregate for road filling or other basic building processes; this is a huge waste of a valuable resource.



Lithium-ion batteries need to be greener and more ethical

Carbon can also be saved by decarbonizing the process of melting the chemical mix during manufacturing. A demonstration project called Furnace for the Future, run by FEVE, makes glass using electricity instead of natural gas to heat recycled glass cullet. If the electricity source were fully decarbonized, it would mean that the entire process of glass-making would effectively be carbon-free.

Glass is an essential material. And it is possible for its manufacture to become almost carbon-free in a relatively short time. But legislation is required to ensure that it is properly collected and recycled, and that it doesn't end up in landfill. Communities and companies should be helped to create infrastructure to collect glass and recycle it. The answers are there, and they are relatively simple. They need to be put into practice — and we can all raise a glass to that.

Nature **599**, 7-8 (2021)

doi: <https://doi.org/10.1038/d41586-021-02992-8>

| [Section menu](#) | [Main menu](#) |

- EDITORIAL
- 03 November 2021

The African Academy of Sciences is in crisis — responsibility must be shared

The pan-African science academy is in turmoil. Funders and fellows must jointly own the crisis, and work to stop it happening again.

The African Academy of Sciences (AAS) is facing its worst crisis since its foundation 36 years ago. The Nairobi-based organization has lost more than half of its staff after key international funders, including the Bill & Melinda Gates Foundation, the UK government and the UK charity Wellcome withdrew from a flagship funding partnership. African researchers and scientific institutions are horror-struck at the resulting devastation of the continent's apex science academy. This did not need to happen.

Funders say they have lost confidence in the academy's governance. This follows internal tensions that led to the suspension of senior staff members. The basis of the disagreement has not been made public, but it does concern the academy's relatively new role as a funding body. In 2015, it was given the extra responsibility of disbursing large amounts of money on behalf of regional and international sponsors. The role is unusual, because academies do not generally process large grants on behalf of other funders. This is partly because they also award their own funding — which is often highly sought-after and prestigious — and partly to avoid conflicts of interest.

Where academies are involved in grant-making, it tends to be on a modest scale, focusing for example on funding for early-career researchers. There are good reasons for this: an organization that represents the interests of scientists should not be responsible for distributing large amounts of

funding to people who would include its own members and fellows. To prevent potential bias, many countries have set up separate grant-funding agencies, which operate at arm's length from both academies and government ministries.

For most of its existence, the AAS was largely responsible for capacity building and science advocacy. But in 2015, the AAS, the African Union and international funders agreed that the academy would host and manage a new and significantly more ambitious funding platform, called the Alliance for Accelerating Excellence in Science in Africa (AESA), to help shift “the centre of gravity” for African research funding closer to Africa.

The platform included schemes such as the US\$176-million Human Heredity & Health in Africa (H3Africa) project, a consortium that undertakes fundamental research into diseases in Africa. Another is a \$100-million initiative called Developing Excellence in Leadership, Training and Science in Africa. Thus, in just 5 or so years, the AAS changed from an organization of 22 staff members doing the work of a conventional academy, into an agency employing almost 70 people and disbursing multi-year grants worth hundreds of millions of dollars.

Some science academies were once much more involved in distributing research grants than they are today. But over time, independent grants agencies have been set up, and are designed such that clear boundaries separate funders and grant recipients; governance and peer review, especially, need to be independent. It's not that the staff of science academies couldn't do the work of a grant-making organization — but that scientists and policymakers agreed that it was not appropriate.

Questions need to be asked about whether this arm's-length principle — which all the AAS funders know well from their home countries — was considered when they set up AESA. Ultimately, of course the fellows who make up the AAS's governing council should never have allowed internal disagreements between members of the leadership to get in the way of the organization's functioning. But funders need to accept their share of responsibility, too.

Good leadership involves learning from failure and accepting responsibility for mistakes. All parties must therefore stay engaged, not walk away, and together assess what has happened and why. That includes determining whether forgoing the arm's-length principle in science funding contributed, even if in a small way, to the present crisis.

This all needs to happen quickly. All those involved have a responsibility to make sure that Africa's premier science academy succeeds and fulfils its mission to represent and boost science on the continent.

Nature **599**, 8 (2021)

doi: <https://doi.org/10.1038/d41586-021-02991-9>

This article was downloaded by **calibre** from <https://www.nature.com/articles/d41586-021-02991-9>

| [Section menu](#) | [Main menu](#) |

- WORLD VIEW
- 02 November 2021

Scientists: don't feed the doubt machine



From climate to COVID, naivety about how science is hijacked promotes more of the same.

- [Cecília Tomori](#) ✉

Researchers at the COP26 climate talks this month know well how doubt can be weaponized to delay action — something many COVID-19 scientists have taken too long to appreciate. They point out problematic methods, poor study design and unjustified claims, but their efforts would be much more effective if they first considered a larger strategy: how ‘sciency-ness’ is used to distract from reality and hinder effective policy.

Much of my own work focuses on how industry exploits scientific credentials to bolster false claims that undermine breastfeeding to increase

sales of formula milk and, ultimately, damage health. The strategies and patterns recur across industries: they have been documented in tobacco, fossil fuels, pharmaceuticals, food and more. This influence is so powerful that public-health researchers consider it a distinct area of study: ‘commercial determinants of health’.

Throughout the pandemic, I’ve been saddened at how science has been hijacked. Arguments around herd immunity exemplify this: proponents claimed that acquiring immunity by infection was fine for most people and also that communities were well on their way to achieving herd immunity. The messages downplayed dangers for those with high risks of exposure or severe illness. Technical arguments over infection rates silently cemented the assumption that disabled or immunocompromised people did not merit collective protective action; nor did the workers whose jobs required dangerous public contact.



Truth decay: when uncertainty is weaponized

Although many scientific champions did provide appropriate context, I watched several respected colleagues step into debates on when, or if, society would reach herd immunity without realizing that the discussion was not simply a scientific debate. Their too-narrow focus unintentionally helped to promote controversy and doubt, and that ultimately impeded an effective public-health response. The same happened around mask use,

vaccination and school policies. This helped to shift public opinion on which public-health measures were ‘acceptable’: the fewer the better.

The field of agnotology (the study of deliberate spreading of confusion) shows how ignorance and doubt can be purposefully manufactured. Famous scholars include David Michaels, Marion Nestle and Naomi Oreskes. In September, Katharine Hayhoe, chief scientist at the Nature Conservancy, a non-profit organization based in Arlington, Virginia, quoted environmentalist Bill McKibben on Twitter in regard to climate change: “We spent a long time thinking we were engaged in an argument about data and reason But now we realize it’s a fight over money and power.” Hayhoe elaborated: “‘Objections’ were always, entirely, professionally, and verrrry cleverly couched in scientific terms. They [industry] focused their lasers on the science and like cats we followed their pointer and their lead.” Some elements of manufactured doubt in this pandemic might seem fuzzier, especially when vested interests are not always clear. Nonetheless, the same lessons apply.



[Beware: transparency rule is a Trojan horse](#)

How can researchers keep from being distracted like cats? By gaining a better understanding of how strategies are deployed to manufacture doubt and ignorance.

First, researchers must learn to identify authors of research, and their relationships with industry and with non-profit groups that have specialized agendas. How the tobacco industry paid scientists and physicians to serve as advisers and consultants to undermine the body of evidence pointing to the harms of tobacco is extensively documented. More recent examples abound. For instance, the non-profit International Life Sciences Institute, based in Washington DC and funded by leading companies in the food and chemical industries, promotes doubt about science that links ultraprocessed foods with health concerns, and provides experts to promote personal responsibility rather than regulations on junk food in policies to combat obesity.

Second, scientists should consider what kinds of argument the data and conclusions serve. How might these shape public opinion? What policy decisions might they affect? A review of corporate determinants of health highlights how media ownership can shape coverage and frame whether health is seen as a matter of ‘personal responsibility’, which suits corporate interests, or a communal and governmental responsibility ([M. McKee and D. Stuckler *Am. J. Public Health* 108, 1167–1170; 2018](#)). This has a key role in whether individual decisions are cast as a matter of ‘freedom’ versus ‘solidarity’, and regulations as restriction or protection. Scientists can point out these framings when talking to reporters or on social media.

Third, scientists can consistently highlight correct information and avoid serving as inadvertent amplifiers of flawed information; they can encourage journalists to do the same. Avoid links to news articles or commentaries that highlight poor studies or otherwise use science irresponsibly. Provoking outrage and controversy helps misleading arguments to spread, which serves to manufacture doubt. And, as documented in anti-vaccine movements and climate denial, controversy around one article can generate attention that legitimizes problematic arguments.

The scientists who gum up the doubt machine do so by constantly pointing to the broader context, by acknowledging genuine scientific debate, by being alert to researchers’ political and commercial connections, and by staying educated on how denialism works. If more scientists did the same, these distorting strategies would be stymied.

Nature **599**, 9 (2021)

doi: <https://doi.org/10.1038/d41586-021-02993-7>

This article was downloaded by **calibre** from <https://www.nature.com/articles/d41586-021-02993-7>

| [Section menu](#) | [Main menu](#) |

- RESEARCH HIGHLIGHT
- 25 October 2021

How climate change will make the hottest tropical days even more extreme

Dryness begets heat, and atmospheric moisture in the tropics is expected to be low on the hottest days in a warmer world.



People cool off in Yemen. Its location in the tropics means that as Earth warms, the temperature of its hottest days will soar as the temperature of its average days rises more moderately. Credit: Yahya Arhab/EPA-EFE/Shutterstock

As Earth's climate changes, the hottest days in the tropics will warm more than average days, thanks to the tropical atmosphere being drier than usual on hot days¹.

Access options

Subscribe to Journal

Get full journal access for 1 year

\$199.00

only \$3.90 per issue

[Subscribe](#)

All prices are NET prices.
VAT will be added later in the checkout.
Tax calculation will be finalised during checkout.

Rent or Buy article

Get time limited or full article access on ReadCube.

from \$8.99

[Rent or Buy](#)

All prices are NET prices.

Additional access options:

- [Log in](#)
- [Learn about institutional subscriptions](#)

Nature **599**, 10 (2021)

doi: <https://doi.org/10.1038/d41586-021-02869-w>

References

1. 1.

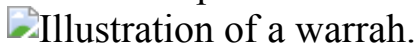
Byrne, M. P. *Nature Geosci.* <https://doi.org/10.1038/s41561-021-00828-8> (2021).

This article was downloaded by **calibre** from <https://www.nature.com/articles/d41586-021-02869-w>

- RESEARCH HIGHLIGHT
- 29 October 2021

Enigmatic Falklands ‘fox’ might have hitched a ride with humans

Findings suggest that people lived on the islands earlier than thought — and could have imported the canid called the warrah.



The warrah, whose origins piqued Charles Darwin’s curiosity, was hunted into extinction by 1876. Credit: The Natural History Museum/Alamy

When Europeans first reached the Falkland Islands in 1690, they found a fox-like animal now called the warrah. Less than 200 years later, it had been hunted to extinction. But how did it get there in the first place? There has been little evidence that humans lived on the islands, which lie east of southernmost South America, before 1690. Nor is there evidence of an ice bridge that the animals could have crossed from the mainland millennia before.

Access options

Subscribe to Journal

Get full journal access for 1 year

\$199.00

only \$3.90 per issue

[Subscribe](#)

All prices are NET prices.
VAT will be added later in the checkout.
Tax calculation will be finalised during checkout.

Rent or Buy article

Get time limited or full article access on ReadCube.

from \$8.99

[Rent or Buy](#)

All prices are NET prices.

Additional access options:

- [Log in](#)
- [Learn about institutional subscriptions](#)

Nature **599**, 10 (2021)

doi: <https://doi.org/10.1038/d41586-021-02946-0>

References

1. 1.

Hamley, K. M. *et al.* *Sci. Adv.* **7**, eabh3803 (2021).

This article was downloaded by **calibre** from <https://www.nature.com/articles/d41586-021-02946-0>

- RESEARCH HIGHLIGHT
- 29 October 2021

All in the mind: what the placebo effect looks like in the brain

When pain relief is expected, specific circuits in the brainstem become more active.



Researchers are uncovering the relationship between pain perception and various brain regions. Credit: Kateryna Kon/Science Photo Library

Expectations sway perceptions of pain: people who take a pill that they think is a painkiller often report relief, even if the pill was just a sugar tablet. Scientists have long known about this ‘placebo effect’ and its inverse, the nocebo effect, which heightens pain if a person anticipates that something will hurt. But the biological basis of these responses has remained elusive.

Access options

Subscribe to Journal

Get full journal access for 1 year

\$199.00

only \$3.90 per issue

[Subscribe](#)

All prices are NET prices.
VAT will be added later in the checkout.
Tax calculation will be finalised during checkout.

Rent or Buy article

Get time limited or full article access on ReadCube.

from \$8.99

[Rent or Buy](#)

All prices are NET prices.

Additional access options:

- [Log in](#)
- [Learn about institutional subscriptions](#)

Nature **599**, 10 (2021)

doi: <https://doi.org/10.1038/d41586-021-02939-z>

References

1. 1.

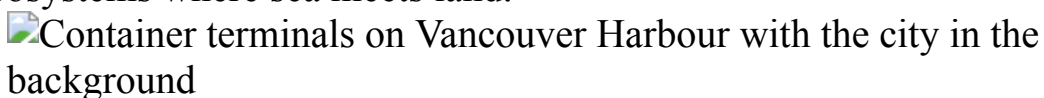
Crawford, L. *et al.* *J. Neurosci.*
<https://doi.org/10.1523/JNEUROSCI.0806-21.2021> (2021).

This article was downloaded by **calibre** from <https://www.nature.com/articles/d41586-021-02939-z>

- RESEARCH HIGHLIGHT
- 26 October 2021

Marine urban sprawl is gobbling up Earth's coastlines

Jetties, docks and other artificial structures are fast replacing the natural ecosystems where sea meets land.



Container terminals in Vancouver, Canada, where artificial structures 'armour' 75% of the coastline. Credit: James MacDonald/Bloomberg/Getty

In coastal cities around the world, artificial coastal infrastructure is likely to swallow up significant proportions of the remaining unspoilt coastal areas in the next 25 years, modelling shows¹.

Access options

Subscribe to Journal

Get full journal access for 1 year

\$199.00

only \$3.90 per issue

[Subscribe](#)

All prices are NET prices.

VAT will be added later in the checkout.

Tax calculation will be finalised during checkout.

Rent or Buy article

Get time limited or full article access on ReadCube.

from \$8.99

[Rent or Buy](#)

All prices are NET prices.

Additional access options:

- [Log in](#)
- [Learn about institutional subscriptions](#)

Nature **599**, 10 (2021)

doi: <https://doi.org/10.1038/d41586-021-02941-5>

References

1. 1.

Floerl, O. *et al.* *Nature Sustain.* <https://doi.org/10.1038/s41893-021-00780-w> (2021).

This article was downloaded by **calibre** from <https://www.nature.com/articles/d41586-021-02941-5>

- RESEARCH HIGHLIGHT
- 29 October 2021

The faint little galaxies that could shed light on the early cosmos

Small galaxies seem to be forming stars the old-fashioned way: in splendid isolation.

Image from SHARDS study

Researchers studied this galaxy cluster, called Abell 370, in their search for galaxies that are in the process of forming stars. Credit: SHARDS research team

The first galaxies coalesced more than 12 billion years ago. Small and fairly short-lived, they helped to bring light and energy to a vast, dark sea of neutral atoms in a process known as reionization. Now, researchers have identified a clutch of galaxies relatively near Earth that could serve as good proxies for the study of those ancient galaxies¹.

Access options

Subscribe to Journal

Get full journal access for 1 year

\$199.00

only \$3.90 per issue

[Subscribe](#)

All prices are NET prices.
VAT will be added later in the checkout.
Tax calculation will be finalised during checkout.

Rent or Buy article

Get time limited or full article access on ReadCube.

from \$8.99

[Rent or Buy](#)

All prices are NET prices.

Additional access options:

- [Log in](#)
- [Learn about institutional subscriptions](#)

Nature **599**, 11 (2021)

doi: <https://doi.org/10.1038/d41586-021-02943-3>

References

1. 1.

Griffiths, A. *et al.* *Mon. Not. R. Astron. Soc.* **508**, 3860–3876 (2021).

This article was downloaded by **calibre** from <https://www.nature.com/articles/d41586-021-02943-3>

- RESEARCH HIGHLIGHT
- 29 October 2021

How ‘sleep misperception’ fools people into thinking they don’t sleep

Research on slumbering volunteers reveals the surprising stage when we feel most deeply asleep.



Humans perceive that they sleep most deeply during the rapid-eye-movement phase, which is also characterized by vivid dreams. Credit: Getty

People with the paradoxical condition called sleep misperception are convinced that they’ve been awake even when their brain activity shows that they were sound asleep. New results suggest that the mismatch stems from brain activity resembling that recorded during wakefulness — but occurring as people sleep¹.

Access options

Subscribe to Journal

Get full journal access for 1 year

\$199.00

only \$3.90 per issue

[Subscribe](#)

All prices are NET prices.
VAT will be added later in the checkout.
Tax calculation will be finalised during checkout.

Rent or Buy article

Get time limited or full article access on ReadCube.

from \$8.99

[Rent or Buy](#)

All prices are NET prices.

Additional access options:

- [Log in](#)
- [Learn about institutional subscriptions](#)

Nature **599**, 11 (2021)

doi: <https://doi.org/10.1038/d41586-021-02942-4>

References

1. 1.

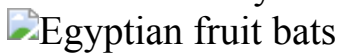
Stephan, A. M., Lecci, S., Cataldi, J. & Siclari, F. *Curr. Biol.*
<https://doi.org/10.1016/j.cub.2021.10.012> (2021).

This article was downloaded by **calibre** from <https://www.nature.com/articles/d41586-021-02942-4>

- RESEARCH HIGHLIGHT
- 27 October 2021

Baby bats try out their ‘sonar’ just after birth

Fruit-bat pups can send short echolocation clicks — and sense those of others — from day zero.



A young Egyptian fruit bat’s navigation clicks sound like those of an adult by the time the pup is 7–8 weeks old, the age of first flight. Credit: Philippe Clement/Nature Picture Library

Move over, early bloomers: baby bats might be the most precocious younglings of the animal kingdom. Researchers have found that, from day zero, newborn Egyptian fruit bats can use the built-in sonar that allows the creatures to navigate in total darkness¹.

Access options

Subscribe to Journal

Get full journal access for 1 year

\$199.00

only \$3.90 per issue

[Subscribe](#)

All prices are NET prices.
VAT will be added later in the checkout.

Tax calculation will be finalised during checkout.

Rent or Buy article

Get time limited or full article access on ReadCube.

from \$8.99

[Rent or Buy](#)

All prices are NET prices.

Additional access options:

- [Log in](#)
- [Learn about institutional subscriptions](#)

Nature **599**, 11 (2021)

doi: <https://doi.org/10.1038/d41586-021-02940-6>

References

1. 1.

Smarsh, G. C., Tarnovsky, Y. & Yovel, Y. *Proc. R. Soc. B* <https://doi.org/10.1098/rspb.2021.1714> (2021).

This article was downloaded by **calibre** from <https://www.nature.com/articles/d41586-021-02940-6>

News in Focus

- **[Africa accelerator, racial-bias fears and UK science budget](#)** [03 November 2021]
News Round-Up • The latest science news, in brief.
 - **[COP26 climate summit: A scientists' guide to a momentous meeting](#)** [25 October 2021]
News Explainer • Despite 30 years of climate diplomacy, urgent and aggressive action is needed to halt global warming. Nature explains what success looks like, and what's on the line.
 - **[What COVID vaccines for young kids could mean for the pandemic](#)** [27 October 2021]
News • As the US Food and Drug Administration authorizes shots for children aged 5 to 11, researchers predict what this might mean for populations.
 - **[DNA reveals surprise ancestry of mysterious Chinese mummies](#)** [27 October 2021]
News • The genomes of 13 remarkably preserved 4,000-year-old mummies from the Tarim Basin suggest they weren't migrants who brought technology from the west, as previously supposed.
 - **[Mysterious 'alien beacon' was false alarm](#)** [25 October 2021]
News • Radio signal seemed to originate from the star Proxima Centauri, and provided a helpful drill for future searches.
 - **[Top climate scientists are sceptical that nations will rein in global warming](#)** [01 November 2021]
News Feature • A Nature survey reveals that many authors of the latest IPCC climate-science report are anxious about the future and expect to see catastrophic changes in their lifetimes.
 - **[African scientists race to test COVID drugs — but face major hurdles](#)** [03 November 2021]
News Feature • In a bid to stave off looming disaster, scientists are trying to repurpose drugs used for malaria and other diseases, but infrastructure and recruitment challenges stymie progress.
-

| [Next section](#) | [Main menu](#) | [Previous section](#) |

- NEWS ROUND-UP
- 03 November 2021

Africa accelerator, racial-bias fears and UK science budget

The latest science news, in brief.



The SESAME synchrotron in Jordan took around 20 years from conception to operation.Credit: Noemi Caraban Gonzalez/SESAME/CERN

African light source needs \$1 billion

Scientists say they need to raise US\$1 billion for [Africa's first synchrotron light source](#), a particle accelerator that produces intense radiation used to probe the structure and behaviour of matter.

Globally, there are some 70 light-source facilities — synchrotrons and free electron lasers — but none is in Africa. “These light sources are just transforming science, and Africa has to be a player,” says Sekazi Mtingwa, a high-energy physicist from the United States and one of the founders of the African Light Source (AfLS) Foundation, which is based in South Africa. The foundation is one of two organizations behind the light-source push.

One-third of the \$1 billion will be needed for the synchrotron hardware; one-third for buildings; and the remainder for investment in researchers, including training programmes. In addition, around \$100 million a year will be needed in running costs, says AfLS executive committee chair Simon Connell, a high-energy physicist at the University of Johannesburg in South Africa. Funding for the project would have to come from African member states.

An early decision will be which country should host the facility. After that, it will take at least ten years before the synchrotron is open for science.

John Mugabe, who studies science and innovation policy at the University of Pretoria, questions whether the project will be able to raise the required funding, at least in the short to medium term. Africa’s governments are struggling to get adequate funding for their existing domestic science projects, he told *Nature*.

Scientists’ fears of racial bias surge amid US crackdown on China ties

The US government’s search for spies in laboratories and businesses has stoked fear among scientists of Chinese descent, according to a [survey of nearly 2,000 researchers](#).

The China Initiative, launched under former US president Donald Trump, has led to several well-publicized arrests of scientists since 2018, often over links to collaborators or institutions in China. The US government has said the goal of the effort is to stop the theft of US trade secrets by the Chinese government.

But civil-rights groups and individual researchers have warned that the US government's scrutiny of scientists under this programme has hampered valuable scientific collaborations with researchers in China and stirred concerns of racial profiling.

"We've seen anecdotal evidence about the chilling effects of the China Initiative," says Ashley Gorski, a senior staff attorney at the American Civil Liberties Union in New York City. "The study makes clear that the effects are far-reaching."

The survey, run between May and July 2021, was supported by the Committee of 100, an organization of Chinese American leaders in New York City. Its results were released on 28 October in a [white paper](#).

About half of the scientists of Chinese descent who participated reported experiencing "considerable" fear, anxiety or a mixture of both that they are being surveilled by the US government. Only 12% of non-Chinese scientists who responded reported that concern (see 'Scientists fearful').

SCIENTISTS FEARFUL

A survey of scientists has confirmed the fear and anxiety that those of Chinese descent have over the US China Initiative. Some 2,000 respondents answered the following prompts, with clear differences between Chinese and non-Chinese scientists.

■ Scientists of Chinese descent ■ Non-Chinese scientists

Feel fear and/or anxiety of US government surveillance



Feel racially profiled by US government



Feel they have had difficulty obtaining US research funding because of their race, nationality or country of origin



Feel they have had professional challenges because of their race, nationality or country of origin



©nature

Source: Jenny Lee/XiaoJie Li/Committee of 100

Among participants who said they conducted research involving China within the past 3 years, about 23% of scientists of Chinese descent said they decided to stop collaborations with researchers in China, whereas only 10% of other respondents said the same.

“The differences are undeniable in ways that are quite profound for those of Chinese descent,” says Jenny Lee, a social scientist at the University of Arizona in Tucson and a co-author of the report.



UK chancellor of the exchequer Rishi Sunak performs the yearly ritual of showing the press the red box in which he carries documents related to the government budget. Credit: Dan Kitwood/Getty

UK research budget nods to Horizon Europe

The United Kingdom has [postponed an ambitious science spending target by two years](#), reveals a plan released on 27 October.

Chancellor of the exchequer Rishi Sunak, the cabinet's senior finance minister, announced that the government will ramp up research and development spending to £22 billion (US\$30.3 billion) per year by 2026 — and not by 2024 as originally planned. The pledge means that in five years, public science spending would be around £5 billion higher than in 2021, a 35% boost.

For the first time, the budget also earmarks funding for the country's participation in the European Union's flagship research programme, Horizon

Europe. The costs of participation were previously covered by the UK subscription to the EU, which ceased after Brexit.

But any deal is contingent on the ultimate status of EU–UK relations. Negotiations have come to a standstill over a row about a customs border between Great Britain and the island of Ireland.

The budget forecasts that foreign-aid spending — which includes funds for researchers in low-income countries — could return to 0.7% of gross national income by 2024–25, after it was cut to 0.5% in the fallout from the COVID-19 pandemic.

Nature **599**, 13 (2021)

doi: <https://doi.org/10.1038/d41586-021-02994-6>

This article was downloaded by **calibre** from <https://www.nature.com/articles/d41586-021-02994-6>

| [Section menu](#) | [Main menu](#) |

COP26 climate summit: A scientists' guide to a momentous meeting

Despite 30 years of climate diplomacy, urgent and aggressive action is needed to halt global warming. *Nature* explains what success looks like, and what's on the line.

By Jeff Tollefson
25 October 2021



Credit: Guglielmo Mangiapane/Reuters

Credit: Guglielmo Mangiapane/Reuters

Some 20,000 people from 196 countries — including world leaders, scientists and activists — will soon converge in Glasgow, UK, for the most anticipated United Nations climate summit in years. Climate researchers [have been warning about the dire and increasing impacts](#) of global warming for more than three decades, and for some, the meeting, set to begin on 31 October, represents one final opportunity for the governments of the world to craft a collective plan to meet their most ambitious goals for curbing climate change.

During the two-week event, the 26th UN Climate Change Conference of the Parties (COP26), government officials and business leaders will present their latest commitments to cut greenhouse-gas emissions, while scientists discuss efforts to track emissions, understand impacts and advance potential climate solutions. Negotiators will also continue discussions of [financial aid for low-income countries](#), which have contributed the least to the climate crisis but

must now prepare for its consequences and develop their economies without relying on fossil fuels.

Arguments still rage over how to define and track climate finance, but even wealthy countries acknowledge that they have yet to meet a commitment, made 12 years ago, to provide US\$100 billion annually to developing nations by 2020. [Scientific assessments have also confirmed](#) that pledges made by governments at the 2015 COP held in Paris haven't been met, and promises made since then still fall short of the official goal to limit global warming to 1.5–2 °C above pre-industrial levels.

"Glasgow is the moment," says Johan Rockström, a climate scientist who heads the Potsdam Institute for Climate Impact Research in Germany. Rockström stresses that countries have a legal obligation under the Paris agreement to submit climate plans that are in line with the latest scientific assessments. "It's a big ask," he says, "but it's actually what every country knows is expected in Glasgow."

Here, *Nature* explains what's on the line at COP26, while taking stock of scientists' hopes and fears for the meeting.

There have been 25 COPs before. Why do researchers say this one is so important?





COP26 will be held at the Scottish Event Campus in the heart of Glasgow.
Credit: Alamy

COP26 will be held at the Scottish Event Campus in the heart of Glasgow.
Credit: Alamy

In 1992, more than 100 nations signed a treaty — called the UN Framework Convention on Climate Change — to cut back global emissions and preserve Earth's climate. Developed and developing countries (as they are described by the treaty) agreed that they had different responsibilities in fighting climate change, but that all nations needed to work together and, by consensus, address the problem. However, it wasn't until the 2015 Paris meeting, the 21st conference of parties to the treaty, that all countries formally agreed to take action to limit warming to 1.5–2 °C (see 'A brief history of climate action').

Six years later, COP26 represents the first major test of the Paris agreement, which committed countries to holding global warming to well below 2 °C above pre-industrial levels and — at the insistence of small island states and developing nations existentially threatened by rising seas and other climate impacts — “pursuing efforts” to prevent more than 1.5 °C of warming. But

scientific assessments showed from the outset that national commitments to curb greenhouse-gas emissions would fall short of that ambitious goal.

As part of the Paris accord, 196 governments agreed to periodically assess their progress, both nationally and collectively, and update their pledges. That was originally supposed to happen for the first time in 2020, but after a delay due to the COVID-19 pandemic, nations are poised to make their first updates in Glasgow. More than 100 countries have submitted new climate pledges so far.

“It’s very clear that Paris is driving action, but it’s just not fast enough,” says Claire Stockwell, a climate-policy analyst with Climate Analytics, a non-profit organization based in Berlin, Germany, that tracks climate commitments and advises developing countries in COP negotiations. Carbon dioxide concentrations in the atmosphere continue to rise at a pace that scientists predict will have dangerous consequences for the planet.

A Brief History of Climate Action

Despite more than 30 years of warnings from scientists, and global efforts, carbon emissions are still increasing.

1958: Charles ‘David’ Keeling takes the first reading of atmospheric carbon dioxide concentrations, registering 313 parts per million.

1988: NASA climate scientist Jim Hansen tells the US Congress: “The greenhouse effect has been detected and is changing our climate now.”

1990: The United Nations Intergovernmental Panel on Climate Change issues its first report on global warming, with a foreword calling it “potentially the greatest global environmental challenge facing mankind”.

1992: At the Earth Summit in Rio de Janeiro, Brazil, 154 nations agree to the UN Framework Convention on Climate Change (UNFCCC), which enters into force two years later.

1995: The first conference of the parties, COP1, is held in Berlin.

1997: Parties to the UNFCCC adopt the Kyoto Protocol, which sets the first binding emission-reduction targets for wealthy nations.

2009: At COP15, global leaders adopt the Copenhagen Accord, setting a goal of limiting warming to 2 °C above pre-industrial temperatures and calling for emissions pledges from all countries for the first time.

2015: Countries sign the Paris Agreement, which sets the first legally binding requirements for all 196 participating governments to limit warming to 1.5–2 °C.

2017: Then-president Donald Trump says he will pull the United States out of the Paris accord, calling it “less about the climate and more about other countries gaining a financial advantage over the United States”.

2021: Under President Joe Biden, the United States rejoins the Paris Agreement as nations prepare to update their pledges for the first time at COP26.

Source: US National Oceanic and Atmospheric Administration

What would a successful outcome look like for COP26?





UN Secretary-General António Guterres has called on world leaders to take decisive action to fight climate change. Credit: Alamy

UN Secretary-General António Guterres has called on world leaders to take decisive action to fight climate change. Credit: Alamy

The simplest answer is a well-defined set of policy commitments from various governments to curb emissions by shutting down power plants that run on coal (the dirtiest fuel), phasing out vehicles running on carbon-emitting internal combustion engines, and ramping up the use of clean-energy technologies. A combination of these actions and many others targeting sectors such as agriculture and industry, researchers say, could achieve the 1.5 °C goal from the Paris agreement.

Most of the major emitters [have already stepped forward with fresh commitments](#) to cut emissions over the next decade, and some countries have even pledged to reach net-zero emissions by around the middle of the century (see ‘Laggards and leaders’). But commitments are just the first step: after Glasgow, leaders will need to implement those policies at home to bend the emissions curve.

Laggards and leaders

The Climate Action Tracker (CAT), a group of scientists and policy experts, assesses the potential impact of countries' climate commitments. Most nations are currently falling short of what is required to meet the goals of the Paris Agreement.

Critically insufficient: Of the nearly 40 countries tracked by the CAT, 6 have climate policies and commitments that have been rated as critically insufficient, indicating that they reflect “minimal to no action” on climate. These nations include Russia and Saudi Arabia, which continue to rely on and export oil and natural gas.

Highly insufficient: The CAT ranks 15 countries — including Canada, Brazil and India — as having highly insufficient climate policies that are inconsistent with the Paris 1.5 °C goal and, in many cases, will lead to rising emissions. For instance, although India has set ambitious targets for the development of renewable energies, including solar power, the country continues to invest in — and subsidize — coal-fired electricity generation.

Insufficient: Eight countries, including the United States and Japan, plus the European Union rank as having insufficient policies, indicating that “substantial improvements” are needed to be compatible with the Paris 1.5 °C goal. Although the United States’ Glasgow pledge to cut emissions by 50% from 2005 levels by 2030 would mark a step forward, Democratic President Joe Biden is struggling to implement his climate policies in the face of opposition from Republicans and some members of his own party.

Almost sufficient: The policies of seven countries ranked as “almost sufficient”, or compatible with the Paris Agreement’s 2 °C goal. They include Kenya, Costa Rica and the United Kingdom, which received the highest rating of any wealthy country. But the United Kingdom has yet to provide a clear road map for achieving its commitment to curb emissions by 68% by 2030, compared with 1990 levels.

Compatible with 1.5 °C: The CAT has ranked only one country, Gambia, as compatible with the 1.5 °C goal. Although policies are not yet in place to achieve the country’s commitments, it is ramping up renewable energy

production and, with international support, could curb emissions by an estimated 55% by 2025, compared with projections in a business-as-usual scenario.

Source: Climate Action Tracker

But COP26 isn't just about national carbon commitments and negotiations between countries. Business and industry associations will be stepping forward with new commitments, as well: this month, the cement industry, for instance, pledged to go carbon neutral by 2050. Philanthropists will also be highlighting their own plans, including a project dedicating several billion dollars to land conservation and Indigenous land rights. Scientists have linked Indigenous land rights with biodiversity conservation and reduced deforestation — and thus carbon emissions — in the Amazon rainforest and across the tropics.

For David Kaimowitz, an economist who heads the forest and farm facility at the Food and Agriculture Organization of the UN in Rome, the emphasis on Indigenous peoples at COP26 represents a refreshing shift in thinking. "I don't think we've seen anything like this at any previous COP, and that's being reflected by a much greater willingness to put money into the topic," Kaimowitz says.

Perhaps the biggest question is whether lingering tensions over commitments, climate finance and a lack of representation owing to travel challenges associated with the COVID-19 pandemic will overshadow any positive developments at COP26. People need to walk away from the summit with a sense of progress, says David Victor, a political scientist at the University of California, San Diego. The idea that this diplomatic process is "credible and alive and well", Victor says, "is really, really important".

Have past COPs actually achieved anything?





Scientists have determined that climate change is causing wildfires to increase in frequency in certain parts of the world. Credit: David McNew/Getty

Scientists have determined that climate change is causing wildfires to increase in frequency in certain parts of the world. Credit: David McNew/Getty

Many, including Swedish youth activist Greta Thunberg, are sceptical that they have. She encapsulated how she feels about past climate pledges at a pre-COP26 meeting of finance ministers in Milan, Italy, in September, with this six-word summary: “Thirty years of blah, blah, blah.” Even seasoned environmental activists and academics have raised questions about whether the UN climate convention, with its tradition of making decisions by consensus among nations rather than majority vote, is capable of meeting the challenge. Nonetheless, the shift away from fossil fuels and towards clean-energy technologies has accelerated over the past decade, and many experts say climate diplomacy has had a role.

“Clearly, we have failed in delivery,” Rockström says, “but we have also made some remarkable progress.” The problem, he says, is one of scale: eliminating fossil fuels represents a wholesale transformation of the modern

global economic system. “It’s not an environmental issue, it’s a massive societal challenge.”

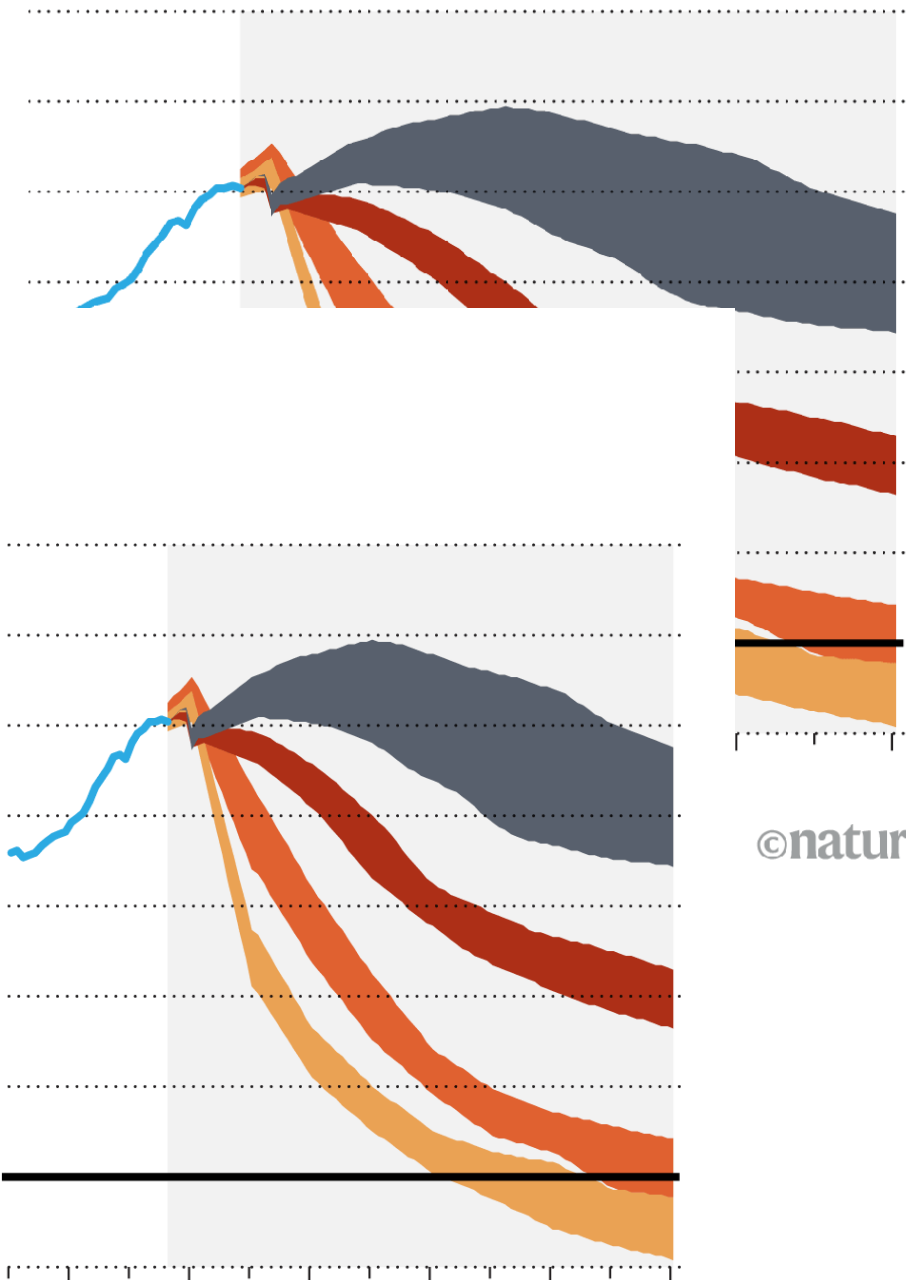
As it stands, the Climate Action Tracker (CAT), a consortium of science and academic organizations, estimates that policies put in place since the Paris agreement could shave 0.7 °C off the predicted increase in average global temperatures this century, resulting in an estimated warming of 2.9 °C above pre-industrial levels by 2100. Fresh government commitments announced ahead of COP26 would strip off another 0.5 °C, the CAT estimates (see ‘The climate multiverse’). And if all 131 countries that have announced or discussed net-zero pledges were to follow through, the projected global temperature increase would be limited to around 2 °C above pre-industrial temperatures. That is still short of the Paris 1.5 °C goal, but a marked improvement compared with the future scientists were predicting a decade ago.

The climate multiverse

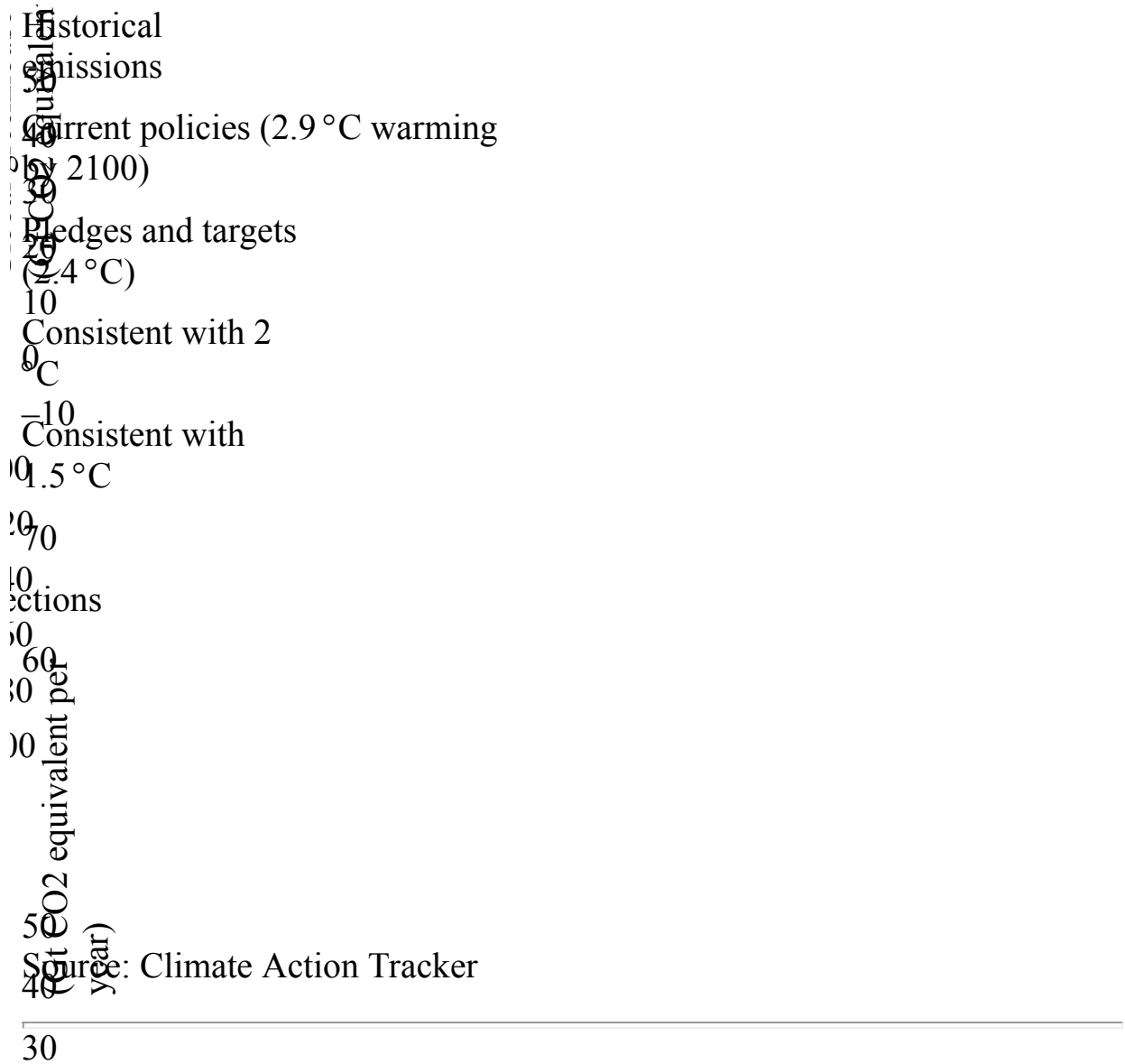
Climate policies put in place since the Paris Agreement was signed have reduced the projected temperature in 2100 by 0.7 °C, to 2.9 °C. New pledges made ahead of COP26 would improve the situation if fully implemented, but still don’t meet the goal of 1.5–2 °C of warming that the globe is aiming for.

H
C
Pl
C
C
70
t per year)

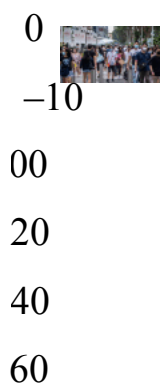
©nature



©nature



Will the COVID-19 pandemic affect the meeting's outcome?



80
00



Credit: [Maverick Asio/SOPA Images/LightRocket/Getty](#)

Credit: [Maverick Asio/SOPA Images/LightRocket/Getty](#)

The ~~nature~~ pandemic has impacted the meeting in multiple ways already. The summit's one-year delay gave countries more time to develop climate ~~Historical~~ ~~targets~~, and gave the UN Intergovernmental Panel on Climate Change ~~emissions~~ to prepare [its latest report on the state of the art in climate science](#). Current policies (2.9 °C warming by 2100)

But travel restrictions and an unequal distribution of COVID-19 vaccines ~~pledges and targets~~ have also created a raft of challenges for attendees.

Although the United Kingdom has pledged to provide vaccines to all negotiators and to pay for hotels for delegates who need to quarantine, some ~~Consistent with~~ ² scientists and environmentalists from non-governmental organizations that serve as both watchdogs and advisers to developing countries [are expected to have trouble attending](#).

1.5 °C

Low-income nations have always been at a political disadvantage in the ~~COP~~ process, and the challenges in accessing vaccines and attending the ~~meetings~~ will only exacerbate those inequities, says Romain Weikmans, a political scientist at the Finnish Institute of International Affairs in Helsinki.

60
er

“With the pandemic, it will be even more difficult for developing countries to get their voices heard,” he says.

Beyond Glasgow: what comes next?



Credit: George Rose/Getty

Credit: George Rose/Getty

For many, the core challenge after Glasgow will be to ensure that governments actually follow through on their promises at home. This is particularly true for vague pledges by some nations to achieve carbon neutrality by mid-century. What scientists want to see is definitive action taken to move away from fossil fuels.

Political promises aren't enough, Stockwell says. “We're not going to stop the climate crisis unless we have implementation of policies that actually reduce emissions.”

In many ways, the economic transformation that scientists are calling for has already begun (see ‘Fuelling the world’). The price of energy from

renewable sources such as wind and solar has plummeted over the past decade, and in many places these sources are now cheaper than fossil fuels. In [a report published on 13 October](#), the International Energy Agency projected that under current policies, coal consumption will peak and begin to decline as early as 2025; a peak in oil consumption will follow around a decade later. But the global economy still runs on fossil fuels, and scientists say the path forward will be anything but easy.

Fuelling the world

Thanks to both government incentives and falling prices, renewables such as wind and solar are expanding quickly. But backing out of existing fossil fuels will be difficult.

Renewable energy consumption has increased more than tenfold over the past two decades, and shows no sign of slowing as prices continue to decline for wind and solar power, as well as battery technologies that are enabling a new generation of electric vehicles.

Hydroelectricity remains fairly level, although a new generation of dams is in the works across the tropics and beyond.

Nuclear energy provides one of the largest sources of carbon-free power, but old plants are being retired faster than new ones can be built. Nuclear power peaked in 2006 and has declined by more than 11% since then.

Natural gas is the cleanest of the fossil fuels, and abundant supplies have helped to suppress demand for coal — the dirtiest of fossil fuels — particularly in the United States. But it too must be phased out if the world is to achieve carbon neutrality.

Oil is at the heart of the transportation industry, whether on the roads, at sea or in the air. The shift toward electric vehicles has caused many energy experts to project that oil consumption will peak over the coming decade, but without further action, the International Energy Agency predicts only a slight decrease by 2050.

Coal provides the world with more than five times as much energy as all of the renewable energy sources combined. Its popularity is declining rapidly across the globe, however, and many hope that COP26 will officially herald its end.

Source: BP Statistical Review of World Energy, 2021

What will this massive energy transformation look like? Scientists and academics have spent years studying everything from carbon taxes to the environmental impacts of wind and solar energy, and the social challenges that will arise around the world as countries rich and poor seek to forgo fossil fuels in favour of clean energy.

Politicians in the United States and other countries that depend on fossil-fuel production often focus on jobs that will be lost owing to this transition, but research suggests that the shift towards clean energy will generate more jobs than it destroys. One study¹ published this year found that the changes required for the world to limit warming to well below 2 °C would generate an extra 5 million jobs in the energy sector by 2050 — an increase of roughly 24% compared with the job gain that would occur if current climate policies stayed in place.

Fossil-energy jobs will disappear and energy prices could increase in many places, however, so there will be clear losers unless governments step in with policies to retrain workers and protect poor people from rising energy costs, says Johannes Emmerling, an economist at the European Institute on Economics and the Environment in Milan and a co-author of the study. The fate of many politicians might well depend on whether and how quickly they can address these challenges as public demands for action increase.

“It’s certainly doable,” Emmerling says, “and I would say it’s also inevitable.”

References

1. Pai, S., Emmerling, J., Drouet, L., Zerriffi, H. & Jewell, J. *One Earth* **4**, 1026–1036 (2021).

[Article](#) [Google Scholar](#)

Research informs action. And the time to act on climate change is now. Explore the latest findings and insights from Springer Nature that will inform how we will mitigate and adapt to our future world.





SPRINGER NATURE

Springer Nature

- [Privacy Policy](#)
- [Use of cookies](#)
- [Legal notice](#)
- [Terms & Conditions](#)
- [Accessibility statement](#)

© 2021 Springer Nature Limited. All rights reserved.

[Top](#)



[Built with Shorthand](#)

This article was downloaded by **calibre** from <https://www.nature.com/articles/d41586-021-02815-w>

| [Section menu](#) | [Main menu](#) |

- NEWS
- 27 October 2021
- Update [29 October 2021](#)

What COVID vaccines for young kids could mean for the pandemic

As the US Food and Drug Administration authorizes shots for children aged 5 to 11, researchers predict what this might mean for populations.

- [Max Kozlov](#)



Modellers predict that vaccinating children against COVID-19 could significantly curtail the spread of any new coronavirus variants of concern. Credit: Alfredo Estrella/AFP via Getty

The US Food and Drug Administration (FDA) has authorized a COVID-19 vaccine for the nation's roughly 28 million 5- to 11-year-olds. The decision comes days after an agency advisory committee reviewed [data from a clinical trial](#) testing a low-dose version of the Pfizer-BioNTech vaccine on children in that age group — and voted nearly unanimously to recommend that the FDA grant emergency approval.



Kids and COVID: why young immune systems are still on top

Anticipating that the US Centers for Disease Control and Prevention (CDC) will also give the vaccine the thumbs up — the last step needed before distribution to US children can begin in the coming weeks — infectious-disease researchers are now looking ahead to how immunizing 5- to 11-year-olds will change the course of the pandemic. This is the largest group of people in the United States not yet eligible for the jab.

“It will save lives in that age group,” says Emma McBryde, an infectious-diseases modeller at the Australian Institute of Tropical Health and Medicine in Townsville. But it could also have a broader impact, given that many US children aged 5 to 11 have returned to school unvaccinated in the past few months, and the group now accounts for a significant portion of new COVID-19 cases, capable of transmitting the coronavirus SARS-CoV-2 to others. “For every child’s life you save, you may well save many, many more adult lives,” she says.

The benefits outweigh the risks

The FDA advisory panel voted in favour of approval on 26 October, on the basis of clinical-trial data showing that the Pfizer–BioNTech vaccine is about 91% effective at preventing symptomatic SARS-CoV-2 infection in 5- to 11-year olds. Around 4,650 children participated in the trial; nearly two-thirds received vaccine doses that were one-third that of an adult jab (the others received a placebo). In a procedure similar to that used to vaccinate adults with the messenger RNA jab in the United States, kids received two doses, three weeks apart.

For the children tested, the data show that the vaccine is safe. mRNA-based vaccines have been linked to a very small risk of myocarditis, an inflammation of the heart muscle, and pericarditis, an inflammation of the lining around the heart, particularly in young men. But there were no reports of either condition in the 5- to 11-year olds involved in the trial, which is a very encouraging sign, says Andrew Pavia, chief of the division of paediatric infectious diseases at University of Utah Health in Salt Lake City. If the shot were distributed to a larger population, however, regulators would need to watch for any sign of the side effects, Pavia notes.



[Should children get COVID vaccines? What the science says](#)

Before the advisory panel's meeting, an independent FDA review of Pfizer's data evaluated six fictional US scenarios, with varying levels of virus in the community, and found that, for the most part, the benefits of the vaccine "clearly outweigh the risks". Officials determined that even if virus levels were very low across the country, the overall benefits of the vaccine would probably still outweigh the potential risks of heart problems, because these conditions typically resolve in a few days after vaccination, unlike COVID-19, which can cause death.

Although SARS-CoV-2 is not nearly as lethal in younger people as in older ones — around 440 children aged 5 to 18 have died of COVID-19 in the United States, compared with around 724,000 in all age groups, according to the CDC — the combination of kids returning to classrooms and a surge caused by the highly transmissible SARS-CoV-2 Delta variant resulted in a sharp rise in paediatric cases beginning in late July. Of the 6.3 million US children who have tested positive for COVID-19 since the pandemic began, nearly one-third were diagnosed in the 11 weeks up to 21 October, [according to an American Academy of Pediatrics report](#).

"To me, the impact of Delta on children in this age group makes the risk side of the equation very compelling," Pavia says. "I don't think it'll be a very difficult decision to approve the vaccine."

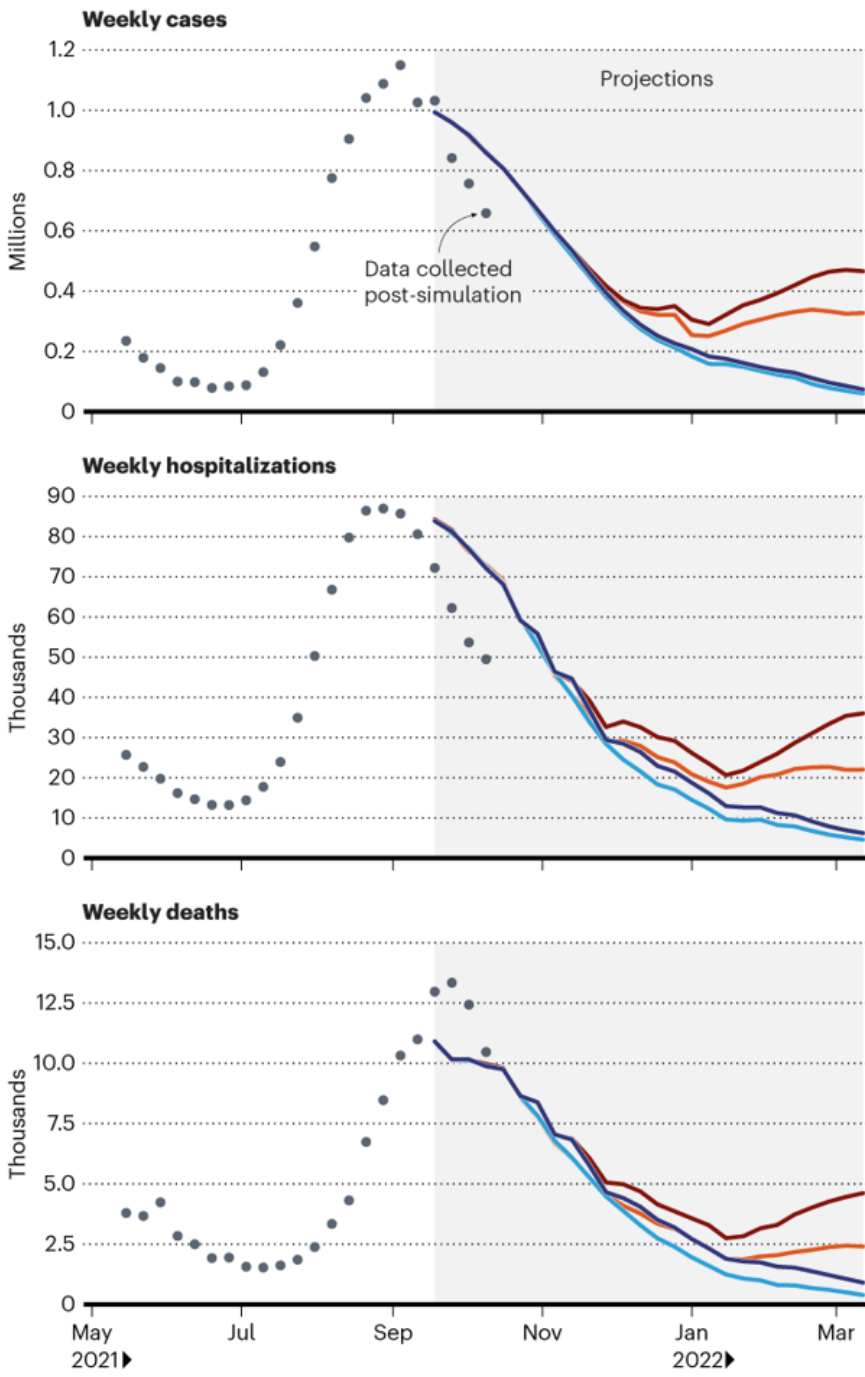
Looking ahead

COVID-19 infections in the United States have been dropping since September, after the Delta surge. Most modellers expect that trend to continue until early 2022, regardless of whether the Pfizer vaccine is authorized for 5- to 11-year-olds. That is, unless another variant of concern emerges, says Katriona Shea, an applied theoretical ecologist tracking the pandemic at Pennsylvania State University in University Park. "If there's a new variant, that's like a slap to the system."

THE KID EFFECT

A simulation of the US pandemic, run in mid-September and averaging multiple models, finds that starting to vaccinate children aged 5 to 11 in early November would not only lower COVID-19's toll, but also have a large impact if a new, more transmissible coronavirus variant emerged later in the month.

- Observed data
- New variant**
 - Childhood vaccination
 - No childhood vaccination
- No new variant**
 - Childhood vaccination
 - No childhood vaccination



Source: [COVID-19 Scenario Modeling Hub](#)

Shea co-leads the COVID-19 Scenario Modeling Hub, which in September [released its ninth forecast](#) of the pandemic's trajectory, factoring in how a vaccine for children aged 5–11 could affect new US infections and deaths. The forecast, which averages the predictions of nine other modelling teams, shows that although vaccines for kids would lead to lower case counts, “it might not make a huge difference at the population level if we are lucky enough just to stick with the Delta variant”, Shea says. But the data show that if a concerning variant were to emerge by mid-November, inoculating children could make a significant difference to the course of the pandemic in the United States (see ‘A kid effect’).

In preparation for US regulators' possible authorization of the jabs, the [White House](#) last week released a plan to distribute the lower-dose shots to paediatrician's offices, hospitals and pharmacies.



[Long COVID and kids: scientists race to find answers](#)

But even if the Pfizer–BioNTech shot is fully approved for emergency use, it remains to be seen how kids in the 5–11 age group will feel about getting vaccinated — and whether their caregivers will allow them to. Mina Fazel, a child and adolescent psychiatrist at the University of Oxford, UK, and her colleagues surveyed¹ nearly 28,000 pupils aged 9 to 18 at 180 UK schools

and found that the younger children were more undecided than their older counterparts.

The survey also suggested that social media plays a part: pupils who spent more than 4 hours a day on social platforms were less willing to receive the vaccine than were those who spent less time on social media. “We have a generation of young people before us who are engaging with information and learning at an unparalleled scale,” Fazel says, adding that it is more important than ever to tailor public-health campaigns for kids.

Global implications

What the authorization of a vaccine for US children aged 5–11 might mean globally also remains to be seen. Almost 70 countries have fully vaccinated less than one-fifth of their populations and will probably not vaccinate younger children for months, or even years, to come. But some countries, including Israel, are waiting to see the US regulators' decision before approving their own jabs.

Other countries, however, are already vaccinating children under age 12. For instance, Chile, China, Cuba and the United Arab Emirates have begun inoculating kids with various COVID-19 vaccines in the past three months.



Deaths from COVID ‘incredibly rare’ among children

In places where the population has a very low natural immunity to the virus because community transmission has remained low throughout the pandemic, McBryde says, childhood vaccination will be essential. Australia, for example, plans to reopen its international border in November, allowing citizens and permanent residents to leave and enter the country if the vaccination rate in their state of residence has hit 80%. The move will “invite the virus” into the country, McBryde says, so it will be essential to “soften the landing” as much as possible by building up people’s immunity to the virus through vaccination — and that includes children. Shots for children under 12 have not yet been submitted to Australia’s regulators for approval.

On 25 October, vaccine maker Moderna, based in Cambridge, Massachusetts, said that a low dose of its mRNA-based jab for children aged 6 to 11 is safe and effective, but it has not yet applied for FDA authorization. Data on Pfizer’s jab for children younger than 5 is expected by the end of the year, according to a statement the company’s chief executive made at an event run by magazine *The Atlantic* last month. Moderna is also conducting a trial with children as young as six months old.

Nature **599**, 18-19 (2021)

doi: <https://doi.org/10.1038/d41586-021-02947-z>

Updates & Corrections

- **Update 29 October 2021:** This story was updated to reflect that the US Food and Drug Administration has authorized the Pfizer-BioNTech COVID-19 vaccine for children.

References

1. 1.

Fazel, M. *et al.* *EClinicalMedicine* **40**, 101144 (2021).

This article was downloaded by **calibre** from <https://www.nature.com/articles/d41586-021-02947-z>

| [Section menu](#) | [Main menu](#) |

- NEWS
- 27 October 2021

DNA reveals surprise ancestry of mysterious Chinese mummies

The genomes of 13 remarkably preserved 4,000-year-old mummies from the Tarim Basin suggest they weren't migrants who brought technology from the west, as previously supposed.

- [Smriti Mallapaty](#)



Cemeteries in the Taklamakan Desert, China, hold human remains up to 4,000 years old. Credit: Wenying Li, Xinjiang Institute of Cultural Relics and Archaeology

Since their discovery a century ago, hundreds of naturally preserved mummies found in China's Tarim Basin have been a mystery to archaeologists. Some thought the Bronze Age remains were from migrants from thousands of kilometres to the west, who had brought farming practices to the area. But now, a genomic analysis suggests they were indigenous people who may have adopted agricultural methods from neighbouring groups.

As they report today in *Nature*¹, researchers have traced the ancestry of these early Chinese farmers to Stone Age hunter-gatherers who lived in Asia some 9,000 years ago. They seem to have been genetically isolated, but despite this had learnt to raise livestock and grow grains in the same way as other groups.

The study hints at “the really diverse ways in which populations move and don’t move, and how ideas can spread with, but also through, populations”, says co-author Christina Warinner, a molecular archaeologist at Harvard University in Boston, Massachusetts.

The finding demonstrates that cultural exchange doesn’t always go hand in hand with genetic ties, says Michael Frachetti, an archaeologist at Washington University in St. Louis, Missouri. “Just because those people are trading, doesn’t necessarily mean that they are marrying one another or having children,” he says.

Perfect preservation environment

Starting in the early twentieth century, the mummies were found in cemeteries belonging to the so-called Xiaohe culture, which are scattered across the Taklamakan Desert in the Xinjiang region of China. The desert “is one of the most hostile places on Earth”, says Alison Betts, an archaeologist at the University of Sydney in Australia.

Here, bodies had been buried in boat-shaped coffins wrapped in cattle hide. The hot, arid and salty environment of the desert naturally preserved them, keeping everything from hair to clothing perfectly intact. Before the latest study, “we knew an awful lot about these people, physically, but we knew nothing about who they were and why they were there”, says Betts.

The mummies — which were buried over a period of 2,000 years or more — date to a significant time in Xinjiang’s history, when ancient communities were shifting from hunter-gatherers to farmers, she adds.



The harsh desert conditions preserved the bodies as natural mummies. Credit: Wenying Li, Xinjiang Institute of Cultural Relics and Archaeology

Some of the later mummies were buried with woollen fabrics and clothing similar to those of cultures found to the west. The graves also contained millet, wheat, animal bones and dairy products — evidence of agricultural and pastoral technologies characteristic of cultures in other regions of Eurasia, which led researchers to hypothesize that these people were

originally migrants from the west, who had passed through Siberia, Afghanistan or Central Asia.

The researchers behind the latest study — based in China, South Korea, Germany and the United States — took DNA from the mummies to test these ideas, but found no evidence to support them.

They sequenced the genomes of 13 individuals who lived between 4,100 and 3,700 years ago and whose bodies were found in the lowest layers of the Tarim Basin cemeteries in southern Xinjiang, as well as another 5 mummies from hundreds of kilometres away in northern Xinjiang, who lived between 5,000 and 4,800 years ago.

They then compared the genetic profiles of these people with previously sequenced genomes from more than 100 ancient groups of people, and those of more than 200 modern populations, from around the world.

Two groups of people

They found that the northern Xinjiang individuals shared some parts of their genomes with Bronze Age migrants from the Altai Mountains of Central Asia who lived about 5,000 years ago — supporting an earlier hypothesis.

But the 13 people from the Tarim Basin did not share this ancestry. They seem to be solely related to hunter-gatherers who lived in southern Siberia and what is now northern Kazakhstan some 9,000 years ago, says co-author Choongwon Jeong, a population and evolutionary geneticist at Seoul National University. The northern Xinjiang individuals also shared some of this ancestry.

[Evidence of dairy products](#) was found alongside the youngest mummies from the upper layers of cemeteries in the Tarim Basin, so the researchers analysed calcified dental plaque on the teeth of some of the older mummies to see how far back dairy farming went. In the plaque, they found milk proteins from cattle, sheep and goats, suggesting that even the earliest settlers here consumed dairy products. “This founding population had already incorporated dairy pastoralism into their way of life,” says Warinner.

But the study raises many more questions about how the people of the Xiaohe culture got these technologies, from where and from whom, says Betts. “That’s the next thing we need to try and resolve.”

Nature **599**, 19-20 (2021)

doi: <https://doi.org/10.1038/d41586-021-02948-y>

Read the related News & Views, ‘[The unexpected ancestry of Inner Asian mummies](#)’.

References

1. 1.

Zhang, F. *et al.* *Nature* <https://doi.org/10.1038/s41586-021-04052-7> (2021).

This article was downloaded by **calibre** from <https://www.nature.com/articles/d41586-021-02948-y>.

| [Section menu](#) | [Main menu](#) |

- NEWS
- 25 October 2021

Mysterious ‘alien beacon’ was false alarm

Radio signal seemed to originate from the star Proxima Centauri, and provided a helpful drill for future searches.

- [Alexandra Witze](#)



The 64-metre Parkes Murriyang telescope is one of the facilities involved in the search for extraterrestrial intelligence, or SETI. Credit: CSIRO/A. Cherney

A radio signal detected by an Australian telescope in 2019, which seemed to be coming from the star closest to the Sun, was not from aliens, researchers report today in two papers in *Nature Astronomy*^{1,2}.

“It is human-made radio interference from some technology, probably on the surface of the Earth,” says Sofia Sheikh, an astronomer at the University of California (UC), Berkeley, and a co-author of both papers.

But the disturbance, detected by Breakthrough Listen — an ambitious and privately funded US\$100-million effort in the search for extraterrestrial intelligence (SETI) — looked intriguing enough at first that it sent astronomers on a nearly year-long quest to understand its origins. It was the first time that data from Breakthrough Listen triggered a detailed search, and the experience puts scientists in a better position to study future candidate detections.

“It’s really valuable for us to have these dry runs,” says Jason Wright, an astronomer at Pennsylvania State University in University Park. “We need these candidate signals so we can learn how we will deal with them — how to prove they are extraterrestrial or human-made.”

Mysterious blips

Since 2016, Breakthrough Listen has used telescopes around the world to listen for possible broadcasts from alien civilizations. The programme has picked up millions of radio blips of unknown origin, nearly all of which could be swiftly classified as coming from radio interference on Earth, from sources such as mobile-phone towers or aircraft radar.

The 2019 signal was different. It was detected by the 64-metre Parkes Murriyang radio telescope in southeastern Australia and came from the direction of Proxima Centauri — the nearest star to the Sun, just 1.3 parsecs (4.2 light years) away. Proxima Centauri is of intense interest to SETI researchers, not just because it is nearby. The star has at least two planets, one of which orbits at the right distance for liquid water to be present on its surface — a prerequisite for life as it exists on Earth³. A sibling initiative to

Breakthrough Listen, known as Breakthrough Starshot, aims to send a tiny spacecraft to this planet in the future to look for life there.

The mysterious signal was first spotted last year by Shane Smith, an undergraduate student at Hillsdale College in Michigan, who was working as a research intern with Breakthrough Listen. Smith was combing through data that Parkes collected over six days in April and May the previous year. The telescope had been making observations in the direction of Proxima Centauri for 26 hours. It was not hunting specifically for aliens at the time, but was instead monitoring flares on the star's surface, which could hurt the chances for life to arise on nearby planets.

The data included more than 4 million signals from the vicinity of the star, but Smith noted one signal near 982 megahertz that seemed to originate from the star itself and lasted for about 5 hours. "I was excited to find a signal that matched all the criteria I was looking for, but I immediately remained sceptical of it and thought there had to be some simple explanation," Smith says. "I did not ever think the signal would cause such excitement."

Smith shared the information with his supervisor, Danny Price, who posted it on a Breakthrough Listen Slack channel, and the team started investigating in earnest. "My first thought was that it must be interference, which I guess is a healthy attitude, to be sceptical," says Price, an astronomer at UC Berkeley and the Breakthrough Listen project scientist in Australia. "But after a while I started thinking, this is exactly the kind of signal we're looking for."

The signal, named BLC1 for 'Breakthrough Listen candidate 1', was the first to pass all of the programme's initial screening tests to rule out obvious sources of interference. "It definitely had me wondering 'what if?' for a bit," says Sheikh.

She, Price and a large group of colleagues began working through possible explanations, from uncatalogued satellites to transmissions from planetary spacecraft. In Australia, the radio-frequency band around 982 megahertz is primarily reserved for aircraft, but the scientists could not identify any

aeroplanes that had been in the area and could account for the signal — and certainly not one lasting 5 hours.

In November 2020, and in January and April this year, the researchers pointed the Parkes telescope at Proxima Centauri to see if they could pick up the signal again. They could not.

Eventually, the team spotted other signals in the original data that looked a lot like the 982-megahertz signal but were at different frequencies. These signals had been tossed out by the team's automated analysis as being earthly interference. Further analysis showed that BLC1 and these 'lookalike' signals were all interference from an unknown source. The signals had modulated and muddied one another, much as a guitar amplifier modulates and distorts a guitar note, which is what made it so difficult to identify BLC1 as interference.

Earthly origins

Because the signal didn't reappear in the 2020 and 2021 observations, it might have been coming from malfunctioning electronic equipment that got shut down or fixed, says Sheikh. The team suspects the equipment was relatively close to Parkes, perhaps within a few hundred kilometres. The frequency of the signal drifts in a way that is consistent with inexpensive crystal oscillators such as those commonly used in computers, phones and radios, says Dan Werthimer, a SETI astronomer at UC Berkeley who specializes in signal processing.

Working with another student, Sheikh is now using machine-learning algorithms to tease out what frequency the interfering equipment was transmitting at, which might help to track down its source. One lingering mystery is why the signal seemed to appear only when the telescope was pointed at Proxima Centauri. That might just be an unfortunate coincidence, if the cadence of the interference mimicked the cadence with which the telescope was looking at the star.

Radio interference has bedevilled other astronomical searches before, such as when flickering signals picked up at Parkes turned out to be the result of

people microwaving their lunches⁴. The famous ‘Wow! ’ signal, detected in 1977 by a radio telescope in Ohio, was a powerful blip so intriguing that the observing scientist scribbled “Wow! ” in the margins of the computer printout — but its origin could never be traced.

Alien searches have become much more sophisticated since then, Sheikh notes. “Many groups assumed that if you had a detection that only showed up when you were pointed at the source, that was it, break out the champagne, you’re done,” she says. “As technology changes, the way we vet signals also has to change — and that hadn’t come together until BLC1.” One of the *Nature Astronomy* papers features a detailed checklist to help astronomers determine whether their signal is truly from aliens or not.

“The Universe gives us a haystack,” says Ravi Kopparapu, a planetary scientist at NASA’s Goddard Space Flight Center in Greenbelt, Maryland. “It is our need to find the needle in it, and make sure that it is actually a needle that we found.”

Nature **599**, 20-21 (2021)

doi: <https://doi.org/10.1038/d41586-021-02931-7>

References

1. 1.

Smith, S. *et al.* *Nature Astron.* <https://doi.org/10.1038/s41550-021-01479-w> (2021).

2. 2.

Sheikh, S. Z. *et al.* *Nature Astron.* <https://doi.org/10.1038/s41550-021-01508-8> (2021).

3. 3.

Anglada-Escudé, G. *et al.* *Nature* **536**, 437–440 (2016).

4. 4.

Petroff, E. *et al.* *Mon. Not. R. Astron. Soc.* **451**, 3933–3940 (2015).

This article was downloaded by **calibre** from <https://www.nature.com/articles/d41586-021-02931-7>

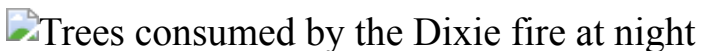
| [Section menu](#) | [Main menu](#) |

- NEWS FEATURE
- 01 November 2021

Top climate scientists are sceptical that nations will rein in global warming

A *Nature* survey reveals that many authors of the latest IPCC climate-science report are anxious about the future and expect to see catastrophic changes in their lifetimes.

- [Jeff Tollefson](#)



The Dixie wildfire in California this year was the second-largest in state history, and was fuelled by high temperatures and drought. Credit: Eric Thayer/Bloomberg/Getty

As a leading climate scientist, Paola Arias doesn't need to look far to see the world changing. Shifting rain patterns threaten water supplies in her home city of Medellín, Colombia, while rising sea levels endanger the country's coastline. She isn't confident that international leaders will slow global warming or that her own government can handle the expected fallout, such as mass migrations and civil unrest over rising inequality. With such an uncertain future, she thought hard several years ago about whether to have children.

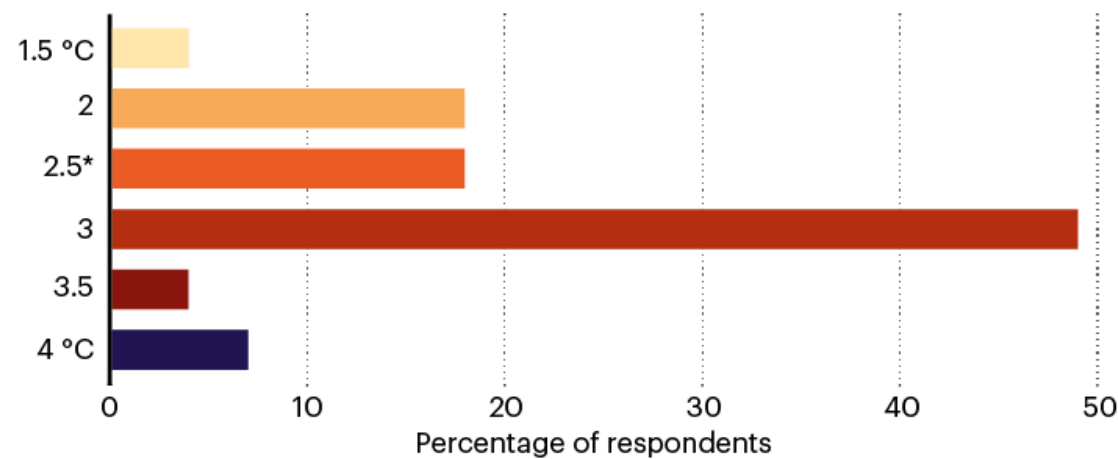
"My answer was no," says Arias, a researcher at the University of Antioquia in Medellín, who was one of the 234 scientists who wrote a [climate-science report](#) published by the Intergovernmental Panel on Climate Change (IPCC) in August (see go.nature.com/3pjupro). That assessment, which makes clear that the world is running out of time to avoid the most severe impacts of

climate change, will figure prominently in climate negotiations over the next two weeks at the COP26 meeting in Glasgow, UK.

Many other leading climate researchers share Arias's concerns about the future. *Nature* conducted an anonymous survey of the 233 living IPCC authors last month and received responses from 92 scientists — about 40% of the group. Their answers suggest strong scepticism that governments will markedly slow the pace of global warming, despite political promises made by international leaders as part of the 2015 Paris climate agreement.

Six in ten of the respondents said that they expect the world to warm by at least 3 °C by the end of the century, compared with what conditions were like before the Industrial Revolution. That is far beyond the Paris agreement's goal to limit warming to 1.5–2 °C.

How much warming above pre-industrial times do you think is likely by 2100?



*Includes 2 responses between 2.7 °C and 2.75 °C; 2.5 °C and 3.5 °C were write-in answers.

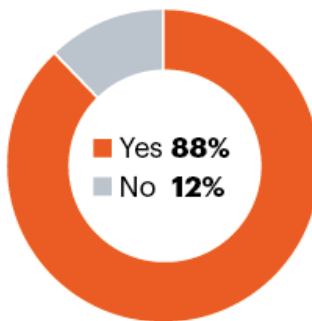
©nature

Source: *Nature* analysis

Most of the survey's respondents — 88% — said they think global warming constitutes a 'crisis', and nearly as many said they expect to see catastrophic impacts of climate change in their lifetimes. Just under half said that global warming has caused them to reconsider major life decisions, such as where to live and whether to have children. More than 60% said that they

experience anxiety, grief or other distress because of concerns over climate change.

Do you think the world is experiencing a 'climate crisis'?

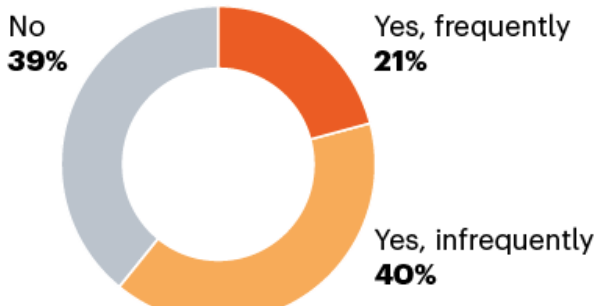


©nature

Source: *Nature* analysis

For Arias, who frequently sees the impacts of political instability out of her office window as immigrants from strife-torn Venezuela wander the streets seeking food and shelter, the choice about children came naturally. She says many friends and colleagues have arrived at the same conclusion. “I’m not saying that that is a decision that everyone should make,” she says, “but it’s not something I am struggling with much any more.”

Do you experience anxiety, grief or other distress because of concerns over climate change?



©nature

Source: *Nature* analysis

The pessimism expressed by some IPCC panellists underscores the vast gulf between hopes and expectations for the climate summit that began this week in Glasgow. In advance of the meeting, the United States, the European Union, China and others have announced new plans to curb greenhouse-gas emissions, although scientific analyses suggest those plans still fall well short of the Paris goals. Over the next two weeks, countries will formalize

— and perhaps even strengthen — those commitments. But making them a reality will require as-yet-unprecedented political mobilization at the national level once leaders return home.

Has global warming caused you or climate researchers you know to reconsider major life decisions such as:

Decisions about where to live

41%

Decisions to have children

17%

Lifestyle choices (including diet, transportation and travel)†

21%

†Write-in answers.

©nature

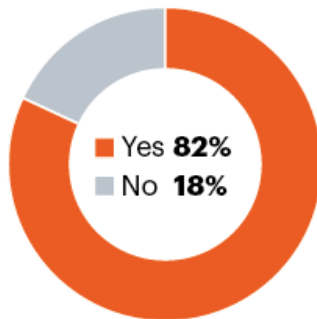
Source: *Nature* analysis

“Right now, governments are just at the stage of providing green promises, but so far we have not seen any actions to curb greenhouse-gas emissions,” says Mouhamadou Bamba Sylla, an IPCC author and climate modeller at the African Institute for Mathematical Sciences in Kigali, Rwanda. Sylla says his home country of Senegal has gone through all the motions and developed adaptation plans for a warming climate, but is anything changing on the ground? “I don’t think so,” he says.

Climate anxiety

The scientists surveyed by *Nature* are part of the IPCC working group charged with assessing the causes and extent of climate change. Their latest report, approved by 195 governments in August, concluded that fossil-fuel emissions are driving unprecedented planetary changes, threatening both people and the ecosystems that humans rely on for food and other resources. “Unless there are immediate, rapid and large-scale reductions in greenhouse gas emissions, limiting warming to close to 1.5 °C or even 2° C will be beyond reach,” the IPCC said. But in announcing the report, IPCC scientists stressed that these goals could still be achieved.

**Do you think you will
see catastrophic
impacts of climate
change in your
lifetime?**



©nature

Source: *Nature* analysis

A separate report from the United Nations Environment Programme last week projected that the climate commitments already announced by nations would put the world on a path towards 2.7 °C of warming by the end of the century (see go.nature.com/3vphvtu). Other projections raise the possibility of even more reductions. The Climate Action Tracker, a consortium of scientific and academic organizations, estimates that warming would be limited to 2.4 °C if countries follow through on their latest pledges under the Paris agreement. One of the goals of the climate negotiations is to prompt more-ambitious steps for limiting greenhouse-gas emissions, but most respondents to the *Nature* survey seemed to be pessimistic about future policies and the amount of warming (see Supplementary information for survey data tables).

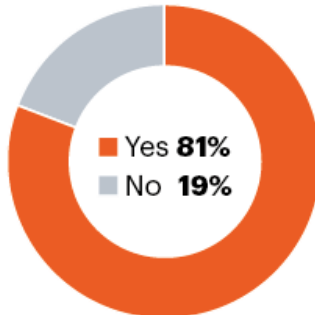
The survey results might not be surprising given the decades of limited progress in tackling climate change, but the opinions of climate researchers should raise alarms, says Diana Liverman, a geographer who studies climate at the University of Arizona in Tucson. “I suppose the fact that they’re pessimistic should make us even more worried.”

The *Nature* survey has limitations: it doesn’t capture the views of 60% of the IPCC authors, and two scientists wrote separately to *Nature* expressing concerns about the poll precisely because it taps into opinions rather than science. Those who took part did so in a personal capacity, not as representatives of the IPCC. Still, the survey provides a snapshot of the views of a significant proportion of the researchers who wrote the report.

Positive signals

Although the results indicate that many harbour deep concerns, the survey also revealed signs of optimism. More than 20% of the scientists said they expect nations to limit global warming to 2 °C, and 4% said the world might indeed meet its most aggressive goal of limiting warming to 1.5 °C — a target that many scientists and academics wrote off from the moment the Paris agreement was signed in 2015.

Do you think that climate scientists should engage in advocacy on this issue?



©nature

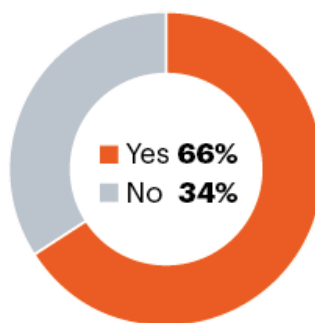
Source: *Nature* analysis

Charles Koven, a climate scientist at Lawrence Berkeley National Laboratory in California, draws hope about the future because of advances in science and technology, and rapidly evolving public opinion. One positive development, he says, is that results in the past few years indicate that global average temperatures will level off quickly once humanity stops emitting greenhouse gases into the atmosphere. This is contrary to long-held expectations that warming would continue for decades even if emissions were halted, owing to a lag in the climate system. He also cites plummeting costs of clean-energy technologies, as well as rising public demand for action in the face of increasingly visible climate impacts — such as the wildfires that he and his family have grown accustomed to each year in California.

“Fundamentally, I believe that the majority of people really do care about the future, and that it is possible for governments to coordinate and avoid the worst climate outcomes,” Koven says.

Two-thirds of the respondents said they engage in climate advocacy, and almost all of those who do said they promote climate science through speeches, publications or videos. Some 43% of those who engage said they have signed letters or petitions, and 40% said they have contacted lawmakers to advocate for climate policies. One-quarter said they have joined demonstrations.

Do you engage in advocacy related to climate change?



Which kind of advocacy activities do you engage in?‡

Promote science through speeches, publications or videos

98%

Contact lawmakers or government officials to advocate specific climate policies

40%

Sign letters or petitions calling for action

43%

Participate in demonstrations

25%

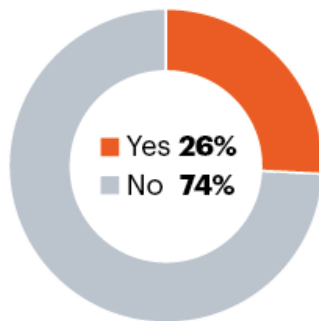
*Respondents could choose multiple answers.

©nature

Source: *Nature* analysis

The tables turned, however, when scientists considered whether the IPCC should take on more of an advocacy role, which would be a sharp break from its remit of neutrally assessing the science: nearly three-quarters of the respondents said the IPCC should refrain from climate advocacy. One survey respondent gave the IPCC credit for sticking to its core mission. “By focusing on the best available scientific information, it has avoided the politicization that has occurred with other scientific issues, such as masking and vaccinating for COVID-19,” the respondent said.

Do you think the IPCC should take on more of an advocacy role related to climate change?



©nature

Source: *Nature* analysis

When asked to name the biggest accomplishments of the IPCC's climate-science working group, nearly 40% of the respondents said the panel effectively informs the public and policymakers about climate change and the part that humans are playing. Many (27%) also value how the IPCC assesses and synthesizes evidence.

What do you think is the biggest accomplishment of the IPCC Working Group I reports?*

Communicates science to public and policymakers

41%

Assesses and synthesizes evidence

29%

Supports international and national policymaking

16%

Provides authoritative source of information

15%

Reaches robust conclusions through rigorous process

14%

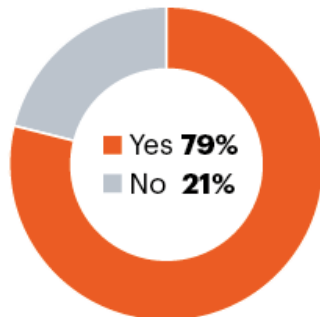
*Respondents were invited to write in answers and 86 people did so. Their answers were divided into categories. Some responses fit multiple categories.

©nature

Source: *Nature* analysis

Since it issued its first report in 1990, the IPCC has gradually increased the representation of researchers from the global south. Nearly 80% of respondents said that the IPCC includes suitable representation of experts from all countries. Arias disagrees, saying it could do more to actively recruit scientists from the global south. Sylla says the IPCC has done an adequate job on that front, given the geographical imbalance in the broader climate-science community. However, he adds, the organization could do more in terms of local outreach to promote the science and to engage policymakers after its reports are published. “I want the IPCC to be more aggressive on that,” he says.

Does the IPCC include suitable representation of experts from all countries?



©nature

Source: *Nature* analysis

Like Arias, Sylla sees the impacts of political and economic instability as people pile aboard small boats leaving Senegal for a perilous journey in search of a better future. He also fears the situation will only get worse as the climate warms. Although he is currently planning to build a house for his family — far from the sea and in a location that is unlikely to flood — Sylla isn’t convinced that Senegal is where he wants to ride out the climate storm. But he is keenly aware of the fact that Europe and the United States are also vulnerable to the inevitable impacts of global warming. “So the question is, where do you go?”

Nature **599**, 22-24 (2021)

doi: <https://doi.org/10.1038/d41586-021-02990-w>

Survey conducted by Richard Monastersky. Additional reporting by Mackenzie White.

This article was downloaded by **calibre** from <https://www.nature.com/articles/d41586-021-02990-w>

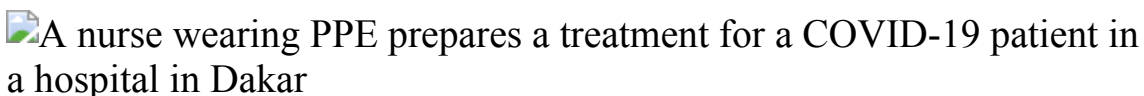
| [Section menu](#) | [Main menu](#) |

- NEWS FEATURE
- 03 November 2021

African scientists race to test COVID drugs — but face major hurdles

In a bid to stave off looming disaster, scientists are trying to repurpose drugs used for malaria and other diseases, but infrastructure and recruitment challenges stymie progress.

- [Abdullahi Tsanni](#) 



A nurse in Senegal treats people who have COVID-19. Credit: Zohra Bensemra/Reuters/Alamy

For more than a year, Adeola Fowotade struggled to recruit people to a clinical trial for COVID-19 treatments. A clinical virologist at University College Hospital in Ibadan, Nigeria, she joined the effort in August 2020, which aims to test the efficacy of a combination of readily available drugs. Her goal was to find 50 volunteers — people diagnosed with COVID-19 who had moderate to severe symptoms and might benefit from the drug cocktail. But the recruitment effort crawled along, even as cases of the virus surged in Nigeria in January and February. After 8 months, she had managed to enlist only 44 people.

“Some patients declined to participate in the study when approached, while some who agreed discontinued midway into the trials,” says Fowotade. Once case rates started to decline in March, it became nearly impossible to find

participants. This made the trial, known as NACOVID, difficult to complete. “We were unable to meet our planned sample size,” she says. The trial ended in September, short of its recruitment goal.

Fowotade’s troubles mirror those faced by other trials in Africa — posing a major problem for those countries in the continent that have been unable to secure enough vaccines against COVID-19. Only 2.7% of people in Nigeria, the continent’s most populous country, have been at least partially vaccinated. That’s just slightly lower than the average rate for low-income countries. Estimates suggest that it could take until at least September 2022 for African nations to obtain enough doses to fully vaccinate 70% of the continent’s population.

That leaves few options for fighting the pandemic now. Although wealthy nations outside Africa have used treatments such as monoclonal antibodies or the antiviral drug remdesivir, these need to be administered in hospitals and are expensive. The drug giant [Merck has agreed to license its pill-based drug molnupiravir](#) to manufacturers that would provide broad access to the drug, but questions remain about how costly it will be if it does get approval. So the hunt is on for affordable, readily available drugs for Africa that could reduce COVID-19 symptoms, lower the burden of disease on health-care systems and reduce deaths.



[How COVID spurred Africa to plot a vaccines revolution](#)

That search has faced numerous hurdles. According to the US-run database clinicaltrials.gov, of nearly 2,000 trials currently exploring drug treatments for COVID-19, only about 150 are registered in Africa, and the vast majority of those are in Egypt and South Africa. The lack of trials is problematic, says Adeniyi Olagunju, a clinical pharmacologist at the University of Liverpool, UK, and the principal investigator for NACOVID. If Africa is largely missing from COVID-19 treatment trials, then the likelihood of it having access to drugs that get approved is very limited, he says. “Add that to the abysmally low access to vaccines,” Olagunju says. “Africa needs effective therapeutics for COVID-19 as an option more than any other continent.”

Some organizations are trying to remedy this shortfall. ANTICOV, a programme run by the non-profit Drugs for Neglected Diseases initiative (DNDi), is currently the largest trial in Africa. It is testing early treatment options for COVID-19 in two trial arms. Another study called Repurposing Anti-Infectives for COVID-19 Therapy (ReACT) — coordinated by the non-profit foundation Medicines for Malaria Venture — will test the safety and efficacy of repurposed drugs in South Africa. But regulatory challenges, a lack of infrastructure and difficulties with recruiting trial participants all present major hurdles to such efforts.

“We have a broken health-care system in sub-Saharan Africa,” says Samba Sow, the national principal investigator for ANTICOV in Mali. That makes the trials hard but all the more necessary, particularly for identifying drugs that will help people during the earliest stages of disease and prevent hospitalizations. For him and many others working on the disease, it is a race against death. “We can’t wait until patients become severely ill,” he says.

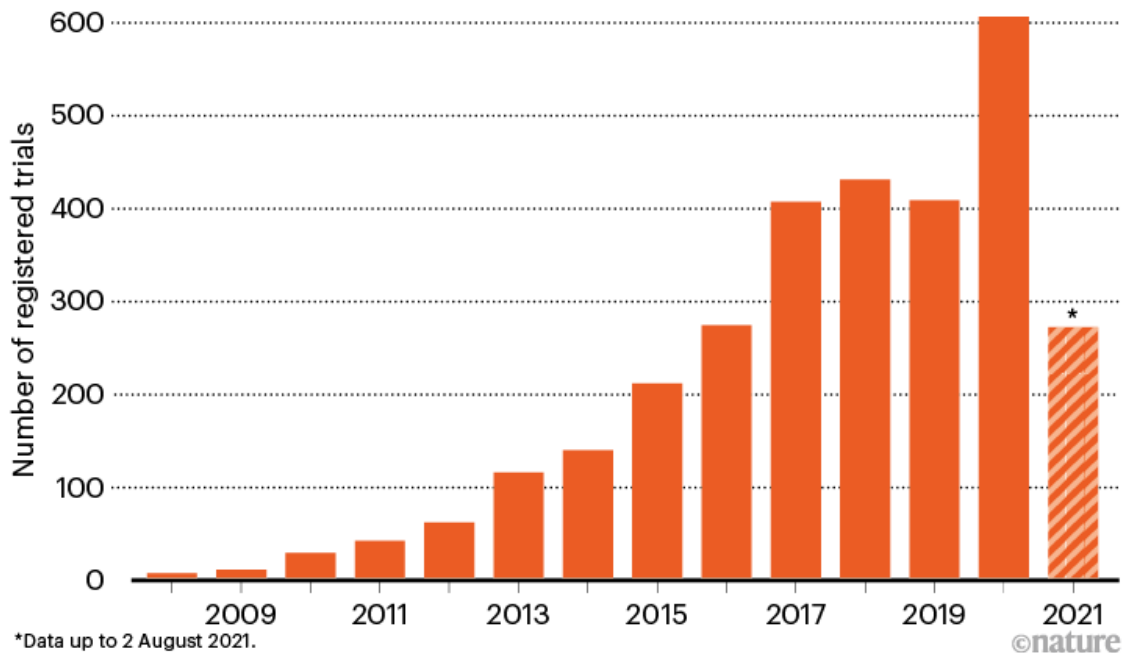
Trials on the up

The coronavirus pandemic has given clinical research in the African continent a boost. Vaccinologist Duduzile Ndwandwe tracks research on experimental treatments at Cochrane South Africa — part of the international group that reviews health evidence — and says that the Pan African Clinical Trials Registry registered a total of 606 clinical trials in

2020, compared with 408 in 2019 (see ‘Clinical trials in Africa’). By August this year, it had registered 271, including trials for both vaccines and drugs. “We’ve seen lots of trials expanding with COVID-19,” Ndawande says.

CLINICAL TRIALS IN AFRICA

Studies registered with the Pan African Clinical Trials Registry increased in 2020, and are on track this year to surpass 2019 levels.



Source: <https://pactr.samrc.ac.za>

Trials for coronavirus treatments are still lacking, however. In March 2020, the World Health Organization (WHO) launched its flagship Solidarity trial, a global study of four potential COVID-19 treatments. Only two African countries participated in the first phase of the study. Challenges in providing health-care services for severely ill patients precluded most nations from joining, says Quarraisha Abdool Karim, a clinical epidemiologist at Columbia University in New York City who is based in Durban, South Africa. “It was an important missed opportunity,” she says, but it laid the groundwork for more COVID-19 treatment trials. In August, the WHO announced the next phase of the Solidarity trial, which will test three other drugs. Five more African countries are participating.

The NACOVID trial that Fowotade worked on aimed to test its combination therapy on 98 people in Ibadan and three other sites in Nigeria. People in that study were given the antiretrovirals atazanavir and ritonavir, and an antiparasitic drug called nitazoxanide. Even though it didn't meet its recruitment goal, Olagunju says that the teams involved are preparing a manuscript for publication and are hopeful that the data will provide some insight about the drugs' effectiveness.



The fight to manufacture COVID vaccines in lower-income countries

South Africa's ReACT trial, sponsored by the South Korean drug company Shin Poong Pharmaceutical in Seoul, aims to test four repurposed drug combinations: the antimalarial therapies artesunate–amodiaquine and pyronaridine–artesunate; the influenza antiviral favipiravir, given with nitazoxanide; and sofosbuvir and daclatasvir, an antiviral combination typically used to treat hepatitis C.

Using repurposed drugs is highly attractive to many researchers, because it could be the most viable route to rapidly finding treatments that can be distributed easily. Africa's lack of infrastructure for pharmaceutical research, development and manufacturing means that countries cannot readily test new compounds and mass-produce drugs. Such efforts are crucial, says Nadia Sam-Agudu, a specialist in paediatric infectious diseases at the University of Maryland in Baltimore, who works at the Institute of Human Virology Nigeria in Abuja. "If effective, these treatments may prevent

severe disease and hospitalization, as well as potentially [stop] onward transmission," she adds.

The continent's largest trial, ANTICOV, was launched in September 2020 in the hope that early treatments could prevent COVID-19 from overwhelming the fragile health-care systems in Africa. It has currently enrolled more than 500 participants across 14 sites in the Democratic Republic of the Congo, Burkina Faso, Guinea, Mali, Ghana, Kenya and Mozambique. It aims to eventually recruit 3,000 participants across 13 countries.



A worker in a cemetery in Dakar, Senegal, in August as a third wave of COVID-19 infections hit. Credit: John Wessels/AFP/Getty

ANTICOV is testing the efficacy of two combination treatments that have seen mixed results elsewhere. The first blends nitazoxanide with inhaled ciclesonide, a corticosteroid used to treat asthma. The second combines artesunate—amodiaquine with the antiparasitic drug ivermectin.

Ivermectin, which is used in veterinary medicine and to treat some neglected tropical diseases in humans, has become controversial in many countries.

Individuals and politicians have been demanding access to it for the treatment of COVID-19 on the basis of anecdotal and scant scientific evidence about its efficacy. Some of the data supporting its use are questionable. A large study in Egypt that supported administering ivermectin in people with COVID-19 [was withdrawn by the preprint server where it was published](#) amid accusations of data irregularities and plagiarism. (The authors of the study have argued they were not given an opportunity by the publishers to defend themselves.) A recent systematic review by the Cochrane Infectious Disease Group found no evidence to support ivermectin's use for treating COVID-19 infections ([M. Popp et al. Cochrane Database Syst. Rev. 7, CD015017; 2021](#)).



[Remember Ebola: stop mass COVID deaths in Africa](#)

Nathalie Strub-Wourgaft, who heads the DNDi's COVID-19 activities, says there are legitimate reasons to test the drug in Africa. She and her colleagues are hopeful that it might act as an anti-inflammatory when given alongside the antimalaria drugs. And the DNDi is poised to test other drugs if this combination is found lacking.

“The issue of ivermectin has been politicized,” says epidemiologist Salim Abdool Karim, director of the Centre for the AIDS Programme of Research in South Africa (CAPRISA), headquartered in Durban. “But if the trials in

Africa can help resolve that or make an important contribution, then that's a good idea.”

Strub-Wourgaft says that the combination of nitazoxanide and ciclesonide looks promising on the basis of existing data so far. “We have encouraging preclinical and clinical data that supported our selection for this combination,” she says. After an interim analysis last September, Strub-Wourgaft says ANTICOV is preparing to test a new arm, and will continue with the two existing treatment arms.

Barriers and bottlenecks

Getting the trials started was a challenge, even for [the DNDi, which has lots of experience working in the continent](#). Regulatory approvals presented a major bottleneck, says Strub-Wourgaft. So, ANTICOV collaborated with the WHO’s African Vaccine Regulatory Forum (AVAREF) to set up an emergency process for joint reviews of clinical studies in 13 countries. This could speed up regulatory and ethical approvals. “It allows us to bring countries, regulators and ethics-review-committee members together,” says Strub-Wourgaft.

Nick White, a specialist in tropical medicine who chairs the COVID-19 Clinical Research Coalition, an international collaboration to find solutions to COVID-19 in low-income countries, says that although the WHO initiative is good, it still takes longer to obtain approvals for studies in low- and middle-income nations than it does in wealthy ones. The reasons include strict regulatory regimes in these nations, and authorities that are unskilled at navigating ethical and regulatory review. This is something that has to change, says White. “If countries want to find the solutions to COVID-19, they should help their researchers to do the necessary research, not obstruct them.”

But the challenges don’t stop there. Fowotade says that logistics and inadequate electrical supplies can stall progress once a trial starts. She was storing COVID-19 samples in a –20 °C freezer at the hospital in Ibadan when it experienced power outages. She also needed to transport the samples

to a centre in Ede for analysis, a two-hour drive away. “I sometimes feel worried about the integrity of the stored samples,” Fowotade says.



How COVID is derailing the fight against HIV, TB and malaria

Olagunju adds that recruiting trial participants became even more difficult when some states stopped funding COVID-19 isolation centres in their hospitals. Without those resources, only patients who could afford to pay were admitted. “We planned and started our trial based on the knowledge that the government was responsible for funding isolation and treatment centres. Nobody expected that to be interrupted,” says Olagunju.

And although it’s generally well resourced, Nigeria is notably not a participant in ANTICOV. “Everybody avoids Nigeria to do clinical trials because we are not organized,” says Oyewale Tomori, a virologist and chair of Nigeria’s Ministerial Expert Advisory Committee on COVID-19, which works to identify effective strategies and best practices for responding to COVID-19.

Babatunde Salako, director-general of the Nigerian Institute of Medical Research in Lagos, disagrees with that view. Salako says that Nigeria has the knowledge to conduct clinical trials as well as hospitals for recruitment and a vibrant ethics-review committee, which coordinates approvals for clinical

trials in Nigeria. “In terms of infrastructure, yes, it may be weak; it can still support clinical trials,” he says.

Ndwandwe wants to encourage more African researchers to join clinical trials so that its citizens can have equitable access to promising therapies. Local trials can help researchers to identify pragmatic treatments. And they can address the specific needs of low-resource settings and contribute to better health outcomes, says Hellen Mnjalla, a clinical-trials manager at the Kenya Medical Research Institute–Wellcome Trust Research Programme in Kilifi.

“COVID-19 is a new infectious disease, so we need to do clinical trials to understand how these interventions are going to work on African populations,” adds Ndwandwe.

Salim Abdool Karim hopes that the crisis will spur African scientists to build on some of the research infrastructure that had been set up to fight the HIV/AIDS epidemic. “The infrastructure is well developed in some countries like Kenya, Uganda and South Africa. But it’s less developed in others,” he says.

To bolster clinical trials for COVID-19 treatments in Africa, Salim Abdool Karim suggests establishing a body such as the Consortium for COVID-19 Vaccine Clinical Trials (CONCVACT; created in July 2020 by the Africa Centres for Disease Control and Prevention) to coordinate treatment trials on the continent. The African Union — the continental body representing the 55 African member states — is well placed to take that responsibility. “They’re already doing it for vaccines, so that could be extended for treatments too,” says Salim Abdool Karim.

The COVID-19 pandemic, says Sow, can be overcome only through international collaboration and equitable partnerships. “In the global fight against infectious diseases, a country can never go alone — not even a continent can,” he says.

Nature **599**, 25–27 (2021)

doi: <https://doi.org/10.1038/d41586-021-02995-5>

This article was downloaded by **calibre** from <https://www.nature.com/articles/d41586-021-02995-5>

| [Section menu](#) | [Main menu](#) |

Books & Arts

- **[The vaccine shots that rang around the world](#)** [01 November 2021]

Book Review • Two books follow key runners in the historic race to immunize the world against COVID.

- BOOK REVIEW
- 01 November 2021

The vaccine shots that rang around the world

Two books follow key runners in the historic race to immunize the world against COVID.

- [Natasha Loder](#) 0



Katalin Karikó worked for decades to harness the power of messenger RNA to fight disease. Credit: Hannah Yoon/Bloomberg/Getty

The First Shots: The Epic Rivalries and Heroic Science Behind the Race to the Coronavirus Vaccine *Brendan Borrell Mariner* (2021)

A Shot to Save the World: The Inside Story of the Life-or-Death Race for a COVID-19 Vaccine *Gregory Zuckerman* Portfolio (2021)

It is almost two years since the first cases of SARS-CoV-2 emerged in hospitals in Wuhan, China. In that time, the virus has left a trail of devastation across the planet. The death toll is estimated at between 10 million and 19 million, according to the unique model of excess deaths built by *The Economist* magazine. Were it not for the extraordinary invention of COVID-19 vaccines, these grim numbers would be higher still.

The race to create those vaccines involved many people. But it started with one: virologist Zhang Yongzhen at Fudan University in Shanghai, China. On 3 January 2020, a metal box arrived in his laboratory. Inside, packed in dry ice, was a sample taken from a person with pneumonia in Wuhan. After 40 hours of labour, he and his colleagues had worked out the genetic sequence of the virus that was responsible for the outbreak. It was a coronavirus. He knew exactly what that could mean.



[The COVID vaccine makers tell all](#)

Zhang was not the first to sequence SARS-CoV-2, but he agreed to the first release of the data. He didn't ask for permission to do so. Nor did he wait until the sequence was published as a paper ([F. Wu et al. *Nature* 579, 265–269; 2020](#)). Instead, it was deposited on the public website Virological.org on 11 January, kick-starting a global chase for vaccines. That effort, unlike any the world had ever seen, saw billions of public and private dollars invested at risk. Now, two books follow key runners in the great vaccine race of 2020 in quite different ways — one close up, one wider angle. Taken together, they give a flavour of some of the people and technologies that stepped up when it mattered the most, and the politics that smoothed or blocked their paths.

Heroes and villains

In *First Shots*, journalist Brendan Borrell relates how the US government, and academics at the US National Institutes of Health (NIH), advanced national vaccine development — particularly that using messenger RNA to prompt cells to make antibodies that fight off the virus, in partnership with the biotechnology company Moderna, based in Cambridge, Massachusetts. Beyond vaccines, there are entertaining digressions into the tortuous US public-health response, the outbreak on the cruise ship *Diamond Princess*, ventilator shortages, US efforts to obtain a supply of masks, and more. One delightful detail features then-president Donald Trump: “Did you see my tweet?” he barks to underlings. “Why hasn’t the FDA approved convalescent plasma?”

Borrell’s book shines in his absorbing account of how, against the odds, the government-backed public–private vaccine-development plan — Operation Warp Speed — arose from the primordial sludge of pandemic policymaking inside the Trump White House. After all, this was an administration that got just about everything 180° wrong on the pandemic and the virus — and, at times, seemed to be at war with science and scientists.

The epic rivalries mentioned in the book’s subtitle are largely down to the egos in an alphabet soup of US government departments and other factions. There are some intriguing minutiae. Early on, a structural biologist — hoping for an inside line on the unpublished genetic sequence of SARS-

CoV-2 — is reputed to have griped when it was uploaded: “Everyone has it now.”



Bali, Indonesia: people receive the vaccine developed by the University of Oxford, UK, and AstraZeneca.Credit: Johanes Christo/NurPhoto/Getty

Yet the pursuit of COVID-19 vaccines is not solely a US story. It is an international one. It also has roots, for example, in the mRNA work of husband-and-wife team Uğur Şahin and Özlem Türeci at the firm BioNTech in Mainz, Germany, which partnered on a vaccine with Pfizer, based in New York City. It is in covering these global angles that *First Shots* comes up short. Borrell’s stateside characters, such as Michael Callahan, a US doctor who travelled to Wuhan in mid-January to witness the devastation in the local hospitals, or vaccine designer and public-engagement star Kizzmekia Corbett are well-drawn and metaphorically square-jawed. That the rights to the book were sold to television channel HBO in July 2020 might have coloured the way the story is told. British scientists, for example, appear as a “standoffish bunch”.

The characterization of University of Oxford vaccinologist Sarah Gilbert is a case in point. Gilbert co-created the adenovirus-based vaccine that the university developed with AstraZeneca, based in Cambridge, UK, and that is now for sale at low cost around the world. Skirting her leadership role, Borrell alights on the detail that the reserved scientist made an appearance in *Vogue* magazine wearing an Armani blouse and Manolo Blahnik boots. He chooses not to pursue the deeper question of why she might be in an article on the “women shaping 2020”. Gilbert certainly found the press attention overwhelming, and initially did not welcome interest in her as a ‘woman’ scientist. Over time, she has come to accept that she is a role model, co-authoring her own book (see [*Nature* 596, 29–30; 2021](#)).

A fuller appraisal of how the world managed to create the 20 or so vaccines that have received limited or full approval so far was always going to be a tall order. In *A Shot to Save the World*, Gregory Zuckerman, a business reporter for the newspaper *The Wall Street Journal*, looks at more of the key vaccines, and takes a broader historical perspective, giving an assured account of the research, the ideas and the personalities.

Hope and promise

Like many great scientific tales, the story features serendipity, failures, tenacity, frustration and temper tantrums. It meanders through the decades-deep origins of the idea of making better recombinant proteins in insect cells. It charts long years of thankless work by Katalin Karikó, latterly at BioNTech, and others, in overcoming the challenges of working with unstable and tricky mRNA molecules. (Karikó and her colleagues’ mRNA triggered worrying immune responses when first injected into mice.) The book also relates the growing pains of the adenoviral approach: in 2007, an HIV vaccine using this technology was found to make participants more likely to be infected, not less.



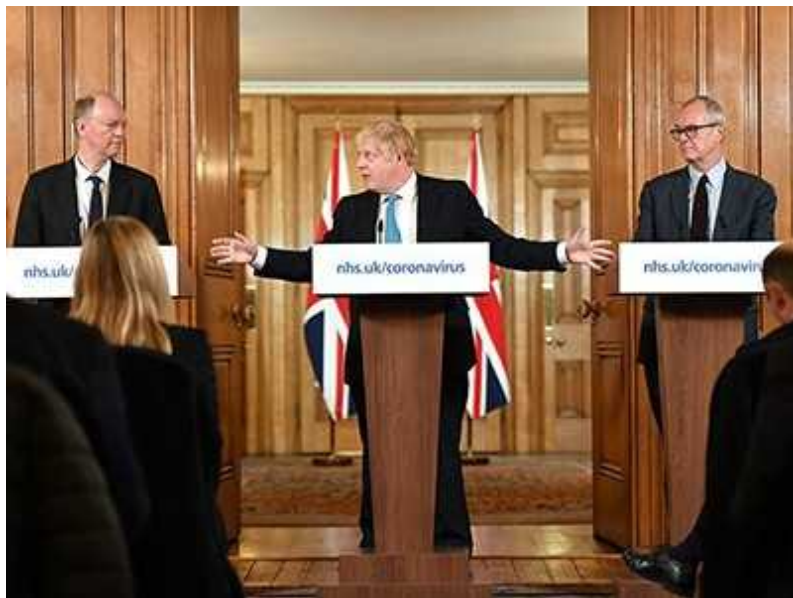
This COVID-vaccine designer is tackling vaccine hesitancy — in churches and on Twitter

Driving this narrative is a strong cast. Stéphane Bancel, the French chief executive of Moderna, emerges as rude and pushy, telling staff: “Fifty percent of you won’t be around in a year.” At BioNTech, meanwhile, Şahin and Türeci have a work ethic that sees them getting married in their lunch break, and celebrating a new piece of data about efficacy with a 30-minute walk. Over at Oxford’s Jenner Institute, director Adrian Hill is painted as overbearing, determined and caustic. Zuckerman relates verbal lashings such as, “That is the most ignorant thing I’ve ever heard.” Some close colleagues are more affectionate, describing Hill as a “Marmite personality” — the sharp taste that one either loves or hates. For anyone who works at the bench, it will come as little surprise that some of these brilliant minds are obsessive, rude or quirky. That is not to excuse bad behaviour. But this is the context in which to view characters who have been thrown into the spotlight. We should not expect them to be heroes from central casting.

Zuckerman dives deeply into a key historical moment. He gives a superb account of the misery of Pfizer executives on the morning of 8 November 2020, a Sunday, as they wait for hours for the results of their phase III clinical trial, the first from any of the vaccine candidates. They squirm in a conference room, wearing black masks printed with “Science Will Win”. Eventually, Kathrin Jansen, Pfizer’s head of vaccine research calls with

news that the jab works: “We made it … we won.” The room erupts with cheers and yelling. Boss Albert Bourla screams, “I love you!” to his colleagues.

That emotion rolled out over the world the following morning, when the news was released. At *The Economist*, my editor picked up the message during our main Monday editorial meeting on Zoom. “Is 90% efficacy good, Natasha?” she asked me. “It’s fucking amazing. Absolutely amazing,” I blurted, feeling a wave of relief and joy. The data came from an interim analysis; the number later improved to 95%.



[Scathing COVID-19 book from Lancet editor — rushed but useful](#)

Pfizer’s result was proof that the gamble on an entirely innovative vaccine had paid off better than anyone dared to hope. It was also evidence that the idea of stimulating immunity against the coronavirus’s ‘spike’ protein was a good one — something that augured well for many other vaccines. Today, as we battle the woes of resistance and distribution, it remains a special moment of hope and of promise.

Neither book tackles the non-Western vaccines; their stories are not easy to tell. But they should be told. The first COVID-19 vaccines did not come from the West at all. In August last year, the Russian vaccine Sputnik V was authorized for use. Shortly after that came the Chinese vaccines CoronaVac

and Sinopharm. These approvals came before the completion of large-scale trials and were seen as ethically dubious and foolhardy.

Yet Chinese vaccines came to the rescue of middle- and low-income countries. China exported early on, and in large quantities. So far, it has sent about 1.1 billion doses to more than 120 countries and territories. By contrast, the US has had a more ambivalent international role. Only in the past few months has it started to donate vaccines; by 21 October, it had given 206 million doses.

Perhaps it is understandable that the messy geopolitics and nationalism that has bedevilled the equitable distribution of vaccines around the planet are not part of either book. That, as they say, is another story — one that is still tragically unfolding.

Nature **599**, 28-29 (2021)

doi: <https://doi.org/10.1038/d41586-021-02996-4>

This article was downloaded by **calibre** from <https://www.nature.com/articles/d41586-021-02996-4>

| [Section menu](#) | [Main menu](#) |

Opinion

- [**Abdul Qadeer Khan \(1936–2021\)**](#) [29 October 2021]
Obituary • Materials scientist behind Pakistan's nuclear-weapons business.
- [**There is no silver bullet against climate change**](#) [02 November 2021]
Correspondence •
- [**Colour blindness: journals should enable image redisplay**](#) [02 November 2021]
Correspondence •
- [**Embrace open-source sensors for local climate studies**](#) [02 November 2021]
Correspondence •
- [**For NGOs, article-processing charges sap conservation funds**](#) [02 November 2021]
Correspondence •

- OBITUARY
- 29 October 2021

Abdul Qadeer Khan (1936–2021)

Materials scientist behind Pakistan's nuclear-weapons business.

- [Ehsan Masood](#)



Credit: Farooq Naeem/AFP/Getty

Scientists designing weapons of mass destruction are usually hidden from the public, watched by security and intelligence agencies. Rarely are they powerful celebrities who give interviews and publish their research. Abdul

Qadeer Khan, the materials scientist who smuggled nuclear-weapons technology into and then out of Pakistan, attended scientific conferences and openly advertised his services. “We have the capability of going nuclear if the politicians decide,” Khan boasted when I interviewed him in the lobby of an Islamabad hotel (see [*Nature* 376, 636–637; 1995](#)). He has died aged 85.

As the world later learnt to its cost, that capability included the first freelance nuclear-weapons technology business, selling uranium-enrichment technology to Iran, North Korea and Libya. Despite confessing to wrongdoing on live television, for millions he died a martyr, restoring a poor country’s pride in matching richer nations in defence technology.

Abdul Qadeer Khan was born in 1936 in Bhopal, India. The family migrated to Pakistan in 1952, after decolonization. Graduating in metallurgy from the University of Karachi, Khan studied further in what was then West Germany, and in the Netherlands. At the Catholic University of Leuven in Belgium he was awarded a PhD in 1972 for work on copper-based martensites, extremely hard forms of steel. Then came the turning point. He went to work for FDO, a company based in Amsterdam that supplied the high-speed centrifuges that enrich uranium for use in nuclear power plants.



[Born secret — the heavy burden of bomb physics](#)

By the early 1970s, Asian countries were in an arms race. China and India had fought one war; India and Pakistan had fought three. China tested a nuclear weapon in 1964. In 1972, Pakistan's then prime minister, Zulfiqar Ali Bhutto, tasked scientists with designing a nuclear device. Bhutto's chief scientific adviser, Abdus Salam, proposed creating a secret theoretical-physics group. This would be in the tradition of the US Manhattan Project, the group's then head, Riazuddin, wrote in his memoir *A Physicist's Journey* (2020).

One of Pakistan's problems was how to acquire the plutonium or uranium needed to produce a nuclear explosion. Weapons can be made using plutonium-239. This was potentially available as a by-product of power plants. But Pakistan's nuclear-energy materials were being monitored by the International Atomic Energy Agency, based in Vienna.

Uranium, too, was a possibility. But Pakistan lacked the enrichment technology to separate the rare fissile isotope — U-235 — from its abundant naturally occurring source. Until, that is, a letter found its way to Bhutto from Khan, then working in the Netherlands, who offered his services to the nuclear-weapons effort.

The timing could not have been better: the missive arrived shortly after India's 1974 nuclear test, as Bhutto was becoming impatient at the lack of progress from his scientists.

Khan relocated to Islamabad — with the designs for high-speed centrifuges to create fissile uranium. He was initially employed by the Pakistan Atomic Energy Commission (PAEC), but fell out with top management, accusing it of stalling on the prime minister's nuclear ambitions. The PAEC administration regarded Khan as unreliable. But Bhutto bought into his vision and granted him strategic and operational independence to establish his own laboratory near Islamabad.



The scientist-spy who spilt secrets of the bomb

In April 1979, Bhutto was hanged after a military coup, but Khan's star continued to rise. He persuaded the army to maintain his funding and operational autonomy. By the 1990s, Khan was at the heart of a web of scientists, engineers, suppliers, fixers and front-companies. They imported nuclear materials, and incorporated these into designs and equipment for export.

Between 1987 and 1997, Khan's network provided Iran with centrifuge designs and components. Next came North Korea, which was supplied with centrifuges, sketches, technical data and uranium hexafluoride gas (UF_6), used in uranium processing. From the late 1990s, Libya bought at least 10,000 centrifuges and 1.87 tonnes of UF_6 .

But Libya was a bridge too far. Western intelligence agencies had been piecing together records of phone conversations, shipments, travel and financial transactions. When Libya gave up its nuclear ambitions, documents passed to the United States named the Khan network as a source for supplies. The administration of US president George W. Bush pressed Pakistan to act and, in 2004, Khan confessed on television, in English. Although later pardoned, Khan spent the rest of his days under effective house arrest.

His reputation in Pakistan remained sky high, however. According to at least one source, he donated millions of dollars to science and education causes, but faced little or no parliamentary scrutiny. Hassan Abbas, former deputy-director of investigations at the country's anti-corruption watchdog, writes in his book *Pakistan's Nuclear Bomb* (2018) that he decided against pursuing a corruption inquiry on the grounds that investigating the country's most popular person was too big for his agency to handle.

In the end, Khan's defenestration proved a convenient distraction for the army, the government and the PAEC. Pakistan, it is estimated, has 165 nuclear warheads, the world's sixth largest nuclear arsenal. The PAEC, as the apex nuclear body, organized Pakistan's 1998 nuclear tests.

Khan was not the 'father' of Pakistan's nuclear-weapons programme, as was widely reported: it was a team effort. But he was a crucial participant, and took advantage of the recklessness and incompetence of a state determined to acquire weapons of mass destruction at any cost, endangering the lives of its own people, and the wider world.

Nature **599**, 31 (2021)

doi: <https://doi.org/10.1038/d41586-021-02997-3>

This article was downloaded by **calibre** from <https://www.nature.com/articles/d41586-021-02997-3>

| [Section menu](#) | [Main menu](#) |

- CORRESPONDENCE
- 02 November 2021

There is no silver bullet against climate change

- [Chandran Nair](#) 0

I find the potential solutions to climate change proposed by Lucas Joppa and colleagues unrealistic ([Nature 597, 629–632; 2021](#)). The scale of the crisis means it cannot be tackled simply by technology, corporations or markets.

Access options

Subscribe to Journal

Get full journal access for 1 year

\$199.00

only \$3.90 per issue

[Subscribe](#)

All prices are NET prices.

VAT will be added later in the checkout.

Tax calculation will be finalised during checkout.

Rent or Buy article

Get time limited or full article access on ReadCube.

from \$8.99

Rent or Buy

All prices are NET prices.

Additional access options:

- [Log in](#)
- [Learn about institutional subscriptions](#)

Nature **599**, 32 (2021)

doi: <https://doi.org/10.1038/d41586-021-02980-y>

This article was downloaded by **calibre** from <https://www.nature.com/articles/d41586-021-02980-y>.

| [Section menu](#) | [Main menu](#) |

- CORRESPONDENCE
- 02 November 2021

Colour blindness: journals should enable image redisplay

- [Jeremy Adler](#) 0

Making the data in figures accessible for people with colour-vision deficiency is difficult (see [Nature 598, 224–225; 2021](#)). For example, a palette optimized for readers with red–green blindness could further disadvantage the smaller group with a blue deficit. And images intended to convey differences in data intensity to colour-blind readers can be problematic for people with full colour vision.

Access options

Subscribe to Journal

Get full journal access for 1 year

\$199.00

only \$3.90 per issue

[Subscribe](#)

All prices are NET prices.

VAT will be added later in the checkout.

Tax calculation will be finalised during checkout.

Rent or Buy article

Get time limited or full article access on ReadCube.

from \$8.99

[Rent or Buy](#)

All prices are NET prices.

Additional access options:

- [Log in](#)
- [Learn about institutional subscriptions](#)

Nature **599**, 32 (2021)

doi: <https://doi.org/10.1038/d41586-021-02982-w>

This article was downloaded by **calibre** from <https://www.nature.com/articles/d41586-021-02982-w>

| [Section menu](#) | [Main menu](#) |

- CORRESPONDENCE
- 02 November 2021

Embrace open-source sensors for local climate studies

- [Elad Levintal](#) ORCID: <http://orcid.org/0000-0002-5029-0742>⁰,
- [Kosana Suvočarev](#) ORCID: <http://orcid.org/0000-0002-5519-2287>¹,
- [Gail Taylor](#) ORCID: <http://orcid.org/0000-0001-8470-6390>² &
- [Helen E. Dahlke](#) ORCID: <http://orcid.org/0000-0001-8757-6982>³

Inexpensive open-source hardware is democratizing science (see [Nature 587, 509–511; 2020](#)). Open-source sensors, for example, are proving to be game-changers for measuring environmental parameters at a fraction of the cost of commercial equipment. They offer opportunities for scientists in low- as well as high-income countries to address local questions around climate change.

Access options

Subscribe to Journal

Get full journal access for 1 year

\$199.00

only \$3.90 per issue

[Subscribe](#)

All prices are NET prices.

VAT will be added later in the checkout.

Tax calculation will be finalised during checkout.

Rent or Buy article

Get time limited or full article access on ReadCube.

from \$8.99

[Rent or Buy](#)

All prices are NET prices.

Additional access options:

- [Log in](#)
- [Learn about institutional subscriptions](#)

Nature **599**, 32 (2021)

doi: <https://doi.org/10.1038/d41586-021-02981-x>

This article was downloaded by **calibre** from <https://www.nature.com/articles/d41586-021-02981-x>

| [Section menu](#) | [Main menu](#) |

- CORRESPONDENCE
- 02 November 2021

For NGOs, article-processing charges sap conservation funds

- [Kevin A. Wood](#) ORCID: <http://orcid.org/0000-0001-9170-6129>^⑨,
- [Julia L. Newth](#) ORCID: <http://orcid.org/0000-0003-3744-1443>^① &
- [Geoff M. Hilton](#) ORCID: <http://orcid.org/0000-0001-9062-3030>^②

The shift from a ‘reader pays’ to an ‘author pays’ model of scientific publishing presents a financial threat to environmental non-governmental organizations (eNGOs). Many of these support, conduct and publish applied research on real-world solutions to the planet’s most pressing challenges. Funded mainly by donations, eNGOs must now choose between taking conservation action and publishing more research papers.

A more equitable publishing system is needed. Platinum and diamond open access (see [L. Barnes *Open Book Publishers* https://doi.org/g3tb: 2018](#)), financed by a third party such as a scientific society, avoid article-processing charges (APCs) for authors and paywalls for readers, and can offer the lowest-cost option for eNGOs. Alternatively, journals could offer APC waivers for authors at eNGOs.

Discussions at this year’s United Nations biodiversity conference (COP15) and climate-change conference (COP26) are informed by eNGO research. Mandatory APCs risk pricing eNGOs out of scientific publishing at a time when their research output is most urgently needed.

Nature **599**, 32 (2021)

doi: <https://doi.org/10.1038/d41586-021-02979-5>

This article was downloaded by **calibre** from <https://www.nature.com/articles/d41586-021-02979-5>

| [Section menu](#) | [Main menu](#) |

Work

- **Tips for managing an industry move without your academic supervisor's support** [02 November 2021]

Career Feature • Struggling with your principal investigator's bias towards academia? Here are some workarounds.

- **Refining the toolkit for sugar analysis** [01 November 2021]

Technology Feature • Antibodies and other reagents for glycans have lagged behind those for proteins and nucleic acids, but the field is catching up.

- **Virus detective: searching for Zika, dengue and SARS-CoV-2** [01 November 2021]

Where I Work • Danielle Bruna Leal de Oliveira tracks pathogens for Brazil's public-health system.

- CAREER FEATURE
- 02 November 2021

Tips for managing an industry move without your academic supervisor's support

Struggling with your principal investigator's bias towards academia? Here are some workarounds.

- [Amy DePaul](#) ⁰

[Find a new job](#)



Catherine Goh (left) was encouraged to move to industry by supervisor Shirish Shenolikar (right) at Duke-NUS Medical School, Singapore. Credit: Duke-NUS Communication

When Catherine Goh started her PhD in 2010, she knew from the outset that her career ambitions lay in commercial science, rather than in academia. Fortunately, Shirish Shenolikar, her supervisor at Duke-NUS Medical School in Singapore, supported her plans.

“There was no problem with my principal investigator (PI). He had also worked in industry and understood what’s involved,” says Goh, who is now an associate product specialist based in Munich, Germany, at PerkinElmer, a biotechnology company specializing in diagnostic and life-science products.

Shenolikar, whose career includes six years working as a senior scientist for global pharmaceutical company Pfizer, helped Goh to secure a postdoctoral research position at siTOOLs Biotech in Munich by inviting her prospective employer to call him to discuss her strengths. “If you want your folks to succeed, you’ve got to get involved,” he says.

Other junior researchers are not so lucky. Many who set their sights on a career in the for-profit sector meet resistance from PIs with a bias towards academic science. For those younger scientists, the career path from academia to industry can be a rocky one.

Scientists who talk about working in industry are commonly referring to start-up, manufacturing and consulting businesses. The roles for people with science PhDs include senior scientist, medical-science liaison, project manager and product manager.

An analysis of the US National Science Foundation’s 2019 Survey of Doctorate Recipients found that, since 2015, more US-trained PhD graduates in science, engineering and health subjects now work in industry than in higher education across the United States.

A report published in 2010 by the Royal Society, which forecast how UK science might further develop over the remainder of the twenty-first century, said: “The majority of people undertaking a PhD will end up in careers

outside scientific research... only a tiny proportion can expect to end up as university professors.”

The implications of these hiring trends haven’t always filtered down to the people who lead academic research and train junior researchers — that is, tenured PIs who steer their trainees towards the pursuit of university careers that mirror their own, and who, in some cases, strongly disfavour industry as a career.



[Planning a postdoc before moving to industry? Think again](#)

Often, a PI’s bias is rooted in the view that pure science research embodies loftier goals than does research serving a commercial purpose, says Anders Ohman, a PhD cancer researcher at Brown University in Providence, Rhode Island.

“A lot of academicians tend to have this sort of stereotype of industry scientists being corporate sell-outs. But, of course, industry also does real science,” says Anders, who is considering a non-academic career path.

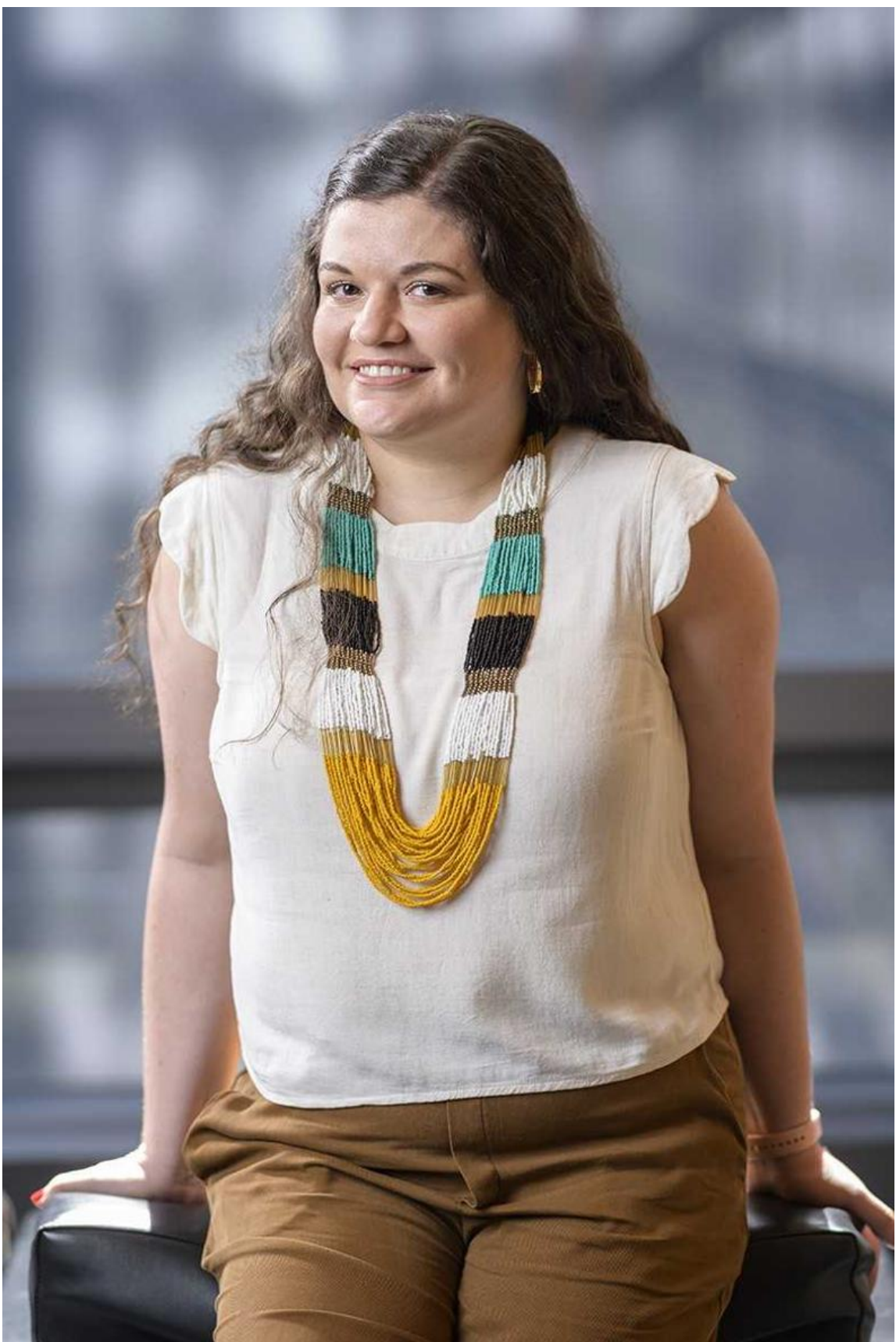
There is a practical reason why some academics want to produce trainees who will follow the same path that they did: professional incentives.

In some institutions, one criterion for tenure is a professor's record in guiding trainees into faculty positions, says Yaihara Fortis Santiago, associate director of postdoctoral affairs and trainee diversity initiatives at Memorial Sloan Kettering Cancer Center in New York City, who informally advises and mentors junior scientists in and outside her institution on career issues.

"Definitely you are going to have to report how many students who went into postdocs are in faculty positions. You have to show how many people you've trained and where they ended up," she says.

Whatever the reason — professional advancement or scientific idealism — an anti-industry bias exists in the minds of some PIs, she says, and it can translate into retaliation. The worst cases include firing junior laboratory members who tell their supervisors they plan to work in industry, or removing them from research projects or not crediting their work in publications, says Fortis Santiago.

But in most cases, she says, the PI's reaction, even when unenthusiastic, is not retaliatory. In fact, she thinks there are more and more PIs who want to help their industry-oriented mentees.



Supervisors are seldom retaliatory, says postdoc mentor Yaihara Fortis Santiago.Credit: Memorial Sloan Kettering

Some younger academic scientists who are considering industry careers echo that sentiment, saying that times have changed for them and many people they know, but not for everyone.

“I have a very supportive adviser,” says Ohman. However, he’s come across stories of unhelpful PIs. “I’ve heard of people hiding their trajectory from their adviser. Those are not the typical case. But it’s definitely not unheard of.”

Anna Drangowska-Way, whose biology PhD research at the University of Virginia in Charlottesville focuses on how organisms regulate fat breakdown during fasting or stress, also received support for her decision to investigate non-academic careers, ranging from science writing to project management in the private sector. But she adds that, although she appreciates her mentor’s encouragement, she didn’t exactly require it: “It’s my life,” she says.



[How to sail smoothly from academia to industry](#)

A change in some PIs’ attitudes is borne out not just by anecdote, but by a 2019 study documenting a shift in thinking among US academic mentors,

who are now more likely to see the value of university career-development services. Approximately one-third of the 817 faculty members who responded to one of two surveys had spent time in a professional position outside academia ([S. W. Watts et al. PLoS ONE 14, e0210189; 2019](#)). The respondents identified an urgent need to broaden career activities to include non-academic options given the paucity of tenure-track positions, but were uncertain about their own knowledge and training to do so effectively.

Still, the anti-industry mindset remains a reality among some PIs. A PhD student in immunology at a US institution, who asked not to be identified, recently told his PI that he planned to work in industry. He got a negative reaction, which left him feeling misunderstood.

“Almost all conversations I had with academics about my plan started with the assumption that money is my only motivation to move to industry, which is disappointing,” he says. “They never considered... [my] genuine interest in the translational nature of industry.”

He is not intimidated by his PI’s disapproval, and money is not a concern he can ignore. “I am not shy about my financial ambition,” he says, “or the pursuit of a secure future for my family.”

Dread of disapproval

Early-career researchers too often dread their PI’s disapproval, which stops them from taking the lead in forging a productive relationship that includes frank conversations about career options, says Fortis Santiago. She encourages a confident mindset instead of a fearful one.

“Always to try to be in partnership with that person [a supervisor], versus seeing them as a parent and asking for permission,” she says.

“You don’t want to go in and say, ‘I’m sorry, I’m leaving academia,’” she explains. Instead, she recommends that junior researchers open with praise for the PI’s mentorship and gratitude for the skills they’ve acquired in the lab, before saying that they hope to pursue a different career path, and that they would appreciate the PI’s support in the transition.



[Collection: Career resources for PhD students](#)

Fortis Santiago recommends, after hopefully securing PI support, that junior lab members then request reasonable amounts of time away from the lab to pursue industry career activities, such as attending a conference or networking with scientists who work in their desired sector.

Tracy Costello, a career coach who assists academics in PhD and postdoctoral programmes, advises clients to be focused when they inform their PIs of their career decision.

“The conversation has to be about what they want out of their career as opposed to PI expectations,” says Costello, who is based in Tampa, Florida. “You are the one in control of your career trajectory. Owning that is terrifying but necessary.”

Costello instructs clients who are walking away from academic research to compile a record of the work that they’ve completed on a project, what the data show so far and what the next steps are.

“Prepare your documentation in the lab so you are ready to step out the door and leave your PI with the resources to be successful in your absence,” she says. “Every postdoc I have coached in that way feels like they left their position in a positive way.”



Klodjan Stafa in the lab at the Estée Lauder Companies in New York City. Credit: Klodjan Stafa

Another point worth bringing up in these conversations is that shifting to an industry path doesn't have to mean underperforming. A 2021 study of ten institutions that offered PhD students professional training (including career panels, skill-building workshops and internships) found that programme participants completed just as many academic papers as those who weren't involved in the programme, and took the same amount of time to complete their degrees ([P. D. Brandt *et al.* *PLoS Biol.* **19**, e3000956; 2021](https://doi.org/10.1371/journal.pbio.3000956)).

Sometimes, a researcher isn't leaving one career for another, but is trying to balance professional opportunities — internships, webinars and networking — alongside their full-time lab duties, which requires their PI's support.

In 2020, Daniela Borges, who is finishing her PhD in molecular biology at Brazil's Federal University of Ceara in Fortaleza, was offered a part-time position at a commercial medical lab, testing people with COVID-19. The job offered more than the chance to collect a pay cheque: she thought it might lead to greater professional opportunities.

“I was worried about my life after finishing my PhD,” she recalls, adding that her PI required that her full-time lab duties were unaffected by her part-time role.

Thus began a schedule of long hours at her lab alongside her job in COVID-19 testing — at nights and at the weekends. As she’d hoped, a job offer came her way as a result of her stint in COVID-19 testing. She’ll face a choice after completing her studies: a full-time position combining scientific and administrative duties at the commercial lab, or a postdoctoral position, offered by her PI, in which she can continue her research.

It’s a tough call because she loves pure science research, but feels that her long-term options in academia are limited, particularly because she doesn’t want to leave Brazil. She has seen some Brazilian PhD-holders working as lab technicians, rather than in academic roles.

“I’m still in love with science,” she says. “But it’s complicated. This is the problem of every student in Brazil.”

The earlier, the better

Sometimes, early-career researchers decide to move from academia to industry during a postdoctoral contract. “It’s harder if you’ve done four-and-a-half years of a postdoc and realize, ‘Oh, I don’t see myself in academia,’” says Costello. In such cases, she adds, “there is less time to pivot and ensure that you have the non-technical skills, or any specific skills — for example, certification in project management — that might be required for the new career path”.

“It’s not too late, but you have to be really efficient,” she says, and advises that researchers in these circumstances prioritize contacting university career-advice services.

Fortunately, she’s found that researchers who have already established a good relationship with their PIs can continue to work productively with them, even if their decision to switch sectors at a later stage disappoints them. But sometimes, a PI’s response necessitates intervention.

If, for example, a researcher commits to a lab where extremely long hours are the norm, making it impossible to allow for exploration of a non-academic career, it might be time to find a different lab, says Shenolikar.



Career resources for postdoctoral researchers

Klodjan Stafa was working as a postdoctoral researcher in neuroscience at the University of California, San Diego, when he decided to take some time out to explore industry career options.

In 2014, he told his PI that he needed a break from his project and possibly from academia, and that he was considering a career in the private sector.

Stafa says he promised to train and advise his replacements for the remaining few months at the lab, but he got the impression that his PI disapproved of his career direction — and he thinks that their working relationship suffered as a result.

In 2015, he landed a job at the Estée Lauder Companies in New York City, where he is now a principal scientist, managing projects and working in cosmetics product development and training.

He's happy with his decision to walk away from the lab, his PI and academic science. He says he finds the pace and collaborative nature of industry

satisfying and validating, and wants young researchers not to feel discouraged about their prospects if they decide to leave academia.

“Your PhD is not a loss of time,” he says. “You can employ it, and industry will compensate you for your education and for your skills.”

Helping a researcher to move from academic to industry science is a goal that any PI can and should try to get behind, however tenuous their connection to the private sector, says Javier García-Martinez, an entrepreneur and molecular-nanotechnology researcher at the University of Alicante in Spain.

“If you don’t have industry contacts, you don’t have industry contacts,” he says. But PIs can put students in touch with colleagues who do, and they can write letters of recommendation or take calls from prospective employers.

The hope is that, in the future, PIs will welcome the chance to train scientists for positions in academia, industry and government, he says.

“We are graduating more doctorates and postdocs than positions are available in academia,” he reminds. “We cannot be ... only training people to become ourselves. That would be a sick system, if I may say so.”

Nature **599**, 165-167 (2021)

doi: <https://doi.org/10.1038/d41586-021-02999-1>

This article was downloaded by **calibre** from <https://www.nature.com/articles/d41586-021-02999-1>

- TECHNOLOGY FEATURE
- 01 November 2021

Refining the toolkit for sugar analysis

Antibodies and other reagents for glycans have lagged behind those for proteins and nucleic acids, but the field is catching up.

- [Amber Dance](#) ⁰

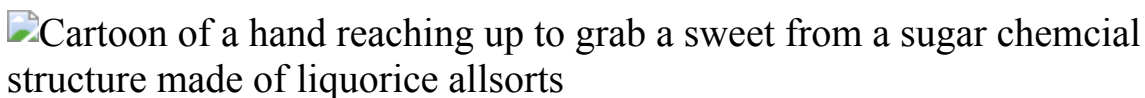


Illustration by project twins

Sugars are everywhere in biology. They decorate cells, proteins and lipids. According to a surprise finding, published in June, they even adorn RNAs¹. Yet these carbohydrates, also called glycans, have garnered little attention in recent decades.

“Glycans form an essential biological language, the glycome,” says Mark von Itzstein, director of the Institute for Glycomics at Griffith University in Brisbane, Australia. They facilitate cell–cell communication and immune responses; are altered in cancer cells; and are exploited by pathogens to get a foothold in host cells. It is slight differences in the glycans on red blood cells that define human blood as being type A, B, AB or O. And it is glycans that both shield SARS-CoV-2 from the immune system and shape the spike protein as the coronavirus attempts to enter our cells². “The spike needs the glycan shield to open,” says Elisa Fadda, a computational glycobiologist at Maynooth University in Ireland and a member of the team that made the discovery.

Most biologists, however, have focused on DNA, RNA and proteins. Part of the reason is that, compared with those neatly encoded biomolecules, glycans are incredibly complex. A small number of simple sugars can link up in a variety of ways, producing variably branching structures with a final form that depends on the presence or absence of dozens of sugar-adding and -removing enzymes. “The sheer complexity, it’s mind-boggling,” says Ajit Varki, a physician and glycobiologist at the University of California, San Diego (UCSD).

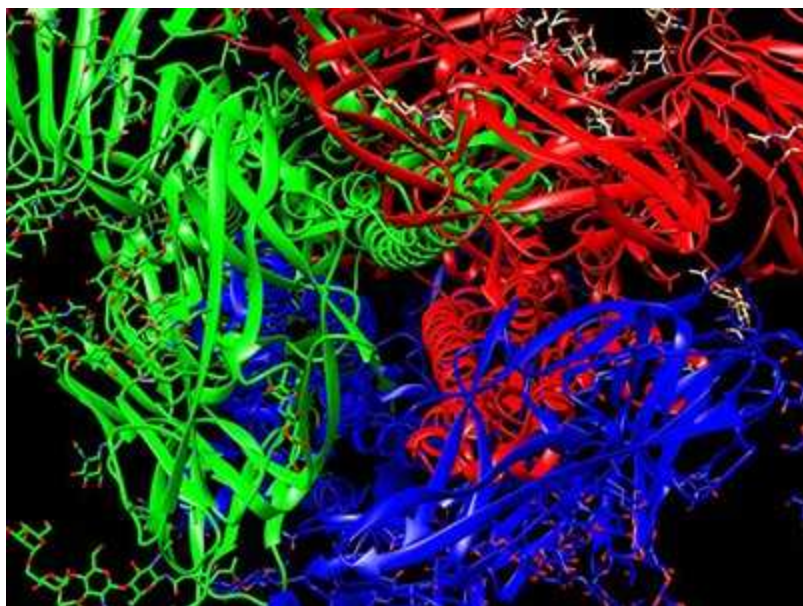
But there’s also a dearth of tools with which to study glycans, says Douglas Sheeley, co-leader of the US National Institutes of Health (NIH) Glycoscience programme in Bethesda, Maryland. The programme aims to build up the toolbox and has, for example, funded its own answer to biomolecule databases such as GenBank, namely GlyGen.org. Researchers can enter a favourite protein on the website and discover what glycans are known to decorate it, or start with a specific glycan structure to find proteins that carry it.

In the laboratory, glycobiologists would like to be able to perform the same assays, western blots, cell stainings and other experiments that antibodies enable for protein studies. But although a handful of glycan-binding ‘affinity reagents’ do exist, most are suboptimal. Some scientists are attempting to improve them; others are seeking fresh options in environments such as the microbiome of the human mouth or the bloodstream of sea lampreys. These new reagents promise to make glycobiology experiments straightforward even for non-specialists.

Upgrading nature

Historically, the leading affinity reagents for glycans have been lectins, natural carbohydrate-binding proteins from diverse organisms. But most researchers in the field have a love–hate relationship with lectins, says glycobiologist Lance Wells at the University of Georgia in Athens. Their prominence comes not so much from superior performance as from the fact that, as he puts it, “they exist” and are easily obtainable. For example, Vector Laboratories in Burlingame, California, sells [lectin-based screening kits to identify diverse pieces of glycans](#).

The downside is that lectins are not particularly specific for individual glycans. Their interface with glycan targets is shallow, less lock-and-key than cup-and-saucer. “Lectins are great for an initial screen, to say, ‘OK, do you have glycoproteins present?’” says Iain Wilson, a glycobiologist at the University of Natural Resources and Life Sciences in Vienna. But “the absence of binding, or the presence of binding, doesn’t prove the structure”.



Exposed: cells' sugary secrets

One exciting approach, says von Itzstein, is to engineer lectins so they fit desired targets better. This was the route that scientists at New England BioLabs (NEB) in Ipswich, Massachusetts, took to find a lectin that would bind to all glycans that attach to asparagine residues in a protein (called *N*-glycans), but not to ones that link to serine and threonine residues (*O*-glycans). The researchers started with Fbs1, a protein normally involved in degrading malformed glycoproteins, and used random mutagenesis and screening to create the reagent that they were after³. The team is happy to share a research-grade version of it, and a commercial-grade version should be available in early 2022, says co-inventor Chris Taron, scientific director of protein expression and modification research at the company. The latter will be part of NEB’s [‘Enzymes for Innovation’ collection](#), products from which typically cost US\$70–\$300.

[Lectenz Bio](#) in Athens, Georgia, is another company using protein engineering to convert highly specific enzymes that act on carbohydrates into refined affinity reagents.

Riches from the sea

It is possible to generate conventional antibodies for use as affinity reagents to glycans, but they rarely bind tightly to their target antigens and can cross-react with other molecules. That's led to a belief that generating antibodies just doesn't work well for carbohydrates, but that's a myth, says glycoimmunologist Rick Cummings, co-director of the Harvard Medical School Center for Glycoscience in Boston, Massachusetts. If you look in the right place, he says, you can find an abundance of specific, high-affinity antibodies to all kinds of carbohydrates.

Around 2000, immunologist Max Cooper at Emory University in Atlanta, Georgia, found one such place: jawless sea lampreys (*Petromyzon marinus*), snakelike creatures with toothy, round mouths. Cooper was comparing their immune systems with those of jawed creatures, and discovered that lamprey antibodies take a different form, with a crescent-shaped binding site⁴. This turns out to be more rigid than the binding site in mammalian antibodies, so it's less likely to flex to fit antigens that are similar to, but not the same as, the intended targets — a characteristic that confers high specificity. “It can distinguish many glycans that, to an antibody, look the same,” says Thomas Boehm, an evolutionary immunologist at the Max Planck Institute of Immunobiology and Epigenetics in Freiburg, Germany.

“You can make antibodies with specificities that have never been seen before,” says Cooper. Cummings, a collaborator on the project, was stunned to identify lamprey antibodies for glycans he didn't even know existed.



[NatureTech hub](#)

In Atlanta, Cooper co-founded a company, NovAb, to produce lamprey antibodies for targets that are difficult to tackle using conventional antibodies. One of its offerings, says co-founder and chief executive Ed Cannon, will be a sort of ‘antibody Velcro’ with multiple copies of the binding domain for a given target, to ensure firm, irreversible binding.

Cummings, meanwhile, has created a diverse array of antibodies, all encoded in yeast libraries, by immunizing lampreys with complex immunogens, such as cells or human milk. His centre can work with collaborators to investigate any given glycan using a microarray, to see whether anything in the library will bind to it. If not, the centre can immunize lampreys to generate new antibodies.

To make the lamprey molecules more convenient for laboratory and, eventually, therapeutic applications, Cooper and Cummings designed hybrid molecules that meld the ‘base’ of mammalian antibodies (the vertical section of their Y-shaped structure) with lamprey binding domains⁵. These ‘smart anti-glycan reagents’ can be detected using the same secondary antibodies that researchers already use to identify more-conventional antibodies.

The reagents right under your nose

Most glycan subunits common in humans have backbones with six carbon atoms, but another class of sugars, called sialic acids, has nine. “If you think glycans are scary to people, sialic acid is scary to glycobiologists, because [these acids are] so much more complex,” says Varki. Sialic acids — of which there are more than 50 types — often cap glycan branches. They’re negatively charged, which allows glycoproteins that contain them to slide past each other and create slippery surfaces such as the interior of the mouth; without them, our mouths would be perpetually dry, says Stefan Ruhl, an oral biologist at the University at Buffalo in New York.

Sialic-acid-tipped glycoproteins also make great handles that enable bacteria to grab on to our teeth, providing a foothold for them to form cavities, says Ruhl, who used to be a practising dentist. He reasoned that those microbes must have evolved to produce excellent sialic-acid-binding molecules, and he has discovered some in streptococci bacteria, the details of which he hopes to publish soon. Reagents based on these molecules will be freely available from Ruhl’s lab as part of the NIH Glycoscience programme.

Varki’s team also used microbes as a source of sialic-acid affinity reagents. The team has assembled a panel of nine reagents, including bacterial lectins and toxins; viral proteins and enzymes; a plant lectin and a chicken antibody⁶. The set includes a general detector for mammalian sialic acids, as well as several for more-specific structures or linkages common in mammals. For tissue staining, the panel’s reagents are easier to use than some lectins that require special buffer conditions, says pathologist Nissi Varki, director of the Histopathology/Mouse Phenotyping Division of UCSD’s Comparative Phenotyping Core. Ajit Varki, her husband, has used them in unpublished work to study the role of sialic acids in a mouse model of the inflammatory disease colitis.

With glycans being so little understood, there’s plenty to learn. “We are like kids in a candy shop,” says Ajit Varki. “The bad part is, there aren’t many kids in the shop.” The new reagents should make it easier for other biologists to get a taste.

Nature **599**, 168–169 (2021)

doi: <https://doi.org/10.1038/d41586-021-03000-9>

References

1. 1.

Flynn, R. A. *et al.* *Cell* **184**, 3109–3124 (2021).

2. 2.

Casalino, L. *et al.* *ACS Cent. Sci.* **6**, 1722–1734 (2020).

3. 3.

Chen, M. *et al.* *Nature Commun.* **8**, 15487 (2017).

4. 4.

Cooper, M. D. & Alder, M. N. *Cell* **124**, 815–822 (2006).

5. 5.

McKittrick, T. R. *et al.* *Commun. Biol.* **3**, 91 (2020).

6. 6.

Srivastava, S. *et al.* Preprint at bioRxiv
<https://doi.org/10.1101/2021.05.28.446202> (2021).

This article was downloaded by **calibre** from <https://www.nature.com/articles/d41586-021-03000-9>

- WHERE I WORK
- 01 November 2021

Virus detective: searching for Zika, dengue and SARS-CoV-2

Danielle Bruna Leal de Oliveira tracks pathogens for Brazil's public-health system.

- [Patrícia Maia Noronha](#) 0



Danielle Bruna Leal de Oliveira is a researcher in microbiology and virology at the University of São Paulo, Brazil. Credit: Pablo Albarenga for *Nature*

In this picture, I'm looking into a digital microscope to observe the structural damage that SARS-CoV-2 does to cells from an African green monkey (*Chlorocebus sabaeus*). I'm inside NB3, the maximum-biosecurity laboratory here at the University of São Paulo (USP) in Brazil, wearing protective equipment. In this room, we look like astronauts.

Nowadays, we can watch molecular mutations as they occur, using computer software alongside advanced lab techniques. We can detect the viruses that cause respiratory disease in just 15 minutes.

I had dreamt of being a researcher since my adolescence. Like most people from Belém (the northern Brazilian city where I grew up), my family has an ethnically mixed background of Europeans and Indigenous people. I wanted to research the genetic impact of this, so for my undergraduate degree I studied genetics at the Federal University of Pará in Belém.

After that, I discovered I had to wait six months to apply to do a PhD in genetics at USP. But the microbiology programme was taking people, and I had useful experience in molecular biology from my first degree.

At USP, I met my husband, a virologist who also works at the university. To us, viruses are almost members of our family. When my daughter was younger, she used to say she knew some viruses better than her brothers.

Our lab works with seven hospitals in the Brazilian public-health system. We inspect samples, looking for 18 respiratory viruses, including the influenza virus H1N1 and SARS-CoV-2; for viruses transmitted by insects, such as dengue, Zika and yellow fever; and for viruses, such as measles, mumps and rubella, that mainly cause disease in children.

This pandemic isn't the first time my lab has worked on a public-health crisis. In 2019, we developed a test for the Zika virus. The kit, created in partnership with a private Brazilian company, is free for public hospitals.

Nature **599**, 172 (2021)

doi: <https://doi.org/10.1038/d41586-021-03001-8>

This article was downloaded by **calibre** from <https://www.nature.com/articles/d41586-021-03001-8>

Research

- **[A whale of an appetite revealed by analysis of prey consumption](#)** [03 November 2021]

News & Views • Reaching a deeper understanding of the ocean ecosystems that maintain whales might aid conservation efforts. Measurements of the animals' krill intake indicate that previous figures were substantial underestimates.

- **[A machine-learning algorithm to target COVID testing of travellers](#)** [22 September 2021]

News & Views • Optimizing the testing of incoming travellers for COVID-19 involves predicting those who are most likely to test positive. A machine-learning algorithm for targeted testing has been implemented at the Greek border.

- **[Relativity could ensure security for cash machines](#)** [03 November 2021]

News & Views • Entering your personal identification number using the keypad of a cash machine is notoriously insecure. A clever application of the special theory of relativity could make identification safer.

- **[A two-step hormone-signalling mechanism that drives physical activity](#)** [13 October 2021]

News & Views • In mice, the ovarian hormone oestradiol sensitizes neurons in a brain region called the hypothalamus to a melanocortin hormone that signals an energy surplus. Their dual activation increases physical activity.

- **[Nanometre-scale imaging and AI reveal the interior of whole cells](#)** [25 October 2021]

News & Views • Efforts to generate nanoscale-resolution images of cell interiors have gained ground through the development and refinement of a microscopy method. The data sets are publicly available as resources for further discoveries.

- **[Ethics of DNA research on human remains: five globally applicable guidelines](#)** [20 October 2021]

Perspective • In this Perspective, a group representing a range of stakeholders makes the case for a set of five proposed globally applicable ethical guidelines for ancient human DNA research.

- **[Experimental relativistic zero-knowledge proofs](#)** [03 November 2021]

Article • A zero-knowledge proof, which can be used to verify secret information, is reported here with security that is enforced by the laws of special relativity.

- **Signatures of bosonic Landau levels in a finite-momentum superconductor** [03 November 2021]

Article • Using torque magnetometry, the thermodynamic signatures of bosonic Landau level transitions are observed in a layered superconductor, owing to the formation of Cooper pairs with finite momentum.

- **Reconstruction of Bloch wavefunctions of holes in a semiconductor** [03 November 2021]

Article • Bloch wavefunctions of two types of hole in gallium arsenide are reconstructed by measuring the polarization of light emitted by collisions of electrons and holes accelerated by a terahertz laser.

- **Percolation transitions in compressed SiO₂ glasses** [03 November 2021]

Article • Amorphous–amorphous phase transitions in silicon dioxide are shown to proceed through a sequence of percolation transitions, a process that has relevance to a range of important liquid and glassy systems.

- **Transition metal-catalysed molecular n-doping of organic semiconductors** [03 November 2021]

Article • Electron doping of organic semiconductors is typically inefficient, but here a precursor molecular dopant is used to deliver higher n-doping efficiency in a much shorter doping time.

- **Episodic deluges in simulated hothouse climates** [03 November 2021]

Article • Through an idealized set of simulations, with a model that incorporates key physics, research reveals dramatic swings between massive rainfall events and extended dry periods in hothouse climates.

- **Carbon implications of marginal oils from market-derived demand shocks** [03 November 2021]

Article • Here the non-linear relationship is revealed between carbon emissions reductions and oil demand reductions, which depends on the magnitude of demand drop and the global oil market structure.

- **Baleen whale prey consumption based on high-resolution foraging measurements** [03 November 2021]

Article • A combination of 3D whale locations and acoustic measurements of prey density is used here to show that whales' consumption of krill is several times larger than often thought.

- **Disease variant prediction with deep generative models of evolutionary data** [27 October 2021]

Article • A new computational method, EVE, classifies human genetic variants in disease genes using deep generative models trained solely on evolutionary sequences.

- **5-HT modulation of a medial septal circuit tunes social memory stability** [06 October 2021]

Article • Experiments in mice identify the medial septum as an extrahippocampal input region that is critical for social memory formation, and show that modulation of the medial septum by serotonin regulates the stability of social memories.

- **Neurotoxic reactive astrocytes induce cell death via saturated lipids** [06 October 2021]

Article • Astrocytes can respond to diseases and injuries of the central nervous system by driving the death of neurons and mature oligodendrocytes through the delivery of long-chain saturated fatty acids contained in lipoparticles.

- **Efficient and targeted COVID-19 border testing via reinforcement learning** [22 September 2021]

Article • A study reports the design and performance of a reinforcement learning algorithm that enabled efficient and targeted SARS-CoV-2 testing of passengers travelling to Greece in the summer of 2020.

- **SARS-CoV-2 B.1.617.2 Delta variant replication and immune evasion** [06 September 2021]

Article • A study of SARS-CoV-2 variants examining their transmission, infectivity, and potential resistance to therapies provides insights into the biology of the Delta variant and its role in the global pandemic.

- **Unravelling the collateral damage of antibiotics on gut bacteria** [13 October 2021]

Article • This study systematically profiles the activity of several classes of antibiotics on gut commensal bacteria and identifies drugs that mitigate their collateral damage on commensal bacteria without compromising their efficacy against pathogens.

- **Regulation of intestinal immunity and tissue repair by enteric glia** [20 October 2021]

Article • Enteric glial cells have tissue-wide immunoregulatory roles through the upregulation of IFN γ -dependent genes both at steady state and after parasite infection, promoting immune homeostasis and CXCL10-mediated tissue repair after pathogen-induced intestinal damage in mice.

- **Oestrogen engages brain MC4R signalling to drive physical activity in female mice** [13 October 2021]

Article • A subset of oestrogen-sensitive neurons integrate melanocortin and oestrogen signalling to rebalance energy allocation in female mice leading to reduced sedentary behaviour and decreasing obesity in oestrogen-depleted female mice

- **SLC25A39 is necessary for mitochondrial glutathione import in mammalian cells** [27 October 2021]

Article • SLC25A39 and its parologue SLC25A40 have redundant roles in the import of glutathione into mitochondria of mammalian cells.

- **Whole-cell organelle segmentation in volume electron microscopy** [06 October 2021]

Article • Focused ion beam scanning electron microscopy (FIB-SEM) combined with deep-learning-based segmentation is used to produce three-dimensional reconstructions of complete cells and tissues, in which up to 35 different organelle classes are annotated.

- **An open-access volume electron microscopy atlas of whole cells and tissues** [06 October 2021]

Article • Open-access 3D images of whole cells and tissues with combined finer resolution and larger sample size are enabled by advances in focused ion beam-scanning electron microscopy.

- **Systems-level effects of allosteric perturbations to a model molecular switch** [13 October 2021]

Article • Interface mutations in the GTPase switch protein Gsp1 (the yeast homologue of human RAN) allosterically affect the kinetics of the switch cycle, revealing a systems-level mechanism of multi-specificity.

- **Structural basis of gating modulation of Kv4 channel complexes** [22 September 2021]

Article • Cryo-electron microscopy structures of the voltage-gated potassium channel Kv4.2 alone and in complex with auxiliary subunits (DPP6S and/or KChIP1) reveal the distinct mechanisms of these two different subunits in modulating channel activity.

- NEWS AND VIEWS
- 03 November 2021

A whale of an appetite revealed by analysis of prey consumption

Reaching a deeper understanding of the ocean ecosystems that maintain whales might aid conservation efforts. Measurements of the animals' krill intake indicate that previous figures were substantial underestimates.

- [Victor Smetacek](#) 0

Baleen whales are the largest known animals that have ever lived. They feed on centimetre-sized prey by filtering seawater through plates of frayed, bristle-like combs, termed baleen, that are fixed to their upper jaws. Previous estimates of the food requirements of whale populations indicate the animals' enormous food demand¹. In the Southern Ocean near Antarctica, before the whaling era, the krill biomass consumed by whales alone is estimated to have been 190 million tonnes annually¹, an amount substantially greater than the entire annual world fish catch in modern times². Intense fishing by humans has decimated ocean fish stocks in a few decades. By contrast, whale feeding seems to be sustainable, as evidenced by hallmarks of the animals' evolution, such as their long lifespan and high degree of specialization geared to the consumption of just one prey — krill.

Access options

Subscribe to Journal

Get full journal access for 1 year

\$199.00

only \$3.90 per issue

Subscribe

All prices are NET prices.

VAT will be added later in the checkout.

Tax calculation will be finalised during checkout.

Rent or Buy article

Get time limited or full article access on ReadCube.

from \$8.99

Rent or Buy

All prices are NET prices.

Additional access options:

- [Log in](#)
- [Learn about institutional subscriptions](#)

Nature **599**, 33-34 (2021)

doi: <https://doi.org/10.1038/d41586-021-02951-3>

References

1. 1.

Laws, R. M. *Phil. Trans. R. Soc. B* **279**, 81–96 (1977).

2. 2.

Pauly, D. & Zeller, D. *Nature Commun.* **7**, 10244 (2016).

3. 3.

Savoca, M. S. *et al.* *Nature* **599**, 85–90 (2021).

4. 4.

Goldbogen, J. A. *et al.* *Science* **366**, 1367–1372 (2019)

5. 5.

Williams, T. M. *Science* **366**, 1316–1317 (2019).

6. 6.

Smetacek, V. in *Impacts of Global Warming on Polar Ecosystems* (ed. Duarte, C. M.) 45–81 (Fund. BBVA, 2008).

7. 7.

Nicol, S. *et al.* *Fish Fish.* **11**, 203–209 (2010).

8. 8.

Smetacek, V. *Protist* **169**, 791–802 (2018).

9. 9.

González, H. E. *Polar Biol.* **12**, 81–91 (1992).

10. 10.

Holm-Hansen, O. & Huntley, M. *J. Crustac. Biol.* **4** (5), 156–173 (1984).

11. 11.

Hart, T. J. *Discov. Rep.* **21**, 261–356 (1942).

12. 12.

Hardy, A. *Great Waters: A Voyage of Natural History to Study Whales, Plankton and the Waters of the Southern Ocean* (Harper & Row, 1967).

13. 13.

Bar-On, Y. M., Phillips, R. & Milo, R. *Proc. Natl Acad. Sci. USA* **115**, 6506–6511 (2018).

This article was downloaded by **calibre** from <https://www.nature.com/articles/d41586-021-02951-3>

| [Section menu](#) | [Main menu](#) |

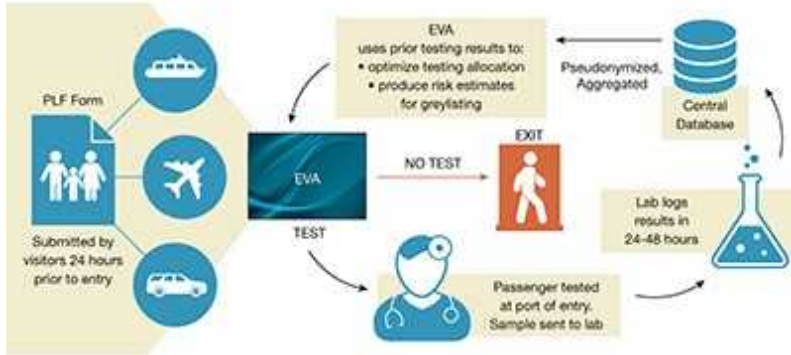
- NEWS AND VIEWS
- 22 September 2021

A machine-learning algorithm to target COVID testing of travellers

Optimizing the testing of incoming travellers for COVID-19 involves predicting those who are most likely to test positive. A machine-learning algorithm for targeted testing has been implemented at the Greek border.

- [Ziad Obermeyer](#) 0

It seems an obvious combination: machine learning and the fight against COVID-19. And yet, despite intense interest and increasing availability of large data sets, success stories of such combinations are few and far between. [Writing in Nature](#), Bastani *et al.*¹ describe a system that they designed and deployed at points of entry into Greece, starting in August 2020. The algorithm, which is built on a method called reinforcement learning, markedly increased the efficiency of testing for the coronavirus SARS-CoV-2, and contributed to Greece's ability to keep its borders open safely. The work also provides a clear warning about the shortcomings of the comparatively blunt policy tools that most other countries continue to use.



[Read the paper: Efficient and targeted COVID-19 border testing via reinforcement learning](#)

Testing is a problem that machine learning is well suited to solve. Imagine a border-control agent on a Greek island. A flight has just landed, and the agent's task is to identify and detain anyone who has COVID-19. The agent might want to test all arriving passengers, but the testing capacity on the island is very limited and, more generally, it is never possible to test 100% of any population 100% of the time. The alternative — shutting down the border completely, in an economy highly dependent on tourism — has its own perils. These would include not only a huge financial cost associated with the loss of jobs and income, but also the negative effects of such losses on public health². So the border agent faces a difficult decision: who should be tested?

As has been noted³, the value of a test depends on its eventual outcome. In this scenario, a negative test generates only costs: the cost of testing and a delay for the traveller. By contrast, a positive test generates tremendous benefit: prevention of all the cases of COVID-19 that a traveller infected with SARS-CoV-2 would have caused. So, in deciding who to test, the border agent's optimal strategy is clear: predict which travellers have the highest likelihood of testing positive, and test them. This strategy maximizes the value of testing, because it detects the most travellers with COVID-19 using the lowest number of tests.

If the border agent could predict which incoming passengers are most likely to test positive, tests could be allocated efficiently (Fig. 1). Conveniently, data about incoming passengers — their country and region of origin, age and sex — are available digitally, on the passenger locator form that all travellers complete 24 hours before arrival in Greece. It seems straightforward enough to use data from past tests of incoming passengers to predict which ‘types’ of passenger might be more likely to test positive in the future. But, as decades of research in statistics and computer science have shown⁴, this strategy runs the risk of getting locked into yesterday’s pandemic: given the rapidly evolving dynamics of COVID-19 spread, an algorithm must quickly adapt its predictions to stay one step ahead and still test the right passengers.

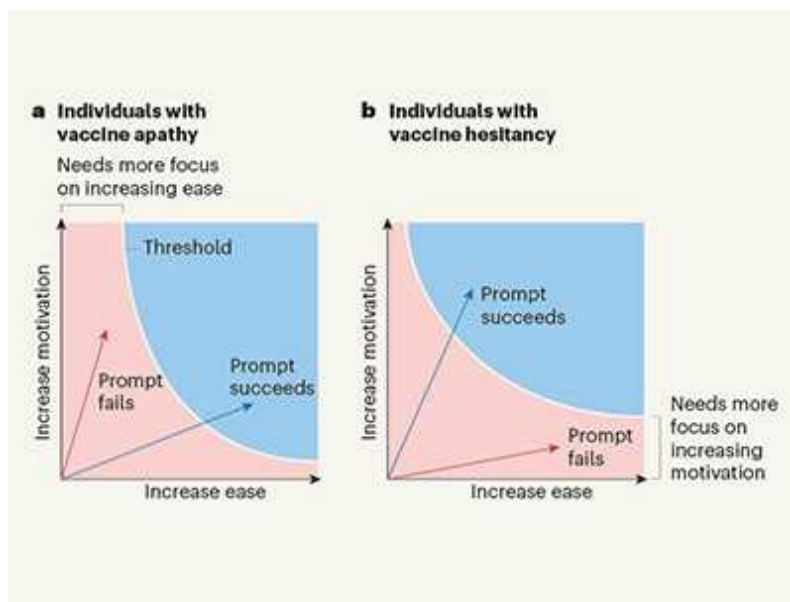


Figure 1 | COVID-19 testing of travellers arriving at Eleftherios Venizelos International Airport in Athens. Credit: Milos Bicanski/Getty

This is where the value of machine learning becomes clear. Just as an algorithm can be trained to play the game Go⁵ by learning which moves lead to winning the game, Bastani and colleagues trained an algorithm to allocate scarce tests, by learning which passengers are likely to test positive.

Crucially, the algorithm balances two goals. The first, and most natural, goal is to test passenger types who are likely to test positive, by exploiting patterns learnt from previous data about the outcome of tests for SARS-CoV-2 in these different groups. The second — perhaps less intuitive, but equally important — is to explore patterns not reflected in previous data, by testing passenger types about which the algorithm knows little.

Then, at a given port of entry on a given day, the algorithm delivers targeted recommendations to border agents about which passengers to test, while respecting the budget and resource constraints imposed by supply chains, staffing, laboratory capacity and delivery logistics for biological samples. These constraints are real and binding: the authors note that, at the peak of the summer tourism season, there was capacity to test only 18.4% of incoming travellers — even after the Greek National COVID-19 Committee of Experts wisely approved group testing to drive efficiency gains in the lab.



Text-message nudges encourage COVID vaccination

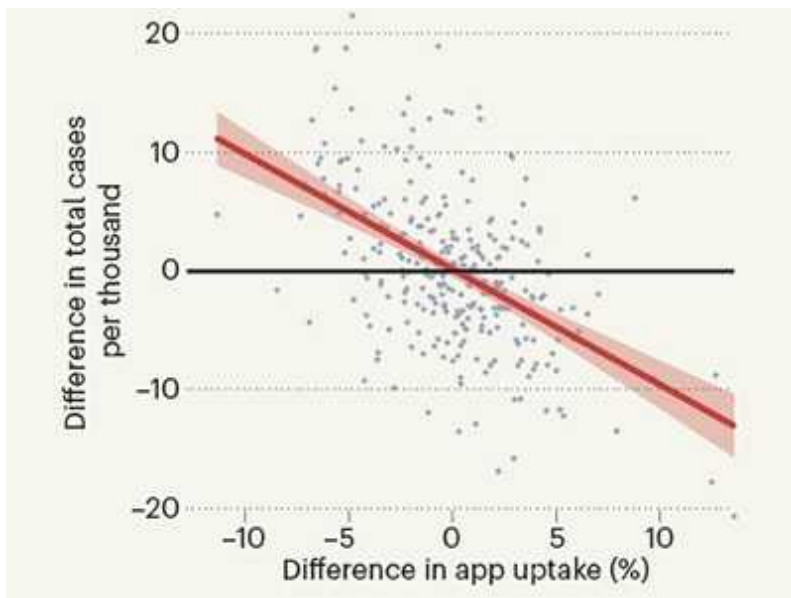
The authors draw on the reinforcement-learning strategies that have powered advances in online commerce and marketing⁶. But using such an algorithm in the real world raises its own technical challenges. For example, the algorithm must learn discontinuously, from large batches of testing results, rather than one-by-one from individual results. And the feedback from batch results is delayed, forcing the algorithm to operate uninformed while waiting

for results. Solving these challenges required substantial tweaking of the algorithms that are typically designed for easier, more data-rich online settings.

The thorniest challenges, however, are legal and political ones. To comply with the European Union's General Data Protection Regulation (GDPR), the authors deliberately limited the data available to the algorithm — and thus its accuracy — in close consultation with lawyers, epidemiologists and policymakers. The potential limit placed on the algorithm's performance by the GDPR highlights how well-intentioned laws to protect privacy can have both positive and negative consequences. In a pandemic that does not respect individuals' privacy, such regulations can ultimately hamper the ability of a government to protect the health of its citizens. The authors also adapted the algorithm with a policymaker audience in mind, choosing their optimization methods to showcase clearly the value of both algorithm goals: testing high-risk passengers and testing high-uncertainty passengers.

The results are impressive. The automated system doubled the efficiency of testing — the number of cases detected per test — allowing border agents to test and quarantine the right passengers, many of whom were asymptomatic, while letting others through to their final destination.

The success of the algorithm presented by Bastani and colleagues highlights the inadequacy of the border policies of nearly all other countries. The decisions underlying these policies — for example, whether to deny all travellers entry to the country or to force the testing or quarantine of all travellers from a given country — have two key flaws. First, these decisions are made about entire countries, rather than individuals, disregarding vast differences between people within countries. Second, they are typically made on the basis of country-level epidemiological data that, as the present study shows, have notable shortcomings.



Contact-tracing app curbed the spread of COVID in England and Wales

Had border agents denied entry to all passengers from countries that had concerning metrics, they would have prevented those people with COVID-19 from entering Greece — but at the cost of crushing a key pillar of the economy. Had they simply tested people proportional to a country's reported COVID-19 metrics rather than algorithmic predictions, however, their testing efficiency would have been much lower. This is because reported COVID-19 metrics can be very different from actual disease prevalence among incoming travellers. Travellers are not randomly drawn from their countries' populations, and passively collected data on cases of COVID-19 or deaths associated with the disease reflect large reporting biases and systemic barriers to access⁷.

Indeed, by efficiently testing incoming passengers, the authors' algorithm was able to anticipate spikes in SARS-CoV-2 infection rates among traveller populations almost 9 days earlier than if they had used country-level epidemiological data alone. This indicates the enormous value of intelligent, deliberate data collection — and the dangers of relying on blunt, flawed, country-level data for important decisions.

Bastani and colleagues' work will be remembered as one of the best examples of using data in the fight against COVID-19. It is a compelling story of how a group of researchers partnered with enlightened policymakers

to produce a tool that has enormous social value. It highlights the best parts of both academic research and the civil service, and shows the great promise of artificial intelligence for making good decisions — which in many settings can be the difference between life and death.

Nature **599**, 34–36 (2021)

doi: <https://doi.org/10.1038/d41586-021-02556-w>

References

1. 1.

Bastani, H. *et al.* *Nature* **599**, 108–113 (2021).

2. 2.

Marmot, M. & Wilkinson, R. (eds) *Social Determinants of Health* (Oxford Univ. Press, 2005).

3. 3.

Mullainathan, S. & Obermeyer, Z. *Diagnosing Physician Error: A Machine Learning Approach to Low-Value Health Care*. National Bureau of Economic Research Working Paper 26168 (2021).

4. 4.

Thompson, W. R. *Biometrika* **25**, 285–294 (1933).

5. 5.

Silver, D. *et al.* *Nature* **529**, 484–489 (2016).

6. 6.

Li, L., Chu, W., Langford, J. & Schapire, R. E. in *Proc. 19th Int. Conf. World Wide Web* 661–670 (2010).

7.7.

Wu, S. L. *et al. Nature Commun.* **11**, 4507 (2020).

This article was downloaded by **calibre** from <https://www.nature.com/articles/d41586-021-02556-w>

| [Section menu](#) | [Main menu](#) |

- NEWS AND VIEWS
- 03 November 2021

Relativity could ensure security for cash machines

Entering your personal identification number using the keypad of a cash machine is notoriously insecure. A clever application of the special theory of relativity could make identification safer.

- [Gilles Brassard](#) 

When you type in your personal identification number (PIN) at a cash machine, you feel safe — provided you cover the keypad with your hand. But even the machines attached to banks are vulnerable to attack by fraudsters, some of whom go as far as to add fake machinery to legitimate machines as a way of stealing PINs (see go.nature.com/3p9r431). To prevent this type of fraud, a solution is needed that allows people to prove their identity without disclosing any secret information. [Writing in Nature](#), Alikhani *et al.*¹ describe an experiment that achieves this goal with unprecedented security, guaranteed by Albert Einstein's special theory of relativity.

Access options

Subscribe to Journal

Get full journal access for 1 year

\$199.00

only \$3.90 per issue

Subscribe

All prices are NET prices.
VAT will be added later in the checkout.
Tax calculation will be finalised during checkout.

Rent or Buy article

Get time limited or full article access on ReadCube.
from \$8.99

Rent or Buy

All prices are NET prices.

Additional access options:

- [Log in](#)
- [Learn about institutional subscriptions](#)

Nature **599**, 36–37 (2021)

doi: <https://doi.org/10.1038/d41586-021-02950-4>

References

1. 1.

Alikhani, P. *et al.* *Nature* **599**, 47–50 (2021).

2. 2.

Goldwasser, S., Micali, S. & Rackoff, C. *SIAM J. Comput.* **18**, 186–208 (1989).

3. 3.

Goldreich, O., Micali, S. & Wigderson, A. *J. Assoc. Comput. Mach.* **38**, 690–728 (1991).

4. 4.

Feige, U., Fiat, A. & Shamir, A. *J. Cryptol.* **1**, 77–94 (1988).

5. 5.

Shor, P. W. *SIAM J. Comput.* **26**, 1484–1509 (1997).

6. 6.

Ben-Or, M., Goldwasser, S., Kilian, J. & Wigderson, A. in *Proc. 20th Annu. ACM Symp. Theory of Computing* 113–131 (ACM, 1988).

7. 7.

Crépeau, C., Massenet, A., Salvail, L., Stinchcombe, L. S. & Yang, N. in *Proc. 1st Conf. Information-Theoretic Cryptography* 4:1–4:18 (LIPIcs, 2020).

8. 8.

Einstein, A., Podolsky, B. & Rosen, N. *Phys. Rev.* **47**, 777–780 (1935).

9. 9.

Bell, J. S. *Physics* **1**, 195–200 (1964).

10. 10.

Crépeau, C., Salvail, L., Simard, J.-R. & Tapp, A. in *Adv. Cryptol. — ASIACRYPT 2011* 407–430 (Springer, 2011).

11. 11.

Chailloux, A. & Leverrier, A. in *Adv. Cryptol. — EUROCRYPT 2017 Part III*, 369–396 (Springer, 2017).

This article was downloaded by **calibre** from <https://www.nature.com/articles/d41586-021-02950-4>

| [Section menu](#) | [Main menu](#) |

- NEWS AND VIEWS
- 13 October 2021

A two-step hormone-signalling mechanism that drives physical activity

In mice, the ovarian hormone oestradiol sensitizes neurons in a brain region called the hypothalamus to a melanocortin hormone that signals an energy surplus. Their dual activation increases physical activity.

- [Stephanie L. Padilla](#) ⁰

Mammals become less physically active with ageing, and, in females, this decline in activity is tied to reproductive ageing. After menopause, women tend to be less active and to develop increased total fat mass and altered fat distribution¹. In rodents, surgical removal of the ovaries (ovariectomy) reduces the levels of ovarian hormones such as oestradiol in a similar way to the effects of menopause, and results in reduced physical activity and corresponding increases in weight. [Writing in Nature](#), Krause *et al.*² identify a population of neurons in the ventrolateral subdivision of the brain's ventromedial hypothalamus (VMH) that are sensitive to oestradiol. These neurons regulate the balance between sedentary behaviour and physical activity on the basis of perceived energy state, with menopause and the associated reduction in oestradiol causing a shift towards sedentary behaviour.

Access options

[Subscribe to Journal](#)

Get full journal access for 1 year

\$199.00

only \$3.90 per issue

[Subscribe](#)

All prices are NET prices.

VAT will be added later in the checkout.

Tax calculation will be finalised during checkout.

Rent or Buy article

Get time limited or full article access on ReadCube.

from \$8.99

[Rent or Buy](#)

All prices are NET prices.

Additional access options:

- [Log in](#)
- [Learn about institutional subscriptions](#)

Nature **599**, 37-39 (2021)

doi: <https://doi.org/10.1038/d41586-021-02725-x>

References

1. 1.

Toth, M. J., Tchernof, A., Sites, C. K. & Poehlman, E. T. *Int. J. Obes. Relat.* **24**, 226–231 (2000).

2. 2.

Krause, W. C. *et al. Nature* **599**, 131–135 (2021).

3. 3.

Heine, P. A., Taylor, J. A., Iwamoto, G. A., Lubahn, D. B. & Cooke, P. S. *Proc. Natl Acad. Sci. USA* **97**, 12729–12734 (2000).

4. 4.

Quarta, C. *et al. Nature Metab.* **3**, 299–308 (2021).

5. 5.

Lee, H. *et al. Nature* **509**, 627–632 (2014).

6. 6.

Xu, Y. *et al. Cell Metab.* **14**, 453–465 (2011).

7. 7.

Musatov, S. *et al. Proc. Natl Acad. Sci. USA* **104**, 2501–2506 (2007).

8. 8.

Matharu, N. *et al. Science* **363**, aau0629 (2019).

This article was downloaded by **calibre** from <https://www.nature.com/articles/d41586-021-02725-x>

- NEWS AND VIEWS
- 25 October 2021

Nanometre-scale imaging and AI reveal the interior of whole cells

Efforts to generate nanoscale-resolution images of cell interiors have gained ground through the development and refinement of a microscopy method. The data sets are publicly available as resources for further discoveries.

- [Jason R. Swedlow](#)⁰ &
- [Lucy Collinson](#)¹

One long-sought goal of cell biology is the full and complete determination of the structure and composition of a single cell. If we could name every molecule that makes up a cell, know each molecule's location, map how the molecules interact, and understand how they come together to construct organelles and determine organelle function, we would have the building blocks needed to understand cellular physiology. Writing in *Nature*, [Xu et al.](#)¹ and [Heinrich et al.](#)² present combined advances in data acquisition and machine-learning (ML)-based analysis in microscopy that move us closer to achieving this objective.

Access options

Subscribe to Journal

Get full journal access for 1 year

\$199.00

only \$3.90 per issue

Subscribe

All prices are NET prices.
VAT will be added later in the checkout.
Tax calculation will be finalised during checkout.

Rent or Buy article

Get time limited or full article access on ReadCube.

from \$8.99

Rent or Buy

All prices are NET prices.

Additional access options:

- [Log in](#)
- [Learn about institutional subscriptions](#)

Nature **599**, 39-40 (2021)

doi: <https://doi.org/10.1038/d41586-021-02776-0>

References

1. 1.

Xu, C. S. *et al.* *Nature* **599**, 147–151 (2021).

2. 2.

Heinrich, L. *et al.* *Nature* **599**, 141–146 (2021).

3. 3.

Heymann, J. A. W. *et al.* *J. Struct. Biol.* **155**, 63–73 (2006).

4. 4.

Hildebrand, D. G. C. *et al.* *Nature* **545**, 345–349 (2017).

5. 5.

Helmstaedter, M. *et al.* *Nature* **500**, 168–174 (2013).

6. 6.

Zheng, Z. *et al.* *Cell* **174**, 730–743 (2018).

7. 7.

Scheffer, L. K. *et al.* *eLife* **9**, e57443 (2020).

8. 8.

Müller, A. *et al.* *J. Cell Biol.* **220**, e202010039 (2021).

9. 9.

Perez, A. J. *et al.* *Front. Neuroanat.* **8**, 126 (2014).

10. 10.

Liu, J. *et al.* *Front. Neurosci.* **14**, 599 (2020).

11. 11.

Guay, M. D. *et al.* *Sci. Rep.* **11**, 2561 (2021).

12. 12.

Spiers, H. *et al.* *Traffic* **22**, 240–253 (2021).

13. 13.

Hollandi, R. *et al.* *Cell Syst.* **10**, 453–458 (2020).

14. 14.

Stringer, C., Wang, T., Michaelos, M. & Pachitariu, M. *Nature Methods* **18**, 100–106 (2021).

15. 15.

Schmidt, U., Weigert, M., Broaddus, C. & Myers, G. in *Medical Image Computing and Computer Assisted Intervention – MICCAI 2018* (eds Frangi, A. F., Schnabel, J. A., Davatzikos, C., López Alberola, C. & Fichtinger, G.) 265–273 (Springer, 2018).

16. 16.

Ellenberg, J. *et al.* *Nature Methods* **15**, 849–854 (2018).

This article was downloaded by **calibre** from <https://www.nature.com/articles/d41586-021-02776-0>

| [Section menu](#) | [Main menu](#) |

- Perspective
- [Published: 20 October 2021](#)

Ethics of DNA research on human remains: five globally applicable guidelines

- [Songül Alpaslan-Roodenberg^{1,2}](#),
- [David Anthony^{3,4}](#),
- [Hiba Babiker⁵](#),
- [Eszter Bánffy](#) [ORCID: orcid.org/0000-0001-5156-826X⁶](#),
- [Thomas Booth⁷](#),
- [Patricia Capone⁸](#),
- [Arati Deshpande-Mukherjee⁹](#),
- [Stefanie Eisenmann](#) [ORCID: orcid.org/0000-0002-6301-5889^{5,10}](#),
- [Lars Fehren-Schmitz](#) [ORCID: orcid.org/0000-0001-5510-1114^{11,12}](#),
- [Michael Frachetti](#) [ORCID: orcid.org/0000-0001-6906-4334¹³](#),
- [Ricardo Fujita¹⁴](#),
- [Catherine J. Frieman](#) [ORCID: orcid.org/0000-0002-9030-4483¹⁵](#),
- [Qiaomei Fu](#) [ORCID: orcid.org/0000-0002-7141-0002¹⁶](#),
- [Victoria Gibbon](#) [ORCID: orcid.org/0000-0001-7875-3297¹⁷](#),
- [Wolfgang Haak](#) [ORCID: orcid.org/0000-0003-2475-2007⁵](#),
- [Mateja Hajdinjak](#) [ORCID: orcid.org/0000-0002-4064-0331⁷](#),
- [Kerstin P. Hofmann](#) [ORCID: orcid.org/0000-0003-4405-5751⁶](#),
- [Brian Holguin¹⁸](#),
- [Takeshi Inomata¹⁹](#),
- [Hideaki Kanzawa-Kiriyama²⁰](#),
- [William Keegan²¹](#),
- [Janet Kelso](#) [ORCID: orcid.org/0000-0002-3618-322X¹⁰](#),
- [Johannes Krause](#) [ORCID: orcid.org/0000-0001-9144-3920¹⁰](#),

- [Ganesan Kumaresan](#) ORCID: orcid.org/0000-0003-0533-3181²²,
- [Chapurukha Kusimba](#)²³,
- [Sibel Kusimba](#)²³,
- [Carles Laluez-Fox](#)²⁴,
- [Bastien Llamas](#) ORCID: orcid.org/0000-0002-5550-9176^{25,26},
- [Scott MacEachern](#) ORCID: orcid.org/0000-0002-4859-3998²⁷,
- [Swapan Mallick](#)^{1,28,29},
- [Hirofumi Matsumura](#) ORCID: orcid.org/0000-0001-5453-7987³⁰,
- [Ana Y. Morales-Arce](#) ORCID: orcid.org/0000-0002-2934-3141³¹,
- [Giedre Motuzaitė Matuzevičiūtė](#) ORCID: orcid.org/0000-0001-9069-1551³²,
- [Veena Mushrif-Tripathy](#) ORCID: orcid.org/0000-0002-4749-1316⁹,
- [Nathan Nakatsuka](#)¹,
- [Rodrigo Nores](#)³³,
- [Christine Ogola](#)³⁴,
- [Mercedes Okumura](#)³⁵,
- [Nick Patterson](#)^{4,29},
- [Ron Pinhasi](#) ORCID: orcid.org/0000-0003-1629-8131^{2,36},
- [Samayamantri P. R. Prasad](#)³⁷,
- [Mary E. Prendergast](#) ORCID: orcid.org/0000-0003-0275-6795³⁸,
- [Jose Luis Punzo](#) ORCID: orcid.org/0000-0002-1025-9169³⁹,
- [David Reich](#) ORCID: orcid.org/0000-0002-7037-5292^{1,4,28,29},
- [Rikai Sawafuji](#) ORCID: orcid.org/0000-0002-8174-2326⁴⁰,
- [Elizabeth Sawchuk](#)^{41,42},
- [Stephan Schiffels](#) ORCID: orcid.org/0000-0002-1017-9150^{5,10},
- [Jakob Sedig](#) ORCID: orcid.org/0000-0001-6642-7734^{1,4},
- [Svetlana Shnaider](#)⁴³,
- [Kendra Sirak](#) ORCID: orcid.org/0000-0003-2347-3479^{1,4},
- [Pontus Skoglund](#) ORCID: orcid.org/0000-0002-3021-5913⁷,
- [Viviane Slon](#)^{44,45},
- [Meradeth Snow](#)⁴⁶,
- [Marie Soressi](#) ORCID: orcid.org/0000-0003-1733-7745⁴⁷,
- [Matthew Spriggs](#) ORCID: orcid.org/0000-0002-7293-6778^{15,48},

- [Philip W. Stockhammer](#) ORCID: [orcid.org/0000-0003-4702-9372](#)^{10,49},
- [Anna Szécsényi-Nagy](#) ORCID: [orcid.org/0000-0003-2095-738X](#)⁵⁰,
- [Kumarasamy Thangaraj](#)^{37,51},
- [Vera Tiesler](#) ORCID: [orcid.org/0000-0003-0532-5819](#)⁵²,
- [Ray Tobler](#)^{23,25},
- [Chuan-Chao Wang](#) ORCID: [orcid.org/0000-0001-9628-0307](#)^{53,54},
- [Christina Warinner](#)^{10,55},
- [Surangi Yasawardene](#) ORCID: [orcid.org/0000-0002-9193-4372](#)⁵⁶ &
- [Muhammad Zahir](#) ORCID: [orcid.org/0000-0002-1765-6319](#)^{5,57}

Nature volume 599, pages 41–46 (2021)

- 15k Accesses
- 290 Altmetric
- [Metrics details](#)

Subjects

- [Archaeology](#)
- [Ethics](#)
- [Genomics](#)

Abstract

We are a group of archaeologists, anthropologists, curators and geneticists representing diverse global communities and 31 countries. All of us met in a virtual workshop dedicated to ethics in ancient DNA research held in November 2020. There was widespread agreement that globally applicable ethical guidelines are needed, but that recent recommendations grounded in discussion about research on human remains from North America are not always generalizable worldwide. Here we propose the following globally applicable guidelines, taking into consideration diverse contexts. These hold that: (1) researchers must ensure that all regulations were followed in

the places where they work and from which the human remains derived; (2) researchers must prepare a detailed plan prior to beginning any study; (3) researchers must minimize damage to human remains; (4) researchers must ensure that data are made available following publication to allow critical re-examination of scientific findings; and (5) researchers must engage with other stakeholders from the beginning of a study and ensure respect and sensitivity to stakeholder perspectives. We commit to adhering to these guidelines and expect they will promote a high ethical standard in DNA research on human remains going forward.

Main

The analysis of ancient human genomes has emerged as a powerful approach for investigating the relationships of people who lived in the past to each other and to people living today. A consistent theme is that people in any given location across time are usually there as the result of a long history of mobility and interaction. Over the past decade, ancient DNA has provided new evidence—adding to that from other disciplines—refuting myths of the ‘purity’ of any population and falsifying racist and nationalistic narratives. While some have sought to misuse genetics as a tool for determining group belonging, in our opinion it is inappropriate for genetic data to be used as an arbiter of identity¹.

The rapid increase in published genome-wide data from ancient humans—from none in 2009 to more than six thousand individuals today—has been accompanied by growing discussions about how to conduct ancient DNA research ethically^{2,3,4,5,6,7,8,9,10,11,12,13,14,15,16}, building on earlier conversations^{17,18,19,20,21,22,23,24}. The ethics of DNA research has a particular urgency because of the rapid growth of the field, the social and political impacts of studying ancestry, and the fact that ancient DNA work analyses once-living people who must be respected.

Institutional or governmental guidelines for obtaining permission to analyse ancient individuals vary and do not always ensure ethical and engaged research. Researchers have an obligation to meet a higher standard than some governing bodies may require, but there is no consensus on what this

entails^{11,25,26,27}. Increasingly, publications on ancient DNA have included statements describing how the research team addressed ethical issues^{28,29,30,31,32,33,34,35,36,37,38}, a development that we support.

Professional organizations are also beginning to articulate guidelines^{15,39}, and at least one grant has been awarded to explore these issues in the context of research on ancient North Americans

(<http://www.adnaethics.org/>). Notably lacking has been a statement on ethics co-signed by an internationally diverse and representative group of scholars engaged in ancient DNA research.

We convened more than 60 archaeologists, anthropologists, curators and geneticists representing more than 30 countries and diverse global communities for a virtual workshop on ethics on 4 and 5 November 2020. All participants are committed to carrying out research on DNA from human remains that is ethically responsible and sensitive to diverse perspectives held by stakeholders (people who have a connection to a study, including descendant communities, those responsible for the stewardship of human remains, and researchers). Here we present case studies from a variety of global contexts to illustrate the breadth of issues surrounding community and Indigenous group consultation, highlighting how the relevant issues vary worldwide. We then provide guidelines for DNA research on human remains that apply globally (Box 1).

Box 1 Five globally applicable guidelines for DNA research on human remains

- (1) Researchers must ensure that all regulations were followed in the places where they work and from which the human remains derived.
- (2) Researchers must prepare a detailed plan prior to beginning any study.
- (3) Researchers must minimize damage to human remains.
- (4) Researchers must ensure that data are made available following publication to allow critical re-examination of scientific findings.

(5) Researchers must engage with stakeholders from the beginning of a study and ensure respect and sensitivity to other stakeholder perspectives.

Community ethical engagement is context-specific

Much of the literature about ethical DNA research on ancient individuals has focused on the USA^{3,4,13,15}. These discussions have produced recommendations to promote engagement between researchers and Indigenous communities, summarized in the research guidance published by the American Society of Human Genetics, which suggests that all ancient DNA studies should involve formal consultation, address cultural and ethical considerations, engage communities and support capacity building, develop plans for reporting and managing data, and develop plans for long-term responsibility and stewardship¹⁵.

Making Indigenous perspectives central is critical in regions with histories of settler colonialism, expropriation of Indigenous lands and artifacts, and persistent disenfranchisement of Indigenous communities; not consulting with communities can cause harm in such contexts^{5,6}. In the USA, all ancient Native American remains held in federally funded institutions fall under the purview of the Native American Graves Protection and Repatriation Act (NAGPRA), which mandates that institutions consult with and seek to transfer the remains of ancient individuals (culturally identifiable or not) to Indigenous groups. In Australia, analogous laws seek to repatriate human remains, in some cases up to 40,000 years old⁴⁰, that have been removed from Aboriginal and Torres Strait Islander communities^{41,42}. However, when carrying out research on the remains of ancient individuals where there are few (if any) material or oral links to present-day groups, or where promoting the idea that some groups have more ownership of cultural heritage than others can contribute to social conflict, an Indigenous-centred ethical framework mandating that each ancient individual be associated with a contemporary group does not fit.

Representation of Indigenous perspectives

In many countries in the Americas, Indigenous heritage is embedded in national identity and integrated into governmental cultural institutions. For instance, following Independence in Mexico, mestizos (people of mixed ancestry)—who form the great majority—embraced legacies from the Nahua (Aztec), Maya, Zapotec and other Indigenous groups as an integral part of national identity^{[43,44,45](#)}. In Peru, the Ministry of Culture was created in the context of *indigenismo*, a movement with the goal of promoting Indigenous culture and fighting discrimination^{[46,47,48](#)}. In such contexts, the process of seeking approval from government or heritage organizations for analysis of human remains can be a robust form of engagement, and adopting a US template can be counterproductive. We have had multiple experiences of writing papers about ancient DNA from Central and South America and receiving reviews stating the work did not conform to standards for Indigenous engagement developed in the USA^{[3,4](#)}. Those of us who are from Mexico and Central and South America have felt that such reviews have been paternalistic at best and colonialist at worst, especially given that many places have embraced Indigenous heritage and embedded it into government approval processes and cultural institutions to a greater extent than has been done in the USA.

There is wide variation, however, in the nature of relationships between governments and Indigenous communities in the Americas, and researchers must take a case-by-case approach to determining when additional consultation is needed. In Peru and Mexico, groups for whom Indigenous heritage is an important part of identity have variable degrees of representation in the government. In Brazil, Indigenous communities are often disenfranchised, and there is no legal mechanism for Indigenous groups to have a voice in the fate of archaeological materials associated with their ancestors^{[49](#)}. In Argentina, a legal mandate that community consent must be obtained to carry out any project involving Indigenous heritage is not always followed. In Guatemala, the Maya and other Indigenous groups who form roughly half the population remain marginalized. In such contexts it is the ethical responsibility of members of an ancient DNA research team to carry out additional outreach beyond what is mandated to incorporate Indigenous perspectives.

Global differences in the meaning of Indigeneity

The meaning of Indigeneity varies globally. In Africa, descendants of colonized groups are now overwhelmingly in power, and Indigeneity often refers more to political or social marginalization on the basis of identity than to traditions of how long groups have been established in a region⁵⁰. Many African communities have complex connections to the lands on which they live, including histories of colonial and postcolonial displacement and disruption. In some regions, people do not recognize past local populations as their relatives. This may be owing to contemporary religious or cultural belief systems being different from past ones⁵¹, collective memories of migrations from elsewhere, fear of reprisal for being linked with other groups, and the continuing aftershocks of decisions made during European colonization that fractured socio-political landscapes and still contribute to violence and displacements. In these situations, careful consultation among stakeholders is necessary, from local groups to government representatives, to ensure that vesting decision-making power about cultural heritage does not aggravate social conflict. In such cases, making Indigeneity a central principle for permitting ancient DNA analysis would probably be harmful.

A more pressing issue related to ancient DNA research in Africa (and in many other regions) is confronting the colonial legacies of human remains collected in unethical ways and often sent abroad^{52,53}. Researchers must work with both the curating institution and with scholars from the country of origin to seek permissions to study the remains of ancient individuals, and engage in discussions about provenance, historical injustices, repatriation and restitution as part of their work^{54,55,56} (<https://www.globalcodeofconduct.org/affiliated-codes/>). A related challenge is the history of non-equitable and often exploitative research in Africa by predominantly European and North American scientists, with minimal local engagement^{25,26,27}. Foreign researchers must prioritize establishing equitable collaborations, which may include training and other capacity building that empowers stakeholders to shape research questions and designs⁵⁷.

Potential harm from emphasizing group identity

There are many places in the world where discussions about who is Indigenous have contributed to xenophobic and nationalistic narratives. In these places, using Indigenous identity to determine who can permit ancient DNA research can be harmful, as it can contribute to conflict among groups and to discrimination.

In India, for example, many people avoid asking about caste and religious background because of a long history of abuse based on group identity, and indeed discrimination on the basis of caste is outlawed. The very exercise of trying to determine what groups today have more of a claim to ancient heritage than others has not only contributed to conflict, but is also made almost meaningless in much of South Asia, owing to the fact that the great majority of groups today are mixtures of the same populations whose ancestors have resided in the subcontinent for millennia^{[58,59](#)}; however, there are cases in which it is clear who is Indigenous, such as in the Andaman Islands^{[60](#)}. There are official procedures in many parts of South Asia for protecting cultural heritage, and working within this framework is an important mechanism for protecting communities from harm.

In West Eurasia, the suggestion that groups who claim local origins should have a special status has contributed to xenophobia and genocide. Nationalists promoting the idea of ‘blood and soil’ during the Nazi period twisted archaeological research to legitimize land seizures by claiming that skeletons excavated in eastern Europe had a ‘Germanic’ morphology^{[61](#)}. European archaeologists have worked for decades to deconstruct narratives that claim ownership of cultural heritage by specific groups. Ancient DNA research ethics in a West Eurasian context must follow this movement away from the use of self-identified notions of ancestral connections to certain lands^{[61,62](#)}, while simultaneously ensuring respect for the perspectives of national minorities who have been the subject of discrimination. The danger of government leaders citing archaeological and ancient DNA research to support favoured narratives of group identity that can then be used to justify exclusionary policies is not just theoretical, but is an ongoing problem in some countries in West Eurasia today, including in Hungary and Israel^{[63,64,65](#)}.

Five globally applicable guidelines

We present five guidelines to promote robust ethical standards in ancient DNA research that apply across the breadth of research contexts discussed above, as well as other major world regions that we have not discussed owing to space limitations, including Central Asia, Siberia, East Asia, Southeast Asia and Oceania (Box 1). We begin with guidelines that address issues of scientific ethics and then return to the topic of ensuring sensitivity of research to perspectives of communities, including Indigenous groups.

(1) *Researchers must ensure that all regulations were followed in the places where they work and from which the human remains derived.* Researchers must consider whether it is ethical to carry out ancient DNA research given the environment in the place from which they sample human remains. Once engaged in a project, researchers must abide by all local regulations. While this may seem obvious, the experience of some co-authors is that ancient DNA researchers have not always followed all agreements. For example, it may be necessary to obtain multiple levels of permission for scientific analysis or export of biological material from institutional, local, regional or national bodies, and to provide reports to curating institutions according to agreed timelines. Where local regulations are insufficient⁶⁶, researchers must adhere to a higher standard following the principles below.

(2) *Researchers must prepare a detailed plan prior to beginning any study.* This should include an articulation of research questions; a description of the techniques to be used and expected impact on remains (including skeletal elements to be studied and quantity to be used); a description of the type of DNA data that will be generated; any plan for material sharing with collaborating laboratories; a timeline for the return of unused material and sharing of results; a plan for how, where and by whom results will be disseminated; a plan for capacity building or training in settings where this can be of value; and a plan for data storage and sharing agreed by stakeholders and complying with open data principles⁶⁷. The plan should define the scope of the research and honestly communicate possible outcomes, recognizing that the analysis of genetic data can lead in unanticipated directions. Such a plan creates a record of the intended research that can be referred to later should there be a deviation from it.

Adjustments to the study design should occur only with the support of those involved in the original agreement: researchers must acknowledge that when permission is granted to study the remains of ancient individuals, they become the stewards of that material for the purpose for which consent was obtained, but that ‘ownership’ is not transferred⁶⁸. It is the responsibility of the researchers to share their plan with those responsible for the human remains and other groups whose perspectives need to be reflected; as such, it should be written in a way that is accessible to a non-specialist audience. If appropriate and agreed upon by all relevant parties, a pathway toward repatriation of human remains curated outside their area of origin may be outlined in the research plan.

(3) *Researchers must minimize damage to human remains.* Minimizing the impact of research on anthropological collections is especially important given the recent focus on a single skeletal element—the petrous bone—that often yields many-fold more human genetic data than other elements^{69,70,71,72}. Researchers should develop a strategy through consultation with other stakeholders to balance concerns about protecting remains with their scientific analysis. Researchers should not collect human remains without training in best practice techniques to minimize damage while maximizing yield of useable data^{11,12,73,74,75,76}. Researchers should not sample more material than necessary to be able to address their scientific questions, should provide documentation to those responsible for human remains noting when sampling occurred, and should report negative results to prevent repeated analysis using similar methods on remains with poor DNA preservation. Before sampling, morphology should be documented with high-resolution photography and bioarchaeological assessment. At least for very ancient individuals or those from unique contexts, micro-CT scans or casts should be produced, and there should be discussion about whether analysis of faunal or non-diagnostic remains should take place first to evaluate DNA preservation at a site.

Once sampling has occurred, responsible treatment of remains can also be promoted through the sharing of material as well as derived molecular products such as DNA extracts and libraries, which reduces the need for additional sampling in subsequent studies. Researchers have the responsibility to maintain derived molecular products for the purposes of

study replication. We also encourage researchers to seek approval for sharing sampled human remains and derived products between laboratories. This facilitates reappraisal of the questions addressed in the original study, as well as additional analyses beyond the scope of the initial study, as long as such uses are consistent with an approved research plan.

(4) Researchers must ensure that data are made available following publication to allow critical re-examination of scientific findings. Ancient DNA data must be published in a timely manner and subsequently made available at least for the purpose of critical reappraisal of results^{77,78}. Scientists cannot ethically participate in a study if there is not a guarantee that data will be available at least for the purpose of verifying the accuracy of published findings, and this guarantee needs to be incorporated into the original permissions for the study. This is important both to prevent the spread of misinformation, and to enable future analyses that seek to re-examine the same questions.

It is best practice to make data fully available following publication, and indeed nearly all ancient genomic data have been published this way in enduring public data repositories, which has been an ethical strength of the field⁷⁹. Beyond contributing to the advancement of scientific knowledge, making data fully available contributes to responsible stewardship of human remains, in that the ability to reuse data reduces the need for further sampling. However, we can envision scenarios in which discussions among stakeholders reveal that it would be ethical to limit the ways in which ancient DNA data can be reused, such as when reporting results from some types of analyses could harm stakeholders, which could outweigh the benefits of fully open data^{6,10,80}. In these cases—which should be identified during a process of engagement prior to the inception of the study—the limitation of data distribution to qualified researchers who agree to only analyse the data for the purpose of reappraising the study findings should be part of the initial research plan.

When data are not made fully publicly available, management and distribution of data for the purpose of critical re-examination of results should be performed by an organization with expertise to prevent data misuse and without an interest in research outcomes. It has been suggested

that stakeholders such as Indigenous groups could be responsible for managing distribution of data after publication to researchers^{10,13,15,81}. However, it is not consistent with professional ethics for researchers to participate in a study where those with a stake in the research findings can deny the sharing of data to qualified researchers whose goal is to critically re-examine the questions covered by the original research agreement. There are established mechanisms for ensuring distribution of non-fully public data to researchers who apply to use it for the purposes of critical re-examination. For example, data could be made available through a repository that shares data only upon formal application and approval from a data access committee that determines whether the applicant's request satisfies the limitations on data use described in the publication. This is sometimes done for modern genomic data to address privacy concerns through mechanisms such as the dbGaP or EGA repositories^{82,83}, although a shortcoming is that the data-acquisition process can be slow⁷⁶. Repositories for data from Indigenous people are also beginning to be established that involve communities in data storage and dissemination^{10,13,79,84,85}. While no stakeholder group—including researchers, community representatives, or curators—should control the distribution of data to researchers who wish to critically re-examine questions covered in the original research agreement, Indigenous data repositories could have an important role in storing and distributing data for purposes beyond those covered by the original research agreement.

(5) Researchers must engage with other stakeholders from the beginning of a study and ensure respect and sensitivity to stakeholder perspectives. A project to generate new ancient DNA data may be initiated by diverse stakeholders, including but not limited to local communities, archaeologists, anthropologists, geneticists or curators, any or all of whom may be members of the research team if they contribute in a scholarly way to the work. Other stakeholders who are consulted should be thanked in the Acknowledgments sections of papers if they consent to be named. Stakeholders—ideally including groups from the place of origin of the human remains being studied—should be actively involved in discussions about study design, research questions and whether a scientific project should proceed. Researchers must accept a negative answer if stakeholders are not collectively supportive of the work taking place¹⁵.

Once a consensus to proceed has been reached, professional scientific ethics requires that researchers are able to pursue their work up to the point of publication without requiring further approval. The suggestion that there should be a requirement for manuscripts to be approved by stakeholder groups who are not members of the research team before publication^{15,81} is not feasible, as researchers cannot ethically participate in a study in which this is mandated. The imperative of scientific independence once a study begins does not mean that researchers should publish results without considering stakeholder perspectives about the implications of the data. It is valuable to invite stakeholders to engage with research results through the addition of their perspectives or by providing critical feedback prior to publication especially when results are surprising and challenge previous assumptions. Continued engagement with other stakeholders after the beginning of a study is an effective mechanism by which researchers can address their professional ethical obligation to understand whether reporting a result in a particular way is likely to cause harm. If these conversations indicate that a result cannot be shared in a way that avoids substantial harm to a stakeholder group, researchers should not publish that result.

Researchers should be available to provide regular updates and must commit to returning results at the culmination of a project. It should be made clear from the outset what the study's potential findings may be, that genetic data may be inconsistent with other forms of knowledge, and that while the results of scientific analyses are reported as scholarly output, they do not discredit, diminish or decrease the importance of traditional expertise and deeply held beliefs. Discrepancies between results from genetic analyses and other lines of evidence should be reported as important elements of the compound nature of understanding the past.

Researchers should commit to working with stakeholders on outreach efforts that create additional outputs accessible to communities. This may involve working with local collaborators to translate the results of papers into local languages^{30,35,36,86,87}, developing children's educational resources^{88,89,90,91}, producing brochures and pamphlets for libraries or other community centres, or working with museums to design exhibits. When relevant, researchers should contribute to training and education, especially for members of stakeholder groups and local communities^{4,15}, and should

consider ways in which to improve the curatorial state of collections¹¹. This can include supplying the resources needed for participating in the generation, interpretation and dissemination of data, for example training in sampling of human remains or laboratory techniques, and financial support for further training or attending professional meetings. It is important for granting agencies to ensure that adequate funding is allocated to capacity building initiatives.

Promoting ethical DNA research on human remains

As part of their work, scholars also have a broader obligation to correct ideologically motivated distortions of research results. Following the technical presentation of data in academic publications, many studies are summarized by science journalists or educators for communication to broad audiences. There have been instances of journalistic and governmental misrepresentation of study findings for political ends, and scientists have an obligation to work to correct misinterpretation when appropriate⁶⁴. Reaching out to the public can include writing essays and books, and contributing to social media and documentaries^{92,93,94,95,96,97,98,99,100}.

Given the overwhelming support for these guidelines among the diverse participants in our workshop, we anticipate that the broader community engaged in ancient DNA research will be supportive of these principles as well, and suggest that they could form a basis for official guidelines from journals, professional organizations and granting agencies going forward. *Translation of this article into more than twenty languages.* This article was reviewed in English. The authors prepared full translations (which were not peer-reviewed or checked for correctness by Springer Nature) into more than twenty languages they speak, including Afrikaans, Arabic, Catalan, Chinese, Croatian, French, German, Hawaiian, Hebrew, Hindi, Hungarian, Japanese, Portuguese, Punjabi, Russian, Sinhala, Spanish, Swahili, Swedish, Tamil, Turkish, Urdu, and Xhosa, and have made them available at figshare
(dx.doi.org/10.6084/m9.figshare.16744552).

References

1. 1.

Booth, T. J. A stranger in a strange land: a perspective on archaeological responses to the palaeogenetic revolution from an archaeologist working amongst palaeogeneticists. *World Archaeol.* **51**, 586–601 (2019). **An archaeologist's perspective on the challenges to and benefits of integrating palaeogenomic data with archaeological evidence to develop a richer understanding of people in the past.**

2. 2.

Austin, R. M., Sholts, S. B., Williams, L., Kistler, L. & Hofman, C. A. To curate the molecular past, museums need a carefully considered set of best practices. *Proc. Natl Acad. Sci. USA* **116**, 1471–1474 (2019). **A museum-based perspective on the responsibility of preserving collections and best practices for evaluating proposals for biomolecular research.**

3. 3.

Bardill, J. et al. Advancing the ethics of paleogenomics. *Science* **360**, 384–385 (2018). **Provides Indigenous perspectives on ethical best practices in ancient DNA research and offers guidance on appropriate engagement with stakeholder communities.**

4. 4.

Claw, K. G. et al. A framework for enhancing ethical genomic research with Indigenous communities. *Nat. Commun.* **9**, 2957 (2018).

5. 5.

Claw, K. G. et al. Chaco Canyon dig unearths ethical concerns. *Hum. Biol.* **89**, 177 (2017).

6. 6.

Cortez, A. D., Bolnick, D. A., Nicholas, G., Bardill, J. & Colwell, C. An ethical crisis in ancient DNA research: Insights from the Chaco Canyon controversy as a case study. *J. Soc. Archaeol.* 146960532199160 (2021).

7. 7.

Crellin, R. J. & Harris, O. J. T. Beyond binaries. Interrogating ancient DNA. *Archaeol. Dial.* 27, 37–56 (2020).

8. 8.

Eisenmann, S. et al. Reconciling material cultures in archaeology with genetic data: the nomenclature of clusters emerging from archaeogenomic analysis. *Sci. Rep.* 8, 13003 (2018).

9. 9.

Gibbon, V. E. African ancient DNA research requires robust ethics and permission protocols. *Nat. Rev. Genet.* 21, 645–647 (2020). **A review emphasizing that ethical guidance developed in Africa for genomic research on living people can be applied with modification to ancient DNA studies, highlighting protocols developed through collaboration among South African institutions, agencies and community groups.**

10. 10.

Hudson, M. et al. Rights, interests and expectations: indigenous perspectives on unrestricted access to genomic data. *Nat. Rev. Genet.* 21, 377–384 (2020).

11. 11.

Prendergast, M. E. & Sawchuk, E. Boots on the ground in Africa’s ancient DNA ‘revolution’: archaeological perspectives on ethics and best practices. *Antiquity* 92, 803–815 (2018). **Reviews ethical issues particular to African bioarchaeological research contexts and**

suggests guidelines for best practices for ancient DNA research in institutional collections.

12. 12.

Sirak, K. A. & Sedig, J. W. Balancing analytical goals and anthropological stewardship in the midst of the paleogenomics revolution. *World Archaeol.* **51**, 560–573 (2019).

13. 13.

Tsosie, K. S., Begay, R. L., Fox, K. & Garrison, N. A. Generations of genomes: advances in paleogenomics technology and engagement for Indigenous people of the Americas. *Curr. Opin. Genet. Dev.* **62**, 91–96 (2020).

14. 14.

Hakenbeck, S. E. Genetics, archaeology and the far right: an unholy trinity. *World Archaeol.* **51**, 517–527 (2019).

15. 15.

Wagner, J. K. et al. Fostering responsible research on ancient DNA. *Am. J. Human Genet.* **107**, 183–195 (2020). **This guidance to promote ethical engagement between researchers and stakeholder communities involved in ancient DNA research was the first set of recommendations to be approved by a professional organization, the American Society of Human Genetics.**

16. 16.

Assessment and Reflection on the Ethical Dimensions of Archaeogenetics Research,
<https://www.eva.mpg.de/archaeogenetics/ethics.html> (Max Planck Institute for Evolutionary Anthropology, 2021).

17. 17.

Evison, M. P. Genetics, ethics and archaeology. *Antiquity* **70**, 512–514 (1996).

18. 18.

Friedlaender, J. S., Gentz, F., Green, K. & Merriwether, D. A. A cautionary tale on ancient migration detection: mitochondrial DNA variation in Santa Cruz Islands, Solomon Islands. *Hum. Biol.* **74**, 453–471 (2002).

19. 19.

Holm, S. The privacy of Tutankhamen—utilising the genetic information in stored tissue samples. *Theor. Med. Bioeth.* **22**, 437–449 (2001).

20. 20.

Hublin, J.-J. et al. Suggested guidelines for invasive sampling of hominid remains. *J. Hum. Evol.* **55**, 756–757 (2008).

21. 21.

Kaestle, F. A. & Horsburgh, K. A. Ancient DNA in anthropology: methods, applications, and ethics. *Am. J. Phys. Anthropol.* **119**, 92–130 (2002).

22. 22.

Lalueza Fox, C. Ancient DNA studies and new bioethic problems. *Hum. Evol.* **12**, 287 (1997).

23. 23.

O'Rourke, D. H., Hayes, M. G. & Carlyle, S. W. Ancient DNA studies in physical anthropology. *Annu. Rev. Anthropol.* **29**, 217–242 (2000).

24. 24.

Sealy, J. Managing collections of human remains in South African museums and universities: ethical policy-making and scientific value: reviews of current issues and research findings: human origins research in South Africa. *S. Afr. J. Sci.* **99**, 238–239 (2003).

25. 25.

Morris, A. Ancient DNA comes of age, but still has some teenage problems. *S. Afr. J. Sci.* **113**, 2 (2017).

26. 26.

Schroeder, D. What is ethics dumping? *Biologist* **66**, 22–25 (2019).

27. 27.

Bockarie, M. J. We need to end “parachute” research which sidelines the work of African scientists. *Quartz Africa* <https://qz.com/africa/1536355/african-scientists-are-sidelined-by-parachute-research-teams/> (2019).

28. 28.

Rasmussen, M. et al. An Aboriginal Australian genome reveals separate human dispersals into Asia. *Science* **334**, 94–98 (2011).

29. 29.

Rasmussen, M. et al. The genome of a Late Pleistocene human from a Clovis burial site in western Montana. *Nature* **506**, 225–229 (2014).

30. 30.

Posth, C. et al. Reconstructing the deep population history of Central and South America. *Cell* **175**, 1185-1197.e22 (2018).

31. 31.

Scheib, C. L. et al. Ancient human parallel lineages within North America contributed to a coastal expansion. *Science* **360**, 1024–1027 (2018).

32. 32.

Bongers, J. L. et al. Integration of ancient DNA with transdisciplinary dataset finds strong support for Inca resettlement in the south Peruvian coast. *Proc. Natl Acad. Sci. USA* **117**, 18359–18368 (2020).

33. 33.

Fernandes, D. M. et al. A genetic history of the pre-contact Caribbean. *Nature* **590**, 103–110 (2021).

34. 34.

Fleskes, R. E. et al. Ancestry, health, and lived experiences of enslaved Africans in 18th century Charleston: an osteobiographical analysis. *Am. J. Phys. Anthropol.* **175**, 3–24 (2021).

35. 35.

Nakatsuka, N. et al. A Paleogenomic reconstruction of the deep population history of the Andes. *Cell* **181**, 1131-1145.e21 (2020).

36. 36.

Nakatsuka, N. et al. Ancient genomes in South Patagonia reveal population movements associated with technological shifts and geography. *Nat. Commun.* **11**, 3868 (2020).

37. 37.

Wang, C.-C. et al. Genomic insights into the formation of human populations in East Asia. *Nature* **591**, 413–419 (2021).

38. 38.

Wibowo, M. C. et al. Reconstruction of ancient microbial genomes from the human gut. *Nature* **594**, 234–239 (2021).

39. 39.

Statement Concerning the Treatment of Human Remains (Society for American Archaeology, 2021).

40. 40.

Pickrell, J. Ancient Australian goes home. *Science* **358**, 853–853 (2017).

41. 41.

Australian government policy on Indigenous repatriation. *Department of Communications and the Arts*
<https://www.arts.gov.au/documents/australian-government-policy-indigenous-repatriation> (2016).

42. 42.

Return of cultural heritage. Australian Institute of Aboriginal and Torres Strait Islander Studies <https://aiatsis.gov.au/about/what-we-do/return-cultural-heritage> (2021).

43. 43.

Moctezuma, E. M. *Las piedras negadas: De la Coatlicue al Templo Mayor* (Consejo Nacional para la Cultura y las Artes, 1998).

44. 44.

Wade, P. *Race and Ethnicity in Latin America: How the East India Company Shaped the Modern Multinational* 2nd edn (Pluto, 2010).

45. 45.

Ortega Muñoz, A. & Tiesler, V. in *Colecciones Esqueléticas Humanas en México: Excavación, Catalogación, Conservación y Aspectos Normativos* (eds Márquez Morfín, L. & Ortega Muñoz, A.) 399–413 (Instituto Nacional de Antropología e Historia, 2011).

46. 46.

Devine, T. L. Indigenous identity and identification in Peru: Indigenismo, education and contradictions in state discourses. *J. Lat. Am. Cult. Stud.* **8**, 63–74 (1999).

47. 47.

Herrera, A. in *Indigenous Peoples and Archaeology in Latin America* (eds. Gnecco, C. et al.) 67–88 (2011).

48. 48.

Silverman, H. Cultural resource management and heritage stewardship in Peru. *J. Heritage Steward.* **3**, 1 (2006).

49. 49.

Endere, M. L., Cali, P. & Funari, P. P. A. in *Indigenous Peoples and Archaeology in Latin America* 159–178 (Routledge, 2016).

50. 50.

Hodgson, D. L. Becoming Indigenous in Africa. *Afr. Stud. Rev.* **52**, 1–32 (2009).

51. 51.

Plackett, B. Arab-World archaeologists must avoid disturbing Islamic graves. *Al-Fanar Media* <https://www.al-fanarmedia.org/2016/05/arab-world-archaeologists-must-avoid-disturbing-islamic-graves/> (2016).

52. 52.

Legassick, M. & Rassool, C. *Skeletons in the Cupboard: South African Museums and the Trade in Human Remains 1907–1917* (South African Museum, McGregor Museum, 2000).

53. 53.

Redman, S. J. *Bone Rooms: From Scientific Racism to Human Prehistory in Museums* (Harvard University Press, 2016).

54. 54.

Gibbon, V. E. & Morris, A. G. UCT Human Skeletal Repository: its stewardship, history, composition and educational use. *J. Compar. Hum. Biol.* **72**, 139–147 (2021).

55. 55.

Steyn, M., Morris, A., Mosothwane, M., Nienaber, C. & Maat, G. Opening the cupboard—lessons in biology and history from African skeletons. *S. Afr. Archaeol. Bull.* **11**, 1–6 (2013).

56. 56.

Smith, A. B. in *African Memory in Danger* (eds. Mayor, A. et al.) 52–60 (2015).

57. 57.

Urassa, M. et al. Cross-cultural research must prioritize equitable collaboration. *Nature Human Behaviour* **5**, 668–671 (2021).

58. 58.

Nakatsuka, N. et al. The promise of discovering population-specific disease-associated genes in South Asia. *Nat. Genet.* **49**, 1403–1407 (2017).

59. 59.

Reich, D., Thangaraj, K., Patterson, N., Price, A. L. & Singh, L. Reconstructing Indian population history. *Nature* **461**, 489–494 (2009).

60. 60.

Thangaraj, K. et al. Reconstructing the origin of Andaman Islanders. *Science* **308**, 996–996 (2005).

61. 61.

Arnold, B. ‘*Arierdämmerung*’: race and archaeology in Nazi Germany. *World Archaeol.* **38**, 8–31 (2006).

62. 62.

Frieman, C. J. & Hofmann, D. Present pasts in the archaeology of genetics, identity, and migration in Europe: a critical essay. *World Archaeol.* **51**, 528–545 (2019).

63. 63.

Moody, O. Hungarian royal lineage traced to Afghanistan as Viktor Orban pushes east. *The Times* (17 July 2020).

64. 64.

Hasson, N. DNA research holds the keys to human history—but it’s being weaponized by politicians. *Haaretz.com*
https://www.haaretz.com/archaeology/_premium-magic-or-a-trap-dna-changes-study-of-the-past-1.8009668 (2019).

65. 65.

Wolinsky, H. Ancient DNA and contemporary politics. *EMBO Rep.* **20**, e49507 (2019).

66. 66.

Ali, J. et al. A scoping review of genetics and genomics research ethics policies and guidelines for Africa. *BMC Med. Ethics* **22**, 39 (2021).

67. 67.

Wilkinson, M. D. et al. The FAIR Guiding Principles for scientific data management and stewardship. *Sci. Data* **3**, 160018 (2016).

68. 68.

Arbour, L. & Cook, D. DNA on loan: issues to consider when carrying out genetic research with aboriginal families and communities. *Community Genet.* **9**, 153–160 (2006).

69. 69.

Gamba, C. et al. Genome flux and stasis in a five millennium transect of European prehistory. *Nat. Commun.* **5**, 5257 (2014).

70. 70.

Pinhasi, R. et al. Optimal ancient DNA yields from the inner ear part of the human petrous bone. *PLoS ONE* **10**, e0129102 (2015).

71. 71.

Hansen, H. B. et al. Comparing ancient DNA preservation in petrous bone and tooth cementum. *PLoS ONE* **12**, e0170940 (2017).

72. 72.

Parker, C. et al. A systematic investigation of human DNA preservation in medieval skeletons. *Sci. Rep.* **10**, 18225 (2020).

73. 73.

Sirak, K. A. et al. A minimally-invasive method for sampling human petrous bones from the cranial base for ancient DNA analysis. *BioTechniques* **62**, 283–289 (2017).

74. 74.

Sirak, K. A. et al. Human auditory ossicles as an alternative optimal source of ancient DNA. *Genome Res.* **30**, 427–436 (2020).

75. 75.

Harney, É. et al. A minimally destructive protocol for DNA extraction from ancient teeth. *Genome Res.* **31**, 472–483 (2021).

76. 76.

Yates, J. A. F. A–Z of ancient DNA protocols for shotgun Illumina Next Generation Sequencing.

<https://doi.org/10.17504/protocols.io.bj8nkrve> (2020).

77. 77.

The next 20 years of human genomics must be more equitable and more open. *Nature* **590**, 183–184 (2021).

78. 78.

Powell, K. The broken promise that undermines human genome research. *Nature* **590**, 198–201 (2021).

79. 79.

Anagnostou, P. et al. When data sharing gets close to 100%: what human paleogenetics can teach the open science movement. *PLoS ONE* **10**, e0121409 (2015). **Discusses the universal practice of fully public data sharing in ancient human DNA research, arguing this is key to establishing reliable and replicable scientific practices.**

80. 80.

Prictor, M., Huebner, S., Teare, H. J. A., Burchill, L. & Kaye, J. Australian Aboriginal and Torres Strait Islander collections of genetic heritage: the legal, ethical and practical considerations of a dynamic

consent approach to decision making. *J. Law Med. Ethics* **48**, 205–217 (2020).

81. 81.

Garrison, N. A. et al. Genomic research through an indigenous lens: understanding the expectations. *Annu. Rev. Genom. Hum. Genet.* **20**, 495–517 (2019).

82. 82.

Mailman, M. D. et al. The NCBI dbGaP database of genotypes and phenotypes. *Nat. Genet.* **39**, 1181–1186 (2007).

83. 83.

Lappalainen, I. et al. The European Genome–Phenome Archive of human data consented for biomedical research. *Nat. Genet.* **47**, 692–695 (2015).

84. 84.

CARE principles of indigenous data governance. *Global Indigenous Data Alliance* <https://www.gida-global.org/care>.

85. 85.

Tsosie, K. S., Fox, K. & Yracheta, J. M. Genomics data: the broken promise is to Indigenous people. *Nature* **591**, 529–529 (2021).

86. 86.

Jeong, C. et al. A dynamic 6,000-year genetic history of eurasia's eastern steppe. *Cell* **183**, 890-904.e29 (2020).

87. 87.

Wilkin, S. et al. Dairy pastoralism sustained eastern Eurasian steppe populations for 5,000 years. *Nat. Ecol. Evol.* **4**, 346–355 (2020).

88. 88.

Stockhammer, P. W., Mitnik, A., Massy, K. & Knipper, C. Mobilität–Die wissenden Frauen vom Lechtal. *Spektrum Wiss. Verl. Ges. Kultur* **4**, 38–41 (2018).

89. 89.

Stockhammer, P. W. BRONZEON: learning by gaming. *Archaeologist* **110**, 24–25 (2020).

90. 90.

Sirak, K., Keegan, W. F. Where did the first people in the Caribbean come from? *Science Journal for Kids and Teens* <https://sciencejournalforkids.org/articles/where-did-the-first-people-in-the-caribbean-come-from/> (2021).

91. 91.

Warinner Group. Adventures in Archaeological Science. <http://christinawarinner.com/outreach/children/adventures-in-archaeological-science/> (2017).

92. 92.

Birney, E., Inouye, M., Raff, J., Rutherford, A. & Scally, A. The language of race, ethnicity, and ancestry in human genetic research. Preprint at <https://arxiv.org/abs/2106.10041> (2021).

93. 93.

Fischer, M., Krause, J. & Richter, S. *Jena Declaration. The concept of race is the result of racism, not its prerequisite.* Opening joint declaration at the 112th Annual Meeting of the German Zoological Society https://www.uni-jena.de/en/190910_JenaerErklaerung_EN (2019).

94. 94.

Gokcumen, O. & Frachetti, M. The impact of ancient genome studies in archaeology. *Annu. Rev. Anthropol.* **49**, 277–298 (2020).

95. 95.

Howe, N. ‘Stick to the science’: when science gets political. *Nature Podcast* <https://doi.org/10.1038/d41586-020-03067-w> (2020).

96. 96.

Krause, J. & Trappe, T. *A Short History of Humanity: A New History of Old Europe* (Random House, 2021).

97. 97.

Orlando, L. et al. Ancient DNA analysis. *Nat. Rev. Methods Prim.* **1**, 1–26 (2021).

98. 98.

Reich, D. *Who We Are and How We Got Here: Ancient DNA and the New Science of the Human Past* (Pantheon, 2018).

99. 99.

Reich, D. & Patterson, O. Ancient DNA is changing how we think about the Caribbean. *The New York Times* (23 December 2020).

100. 100.

Motti, J. M. B., Luisi, P., Salemme, M., Santiago, F. & Nores, R. 7.000 años de historia en el fin del mundo. *Desde la Patagonia Difundiendo Saberes* **17**, 12–20 (2020).

Acknowledgements

The participants in the workshop on ancient DNA ethics who are authors thank many colleagues who improved this article through discussions and

critical comments. To ensure open access, the authors have applied a CC BY licence to any accepted manuscript arising from this submission. C.J.F. acknowledges support from the Australian Research Council Discovery Project DP160100811. V.G. acknowledges support from the National Research Foundation (NRF) South Africa; opinions expressed and conclusions arrived at are those of the authors and are not necessarily attributed to the NRF. M.O. acknowledges support from Conselho Nacional de Desenvolvimento Científico e Tecnológico grant 302163/2017-4 and from Fundação de Amparo à Pesquisa do Estado de São Paulo grant 2018/23282-5. P.S. acknowledges Francis Crick Institute core funding (FC001595) from Cancer Research UK, the UK Medical Research Council and the Wellcome Trust. V.S. acknowledges funding from the Alon Fellowship. M. Soressi acknowledges support from Dutch Research council grant VI.C.191.070. A.S.-N. acknowledges the János Bolyai Research Scholarship of the Hungarian Academy of Sciences. K.T. was supported by a J. C. Bose Fellowship (JCB/2019/000027), SERB and CSIR, Ministry of Science and Technology, Government of India. C.W. acknowledges support from the European Research Council (ERC-2017-StG 804844- DAIRYCULTURES) and the Werner Siemens Stiftung. The authors from Harvard Medical School acknowledge support from the John Templeton Foundation (6122) and the Howard Hughes Medical Institute. The authors from MPI Leipzig and MPI Jena are funded by the Max Planck Society and the Max Planck Harvard Research Center for the Archaeoscience of the Ancient Mediterranean. R.N., E.S., J.S., K.S., V.T., and J.L.P. acknowledge support from the National Geographic Society.

Author information

Affiliations

1. Department of Genetics, Harvard Medical School, Boston, MA, USA
Songül Alpaslan-Roodenberg, Swapan Mallick, Nathan Nakatsuka, David Reich, Jakob Sedig & Kendra Sirak
2. Department of Evolutionary Anthropology, University of Vienna, Vienna, Austria

Songül Alpaslan-Roodenberg & Ron Pinhasi

3. Department of Anthropology, Hartwick College, Oneonta, NY, USA

David Anthony

4. Department of Human Evolutionary Biology, Harvard University, Cambridge, MA, USA

David Anthony, Nick Patterson, David Reich, Jakob Sedig & Kendra Sirak

5. Max Planck Institute for the Science of Human History, Jena, Germany

Hiba Babiker, Stefanie Eisenmann, Wolfgang Haak, Stephan Schiffels & Muhammad Zahir

6. Romano-Germanic Commission of the German Archaeological Institute, Frankfurt am Main, Germany

Eszter Bánffy & Kerstin P. Hofmann

7. Francis Crick Institute, London, UK

Thomas Booth, Mateja Hajdinjak & Pontus Skoglund

8. Peabody Museum of Archaeology and Ethnology, Harvard University, Cambridge, MA, USA

Patricia Capone

9. Department of Ancient Indian History Culture and Archaeology, Deccan College Post Graduate and Research Institute, Pune, India

Arati Deshpande-Mukherjee & Veena Mushrif-Tripathy

10. Max Planck Institute for Evolutionary Anthropology, Leipzig, Germany

Stefanie Eisenmann, Janet Kelso, Johannes Krause, Stephan Schiffels, Philipp W. Stockhammer & Christina Warinner

11. Department of Anthropology, University of California, Santa Cruz, CA, USA

Lars Fehren-Schmitz

12. UCSC Genomics Institute, University of California, Santa Cruz, CA, USA

Lars Fehren-Schmitz

13. Department of Anthropology, Washington University in St Louis, St Louis, MO, USA

Michael Frachetti

14. Centro de Genética y Biología Molecular, Facultad de Medicina, Universidad de San Martín de Porres, Lima, Peru

Ricardo Fujita

15. School of Archaeology and Anthropology, The Australian National University, Canberra, Australian Capital Territory, Australia

Catherine J. Frieman & Matthew Spriggs

16. Key Laboratory of Vertebrate Evolution and Human Origins, Institute of Vertebrate Paleontology and Paleoanthropology, Center for Excellence in Life and Paleoenvironment, Chinese Academy of Sciences, Beijing, China

Qiaomei Fu

17. Division of Clinical Anatomy and Biological Anthropology, Department of Human Biology, University of Cape Town, Cape Town, South Africa

Victoria Gibbon

18. Department of Anthropology, University of California, Santa Barbara,
CA, USA

Brian Holguin

19. School of Anthropology, University of Arizona, Tucson, AZ, USA

Takeshi Inomata

20. National Museum of Nature and Science, Ibaraki, Japan

Hideaki Kanzawa-Kiriyama

21. Florida Museum of Natural History, Gainesville, FL, USA

William Keegan

22. Department of Genetics, School of Biological Sciences, Madurai
Kamaraj University, Madurai, India

Ganesan Kumaresan

23. Department of Anthropology, University of South Florida, Tampa, FL,
USA

Chapurukha Kusimba, Sibel Kusimba & Ray Tobler

24. Institute of Evolutionary Biology (CSIC-UPF), Barcelona, Spain

Carles Lalueza-Fox

25. Australian Centre for Ancient DNA, School of Biological Sciences
and The Environment Institute, University of Adelaide, Adelaide,
South Australia, Australia

Bastien Llamas & Ray Tobler

26. ARC Centre of Excellence for Australian Biodiversity and Heritage,
University of Adelaide, Adelaide, South Australia, Australia

Bastien Llamas

27. Office of the Chancellors, Duke Kunshan University, Jiangsu, China

Scott MacEachern

28. Howard Hughes Medical Institute, Boston, MA, USA

Swapan Mallick & David Reich

29. Broad Institute of MIT and Harvard, Cambridge, MA, USA

Swapan Mallick, Nick Patterson & David Reich

30. School of Health Science, Sapporo Medical University, Sapporo, Japan

Hirofumi Matsumura

31. Institute of Ecology and Evolution, University of Bern, Bern,
Switzerland

Ana Y. Morales-Arce

32. Lithuanian Institute of History and Department of Archaeology,
History Faculty, Vilnius University, Vilnius, Lithuania

Giedre Motuzaitė Matuzevičiūtė

33. Departamento de Antropología, Facultad de Filosofía y Humanidades,
Universidad Nacional de Córdoba, Instituto de Antropología de
Córdoba (IDACOR), CONICET, Córdoba, Argentina

Rodrigo Nores

34. Earth Sciences Department, National Museums of Kenya, Nairobi,
Kenya

Christine Ogola

35. Department of Genetics and Evolutionary Biology, University of São Paulo, São Paulo, Brazil

Mercedes Okumura

36. Human Evolution and Archaeological Sciences, University of Vienna, Vienna, Austria

Ron Pinhasi

37. DBT-Centre for DNA Fingerprinting and Diagnostics, Hyderabad, India

Samayamantri P. R. Prasad & Kumarasamy Thangaraj

38. Department of Anthropology, Rice University, Houston, TX, USA

Mary E. Prendergast

39. Instituto Nacional de Antropología e Historia, Michoacán, Mexico

Jose Luis Punzo

40. School of Advanced Sciences, The Graduate University for Advanced Studies (SOKENDAI), Kanagawa, Japan

Rikai Sawafuji

41. Department of Anthropology, University of Alberta, Edmonton, Alberta, Canada

Elizabeth Sawchuk

42. Department of Anthropology, Stony Brook University, Stony Brook, NY, USA

Elizabeth Sawchuk

43. ArchaeoZOOlogy in Siberia and Central Asia–ZooSCAN, CNRS–IAET SB RAS International Research Laboratory, Novosibirsk, Russia

Svetlana Shnaider

44. Department of Anatomy and Anthropology and Department of Human Molecular Genetics and Biochemistry, Sackler Faculty of Medicine, Tel Aviv University, Tel Aviv, Israel

Viviane Slon

45. The Dan David Center for Human Evolution and Biohistory Research, Tel Aviv University, Tel Aviv, Israel

Viviane Slon

46. Anthropology Department, University of Montana, Missoula, MO, USA

Meradeth Snow

47. Faculty of Archaeology, Leiden University, Leiden, Netherlands

Marie Soressi

48. Vanuatu Cultural Centre, Port Vila, Vanuatu

Matthew Spriggs

49. Institute for Pre- and Protohistoric Archaeology and Archaeology of the Roman Provinces, Ludwig Maximilian University, Munich, Germany

Philipp W. Stockhammer

50. Institute of Archaeogenomics, Research Centre for the Humanities, Eötvös Loránd Research Network, Budapest, Hungary

Anna Szécsényi-Nagy

51. CSIR-Centre for Cellular and Molecular Biology, Hyderabad, India

Kumarasamy Thangaraj

52. School of Anthropological Sciences, Universidad Autónoma de Yucatán, Mérida, Mexico

Vera Tiesler

53. Department of Anthropology and Ethnology, Institute of Anthropology, School of Sociology and Anthropology, State Key Laboratory of Cellular Stress Biology, School of Life Sciences, Xiamen University, Xiamen, China

Chuan-Chao Wang

54. School of Basic Medical Sciences, Zhejiang University School of Medicine, and Institute of Asian Civilizations, Zhejiang University, Hangzhou, China

Chuan-Chao Wang

55. Department of Anthropology, Harvard University, Cambridge, MA, USA

Christina Warinner

56. Department of Anatomy, University of Sri Jayewardenepura, Nugegoda, Sri Lanka

Surangi Yasawardene

57. Department of Archaeology, Hazara University, Mansehra, Pakistan

Muhammad Zahir

Contributions

All authors participated in discussions and are listed alphabetically.

Corresponding authors

Correspondence to Lars Fehren-Schmitz, Mary E. Prendergast, David Reich, Jakob Sedig, Kendra Sirak or Philipp W. Stockhammer.

Ethics declarations

Competing interests

The authors declare no competing interests.

Additional information

Peer review information *Nature* thanks Shadreck Chirikure, Emma Kowal, Wibhu Kutanan, Kirsty Squires and the other, anonymous, reviewer(s) for their contribution to the peer review of this work.

Publisher's note Springer Nature remains neutral with regard to jurisdictional claims in published maps and institutional affiliations.

Rights and permissions

[Reprints and Permissions](#)

About this article

Cite this article

Alpaslan-Roodenberg, S., Anthony, D., Babiker, H. *et al.* Ethics of DNA research on human remains: five globally applicable guidelines. *Nature* **599**, 41–46 (2021). <https://doi.org/10.1038/s41586-021-04008-x>

- Received: 20 March 2021
- Accepted: 08 September 2021

- Published: 20 October 2021
- Issue Date: 04 November 2021
- DOI: <https://doi.org/10.1038/s41586-021-04008-x>

Share this article

Anyone you share the following link with will be able to read this content:

[Get shareable link](#)

Sorry, a shareable link is not currently available for this article.

[Copy to clipboard](#)

Provided by the Springer Nature SharedIt content-sharing initiative

This article was downloaded by **calibre** from <https://www.nature.com/articles/s41586-021-04008-x>

| [Section menu](#) | [Main menu](#) |

- Article
- [Published: 03 November 2021](#)

Experimental relativistic zero-knowledge proofs

- [Pourya Alikhani](#)¹,
- [Nicolas Brunner](#)²,
- [Claude Crépeau](#) [ORCID: orcid.org/0000-0002-9990-8005](#)¹,
- [Sébastien Designolle](#) [ORCID: orcid.org/0000-0003-0303-3556](#)²,
- [Raphaël Houlmann](#)²,
- [Weixu Shi](#)^{2,3},
- [Nan Yang](#)⁴ &
- [Hugo Zbinden](#) [ORCID: orcid.org/0000-0002-9237-1700](#)²

[Nature](#) volume **599**, pages 47–50 (2021)

- 2270 Accesses
- 41 Altmetric
- [Metrics details](#)

Subjects

- [Computer science](#)
- [Quantum physics](#)

Abstract

Protecting secrets is a key challenge in our contemporary information-based era. In common situations, however, revealing secrets appears unavoidable;

for instance, when identifying oneself in a bank to retrieve money. In turn, this may have highly undesirable consequences in the unlikely, yet not unrealistic, case where the bank's security gets compromised. This naturally raises the question of whether disclosing secrets is fundamentally necessary for identifying oneself, or more generally for proving a statement to be correct. Developments in computer science provide an elegant solution via the concept of zero-knowledge proofs: a prover can convince a verifier of the validity of a certain statement without facilitating the elaboration of a proof at all¹. In this work, we report the experimental realization of such a zero-knowledge protocol involving two separated verifier–prover pairs². Security is enforced via the physical principle of special relativity³, and no computational assumption (such as the existence of one-way functions) is required. Our implementation exclusively relies on off-the-shelf equipment and works at both short (60 m) and long distances (≥ 400 m) in about one second. This demonstrates the practical potential of multi-prover zero-knowledge protocols, promising for identification tasks and blockchain applications such as cryptocurrencies or smart contracts⁴.

Access options

Subscribe to Journal

Get full journal access for 1 year

\$199.00

only \$3.90 per issue

[Subscribe](#)

All prices are NET prices.

VAT will be added later in the checkout.

Tax calculation will be finalised during checkout.

Rent or Buy article

Get time limited or full article access on ReadCube.

from \$8.99

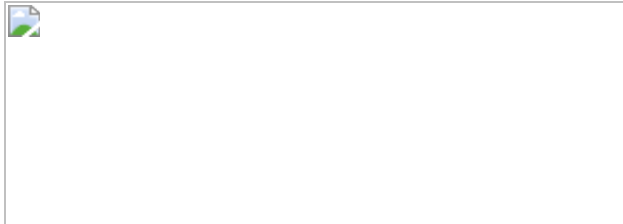
[Rent or Buy](#)

All prices are NET prices.

Additional access options:

- [Log in](#)
- [Access through your institution](#)
- [Learn about institutional subscriptions](#)

Fig. 1: Relativistic zero-knowledge protocol for three-colourability on a short distance.



Data availability

All data supporting the findings of this article are available from the corresponding authors upon request.

Code availability

All code supporting the findings of this article are available from the corresponding authors upon request.

References

1. 1.

Goldwasser, S., Micali, S. & Rackoff, C. The knowledge complexity of interactive proof systems. In *Proc. Seventeenth Annual ACM*

Symposium on Theory of Computing 291–304 (ACM, 1985).

2. 2.

Ben-Or, M., Goldwasser, S., Kilian, J. & Wigder-son, A. Multi-prover interactive proofs: how to remove intractability assumptions. In *Proc. Twentieth Annual ACM Symposium on Theory of Computing* 113–131 (ACM, 1988).

3. 3.

Kilian, J. Strong separation models of multi prover interactive proofs. In *DIMACS Workshop on Cryptography* (DIMACS, 1990).

4. 4.

Ben-Sasson, E., Bentov, I., Horesh, Y. & Riabzev, M. Scalable, transparent, and post-quantum secure computational integrity. Preprint at <https://eprint.iacr.org/2018/046.pdf> (2018).

5. 5.

Goldwasser, S., Micali, S. & Rackoff, C. The knowledge complexity of interactive proof systems. *SIAM J. Comput.* **18**, 186–208 (1989).

6. 6.

Rivest, R. L., Shamir, A. & Adleman, L. A method for obtaining digital signatures and public-key cryptosystems. *Commun. ACM* **21**, 120–126 (1978).

7. 7.

Garey, M. R. & Johnson, D. S. *Computers and Intractability: A Guide to the Theory of NP-Completeness* (W. H. Freeman & Co., 1979).

8. 8.

Goldreich, O., Micali, S. & Wigderson, A. Proofs that yield nothing but their validity or all languages in NP have zero-knowledge proof systems. *J. ACM* **38**, 690–728 (1991).

9. 9.

Fortnow, L. The complexity of perfect zero-knowledge. In *Proc. Nineteenth Annual ACM Symposium on Theory of Computing* 204–209 (ACM, 1987).

10. 10.

Ben Sasson, E. et al. Zerocash: decentralized anonymous payments from Bitcoin. In *Proc. IEEE Symp. Security and Privacy* 459–474 (IEEE, 2014).

11. 11.

Bernstein, D. J. & Lange, T. Post-quantum cryptography. *Nature* **549**, 188–194 (2017).

12. 12.

Arute, F. et al. Quantum supremacy using a programmable superconducting processor. *Nature* **574**, 505–510 (2019).

13. 13.

Kent, A. Unconditionally secure bit commitment. *Phys. Rev. Lett.* **83**, 1447–1450 (1999).

14. 14.

Crépeau, C., Massenet, A., Salvail, L., Stinchcombe, L. & Yang, N. Practical relativistic zero-knowledge for NP. In *Proc. 1st Conf. Information-Theoretic Cryptography* 4, 1–18 (LIPiCS, 2020).

15. 15.

Mizuno, K. & Nishihara, S. Constructive generation of very hard 3-colorability instances. *Discret. Appl. Math.* **156**, 218–229 (2008).

16. 16.

Katz, J. & Lindell, Y. *Introduction to Modern Cryptography* 3rd edn (CRC, 2020).

17. 17.

Verbanis, E. et al. 24-hour relativistic bit commitment. *Phys. Rev. Lett.* **117**, 140506 (2016).

18. 18.

Li, N., Li, C., Helleseth, T., Ding, C. & Tang, X. Optimal ternary cyclic codes with minimum distance four and five. *Finite Fields their Appl.* **30**, 100–120 (2014).

19. 19.

Tassa, T. & Villar, J. L. On proper secrets, (t, k) -bases and linear codes. *Des. Codes Cryptogr.* **52**, 129–154 (2009).

20. 20.

Lunghi, T. et al. Practical relativistic bit commitment. *Phys. Rev. Lett.* **115**, 030502 (2015).

21. 21.

Bell, J. S. On the Einstein–Podolsky–Rosen paradox. *Phys. Phys. Fiz.* **1**, 195–200 (1964).

22. 22.

Kempe, J., Kobayashi, H., Matsumoto, K., Toner, B. & Vidick, T. Entangled games are hard to approximate. *SIAM J. Comput.* **40**, 848–877 (2011).

23. 23.

Chailloux, A. & Leverrier, A. Relativistic (or 2-prover 1-round) zero-knowledge protocol for NP secure against quantum adversaries. In *Advances in Cryptology – EUROCRYPT 2017* (eds. Coron, J. S. & Nielsen, J.) 369–396 (Springer, 2017).

24. 24.

Ji, Z. Binary constraint system games and locally commutative reductions. Preprint at <https://arxiv.org/abs/1310.3794> (2013).

25. 25.

Groth, J. Non-interactive zero-knowledge arguments for voting. In *Applied Cryptography and Network Security* (eds. Ioannidis, J., Keromytis, A. & Yung, M.) 467–482 (Springer, 2005).

26. 26.

Micali, S. & Rabin, M. O. Cryptography miracles, secure auctions, matching problem verification. *Commun. ACM* **57**, 85–93 (2014).

27. 27.

Glaser, A., Barak, B. & Goldston, R. J. A zero-knowledge protocol for nuclear warhead verification. *Nature* **510**, 497–502 (2014).

28. 28.

Group of Applied Physics. *Google Maps*
<https://goo.gl/maps/qhriiVPu8ktAqfZd9> (2020).

Acknowledgements

Financial supports by the Swiss National Science Foundation (starting grant DIAQ, NCCR-QSIT) and the European project OpenQKD are gratefully acknowledged by N.B., S.D., R.H., W.X. and H.Z. P.A., C.C. and N.Y. are

grateful to Québec's FRQNT and Canada's NSERC for making this work financially possible.

Author information

Affiliations

1. School of Computer Science, McGill University, Montréal, Québec, Canada

Pouriya Alikhani & Claude Crépeau

2. Department of Applied Physics, University of Geneva, Genève, Switzerland

Nicolas Brunner, Sébastien Designolle, Raphaël Houlmann, Weixu Shi & Hugo Zbinden

3. Department of Electronic Science, National University of Defense Technology, Changsha, China

Weixu Shi

4. Department of Computer Science and Software Engineering, Concordia University, Montréal, Québec, Canada

Nan Yang

Contributions

P.A. and C.C. generated the graph used. N.B. and H.Z. supervised the research. C.C. and N.Y. came up with the protocol and C.C. was the theoretical leader. S.D. ensured the link between theory and experiment. R.H. was responsible for the experimental implementation, with support by S.D. and H.Z. W.X. contributed at early stage of the project. S.D. and C.C. wrote the initial draft, with the other authors providing editorial comments.

Corresponding authors

Correspondence to Claude Crépeau or Sébastien Designolle.

Ethics declarations

Competing interests

The authors declare no competing interests.

Additional information

Peer review information *Nature* thanks Thomas Vidick and the other, anonymous, reviewer(s) for their contribution to the peer review of this work. Peer reviewer reports are available.

Publisher's note Springer Nature remains neutral with regard to jurisdictional claims in published maps and institutional affiliations.

Extended data figures and tables

[Extended Data Fig. 1 Illustration of a round of the protocol.](#)

The colours are consistent with those of Fig. 1a and depict a typical round where the verifiers ask the same edge to the provers, here $\backslash(\{1,2\}\backslash)$, but where $\backslash(b\backslashneq b\backslashtext{'})\backslash$ so that they check in the end that \backslash
 $\{{a}_0+a\backslashtext{'}}_0\backslash \not\equiv \{{a}_1+a\backslashtext{'}}_1\backslash(\backslash rm{m}\backslash$
 $\backslash rm{o}\backslash\backslash rm{d}\backslash,3\backslash)\backslash$. In this example we have $\backslash\{{\backslash ell}\}_1^0=2$,
 $\backslash\{{\backslash ell}\}_1^1=1$, $\backslash\{{\backslash ell}\}_2^0=0$, $\backslash\{{\backslash ell}\}_2^1=1\backslash$; note
that, despite the adjacency of the vertices 1 and 2, the equality $\backslash\{{\backslash ell}\}_1^1=\backslash\{{\backslash ell}\}_2^1\backslash$ is legal as the labellings $\backslash\{{\backslash ell}\}_k^b\backslash$ do not need to be colourings.

[Extended Data Fig. 2 Illustration of the hardware used in our two implementations.](#)

a, b, The GPS version (**a**) and the triggered version (**b**). The essential difference is the method used for synchronizing the verifiers' questions. In **a** the connection is wireless as it uses communication with satellites at the expense of a higher imprecision thus further verifier–prover pairs. In **b** the connection is physical and oriented from the first to the second verifier; the former sends a trigger through the fibre and delays their action by the time needed for this signal to reach the latter. With a better accuracy this second method allows for shorter distances between the verifier–prover pairs, here 60 m but arguably improvable.

Supplementary information

[Peer Review File](#)

Rights and permissions

[Reprints and Permissions](#)

About this article

Cite this article

Alikhani, P., Brunner, N., Crépeau, C. *et al.* Experimental relativistic zero-knowledge proofs. *Nature* **599**, 47–50 (2021).
<https://doi.org/10.1038/s41586-021-03998-y>

- Received: 15 January 2021
- Accepted: 06 September 2021
- Published: 03 November 2021
- Issue Date: 04 November 2021
- DOI: <https://doi.org/10.1038/s41586-021-03998-y>

Share this article

Anyone you share the following link with will be able to read this content:

[Get shareable link](#)

Sorry, a shareable link is not currently available for this article.

[Copy to clipboard](#)

Provided by the Springer Nature SharedIt content-sharing initiative

[Relativity could ensure security for cash machines](#)

- Gilles Brassard

News & Views 03 Nov 2021

This article was downloaded by **calibre** from <https://www.nature.com/articles/s41586-021-03998-y>.

| [Section menu](#) | [Main menu](#) |

- Article
- [Published: 03 November 2021](#)

Signatures of bosonic Landau levels in a finite-momentum superconductor

- [A. Devarakonda](#) ORCID: [orcid.org/0000-0002-6095-7854¹](https://orcid.org/0000-0002-6095-7854),
- [T. Suzuki](#) ORCID: [orcid.org/0000-0002-5670-2103¹](https://orcid.org/0000-0002-5670-2103) nAff7,
- [S. Fang](#) ORCID: [orcid.org/0000-0002-9412-6426²](https://orcid.org/0000-0002-9412-6426),
- [J. Zhu¹](#),
- [D. Graf](#) ORCID: [orcid.org/0000-0001-6195-0462³](https://orcid.org/0000-0001-6195-0462),
- [M. Kriener](#) ORCID: [orcid.org/0000-0001-5220-8792⁴](https://orcid.org/0000-0001-5220-8792),
- [L. Fu¹](#),
- [E. Kaxiras](#) ORCID: [orcid.org/0000-0002-4682-0165^{5,6}](https://orcid.org/0000-0002-4682-0165) &
- [J. G. Checkelsky](#) ORCID: [orcid.org/0000-0003-0325-5204¹](https://orcid.org/0000-0003-0325-5204)

[Nature](#) volume 599, pages 51–56 (2021)

- 1391 Accesses
- 8 Altmetric
- [Metrics details](#)

Subjects

- [Electronic properties and materials](#)
- [Superconducting properties and materials](#)
- [Topological insulators](#)

Abstract

Charged particles subjected to magnetic fields form Landau levels (LLs). Originally studied in the context of electrons in metals¹, fermionic LLs continue to attract interest as hosts of exotic electronic phenomena^{2,3}. Bosonic LLs are also expected to realize novel quantum phenomena^{4,5}, but, apart from recent advances in synthetic systems^{6,7}, they remain relatively unexplored. Cooper pairs in superconductors—composite bosons formed by electrons—represent a potential condensed-matter platform for bosonic LLs. Under certain conditions, an applied magnetic field is expected to stabilize an unusual superconductor with finite-momentum Cooper pairs^{8,9} and exert control over bosonic LLs^{10,11,12,13}. Here we report thermodynamic signatures, observed by torque magnetometry, of bosonic LL transitions in the layered superconductor Ba₆Nb₁₁S₂₈. By applying an in-plane magnetic field, we observe an abrupt, partial suppression of diamagnetism below the upper critical magnetic field, which is suggestive of an emergent phase within the superconducting state. With increasing out-of-plane magnetic field, we observe a series of sharp modulations in the upper critical magnetic field that are indicative of distinct vortex states and with a structure that agrees with predictions for Cooper pair LL transitions in a finite-momentum superconductor^{10,11,12,13,14}. By applying Onsager’s quantization rule¹⁵, we extract the momentum. Furthermore, study of the fermionic LLs shows evidence for a non-zero Berry phase. This suggests opportunities to study bosonic LLs, topological superconductivity, and their interplay via transport¹⁶, scattering¹⁷, scanning probe¹⁸ and exfoliation techniques¹⁹.

Access options

Subscribe to Journal

Get full journal access for 1 year

\$199.00

only \$3.90 per issue

[Subscribe](#)

All prices are NET prices.

VAT will be added later in the checkout.

Tax calculation will be finalised during checkout.

Rent or Buy article

Get time limited or full article access on ReadCube.

from \$8.99

[Rent or Buy](#)

All prices are NET prices.

Additional access options:

- [Log in](#)
- [Access through your institution](#)
- [Learn about institutional subscriptions](#)

Fig. 1: Bosonic LLs, finite- q superconductivity and torque magnetization of $\text{Ba}_6\text{Nb}_{11}\text{S}_{28}$.

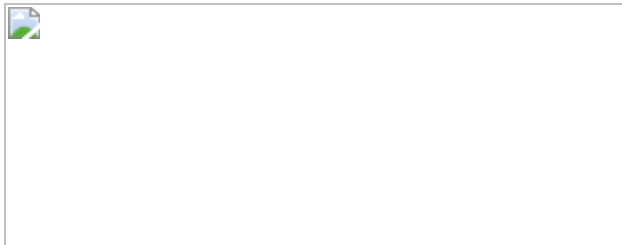


Fig. 2: Evidence of an emergent superconducting state.

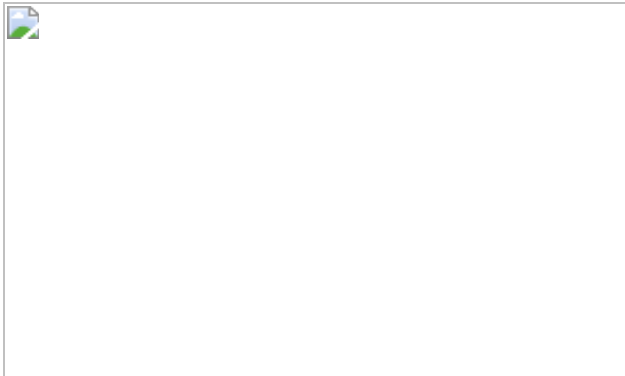


Fig. 3: Signatures of bosonic LL transitions.

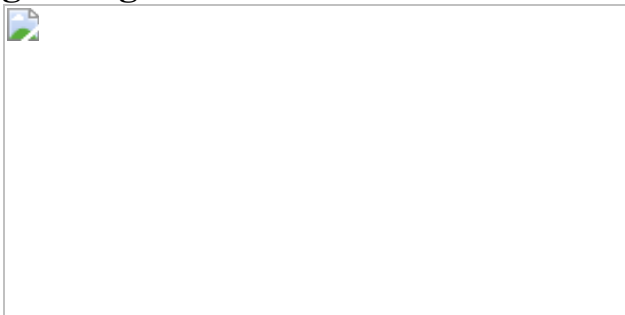
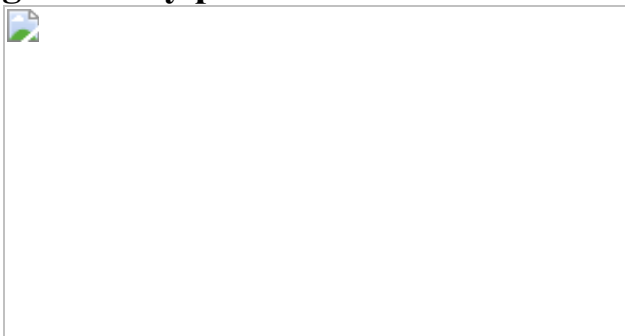


Fig. 4: Berry phase of fermionic LLs.



Data availability

The data presented in this article are available from the Harvard Dataverse at <https://doi.org/10.7910/DVN/PLWWKA>.

Code availability

The codes used for the density functional theory and analytical calculations in this study are available from the corresponding author upon reasonable request.

References

1. 1.

Shoenberg, D. The de Haas–Van Alphen Effect. *Phil. Trans. R. Soc. A* **245**, 1–57 (1952).

2. 2.

Bartolomei, H. et al. Fractional statistics in anyon collisions. *Science* **368**, 173–177 (2020).

3. 3.

Nakamura, J., Liang, S., Gardner, G. C. & Manfra, M. J. Direct observation of anyonic braiding statistics. *Nat. Phys.* **16**, 931–936 (2020).

4. 4.

Cooper, N. R., Wilkin, N. K. & Gunn, J. M. F. Quantum phases of vortices in rotating Bose–Einstein condensates. *Phys. Rev. Lett.* **87**, 120405 (2001).

5. 5.

Senthil, T. & Levin, M. Integer quantum Hall effect for bosons. *Phys. Rev. Lett.* **110**, 046801 (2013).

6. 6.

Schine, N., Ryou, A., Gromov, A., Sommer, A. & Simon, J. Synthetic Landau levels for photons. *Nature* **534**, 671–675 (2016).

7. 7.

Fletcher, R. J. et al. Geometric squeezing into the lowest Landau level. *Science* **372**, 1318–1322 (2021).

8. 8.

Fulde, P. & Ferrell, R. A. Superconductivity in a strong spin-exchange field. *Phys. Rev.* **135**, A550–A563 (1964).

9. 9.

Larkin, A. I. & Ovchinnikov, Y. I. Inhomogeneous state of superconductors. *Sov. Phys. JETP* **20**, 762–769 (1965).

10. 10.

Bulaevskii, L. N. Inhomogeneous state and the anisotropy of the upper critical field in layered superconductors with Josephson layer interaction. *Sov. Phys. JETP* **38**, 634–639 (1974).

11. 11.

Shimahara, H. & Rainer, D. Crossover from vortex states to the Fulde–Ferrell–Larkin–Ovchinnikov state in two-dimensional *s*- and *d*-wave superconductors. *J. Phys. Soc. Jpn* **66**, 3591–3599 (1997).

12. 12.

Klein, U. Two-dimensional superconductor in a tilted magnetic field: states with finite Cooper-pair momentum. *Phys. Rev. B* **69**, 134518 (2004).

13. 13.

Yang, K. & MacDonald, A. H. Vortex-lattice structure of Fulde–Ferrell–Larkin–Ovchinnikov superconductors. *Phys. Rev. B* **70**, 094512 (2004).

14. 14.

Bulaevskii, L. N. Magnetic properties of layered superconductors with weak interaction between the layers. *Sov. Phys. JETP* **37**, 1133–1136 (1973).

15. 15.

Onsager, L. Interpretation of the de Haas–van Alphen effect. *Phil. Mag.* **43**, 1006–1008 (1952).

16. 16.

Kasahara, Y. et al. Majorana quantization and half-integer thermal quantum Hall effect in a Kitaev spin liquid. *Nature* **559**, 227–231 (2018).

17. 17.

Huxley, A. et al. Realignment of the flux-line lattice by a change in the symmetry of superconductivity in UPt₃. *Nature* **406**, 160–164 (2000).

18. 18.

Wang, D. et al. Evidence for Majorana bound states in an iron-based superconductor. *Science* **362**, 333–335 (2018).

19. 19.

Yang, K. & Agterberg, D. F. Josephson effect in Fulde–Ferrell–Larkin–Ovchinnikov superconductors. *Phys. Rev. Lett.* **84**, 4970–4973 (2000).

20. 20.

Wen, X.-G. Topological orders and edge excitations in fractional quantum Hall states. *Adv. Phys.* **44**, 405–473 (1995).

21. 21.

Lilly, M. P., Cooper, K. B., Eisenstein, J. P., Pfeiffer, L. N. & West, K. W. Evidence for an anisotropic state of two-dimensional electrons in high Landau levels. *Phys. Rev. Lett.* **82**, 394–397 (1999).

22. 22.

Amet, F. et al. Supercurrent in the quantum Hall regime. *Science* **352**, 966–969 (2016).

23. 23.

Klemm, R. A. *Layered Superconductors* (Oxford Univ. Press, 2012).

24. 24.

Burkhardt, H. & Rainer, D. Fulde–Ferrell–Larkin–Ovchinnikov state in layered superconductors. *Ann. Phys.* **506**, 181–194 (1994).

25. 25.

Dao, V. H., Denisov, D., Buzdin, A. & Brison, J.-P. Role of crystal anisotropy on the vortex state in the Fulde–Ferrell–Larkin–Ovchinnikov (FFLO) phase. *Phys. Rev. B* **87**, 174509 (2013).

26. 26.

Matsuda, Y. & Shimahara, H. Fulde–Ferrell–Larkin–Ovchinnikov state in heavy fermion superconductors. *J. Phys. Soc. Jpn* **76**, 051005 (2007).

27. 27.

Wosnitza, J. FFLO states in layered organic superconductors. *Ann. Phys.* **530**, 1700282 (2018).

28. 28.

Devarakonda, A. et al. Clean 2D superconductivity in a bulk van der Waals superlattice. *Science* **370**, 231–236 (2020).

29. 29.

Tinkham, M. *Introduction to Superconductivity* (Dover Publications, 2004).

30. 30.

Gruenberg, L. W. & Gunther, L. Fulde–Ferrell effect in type-II superconductors. *Phys. Rev. Lett.* **16**, 996–998 (1966).

31. 31.

Klemm, R. A., Luther, A. & Beasley, M. R. Theory of the upper critical field in layered superconductors. *Phys. Rev. B* **12**, 877–891 (1975).

32. 32.

Lu, J. M. et al. Evidence for two-dimensional Ising superconductivity in gated MoS₂. *Science* **350**, 1353–1357 (2015).

33. 33.

Uji, S. et al. Quantum vortex melting and phase diagram in the layered organic superconductor κ-(BEDT-TTF)₂Cu(NCS)₂. *Phys. Rev. B* **97**, 024505 (2018).

34. 34.

Modler, R. “Anomalous peak effect”—Is it indicative of a generalized Fulde–Ferrell–Larkin–Ovchinnikov state? *Czech. J. Phys.* **46**, 3123–3130 (1996).

35. 35.

Kawamata, S., Itoh, N., Okuda, K., Mochiku, T. & Kadowaki, K. Observation of anisotropic pinning effect in Bi₂Sr₂CaCu₂O_{8+δ} single crystals. *Physica C* **195**, 103–108 (1992).

36. 36.

Abrikosov, A. A. Nobel Lecture: Type-II superconductors and the vortex lattice. *Rev. Mod. Phys.* **76**, 975–979 (2004).

37. 37.

Shoenberg, D. *Magnetic Oscillations in Metals* (Cambridge Univ. Press, 2009).

38. 38.

Smidman, M., Salamon, M. B., Yuan, H. Q. & Agterberg, D. F. Superconductivity and spin–orbit coupling in non-centrosymmetric materials: a review. *Rep. Prog. Phys.* **80**, 036501 (2017).

39. 39.

Mikitik, G. P. & Sharlai, Y. V. Manifestation of Berry’s phase in metal physics. *Phys. Rev. Lett.* **82**, 2147–2150 (1999).

40. 40.

Falicov, L. M. & Sievert, P. R. Magnetoresistance and magnetic breakdown. *Phys. Rev. Lett.* **12**, 558–561 (1964).

41. 41.

Schneider, J. M., Piot, B. A., Sheikin, I. & Maude, D. K. Using the de Haas–van Alphen effect to map out the closed three-dimensional Fermi surface of natural graphite. *Phys. Rev. Lett.* **108**, 117401 (2012).

42. 42.

Manchon, A., Koo, H. C., Nitta, J., Frolov, S. M. & Duine, R. A. New perspectives for Rashba spin–orbit coupling. *Nat. Mater.* **14**, 871–882 (2015).

43. 43.

Zhang, P. et al. Observation of topological superconductivity on the surface of an iron-based superconductor. *Science* **360**, 182–186 (2018).

44. 44.

Potter, A. C. & Lee, P. A. Engineering a $p + ip$ superconductor: comparison of topological insulator and Rashba spin–orbit-coupled materials. *Phys. Rev. B* **83**, 184520 (2011).

45. 45.

Hu, L. H., Liu, C. X. & Zhang, F. C. Topological Larkin–Ovchinnikov phase and Majorana zero mode chain in bilayer superconducting topological insulator films. *Commun. Phys.* **2**, 25 (2019).

46. 46.

Wang, Y. et al. Field-enhanced diamagnetism in the pseudogap state of the cuprate $\text{Bi}_2\text{Sr}_2\text{CaCu}_2\text{O}_{8+\delta}$ superconductor in an intense magnetic field. *Phys. Rev. Lett.* **95**, 247002 (2005).

47. 47.

Bergemann, C. et al. Superconducting magnetization above the irreversibility line in $\text{Tl}_2\text{Ba}_2\text{CuO}_{6+\delta}$. *Phys. Rev. B* **57**, 14387–14396 (1998).

48. 48.

Li, L. et al. Diamagnetism and Cooper pairing above T_c in cuprates. *Phys. Rev. B* **81**, 054510 (2010).

49. 49.

Sugiura, S. et al. Fulde–Ferrell–Larkin–Ovchinnikov and vortex phases in a layered organic superconductor. *npj Quantum Mater.* **4**, 7 (2019).

50. 50.

Campbell, A. M., Evetts, J. E. & Dew-hughes, D. The behaviour of type II superconductors. *Phil. Mag.* **10**, 333–338 (1964).

51. 51.

Finnemore, D. K., Stromberg, T. F. & Swenson, C. A. Superconducting properties of high-purity niobium. *Phys. Rev.* **149**, 231–243 (1966).

52. 52.

Altshuler, E. & Johansen, T. H. Colloquium: Experiments in vortex avalanches. *Rev. Mod. Phys.* **76**, 471–487 (2004).

53. 53.

Swanson, A. G. et al. Flux jumps, critical fields, and de Haas–van Alphen effect in κ -(BEDT-TTF)₂Cu(NCS)₂. *Solid State Commun.* **73**, 353–356 (1990).

54. 54.

Tenya, K. et al. Anomalous pinning behavior in Sr₂RuO₄. *Physica B* **403**, 1101–1103 (2008).

55. 55.

Li, L., Checkelsky, J. G., Komiya, S., Ando, Y. & Ong, N. P. Low-temperature vortex liquid in La_{2-x}Sr_xCuO₄. *Nat. Phys.* **3**, 311–314 (2007).

56. 56.

Chaikin, P. M. & Lubensky, T. C. *Principles of Condensed Matter Physics* (Cambridge Univ. Press, 1995).

57. 57.

Takahashi, M., Mizushima, T. & Machida, K. Multiband effects on Fulde–Ferrell–Larkin–Ovchinnikov states of Pauli-limited superconductors. *Phys. Rev. B* **89**, 064505 (2014).

58. 58.

Campbell, A. M. & Evetts, J. E. Flux vortices and transport currents in type II superconductors. *Adv. Phys.* **21**, 199–428 (1972).

59. 59.

Roy, S. B. & Chaddah, P. Anomalous superconducting properties in CeRu₂: effects of magnetic and nonmagnetic substitutions. *Phys. Rev. B* **55**, 11100–11102 (1997).

60. 60.

Lortz, R. et al. Calorimetric evidence for a Fulde–Ferrell–Larkin–Ovchinnikov superconducting state in the layered organic superconductor κ-(BEDT-TTF)₂Cu(NCS)₂. *Phys. Rev. Lett.* **99**, 187002 (2007).

61. 61.

Farrell, D. E., Rice, J. P. & Ginsberg, D. M. Experimental evidence for flux-lattice melting. *Phys. Rev. Lett.* **67**, 1165–1168 (1991).

62. 62.

Beck, R. G., Farrell, D. E., Rice, J. P., Ginsberg, D. M. & Kogan, V. G. Melting of the Abrikosov flux lattice in anisotropic superconductors. *Phys. Rev. Lett.* **68**, 1594–1596 (1992).

63. 63.

Ooi, S., Shibauchi, T., Okuda, N. & Tamegai, T. Novel angular scaling of vortex phase transitions in Bi₂Sr₂CaCu₂O_{8+y}. *Phys. Rev. Lett.* **82**, 4308–4311 (1999).

64. 64.

Uji, S. et al. Orbital effect on FFLO phase and energy dissipation due to vortex dynamics in magnetic-field-induced superconductor λ - $(\text{BETS})_2\text{FeCl}_4$. *J. Phys. Soc. Jpn* **82**, 034715 (2013).

65. 65.

Martínez, J. C. et al. Magnetic anisotropy of a $\text{Bi}_2\text{Sr}_2\text{CaCu}_2\text{O}_x$ single crystal. *Phys. Rev. Lett.* **69**, 2276–2279 (1992).

66. 66.

Feinberg, D. & Villard, C. Intrinsic pinning and lock-in transition of flux lines in layered type-II superconductors. *Phys. Rev. Lett.* **65**, 919–922 (1990).

67. 67.

Buzdin, A. I. & Kachkachi, H. Generalized Ginzburg–Landau theory for nonuniform FFLO superconductors. *Phys. Lett. A* **225**, 341–348 (1997).

68. 68.

Houzet, M. & Buzdin, A. Influence of the paramagnetic effect on the vortex lattice in 2D superconductors. *Europhys. Lett.* **50**, 375–381 (2000).

69. 69.

Denisov, D., Buzdin, A. & Shimahara, H. Types of Fulde–Ferrell–Larkin–Ovchinnikov states induced by anisotropy effects. *Phys. Rev. B* **79**, 064506 (2009).

70. 70.

Shoenberg, D. Magnetization of a two-dimensional electron gas. *J. Low Temp. Phys.* **56**, 417–440 (1984).

71. 71.

Yoshida, T., Sigrist, M. & Yanase, Y. Complex-stripe phases induced by staggered Rashba spin–orbit coupling. *J. Phys. Soc. Jpn* **82**, 074714 (2013).

72. 72.

Zhou, T. & Ting, C. S. Phase diagram and local tunneling spectroscopy of the Fulde–Ferrell–Larkin–Ovchinnikov states of a two-dimensional square-lattice *d*-wave superconductor. *Phys. Rev. B* **80**, 224515 (2009).

73. 73.

Yuan, N. F. Q. & Fu, L. Topological metals and finite-momentum superconductors. *Proc. Natl Acad. Sci. USA* **118**, e2019063118 (2021).

74. 74.

Agterberg, D. F. & Kaur, R. P. Magnetic-field-induced helical and stripe phases in Rashba superconductors. *Phys. Rev. B* **75**, 064511 (2007).

75. 75.

Kresse, G. & Furthmüller, J. Efficiency of ab-initio total energy calculations for metals and semiconductors using a plane-wave basis set. *Comput. Mater. Sci.* **6**, 15–50 (1996).

76. 76.

Kresse, G. & Furthmüller, J. Efficient iterative schemes for ab initio total-energy calculations using a plane-wave basis set. *Phys. Rev. B* **54**, 11169–11186 (1996).

77. 77.

Blöchl, P. E. Projector augmented-wave method. *Phys. Rev. B* **50**, 17953–17979 (1994).

78. 78.

Perdew, J. P., Burke, K. & Ernzerhof, M. Generalized gradient approximation made simple. *Phys. Rev. Lett.* **77**, 3865–3868 (1996).

79. 79.

Monkhorst, H. J. & Pack, J. D. Special points for Brillouin-zone integrations. *Phys. Rev. B* **13**, 5188–5192 (1976).

80. 80.

Marzari, N., Mostofi, A. A., Yates, J. R., Souza, I. & Vanderbilt, D. Maximally localized Wannier functions: theory and applications. *Rev. Mod. Phys.* **84**, 1419–1475 (2012).

81. 81.

Mostofi, A. A. et al. wannier90: a tool for obtaining maximally-localised Wannier functions. *Comput. Phys. Commun.* **178**, 685–699 (2008).

82. 82.

Mostofi, A. A. et al. An updated version of wannier90: a tool for obtaining maximally-localised Wannier functions. *Comput. Phys. Commun.* **185**, 2309–2310 (2014).

83. 83.

Liu, G.-B., Shan, W.-Y., Yao, Y., Yao, W. & Xiao, D. Three-band tight-binding model for monolayers of group-VIB transition metal dichalcogenides. *Phys. Rev. B* **88**, 085433 (2013).

84. 84.

Fang, S. et al. Ab initio tight-binding Hamiltonian for transition metal dichalcogenides. *Phys. Rev. B* **92**, 205108 (2015).

85. 85.

Xi, X. et al. Ising pairing in superconducting NbSe₂ atomic layers. *Nat. Phys.* **12**, 139–143 (2016).

86. 86.

Saito, Y. et al. Superconductivity protected by spin–valley locking in ion-gated MoS₂. *Nat. Phys.* **12**, 144–149 (2016).

87. 87.

Xiao, D., Chang, M. C. & Niu, Q. Berry phase effects on electronic properties. *Rev. Mod. Phys.* **82**, 1959–2007 (2010).

88. 88.

Fukui, T., Hatsugai, Y. & Suzuki, H. Chern numbers in discretized Brillouin zone: efficient method of computing (spin) Hall conductances. *J. Phys. Soc. Jpn* **74**, 1674–1677 (2005).

89. 89.

Aroyo, M. I. et al. Crystallography online: Bilbao Crystallographic Server. *Bulg. Chem. Commun.* **43**, 183–197 (2011).

90. 90.

Aroyo, M. I. et al. Bilbao Crystallographic Server: I. Databases and crystallographic computing programs. *Z. Kristallogr. Cryst. Mater.* **221**, 15–27 (2006).

91. 91.

Aroyo, M. I., Kirov, A., Capillas, C., Perez-Mato, J. M. & Wondratschek, H. Bilbao Crystallographic Server. II. Representations of crystallographic point groups and space groups. *Acta Crystallogr. A* **62**, 115–128 (2006).

92. 92.

Culcer, D., MacDonald, A. & Niu, Q. Anomalous Hall effect in paramagnetic two-dimensional systems. *Phys. Rev. B* **68**, 045327 (2003).

93. 93.

Wright, A. R. & McKenzie, R. H. Quantum oscillations and Berry's phase in topological insulator surface states with broken particle–hole symmetry. *Phys. Rev. B* **87**, 085411 (2013).

94. 94.

Alexandradinata, A., Wang, C., Duan, W. & Glazman, L. Revealing the topology of Fermi-surface wave functions from magnetic quantum oscillations. *Phys. Rev. X* **8**, 011027 (2018).

95. 95.

Kaganov, M. I. & Slutskin, A. A. Coherent magnetic breakdown. *Phys. Rep.* **98**, 189–271 (1983).

96. 96.

Harrison, N. et al. Magnetic breakdown and quantum interference in the quasi-two-dimensional superconductor κ -(BEDT-TTF)₂Cu(NCS)₂ in high magnetic fields. *J. Phys. Condens. Matter* **8**, 5415–5435 (1996).

97. 97.

Gvozdikov, V. M. & Taut, M. Magnetic quantum oscillations of electrons on a two-dimensional lattice: Numerical simulations and the magnetic breakdown approach. *Phys. Rev. B* **75**, 155436 (2007).

98. 98.

Fuchs, J. N., Piéchon, F., Goerbig, M. O. & Montambaux, G. Topological Berry phase and semiclassical quantization of cyclotron orbits for two dimensional electrons in coupled band models. *Eur. Phys. J. B* **77**, 351–362 (2010).

99. 99.

Zhang, Y., Tan, Y.-W., Stormer, H. L. & Kim, P. Experimental observation of the quantum Hall effect and Berry's phase in graphene. *Nature* **438**, 201–204 (2005).

100. 100.

Analytis, J. G. et al. Two-dimensional surface state in the quantum limit of a topological insulator. *Nat. Phys.* **6**, 960–964 (2010).

101. 101.

Xiong, J. et al. High-field Shubnikov–de Haas oscillations in the topological insulator Bi₂Te₂Se. *Phys. Rev. B* **86**, 045314 (2012).

102. 102.

Das, B. et al. Evidence for spin splitting in In_xGa_{1-x}As/In_{0.52}Al_{0.48}As heterostructures as $B \rightarrow 0$. *Phys. Rev. B* **39**, 1411–1414 (1989).

103. 103.

Nakamura, H., Koga, T. & Kimura, T. Experimental evidence of cubic Rashba effect in an inversion-symmetric oxide. *Phys. Rev. Lett.* **108**, 206601 (2012).

104. 104.

Winkler, R. *Spin–Orbit Coupling Effects in Two-dimensional Electron and Hole Systems* (Springer, 2003).

105. 105.

Forsythe, C. et al. Band structure engineering of 2D materials using patterned dielectric superlattices. *Nat. Nanotechnol.* **13**, 566–571 (2018).

106. 106.

Alicea, J. Majorana fermions in a tunable semiconductor device. *Phys. Rev. B* **81**, 125318 (2010).

107. 107.

Nakosai, S., Tanaka, Y. & Nagaosa, N. Topological superconductivity in bilayer Rashba system. *Phys. Rev. Lett.* **108**, 147003 (2012).

Acknowledgements

We are grateful to S. K. Yip, M. Shayegan and M. T. Randeria for discussions. This research is funded in part by the Gordon and Betty Moore Foundation through grant GBMF9070 to J.G.C. (instrumentation development), the Office of Naval Research (ONR) under award N00014-21-1-2591 (advanced characterization), the US Department of Energy (DOE) Office of Science, Basic Energy Sciences, under award DE-SC0019300 (material synthesis) and award DE-SC0022028 (structure analysis), the STC Center for Integrated Quantum Materials, NSF grant DMR-1231319 (E.K.) and the DOE Office of Basic Energy Sciences under award DE-SC0018945 (L.F.). S.F. acknowledges support from the Rutgers Center for Materials Theory Distinguished Postdoctoral Fellowship. Computations were performed on the Cannon cluster supported by the FAS Division of Science Research Computing Group (FASRC) at Harvard University. A portion of this work was performed at the National High Magnetic Field Laboratory, which is supported by NSF Cooperative Agreement DMR-1157490, the State of Florida, and DOE.

Author information

Author notes

1. T. Suzuki

Present address: Department of Physics, Toho University, Funabashi, Japan

Affiliations

1. Department of Physics, Massachusetts Institute of Technology, Cambridge, MA, USA

A. Devarakonda, T. Suzuki, J. Zhu, L. Fu & J. G. Checkelsky

2. Department of Physics and Astronomy, Center for Materials Theory, Rutgers University, Piscataway, NJ, USA

S. Fang

3. National High Magnetic Field Laboratory, Tallahassee, FL, USA

D. Graf

4. RIKEN Center for Emergent Matter Science (CEMS), Wako, Japan

M. Kriener

5. Department of Physics, Harvard University, Cambridge, MA, USA

E. Kaxiras

6. John A. Paulson School of Engineering and Applied Sciences, Harvard University, Cambridge, MA, USA

E. Kaxiras

Contributions

A.D. and J.G.C. conceived the project. A.D. grew the single crystals, characterized the materials, and performed the measurements with T.S.,

J.Z., D.G. and M.K. supporting. A.D. performed the analytical calculations and S.F. and A.D. the electronic structure calculations with L.F. and E.K. supporting. A.D. and J.G.C. wrote the manuscript with contributions and discussions from all authors. J.G.C. supervised the project.

Corresponding author

Correspondence to J. G. Checkelsky.

Ethics declarations

Competing interests

The authors declare no competing interests.

Additional information

Peer review information *Nature* thanks the anonymous reviewers for their contribution to the peer review of this work.

Publisher's note Springer Nature remains neutral with regard to jurisdictional claims in published maps and institutional affiliations.

Extended data figures and tables

[Extended Data Fig. 1 Torque magnetometry.](#)

a Non-collinear response of M to H results in τ which can be measured using torque magnetometry techniques. **b** Capacitive torque magnetometer (sample S1). **c** Resistive torque magnetometer (sample S2). Scale bars are 1 mm. **d** $\delta C(H)$ at $\theta = 89.7^\circ$ and $T = 0.3$ K for sample S1. (inset) The experimental geometry for S1. $\delta C < 0$ is consistent with diamagnetic response of $\langle M \rangle$. **e** Comparison of $\rho_{xx}(T)$ and $M_\tau(T)$ measured with $\mu_0 H_\perp = 0.4$ mT for sample S1. **f** Comparison of $\rho_{xx}(H)$ and $M_\tau(H)$ at $\theta = 89.7^\circ$ and $T = 0.3$ K for sample S1. **g** $\langle M(H) \rangle$ loop for $\theta = 0^\circ$ at $T = 0.4$ K measured by

SQUID. **h** $M_\tau(H)$ loop for $\theta = 46^\circ$ at $T = 0.3$ K measured by torque magnetometry (S1). (inset) $\tau(H)$ from which we obtain $M_\tau(H)$ in the main panel. **i** δ quantum oscillation frequency $F(\theta_H)$ (orange points) with fit to equation (2) (dashed line). (inset) θ where $M_\tau(H)$ oscillates around zero corresponds to $\theta = 90^\circ$.

Extended Data Fig. 2 Survey of H - T - θ phase space (sample S1).

a $\partial M_\tau(H)/\partial H$ of up-sweep $M_\tau(H)$ (see Fig. 2a) at $\theta = 89.7^\circ$ and various fixed temperatures, vertically offset for clarity. The peak-like structure marking H^* is traced by a dashed guide to the eye. **b** Up- (solid) and down-sweep (dashed) $M_\tau(H)$ measured at $T = 0.31$ K at various angles between 80° and 90° , vertically offset for clarity. **c** Up- (solid) and down-sweep (dashed) $M_\tau(H)$ measured at $\theta = 89.2^\circ$ at various fixed temperatures, vertically offset for clarity. **d** $\partial M_\tau(H)/\partial H$ of up-sweep $M_\tau(H)$ at $\theta = 89.2^\circ$ (shown in c) for various fixed temperatures, vertically offset for clarity. The peak-like structure marking H^* is absent here. **e** T - H phase diagram at $\theta = 89.2^\circ$ showing H_{c2} and H_{c1} .

Extended Data Fig. 3 H - T phase diagram (sample S2).

a Up- (solid) and down-sweep (dashed) $M_\tau(H)$ measured at $\theta = 88.9^\circ$ for various temperatures, vertically offset for clarity. **b** $\partial M_\tau(H)/\partial H$ of up-sweep $M_\tau(H)$ at $\theta = 88.9^\circ$ (shown in a) for fixed temperatures down to $T = 33$ mK, vertically offset for clarity. The peak-like structure at H^* is traced by a dashed guide to the eye. **c** T - H phase diagram at $\theta = 88.9^\circ$ showing H_{c2} , H^* , and H_{c1} . Black circle marks T_c .

Extended Data Fig. 4 $M_\tau(H)$ at fixed T and θ (sample S1).

a Up- (solid) and down-sweeps (dashed) of $M_\tau(H)$ for $T = 395$ mK at equally spaced, fixed θ between 89.30° and 89.95° , vertically offset for clarity. **b** $\partial M_\tau(H)/\partial H$ of up-sweep in (a), vertically offset for clarity. Guide

to the eye (grey dashed line) traces corrugation of $H^*(\theta)$. **c** Up- (solid) and down-sweeps (dashed) of $M_\tau(H)$ for $T = 460$ mK at equally spaced, fixed θ between 89.75° and 89.95° , vertically offset for clarity. **d** $\partial M_\tau(H)/\partial H$ of up-sweep in (c), vertically offset for clarity. Guide to the eye (grey dashed line) traces corrugation of $H^*(\theta)$.

Extended Data Fig. 5 Low temperature $M_\tau(H)$ at fixed θ .

a Up- and **b** down-sweeps of $M_\tau(H)$ for $T = 20$ mK at equally spaced, fixed θ between 88.45° and 89.95° , vertically offset for clarity. Guide to the eye (grey dashed line) in (b) traces angular evolution of $H'(\theta)$ **c** $\partial M_\tau(H)/\partial H$ of up-sweep $M_\tau(H)$ in (a), vertically offset for clarity. Guide to the eye (grey dashed line) traces corrugation of $H^*(\theta)$ (inset) Up- and down-sweep $M_\tau(H)$ (solid and dashed, respectively) at fixed angles near 90° for a third sample, S3.

Extended Data Fig. 6 Ginzburg-Landau modeling.

a GL free energy $\delta F(q_x, q_y)$ in the finite- q pairing state of an isotropic superconductor. Finite- q pairing with $|\mathbf{q}| = q_0$ minimizes δF (red contour). **b** (black line) Radial cut of $\delta F(q)$ for $H_\perp = 0$. (orange points) For $H_\perp \neq 0$, discrete LLs are formed. The LL with $(2n+1)^{1/2}/l_\perp$ closest to q_0 is the optimal solution. **c** Superconductivity opens a gap Δ_{SC} around the Fermi energy E_F (orange). **d** Magnetic field causes Zeeman splitting of a spin-degenerate band (dashed) into spin-up (blue) and spin-down (red) bands. **e** Zeeman split bands create two Fermi surface contours in k -space separated by q .

Extended Data Fig. 7 Electronic structure modeling.

a The Fermi surface contours for monolayer H -NbS₂. The supercell Brillouin zones and corresponding M points are shown as white lines and open blue circles, respectively. **b** Electronic structure resulting from 3×3 zone-folding. This is formed by overlapping the nine cells marked by white

lines in (a). **c** Fermi surface contours from first-principles calculations capturing monolayer $H\text{-NbS}_2$ and the spacer layer 3×3 perturbation. This resembles (b) but with additional band gaps and renormalization due to the spacer layer perturbation. **d** Electronic structure around K, K' from first-principles with the δ pocket corresponding to f_δ identified. **e** Electronic structure around M from first-principles showing the inner α_1 and outer α_2 pockets. **f** Bloch sphere showing spin-texture along the δ pocket. (inset) Expanded view near the north pole of the Bloch sphere. Blue arrow shows sense of spin evolution for clockwise motion along the δ pocket, see white arrow in (d). **g** Bloch sphere showing spin-texture along the α_1 (blue) and α_2 (red) pockets. Blue (red) arrow shows sense of spin evolution for clockwise motion along the α_1 (α_2) pocket, see white arrows in (e). **h** Coordinate system used for M point $\mathbf{k} \cdot \mathbf{p}$ model. **i** Bloch sphere showing the segments $\backslash(\{\mathfrak{C}\}\}_{\{a\}}\backslash$ (red) and $\backslash(\{\mathfrak{C}\}\}_{\{b\}}\backslash$ (blue) traced by the spin-1/2 eigenvector $\backslash(\{\mathrm{rm}\}\}\backslash\mathrm{varPsi}\backslash\mathrm{rm}\{\rangle\})$ which together form a closed contour $\backslash(\{\mathfrak{C}\}\backslash)$. **j** Berry curvature $\Omega_B(k_x, k_y)$. For $\Delta_M \neq 0$, Ω_B integrated over the area A_k defined by the FS contour yields $\varphi_B \neq \pi$.

Extended Data Fig. 8 de Haas-van Alphen oscillations.

a $\langle(M)_\tau^\alpha \rangle(H_\perp)$ at $T = 0.3$ K for various angles. The oscillations are aligned across 75° when plotted versus H_\perp indicating the two-dimensionality of the FSs. **b** $\langle(M)_\tau^\alpha \rangle(H)$ at $\theta = 18^\circ$ for various temperatures. **c** $\langle(\widetilde{A})_{\widetilde{\alpha}}(T)\rangle$ for the α and δ oscillations (points) with fits to $\langle(R)_T^i\rangle$ (Methods) to extract the effective mass. **d** $\langle(M)_\tau^\alpha \rangle(1/H)$ measured at $T = 20$ mK for $\theta = 8.2^\circ$ (blue). The result of applying a sliding window centered at various equally spaced $1/H_0$ are shown as gray and orange traces, vertically offset for clarity. **e** FFT of un-windowed (blue) and windowed (gray) $\langle(M)_\tau^\alpha \rangle(1/H)$ in (d), vertically offset for clarity. The peak at $\langle f \rangle_{\alpha}^{\star}$ (grey dashed guide) appears for $1/\mu_0 H_0 < 0.21$ T $^{-1}$, orange trace in (d) and (e).

Extended Data Fig. 9 Phase analysis.

a $M_\tau(H)$ measured at $T = 0.3$ K and $\theta = 80^\circ$ showing both the Meissner effect (left) and dHvA quantum oscillation (right). **b** $(M_\tau \tau)^{\text{osc}}(1/H_\perp)$ at $T = 0.3$ K ($T = 20$ mK) for sample(s) S1 (S4-S5) at angles near $\theta = 16^\circ$. **c-f** Phase-shift function $K(f, \varphi_B)$ around the δ (left) and α (right) oscillations for samples S1, S3, S4, and S5 using $(M_\tau \tau)^{\text{osc}}$ shown in (b). The red contours are drawn at 98% of the local maxima. $K(f, \varphi_B)$ for S2 is shown in Fig. 4b.

Extended Data Fig. 10 Calculated Landau level spectrum.

a (M) -point pockets resulting from the $\mathbf{k} \cdot \mathbf{p}$ model with the experimentally determined SOC parameters. The inner (outer) contour in red (blue) corresponds to the measured $(f_{\rm rm\alpha})_1$ ($(f_{\rm rm\alpha})_2$) frequency. The intersecting dashed green circles are the contours in the presence of mirror symmetry. **b** Calculated density of states in the presence of H showing oscillations due to Landau quantization of the electronic structure in (a). (inset) FFT power spectrum shows three modes corresponding to $(f_{\rm rm\alpha})_1$ (red), $(f_{\rm rm\alpha})_2$ (blue), and the breakdown frequency $(f_{\rm rm\alpha})^*$ (green). **c** The breakdown contribution at $(f_{\rm rm\alpha})^*$ in the FFT power spectrum vanishes at $\mu_0 H_{\text{mb}} \approx 6$ T. **d** FFT power spectrum at various values of the chemical potential E_F showing a Landau fan. By comparing with the observed pocket sizes, we can estimate E_F .

Rights and permissions

[Reprints and Permissions](#)

About this article

Cite this article

Devarakonda, A., Suzuki, T., Fang, S. *et al.* Signatures of bosonic Landau levels in a finite-momentum superconductor. *Nature* **599**, 51–56 (2021).

<https://doi.org/10.1038/s41586-021-03915-3>

- Received: 15 February 2021
- Accepted: 16 August 2021
- Published: 03 November 2021
- Issue Date: 04 November 2021
- DOI: <https://doi.org/10.1038/s41586-021-03915-3>

Share this article

Anyone you share the following link with will be able to read this content:

[Get shareable link](#)

Sorry, a shareable link is not currently available for this article.

[Copy to clipboard](#)

Provided by the Springer Nature SharedIt content-sharing initiative

This article was downloaded by **calibre** from <https://www.nature.com/articles/s41586-021-03915-3>

| [Section menu](#) | [Main menu](#) |

- Article
- [Published: 03 November 2021](#)

Reconstruction of Bloch wavefunctions of holes in a semiconductor

- [J. B. Costello](#) ORCID: orcid.org/0000-0002-7764-2701^{1 na1},
- [S. D. O'Hara](#) ORCID: orcid.org/0000-0001-7650-8589^{1 na1},
- [Q. Wu](#) ORCID: orcid.org/0000-0002-6218-3338^{1 na1},
- [D. C. Valoycin](#)²,
- [L. N. Pfeiffer](#)³,
- [K. W. West](#)³ &
- [M. S. Sherwin](#) ORCID: orcid.org/0000-0002-3869-1893¹

Nature volume **599**, pages 57–61 (2021)

- 1076 Accesses
- 6 Altmetric
- [Metrics details](#)

Subjects

- [Electronic properties and materials](#)
- [High-harmonic generation](#)
- [Terahertz optics](#)

Abstract

A central goal of condensed-matter physics is to understand how the diverse electronic and optical properties of crystalline materials emerge from the wavelike motion of electrons through periodically arranged atoms.

However, more than 90 years after Bloch derived the functional forms of electronic waves in crystals¹ (now known as Bloch wavefunctions), rapid scattering processes have so far prevented their direct experimental reconstruction. In high-order sideband generation^{2,3,4,5,6,7,8,9}, electrons and holes generated in semiconductors by a near-infrared laser are accelerated to a high kinetic energy by a strong terahertz field, and recollide to emit near-infrared sidebands before they are scattered. Here we reconstruct the Bloch wavefunctions of two types of hole in gallium arsenide at wavelengths much longer than the spacing between atoms by experimentally measuring sideband polarizations and introducing an elegant theory that ties those polarizations to quantum interference between different recollision pathways. These Bloch wavefunctions are compactly visualized on the surface of a sphere. High-order sideband generation can, in principle, be observed from any direct-gap semiconductor or insulator. We thus expect that the method introduced here can be used to reconstruct low-energy Bloch wavefunctions in many of these materials, enabling important insights into the origin and engineering of the electronic and optical properties of condensed matter.

Access options

Subscribe to Journal

Get full journal access for 1 year

\$199.00

only \$3.90 per issue

[Subscribe](#)

All prices are NET prices.

VAT will be added later in the checkout.

Tax calculation will be finalised during checkout.

Rent or Buy article

Get time limited or full article access on ReadCube.

from \$8.99

[Rent or Buy](#)

All prices are NET prices.

Additional access options:

- [Log in](#)
- [Access through your institution](#)
- [Learn about institutional subscriptions](#)

Fig. 1: High-order sideband generation in bulk GaAs.

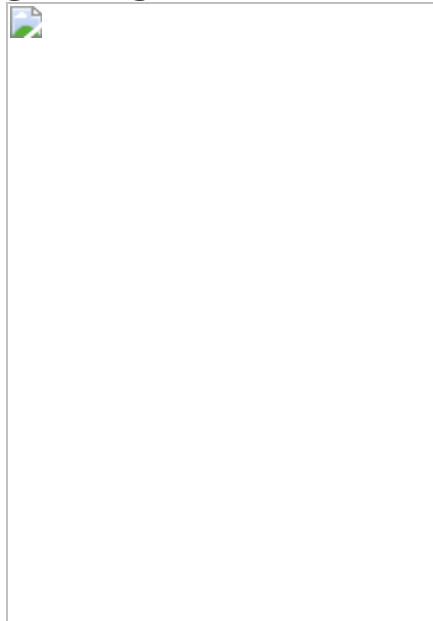


Fig. 2: Quantum interference leading to sideband polarization.

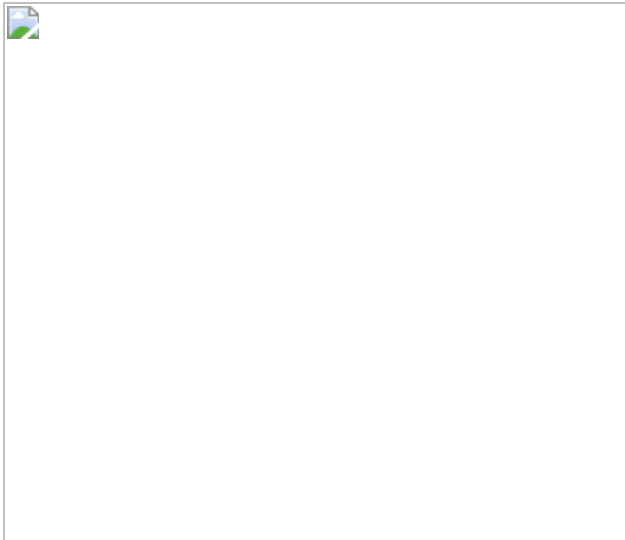


Fig. 3: Ratios of Jones matrix elements, $\xi_n(\theta) \equiv T_{++,n}(\theta)/T_{--,n}(\theta)$ and $\chi_n(\theta) \equiv T_{+-,n}(\theta)/T_{-+,n}(\theta)$, **measured by Stokes polarimetry.**

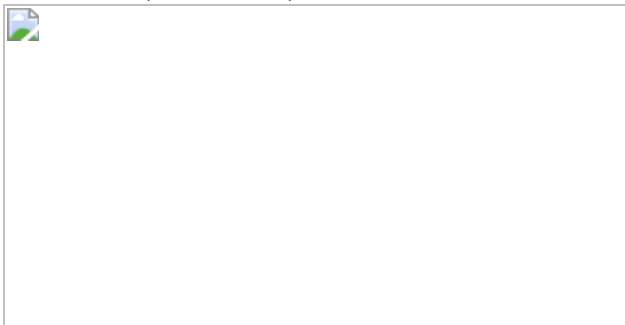
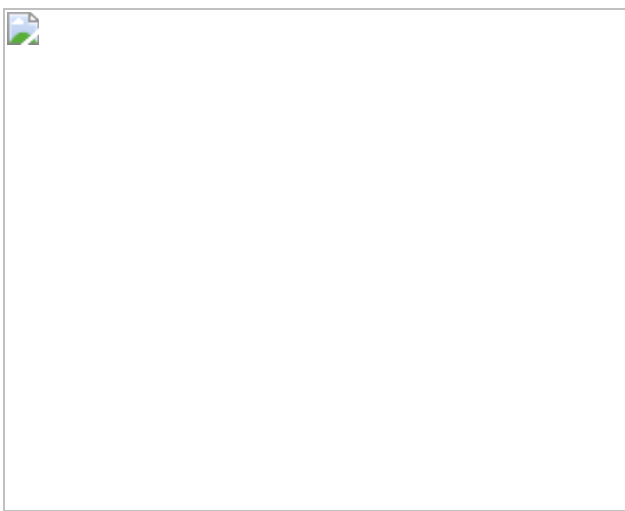


Fig. 4: Reconstruction of the Bloch wavefunctions for $k_z = 0$.



Data availability

The datasets generated and/or analysed during the current study are available in the Materials Cloud repository^{[36](#)}. [Source data](#) are provided with this paper.

Code availability

The codes used in the data analysis are available at Zenodo^{[37](#)}.

References

1. 1.

Bloch, F. *Über die quantenmechanik der elektronen in kristallgittern.* *Z. Phys.* **52**, 555–600 (1929).

2. 2.

Zaks, B., Liu, R. B. & Sherwin, M. S. Experimental observation of electron–hole recollisions. *Nature* **483**, 580–583 (2012).

3. 3.

Banks, H. et al. Terahertz electron–hole recollisions in GaAs/AlGaAs quantum wells: robustness to scattering by optical phonons and thermal fluctuations. *Phys. Rev. Lett.* **111**, 267402 (2013).

4. 4.

Zaks, B., Banks, H. & Sherwin, M. S. High-order sideband generation in bulk GaAs. *Appl. Phys. Lett.* **102**, 012104 (2013).

5. 5.

Langer, F. et al. Lightwave-driven quasiparticle collisions on a subcycle timescale. *Nature* **533**, 225–229 (2016).

6. 6.

Banks, H. B. et al. Dynamical birefringence: electron–hole recollisions as probes of Berry curvature. *Phys. Rev. X* **7**, 041042 (2017).

7. 7.

Valovcin, D. C. et al. Optical frequency combs from high-order sideband generation. *Opt. Express* **26**, 29807–29816 (2018).

8. 8.

Langer, F. et al. Lightwave valleytronics in a monolayer of tungsten diselenide. *Nature* **557**, 76–80 (2018).

9. 9.

Borsch, M. et al. Super-resolution lightwave tomography of electronic bands in quantum materials. *Science* **370**, 1204–1207 (2020).

10. 10.

Yang, H. F. et al. Visualizing electronic structures of quantum materials by angle-resolved photoemission spectroscopy. *Nat. Rev. Mater.* **3**, 341–353 (2018).

11. 11.

Damascelli, A., Hussain, Z. & Shen, Z. X. Angle-resolved photoemission studies of the cuprate superconductors. *Rev. Mod. Phys.* **75**, 473–541 (2003).

12. 12.

Lawaetz, P. Valence-band parameters in cubic semiconductors. *Phys. Rev. B* **4**, 3460–3467 (1971).

13. 13.

Vurgaftman, I., Meyer, J. R. & Ram-Mohan, L. R. Band parameters for III–V compound semiconductors and their alloys. *J. Appl. Phys.* **89**,

5815–5875 (2001).

14. 14.

Skolnick, M. S. et al. An investigation of anisotropy of valence band of GaAs by cyclotron-resonance. *J. Phys. C* **9**, 2809–2821 (1976).

15. 15.

Itatani, J. et al. Tomographic imaging of molecular orbitals. *Nature* **432**, 867–871 (2004).

16. 16.

Luftner, D. et al. Imaging the wave functions of adsorbed molecules. *Proc. Natl Acad. Sci. USA* **111**, 605–610 (2014).

17. 17.

Shafir, D., Mairesse, Y., Villeneuve, D. M., Corkum, P. B. & Dudovich, N. Atomic wavefunctions probed through strong-field light-matter interaction. *Nat. Phys.* **5**, 412–416 (2009).

18. 18.

Ghimire, S. & Reis, D. A. High-harmonic generation from solids. *Nat. Phys.* **15**, 10–16 (2019).

19. 19.

Hohenleutner, M. et al. Real-time observation of interfering crystal electrons in high-harmonic generation. *Nature* **523**, 572–575 (2015).

20. 20.

Ghimire, S. & Reis, D. A. High-harmonic generation from solids. *Nat. Phys.* **15**, 10–16 (2019).

21. 21.

Liu, H. Z. et al. High-harmonic generation from an atomically thin semiconductor. *Nat. Phys.* **13**, 262–265 (2017).

22. 22.

Vampa, G. et al. All-optical reconstruction of crystal band structure. *Phys. Rev. Lett.* **115**, 193603 (2015).

23. 23.

Luu, T. T. et al. Extreme ultraviolet high-harmonic spectroscopy of solids. *Nature* **521**, 498–502 (2015).

24. 24.

Ramian, G. The new UCSB free-electron lasers. *Nucl. Instrum. Methods Phys. A* **318**, 225–229 (1992).

25. 25.

Luttinger, J. M. & Kohn, W. Motion of electrons and holes in perturbed periodic fields. *Phys. Rev.* **97**, 869–883 (1955).

26. 26.

Bernevig, B. A., Hughes, T. L. & Zhang, S. C. Quantum spin Hall effect and topological phase transition in HgTe quantum wells. *Science* **314**, 1757–1761 (2006).

27. 27.

Fulop, J. A., Tzortzakis, S. & Kampfrath, T. Laser-driven strong-field terahertz sources. *Adv. Opt. Mater.* **8**, 1900681 (2020).

28. 28.

Yablonovitch, E., Hwang, D. M., Gmitter, T. J., Florez, L. T., Harbison, J. P. Van der Waals bonding of GaAs epitaxial liftoff films onto arbitrary substrates. *Appl. Phys. Lett.* **56**, 2419–2421 (1990).

29. 29.

Cole, G. D. et al. High-performance near- and mid-infrared crystalline coatings. *Optica* **3**, 647–656 (2016).

30. 30.

Yablonovitch, E., Gmitter, T., Harbison, J. P., Bhat, R. Extreme selectivity in the lift-off of epitaxial GaAs films. *Appl. Phys. Lett.* **51**, 2222–2224 (1987).

31. 31.

Cole, G. D., Zhang, W., Martin, M. J., Ye, J., Aspelmeyer, M. Tenfold reduction of Brownian noise in high-reflectivity optical coatings. *Nat. Photon.* **7**, 644–650 (2013).

32. 32.

Wilmer, B. L., Webber, D., Ashley, J. M., Hall, K. C., Bristow, A. D. Role of strain on the coherent properties of GaAs excitons and biexcitons. *Phys. Rev. B* **94**, 075207 (2016).

33. 33.

Kaminski, J. P. et al. Far-infrared cavity dump coupling of the UC Santa Barbara free-electron laser. *Appl. Phys. Lett.* **57**, 2770–2772 (1990).

34. 34.

Takahashi, S., Ramian, G., Sherwin, M. S. Cavity dumping of an injection-locked free-electron laser. *Appl. Phys. Lett.* **95**, 234102 (2009).

35. 35.

Voon, L. C. L. Y. & Willatzen, M. *The k p Method: Electronic Properties of Semiconductors* (Springer Science & Business Media,

2009).

36. 36.

Costello, J. B. et al. Reconstruction of Bloch wavefunctions of holes in a semiconductor. *Materials Cloud Archive* 2021.113
<https://doi.org/10.24435/materialscloud:m0-t8> (2021).

37. 37.

Banks, H. B., Valovcin, D. C., O'Hara, S. D. & Costello, J. B. SherwinGroup/HSG-turbo: 2021 release. *Zenodo*
<https://doi.org/10.5281/zenodo.5116718> (2021).

Acknowledgements

We acknowledge R. B. Liu and M. Kira for reading an earlier version of the manuscript; G. Cole and P. Heu for assistance with GaAs membrane fabrication; A. Peñaloza for assistance with the design and fabrication of cryostat modifications; C. Cannon for implementing software for Monte Carlo error estimation; D. Enyeart and N. Agladze for assistance with maintaining and operating the UCSB millimetre-wave free-electron laser; and J. Meyer and I. Vurgaftman for a discussion. The portion of this research conducted at UCSB was funded by NSF-DMR 1710639 and NSF-DMR 2004995. Upgrades to the UCSB terahertz facility that was used for this research were funded by NSF-DMR 1626681 and NSF-DMR 1126894. The portion of this research conducted at Princeton was funded in part by the Gordon and Betty Moore Foundation's EPiQS Initiative, Grant GBMF9615 to L.N.P., and by the National Science Foundation MRSEC grant DMR 1420541.

Author information

Author notes

1. These authors contributed equally: J. B. Costello, S. D. O'Hara, Q. Wu

Affiliations

1. Physics Department and Institute for Terahertz Science and Technology, University of California, Santa Barbara, Santa Barbara, CA, USA

J. B. Costello, S. D. O'Hara, Q. Wu & M. S. Sherwin

2. Mathworks, Natick, MA, USA

D. C. Valovcin

3. Department of Electrical Engineering, Princeton University, Princeton, NJ, USA

L. N. Pfeiffer & K. W. West

Contributions

Performing experiments, data collection and analysis: S.D.O. and J.B.C. Software: J.B.C., D.C.V. and S.D.O. Theory: Q.W. Conceptualization: M.S.S. and Q.W. Resources (GaAs epilayer growth): K.W.W. and L.N.P. Development of broad-band polarimetry: D.C.V. Writing: M.S.S., Q.W., S.D.O. and J.B.C. Supervision, funding acquisition and project administration: M.S.S.

Corresponding author

Correspondence to M. S. Sherwin.

Ethics declarations

Competing interests

The authors declare no competing interests.

Additional information

Peer review information *Nature* thanks the anonymous reviewers for their contribution to the peer review of this work. Peer reviewer reports are available.

Publisher's note Springer Nature remains neutral with regard to jurisdictional claims in published maps and institutional affiliations.

Extended data figures and tables

Extended Data Fig. 1 Field enhancement at the GaAs epilayer from the ITO-coated sapphire substrate.

The field enhancement is calculated as $\left(1+r(f_{\text{THz}})\right)$ with the complex reflection coefficient $r(f_{\text{THz}})$ measured by a Vector Network Analyzer.

Extended Data Fig. 2 An absorbance spectrum of the GaAs epilayer mounted on the ITO-coated sapphire substrate.

The measurement was taken at the spot illuminated by a white light source (left inset). The right inset shows a zoom-in of the spectrum, with the bandgap and the photon energy of the NIR laser denoted by dash-dot blue and red lines, respectively. The two peaks are strain-split exciton resonances associated with band-edge states with different angular momenta. The temperature was 60 K.

Extended Data Fig. 3 Stokes polarimetry with linearly polarized NIR laser ($\gamma_{\text{NIR}}=0^\circ$).

a, Polarograms for sideband index ($n=12$) and orientation angle of the NIR laser ($\alpha_{\text{NIR}}=0^\circ$). **b**, The polarization state of the sideband extracted from the polarograms in **a**. **c**, Polarograms for sideband index ($n=24$) and orientation angle of the NIR laser (α_{NIR}

$\{\rm{NIR}\} = 45^\circ$. **d**, The polarization state of the sideband extracted from the polarograms in **c**. In **a** and **c**, the black dots show the measured polarograms, with error bars showing the standard deviation over 4 measurements, and the red solid lines are the reconstructed polarogram through Fourier transform, with the red dotted lines showing the bounds. In **b** and **d**, the polarization states of the sidebands are represented as trajectories of the tips of the electric field vectors (E_x, E_y) over time. The orientation angle α and ellipticity angle γ are defined in the inset in **b**.

Extended Data Fig. 4 Quantum interference in three-step model of HSG leading to sideband polarization.

A photon from the NIR laser is decomposed into components $(\sigma_{\rm{NIR}}^{\pm})$, with helicity ± 1 . **a**, A $\sigma_{\rm{NIR}}^{-}$ photon excites either a spin-up electron and hole of spin $-3/2$ or a spin-down electron and hole of spin $-1/2$. A $\sigma_{\rm{NIR}}^{+}$ photon excites either a spin-up electron and hole of spin $+1/2$ or a spin-down electron and hole of spin $+3/2$. **b**, Driven by the THz field, an electron-hole pair accumulates dynamic phase $(A_{\rm{HH}})$ or $(A_{\rm{LH}})$, depending on the band of the hole state (HH or LH). The electron spin is unchanged, while the hole states originating from the spin $-3/2$ state are superpositions of spin $-3/2$ and $+1/2$ states and the states originating from the spin $-1/2$ state are superpositions of spin $-1/2$ and $+3/2$ states. **c**, Upon recollision, either $\sigma_{\rm{HSG}}^{+}$ or $\sigma_{\rm{HSG}}^{-}$ photons are produced following angular momentum conservation—for example, a spin $+3/2$ hole recombining with a spin-down ($-1/2$) electron produces a $\sigma_{\rm{HSG}}^{+}$ photon with helicity $+3/2 - 1/2 = +1$. The interference of the evolution pathways from $\sigma_{\rm{NIR}}^{\pm}$ to $\sigma_{\rm{HSG}}^{+}$ ($\sigma_{\rm{HSG}}^{-}$) produces the dynamical Jones matrix element $(T_{\pm\pm})$.

Extended Data Fig. 5 Additional data for ratios of Jones matrix elements, $(\boldsymbol{\xi})/\boldsymbol{n}$.

({\boldsymbol{\theta}}) and {\boldsymbol{\chi}}_n({\boldsymbol{\theta}}).

a, The argument of $\langle \{ \boldsymbol{\xi} \} \rangle_n$. The dash-dot line marks the expected value of 0. **b**, The magnitude of $\langle \{ \boldsymbol{\xi} \} \rangle_n$. The dash-dot line marks the expected value of 1. **c**, The magnitude of $\langle \{ \boldsymbol{\chi} \} \rangle_n$. All quantities are presented as functions of sideband index n for eight values of angle θ . Inset, The definition of $\langle \{ \boldsymbol{\theta} \} \rangle$ by using the GaAs crystal lattice and the THz electric field.

Extended Data Fig. 6 Monte Carlo simulation in calculating the dynamical Jones matrices.

a, The polarization state of the $(n=12)$ sideband ($\theta = 23^\circ$) for all 4 initial NIR polarizations (i- $\alpha_{\rm NIR} = 0^\circ$, ii- $\alpha_{\rm NIR} = 45^\circ$, iii- $\alpha_{\rm NIR} = 90^\circ$, iv- $\alpha_{\rm NIR} = -45^\circ$). The horizontal and vertical axes represent α and γ , respectively. Dashed ovals correspond to confidence intervals in the measurement of α and γ . **b**, Histograms of α and γ for the 4 measured sidebands' polarizations. Normal distributions of α and γ were sampled, with the central value and standard deviation of the distributions set by the measured values. In this figure, 1,000 iterations are shown, but the results of this paper are calculated from 10,000 iterations. **c**, The complex \mathcal{J} -matrix elements resulting from the α and γ in **b**. The horizontal and vertical axes represent the real and imaginary part, respectively. Each red dashed line shows one standard deviation of the distribution of each \mathcal{J} -matrix element resulting from the Monte Carlo simulation. All three plots have the same scale. The value of $\langle \mathcal{J}_{xx} \rangle_n$ is set as 1 in these calculations.

Extended Data Fig. 7 Berry connection matrix element $\langle \mathbf{A}^{\pm}, \mathbf{H}^{\pm} \rangle$ in the $k_z = 0$ plane of the Brillouin zone.

The double-headed black dotted arrow represents a path of a hole accelerated by a linearly polarized THz field, which is perpendicular to the Berry connection (color arrows) at all points. The Berry connection is plotted in units of $\langle a \rangle$, which is the lattice constant of GaAs.

Extended Data Fig. 8 Effect of a biaxial strain on the valence band structure and non-Abelian Berry connection along the direction of quasi-momentum k in the $k_z=0$ plane of the Brillouin zone.

The strain is chosen as tensile along [001] direction to be consistent with the splitting of the exciton peaks in the absorbance spectrum (Extended Data Fig. 2). **a**, Valence band structures along $(k_x=k_z=0)$ for unstrained (top) and strained (bottom) GaAs. The blue and orange curves represent the heavy-hole and light-hole bands, respectively. **b**, The magnitude of the diagonal Berry connection matrix element $\langle A^{\pm}, H^{\pm} \rangle$ along the direction of quasi-momentum for unstrained (top) and strained (bottom) GaAs. **c**, The magnitude of the off-diagonal Berry connection matrix element $\langle A^{\pm}, H^{\pm}, L^{\pm} \rangle$ along the direction of quasi-momentum for unstrained (top) and strained (bottom) GaAs. For the unstrained case, the Berry connection along the quasi-momentum is identically zero in the plots except for the singularity at $k=0$. The Berry connection is plotted in units of $\langle a \rangle$, which is the lattice constant of GaAs.

Supplementary information

Supplementary Information

This file contains Supplementary Methods, a Supplementary Discussion and Supplementary References.

Peer Review File

Source data

Source Data Fig. 1

Source Data Fig. 3

Rights and permissions

Reprints and Permissions

About this article

Cite this article

Costello, J.B., O'Hara, S.D., Wu, Q. *et al.* Reconstruction of Bloch wavefunctions of holes in a semiconductor. *Nature* **599**, 57–61 (2021). <https://doi.org/10.1038/s41586-021-03940-2>

- Received: 02 February 2021
- Accepted: 20 August 2021
- Published: 03 November 2021
- Issue Date: 04 November 2021
- DOI: <https://doi.org/10.1038/s41586-021-03940-2>

Share this article

Anyone you share the following link with will be able to read this content:

[Get shareable link](#)

Sorry, a shareable link is not currently available for this article.

[Copy to clipboard](#)

Provided by the Springer Nature SharedIt content-sharing initiative

This article was downloaded by **calibre** from <https://www.nature.com/articles/s41586-021-03940-2>

| [Section menu](#) | [Main menu](#) |

- Article
- [Published: 03 November 2021](#)

Percolation transitions in compressed SiO₂ glasses

- [A. Hasmy ORCID: orcid.org/0000-0001-8194-6532^{1,2}](#),
- [S. Ispas ORCID: orcid.org/0000-0002-8537-8461¹](#) &
- [B. Hehlen ORCID: orcid.org/0000-0003-4019-683X¹](#)

Nature volume 599, pages 62–66 (2021)

- 999 Accesses
- 1 Altmetric
- [Metrics details](#)

Subjects

- [Phase transitions and critical phenomena](#)
- [Structure of solids and liquids](#)

Abstract

Amorphous–amorphous transformations under pressure are generally explained by changes in the local structure from low- to higher-fold coordinated polyhedra^{1,2,3,4}. However, as the notion of scale invariance at the critical thresholds has not been addressed, it is still unclear whether these transformations behave similarly to true phase transitions in related crystals and liquids. Here we report ab initio-based calculations of compressed silica (SiO₂) glasses, showing that the structural changes from

low- to high-density amorphous structures occur through a sequence of percolation transitions. When the pressure is increased to 82 GPa, a series of long-range ('infinite') percolating clusters composed of corner- or edge-shared tetrahedra, pentahedra and eventually octahedra emerge at critical pressures and replace the previous 'phase' of lower-fold coordinated polyhedra and lower connectivity. This mechanism provides a natural explanation for the well-known mechanical anomaly around 3 GPa, as well as the structural irreversibility beyond 10 GPa, among other features. Some of the amorphous structures that have been discovered mimic those of coesite IV and V crystals reported recently^{5,6}, highlighting the major role of SiO₅ pentahedron-based polyamorphs in the densification process of vitreous silica. Our results demonstrate that percolation theory provides a robust framework to understand the nature and pathway of amorphous–amorphous transformations and open a new avenue to predict unravelled amorphous solid states and related liquid phases^{7,8}.

Access options

Subscribe to Journal

Get full journal access for 1 year

\$199.00

only \$3.90 per issue

[Subscribe](#)

All prices are NET prices.

VAT will be added later in the checkout.

Tax calculation will be finalised during checkout.

Rent or Buy article

Get time limited or full article access on ReadCube.

from \$8.99

Rent or Buy

All prices are NET prices.

Additional access options:

- [Log in](#)
- [Access through your institution](#)
- [Learn about institutional subscriptions](#)

Fig. 1: v-SiO₂ local structures and connectivities.

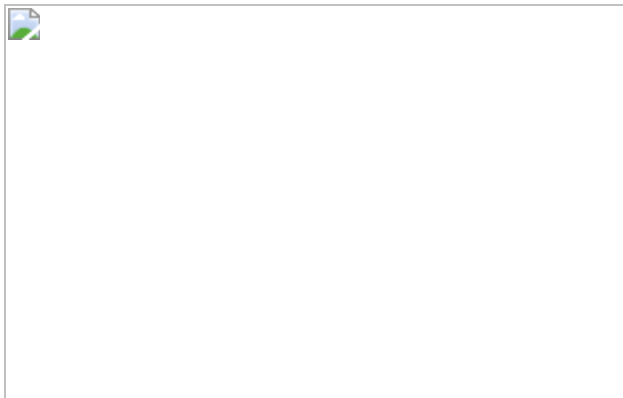


Fig. 2: Sequence of percolation transitions in v-SiO₂.

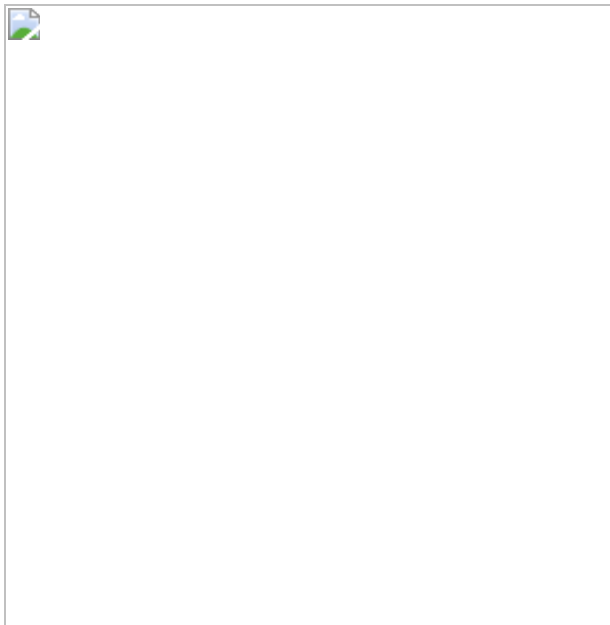
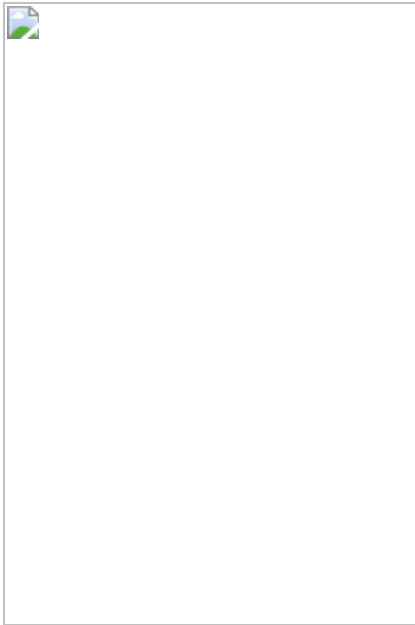


Fig. 3: Fractal percolating clusters at threshold.



Data availability

Figures and corresponding datasets (agr format), as well as sample trajectories at selected pressures are available at Zenodo (<https://doi.org/10.5281/zenodo.5056541>).

Code availability

The DFTB+ code is publicly available at <https://dftbplus.org/>. Additional information may be found there. The percolation code is available freely for non-commercial research at Zenodo (<https://doi.org/10.5281/zenodo.5064069>). Other codes for structural characterization are available from B.H.

References

1. 1.

McMillan, P. F., Wilson, M., Daisenberger, D. & Machon, D. A density-driven phase transition between semiconducting and metallic polyamorphs of silicon. *Nat. Mater.* **4**, 680–684 (2005).

2. 2.

Sheng, H. W. et al. Polyamorphism in a metallic glass. *Nat. Mater.* **6**, 192–197 (2007).

3. 3.

Prescher, C. et al. Beyond 6-fold coordinated Si in SiO₂ glass at ultrahigh pressures. *Proc. Natl Acad. Sci. USA* **114**, 10041–10046 (2017).

4. 4.

Deringer, V. L. et al. Origins of structural and electronic transitions in disordered silicon. *Nature* **589**, 59–64 (2021).

5. 5.

Hu, Q. Y. et al. Polymorphic phase transition mechanism of compressed coesite. *Nat. Commun.* **6**, 6630 (2015).

6. 6.

Bykova, E. et al. Metastable silica high pressure polymorphs as structural proxies of deep Earth silicate melts. *Nat. Commun.* **9**, 4789 (2018).

7. 7.

Debenedetti, P. G. & Stillinger, F. H. Supercooled liquids and the glass transition. *Nature* **410**, 259–267 (2001).

8. 8.

Loerting, T., Brazhkin, V. V. & Morishita, T. Multiple amorphous–amorphous transitions. *Adv. Chem. Phys.* **143**, 29–82 (2009).

9. 9.

Brazhkin, V. V., Lyapin, A. G. & Trachenko, K. Atomistic modeling of multiple amorphous–amorphous transitions in SiO_2 and GeO_2 glasses at megabar pressures. *Phys. Rev. B* **83**, 132103 (2011).

10. 10.

Lin, J.-F. et al. Electronic bonding transition in compressed SiO_2 glass. *Phys. Rev. B* **75**, 012201 (2007).

11. 11.

Zeidler, A. et al. High pressure transformation of SiO_2 glass from a tetrahedral to an octahedral network: a joint approach using neutron diffraction and molecular dynamics. *Phys. Rev. Lett.* **113**, 135501 (2014).

12. 12.

Ryuo, E., Wakabayashi, D., Koura, A. & Shimojo, F. Ab initio simulation of permanent densification in silica glass. *Phys. Rev. B* **96**, 054206 (2017).

13. 13.

Tsiok, O. B., Brazhkin, V. V., Lyapin, A. G. & Khvostantsev, L. G. Logarithmic kinetics of the amorphous–amorphous transformations in SiO_2 and GeO_2 glasses under high pressure. *Phys. Rev. Lett.* **80**, 999–1002 (1998).

14. 14.

Weigel, C. et al. Pressure-induced densification of vitreous silica: insight from elastic properties. *Phys. Rev. B* **100**, 094102 (2019).

15. 15.

Trachenko, K., Dove, M. T., Brazhkin, V. & El’kin, F. S. Network rigidity and properties of SiO_2 and GeO_2 glasses under pressure. *Phys.*

Rev. Lett. **93**, 135502 (2004).

16. 16.

Liang, Y., Miranda, C. R. & Scandolo, S. Mechanical strength and coordination defects in compressed silica glass: molecular dynamics simulations. *Phys. Rev. B* **75**, 024205 (2007).

17. 17.

Sarnthein, J., Pasquarello, A. & Car, R. Origin of the high-frequency doublet in the vibrational spectrum of vitreous SiO₂. *Science* **275**, 1925–1927 (1997).

18. 18.

Hosokawa, S. et al. Oxygen 2p partial density of states and bond angles around O atoms in SiO₂ glass. *J. Phys. Soc. Jpn* **84**, 024605 (2015).

19. 19.

Wu, M., Liang, Y., Jiang, J.-Z. & Tse, J. S. Structure and properties of dense silica glass. *Sci. Rep.* **2**, 398 (2012).

20. 20.

Murakami, M. et al. Ultrahigh-pressure form of SiO₂ glass with dense pyrite-type crystalline homology. *Phys. Rev. B* **99**, 045153 (2019).

21. 21.

Harvey, J. P. & Asimow, P. D. Current limitations of molecular dynamic simulations as probes of thermo-physical behavior of silicate melts. *Am. Min.* **100**, 1866–1882 (2015).

22. 22.

Kob, W. & Ispas, S. in *Encyclopedia of Glass Science, Technology, History, and Culture* (ed. Richet, P.) Ch. 2.9 (Wiley, 2020).

23. 23.

Aradi, B., Hourahine, B. & Frauenheim, T. DFTB+, a sparse matrix-based implementation of the DFTB method. *J. Phys. Chem. A* **111**, 5678–5684 (2007).

24. 24.

Pauling, L. The principles determining the structure of complex ionic crystals. *J. Am. Chem. Soc.* **51**, 1010–1026 (1929).

25. 25.

Sato, T. & Funamori, N. High pressure structural transformation of SiO₂ glass up to 100 GPa. *Phys. Rev. B* **82**, 184102 (2010).

26. 26.

Phillips, J. C. & Thorpe, M. F. Constraint, vector percolation and glass formation. *Solid State Commun.* **53**, 699–702 (1985).

27. 27.

Sauffer, D. & Aharony, A. *Introduction to Percolation Theory* (Taylor & Francis, 2003).

28. 28.

Hu, Q. Y. et al. Stability limits and transformation pathways of α-quartz under high pressure. *Phys. Rev. B* **95**, 104112 (2017).

29. 29.

Pabst, W. & Gregorová, E. Elastic properties of silica polymorphs—a review. *Ceramics Silikáty* **57**, 167–184 (2013).

30. 30.

Machon, D., Meersman, F., Wilding, M. C., Wilson, M. & McMillan, P. F. Pressure-induced amorphization and polyamorphism: inorganic and biochemical systems. *Prog. Mater. Sci.* **61**, 216–282 (2014).

31. 31.

Brovchenko, I. & Oleinikova, A. Multiple phases of liquid water. *ChemPhysChem* **9**, 2660–2675 (2008).

32. 32.

Yang, X., Tong, H., Wang, W. H. & Chen, K. Emergence and percolation of rigid domains during the colloidal glass transition. *Phys. Rev. E* **99**, 062610 (2019).

33. 33.

Ojovan, M. I. & Louzguine-Luzgin, D. V. Revealing structural changes at glass transition via radial distribution functions. *J. Phys. Chem. B* **124**, 3186–3194 (2020).

34. 34.

Tong, H., Sengupta, S. & Tanaka, H. Emergent solidity of amorphous materials as a consequence of mechanical self-organisation. *Nat. Commun.* **11**, 4863 (2020).

35. 35.

Trave, A., Tangney, P., Scandolo, S., Pasquarello, A. & Car, R. Pressure-induced structural changes in liquid SiO₂ from ab initio simulations. *Phys. Rev. Lett.* **89**, 245504 (2002).

36. 36.

Karki, B. B., Bhattacharai, D. & Stixrude, L. First-principles simulations of liquid silica: structural and dynamical behavior at high pressure.

Phys. Rev. B **76**, 104205 (2007).

37. 37.

Zhu, X. F. & Chen, L. F. First-principles molecular dynamics simulations of the structure of germanium dioxide under pressures. *Phys. B* **404**, 4178–4184 (2009).

38. 38.

Gartner, T. E. III, Torquato, S., Car, R. & Debenedetti, P. G. Manifestations of metastable criticality in the long-range structure of model water glasses. *Nat. Commun.* **12**, 3398 (2021).

39. 39.

Carré, A., Berthier, L., Horbach, J., Ispas, S. & Kob, W. Amorphous silica modeled with truncated and screened Coulomb interactions: a molecular dynamics simulation study. *J. Chem. Phys.* **127**, 114512 (2007).

40. 40.

Koehler, C., Hajnal, Z., Deak, P., Frauenheim, T. & Suhai, S. Theoretical investigation of carbon defects and diffusion in α -quartz. *Phys. Rev. B* **64**, 085333 (2001).

41. 41.

Zwijnenburg, M. A., van Alsenoy, C. & Maschmeyer, T. Factors affecting ionicity in all-silica materials: a density functional cluster study. *J. Phys. Chem. A* **106**, 12376–12385 (2002).

42. 42.

Gibbs, G. V. et al. Bonded interactions in silica polymorphs, silicates and siloxane molecules. *Am. Min.* **94**, 1085–1102 (2009).

43. 43.

Binder, K. & Kob, W. *Glassy Materials and Disordered Solids* (Word Scientific, 2005).

44. 44.

Neutron Scattering Lengths and Cross Sections (NIST Center for Neutron Research, 2021); <https://www.ncnr.nist.gov/resources/n-lengths/>

45. 45.

Fischer, H. E., Barnes, A. C. & Salmon, P. S. Neutron and X-ray diffraction studies of liquids and glasses. *Rep. Prog. Phys.* **69**, 233–299 (2006).

46. 46.

Waasmaier, D. & Kirfel, A. New analytical scattering-factor functions for free atoms and ions for free atoms and ions. *Acta Crystallogr.* **A51**, 416–431 (1995).

47. 47.

More, S., Andrey, V., Kravtsov, A. V., Dalal, N. & Gottlöber, S. The overdensity and masses of the friends-of-friends halos and universality of halo mass function. *Astrophys. J. Suppl. Ser.* **195**, 4 (2011).

48. 48.

Zha, C.-S., Hemley, R. J., Maom, H.-K., Duffy, T. S. & Meade, C. Acoustic velocities and refractive index of SiO₂ glass to 57.5 GPa by Brillouin scattering. *Phys. Rev. B* **50**, 13105–13112 (1994).

49. 49.

Petitgirard, S. et al. SiO₂ glass density to lower-mantle pressures. *Phys. Rev. Lett.* **119**, 215701 (2017).

50. 50.
- American Mineralogist Crystal Structure Database* (AMCSD, 2021);
<http://rruff.geo.arizona.edu/AMS/amcsd.php>
51. 51.
- Yi, Y. S. & Lee, K. L. Pressure-induced changes in local electronic structures of SiO_2 and MgSiO_3 polymorphs: insights from ab initio calculations of O K-edge energy-loss near-edge structure spectroscopy. *Am. Min.* **97**, 897–909 (2012).
52. 52.
- Scheidl, K. S., Kurnosov, A., Boffa Ballaran, D. M., Angel, R. J., & Miletich, R. Extending the single-crystal quartz pressure gauge up to hydrostatic pressure of 19 GPa, *J. Appl. Crystallogr.* **49**, 2129–2137 (2016).
53. 53.
- Buchen, J. et al. Equation of state of polycrystalline stishovite across the tetragonal–orthorhombic phase transition. *J. Geophys. Res. Solid Earth* **123**, 7347–7360 (2018).
54. 54.
- Hasmy, A., Foret, M., Pelous, J., & Jullien, R. Small-angle neutron-scattering investigation of short-range correlations in fractal aerogels: simulations and experiments. *Phys. Rev. B* **48**, 9345–9353 (1993).
55. 55.
- O’Keeffe M. & Hyde B. G. in *Structure and Bonding in Crystals* (eds O’Keeffe, M. & Navrotsky, A.) 227–254 (Academic, 1981).
56. 56.

Kono, Y., Shu, Y., Kenney-Benson, C., Wang, Y., & Shen, G. Structural evolution of SiO₂ glass with Si coordination number greater than 6. *Phys. Rev. Lett.* **125**, 205701 (2020).

Acknowledgements

We thank the BioNano-NMRI team (L2C, UM) for computer facilities. A.H. thanks the CNRS (France) for funding, L. C. Rincón for introducing him to the SCC-DFTB method and E. Anglaret and F. Piuzzi for support that enabled him to participate in the conception of this project. This work was granted access to the high-performance computing resources of CINES by GENCI (Grand Equipement National de Calcul Intensif) under allocation grants nos. A0060910788, A0080910788 and A0100910788. BH acknowledges support from the French National Research Agency program PIPOG ANR-17-CE30-0009.

Author information

Affiliations

1. Laboratoire Charles Coulomb (L2C), CNRS – Université Montpellier, Montpellier, France
A. Hasmy, S. Ispas & B. Hehlen
2. Departamento de Física, Universidad Simón Bolívar, Caracas, Venezuela
A. Hasmy

Contributions

All authors initiated the project. A.H. and B.H. performed the MD tight-binding (SCC-DFTB) calculations of the pressurized glasses, after S.I. prepared the initial glass at ambient pressure by classical MD simulations. A.H. performed the tight-binding calculations of the crystals and computed

the percolation tools. All authors contributed to data analysis: atomic structure (A.H., B.H. and S.I.), electronic structure and percolation (A.H.) and inelastic structure factors (S.I.). A.H. and B.H. developed the main conclusions and wrote the paper. S.I. contributed to the final version of the paper.

Corresponding authors

Correspondence to A. Hasmy or B. Hehlen.

Ethics declarations

Competing interests

The authors declare no competing interests.

Additional information

Peer review information *Nature* thanks the anonymous reviewers for their contribution to the peer review of this work. Peer reviewer reports are available.

Publisher's note Springer Nature remains neutral with regard to jurisdictional claims in published maps and institutional affiliations.

Extended data figures and tables

[Extended Data Fig. 1 Electronic structure of compressed v-SiO₂.](#)

Total DOS for a SiO₂ glass at ambient pressure, with its corresponding projected DOS (a) and compared to different SiO₄ crystalline polymorphs (b). Fermi energy (c) and total DOS (d) when the pressure increases. The

results are compared with those corresponding to different SiO_2 crystalline polymorphs.

Extended Data Fig. 2 Ionic bonding of v- SiO_2 .

Mulliken atomic charges for Si (a) and O (b), and the average Mulliken ionicity of the Si-O bond (c) in v- SiO_2 as a function of pressure. The results (circles) are compared with those corresponding to different SiO_2 crystalline polymorphs. The error bars in (b) correspond to the standard deviation of the average of the charges of all O atoms. Similar relative errors were estimated for (a) and (c).

Extended Data Fig 3 v- SiO_2 atomic structures.

(a) $S_X(q)$ of our densified vitreous silicas compared to X-ray data reproduced from Prescher et al.³ and (b) Evolution of the maximum of the first sharp diffraction peak FSDP. (c) Calculated $S_N(q)$ compared to neutron data (black lines) reproduced from Zeidler et al.¹¹.

Extended Data Fig. 4 v- SiO_2 interatomic distances and angles.

(a) Calculated Si-O, O-O, and Si-Si distances at maximum of the distribution in our densified vitreous silicas. Si-O bond length are compared to X-Ray (squares) and neutron (+) scattering data. Si-Si distances are compared to those in the crystalline polymorphs. For stishovite, the interval corresponds to pressures between 10 GPa and 30 GPa. (b) Si-O-Si bond angle distribution (BAD) and pressure dependence of the Si-O-Si BAD marked by the arrow. The average value has been calculated from 110° to 175° . (c) Pressure dependence of the O-Si-O and examples of bond angle distributions (BAD).

Extended Data Fig 5 Face-shared SiO_n polyhedra.

Number of face-sharing per polyhedron unit for dominant SiO_n - SiO_m connectivities as a function of pressure.

Extended Data Fig. 6 Percolation transitions.

(a) Percolation probability, P_∞ , versus v- SiO_2 density for the different 4-, 5- and 6-folded coordinated Si, and their combinations. (b) P_∞ versus the fractions of SiO_n .

Extended Data Fig. 7 OSi_Z structures.

(a) Coordination numbers Z and Z' of SiO_Z polyhedra and $\text{OSi}_{Z'}$ structures, (b) fraction of OSi_n , and (c) percolation probability of $(\text{OSi}_2\text{-OSi}_2)_\infty$, $(\text{OSi}_2\text{-OSi}_3)_\infty$, and $(\text{OSi}_3\text{-OSi}_3)_\infty$ clusters.

Extended Data Table 1 Vitreous silica versus crystalline silicas

Supplementary information

Peer Review File

Rights and permissions

Reprints and Permissions

About this article

Cite this article

Hasmy, A., Ispas, S. & Hehlen, B. Percolation transitions in compressed SiO_2 glasses. *Nature* **599**, 62–66 (2021). <https://doi.org/10.1038/s41586-021-03918-0>

- Received: 31 March 2021

- Accepted: 16 August 2021
- Published: 03 November 2021
- Issue Date: 04 November 2021
- DOI: <https://doi.org/10.1038/s41586-021-03918-0>

Share this article

Anyone you share the following link with will be able to read this content:

[Get shareable link](#)

Sorry, a shareable link is not currently available for this article.

[Copy to clipboard](#)

Provided by the Springer Nature SharedIt content-sharing initiative

This article was downloaded by **calibre** from <https://www.nature.com/articles/s41586-021-03918-0>

| [Section menu](#) | [Main menu](#) |

- Article
- [Published: 03 November 2021](#)

Transition metal-catalysed molecular n-doping of organic semiconductors

- [Han Guo¹](#),
- [Chi-Yuan Yang](#) ORCID: [orcid.org/0000-0003-4270-1131²](#),
- [Xianhe Zhang¹](#),
- [Alessandro Motta³](#),
- [Kui Feng¹](#),
- [Yu Xia⁴](#),
- [Yongqiang Shi¹](#),
- [Ziang Wu⁵](#),
- [Kun Yang¹](#),
- [Jianhua Chen¹](#),
- [Qiaogan Liao¹](#),
- [Yumin Tang¹](#),
- [Huiliang Sun¹](#),
- [Han Young Woo](#) ORCID: [orcid.org/0000-0001-5650-7482⁵](#),
- [Simone Fabiano](#) ORCID: [orcid.org/0000-0001-7016-6514²](#),
- [Antonio Facchetti](#) ORCID: [orcid.org/0000-0002-8175-7958^{2,4,6}](#) &
- [Xugang Guo](#) ORCID: [orcid.org/0000-0001-6193-637X¹](#)

[Nature](#) volume 599, pages 67–73 (2021)

- 3100 Accesses
- 6 Altmetric

- [Metrics details](#)

Subjects

- [Electrical and electronic engineering](#)
- [Materials for devices](#)
- [Materials for energy and catalysis](#)

Abstract

Chemical doping is a key process for investigating charge transport in organic semiconductors and improving certain (opto)electronic devices^{1,2,3,4,5,6,7,8,9}. N(electron)-doping is fundamentally more challenging than p(hole)-doping and typically achieves a very low doping efficiency (η) of less than 10%^{1,10}. An efficient molecular n-dopant should simultaneously exhibit a high reducing power and air stability for broad applicability^{1,5,6,9,11}, which is very challenging. Here we show a general concept of catalysed n-doping of organic semiconductors using air-stable precursor-type molecular dopants. Incorporation of a transition metal (for example, Pt, Au, Pd) as vapour-deposited nanoparticles or solution-processable organometallic complexes (for example, Pd₂(dba)₃) catalyses the reaction, as assessed by experimental and theoretical evidence, enabling greatly increased η in a much shorter doping time and high electrical conductivities (above 100 S cm⁻¹; ref. ¹²). This methodology has technological implications for realizing improved semiconductor devices and offers a broad exploration space of ternary systems comprising catalysts, molecular dopants and semiconductors, thus opening new opportunities in n-doping research and applications^{12, 13}.

Access options

Subscribe to Journal

Get full journal access for 1 year

\$199.00

only \$3.90 per issue

[Subscribe](#)

All prices are NET prices.

VAT will be added later in the checkout.

Tax calculation will be finalised during checkout.

Rent or Buy article

Get time limited or full article access on ReadCube.

from \$8.99

[Rent or Buy](#)

All prices are NET prices.

Additional access options:

- [Log in](#)
- [Access through your institution](#)
- [Learn about institutional subscriptions](#)

Fig. 1: The TM catalysed n-doping concept.

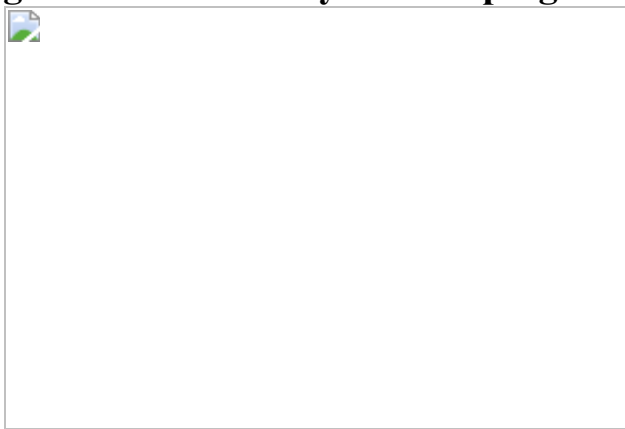


Fig. 2: AuNP catalysed n-doping of PDTzTI with N-DMBI-H.

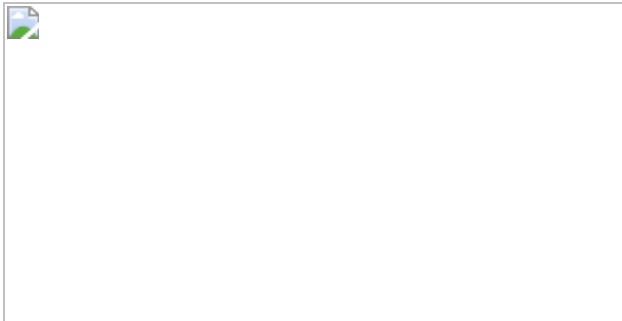


Fig. 3: The generality of metal-catalysed N-DMBI-H doping method.

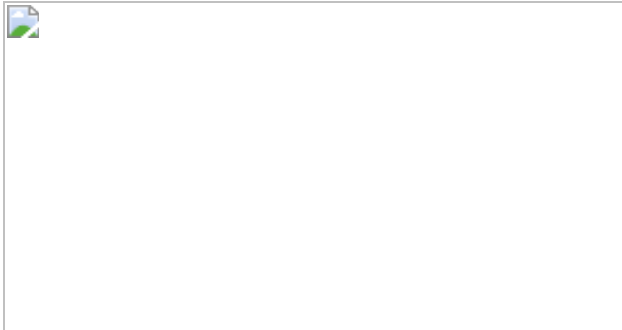


Fig. 4: AuNP-catalysed N-DMBI-H doping mechanism.



Data availability

All relevant data are contained within the Article and its [Supplementary Information](#), or are available from the corresponding authors upon request.

References

1. 1.

Lüssem, B., Riede, M. & Leo, K. Doping of organic semiconductors. *Phys. Status Solidi A* **210**, 9–43 (2013).

2. 2.

Kang, K. et al. 2D coherent charge transport in highly ordered conducting polymers doped by solid state diffusion. *Nat. Mater.* **15**, 896–902 (2016).

3. 3.

Kiefer, D. et al. Double doping of conjugated polymers with monomer molecular dopants. *Nat. Mater.* **18**, 149–155 (2019).

4. 4.

Yamashita, Y. et al. Efficient molecular doping of polymeric semiconductors driven by anion exchange. *Nature* **572**, 634–638 (2019).

5. 5.

Wei, P., Oh, J. H., Dong, G. & Bao, Z. Use of a 1H-benzoimidazole derivative as an n-type dopant and to enable air-stable solution-processed n-channel organic thin-film transistors. *J. Am. Chem. Soc.* **132**, 8852–8853 (2010).

6. 6.

Lin, X. et al. Beating the thermodynamic limit with photo-activation of n-doping in organic semiconductors. *Nat. Mater.* **16**, 1209–1215 (2017).

7. 7.

Tang, C. G. et al. Doped polymer semiconductors with ultrahigh and ultralow work functions for ohmic contacts. *Nature* **539**, 536–540

(2016).

8. 8.

Tang, C. G. et al. Multivalent anions as universal latent electron donors. *Nature* **573**, 519–525 (2019).

9. 9.

Gruessing, A. et al. Use of heterocyclic radicals for doping of organic semiconductors. *EP patent EP06005834A* (2006).

10. 10.

Lüssem, B. et al. Doped organic transistors. *Chem. Rev.* **116**, 13714–13751 (2016).

11. 11.

Guo, S. et al. N-doping of organic electronic materials using air-stable organometallics. *Adv. Mater.* **24**, 699–703 (2012).

12. 12.

Sun, Y., Di, C.-A., Xu, W. & Zhu, D. Advances in n-type organic thermoelectric materials and devices. *Adv. Electron. Mater.* **5**, 1800825 (2019).

13. 13.

Russ, B. et al. Organic thermoelectric materials for energy harvesting and temperature control. *Nat. Rev. Mater.* **1**, 16050 (2016).

14. 14.

Wei, P. et al. Tuning the Dirac point in CVD-grown graphene through solution processed n-type doping with 2-(2-methoxyphenyl)-1,3-dimethyl-2,3-dihydro-1H-benzoimidazole. *Nano Lett.* **13**, 1890–1897 (2013).

15. 15.

Li, F. H. et al. Leuco crystal violet as a dopant for n-doping of organic thin films of fullerene C₆₀. *J. Phys. Chem. B* **108**, 17076–17082 (2004).

16. 16.

Chan, C. K., Kim, E. G., Brédas, J. L. & Kahn, A. Molecular n-type doping of 1,4,5,8-naphthalene tetracarboxylic dianhydride by pyronin B studied using direct and inverse photoelectron spectroscopies. *Adv. Funct. Mater.* **16**, 831–837 (2006).

17. 17.

Shi, K. et al. A novel solution-processable n-dopant based on 1,4-dihdropyridine motif for high electrical conductivity of organic semiconductors. *Adv. Electron. Mater.* **3**, 1700164 (2017).

18. 18.

Yang, C.-Y. et al. A thermally activated and highly miscible dopant for n-type organic thermoelectrics. *Nat. Commun.* **11**, 3292 (2020).

19. 19.

Naab, B. D. et al. Effective solution- and vacuum-processed n-doping by dimers of benzimidazoline radicals. *Adv. Mater.* **26**, 4268–4272 (2014).

20. 20.

Un, H.-I. et al. Understanding the effects of molecular dopant on n-type organic thermoelectric properties. *Adv. Energy Mater.* **9**, 1900817 (2019).

21. 21.

Guha, S., Goodson, F. S., Corson, L. J. & Saha, S. Boundaries of anion/naphthalenediimide interactions: from anion- π interactions to anion-induced charge-transfer and electron-transfer phenomena. *J. Am. Chem. Soc.* **134**, 13679–13691 (2012).

22. 22.

Li, C.-Z. et al. Doping of fullerenes via anion-induced electron transfer and its implication for surfactant facilitated high performance polymer solar cells. *Adv. Mater.* **25**, 4425–4430 (2013).

23. 23.

Naab, B. D. et al. Mechanistic study on the solution-phase n-doping of 1,3-dimethyl-2-aryl-2,3-dihydro-1H-benzoimidazole derivatives. *J. Am. Chem. Soc.* **135**, 15018–15025 (2013).

24. 24.

Guo, S. et al. N-doping of organic electronic materials using air-stable organometallics: A mechanistic study of reduction by dimeric sandwich compounds. *Chem. Eur. J.* **18**, 14760–14772 (2012).

25. 25.

Mohapatra, S. K. et al. Dimers of nineteen-electron sandwich compounds: crystal and electronic structures, and comparison of reducing strengths. *Chem. Eur. J.* **20**, 15385–15394 (2014).

26. 26.

Jhulkı, S. et al. Reactivity of an air-stable dihydrobenzoimidazole n-dopant with organic semiconductor molecules. *Chem* **7**, 1050–1065 (2021).

27. 27.

Daniel, M. C. & Astruc, D. Gold nanoparticles: assembly, supramolecular chemistry, quantum-size-related properties, and

applications toward biology, catalysis, and nanotechnology. *Chem. Rev.* **104**, 293–346 (2004).

28. 28.

Wang, D. & Astruc, D. The golden age of transfer hydrogenation. *Chem. Rev.* **115**, 6621–6686 (2015).

29. 29.

Wang, H. et al. Tuning the threshold voltage of carbon nanotube transistors by n-type molecular doping for robust and flexible complementary circuits. *Proc. Natl Acad. Sci. USA* **111**, 4776–4781 (2014).

30. 30.

Tarasov, A. et al. Controlled doping of large-area trilayer MoS₂ with molecular reductants and oxidants. *Adv. Mater.* **27**, 1175–1181 (2015).

31. 31.

Jia, C.-J. & Schüth, F. Colloidal metal nanoparticles as a component of designed catalyst. *Phys. Chem. Chem. Phys.* **13**, 2457–2487 (2011).

32. 32.

Shi, Y. et al. Thiazole imide-based all-acceptor homopolymer: achieving high-performance unipolar electron transport in organic thin-film transistors. *Adv. Mater.* **30**, 1705745 (2018).

33. 33.

Tanaka, H., Nishio, S., Ito, H. & Kuroda, S.-I. Microscopic signature of insulator-to-metal transition in highly doped semicrystalline conducting polymers in ionic-liquid-gated transistors. *Appl. Phys. Lett.* **107**, 243302 (2015).

34. 34.

Zuo, G. et al. Molecular doping and trap filling in organic semiconductor host–guest systems. *J. Phys. Chem. C* **121**, 7767–7775 (2017).

35. 35.

Maxwell, A. J. et al. Electronic and geometric structure of C₆₀ on Al(111) and Al(110). *Phys. Rev. B* **57**, 7312–7326 (1998).

36. 36.

Scholes, D. T. et al. Overcoming film quality issues for conjugated polymers doped with F₄TCNQ by solution sequential processing: Hall effect, structural, and optical measurements. *J. Phys. Chem. Lett.* **6**, 4786–4793 (2015).

37. 37.

Shi, Y. et al. Imide-functionalized thiazole-based polymer semiconductors: Synthesis, structure-property correlations, charge carrier polarity, and thin-film transistor performance. *Chem. Mater.* **30**, 7988–8001 (2018).

38. 38.

Yan, H. et al. A high-mobility electron-transporting polymer for printed transistors. *Nature* **457**, 679–686 (2009).

39. 39.

Schlitz, R. A. et al. Solubility-limited extrinsic n-type doping of a high electron mobility polymer for thermoelectric applications. *Adv. Mater.* **26**, 2825–2830 (2014).

40. 40.

Wang, S. et al. Thermoelectric properties of solution-processed n-doped ladder-type conducting polymers. *Adv. Mater.* **28**, 10764–10771

(2016).

41. 41.

Naab, B. D. et al. Role of polymer structure on the conductivity of n-doped polymers. *Adv. Electron. Mater.* **2**, 1600004 (2016).

42. 42.

Fratini, S. et al. Charge transport in high-mobility conjugated polymers and molecular semiconductors. *Nat. Mater.* **19**, 491–502 (2020).

43. 43.

Rousseaux, S., Gorelsky, S. I., Chung, B. K. W. & Fagnou, K. Investigation of the mechanism of C(sp³)–H bond cleavage in Pd(0)-catalyzed intramolecular alkane arylation adjacent to amides and sulfonamides. *J. Am. Chem. Soc.* **132**, 10692–10705 (2010).

44. 44.

Zalesskiy, S. S. & Ananikov, V. P. Pd₂(dba)₃ as a precursor of soluble metal complexes and nanoparticles: Determination of palladium active species for catalysis and synthesis. *Organometallics* **31**, 2302–2309 (2012).

45. 45.

Lyons, M. E. G. *Electroactive Polymer Electrochemistry Part 1: Fundamentals* Ch. 1, (Springer, 1994).

46. 46.

Lu, Y. et al. Persistent conjugated backbone and disordered lamellar packing impart polymers with efficient n-doping and high conductivities. *Adv. Mater.* **33**, 2005946 (2021).

47. 47.

Baeg, K.-J., Caironi, M. & Noh, Y.-Y. Toward printed integrated circuits based on unipolar or ambipolar polymer semiconductors. *Adv. Mater.* **25**, 4210–4244 (2013).

48. 48.

Chueh, C.-C., Li, C.-Z. & Jen, A. K. Y. Recent progress and perspective in solution-processed interfacial materials for efficient and stable polymer and organometal perovskite solar cells. *Energy Environ. Sci.* **8**, 1160–1189 (2015).

49. 49.

Walzer, K., Maennig, B., Pfeiffer, M. & Leo, K. Highly efficient organic devices based on electrically doped transport layers. *Chem. Rev.* **107**, 1233–1271 (2007).

50. 50.

Shi, Y. et al. Distannylated bithiophene imide: enabling high-performance n-type polymer semiconductors with an acceptor-acceptor backbone. *Angew. Chem. Int. Ed.* **59**, 14449–14457 (2020).

51. 51.

Wang, Y. et al. Effects of bithiophene imide fusion on the device performance of organic thin-film transistors and all-polymer solar cells. *Angew. Chem. Int. Ed.* **56**, 15304–15308 (2017).

52. 52.

Küehne, T. D. et al. CP2K: an electronic structure and molecular dynamics software package - quickstep: efficient and accurate electronic structure calculations. *J. Chem. Phys.* **152**, 194103 (2020).

53. 53.

VandeVondele, J. & Hutter, J. Gaussian basis sets for accurate calculations on molecular systems in gas and condensed phases. *J.*

Chem. Phys. **127**, 114105 (2007).

54. 54.

Goedecker, S., Teter, M. & Hutter, J. Separable dual-space gaussian pseudopotentials. *Phys. Rev. B* **54**, 1703–1710 (1996).

55. 55.

Perdew, J. P., Burke, K. & Ernzerhof, M. Generalized gradient approximation made simple. *Phys. Rev. Lett.* **77**, 3865–3868 (1996).

56. 56.

Grimme, S., Antony, J., Ehrlich, S. & Krieg, H. A consistent and accurate ab initio parametrization of density functional dispersion correction (DFT-D) for the 94 elements H-Pu. *J. Chem. Phys.* **132**, 154104 (2010).

57. 57.

Frisch, M. J. et al. Gaussian 16 rev. B.01 (Gaussian Inc., Wallingford, CT, 2016).

58. 58.

Liu, J. et al. Overcoming coulomb interaction improves free-charge generation and thermoelectric properties for n-doped conjugated polymers. *ACS Energy Lett.* **4**, 1556–1564 (2019).

59. 59.

Kiefer, D. et al. Enhanced n-doping efficiency of a naphthalenediimide-based copolymer through polar side chains for organic thermoelectrics. *ACS Energy Lett.* **3**, 278–285 (2018).

Acknowledgements

H.G. and X.G. gratefully acknowledge financial support from the National Natural Science Foundation of China (51903117 and 21774055) and the Shenzhen Science and Technology Innovation Commission (JCYJ20180504165709042). A.F. acknowledges AFOSR grant FA9550-18-1-0320. S.F. and C.-Y.Y. acknowledge financial support from the Swedish Research Council (2020-03243), Olle Engkvists Stiftelse (204-0256), VINNOVA (2020-05223), Swedish Government Strategic Research Area in Materials Science on Functional Materials at Linköping University (Faculty Grant SFO-Mat-LiU 2009-00971), and the European Commission through the Marie Skłodowska-Curie project HORATES (GA-955837). A.M. acknowledges CINECA award no. HP10CC5WSY 2020 under the ISCRA initiative for computational resources. H.Y.W. acknowledges financial support from the National Research Foundation (NRF) of Korea (NRF-2019R1A2C2085290). We also acknowledge technical support from SUSTech Core Research Facilities. We thank H. Li, L. Lin, Z.-Y. Ren and Y.-H. Yang for performing ESI-MS and ESR measurements. We thank L. Safaric, Q. Li and Y. Liu (Linköping University) for assistance with GC, absorption and NMR measurements.

Author information

Affiliations

1. Department of Materials Science and Engineering, Southern University of Science and Technology (SUSTech), Shenzhen, Guangdong, China

Han Guo, Xianhe Zhang, Kui Feng, Yongqiang Shi, Kun Yang, Jianhua Chen, Qiaogan Liao, Yumin Tang, Huiliang Sun & Xugang Guo

2. Laboratory of Organic Electronics, Department of Science and Technology, Linköping University, Norrköping, Sweden

Chi-Yuan Yang, Simone Fabiano & Antonio Facchetti

3. Dipartimento di Scienze Chimiche, Università di Roma “La Sapienza”
and INSTM, UdR Roma, Roma, Italy

Alessandro Motta

4. Flexterra Corporation, Skokie, IL, USA

Yu Xia & Antonio Facchetti

5. Department of Chemistry, Korea University, Seoul, South Korea

Ziang Wu & Han Young Woo

6. Department of Chemistry and the Materials Research Center,
Northwestern University, Evanston, IL, USA

Antonio Facchetti

Contributions

H.G., A.F. and X.G. conceived and designed the project. H.G. prepared the samples and performed the electrical, optical absorption, MIS diode, AFM and Seebeck coefficient measurements. C.-Y.Y. and S.F. conducted the doping kinetics study and H₂ product analysis. X.Z. initiated the study with organometallic complex catalyst. A.M. performed the DFT calculations. K.F., Y.S., K.Y., J.C. and H.S. synthesized the organic semiconductors. Y.X. and A.F. fabricated and characterized OTFT devices. Q.L. fabricated and characterized perovskite solar cells. Z.W. and H.Y.W. conducted the GIWAXS measurement. Y.T. performed the TEM measurement. C.-Y.Y., A.M., S.F. and A.F. contributed to data analysis and scientific discussion. H.G., A.F. and X.G. wrote the manuscript. All authors discussed the experimental results and approved the manuscript.

Corresponding authors

Correspondence to Antonio Facchetti or Xugang Guo.

Ethics declarations

Competing interests

X.G. and H.G. have filed a provisional patent application based on this work. S.F. is the chief scientific officer of n-Ink AB, a company developing organic conductive inks. A.F. is the chief technology officer of Flexterra corporation, a company developing organic semiconductors.

Additional information

Peer review information *Nature* thanks Peter Ho, Karl Leo and Shun Watanabe for their contribution to the peer review of this work.

Publisher's note Springer Nature remains neutral with regard to jurisdictional claims in published maps and institutional affiliations.

Extended data figures and tables

[**Extended Data Fig. 1 TEM images of thermally evaporated AuNP films on TEM grids coated with a thin carbon film with the nanoparticle size \(diameter \$d\$ \) distribution as a function of the nominal film thickness.**](#)

a–e, The nominal AuNP film thickness is 0.1 nm (**a**), 0.2 nm (**b**), 0.4 nm (**c**), 0.8 nm (**d**) and 1.5 nm (**e**). The TEM images are shown in both high magnification (left column; scale bar, 10 nm) and lower magnification (middle column; scale bar, 50 nm). The AuNP size distribution probability plots in the right column are all from statistical analysis of more than 150 nanoparticles, with their average sizes and standard deviations shown inside.

[**Extended Data Fig. 2 Electrical conductivity measurements for blend doped PDTzTI films on glass and PET substrates with**](#)

different electrical contact materials.

a–c, Representative I – V characteristics of 60 mol% N-DMBI-H blend doped PDTzTI films on glass substrates as plotted in log scale (**a**) and linear scale (**b**, **c**), respectively. When using AuNPs, there is a significant charge injection barrier between the Al electrode and the highly conductive PDTzTI film as shown by the non-linear I – V characteristics in panel **b**. Nonetheless, the σ of the Al device, estimated from the currents at $|V| = 5$ V, is 3.6 ± 0.3 S cm $^{-1}$, which is in the same order of magnitude of that of the Au device (14.1 ± 0.7 S cm $^{-1}$). **c**, Without using AuNP catalyst, the device current is orders of magnitude lower than that of the device with AuNP, with a $\sigma = (2.6 \pm 0.2) \times 10^{-4}$ S cm $^{-1}$ for the Al device and $(4.6 \pm 1.2) \times 10^{-4}$ S cm $^{-1}$ for the Au device. In all these experiments, the electrodes were fabricated by thermal evaporation using a shadow mask except for the control Au device (without AuNPs), which was prepared by lift-off photolithography to avoid that residual Au clusters catalyse the reaction as we show clearly in Supplementary Fig. 8. **d**, Representative I – V characteristics of 60 mol% N-DMBI-H plus AuNPs blend doped PDTzTI films on glass (blue line) and plastic (PET, red line) substrates. In all these experiments $d = 1.4$ nm, $T_{\text{ann}} = 120$ °C, $t_{\text{ann}} = 10$ s when using AuNP catalyst or $t_{\text{ann}} = 10$ min when not using catalyst, demonstrating that the catalysed n-doping method is fully compatible with PET substrates. All contact geometries are 100 μm (channel length) and 2 mm (channel width).

Extended Data Fig. 3 AuNP catalysed N-DMBI-H doping efficiency estimation from electrical conductivity.

a–f, N-DMBI-H doping efficiency (η) versus dopant molar ratio in blend-doped PDTzTI (**a**), PDTzTIT-2F (**b**), PDTzTIT (**c**), PBTzI (**d**), N2200 (**e**), and f-BTI2TEG-FT (**f**) films calculated using the measured electrical conductivity and various electron mobility values. The red curves originate using the measured OTFT mobility ($\mu_{\text{e,OTFT}}$ values from our published results^{32,37,58} or Supplementary Table 6 for f-BTI2TEG-FT). The plots show that the $\mu_{\text{e,OTFT}}$ is a reasonable assumption for the actual carrier mobility of doped films ($\mu_{\text{e,doped}}$) at high charge density for PDTzTI,

PDTzTIT-2F, PDTzTIT and PBTzI (Extended Data Fig. 3a–d and Supplementary Table 3). The estimated high η is in good agreement with our experimental observations of strong film colour change in their UV-vis–NIR spectra and high electrical conductivity (for example, Fig. 2b, Supplementary Figs. 9 and 10, Table 1). Obviously, the $\mu_{e,\text{doped}}$ at different dopant loading must afford a $\eta < 100\%$, to be realistic. $\mu_{e,\text{doped}}$ is likely to be charge density dependent and also changes with the N-DMBI-H loading and variation of film morphology, and also may differ significantly from the $\mu_{e,\text{OTFT}}$ as exemplified by N2200 (e) and f-BTI2TEG-FT (f) analysis. For N2200, the calculated η_{max} using the $\mu_{e,\text{OTFT}}$ is $<0.1\%$, which does not agree with the experimental ESR results ($>40\%$) and the strong variation of the optical absorption. Thus, the actual $\mu_{e,\text{doped}}$ must be $\ll \mu_{e,\text{OTFT}}$ and possibly $<0.001 \text{ cm}^2 \text{ V}^{-1} \text{ s}^{-1}$ when examining the η -dopant molar ratio graph in panel e. For the polymer f-BTI2TEG-FT, a $\eta_{\text{max}} > 3,000\%$ is calculated using the $\mu_{e,\text{OTFT}}$, which is unrealistic. Thus, the actual $\mu_{e,\text{doped}}$ is $\gg \mu_{e,\text{OTFT}}$ and possibly around $1 \text{ cm}^2 \text{ V}^{-1} \text{ s}^{-1}$ at high charge densities, as estimated from the graph in panel f.

Extended Data Fig. 4 2D-GIWAXS images of N-DMBI-H + AuNP doped organic semiconductor films.

The semiconductor films were spin-cast from their pristine or blend solutions with N-DMBI-H in CHCl_3 (5 mg ml $^{-1}$ for PDTzTI and N2200, 20 mg ml $^{-1}$ for PDI-C $_6$ C $_7$), then annealed at $T_{\text{ann}} = 120^\circ\text{C}$, $t_{\text{ann}} = 10$ s. In all these experiments, AuNP $d = 1.4$ nm and the substrate is silicon. The images clearly show that, as the N-DMBI-H loading increases, the doped film crystallinity gradually decreases, eventually to a very low degree of crystallinity and near amorphous structure for all these organic semiconductor films at 100mol% N-DMBI-H loading.

Extended Data Fig. 5 Explored AuNP catalysed N-DMBI-H doping mechanisms.

All the investigated routes share the same first step, namely the hydride transfer from N-DMBI-H to AuNP surface. Depending on the possible active-doping-species, we propose four different reaction routes after the initial hydride transfer step. In route a, $\text{Au}_x\text{--H}^-$ directly acts as the active-doping-species and forms $\text{Au}_x\text{--H}^\bullet$ after electron transfer to PDI, then, the H^\bullet on AuNP surface combines and releases H_2 gas to regenerate clean AuNP surface for the next catalytic cycle. In route b, H^\bullet is released from $\text{Au}_x\text{--H}^-$ to form $\text{Au}_x^{\bullet-}$ as the active-doping-species, then H^\bullet combines to give H_2 gas, while $\text{Au}_x^{\bullet-}$ transfers the electron to the PDI and goes to the next catalytic cycle. In route c, H^- is transferred from $\text{Au}_x\text{--H}^-$ to PDI and forms hydrogenated PDI anion (denoted as PDI--H^-) as the active-doping-species, which transfers electron to another PDI molecule and forms PDI--H^\bullet , then two PDI--H^\bullet combine each other to give H_2 gas while PDI is regenerated for the next doping reaction cycle. Finally, in route d, H^- is released from $\text{Au}_x\text{--H}^-$ and serves as the active-doping-species, the clean AuNP surface goes to next catalytic cycle, while H^- transfers the electron to the PDI and forms H^\bullet which combines to give H_2 gas. For all the reaction routes, the final reaction products are N-DMBI^+ , $\text{PDI}^{\bullet-}$ and H_2 gas, AuNP only serves as the reaction catalyst. PDI-C₆C₇ molecule is modelled by a simpler PDI in which the 1-hexylheptyl side chain is replaced by a methyl group.

Extended Data Fig. 6 Gibbs free energy profile (kcal mol⁻¹) of the investigated nanoparticle catalysed N-DMBI-H doping mechanisms.

PDI-C₆C₇ molecule is modelled by a simpler PDI in which the 1-hexylheptyl side chain is replaced by a methyl group. AuNP is modelled by the Au (111) surface. Solvation effects are taken into account for all the molecular species. Route a is most energetically favourable with its Gibbs free energy diagram also given in Fig. 4f of the main text.

Extended Data Fig. 7 Application of catalysed n-doping of organic polymers to n-type organic thermoelectronic devices.

a, Illustration of an n-type thermoelectric device where this method can be used to generate an n-doped organic semiconductor film. **b**, N-type thermoelectric performance of an off-centre spin-casted, sequentially doped f-BTI2TEG-FT+PBTI blend films, using AuNP catalyst. Recently, side-chain engineering of conjugated polymers with hydrophilic groups⁵⁹ has shown improved n-dopability and conductivity with N-DMBI-H due to enhanced dopant/semiconductor miscibility. For example, by simply replacing the hydrophobic alkyl chain (2-octyldodecyl) in f-BTI2-FT⁵¹ with triethylene glycol (TEG)-based chain in f-BTI2TEG-FT (Supplementary scheme 1, Supplementary Figs. 34–41), σ of uncatalysed N-DMBI-H doping was found to increase from $(8.9 \pm 0.5) \times 10^{-3} \text{ S cm}^{-1}$ to $1.4 \pm 0.1 \text{ S cm}^{-1}$, respectively. However, N-DMBI-H+AuNP doping of f-BTI2TEG-FT can achieve a σ of $25.1 \pm 0.6 \text{ S cm}^{-1}$ (blend doping), $38.4 \pm 2.2 \text{ S cm}^{-1}$ (sequential doping, on-centre), and $74.3 \pm 4.6 \text{ S cm}^{-1}$ (sequential doping, off-centre) (Table 1, Supplementary Figs. 42, 43), despite a low transistor mobility of $0.018 \text{ cm}^2 \text{ V}^{-1} \text{ s}^{-1}$ (Supplementary Fig. 44, Supplementary Table 6). Impressively, an even higher σ of $104.0 \pm 7.9 \text{ S cm}^{-1}$ (maximum 116.3 S cm^{-1}) can be obtained by adding a small amount (15wt%) of the high mobility PBTI polymer⁵⁰ ($M_n = 35.5 \text{ kDa}$) to f-BTI2TEG-FT, which serves as high-mobility pathways between doped f-BTI2TEG-FT domains for improved charge transport⁴². Thus, based on the latter blend, we fabricated an organic thermoelectric device which showed a remarkable power factor (PF) of $65.7 \pm 5.5 \mu\text{W m}^{-1} \text{ K}^{-2}$ with a Seebeck coefficient of $-79.5 \pm 2.8 \mu\text{V K}^{-1}$ (Extended Data Fig. 7b, Supplementary Fig. 45). The conductivity and power factor values are among the highest to date for solution-processed molecular n-doped conjugated polymers^{12,46}. Error bars represent the standard deviations from their mean values.

Extended Data Fig. 8 Application of catalysed n-doping of organic polymers to organic thin-film transistor (OTFT) devices.

a, Chemical structure of the polymer N2200-EG7 (P) and the PDIR-CN2 semiconductor (OSC) used for OTFT devices. **b**, Top-gate bottom-contact OTFT structure with Au source/drain/gate electrodes and using Au contacts

to catalyse the n-doping of the NDI polymer P with N-DMBI-H (blend method). **c–e**, Corresponding transfer plots (**c**), mobility evolutions (**d**) and low-drain voltage output plots (**e**) of the indicated devices. **f**, Top-gate bottom-contact OTFT structure with Ag source/drain/gate electrodes using $\text{Pd}_2(\text{dba})_3$ to catalyse the n-doping of the NDI polymer P with N-DMBI-H (blend method). **g–i**, Corresponding transfer plots (**g**), mobility evolutions (**h**) and low-drain voltage output plots (**i**) of the indicated devices.

Extended Data Fig. 9 Perovskite solar cells fabricated with undoped/doped polymer films as the electron transporting layer (ETL).

a, Perovskite cell structure, chemical structures of the hole transporting layer (HTL) and ETL polymers used in this study. **b**, $J-V$ plots of the best device using PDTzTIT polymer as ETL. **c**, $J-V$ plots of the best device using PDTzTIT-2F polymer as ETL.

Supplementary information

Supplementary Information

This file contains Supplementary Figs. 1–46, Supplementary Tables 1–7, Supplementary scheme 1 and Supplementary references.

Supplementary Video 1

Video showing that fast N-DMBI-H doping reaction happens in the presence of AuNP. The PDI-C₆C₇ + N-DMBI-H (10 eq.) blend solutions in CH₂Cl₂ were drop-casted in ambient air at 25 °C onto bare glass substrate (left) or glass with pre-deposited AuNP (right, nominal evaporation thickness 1.2 nm, estimated NP size $d \approx 6.4$ nm). An immediate colour change was observed when the blend solution contacted AuNP, while there was no obvious change without AuNP, thus clearly demonstrating the high catalytic activity of AuNP which significantly enhances the N-DMBI-H doping reaction.

Rights and permissions

[Reprints and Permissions](#)

About this article

Cite this article

Guo, H., Yang, CY., Zhang, X. *et al.* Transition metal-catalysed molecular n-doping of organic semiconductors. *Nature* **599**, 67–73 (2021).
<https://doi.org/10.1038/s41586-021-03942-0>

- Received: 29 January 2020
- Accepted: 24 August 2021
- Published: 03 November 2021
- Issue Date: 04 November 2021
- DOI: <https://doi.org/10.1038/s41586-021-03942-0>

Share this article

Anyone you share the following link with will be able to read this content:

[Get shareable link](#)

Sorry, a shareable link is not currently available for this article.

[Copy to clipboard](#)

Provided by the Springer Nature SharedIt content-sharing initiative

| [Section menu](#) | [Main menu](#) |

- Article
- [Published: 03 November 2021](#)

Episodic deluges in simulated hothouse climates

- [Jacob T. Seeley](#) ORCID: [orcid.org/0000-0003-0769-292X¹](https://orcid.org/0000-0003-0769-292X) &
- [Robin D. Wordsworth](#) ORCID: [orcid.org/0000-0003-1127-8334^{1,2}](https://orcid.org/0000-0003-1127-8334)

Nature volume **599**, pages 74–79 (2021)

- 748 Accesses
- 48 Altmetric
- [Metrics details](#)

Subjects

- [Atmospheric dynamics](#)
- [Climate and Earth system modelling](#)
- [Phase transitions and critical phenomena](#)

Abstract

Earth's distant past and potentially its future include extremely warm 'hothouse'¹ climate states, but little is known about how the atmosphere behaves in such states. One distinguishing characteristic of hothouse climates is that they feature lower-tropospheric radiative heating, rather than cooling, due to the closing of the water vapour infrared window regions². Previous work has suggested that this could lead to temperature inversions and substantial changes in cloud cover^{3,4,5,6}, but no previous

modelling of the hothouse regime has resolved convective-scale turbulent air motions and cloud cover directly, thus leaving many questions about hothouse radiative heating unanswered. Here we conduct simulations that explicitly resolve convection and find that lower-tropospheric radiative heating in hothouse climates causes the hydrologic cycle to shift from a quasi-steady regime to a ‘relaxation oscillator’ regime, in which precipitation occurs in short and intense outbursts separated by multi-day dry spells. The transition to the oscillatory regime is accompanied by strongly enhanced local precipitation fluxes, a substantial increase in cloud cover, and a transiently positive (unstable) climate feedback parameter. Our results indicate that hothouse climates may feature a novel form of ‘temporal’ convective self-organization, with implications for both cloud coverage and erosion processes.

Access options

Subscribe to Journal

Get full journal access for 1 year

\$199.00

only \$3.90 per issue

[Subscribe](#)

All prices are NET prices.

VAT will be added later in the checkout.

Tax calculation will be finalised during checkout.

Rent or Buy article

Get time limited or full article access on ReadCube.

from \$8.99

[Rent or Buy](#)

All prices are NET prices.

Additional access options:

- [Log in](#)
- [Access through your institution](#)
- [Learn about institutional subscriptions](#)

Fig. 1: Transition to the relaxation oscillator regime due to increased insolation.

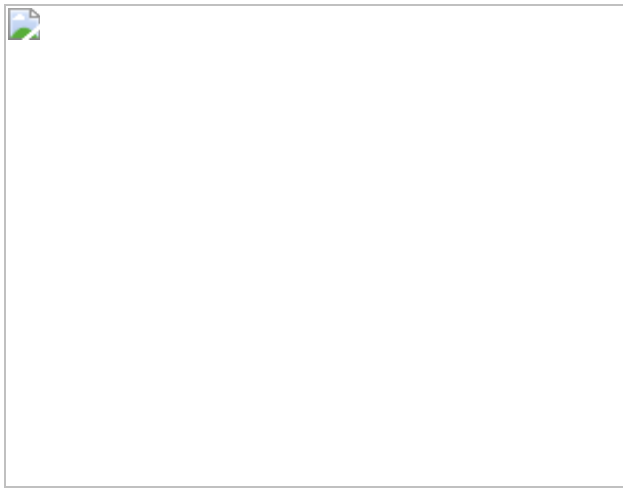


Fig. 2: The oscillatory regime is induced by LTRH.

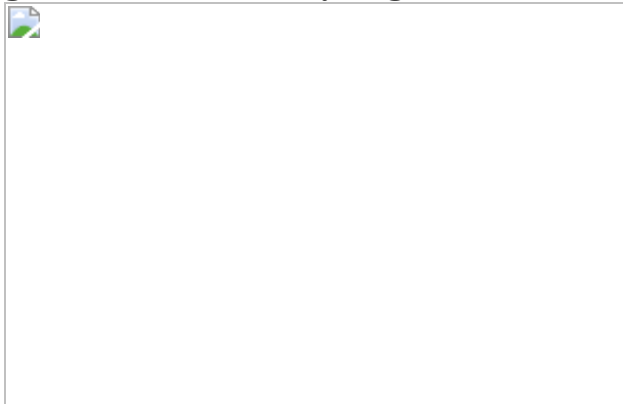


Fig. 3: Mechanism of the oscillatory regime as revealed by high-frequency model output.

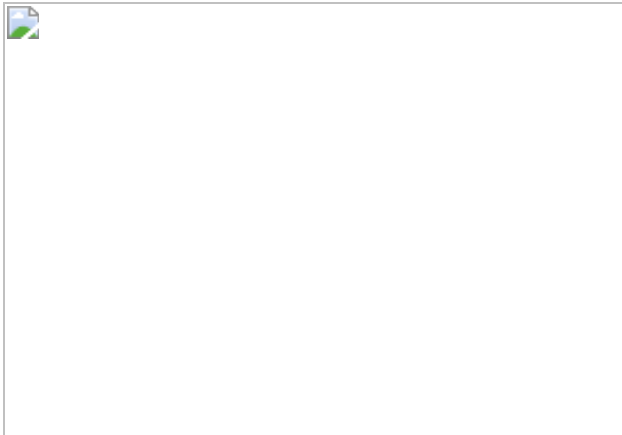
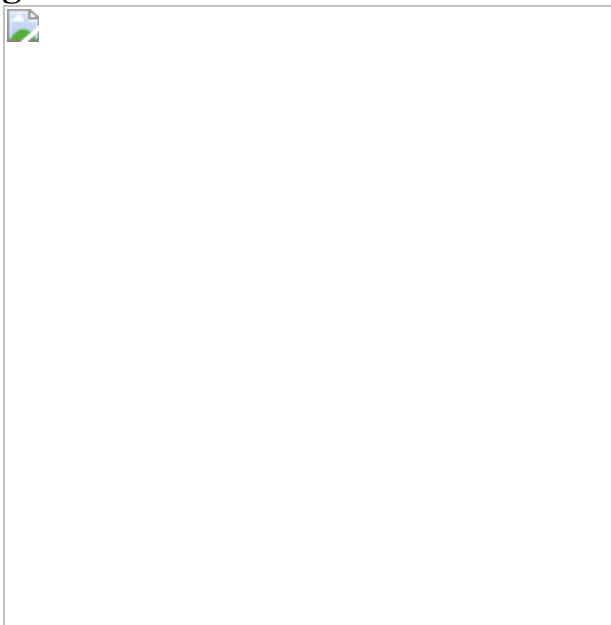


Fig. 4: Overview of the relaxation oscillator convective regime.



Data availability

Input data files and cloud-resolving model output associated with this work are available in a Zenodo repository at
<https://doi.org/10.5281/zenodo.5117529>.

Code availability

Source code for the stochastic two-layer model, processing cloud-resolving model output, and generating figures is available in a Zenodo repository at
<https://doi.org/10.5281/zenodo.5117529>.

References

1. 1.

Steffen, W. et al. Trajectories of the Earth System in the Anthropocene. *Proc. Natl Acad. Sci. USA* **115**, 8252–8259 (2018).

2. 2.

Wordsworth, R. D. & Pierrehumbert, R. T. Water loss from terrestrial planets with CO₂-rich atmospheres. *Astrophys. J.* **778**, 154 (2013).

3. 3.

Wolf, E. T. & Toon, O. B. The evolution of habitable climates under the brightening Sun. *J. Geophys. Res. Atmos.* **120**, 5775–5794 (2015).

4. 4.

Kopparapu, R. K. et al. The inner edge of the habitable zone for synchronously rotating planets around low-mass stars using general circulation models. *Astrophys. J.* **819**, 84 (2016).

5. 5.

Popp, M., Schmidt, H. & Marotzke, J. Transition to a Moist Greenhouse with CO₂ and solar forcing. *Nat. Commun.* **7**, 10627 (2016).

6. 6.

Wolf, E. T., Haqq-Misra, J. & Toon, O. B. Evaluating climate sensitivity to CO₂ across Earth’s history. *J. Geophys. Res. Atmos.* **123**, 11861–11874 (2018).

7. 7.

Snyder, C. W. Evolution of global temperature over the past two million years. *Nature* **538**, 226–228 (2016).

8. 8.

Sleep, N. H. The Hadean-Archaean environment. *Cold Spring Harb. Perspect. Biol.* <https://doi.org/10.1101/cshperspect.a002527> (2010).

9. 9.

Charnay, B., Le Hir, G., Fluteau, F., Forget, F. & Catling, D. C. A warm or a cold early Earth? New insights from a 3-D climate-carbon model. *Earth Planet. Sci. Lett.* **474**, 97–109 (2017).

10. 10.

Pierrehumbert, R., Abbot, D., Voigt, A. & Koll, D. Climate of the Neoproterozoic. *Annu. Rev. Earth Planet. Sci.* **39**, 417–460 (2011).

11. 11.

Goldblatt, C. & Watson, A. J. The runaway greenhouse: implications for future climate change, geoengineering and planetary atmospheres. *Philos. Trans. R. Soc. A* **370**, 4197–4216 (2012).

12. 12.

Koll, D. D. B. & Cronin, T. W. Earth's outgoing longwave radiation linear due to H_2O greenhouse effect. *Proc. Natl Acad. Sci. USA* **115**, 10293–10298 (2018).

13. 13.

Seeley, J. T. & Jeevanjee, N. H_2O windows and CO_2 radiator fins: a clear-sky explanation for the peak in equilibrium climate sensitivity. *Geophys. Res. Lett.* **48**, e2020GL089609 (2021).

14. 14.

Yang, J., Cowan, N. B. & Abbot, D. S. Stabilizing cloud feedback dramatically expands the habitable zone of tidally locked planets. *Astrophys. J. Lett.* **771**, L45 (2013).

15. 15.

Sergeev, D. E. et al. Atmospheric convection plays a key role in the climate of tidally-locked terrestrial exoplanets: insights from high-resolution simulations. *Astrophys. J.* **894**, 84 (2020).

16. 16.

Lefèvre, M., Turbet, M. & Pierrehumbert, R. 3D convection-resolving model of temperate, tidally locked exoplanets. *Astrophys. J.* **913**, 101 (2021).

17. 17.

Romps, D. M. The dry-entropy budget of a moist atmosphere. *J. Atmos. Sci.* **65**, 3779–3799 (2008).

18. 18.

Wang, D. in *Wiley Encyclopedia of Electrical and Electronics Engineering* (ed. Webster, J. G.) Vol. 18, 396–405 (Wiley, 1999).

19. 19.

Ginoux, J.-M. & Letellier, C. Van der Pol and the history of relaxation oscillations: toward the emergence of a concept. *Chaos* **22**, 023120 (2012).

20. 20.

Pendergrass, A. G. & Hartmann, D. L. The atmospheric energy constraint on global-mean precipitation change. *J. Clim.* **27**, 757–768 (2014).

21. 21.

Jeevanjee, N. & Romps, D. M. Mean precipitation change from a deepening troposphere. *Proc. Natl Acad. Sci. USA* **115**, 11465–11470 (2018).

22. 22.

Torri, G., Kuang, Z. & Tian, Y. Mechanisms for convection triggering by cold pools. *Geophys. Res. Lett.* **42**, 1943–1950 (2015).

23. 23.

Jeevanjee, N. & Romps, D. M. Effective buoyancy, inertial pressure, and the mechanical generation of boundary layer mass flux by cold pools. *J. Atmos. Sci.* **72**, 3199–3213 (2015).

24. 24.

Feng, Z. et al. Mechanisms of convective cloud organization by cold pools over tropical warm ocean during the AMIE/DYNAMO field campaign. *J. Adv. Model. Earth Syst.* **7**, 357–381 (2015).

25. 25.

Torri, G. & Kuang, Z. On cold pool collisions in tropical boundary layers. *Geophys. Res. Lett.* **46**, 399–407 (2019).

26. 26.

Singh, M. S. & O’Gorman, P. A. Influence of entrainment on the thermal stratification in simulations of radiative-convective equilibrium. *Geophys. Res. Lett.* **40**, 4398–4403 (2013).

27. 27.

Seeley, J. T. & Romps, D. M. Why does tropical convective available potential energy (CAPE) increase with warming? *Geophys. Res. Lett.* **42**, 10,429–10,437 (2015).

28. 28.

Zhao, M. Uncertainty in model climate sensitivity traced to representations of cumulus precipitation microphysics. *J. Clim.* **29**, 543–560 (2016).

29. 29.

Popp, M., Schmidt, H. & Marotzke, J. Initiation of a runaway greenhouse in a cloudy column. *J. Atmos. Sci.* **72**, 452–471 (2015).

30. 30.

Wing, A. A. et al. Clouds and convective self-aggregation in a multimodel ensemble of radiative-convective equilibrium simulations. *J. Adv. Model. Earth Syst.* **12**, e2020MS002138 (2020).

31. 31.

Becker, T. & Wing, A. A. Understanding the extreme spread in climate sensitivity within the radiative-convective equilibrium model intercomparison project. *J. Adv. Model. Earth Syst.* **12**, e2020MS002165 (2020).

32. 32.

Romps, D. M. Climate sensitivity and the direct effect of carbon dioxide in a limited-area cloud-resolving model. *J. Clim.* **33**, 3413–3429 (2020).

33. 33.

Wing, A. A., Emanuel, K., Holloway, C. E. & Muller, C. Convective self-aggregation in numerical simulations: a review. *Surv. Geophys.* **38**, 1173–1197 (2017).

34. 34.

Mirollo, R. E. & Strogatz, S. H. Synchronization of pulse-coupled biological oscillators. *SIAM J. Appl. Math.* **50**, 1645–1662 (1990).

35. 35.

Pantaleone, J. Synchronization of metronomes. *Am. J. Phys.* **70**, 992–1000 (2002).

36. 36.

Buck, J. & Buck, E. Biology of synchronous flashing of fireflies. *Nature* **211**, 562–564 (1966).

37. 37.

Bretherton, C. S. & Smolarkiewicz, P. K. Gravity waves, compensating subsidence, and detrainment around cumulus clouds. *J. Atmos. Sci.* **46**, 740–759 (1989).

38. 38.

Edman, J. P. & Romps, D. M. Beyond the rigid lid: baroclinic modes in a structured atmosphere. *J. Atmos. Sci.* **74**, 3551–3566 (2017).

39. 39.

Carlson, T. N., Benjamin, S. G. & Forbes, G. S. Elevated mixed layers in the regional severe storm environment: conceptual model and case studies. *Mon. Weather Rev.* **11**, 1453–1473 (1983).

40. 40.

Schultz, D. M., Richardson, Y. P., Markowski, P. M. & Doswell, C. A. Tornadoes in the central United States and the “clash of air masses”. *Bull. Am. Meteorol. Soc.* **95**, 1704–1712 (2014).

41. 41.

Agard, V. & Emanuel, K. Clausius–Clapeyron scaling of peak CAPE in continental convective storm environments. *J. Atmos. Sci.* **74**, 3043–3054 (2017).

42. 42.

Arakawa, A. & Schubert, W. H. Interaction of a cumulus cloud ensemble with the large-scale environment, part I. *J. Atmos. Sci.* **31**, 674–701 (1974).

43. 43.

Raymond, D. in *The Physics and Parameterization of Moist Atmospheric Convection* (ed. Smith, R. K.) 387–397 (Kluwer Academic Publishers, 1997).

44. 44.

Melosh, H. J. in *Planetary Surface Processes* Ch. 10, 382–433 (Cambridge Univ. Press, 2011).

45. 45.

Villarini, G., Smith, J. A., Baeck, M. L., Marchok, T. & Vecchi, G. A. Characterization of rainfall distribution and flooding associated with U.S. landfalling tropical cyclones: analyses of Hurricanes Frances, Ivan, and Jeanne (2004). *J. Geophys. Res. Atmos.* **116**, D23116 (2011).

46. 46.

Graham, R. J. & Pierrehumbert, R. Thermodynamic and energetic limits on continental silicate weathering strongly impact the climate and habitability of wet, rocky worlds. *Astrophys. J.* **896**, 115 (2020).

47. 47.

Dansgaard, W. Stable isotopes in precipitation. *Tellus* **16**, 436–468 (1964).

48. 48.

Pausata, F. S., Battisti, D. S., Nisancioglu, K. H. & Bitz, C. M. Chinese stalagmite $\delta^{18}\text{O}$ controlled by changes in the indian monsoon during a

simulated heinrich event. *Nat. Geosci.* **4**, 474–480 (2011).

49. 49.

Frieling, J. et al. Extreme warmth and heat-stressed plankton in the tropics during the Paleocene-Eocene Thermal Maximum. *Sci. Adv.* **3**, e1600891 (2017).

50. 50.

Wing, A. A. et al. Radiative-Convective Equilibrium Model Intercomparison Project. *Geosci. Model Dev.* **11**, 793–813 (2018).

51. 51.

Romps, D. M. Response of tropical precipitation to global warming. *J. Atmos. Sci.* **68**, 123–138 (2011).

52. 52.

Clough, S. A. et al. Atmospheric radiative transfer modeling: a summary of the AER codes. *J. Quant. Spectrosc. Radiat. Transf.* **91**, 233–244 (2005).

53. 53.

Iacono, M. J. et al. Radiative forcing by long-lived greenhouse gases: calculations with the AER radiative transfer models. *J. Geophys. Res. Atmos.* **113**, 2–9 (2008).

54. 54.

Wordsworth, R. et al. Transient reducing greenhouse warming on early Mars. *Geophys. Res. Lett.* **44**, 665–671 (2017).

55. 55.

Ding, F. & Wordsworth, R. D. A new line-by-line general circulation model for simulations of diverse planetary atmospheres: initial

validation and application to the exoplanet GJ 1132B. *Astrophys. J.* **878**, 117 (2019).

56. 56.

Schaefer, L., Wordsworth, R. D., Berta-Thompson, Z. & Sasselov, D. Predictions of the atmospheric composition of GJ 1132b. *Astrophys. J.* **829**, 63 (2016).

57. 57.

Clough, S. A., Iacono, M. J. & Moncet, J.-L. Line-by-line calculations of atmospheric fluxes and cooling rates: application to water vapor. *J. Geophys. Res.* **97**, 15761 (1992).

58. 58.

Gordon, I. E. et al. The HITRAN2016 molecular spectroscopic database. *J. Quant. Spectrosc. Radiat. Transf.* **203**, 3–69 (2017).

59. 59.

Dudhia, A. The Reference Forward Model (RFM). *J. Quant. Spectrosc. Radiat. Transf.* **186**, 243–253 (2017).

60. 60.

Mlawer, E. J. et al. Development and recent evaluation of the MT_CKD model of continuum absorption. *Philos. Trans. R. Soc. A* **370**, 2520–2556 (2012).

61. 61.

Claire, M. W. et al. The evolution of solar flux from 0.1 nm to 160 μm : quantitative estimates for planetary studies. *Astrophys. J.* **757**, 95 (2012).

62. 62.

Segura, A. et al. Biosignatures from Earth-like planets around M dwarfs. *Astrobiology* **5**, 706–725 (2005).

63. 63.

Krueger, S. K., Fu, Q., Liou, K. N. & Chin, H.-N. S. Improvements of an ice-phase microphysics parameterization for use in numerical simulations of tropical convection. *J. Appl. Meteorol.* **34**, 281–286 (1995).

64. 64.

Lin, Y.-L., Farley, R. D. & Orville, H. D. Bulk parameterization of the snow field in a cloud model. *J. Clim. Appl. Meteorol.* **22**, 1065–1092 (1983).

65. 65.

Lord, S. J., Willoughby, H. E. & Piotrowicz, J. M. Role of a parameterized ice-phase microphysics in an axisymmetric, nonhydrostatic tropical cyclone model. *J. Atmos. Sci.* **41**, 2836–2848 (1984).

66. 66.

Seeley, J. T., Jeevanjee, N. & Romps, D. M. FAT or FiTT: are anvil clouds or the tropopause temperature-invariant? *Geophys. Res. Lett.* **46**, 1842–1850 (2019).

67. 67.

Seeley, J. T., Lutsko, N. J. & Keith, D. W. Designing a radiative antidote to CO₂. *Geophys. Res. Lett.* **48**, e2020GL090876 (2021).

68. 68.

Romps, D. M. & Kuang, Z. Nature versus nurture in shallow convection. *J. Atmos. Sci.* **67**, 1655–1666 (2010).

69. 69.

Khairoutdinov, M. F. & Randall, D. A. Cloud resolving modeling of the ARM summer 1997 IOP: model formulation, results, uncertainties, and sensitivities. *J. Atmos. Sci.* **60**, 607–625 (2003).

70. 70.

Bryan, G. & Fritsch, J. A benchmark simulation for moist nonhydrostatic numerical models. *Mon. Weather Rev.* **130**, 2917–2928 (2002).

71. 71.

Morrison, H., Curry, J. A. & Khvorostyanov, V. I. A new double-moment microphysics parameterization for application in cloud and climate models. Part I: description. *J. Atmos. Sci.* **62**, 1665–1677 (2005).

72. 72.

Cess, R. D. et al. Intercomparison and interpretation of climate feedback processes in 19 atmospheric general circulation models. *J. Geophys. Res. Atmos.* **95**, 16601–16615 (1990).

Acknowledgements

We are grateful to the authors of the cloud-resolving models used in this work: D. Romps, M. Khairoutdinov and G. Bryan. We also thank A. Dudhia for sharing with us the Reference Forward Model. We thank X. Wei for conducting exploratory simulations with SAM. J.T.S. thanks N. Jeevanjee, A. Match, N. Tarshish and Z. Kuang for discussions.

Author information

Affiliations

1. Department of Earth and Planetary Sciences, Harvard University,
Cambridge, MA, USA

Jacob T. Seeley & Robin D. Wordsworth

2. School of Engineering and Applied Sciences, Harvard University,
Cambridge, MA, USA

Robin D. Wordsworth

Contributions

J.T.S. and R.D.W. designed the research. J.T.S. performed the simulations, analysed the results and prepared the figures. The manuscript was written jointly by J.T.S. and R.D.W.

Corresponding author

Correspondence to Jacob T. Seeley.

Ethics declarations

Competing interests

The authors declare no competing interests.

Additional information

Peer review information *Nature* thanks the anonymous reviewers for their contribution to the peer review of this work.

Publisher's note Springer Nature remains neutral with regard to jurisdictional claims in published maps and institutional affiliations.

Extended data figures and tables

Extended Data Fig. 1 Errors in clear-sky RRTM radiative heating rates are corrected by using line-by-line radiative transfer.

Comparison of net (LW+SW; panels **a–d**), longwave (LW; panels **e–h**), and shortwave (SW; panels **i–l**) radiative heating rates as computed by RRTM (black) and PCM_LBL (red). The heating rates are computed for moist-adiabatic temperature-pressure profiles with surface temperatures ranging from 305 K to 335 K in 10-K increments (columns, left to right). All columns have a surface pressure of 101325 Pa, 75% tropospheric relative humidity, 400 ppm CO₂, and an isothermal stratosphere at 160 K. Note that the discontinuous heating rates calculated by RRTM for the warmer atmospheres (around 20 km altitude) do not appear in the PCM_LBL results.

Extended Data Fig. 2 Top-of-atmosphere radiative fluxes and heating rates from DAM snapshots.

(a–c) Outgoing longwave radiation (OLR) from a snapshot from the fixedSST_hires DAM simulation with a surface temperature of 305 K, computed by three different combinations of radiative transfer codes and approximations. Panel **(a)** is from RRTM alone, panel **(b)** shows the result of swapping out the clear-sky radiative fluxes from RRTM with those calculated by PCM_LBL, and panel **(c)** shows the result of swapping out each column's clear-sky radiative fluxes for those calculated by PCM_LBL for the horizontal-mean column, which is the approach taken for the simulations associated with this work. Panel **(d)** shows the horizontal-mean longwave radiative heating rates for this snapshot. **(e–h)** As in **(a–d)**, but for absorbed shortwave radiation (ASR). **(i–p)** As in **(a–h)**, but for a snapshot from the simulation with a surface temperature of 330 K.

Extended Data Fig. 3 Tests of the robustness of the oscillatory transition.

Domain-mean precipitation from two periods of **(a)** the FCO2 simulation with mean SSTs of 306.1 K and 331.5 K; **(b)** the fixedSST suite at 305 K

and 330 K; (c) the fixedSST_sm suite, which use the simplified microphysics parameterization described in the Methods; (d) fixed-SST simulations with finer horizontal resolution ($\Delta x = 250$ m; fixedSST_hires) or on a larger domain ($L_x = 512$ km; fixedSST_large). (e) The same quantity from simulations conducted with the System for Atmospheric Modeling (SAM)⁶⁹ at fixed SSTs of 305 and 325 K. (f) As in (e), but for the Cloud Model 1 (CM1)⁷⁰.

Extended Data Fig. 4 Mean profiles of temperature and cloud fraction.

From the fixedSST simulations, profiles of (a) mean temperature and (b) mean cloud fraction (fraction of grid cells with non-precipitating cloud condensate mass fraction greater than 10^{-5} kg/kg). In (a), the variability is indicated by the shading, which shows ± 2 standard deviations of hourly-mean temperatures at each altitude. In (a), the dashed line shows the mean temperature profile from the simulation without evaporation of precipitating hydrometeors (prevap0) at 330 K.

Extended Data Fig. 5 Sign reversal of the climate feedback parameter indicates transient climate instability.

The feedback parameter λ is defined here as minus the change in net radiative flux at the top-of-atmosphere (TOA) per degree of surface warming (positive downward, so that a negative feedback indicates more radiation escaping to space with warming and hence climate stability, and a positive feedback indicates climate instability; this is often called the “Cess sensitivity”⁷²). We calculated feedbacks using finite differences on a staggered surface temperature grid that interpolates between the surface temperatures of the fixedSST experiment. (a) The solid line shows clear-sky feedbacks calculated for TOA fluxes averaged over the final 100 days of the fixedSST simulations, while the dashed and dot-dashed lines show the feedbacks calculated using the time-mean columns from those simulations with actual or fixed 100% relative humidity profiles, respectively. (b) As in (a), but for the all-sky feedbacks from fixedSST experiments broken down into longwave and shortwave components. The

dashed line shows the net all-sky feedback from the final 50 days of the LTRH_off experiment, which does not undergo a steady-to-oscillatory transition and remains stable at all temperatures. (c) Time-mean profiles of relative humidity (RH) in the fixedSST experiments, using temperature within the atmosphere as a vertical coordinate to emphasize the increases in upper-tropospheric relative humidity that occur during the oscillatory transition between 320 and 325 and K. Since the clear-sky climate instability is eliminated by using a fixed relative humidity of 100% (panel a), we attribute the clear-sky climate instability to the increase in upper-tropospheric RH, which lowers spectral emission temperatures and hence OLR.

Extended Data Fig. 6 Spatially-separated subdomains exhibit in-phase pulses of convection.

Timeseries of (a,c) moist static energy in the lowest model level ($z = 12.5$ m; MSE_{surf}), and (b,d) precipitation rate, averaged over five different subdomains of the fixedSST_large simulations at 305 K (top row) and 330 K (bottom row). The subdomains (color-coded in panel e) each have an area of 256 km^2 and are located an average of 215 km apart from each other.

Extended Data Fig. 7 The steady-to-oscillatory transition in the convection-resolving model and the stochastic two-layer model.

(a) In the convection-resolving model, the radiative heating profile is switched from cool-climate-type to hothouse-type (LTRH_off to LTRH_on) on model day 0 (the transient_SO simulation). (b) In the two-layer model, the inhibition parameter is increased linearly in time between days 0 and 2 and held fixed thereafter.

Extended Data Fig. 8 Probability density functions (PDFs) of 6-hour local rain accumulations.

The precipitation data are from 20-day periods of (a) the fixedSST_large simulations, and (b) the transient_SO simulation in the steady and oscillatory regime. The PDFs are constructed by first dividing the model

domains into watershed-sized subdomains ($16 \times 16 \text{ km}^2$ for fixedSST_large, and $12 \times 12 \text{ km}^2$ for transient_SO). Precipitation is then accumulated in each subdomain for all 6-hour periods during the 20-day intervals, producing the 6-hour local rain accumulations from which the PDFs are constructed. The 99.9th percentile of each of the PDFs is indicated at the top of each plot.

Extended Data Fig. 9 The oscillatory transition occurs more readily for climates instigated by an M-star spectrum.

Comparison of tropospheric radiative heating rates (panels **a,b**) and timeseries of surface precipitation (panels **c,d**) in fixed-SST simulations with either the solar instellation spectrum or that of the M-star AD Leonis⁶². Panel (e) shows the spectral flux for these two stars (normalized to the same total flux), as well as the logarithm of the H₂O absorption coefficient at a reference temperature and pressure.

Extended Data Table 1 Summary of key aspects of the suite of DAM simulations conducted for this work

Supplementary information

Supplementary Video 1

The supplementary video is an animation of DAM model output from the fixed-SST simulation at 330 K (from our fixedSST_hires suite; Extended Data Table 1). Each frame in the video consists of six panels showing, from top to bottom and left to right: buoyancy in the near-surface layer, wind speed in the near-surface layer, outgoing solar radiation, temperature anomaly in the near-surface layer, specific humidity anomaly in the near-surface layer, and accumulated rainfall over the preceding 6 h. Anomalies are calculated with respect to the horizontal and time mean. The sampling interval between frames is 15 min, and the animation covers 7 days of model time. The video is also available at <https://youtu.be/NALhYFiaeos>.

Rights and permissions

[Reprints and Permissions](#)

About this article

Cite this article

Seeley, J.T., Wordsworth, R.D. Episodic deluges in simulated hothouse climates. *Nature* **599**, 74–79 (2021). <https://doi.org/10.1038/s41586-021-03919-z>

- Received: 21 April 2021
- Accepted: 16 August 2021
- Published: 03 November 2021
- Issue Date: 04 November 2021
- DOI: <https://doi.org/10.1038/s41586-021-03919-z>

Share this article

Anyone you share the following link with will be able to read this content:

[Get shareable link](#)

Sorry, a shareable link is not currently available for this article.

[Copy to clipboard](#)

Provided by the Springer Nature SharedIt content-sharing initiative

| [Section menu](#) | [Main menu](#) |

- Article
- [Published: 03 November 2021](#)

Carbon implications of marginal oils from market-derived demand shocks

- [Mohammad S. Masnadi](#) ORCID: orcid.org/0000-0002-3834-0241¹,
- [Giacomo Benini](#)²,
- [Hassan M. El-Houjeiri](#)³,
- [Alice Milivinti](#)⁴,
- [James E. Anderson](#) ORCID: orcid.org/0000-0003-0878-5271⁵,
- [Timothy J. Wallington](#) ORCID: orcid.org/0000-0002-9810-6326⁵,
- [Robert De Kleine](#)⁵,
- [Valerio Dotti](#)⁶,
- [Patrick Jochem](#) ORCID: orcid.org/0000-0002-7486-4958⁷ &
- [Adam R. Brandt](#) ORCID: orcid.org/0000-0002-2528-1473²

Nature volume **599**, pages 80–84 (2021)

- 1171 Accesses
- 14 Altmetric
- [Metrics details](#)

Subjects

- [Climate-change mitigation](#)
- [Environmental economics](#)
- [Environmental impact](#)

Abstract

Expanded use of novel oil extraction technologies has increased the variability of petroleum resources and diversified the carbon footprint of the global oil supply¹. Past life-cycle assessment (LCA) studies overlooked upstream emission heterogeneity by assuming that a decline in oil demand will displace average crude oil². We explore the

life-cycle greenhouse gas emissions impacts of marginal crude sources, identifying the upstream carbon intensity (CI) of the producers most sensitive to an oil demand decline (for example, due to a shift to alternative vehicles). We link econometric models of production profitability of 1,933 oilfields (~90% of the 2015 world supply) with their production CI. Then, we examine their response to a decline in demand under three oil market structures. According to our estimates, small demand shocks have different upstream CI implications than large shocks. Irrespective of the market structure, small shocks (~2.5% demand) displace mostly heavy crudes with ~25–54% higher CI than that of the global average. However, this imbalance diminishes as the shocks become bigger and if producers with market power coordinate their response to a demand decline. The carbon emissions benefits of reduction in oil demand are systematically dependent on the magnitude of demand drop and the global oil market structure.

[Download PDF](#)

Main

The energy sector is in a state of rapid change. Several countries announced a variety of ‘green’ policies to recover from the 2020 COVID-19 downturn. Many of these policies could have a long lasting effect on the oil and gas industry^{3,4}. The industry could enter into an era of declining demand, technology-led supply response, intense competition, investors’ scepticism, and increasing public and government pressure regarding impacts of the oil sector on the environment⁴.

Environmental impacts of oil are commonly measured using LCA methods. The life-cycle carbon footprint, or CI of oil-derived transportation fuels (for example, gasoline) includes the greenhouse gas (GHG) emissions resulting from the combustion of fuels themselves as well as emissions from production and refining of petroleum products. So-called upstream emissions from exploration, extraction and transportation of crude oil differ widely between oilfields (~20–300 kg of CO₂ equivalent per barrel (kgCO₂e bbl⁻¹) due to diverse sub-surface geological properties of the deposit, physical and thermodynamic properties of the hydrocarbons, and production and resource management practices¹. Similarly, ‘midstream’ emissions from refining vary widely (~10–60 kgCO₂e bbl⁻¹ oil) due to the quality of stream of processed crude and the refining technologies applied⁵. These emissions contribute to variability in the life-cycle CI of different crude oil supply chains.

The profitability of crude oil production somewhat mirrors the heterogeneity in GHG emissions. The cost-effectiveness of the upstream sector varies due to the properties of the crude extracted, the marginal production costs, the capacity of the producers to

affect the global oil price, and the global oil demand elasticity. Thus, some fields are very profitable, while others barely break even.

Recent studies have separately analysed the heterogeneity in the GHG emissions^{1,5} and the economics of the oil market (Benini, G. et al., manuscript in preparation). However, the interaction between the two remains poorly understood. As a result, the characteristics of marginally economic oilfields are not systematically available. This interaction is important because it affects the magnitude of emissions mitigation potential as less profitable oil producers are displaced when demand declines. The demand drops can be due to socio-economic effects (for example, recessions or the ongoing COVID-19 pandemic), substitution effects (for example, more extensive use of alternative fuels/vehicles), and technological change within the transportation sector (for example, greater fuel efficiency).

In the past decade, development of ‘consequential’ LCA aimed to incorporate numerous economic factors into previously static engineering-based analysis^{2,6,7,8}. These analyses attempt to model income and substitution effects of introducing alternatives, instead of simply assuming that a new product directly displaces an old product. To date, this consequential LCA paradigm has not reached crude oil LCA, and studies of alternatives to crude oil (for example, electric vehicles (EVs)) nearly always assume that an alternative simply displaces average crude oil. The merging of CI and profitability allow us to conduct the first consequential LCA study of the global oil supply (to the best of our knowledge).

The present work connects the upstream CI of 1,933 oilfields (~90% of 2015 global crude production) with their profitability. The CI of fields is calculated using a well-to-refinery estimation tool, which assesses the emissions due to the production of an additional barrel of crude from a particular oilfield. The profitability is calculated using a microeconomic model, which determines how much money a company is willing to pay to manage an additional barrel of crude located in a particular oilfield (see [Methods](#)). The integration of field-specific CI and profitability allows us to identify the emissions of fields close to the break-even point (extensive margin of the industry). In other words, we isolate the emissions of those fields where the management choice hangs in the balance between ‘how much should I produce?’ and ‘should I keep producing or cease business operations?’

Our results suggest that an environmental policy designed around non-market informed LCA results could ignore first-order effects. In addition, the structure of the global oil market systematically affects the life-cycle benefits from a decline in oil demand. These results could serve public (for example, the US Department of Energy National Energy Modeling System) and private energy system models to better assess the benefits of technological change within the transportation sector.

Results and discussion

Country-level

Figure 1 presents the global map of national volume-weighted average (VWA) marginal production costs (MC) in 2015. The numbers below the name of each country in the map are the corresponding upstream VWA CIs (in $\text{kgCO}_2\text{e bbl}^{-1}$). The global average MC estimate—shown by the horizontal dashed line in Fig. 1—is $\sim\text{US\$5.9 bbl}^{-1}$ crude oil, with country-level MCs ranging from 2.8 (Iraq (IRQ)) to $\text{US\$21.5 bbl}^{-1}$ (Columbia (COL)). Fields with the lowest production costs are mainly conventional resources located in the Middle East and North Africa. There is a wide range of production emissions associated with these regions, with routine flaring as the major driver of high CI due to lack of investment/infrastructure for gas handling (see Supplementary Information section 3.3).

Fig. 1: Estimated global crude oil upstream marginal cost of production (2015).



National volume weighted average (VWA) upstream marginal cost of production in $\text{US\$ bbl}^{-1}$ crude oil produced. Map shows national VWA upstream marginal CI below each country name (in $\text{kgCO}_2\text{e bbl}^{-1}$ crude oil delivered to refinery). The global VWA

MC estimate is shown by the horizontal dashed line (\sim US\$5.6 bbl $^{-1}$). Reference year is 2015. Top 30 global producers are mapped (see Supplementary Data 1 for full list). Countries are named based on their ISO 3 code. Colour scheme reflects national VWA MC: dark blue for lowest MC, dark red for highest MC.

Among large producers, Venezuelan, Mexican and Canadian oils are the most expensive and tend to have high production CIs. The US oil industry stands near the global average in terms of GHG emissions and has a high MC (\sim US\$7.3 bbl $^{-1}$).

Note that the dynamics of the emissions presented in Fig. 1 can vary over time^{9,10}. However, due to the fact that substantial change in production strategies takes time, the relative magnitude of the presented emissions can be expected to hold for a short-term outlook of <5–10 years. See Supplementary Information section 3.1 for production economics time-series dissection.

Crude type

Table 1 groups field-level results into summary statistics of a set of global crude classes. Heavy fields (most commonly located in Venezuela) and extra heavy fields (mostly located in Canada) are the least profitable fields with relatively high MC and low selling price (due to low API gravity). Oil sands have the lowest selling oil price due to low API gravity and high sulfur content. However, their MCs have substantially decreased in recent years^{11,12} making them more competitive vis-à-vis heavy and extra heavy crudes. Contrary to all the other types of crude, oil sands are all located in a single country (Canada). Therefore, they are particularly sensitive to national-specific shocks and transport logistics issues. Shale and tight oil resources are somewhat more competitive, with relatively higher profit margins in all three economic cases, lower emissions, and lighter density crude (higher selling price and lower refining emissions). Conventional light and medium fields are the largest and cheapest to extract crude oil with high selling price, low MC and relatively low CI.

Table 1 2015 global oilfields characteristics based on crude type

The average profitability (shadow price (SP)) of different crude types changes accordingly to the assumption on the market structure. In perfect competition (PC), every field is an independent firm, which exerts no market power. In oligopolistic competition (oligopoly), a limited number of firms owns many fields. In cartel competition (cartel), a limited number of firms coordinate their production decisions via a syndicate (for example, the Organization of the Petroleum Exporting Countries (OPEC)—see [Methods](#)). In PC, the oilfield SP is the difference between the price at which it sells its output and the MC. The conventional light and medium fields are the most profitable producing units (see SP-PC in Table 1). In oligopoly, the volume of

production of the firm, which owns the field, affects its SP. In cartel, the volume of production of OPEC affects the SP of the field's member of the union. As a result, in oligopoly and cartel cases, shutting down or reducing production from individually profitable oilfields is rational, since the firm/cartel will sell less output but at a higher price. As a result, in oligopoly and in cartel cases many light and medium fields owned by large international or national oil companies shift to a least profitable position.

Irrespective of the underlying market structure, heavy fields tend to remain the least profitable formation. Thus, these are the crudes most likely to be displaced by an oil demand reduction. Carbon taxation would also significantly affect their profitability due to their high production CI. Gas management (that is, routine flaring and methane venting and fugitives) is the major CI contributor for light and medium, and shale and tight oil crudes. The profitability of these fields is therefore exposed to gas management regulations (for example, production restriction as imposed in eastern Canada¹³).

Field-level

To estimate field-level CI (see [Methods](#)), we separate the GHG emissions due to the production of the next barrel from the emissions due to the exploration, and drilling and development. The former identifies the environmental footprint linked to the SP of discovered oil (that is, the one identified in the econometric analysis). The latter—exploration and development emissions—are smaller in most cases and are coupled to the SP of undiscovered oil (not included in this work). Next, the computed SPs of discovered oilfields are sorted from smallest to largest (that is, low to high profitability). As a result, we obtain a merit base curve, which links profitability to production CI for the three market structures (PC, oligopoly and cartel—see [Methods](#)).

Figure 2 combines the upstream cumulative VWA CIs (right axis) and the sorted SPs (left axis), against the percentage of total oil production covered in this work.

Analogous to the upstream CI¹, the presented wide range of SPs illustrates heterogeneity of production costs due to diverse operational, physical, chemical, and geological properties of different oilfields. Fields in the highest fifth percentile (\sim US\$53 bbl $^{-1}$) make over 17% more marginal profit per barrel than the median field (\sim US\$46 bbl $^{-1}$) for all economic cases.

Fig. 2: Upstream cumulative volume-weighted average CIs (right axis) and sorted SPs (left axis) of global oilfields for PC, oligopoly and cartel economic cases versus the percentage of total oil production in 2015.



The oil demand elasticity of $\eta = -0.35$ is used for both oligopoly and cartel competition cases. See Supplementary Information section [3.2](#) (Supplementary Figs. [10](#) and [11](#)) for results variation based on different oil demand elasticities and further discussions.

Each local peak along the CI curve in Fig. [2](#) indicates an addition of a field with relatively high CI and production rate compared to the preceding covered fields. For example, the early sharp peaks by using the cartel model (black curve in Fig. [2](#)) correspond to Venezuelan heavy fields. Large peaks in cumulative CIs at the beginning (0–20% of total production) imply that many less-economic fields with relatively low SPs also emit high GHG emissions (few exceptions are unprofitable depleted conventional fields with low SP and low emissions). These marginal oilfields are consequently more vulnerable to any future carbon taxation/regulation regime and more likely to be displaced by a demand shift.

In all economic cases, the cumulative CI curve trends downward due to covering fewer emitting fields. This trend continues for the PC case until reaching $51.9 \text{ kgCO}_2\text{e bbl}^{-1}$ (at 100% production coverage), which is the global VWA marginal CI (see Table [1](#)). However, for the other two cases (that is, oligopoly and cartel), including the global oil demand elasticity and market power correction in computing the SP results in less profitability of several low-emitting conventional producers. Thus, for oligopoly and cartel models after few high peaks, the cumulative CI curve first trends descending (conventional with low CI) and later trends ascending (remaining fields with higher CI than conventional closer to margin). See Supplementary Information section [3.3](#) and Supplementary Data 1 for field-level additional data.

Displacement implications

Many reports estimate near and long-term volume of oil that is going to be displaced and/or stranded by technological developments and/or policy measures^{14,15,16,17,18}. These estimates depend on numerous scenario assumptions (for example, growth rate of EVs, global income growth and the way these factors interact) and their conclusions differ markedly.

Instead of selecting any one scenario, we create abstract round number shocks to identify the environmental effect resulting from the displacement of the extensive margin of the oil industry. Such shocks might stem from policies to counter climate change, economic slowdowns, geopolitical conflict, or (as the case in 2020) global diseases like COVID-19. We first consider an oil demand reduction of 2.5% relative to the baseline (~1.8 million barrels per day (MMbbl d⁻¹)), which we call small shock scenario. Then, we consider a reduction of ~5% (~3.6 MMbbl d⁻¹), which we call COVID-19 pandemic scenario due to its resemblance with the contraction in oil demand observed during the 2020 pandemic^{19,20}. Finally, we consider a reduction of ~10% (~7.1 MMbbl d⁻¹), which we call medium shock. The latter could result from a vigorous adoption of alternatives or major macroeconomic downturns like a global financial recession. Note that in medium and large demand reduction scenarios (that is, roughly >5–10%), only the PC-SP is informative. In the other two cases (that is, oligopoly and cartel), the estimated SP is likely to become uninformative, since the market power correction term would change due to a transformation of the market structure (for example, countries leave/join OPEC, different propensity of countries to respect OPEC quotas, or different outcomes of the game-in-quantities played among oligopolists).

Table 2 characterizes the small, COVID-19, and medium shock scenarios using the different market structures. In PC, the marginal fields are mostly small producers, with median production of ~8,000–10,000 bbl d⁻¹. The oligopoly and cartel cases shift few large conventional producers close to the industry margins (Table 2, and bar widths in Supplementary Figs. 12–14). The shift occurs for the same reasons explained above. Namely, oligopolists and members of the cartel adjust production from profitable fields to maximize their total profit.

Table 2 Characteristics of small and COVID-19 shock scenarios for crude oil demand reduction using different economic models

In all three economic models, the VWA MC of the marginal fields is much higher (25–375%) than the global average MC of ~US\$5.6 bbl⁻¹. Shifting low carbon intensive light and medium conventional fields towards the margin lowers the average CI of the displaced oil, but several heavy fields stay at the margin. We conclude that oil demand shocks result in nonlinear carbon emissions reduction. In all three economic cases, the CI of the crudes displaced by the small shock is ~25–54% larger than the global

average of $51.9 \text{ kgCO}_2\text{e bbl}^{-1}$. The CI of the displaced crudes by COVID-19 shock is ~35% larger than the global average for PC, but is close to the global average CI using oligopolistic and cartel competition. The PC model still provides accurate estimates for 10% reduction shock where the CI of the displaced crudes is ~37% larger than the global average. However, the oligopoly and cartel models might not capture the market behaviour for such a large shock. The average CIs for these two economic cases due to 10% demand reduction are lower than global average with large volume share of light and medium crudes being displaced due to market power considerations.

The demand reduction magnitude affects the average CI of displaced crudes. Heavy oilfields with high CI (mostly located in Venezuela) have consistent contribution in all demand reduction scenarios and across all economic models. The total share of unconventional crudes (by volume) generally decreases by including market power corrections in the economic model, as it becomes more viable for large national oil companies to exert market power by reducing production from productive conventional fields. Our results show that given the proposed three economic cases, the small, COVID-19 and 10% reduction shocks in the global oil demand would result in the elimination of 39–54, 61–92 and 109–184 MtCO₂e per year of upstream emissions, respectively. Supplementary Figure 15 shows a full range of annual carbon mitigation potential versus the amount of oil displaced using the three economic models. Larger reductions of GHG emissions associated with refining of oil and the final combustion of corresponding products would also occur, but are not included in these calculations. See Supplementary Information section 4.2 and Supplementary Table 8 for well-to-wheel mitigation potential estimate ranges and further discussions on demand sector GHG emissions.

In this work, we only included the production economics and identified the extensive margin of the oil industry. However, various other dynamic forces such as production agreements, region-specific fiscal regimes, regulations (for example, fuel standard policies), geopolitics (for example, sanctions, trade wars), technical advances and incidental events could move a particular oilfield toward or away from the margin. Further analysis of these factors is beyond the scope of this work, but could be pursued in future research (see Supplementary Information section 5).

Methods

Research scope

This work covers upstream emissions (including production and transport of crude oil to refinery gate) and costs. Due to lack of access to refinery cost data, we cannot generate a fully market-informed (consequential) well-to-wheel emissions analysis

that goes all the way to refined fuels. Nevertheless, we provide a discussion on how upstream displacement could affect the emissions of the demand side (see Supplementary Information section [4.2](#)).

Carbon intensity model

The field-level CI is estimated using the Oil Production Greenhouse Gas Emissions Estimator (OPGEE version 2.0)[21,22,23](#). OPGEE is an open-source, peer-reviewed[9,10,21,24,25,26,27,28,29,30,31](#), bottom-up, engineering-based model. The OPGEE system boundary is ‘well-to-refinery’ (WTR, that is, exploration, drilling and development, production and extraction, surface processing, maintenance, waste disposal, and crude transport to the refinery). Reported emissions are measured in gCO₂e emitted per 1 MJ lower heating value (LHV) of crude petroleum delivered to the refinery entrance gate. All GHGs are converted to gCO₂e using AR5 GWP100 conversion factors (without carbon feedback)[32](#). See the OPGEE user guide[21](#) for more details of each process stage.

OPGEE estimates CI using up to 50 parameters as input data for each modelled oilfield. If input data are not available for some parameters (common), OPGEE supplies defaults based on statistical analysis of petroleum engineering literature and commercial data sources (for example *Oil & Gas Journal* (O&GJ)[33](#)) enabling the software to estimate a field’s CI without complete data[21,33](#).

In this work, field exploration, and drilling and development emissions are excluded from CIs reported in prior work¹ to estimate GHG emissions associated with production of the next barrel of crude oil (that is, marginal upstream CIs). These two sectors hold a very low share of the total upstream GHG emissions (see supplementary Fig. S[20](#) of ref. ¹).

Global oilfields

In the previous work¹, CIs were estimated for 8,966 global active oilfields (so-called child fields) supplying 78.9 million barrels per day (MMbbl d⁻¹), and capturing ~98% of 2015 global crude oil and condensate production³⁴. A combination of government reported data (Norway[35,36](#), Canada[37,38,39,40](#), Denmark[41](#), UK[42](#), Nigeria[43](#), and US California[44](#), US Alaska[45](#) and US shale oils[46](#)), public literature (total of nearly 800 sources) and proprietary/commercial data sources (O&GJ 2015 survey[33](#) and Wood Mackenzie (WM) oilfield datasets⁴⁷) were used as input data¹. Government and public literature data were collected and used for 1,009 global fields, accounting for about 64.3% of global crude oil production. Commercial data are utilized for the remainder

(mostly small fields). We select 2015 as the reference year due to lags in some data sources. See our previous study supplementary materials document¹ for further details.

Economic model

We frame our economic model as a profit-maximization problem. We study three different cases described here heuristically with mathematical details presented in the [Supplementary Information](#). In the perfect competition (PC) case, every field is an independent firm which exerts no market power. In this context, the field management solves the profit-maximization problem taking the oil price as given. In the oligopolistic competition (oligopoly) case, a limited number of firms owns many fields. In this context, the field management solves the profit-maximization problem knowing that the quantity of oil produced by the firm who owns the field as well as its competitors influences the oil price. In the cartel competition (cartel) case, a limited number of firms coordinate their production decisions via a syndicate. In this context, the field management solves the profit-maximization problem knowing that the quantity of oil produced by the members of the syndicate influences the oil price. Said differently, in the oligopoly case a small number of oligopolistic competitors play a game-in-quantities. In the cartel case, a few firms work together to coordinate their production decisions around a union. In our model, the members of the cartel are the national oil companies associated with OPEC. Due to the complexities in modelling the realities of cartel dynamics, our cartel case assumes that the cartel operates in unison. The effect of a cartel with imperfect coordination would fall somewhere between individual company market power (oligopoly case) and the perfect cartel (cartel case).

In the PC case, field profits are the difference between field revenues and field costs, which we divide into two macro-classes: (1) costs to extract the oil (extraction costs) and (2) costs to discover new oil (exploration costs),

$$\text{Profits} = (\text{oil price} \times \text{volumes of oil extracted}) - (\text{extraction costs} + \text{exploration costs}).$$

In the oligopoly and cartel cases, the field profits are the same. However, in the oligopoly case the management takes into consideration the effect of the volumes of oil produced by the firm who owns the field on the oil price, while in the cartel case the management takes into consideration the effect of the volumes of oil produced by the cartel on the oil price.

In all three cases, the decision choices are: what volume of oil to extract and how much money to spend in exploration^{48,49}. While making these decisions the management faces two physical constraints. First, the quantity of reserves available at

time t equals the reserves at time $t - 1$ minus the volumes of oil extracted at time t plus the quantity of oil discovered at time t . Second, the cumulative discoveries at time t equals the cumulative discoveries until time $t - 1$ plus the discoveries at time t .

The first-order condition of the optimization problem with respect to the volumes of oil extracted identifies how much money a producer is willing to spend to manage one extra barrel of oil. This value is called shadow price (of discovered oil),

$$\text{Shadow price} = \text{oil price} - \text{marginal extraction cost} + \text{market power correction term}.$$

The shadow price (SP) equals the difference between the oil price and the marginal extraction cost (MC)⁵⁰ (that is, the cost of extracting the next barrel; this quantity is obtained by taking the first-order derivative of the extraction costs with respect to volumes of oil extracted) readjusted by a market power correction term.

If every field is an independent firm with no capacity to influence price (that is, PC), the market power correction term shrinks to zero and the SP becomes the difference between the oil price and the MC. For example, if a field sells its output at US\$50 bbl⁻¹ and its MC is US\$40 bbl⁻¹, the owner of the field is willing to spend (up to) US\$10 to manage one more barrel located in that particular deposit. In the case of oligopolistic competition/perfect collusion behaviour, the SP takes into account the capacity of the firm/cartel to influence the global (average) oil price rescaled by the propensity of consumers to decrease the quantity of oil consumed due to an increase in oil price. Section 1 of the [Supplementary Information](#) provides the mathematical details of the economic framework linking the concept of SP to standard oil economics.

As the SP of a field approaches zero, the management problem shifts from ‘how much should I produce?’ (intensive margin choice) to ‘should I produce or not?’ (extensive margin choice). In other words, the fields with a SP close to zero identify the extensive margin of the oil industry. The emissions of this portion of the industry are the most sensitive to a drop in oil price caused by a reduction in the transportation fuel demand.

Note that estimating field-level gross profit was the main aim of this work, not the net profit. The gross profit is a better representative of fields’ geological and physical characteristics and production practices, whereas the net profit includes additional fiscal regimes (that is, royalties, severance taxes, income taxes, production sharing and so on), which are complex, country/region-specific and subject to change. Incorporating these fiscal terms is out of the capacity and the scope of the presented work.

Econometric analysis

All three variables making up SP are unobserved. To estimate them, we face three econometric problems: (1) the non-stationary nature of oil prices, (2) the endogenous link between costs, quantities and reserves, and (3) the uncertainty about the magnitude of the oil demand elasticity.

We do not know the price at which a field sells its output because we do not have access to commercial agreements between oil producers and oil refiners. However, we know the prices of publicly traded oil classes. More precisely, we know the landed costs of imported crudes in the United States from 1979 to 2018⁵¹, as well as some key physical and chemical characteristics of every traded class⁵² (see Supplementary Fig. 1 and Supplementary Table 1). In the same way, we know the average price at which US refineries buy imported crudes⁵³ and the average physical and chemical characteristics of crudes imported in the United States⁵⁴. The physical and chemical characteristics most important to refineries are the crude density (measured as API gravity) and the sulfur content (measured as wt% sulfur).

We regress the difference between the price of a particular oil class and the average price at which refineries buy imported crudes on the differences between the API gravity of the oil class and the average API gravity of imported crudes as well as on the difference between the sulfur content of the oil class and the average sulfur content of imported crudes^{55,56,57}. In doing so, we solve the non-stationarity problem while assuming that the difference between the price of a particular oil class and the average one is a linear function of the oil's characteristics. We allow these linear deviations to be time-specific to adjust for changing in demand of transportation fuels as well as for technological change within the refinery sector. For example, in 2015 the average oil price was US\$50.39 bbl⁻¹, its API gravity 31.46, and its sulfur content 1.40%. In 2015 increasing the API gravity by one degree increased the value of a crude stream by US\$0.13 bbl⁻¹, while increasing sulfur content by 1% lowered the value of a crude stream by US\$2.86 bbl⁻¹. In 2016, these two quantities were +US\$0.03 bbl⁻¹ and -US\$0.85 bbl⁻¹. This change could be due to (1) a modification in the composition of the demand for transportation fuels (for example, more demand for gasoline, less demand for diesel), (2) a change in the technologies employed by US refineries, and (3) a combination of (1) and (2). Our econometric model is flexible enough to take into account all three possibilities (see Supplementary Information section 2.1).

We can use the two structural coefficients, which weight the impact of API gravity and sulfur content, to estimate field-level selling prices (see Supplementary Information section 2.1, equation 8). Using the API gravity and sulfur content reported in the 2018 WM dataset⁴⁷, we estimate the selling price of 1,933 ‘parent project’ fields over the decade 2009–2018, thereby obtaining $1,933 \times 10 = 19,330$ simulated selling prices (see Supplementary Information section 2.1 for a detailed discussion on the results). See Supplementary Figs. 2 and 3 for a cross-sectional snapshot.

Next, we estimate the MC. An accurate measurement of MC is complicated because it is difficult to determine which factors of production are fixed and which are variable. However, the use of detailed accounting data, combined with standard econometric techniques, allows us to have a good first-order approximation of the MC of different types of fields. We use the WM dataset to obtain yearly cost data for the same 1,933 fields over the time interval 2009–2018. Then, we obtain the extraction costs summing the operational expenditures (OPEX), which include consumable inputs, labour, maintenance, repairs, accounting costs, license fees, office expenses, utilities and insurance. We also include capital expenditures not linked to exploration activities (non-exploration CAPEX, which include installation, acquisition, upgrading and restoring of the physical assets used to extract the oil).

After computing the extraction costs, we regress them against the volumes of oil extracted while controlling for the depletion level of the field, the geological characteristics of the field, and technological trends in the broader oil industry⁵⁸. We estimate the structural coefficients of the cost function re-expressing the regression in first differences. The combination of the longitudinal structure of the dataset with the first-difference estimation method allows us to attenuate (or in the best case scenario to solve) eventual endogeneity problems⁵⁹. The first-order derivative of the fit returns the estimated MC. Section 2.3 of [Supplementary Information](#) provides all the econometric details.

Finally, for two of the three cases analysed, we compute the market power correction term. Its expression is the same in both cases. Namely, the capacity of the firm/cartel to influence the average oil price rescaled by the capacity of consumers to lower their demand for oil-derived products when their prices increase. Said differently, the market power correction term adjusts the SP of every field by capturing the effect of a unit increase in the production of a specific field on the equilibrium oil price and, in turn, on the firm's profits. Higher market power—corresponding to larger firm size—implies, *ceteris paribus*, a lower shadow price, because the effect of a fall in price due to the production of an extra unit of crude on the firm total revenues is proportional to the total production. For instance, if the production of an extra barrel causes the oil price to fall by 0.01 cents, then the firm must trade-off the profits generated by selling that extra barrel and a loss of 0.01 cents per barrel times the total number of barrels produced by the firm. Thus, accounting for market power makes the marginal unit produced by each firm/cartel less valuable, resulting in lower SPs. This effect is increasing in the firm/cartel size. Since the magnitude of the oil demand elasticity is object of econometric debate⁶⁰, we validate our results using different point estimates within the interval –0.20 up to –0.35.

Data matching and coverage

The previous work on the CI of global oilfields¹ is provided at a child field level. Child fields are individual discoveries that are part of a parent project. Parent fields are combinations of geologic deposits collected for the purposes of a combined valuation. The linkage with the economic data, available only at parent level, requires us to match the child field CIs¹ to parent fields. The majority of the child non-technical oilfields from WM datasets⁴⁷ (accessed 2018)—whose corresponding parent fields are available—directly matched with the OPGEE global dataset. We paired the remaining with smart string search and string distance matching using *R* as well as manual matching for the countries with poor total production coverage. Finally, we conduct an additional treatment on two important global producers (Canada and United States) based on the available data (see Supplementary Information section [2.2](#)).

After the matching process is completed, we examine the representativeness of our techno-economic dataset. In total, we matched 1,933 parent fields located in 77 countries. Their combined production is \sim 71 MMBbl d⁻¹ and it captures \sim 90% of the 2015 global crude oil and condensate production³⁴. Supplementary Table [5](#) returns the coverage summary of the top 20 largest global producers, and Supplementary Fig. [4](#) zooms in on the geographic location and the CI of the mapped fields.

Data availability

The field-level environmental and economic dataset generated during the current study are provided as a separate Excel file at <https://doi.org/10.6084/m9.figshare.15029565>. The carbon intensity data are taken from <https://doi.org/10.1126/science.aar6859>. The core economic datasets used during the current study (that is, the Wood Mackenzie dataset) are not publicly available due to them being proprietary/commercial datasets.

Code availability

The custom software or code is not central to the paper or required to support the main results being reported in the manuscript. Thus, all custom codes are available upon request.

References

1. 1.

Masnadi, M. S. et al. Global carbon intensity of crude oil production. *Science* **361**, 851–853 (2018).

2. 2.

Wallington, T. J. et al. When comparing alternative fuel-vehicle systems, life cycle assessment studies should consider trends in oil production. *J. Ind. Ecol.* **21**, 244–248 (2017).

3. 3.

Mintz-Woo, K., Dennig, F., Liu, H. & Schinko, T. Carbon pricing and COVID-19. *Clim. Policy* <https://doi.org/10.1080/14693062.2020.1831432> (2020).

4. 4.

Barbosa, F., Bresciani, G., Graham, P., Nyquist, S. & Yanosek, K. *Oil and Gas After COVID-19: The Day of Reckoning or a New Age of Opportunity* (McKinsey Company, 2020).

5. 5.

Jing, L. et al. Carbon intensity of global crude oil refining and mitigation potential. *Nat. Clim. Change* **10**, 526–532 (2020).

6. 6.

Earles, J. M. & Halog, A. Consequential life cycle assessment: a review. *Int. J. Life Cycle Assess.* **16**, 445–453 (2011).

7. 7.

Plevin, R. J., Delucchi, M. A. & Creutzig, F. Using attributional life cycle assessment to estimate climate-change mitigation benefits misleads policy makers. *J. Ind. Ecol.* **18**, 73–83 (2014).

8. 8.

Yang, Y. & Heijungs, R. On the use of different models for consequential life cycle assessment. *Int. J. Life Cycle Assess.* **23**, 751–758 (2018).

9. 9.

Masnadi, M. S. & Brandt, A. R. Climate impacts of oil extraction increase significantly with oilfield age. *Nat. Clim. Change* **7**, 551–556 (2017).

10. 10.

Masnadi, M. S. & Brandt, A. R. Energetic productivity dynamics of global super-giant oilfields. *Energy Environ. Sci.* **10**, 1493–1504 (2017).

11. 11.

Costs of Canadian oil sands projects fell dramatically in recent years; but pipeline constraints and other factors will moderate. *Bloomberg* <https://www.bloomberg.com/press-releases/2019-05- 01/costs-of-canadian-oil-sands-projects-fell-dramatically-in-recent-years- but-pipeline-constraints- and-other-factors-will-moderate> (1 May 2019).

12. 12.

Canadian oil sands dialogue. *HIS Markit* <https://ihsmarkit.com/products/energy-industry-oil-sands-dialogue.html?ocid=cera- osd:energy:print:0001> (accessed: 30 June 2020).

13. 13.

Newfoundland and Labrador Offshore Area Gas Flaring Reduction Implementation Plan (The Canada-Newfoundland and Labrador Offshore Petroleum Board, 2017); <https://www.cnlopb.ca/legislation/regulations/>

14. 14.

Eberhart, D. The oil sector will survive the arrival of the electric car just fine. *Forbes* <https://www.forbes.com/sites/daneberhart/2018/03/22/the- oil-sector-will-survive-the-arrival-of-the- electric-car-just-fine/#273b75267155> (22 May 2018).

15. 15.

Kah, M. *Electric Vehicle Penetration and Its Impact On Global Oil Demand: A Survey of 2019 Forecast Trends* (Columbia University Center Global Energy Policy, 2019).

16. 16.

Sharma, G. Are electric vehicles really about to plateau oil demand? *Forbes* <https://www.forbes.com/sites/gauravsharma/2019/11/25/are- electric-vehicles-really-about-to-plateau-oil-demand/#7f0853083b13> (25 November 2019).

17. 17.

Electric Vehicle Outlook 2020 (BloombergNEF, 2020);
<https://about.bnef.com/electric-vehicle-outlook/>

18. 18.

Global EV Outlook 2019 (IEA, 2019); <https://www.iea.org/reports/global-ev-outlook-2019#executive-summary>.

19. 19.

Short-Term Energy Outlook (EIA, 2020);
https://www.eia.gov/outlooks/steo/report/global_oil.php

20. 20.

Global Energy Review 2020 (IEA, 2020); <https://www.iea.org/reports/global-energy-review-2020/>

21. 21.

El-Houjeiri, H. M., Masnadi, M. S., Vafi, K., Duffy, J. & Brandt, A. R. *Oil Production Greenhouse Gas Emissions Estimator OPGEE v2.0a: User Guide & Technical Documentation* (California Environmental Protection Agency, 2017).

22. 22.

LCFS Crude Oil Lifecycle Assessment (California Air Resources Board, 2017);
<https://www.arb.ca.gov/fuels/lcfs/crude-oil/crude-oil.htm>

23. 23.

OPGEE: The Oil Production Greenhouse gas Emissions Estimator (Environmental Assessment & Optimization Group, 2017);
<https://eao.stanford.edu/research-areas/opgee>

24. 24.

Vafi, K. & Brandt, A. GHGfrack: an open-source model for estimating greenhouse gas emissions from combustion of fuel during drilling and hydraulic fracturing. *Environ. Sci. Technol.* **50**, 7913–7920 (2016).

25. 25.

El-Houjeiri, H. M., Brandt, A. R. & Duffy, J. E. Open-source LCA tool for estimating greenhouse gas emissions from crude oil production using field characteristics. *Environ. Sci.* **47**, 5998–6006 (2013).

26. 26.

Masnadi, M. S. et al. Well-to-refinery emissions and net-energy analysis of China's crude oil supply. *Nat. Energy* **3**, 220–226 (2018).

27. 27.

Brandt, A. R., Masnadi, M. S., Englander, J. G., Koomey, J. & Gordon, D. Climate-wise choices in a world of oil abundance. *Environ. Res. Lett.* **13**, 044027 (2018).

28. 28.

Brandt, A. R., Sun, Y., Bharadwaj, S., Livingston, D. & Tan, E. Energy return on investment (EROI) for forty global oilfields using a detailed engineering-based model of oil production. *PLoS ONE* **10**, e0144141 (2015).

29. 29.

Brandt, A. R., Englander, J. & Bharadwaj, S. The energy efficiency of oil sands extraction: energy return ratios from 1970 to 2010. *Energy* **55**, 693–702 (2013).

30. 30.

Brandt, A. R., Sun, Y. & Vafi, K. Uncertainty in regional-average petroleum GHG intensities: countering information gaps with targeted data gathering. *Environ. Sci. Technol.* **49**, 679–686 (2014).

31. 31.

Tripathi, V. & Brandt, A. Estimating decades-long trends in petroleum field energy return on investment (EROI) with an engineering-based model. *PLoS ONE* **12**, e0171083 (2017).

32. 32.

Myhre, G. et al. Anthropogenic and natural radiative forcing. In *Climate Change 2013: The Physical Science Basis. Contribution of Working Group I to the Fifth Assessment Report of the Intergovernmental Panel on Climate Change* (eds. Stocker, T. F. et al.) (Cambridge Univ. Press, 2013).

33. 33.

Worldwide Oil Field Production Survey 2015 (PenWell, 2015).

34. 34.

Total Petroleum and Other Liquids Production - 2016 (EIA, 2017);
<https://go.nature.com/3jfink3>

35. 35.

Norway Petroleum Directorate (NPD, 2017);
<https://factpages.npd.no/en/field/PageView>

36. 36.

Feltpesifikke Utslippsrapporter 2015 (Norsk Olje & Gass, 2015);
<https://www.norskoljeoggass.no/page-not-found/migrering/feltpesifikke-utslippsrapporter-2015/>

37. 37.

Statistical Reports (ST) (Alberta Energy Regulator, 2015);
<https://portal.aer.ca/providing-information/data-and-reports/statistical-reports.html>

38. 38.

Statistical information (C-NLOPB, 2021);
<https://www.cnlopbc.ca/information/statistics/#rm>

39. 39.

Estimated Production of Canadian Crude Oil and Equivalent (National Energy Board, 2017); <https://www.cer-rec.gc.ca/en/data-analysis/energy-commodities/crude-oil-petroleum-products/statistics/estimated-production-canadian-crude-oil-equivalent.html>

40. 40.

BASIN database. *Natural Resources Canada*
http://basin.gdr.nrcan.gc.ca/index_e.php (accessed: 15 November 2017).

41. 41.

2015 Production (Danish Energy Agency, 2016); <https://ens.dk/en/our-responsibilities/oil-gas>

42. 42.

Oil and Gas: Field Data (UK Government, 2017);
<https://www.gov.uk/guidance/oil-and-gas-uk-field-data>

43. 43.

Annual Statistical: 2015 Statistical Bulletin (Nigerian National Petroleum Corporation, 2015); <https://nnpcgroup.com/Public-Relations/Oil-and-Gas-Statistics/Pages/Annual-Statistics-Bulletin.aspx>

44. 44.

2015 Report of California Oil and Gas Production Statistics (State of California Department of Conservation, the Division of Oil, Gas, & Geothermal Resources, 2015); ftp://ftp.consrv.ca.gov/pub/oil/annual_reports/2015/PR03_2015.pdf

45. 45.

Alaska Oil and Gas Conservation Commission (Alaska Department of Administration, 2017); <https://www.commerce.alaska.gov/web/aogcc/Data.aspx>

46. 46.

Drilling Productivity Report (EIA, 2021);
<https://www.eia.gov/petroleum/drilling/>

47. 47.

Upstream data tool. *Wood Mackenzie*
<https://www.woodmac.com/research/products/upstream/upstream-data-tool/>
(2018)

48. 48.

Devarajan, S. & Fisher, A. C. Exploration and scarcity. *J. Polit. Econ.* **90**, 1279–1290 (1982).

49. 49.

Pindyck, R. S. The optimal exploration and production of nonrenewable resources. *J. Polit. Econ.* **86**, 841–861 (1978).

50. 50.

Pesaran, M. H. An econometric analysis of exploration and extraction of oil in the UK Continental Shelf. *Econ. J.* **100**, 367–390 (1990).

51. 51.

Landed Costs of Imported Crude for Selected Crude Streams (EIA, 2020);
https://www.eia.gov/dnav/pet/pet_move_land2_k_a.htm

52. 52.

The Crude Oils And Their Key Characteristics (PSA, 2020); <https://www.psa-bv.nl/files/CrudeOils.pdf>

53. 53.

Total Energy Data (EIA, 2021);
<https://www.eia.gov/totalenergy/data/browser/csv.php?tbl=T09.01>

54. 54.

Crude Oil Input Qualities (EIA, 2021);
https://www.eia.gov/dnav/pet/pet_pnp_crq_dcu_nus_a.htm

55. 55.

Kilian, L. & Murphy, D. P. Why agnostic sign restrictions are not enough: understanding the dynamics of oil market VAR models. *J. Eur. Econ. Assoc.* **10**, 1166–1188 (2012).

56. 56.

Fattouh, B. The dynamics of crude oil price differentials. *Energy Econ.* **32**, 334–342 (2010).

57. 57.

Bacon, R. & Tordo, S. *Crude Oil Price Differentials and Differences in Oil Qualities: A Statistical Analysis* Technical Paper No. 81 (ESMAP, 2005);
<https://openknowledge.worldbank.org/handle/10986/18006>

58. 58.

Henningsen, A. *Introduction to Econometric Production Analysis with R* (Leanpub, 2014).

59. 59.

Kawaguchi, K. ECON5630 Topics in empirical industrial organization. *GitHub* <https://kohei-kawaguchi.github.io/EmpiricalIO/> (last accessed 31 January 2021).

60. 60.

Kilian, L. Understanding the estimation of oil demand and oil supply elasticities (2020).

61. 61.

Sleep, S. et al. Improving robustness of LCA results through stakeholder engagement: a case study of emerging oil sands technologies. *J. Clean. Prod.* **281**, 125277 (2021).

Acknowledgements

The authors want to thank J.-C. Monfort from Aramco Americas for help creating the global map display.

Author information

Affiliations

1. Department of Chemical and Petroleum Engineering, University of Pittsburgh, Pittsburgh, PA, USA

Mohammad S. Masnadi

2. Department of Energy Resources Engineering, Stanford University, Stanford, CA, USA

Giacomo Benini & Adam R. Brandt

3. Technology Outlook, Technology Strategy and Planning Department, Saudi Aramco, Dhahran, Saudi Arabia

Hassan M. El-Houjeiri

4. Center for Population Health Sciences, School of Medicine, Stanford University, Stanford, CA, USA

Alice Milivinti

5. Research and Advanced Engineering, Ford Motor Company, Dearborn, MI, USA

James E. Anderson, Timothy J. Wallington & Robert De Kleine

6. Department of Economics, Ca' Foscari University of Venice, Venice, Italy

Valerio Dotti

7. Institute of Networked Energy Systems, German Aerospace Center (DLR), Cologne, Germany

Patrick Jochem

Contributions

M.S.M., G.B. and A.R.B. developed the carbon model and linked the economic and environmental data. G.B., A.M., V.D., H.M.E., M.S.M. and P.J. developed the economic model. M.S.M., G.B., A.R.B., J.E.A., T.J.W., R.D.K. and H.M.E. contributed on the broader implications of the study. M.S.M., G.B., A.M. and H.M.E. contributed to improve the manuscript displays. M.S.M. organized and processed the material and wrote the paper.

Corresponding authors

Correspondence to Mohammad S. Masnadi or Adam R. Brandt.

Ethics declarations

Competing interests

Work at Stanford University on this project was primarily funded by Ford Motor Company through a gift to Stanford University. Other funding at Stanford University was provided by Aramco Americas. Some co-authors are employed by industry. Every effort was made to maintain independence and accuracy in this work. Industry

collaborations were vital to obtaining and accurately analysing the detailed oilfield financial data used in this study.

Additional information

Peer review information *Nature* thanks Kausik Chaudhuri, Sujit Das and the other, anonymous, reviewer(s) for their contribution to the peer review of this work. Peer reviewer reports are available.

Publisher's note Springer Nature remains neutral with regard to jurisdictional claims in published maps and institutional affiliations.

Supplementary information

Supplementary Information

This Supplementary Information file contains the following five sections: (1) theoretical economic model; (2) empirical economic model; (3) shadow prices; (4) life cycle analysis; (5) limitations and future research.

Peer Review File

Supplementary Data 1

Rights and permissions

Reprints and Permissions

About this article

Cite this article

Masnadi, M.S., Benini, G., El-Houjeiri, H.M. *et al.* Carbon implications of marginal oils from market-derived demand shocks. *Nature* **599**, 80–84 (2021).

<https://doi.org/10.1038/s41586-021-03932-2>

- Received: 21 November 2020
- Accepted: 18 August 2021

- Published: 03 November 2021
- Issue Date: 04 November 2021
- DOI: <https://doi.org/10.1038/s41586-021-03932-2>

Share this article

Anyone you share the following link with will be able to read this content:

[Get shareable link](#)

Sorry, a shareable link is not currently available for this article.

[Copy to clipboard](#)

Provided by the Springer Nature SharedIt content-sharing initiative

This article was downloaded by **calibre** from <https://www.nature.com/articles/s41586-021-03932-2>

| [Section menu](#) | [Main menu](#) |

- Article
- [Published: 03 November 2021](#)

Baleen whale prey consumption based on high-resolution foraging measurements

- [Matthew S. Savoca](#) [ORCID: orcid.org/0000-0002-7318-4977¹](#),
- [Max F. Czapanskiy¹](#),
- [Shirel R. Kahane-Rapport¹](#),
- [William T. Gough](#) [ORCID: orcid.org/0000-0003-2701-5299¹](#),
- [James A. Fahlbusch](#) [ORCID: orcid.org/0000-0001-9275-013X^{1,2}](#),
- [K. C. Bierlich^{3,4}](#),
- [Paolo S. Segre](#) [ORCID: orcid.org/0000-0002-2396-2670¹](#),
- [Jacopo Di Clemente^{5,6,7}](#),
- [Gwenith S. Penry](#) [ORCID: orcid.org/0000-0003-0545-7723⁸](#),
- [David N. Wiley⁹](#),
- [John Calambokidis](#) [ORCID: orcid.org/0000-0002-5028-7172²](#),
- [Douglas P. Nowacek](#) [ORCID: orcid.org/0000-0002-8137-1836³](#),
- [David W. Johnston](#) [ORCID: orcid.org/0000-0003-2424-036X³](#),
- [Nicholas D. Pyenson](#) [ORCID: orcid.org/0000-0003-4678-5782^{10,11}](#),
- [Ari S. Friedlaender¹²](#),
- [Elliott L. Hazen](#) [ORCID: orcid.org/0000-0002-0412-7178^{1,12,13}](#) &
- [Jeremy A. Goldbogen](#) [ORCID: orcid.org/0000-0002-4170-7294¹](#)

[Nature](#) volume 599, pages 85–90 (2021)

- 3223 Accesses
- 405 Altmetric

- [Metrics details](#)

Subjects

- [Behavioural ecology](#)
- [Carbon cycle](#)
- [Ecosystem services](#)
- [Element cycles](#)

Abstract

Baleen whales influence their ecosystems through immense prey consumption and nutrient recycling^{1,2,3}. It is difficult to accurately gauge the magnitude of their current or historic ecosystem role without measuring feeding rates and prey consumed. To date, prey consumption of the largest species has been estimated using metabolic models^{3,4,5,6,7,8,9} based on extrapolations that lack empirical validation. Here, we used tags deployed on seven baleen whale (*Mysticeti*) species ($n = 321$ tag deployments) in conjunction with acoustic measurements of prey density to calculate prey consumption at daily to annual scales from the Atlantic, Pacific, and Southern Oceans. Our results suggest that previous studies^{3,4,5,6,7,8,9} have underestimated baleen whale prey consumption by threefold or more in some ecosystems. In the Southern Ocean alone, we calculate that pre-whaling populations of mysticetes annually consumed 430 million tonnes of Antarctic krill (*Euphausia superba*), twice the current estimated total biomass of *E. superba*¹⁰, and more than twice the global catch of marine fisheries today¹¹. Larger whale populations may have supported higher productivity in large marine regions through enhanced nutrient recycling: our findings suggest mysticetes recycled 1.2×10^4 tonnes iron yr^{-1} in the Southern Ocean before whaling compared to 1.2×10^3 tonnes iron yr^{-1} recycled by whales today. The recovery of baleen whales and their nutrient recycling services^{2,3,7} could augment productivity and restore ecosystem function lost during 20th century whaling^{12,13}.

Access options

[Subscribe to Journal](#)

Get full journal access for 1 year

\$199.00

only \$3.90 per issue

[Subscribe](#)

All prices are NET prices.

VAT will be added later in the checkout.

Tax calculation will be finalised during checkout.

Rent or Buy article

Get time limited or full article access on ReadCube.

from \$8.99

[Rent or Buy](#)

All prices are NET prices.

Additional access options:

- [Log in](#)
- [Access through your institution](#)
- [Learn about institutional subscriptions](#)

Fig. 1: Field measurements informing baleen whale prey consumption and nutrient recycling.

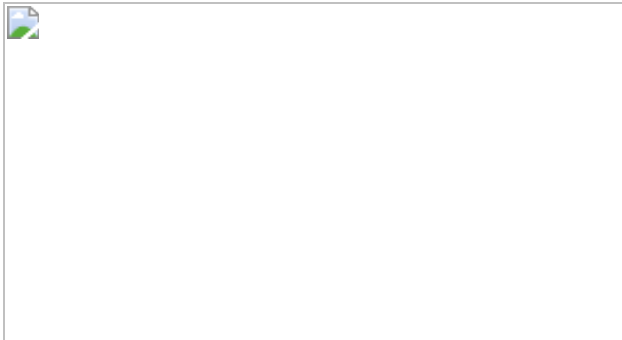


Fig. 2: Individual rorqual daily feeding rate, water filtered and krill consumed.

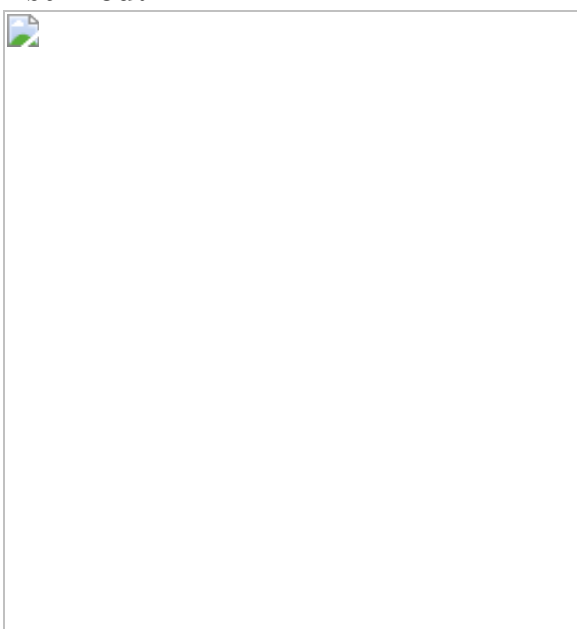


Fig. 3: Individual annual prey consumption estimates, with comparison to prior estimates.

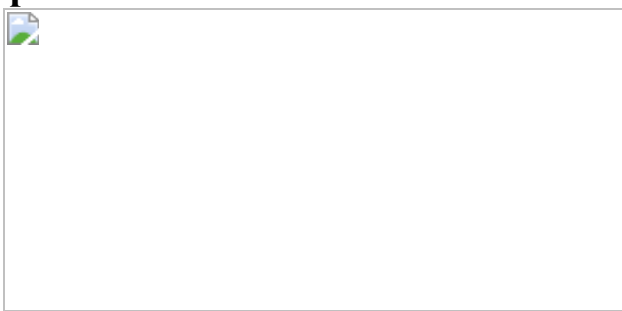
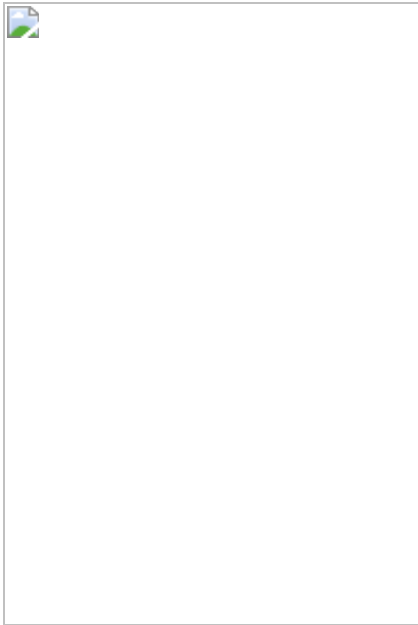


Fig. 4: Southern Ocean rorqual population-level water filtration, prey consumption and iron recycling.



Data availability

Code to reproduce the figures and analyses in this paper are available at: https://github.com/mssavoca/prey_consumption_paper; all data and code are available on GitHub.

References

1. 1.

Enquist, B. J., Abraham, A. J., Harfoot, M. B. J., Malhi, Y. & Doughty, C. E. The megabiota are disproportionately important for biosphere functioning. *Nat. Commun.* **11**, 699 (2020).

2. 2.

Doughty, C. E. et al. Global nutrient transport in a world of giants. *Proc. Natl Acad. Sci. USA* **113**, 868–873 (2016).

3. 3.

Roman, J. & McCarthy, J. J. The whale pump: marine mammals enhance primary productivity in a coastal basin. *PLoS ONE* **5**, e13255 (2010).

4. 4.

Barlow, J., Kahru, M. & Mitchell, B. G. Cetacean biomass, prey consumption, and primary production requirements in the California Current ecosystem. *Mar. Ecol. Prog. Ser.* **371**, 285–295 (2008).

5. 5.

Fortune, S. M. E., Trites, A. W., Mayo, C. A., Rosen, D. A. S. & Hamilton, P. K. Energetic requirements of North Atlantic right whales and the implications for species recovery. *Mar. Ecol. Prog. Ser.* **478**, 253–272 (2013).

6. 6.

Trites, A. W., Christensen, V. & Pauly, D. Competition between fisheries and marine mammals for prey and primary production in the Pacific Ocean. *J. Northwest Atl. Fish. Sci.* **22**, 173–187 (1997).

7. 7.

Lavery, T. J. et al. Whales sustain fisheries: blue whales stimulate primary production in the Southern Ocean. *Mar. Mammal Sci.* **30**, 888–904 (2014).

8. 8.

Croll, D. A., Kudela, R. & Tershy, B. R. in *Whales, Whaling, and Ocean Ecosystems* (eds. Estes, J. A. et al.) 202–214 (Univ. California Press, 2006).

9. 9.

Smith, L. A., Link, J. S., Cadin, S. X. & Palka, D. L. Consumption by marine mammals on the Northeast U.S. continental shelf. *Ecol. Appl.*

25, 373–389 (2015).

10. 10.

Atkinson, A., Siegel, V., Pakhomov, E. A., Jessopp, M. J. & Loeb, V. A re-appraisal of the total biomass and annual production of Antarctic krill. *Deep. Res. Part I Oceanogr. Res. Pap.* **56**, 727–740 (2009).

11. 11.

Pauly, D. & Zeller, D. Catch reconstructions reveal that global marine fisheries catches are higher than reported and declining. *Nat. Commun.* **7**, 10244 (2016).

12. 12.

Estes, J. A., Heithaus, M., McCauley, D. J., Rasher, D. B. & Worm, B. Megafaunal Impacts on Structure and Function of Ocean Ecosystems. *Annu. Rev. Environ. Resour.* **41**, 83–116 (2016).

13. 13.

Smetacek, V. in *Impacts of Global Warming on Polar Ecosystems* (ed. Duarte, C. M.) 46–80 (Fundacion BBVA, 2008).

14. 14.

Wing, S. et al. Seabirds and marine mammals redistribute bioavailable iron in the Southern Ocean. *Mar. Ecol. Prog. Ser.* **510**, 1–13 (2014).

15. 15.

Nicol, S. et al. Southern Ocean iron fertilization by baleen whales and Antarctic krill. *Fish Fish.* **11**, 203–209 (2010).

16. 16.

Ripple, W. J., Wolf, C., Newsome, T. M., Hoffmann, M. & Wirsing, A. J. Extinction risk is most acute for the world's largest and smallest

vertebrates. *Proc. Natl Acad. Sci. USA* **114**, 10678–10683 (2017).

17. 17.

McCauley, D. J. et al. Marine defaunation: animal loss in the global ocean. *Science* **347**, 1255641 (2015).

18. 18.

Goldbogen, J. A. et al. How baleen whales feed: the biomechanics of engulfment and filtration. *Ann. Rev. Mar. Sci.* **9**, 367–386 (2017).

19. 19.

Kleiber, M. *The Fire of Life: An Introduction to Animal Energetics* (Krieger, 1975).

20. 20.

Nagy, K. A. Field metabolic rate and body size. *J. Exp. Biol.* **208**, 1621–1625 (2005).

21. 21.

Roman, J. et al. Whales as marine ecosystem engineers. *Front. Ecol. Environ.* **12**, 377–385 (2014).

22. 22.

Atkinson, A., Siegel, V., Pakhomov, E. & Rothery, P. Long-term decline in krill stock and increase in salps within the Southern Ocean. *Nature* **432**, 100–103 (2004).

23. 23.

Lee, C. I. L., Pakhomov, E., Atkinson, A. & Siegel, V. Long-term relationships between the marine environment, krill and salps in the Southern Ocean. *J. Mar. Biol.* **2010**, 410129 (2010).

24. 24.

Kahane-Rapport, S. R. & Goldbogen, J. A. Allometric scaling of morphology and engulfment capacity in rorqual whales. *J. Morphol.* **279**, 1256–1268 (2018).

25. 25.

Goldbogen, J. A. et al. Why whales are big but not bigger: physiological drivers and ecological limits in the age of ocean giants. *Science* **366**, 1367–1372 (2019).

26. 26.

Nickels, C. F., Sala, L. M. & Ohman, M. D. The morphology of euphausiid mandibles used to assess selective predation by blue whales in the southern sector of the California Current System. *J. Crustac. Biol.* **38**, 563–573 (2018).

27. 27.

Croll, D. A., Kudela, R. & Tershy, B. R. in *Whales, Whaling, and Ocean Ecosystems* (eds. Estes, J. A. et al.) 202–214 (Univ. California Press, 2006).

28. 28.

Fleming, A. H., Clark, C. T., Calambokidis, J. & Barlow, J. Humpback whale diets respond to variance in ocean climate and ecosystem conditions in the California Current. *Glob. Chang. Biol.* **22**, 1214–1224 (2015).

29. 29.

Katija, K. Biogenic inputs to ocean mixing. *J. Exp. Biol.* **215**, 1040–1049 (2012).

30. 30.

Katija, K., Sherlock, R. E., Sherman, A. D. & Robison, B. H. New technology reveals the role of giant larvaceans in oceanic carbon cycling. *Sci. Adv.* **3**, e1602374 (2017).

31. 31.

Riisgård, H. U. On measurement of filtration rates in bivalves — the stony road to reliable data: review and interpretation. *Mar. Ecol. Prog. Ser.* **211**, 275–291 (2001).

32. 32.

Drenner, R. W., Mummert, J. R. & O'Brien, W. J. Filter-feeding rates of gizzard shad. *Trans. Am. Fish. Soc.* **111**, 210–215 (1982).

33. 33.

Rocha, R. C. Jr, Clapham, P. J. & Ivashchenko, Y. V. Emptying the oceans: a summary of industrial whaling catches in the 20th century. *Mar. Fish. Rev.* **76**, 37–48 (2014).

34. 34.

Christensen, L. B. Marine mammal populations: reconstructing historical abundances at the global scale. *Fish. Cent. Res. Reports* **14**, 167 (2006).

35. 35.

Laws, R. M. Seals and whales of the Southern Ocean. *Philos. Trans. R. Soc. B Biol. Sci.* **279**, 81–96 (1977).

36. 36.

Myers, R. A. & Worm, B. Rapid worldwide depletion of predatory fish communities. *Nature* **423**, 280–283 (2003).

37. 37.

Trathan, P. N., Ratcliffe, N. & Masden, E. A. Ecological drivers of change at South Georgia: the krill surplus, or climate variability. *Ecography* **35**, 983–993 (2012).

38. 38.

Dunn, M. J. et al. Population size and decadal trends of three penguin species nesting at Signy Island, South Orkney Islands. *PLoS ONE* **11**, e0164025 (2016).

39. 39.

Falkowski, P. G., Barber, R. T. & Smetacek, V. Biogeochemical controls and feedbacks on ocean primary production. *Science* **281**, 200–206 (1998).

40. 40.

Ratnarajah, L. et al. A preliminary model of iron fertilisation by baleen whales and Antarctic krill in the Southern Ocean: sensitivity of primary productivity estimates to parameter uncertainty. *Ecol. Modell.* **320**, 203–212 (2016).

41. 41.

Willis, J. Whales maintained a high abundance of krill; both are ecosystem engineers in the Southern Ocean. *Mar. Ecol. Prog. Ser.* **513**, 51–69 (2014).

42. 42.

Gerber, L. R., Morissette, L., Kaschner, K. & Pauly, D. Should whales be culled to increase fishery yield? *Science* **323**, 880–881 (2009).

43. 43.

Ruzicka, J. J., Steele, J. H., Ballerini, T., Gaichas, S. K. & Ainley, D. G. Dividing up the pie: whales, fish, and humans as competitors. *Prog. Oceanogr.* **116**, 207–219 (2013).

44. 44.

Arrigo, K. R., van Dijken, G. L. & Bushinsky, S. Primary production in the Southern Ocean, 1997-2006. *J. Geophys. Res. Ocean.* **113**, C08004 (2008).

45. 45.

Geremia, C. et al. Migrating bison engineer the green wave. *Proc. Natl Acad. Sci. USA* **116**, 25707–25713 (2019).

46. 46.

Abrahms, B. et al. Memory and resource tracking drive blue whale migrations. *Proc. Natl Acad. Sci. USA* **116**, 5582–5587 (2019).

47. 47.

Bar-on, Y. M., Phillips, R. & Milo, R. The biomass distribution on Earth. *Proc. Natl Acad. Sci. USA* **115**, 6506–6511 (2018).

48. 48.

Pallin, L. J. et al. High pregnancy rates in humpback whales (*Megaptera novaeangliae*) around the Western Antarctic Peninsula, evidence of a rapidly growing population. *R. Soc. Open Sci.* **5**, 180017 (2018).

49. 49.

Aksnes, D. L. & Ohman, M. D. Multi-decadal shoaling of the euphotic zone in the southern sector of the California Current System. *Limnol. Oceanogr.* **54**, 1272–1281 (2009).

50. 50.

Krogh, A. The physiology of the blue whale. *Nature* **133**, 635–637 (1934).

51. 51.

Lockyer, C. in *Mammals in the Seas: Large Cetaceans* (eds. Clarke, J. G., Goodman, J. & Soave, G. A.) 379–487 (FAO, 1981).

52. 52.

Tamura, T. & Ohsumi, S. Regional assessments of prey consumption by marine cetaceans in the world. *International Whaling Comission Scientific Report* (2000); <https://doi.org/10.1079/9780851996332.0143>

53. 53.

Leaper, R. & Lavigne, D. How much do large whales eat? *J. Cetacean Res. Manag.* **9**, 179–188 (2007).

54. 54.

Klumov, S. K. Food and helminth fauna of whalebone whales (Mystacoceti) in the main whaling regions of the world ocean. *Tr. Instituta Okeanol.* **71**, 94–194 (1963).

55. 55.

Sigurjónsson, J. & Vikingsson, G. A. Estimation of food consumption by cetaceans in Icelandic and adjacent waters. *J. Northw. Atl. Fish. Sci* **22**, 271–287 (1997).

56. 56.

Tamura, T. & Konishi, K. Food habit and prey consumption of Antarctic minke whale *Balaenoptera bonaerensis* in JARPA research area. *Inst. Cetacean Res. Rep.* SC/D06/J18 (2006).

57. 57.

Kenney, R. D., Scott, G. P., Thompson, T. J. & Winn, H. E. Estimates of prey consumption and trophic impacts of cetaceans in the USA

northeast continental shelf ecosystem. *J. Northwest Atl. Fish. Sci.* **22**, 155–171 (1997).

58. 58.

Innes, B. Y. S., Lavigne, D. M., Earle, W. M. & Kovacs, K. M. Feeding rates of seals and whales. *J. Anim. Ecol.* **56**, 115–130 (1987).

59. 59.

Tamura, T. & Konishi, K. Prey composition and consumption rate by Antarctic minke whales based on JARPA and JARPAII data. *Inst. Cetacean Res. Rep.* SC/F14/J15 (2014).

60. 60.

Tamura, T. Preliminary analyses on prey consumption by fin whales based on JARPAII data. *Inst. Cetacean Res. Rep.* SC/F14/J16 (2014).

61. 61.

Tamura, T., Konishi, K. & Isoda, T. Updated estimation of prey consumption by common minke, Bryde's and sei whales in the western North Pacific. *Inst. Cetacean Res. Rep.* SC/F16/JR15 (2016).

62. 62.

Lockyer, C. All creatures great and smaller: a study in cetacean life history energetics. *J. Mar. Biol. Assoc. UK* **87**, 1035–1045 (2007).

63. 63.

Víkingsson, G. A. Feeding of fin whales (*Balaenoptera physalus*) off Iceland - diurnal and seasonal variation and possible rates. *J. Northwest Atl. Fish. Sci.* **22**, 77–89 (1997).

64. 64.

Ichii, T. & Kato, H. Food and daily food consumption of southern minke whales in the Antarctic (*Balaenoptera acutorostrata*). *Polar Biol.* **11**, 479–487 (1991).

65. 65.

Tamura, T. & Konishi, K. Feeding habits and prey consumption of Antarctic minke whale (*Balaenoptera bonaerensis*) in the Southern Ocean. *J. Northwest Atl. Fish. Sci.* **42**, 13–25 (2009).

66. 66.

Lockyer, C. Body fat condition in northeast Atlantic fin whales, *Balaenoptera physalus*, and its relationship with reproduction and food resource. *Can. J. Fish. Aquat. Sci.* **43**, 142–147 (1986).

67. 67.

Goldbogen, J. A. et al. Using digital tags with integrated video and inertial sensors to study moving morphology and associated function in large aquatic vertebrates. *Anat. Rec.* **300**, 1935–1941 (2017).

68. 68.

Sumich, J. L. Swimming velocities, breathing patterns, and estimated costs of locomotion in migrating gray whales, *Eschrichtius robustus*. *Can. J. Zool.* **61**, 647–652 (1983).

69. 69.

Pauly, D., Trites, A. W., Capuli, E. & Christensen, V. Diet composition and trophic levels of marine mammals. *ICES J. Mar. Sci.* **55**, 467–481 (1998).

70. 70.

White, C. R. & Kearney, M. R. Metabolic scaling in animals: methods, empirical results, and theoretical explanations. *Compr. Physiol.* **4**, 231–256 (2014).

71. 71.

Schmitz, O. J. & Lavigne, D. M. Intrinsic rate of increase, body size, and specific metabolic rate in marine mammals. *Oecologia* **62**, 305–309 (1984).

72. 72.

Nagy, K. A., Girard, I. A. & Brown, T. K. Energetics of free-ranging mammals, reptiles, and birds. *Annu. Rev. Nutr.* **19**, 247–277 (1999).

73. 73.

Rivero, J.-L. L. Locomotor muscle fibre heterogeneity and metabolism in the fastest large-bodied rorqual: the fin whale (*Balaenoptera physalus*). *J. Exp. Biol.* **221**, jeb177758 (2018).

74. 74.

Friedlaender, A. S. et al. The advantages of diving deep: Fin whales quadruple their energy intake when targeting deep krill patches. *Funct. Ecol.* **34**, 497–506 (2019).

75. 75.

Calambokidis, J. et al. Differential vulnerability to ship strikes between day and night for blue, fin, and humpback whales based on dive and movement data from medium duration archival tags. *Front. Mar. Sci.* **6**, 543 (2019).

76. 76.

Cade, D. E., Friedlaender, A. S., Calambokidis, J. & Goldbogen, J. A. Kinematic diversity in rorqual whale feeding mechanisms. *Curr. Biol.* **26**, 2617–2624 (2016).

77. 77.

Gough, W. T. et al. Scaling of swimming performance in baleen whales. *J. Exp. Biol.* **222**, jeb204172 (2019).

78. 78.

Parks, S. E., Warren, J. D., Stamieszkin, K., Mayo, C. A. & Wiley, D. Dangerous dining: Surface foraging of North Atlantic right whales increases risk of vessel collisions. *Biol. Lett.* **8**, 57–60 (2012).

79. 79.

Nowacek, D. P. et al. Buoyant balaenids: the ups and downs of buoyancy in right whales. *Proc. R. Soc. B Biol. Sci.* **268**, 1811–1816 (2001).

80. 80.

Johnson, M. P. & Tyack, P. L. A digital acoustic recording tag for measuring the response of wild marine mammals to sound. *IEEE J. Ocean. Eng.* **28**, 3–12 (2003).

81. 81.

Cade, D. E., Barr, K. R., Calambokidis, J., Friedlaender, A. S. & Goldbogen, J. A. Determining forward speed from accelerometer jiggle in aquatic environments. *J. Exp. Biol.* **221**, 170449 (2018).

82. 82.

Goldbogen, J. A. et al. Integrative approaches to the study of baleen whale diving behavior, feeding performance, and foraging ecology. *Bioscience* **63**, 90–100 (2013).

83. 83.

Hazen, E. L., Friedlaender, A. S. & Goldbogen, J. A. Blue whales (*Balaenoptera musculus*) optimize foraging efficiency by balancing oxygen use and energy gain as a function of prey density. *Sci. Adv.* **1**, e1500469 (2015).

84. 84.

Cade, D. E. et al. Predator-scale spatial analysis of intra-patch prey distribution reveals the energetic drivers of rorqual whale super group formation. *Functional Ecol.* **35**, 894–908 (2021).

85. 85.

Nowacek, D. P. et al. Super-aggregations of krill and humpback whales in Wilhelmina bay, Antarctic Peninsula. *PLoS ONE* **6**, 2–6 (2011).

86. 86.

Goldbogen, J. A. et al. Prey density and distribution drive the three-dimensional foraging strategies of the largest filter feeder. *Funct. Ecol.* **29**, 951–961 (2015).

87. 87.

Cade, D. E., Carey, N., Domenici, P., Potvin, J. & Goldbogen, J. A. Predator-informed looming stimulus experiments reveal how large filter feeding whales capture highly maneuverable forage fish. *Proc. Natl Acad. Sci. USA* **117**, 472–478 (2020).

88. 88.

Goldbogen, J. A. et al. Mechanics, hydrodynamics and energetics of blue whale lunge feeding: efficiency dependence on krill density. *J. Exp. Biol.* **214**, 131–146 (2011).

89. 89.

Hamner, W. M. Aspects of schooling in *Euphausia superba*. *J. Crustac. Biol.* **4**, 67–74 (1984).

90. 90.

Potvin, J., Goldbogen, J. A. & Shadwick, R. E. Passive versus active engulfment: verdict from trajectory simulations of lunge-feeding fin

whales *Balaenoptera physalus*. *J. R. Soc. Interface* **6**, 1005–1025 (2009).

91. 91.

Potvin, J., Goldbogen, J. A. & Shadwick, R. E. Scaling of lunge feeding in rorqual whales: an integrated model of engulfment duration. *J. Theor. Biol.* **267**, 437–453 (2010).

92. 92.

Goldbogen, J. A. et al. Underwater acrobatics by the world's largest predator: 360° rolling manoeuvres by lunge-feeding blue whales. *Biol. Lett.* **9**, 20120986 (2013).

93. 93.

Rodriguez-Romero, J., Palacios-Salgado, D. S., Lopez-Martinez, J., Vazquez, S. H. & Velazquez-Abunader, J. I. The length – weight relationship parameters of demersal fish species off the western coast of Baja California Sur, Mexico. *J. Appl. Ichthology* **25**, 114–116 (2009).

94. 94.

Pitcher, T. J. & Partridge, B. L. Fish school density and volume. *Mar. Biol.* **394**, 383–394 (1979).

95. 95.

Laidre, K. L., Heide-Jørgensen, M. P. & Nielsen, T. G. Role of the bowhead whale as a predator in West Greenland. *Mar. Ecol. Prog. Ser.* **346**, 285–297 (2007).

96. 96.

Simon, M., Johnson, M., Tyack, P. & Madsen, P. T. Behaviour and kinematics of continuous ram filtration in bowhead whales (*Balaena mysticetus*). *Proc. R. Soc. B Biol. Sci.* **276**, 3819–3828 (2009).

97. 97.

Baumgartner, M. F. & Mate, B. R. Summertime foraging ecology of North Atlantic right whales. *Mar. Ecol. Prog. Ser.* **264**, 123–135 (2003).

98. 98.

van der Hoop, J. M. et al. Foraging rates of ram-filtering North Atlantic right whales. *Funct. Ecol.* **33**, 1290–1306 (2019).

99. 99.

Burnett, J. D. et al. Estimating morphometric attributes of baleen whales with photogrammetry from small UASs: a case study with blue and gray whales. *Mar. Mammal Sci.* **35**, 108–139 (2019).

100. 100.

Torres, W. I. & Bierlich, K. C. MorphoMetriX: a photogrammetric measurement GUI for morphometric analysis of megafauna. *J. Open Source Softw.* **5**, 1825 (2020).

101. 101.

Johnston, D. W. Unoccupied aircraft systems in marine science and conservation. *Ann. Rev. Mar. Sci.* **11**, 439–463 (2019).

102. 102.

Durban, J. W. et al. Photogrammetry of blue whales with an unmanned hexacopter. *Mar. Mammal Sci.* **32**, 1510–1515 (2016).

103. 103.

Kelley, D. & Richards, C. *oce: Analysis of Oceanographic Data R Package v. 1.1* (2019).

104. 104.

Dubreuil, J. & Petitgas, P. Energy density of anchovy *Engraulis encrasiculus* in the Bay of Biscay. *J. Fish Biol.* **74**, 521–534 (2009).

105. 105.

Chenowith, E. M. *Bioenergetic and Economic Impacts of Humpback Whale Depredation at Salmon Hatchery Release Sites*. PhD thesis, Univ. Alaska (2018).

106. 106.

Werth, A. J. Models of hydrodynamic flow in the bowhead whale filter feeding apparatus. *J. Exp. Biol.* **207**, 3569–3580 (2004).

107. 107.

Werth, A. in *Feeding: Form, Function, and Evolution in Tetrapod Vertebrates* (ed. Schwenk, K.) 487–526 (Academic, 2000).

108. 108.

Mckinstry, C. A. E., Westgate, A. J. & Koopman, H. N. Annual variation in the nutritional value of stage V *Calanus finmarchicus*: implications for right whales and other copepod predators. *Endang. Species Res.* **20**, 195–204 (2013).

109. 109.

Folkow, L. P., Haug, T., Nilssen, K. T. & Nordy, E. S. Estimated food consumption of minke whales *Balaenoptera acutorostrata* in Northeast Atlantic waters in 1992-1995. *NAMMCO Sci. Publ.* **2**, 65–80 (2000).

110. 110.

Brodie, P. F. Cetacean energetics, an overview of intraspecific size variation. *Ecology* **56**, 152–161 (1975).

111. 111.

Hill, S. L. et al. Is current management of the antarctic krill fishery in the atlantic sector of the southern ocean precautionary? *CCAMLR Sci.* **23**, 31–51 (2016).

112. 112.

Atkinson, A. et al. Oceanic circumpolar habitats of Antarctic krill. *Mar. Ecol. Prog. Ser.* **362**, 1–23 (2008).

113. 113.

Ratnarajah, L., Bowie, A. R., Lannuzel, D., Meiners, K. M. & Nicol, S. The biogeochemical role of baleen whales and krill in Southern Ocean nutrient cycling. *PLoS ONE* **9**, e114067 (2014).

114. 114.

Rose, C., Parker, A., Jefferson, B. & Cartmell, E. The characterization of feces and urine: a review of the literature to inform advanced treatment technology. *Crit. Rev. Environ. Sci. Technol.* **45**, 1827–1879 (2015).

115. 115.

Candela, E., Camacho, M. V. & Perdomo, J. Iron absorption by humans and swine from Fe (III)-EDTA. Further studies. *J. Nutr.* **114**, 2204–2211 (1984).

116. 116.

Ratnarajah, L. et al. A preliminary model of iron fertilisation by baleen whales and Antarctic krill in the Southern Ocean: sensitivity of primary productivity estimates to parameter uncertainty. *Ecol. Modell.* **320**, 203–212 (2016).

117. 117.

Twining, B. S., Baines, S. B. & Fisher, N. S. Element stoichiometries of individual plankton cells collected during the Southern Ocean Iron

Experiment (SOFeX). *Limnol. Oceanogr.* **49**, 2115–2128 (2004).

118. 118.

Strzepek, R. F., Maldonado, M. T., Hunter, K. A., Frew, R. D. & Boyd, P. W. Adaptive strategies by Southern Ocean phytoplankton to lessen iron limitation: uptake of organically complexed iron and reduced cellular iron requirements. *Limnol. Oceanogr.* **56**, 1983–2002 (2011).

119. 119.

Quigg, A. et al. The evolutionary inheritance of elemental stoichiometry in marine phytoplankton. *Nature* **425**, 291–294 (2003).

120. 120.

Wickham, H. *ggplot2: Elegant Graphics for Data Analysis* 2nd edn (Springer, 2016).

121. 121.

Lockyer, C. Body weights of some species of large whales. *ICES J. Mar. Sci.* **36**, 259–273 (1976).

122. 122.

Blix, A. S. & Folkow, L. P. Daily energy expenditure in free living minke whales (*Balaenoptera acutorostrata*). *Acta Physiol. Scand.* **153**, 61–66 (1995).

123. 123.

Nordoy, E. S., Folkow, L. P., Martensson, P. & Blix, A. S. Food requirements of Northeast Atlantic minke whales. *Dev. Mar. Biol.* **4**, 307–317 (1995).

124. 124.

Murase, H., Tamura, T., Matsuoka, K. & Hakamada, T. First attempt of estimation of feeding impact on krill standing stock by three baleen whale species (Antarctic minke, humpback and fin whales) in Areas IV and V using JARPA dat. *Inst. Cetacean Res. Rep.* SC/D06/J22 (2006).

125. 125.

Southall, B. L. et al. Behavioral responses of individual blue whales (*Balaenoptera musculus*) to mid-frequency military sonar. *J. Exp. Biol.* **222**, jeb190637 (2019).

126. 126.

Goldbogen, J. A. et al. Blue whales respond to simulated mid-frequency military sonar. *Proc. R. Soc. B* **280**, 20130657 (2013).

127. 127.

Stimpert, A. K. et al. Sound production and associated behavior of tagged fin whales (*Balaenoptera physalus*) in the Southern California Bight. *Anim. Biotelemetry* **3**, 1–12 (2015).

128. 128.

Goldbogen, J. A. et al. Foraging behavior of humpback whales: kinematic and respiratory patterns suggest a high cost for a lunge. *J. Exp. Biol.* **211**, 3712–3719 (2008).

129. 129.

Wiley, D. et al. Underwater components of humpback whale bubble-net feeding behaviour. *Behaviour* **148**, 575–602 (2011).

130. 130.

Friedlaender, A. S., Tyson, R. B., Stimpert, A. K., Read, A. J. & Nowacek, D. P. Extreme diel variation in the feeding behavior of

humpback whales along the western Antarctic Peninsula during autumn. *Mar. Ecol. Prog. Ser.* **494**, 281–289 (2013).

131. 131.

Kahane-Rapport, S. R. et al. Lunge filter feeding biomechanics constrain rorqual foraging ecology across scale. *J. Exp. Biol.* **223**, jeb224196 (2020).

132. 132.

Friedlaender, A. S. et al. Feeding rates and under-ice foraging strategies of the smallest lunge filter feeder, the Antarctic minke whale (*Balaenoptera bonaerensis*). *J. Exp. Biol.* **217**, 2851–2854 (2014).

133. 133.

Domenici, P., Batty, R. S. & Similä, T. Spacing of wild schooling herring while encircled by killer whales. *J. Fish Biol.* **57**, 831–836 (2000).

134. 134.

Tamura, T. et al. *Some examinations of uncertainties in the prey consumption estimates of common minke, sei and Bryde's whales in the western North Pacific.* (2009).

135. 135.

Innes, S., Lavigne, D. M., Earle, W. M. & Kovacs, K. M. Estimating feeding rates of marine mammals from heart mass to body mass ratios. *Mar. Mammal Sci.* **2**, 227–229 (1986).

136. 136.

Armstrong, A. J. & Siegfried, W. R. Consumption of Antarctic krill by minke whales (*Balaenoptera acutorostrata*). *Antarct. Sci.* **3(1)** 13–18. 1991. **3**, 13–18 (1991).

137. 137.

Reilly, S. et al. Biomass and energy transfer to baleen whales in the South Atlantic sector of the Southern Ocean. *Deep. Res. Part II Top. Stud. Oceanogr.* **51**, 1397–1409 (2004).

138. 138.

Read, A. J. & Brownstein, C. R. Considering other consumers: Fisheries, predators, and Atlantic herring in the Gulf of Maine. *Conserv. Ecol.* **7** (2003).

139. 139.

Nagy, K. Food requirements of wild animals: predictive equations for free-living mammals, reptiles, and birds. *Nutr. Abstr. Rev. Ser. B* **71**, 21R–31R (2001).

140. 140.

Stevick, P. T. et al. Trophic relationships and oceanography on and around a small offshore bank. *Mar. Ecol. Prog. Ser.* **363**, 15–28 (2008).

Acknowledgements

We would like to thank J. Barlow at NOAA's Southwest Fisheries Science Center for an internal review of our manuscript, and R. Anderson for editorial assistance. D. Cade was integral in the fieldwork and on advising with the methods used in the manuscript. A. Atkinson and O. Schofield advised on the methods relating to Southern Ocean productivity.

Illustrations in Fig. 3 were provided by K. Duthie, all other illustrations were provided by A. Boersma. Funding for this work was provided by the National Science Foundation (IOS 1656691, OPP 1644209, 1643877, 1250208, 1440435, PRFB 1906332), the Office of Naval Research Young Investigator Program (N000141612477), the Defense University Research Instrumentation Program (N00014-16-1-2546), the National Geographic Society (EC-53352R-18), the Percy Sladen Memorial Trust, the PADI

Foundation, the Society for Marine Mammalogy, Torben og Alice Frimodts Fond, the Volgenau Foundation, the International Fund for Animal Welfare, and MAC3 Impact Philanthropies. Data collection was also supported by NSF Palmer LTER, WWF, OneOcean Expeditions, the Hogwarts Running Club, Cheeseman's Ecology Safaris, and the American Cetacean Society.

Author information

Affiliations

1. Hopkins Marine Station, Stanford University, Pacific Grove, CA, USA

Matthew S. Savoca, Max F. Czapanskiy, Shirel R. Kahane-Rapport, William T. Gough, James A. Fahlbusch, Paolo S. Segre, Elliott L. Hazen & Jeremy A. Goldbogen

2. Cascadia Research Collective, Olympia, WA, USA

James A. Fahlbusch & John Calambokidis

3. Duke University Marine Laboratory, Duke University, Beaufort, NC, USA

K. C. Bierlich, Douglas P. Nowacek & David W. Johnston

4. Marine Mammal Institute, Hatfield Marine Science Center, Oregon State University, Newport, OR, USA

K. C. Bierlich

5. Department of Biology, University of Copenhagen, Copenhagen, Denmark

Jacopo Di Clemente

6. Department of Biology, University of Southern Denmark, Odense, Denmark

Jacopo Di Clemente

7. Department of Bioscience, Aarhus University, Aarhus, Denmark

Jacopo Di Clemente

8. Institute for Coastal and Marine Research, Nelson Mandela University,
Port Elizabeth, South Africa

Gwenith S. Penry

9. Stellwagen Bank National Marine Sanctuary, NOAA National Ocean
Service, Scituate, MA, USA

David N. Wiley

10. Department of Paleobiology, National Museum of Natural History,
Washington, DC, USA

Nicholas D. Pyenson

11. Department of Paleontology and Geology, Burke Museum of Natural
History and Culture, Seattle, WA, USA

Nicholas D. Pyenson

12. Long Marine Laboratory, University of California, Santa Cruz, Santa
Cruz, CA, USA

Ari S. Friedlaender & Elliott L. Hazen

13. Environmental Research Division, NOAA Southwest Fisheries
Science Center, Monterey, CA, USA

Elliott L. Hazen

Contributions

M.S.S. and J.A.G. conceived and led the project. Data collection and initial processing by S.R.K-R., W.T.G., J.A.F., K.C.B., P.S.S., J.D., G.S.P., D.N.W., J.C., D.W.J., A.S.F., E.L.H. and J.A.G. Data analysed and visualized by M.F.C. and M.S.S. Manuscript drafted by M.S.S. with substantial contributions from M.F.C., E.L.H., N.D.P. and J.A.G. All authors edited and proofread the paper.

Corresponding author

Correspondence to Matthew S. Savoca.

Ethics declarations

Competing interests

The authors declare no competing interests.

Additional information

Peer review information *Nature* thanks Peter Corkeron, Kimberly Davies, Victor Smetacek and the other, anonymous, reviewer(s) for their contribution to the peer review of this work. Peer reviewer reports are available.

Publisher's note Springer Nature remains neutral with regard to jurisdictional claims in published maps and institutional affiliations.

Extended data figures and tables

[Extended Data Fig. 1 Prior estimates of daily prey consumption.](#)

See Extended Data Table 3 for studies that use specific parameter values plotted in panels **d**, **e** and **f**. **a**, Daily ration (R) estimate using equation (1). Note that here *B. edeni* is representative of the Bryde's whale complex that

includes *B. brydei*. **b**, Mean daily consumption (MDC) estimate using equation (1) if 120 days spent feeding. **c**, Mean daily consumption (MDC) estimate using equation (1) if 90 days spent feeding. **d**, Daily ration (R) estimate using equation (2). **e**, Mean daily consumption (MDC) estimate using equation (2) if 120 days spent feeding. **f**, Mean daily consumption (MDC) estimate using equation (2) if 90 days spent feeding.

Extended Data Fig. 2 Map of field data.

Each point represents a tag deployment, coloured by species. The world map was generated from ref. [120](#). The icons of the RHIB with the echosounder represent regions where we have prey mapping data and were illustrated by Alex Boersma; drone icons indicate where we conducted drone measurements.

Extended Data Fig. 3 Analysis flowchart.

The outline of the analytical steps from field measurements to modelled daily krill consumption, and finally to projected annual consumption, and nutrients (for example, iron) recycled. Boxes with solid lines are data we collected, modelled and projected; dashed boxes are data we retrieved from other sources. The majority of our data, analyses, results, and inferences focused on krill-feeding rorqual whales (207 of 321 tag deployments), and this flow chart highlights those methods in particular. For details on the measured data, see: Methods sections ‘Tagging data’ and ‘Lunge detection methods’ for tag data; Methods section ‘Prey methods’ for prey data; Methods section ‘Drone/engulfment capacity methods’ for drone data; Methods section ‘Iron recycling and primary production’ for fecal iron concentrations. For details on the calculated information from the field data, see: Methods sections ‘Rorqual feeding rate methods’ and ‘Feeding rate validation’ for feeding rate (lunges h^{-1}) calculations; Methods section ‘Prey methods’ for prey biomass calculations; Methods section ‘Drone/engulfment capacity methods’ for engulfment capacity calculations; Methods section ‘Annual and population-level projections’ for population size information. For details on the modelled outputs of daily prey ingestion and water filtration, see: Methods section ‘Daily prey consumption methods for rorquals’ for rorquals; Methods section ‘Balaenid water filtration and

prey estimation methods' for balaenids. For details on annual projected prey ingested, water filtered and iron recycled see: Methods section 'Annual and population-level projections' for prey ingested; Methods section 'Iron recycling and primary production' for iron recycled. For specific methods on fish-feeding rorquals see the 'Fish' subsection of the 'Prey methods' section, and for specific details on methods regarding balaenids, see the 'Copepod' portion of the 'Prey methods' section as well as section 'Balaenid water filtration and prey estimation methods'.

Extended Data Fig. 4 Balaenid daily water filtration and prey consumption.

a, Visualization of an example bowhead whale (*Ba. mysticetus*) showing how water filtration was calculated. **b**, Water filtered per day for an individual bowhead (*Ba. mysticetus*) and North Atlantic right whale (*Eu. glacialis*). Density plots illustrate the full scope of all daily simulations with the height representing the relative probability of each output; the boxplots show the quartiles of these outputs with the thick line representing the median and the shaded region representing the Q1–Q3 range (25th–75th percentiles) of all modelled daily rates. For each species, the lower distribution represents a low effort foraging day (10 h feeding) and the higher distribution represents a high effort foraging day (15 h feeding). **c**, Prey consumed per day for an individual bowhead and North Atlantic right whale. Density plots illustrate the full scope of all daily simulations with the height representing the relative probability of each output; the boxplots show the quartiles of these outputs with the thick line representing the median and the shaded region representing the Q1–Q3 range (25th–75th percentiles) of all modelled daily rates. For each species, the lower distribution represents a low effort foraging day (10 h feeding) and the higher distribution represents a high effort foraging day (15 h feeding).

Extended Data Fig. 5 Additional daily prey consumption results.

a–c, Estimated individual daily feeding rates, filtration volumes and prey consumption for fish-feeding humpback whales (*M. novaeangliae*) from the

California Current and North Atlantic Ocean (Stellwagen Bank, Gulf of Maine), as well as for Bryde's whales (*Balaenoptera brydei*) tagged off South Africa. The smaller distributions assume smaller fish schools that are 29% of the size of the engulfment volume (see [Methods](#)). Density plots illustrate the full scope of all daily simulations with the height representing the relative probability of each output; the boxplots show the quartiles of these outputs with the thick line representing the median and the shaded region representing the 25th–75th percentiles of all modelled daily rates. **d**, Non-Antarctic humpback, fin (*B. physalus*), and blue whales (*B. musculus*) prey consumption estimates. Density plots illustrate the full scope of all daily simulations with the height representing the relative probability of each output; the boxplots show the quartiles of these outputs with the thick line representing the median and the shaded region representing the 25th–75th percentiles of all modelled daily rates. **e**, Mass-specific daily energy intake. Species-specific average whale mass was calculated using our drone-length measurements (Extended Data Table 1), converting to body weight according to ref. [121](#). Average prey energy density for Antarctic krill, eastern North Pacific krill (2 spp.), forage fish, and copepods described in sections 'Daily prey consumption methods for rorquals' and 'Balaenid water filtration and prey estimation methods'. Dashed horizontal line represents $80 \text{ kJ kg}^{-1} \text{ d}^{-1}$ (converted to $242.36 \text{ kJ kg}^{-1} \text{ d}^{-1}$ via MDC methodology), which previous studies have used to estimate mysticete prey consumption[122,123,124](#). Boxplots show the quartiles of all modelled daily outputs with the thick line representing the median and the shaded region representing the 25th–75th percentiles of all modelled daily rates. **f**, Mass-specific daily energy intake using Antarctic krill TS–L equations for North Pacific krill, as has been used in previous studies[74,83,86](#). Boxplots show the quartiles of all modelled daily outputs with the thick line representing the median and the shaded region representing the 25th–75th percentiles of all modelled daily rates. Dashed horizontal line represents $80 \text{ kJ kg}^{-1} \text{ d}^{-1}$ (converted to $242.36 \text{ kJ kg}^{-1} \text{ d}^{-1}$ via MDC methodology), which previous studies have used to estimate mysticete prey consumption[122,123,124](#). Falling largely below the horizontal dashed line, this level of prey consumption would probably not be possible for these rorqual species to meet their energetic demands.

Extended Data Fig. 6 Feeding rate validation measurements and weighting curve.

a, Using medium term tags attached to ENP blue whales (*B. musculus*), we calculated the mean absolute error in daily lunge rate estimation when randomly subsampling and quantifying hourly lunge rates from different duration blocks of multi-day tag deployments. This analysis showed that the longer a sub-daily deployment is, the more accurate and precise it becomes in estimating the daily lunge rate. **b**, Using data from panel **a**, we generated a custom weighting function which we applied to all deployments in our dataset, accounting for our increased confidence in the lunge rates of longer deployments. Deployments ≥ 10 h were weighted equally.

Extended Data Table 1 Summary of baleen whale data measured, calculated, and modelled

Extended Data Table 2 Calculations to estimate primary production stimulated by whale recycled iron in the Southern Ocean

Extended Data Table 3 Parameters used to estimate mysticete prey consumption

Extended Data Table 4 Summary of tag deployments

Supplementary information

[**Reporting Summary**](#)

[**Peer Review File**](#)

Rights and permissions

[Reprints and Permissions](#)

About this article

Cite this article

Savoca, M.S., Czapanskiy, M.F., Kahane-Rapport, S.R. *et al.* Baleen whale prey consumption based on high-resolution foraging measurements. *Nature* **599**, 85–90 (2021). <https://doi.org/10.1038/s41586-021-03991-5>

- Received: 05 July 2020
- Accepted: 01 September 2021
- Published: 03 November 2021
- Issue Date: 04 November 2021
- DOI: <https://doi.org/10.1038/s41586-021-03991-5>

Share this article

Anyone you share the following link with will be able to read this content:

[Get shareable link](#)

Sorry, a shareable link is not currently available for this article.

[Copy to clipboard](#)

Provided by the Springer Nature SharedIt content-sharing initiative

[A whale of an appetite revealed by analysis of prey consumption](#)

- Victor Smetacek

News & Views 03 Nov 2021

[Whale-cams reveal how much they really eat](#)

- Sara Reardon

Nature Video 05 Nov 2021

This article was downloaded by **calibre** from <https://www.nature.com/articles/s41586-021-03991-5>

| [Section menu](#) | [Main menu](#) |

- Article
- [Published: 27 October 2021](#)

Disease variant prediction with deep generative models of evolutionary data

- [Jonathan Frazer](#)¹ na1,
- [Pascal Notin](#)² na1,
- [Mafalda Dias](#)¹ na1,
- [Aidan Gomez](#)²,
- [Joseph K. Min](#) [ORCID: orcid.org/0000-0002-2781-7390](#)¹,
- [Kelly Brock](#)¹,
- [Yarin Gal](#) [ORCID: orcid.org/0000-0002-2733-2078](#)² &
- [Debora S. Marks](#) [ORCID: orcid.org/0000-0001-9388-2281](#)^{1,3}

[Nature](#) volume 599, pages 91–95 (2021)

- 16k Accesses
- 339 Altmetric
- [Metrics details](#)

Subjects

- [Computational models](#)
- [Disease genetics](#)
- [Genetic variation](#)
- [Genetics research](#)
- [Machine learning](#)

Abstract

Quantifying the pathogenicity of protein variants in human disease-related genes would have a marked effect on clinical decisions, yet the overwhelming majority (over 98%) of these variants still have unknown consequences^{1,2,3}. In principle, computational methods could support the large-scale interpretation of genetic variants. However, state-of-the-art methods^{4,5,6,7,8,9,10} have relied on training machine learning models on known disease labels. As these labels are sparse, biased and of variable quality, the resulting models have been considered insufficiently reliable¹¹. Here we propose an approach that leverages deep generative models to predict variant pathogenicity without relying on labels. By modelling the distribution of sequence variation across organisms, we implicitly capture constraints on the protein sequences that maintain fitness. Our model EVE (evolutionary model of variant effect) not only outperforms computational approaches that rely on labelled data but also performs on par with, if not better than, predictions from high-throughput experiments, which are increasingly used as evidence for variant classification^{12,13,14,15,16}. We predict the pathogenicity of more than 36 million variants across 3,219 disease genes and provide evidence for the classification of more than 256,000 variants of unknown significance. Our work suggests that models of evolutionary information can provide valuable independent evidence for variant interpretation that will be widely useful in research and clinical settings.

Access options

Subscribe to Journal

Get full journal access for 1 year

\$199.00

only \$3.90 per issue

[Subscribe](#)

All prices are NET prices.
VAT will be added later in the checkout.
Tax calculation will be finalised during checkout.

Rent or Buy article

Get time limited or full article access on ReadCube.

from \$8.99

[Rent or Buy](#)

All prices are NET prices.

Additional access options:

- [Log in](#)
- [Access through your institution](#)
- [Learn about institutional subscriptions](#)

Fig. 1: Modelling strategy.

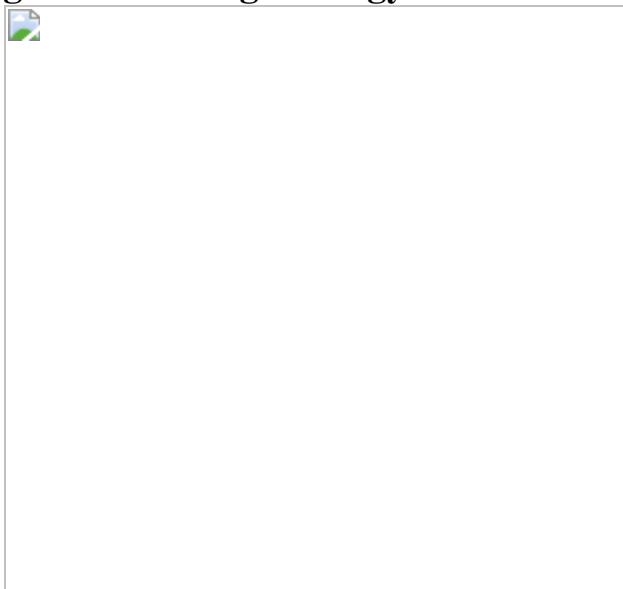


Fig. 2: EVE accurately predicts disease-causing variants.

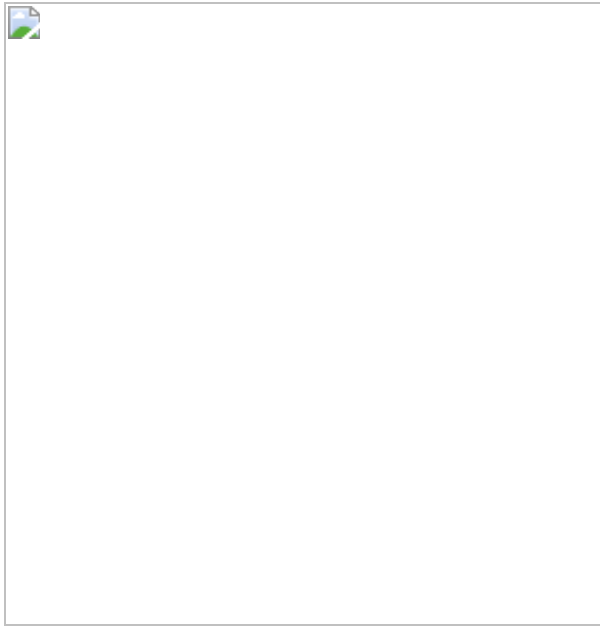


Fig. 3: EVE is as good as functional experiments at predicting clinical interpretations of variants.

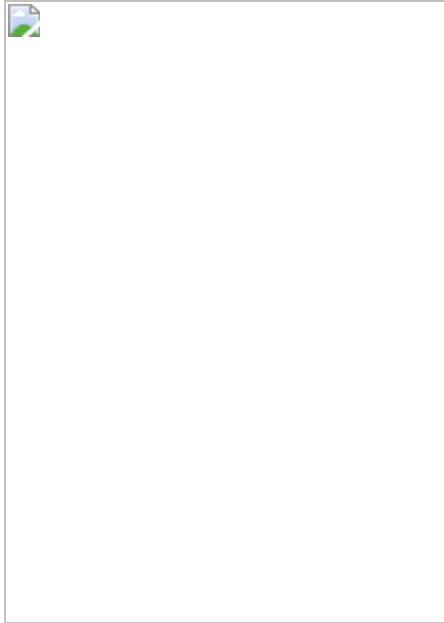
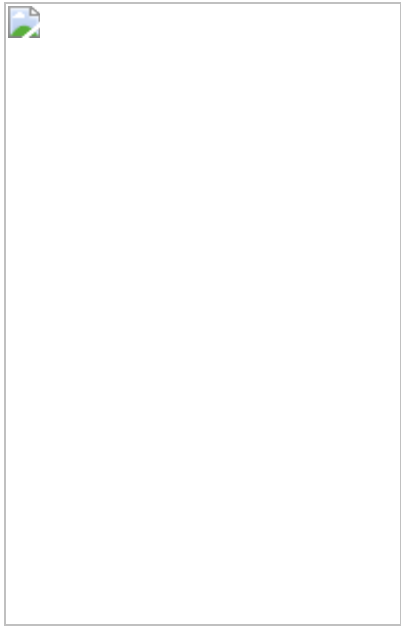


Fig. 4: Predictions for variants in 3,219 genes.



Data availability

The data analysed and generated in this study, including multiple sequence alignments used in training, ClinVar annotations used for validation, population frequencies and predictions from our model, are available in [Supplementary Information](#) and at [evemodel.org](#). Predictions from other computational models are available through <http://database.liulab.science/dbNSFP>. [Source data](#) are provided with this paper.

Code availability

The model code is available at <https://github.com/OATML-Markslab/EVE>, <https://doi.org/10.5281/zenodo.5389490>.

References

1. 1.

Van Hout, C. V. et al. Exome sequencing and characterization of 49,960 individuals in the UK Biobank. *Nature* **586**, 749–756 (2020).

2. 2.

Karczewski, K. J. et al. The mutational constraint spectrum quantified from variation in 141,456 humans. *Nature* **581**, 434–443 (2020).

3. 3.

Landrum, M. J. & Kattman, B. L. ClinVar at five years: delivering on the promise. *Hum. Mutat.* **39**, 1623–1630 (2018).

4. 4.

Raimondi, D. et al. DEOGEN2: prediction and interactive visualization of single amino acid variant deleteriousness in human proteins. *Nucleic Acids Res.* **45**, W201-W206 (2017).

5. 5.

Feng, B. J. PERCH: a unified framework for disease gene prioritization. *Hum. Mutat.* **38**, 243–251 (2017).

6. 6.

Ioannidis, N. M. et al. REVEL: an ensemble method for predicting the pathogenicity of rare missense variants. *Am. J. Hum. Genet.* **99**, 877–885 (2016).

7. 7.

Ionita-Laza, I., McCallum, K., Xu, B. & Buxbaum, J. D. A spectral approach integrating functional genomic annotations for coding and noncoding variants. *Nat. Genet.* **48**, 214–220 (2016).

8. 8.

Jagadeesh, K. A. et al. M-CAP eliminates a majority of variants of uncertain significance in clinical exomes at high sensitivity. *Nat. Genet.* **48**, 1581-1586 (2016).

9. 9.

Rentzsch, P., Witten, D., Cooper, G. M., Shendure, J. & Kircher, M. CADD: predicting the deleteriousness of variants throughout the human genome. *Nucleic Acids Res.* **47**, D886–D894 (2019).

10. 10.

Adzhubei, I. A. et al. A method and server for predicting damaging missense mutations. *Nat. Methods* **7**, 248–249 (2010).

11. 11.

Richards, S. et al. Standards and guidelines for the interpretation of sequence variants: a joint consensus recommendation of the American College of Medical Genetics and Genomics and the Association for Molecular Pathology. *Genet. Med.* **17**, 405–424 (2015).

12. 12.

Findlay, G. M. et al. Accurate classification of BRCA1 variants with saturation genome editing. *Nature* **562**, 217–222 (2018).

13. 13.

Glazer, A. M. et al. High-throughput reclassification of SCN5A variants. *Am. J. Hum. Genet.* **107**, 111–123 (2020).

14. 14.

Giacomelli, A. O. et al. Mutational processes shape the landscape of TP53 mutations in human cancer. *Nat. Genet.* **50**, 1381–1387 (2018).

15. 15.

Mighell, T. L., Evans-Dutson, S. & O’Roak, B. J. A saturation mutagenesis approach to understanding PTEN lipid phosphatase activity and genotype–phenotype relationships. *Am. J. Hum. Genet.* **102**, 943–955 (2018).

16. 16.

Jia, X. et al. Massively parallel functional testing of MSH2 missense variants conferring Lynch syndrome risk. *Am. J. Hum. Genet.* **108**, 163–175 (2021).

17. 17.

Cao, Y. et al. The ChinaMAP analytics of deep whole genome sequences in 10,588 individuals. *Cell Res.* **30**, 717–731 (2020).

18. 18.

Gudbjartsson, D. F. et al. Large-scale whole-genome sequencing of the Icelandic population. *Nat. Genet.* **47**, 435–444 (2015).

19. 19.

Esposito, D. et al. MaveDB: an open-source platform to distribute and interpret data from multiplexed assays of variant effect. *Genome Biol.* **20**, 223 (2019).

20. 20.

Trenkmann, M. Putting genetic variants to a fitness test. *Nat. Rev. Genet.* **19**, 667 (2018).

21. 21.

Rehm, H. L. et al. ClinGen—the Clinical Genome Resource. *N. Engl. J. Med.* **372**, 2235–2242 (2015).

22. 22.

Grimm, D. G. et al. The evaluation of tools used to predict the impact of missense variants is hindered by two types of circularity. *Hum. Mutat.* **36**, 513–523 (2015).

23. 23.

Hopf, T. A. et al. Mutation effects predicted from sequence co-variation. *Nat. Biotechnol.* **35**, 128–135 (2017).

24. 24.

Marks, D. S. et al. Protein 3D structure computed from evolutionary sequence variation. *PLoS ONE* **6**, e28766 (2011).

25. 25.

Hopf, T. A. et al. Sequence co-evolution gives 3D contacts and structures of protein complexes. *eLife* **3**, e03430 (2014).

26. 26.

Lapedes, A., Giraud, B. & Jarzynski, C. Using sequence alignments to predict protein structure and stability with high accuracy. Preprint at <https://arxiv.org/abs/1207.2484v1> (2012).

27. 27.

Vaser, R., Adusumalli, S., Leng, S. N., Sikic, M. & Ng, P. C. SIFT missense predictions for genomes. *Nat. Protoc.* **11**, 1–9 (2016).

28. 28.

Reva, B., Antipin, Y. & Sander, C. Predicting the functional impact of protein mutations: application to cancer genomics. *Nucleic Acids Res.* **39**, e118 (2011).

29. 29.

Rezende, D. J., Mohamed, S. & Wierstra, D. in *Proceedings of the 31st International Conference on Machine Learning* vol. 32 (eds Xing, E. P. & Jebara, T.) 1278–1286 (PMLR, 2014).

30. 30.

Kingma, D. P. & Welling, M. Auto-encoding variational Bayes. Preprint at <https://arxiv.org/abs/1312.6114> (2013).

31. 31.

Riesselman, A. J., Ingraham, J. B. & Marks, D. S. Deep generative models of genetic variation capture the effects of mutations. *Nat. Methods* **15**, 816–822 (2018).

32. 32.

Suzek, B. E., Wang, Y., Huang, H., McGarvey, P. B. & Wu, C. H. UniRef clusters: a comprehensive and scalable alternative for improving sequence similarity searches. *Bioinformatics* **31**, 926–932 (2015).

33. 33.

Kalia, S. S. et al. Recommendations for reporting of secondary findings in clinical exome and genome sequencing, 2016 update (ACMG SF v2.0): a policy statement of the American College of Medical Genetics and Genomics. *Genet. Med.* **19**, 249–255 (2017).

34. 34.

Frigo, G. et al. Homozygous SCN5A mutation in Brugada syndrome with monomorphic ventricular tachycardia and structural heart abnormalities. *Europace* **9**, 391–397 (2007).

35. 35.

Itoh, H. et al. Asymmetry of parental origin in long QT syndrome: preferential maternal transmission of KCNQ1 variants linked to channel dysfunction. *Eur. J. Hum. Genet.* **24**, 1160–1166 (2016).

36. 36.

Glazer, A. M. et al. Deep mutational scan of an SCN5A voltage sensor. *Circ. Genom. Precis. Med.* **13**, e002786 (2020).

37. 37.

Bouvet, D. et al. Methylation tolerance-based functional assay to assess variants of unknown significance in the MLH1 and MSH2 genes and identify patients with Lynch syndrome. *Gastroenterology* **157**, 421–431 (2019).

38. 38.

Pan, X. et al. Structure of the human voltage-gated sodium channel Na_v1.4 in complex with β1. *Science* **362**, eaau2486 (2018).

39. 39.

Fishel, R. et al. The human mutator gene homolog MSH2 and its association with hereditary nonpolyposis colon cancer. *Cell* **75**, 1027–1038 (1993).

40. 40.

Peltomaki, P. Role of DNA mismatch repair defects in the pathogenesis of human cancer. *J. Clin. Oncol.* **21**, 1174-1179 (2003).

41. 41.

Warren, J. J. et al. Structure of the human MutSα DNA lesion recognition complex. *Mol. Cell* **26**, 579–592 (2007).

42. 42.

Brnich, S. E. et al. Recommendations for application of the functional evidence PS3/BS3 criterion using the ACMG/AMP sequence variant interpretation framework. *Genome Med.* **12**, 3 (2019).

43. 43.

Lewontin, R. C. *The Genetic Basis of Evolutionary Change* (Columbia Univ. Press, 1974).

44. 44.

Kreitman, M. Nucleotide polymorphism at the alcohol dehydrogenase locus of *Drosophila melanogaster*. *Nature* **304**, 412-417 (1983).

45. 45.

Sunyaev, S. et al. Prediction of deleterious human alleles. *Hum. Mol. Genet.* **10**, 591–597 (2001).

46. 46.

IUCN. The IUCN red list of threatened species. *IUCN* <https://www.iucnredlist.org> (2020).

Acknowledgements

We thank members of the Marks laboratory, OATML and C. Sander for many valuable discussions. J.F., M.D. and K.B. are supported by the Chan Zuckerberg Initiative CZI2018-191853. K.B. is also supported by the US National Institutes of Health (R01 R01GM120574). P.N. is supported by GSK and the UK Engineering and Physical Sciences Research Council (EPSRC ICASE award no. 18000077). A.G. is a Clarendon Scholar and Open Philanthropy AI Fellow. Y.G. holds a Turing AI Fellowship (Phase 1) at the Alan Turing Institute, which is supported by EPSRC grant reference V030302/1. D.S.M. holds a Ben Barres Early Career Award by the Chan Zuckerberg Initiative as part of the Neurodegeneration Challenge Network, CZI2018-191853.

Author information

Author notes

1. These authors contributed equally: Jonathan Frazer, Pascal Notin, Mafalda Dias

Affiliations

1. Marks Group, Department of Systems Biology, Harvard Medical School, Boston, MA, USA
Jonathan Frazer, Mafalda Dias, Joseph K. Min, Kelly Brock & Debora S. Marks
2. OATML Group, Department of Computer Science, University of Oxford, Oxford, UK
Pascal Notin, Aidan Gomez & Yarin Gal
3. Broad Institute of Harvard and MIT, Cambridge, MA, USA
Debora S. Marks

Contributions

D.S.M. and Y.G. led the research. J.F., P.N. and M.D. conceived and implemented the end-to-end approach. A.G. contributed technical advice. K.B. supported with data preparation. J.K.M. developed the website. J.F., P.N., M.D., Y.G. and D.S.M. wrote the manuscript.

Corresponding authors

Correspondence to Yarin Gal or Debora S. Marks.

Ethics declarations

Competing interests

The authors declare no competing interests.

Additional information

Peer review information *Nature* thanks Martin Kircher and the other, anonymous, reviewer(s) for their contribution to the peer review of this

work.

Publisher's note Springer Nature remains neutral with regard to jurisdictional claims in published maps and institutional affiliations.

Extended data figures and tables

Extended Data Fig. 1 Bayesian VAE architecture details.

The Bayesian VAE architecture in EVE is comprised of a symmetric 3-layer encoder & decoder architecture (with 2,000-1,000-300 and 300-1,000-2,000 units respectively) and a latent space of dimension 50. After performing a one-hot encoding of the input sequence across amino acids (zeros in white, ones in green), we flatten the input before performing the forward pass through the network. We use a single set of parameters for the encoder (ϕ_p) and learn a fully-factorized gaussian distribution over the weights of the decoder (θ_p): weight samples for the decoder are obtained by sampling a random normal variable (rnv), multiplying that sample by the standard deviation parameters, and subsequently adding the mean parameters. A one-dimensional convolution is applied on the un-flattened output of the decoder to capture potential correlations between amino-acid usage. Finally, a softmax activation turns the final output into probabilities over amino acids at each position of the sequence (low values in white, high values in dark green). The overall network is trained by maximizing the Evidence Lower Bound (ELBO), which forms a tractable lower bound to the log-marginal likelihood ([Supplementary Methods](#) and Fig. 1).

Extended Data Fig. 2 Comparison of performance of Bayesian VAE and DeepSequence against 38 deep mutation scans.

Comparison between the performance of the Bayesian VAE architecture in EVE and DeepSequence⁴⁶ which achieves state-of-the-art performance on the protein function prediction task. “Evolutionary indices” were computed by sampling 2k times from the approximate posterior distribution and by ensembling the obtained indices over 5 independently trained VAEs ([Supplementary Methods](#)).

Extended Data Fig. 3 Evolutionary index separates pathogenic and benign variants.

a, Average evolutionary index per protein, and corresponding standard deviations, for variants with known Benign and Pathogenic ClinVar labels across 3,219 proteins (sorted by alphabetical order). On the right, marginal distributions of the means over the 3,219 proteins. Evolutionary index separates pathogenic and benign labels consistently across proteins. **b**, Two-component Gaussian Mixture Models (GMM) over the distributions of the evolutionary indices (histograms) for all the single amino acid variants of 3,219 proteins combined (top, left) and for P53, PTEN and SCN5A separately (top right, bottom left and right, respectively). The dashed black line is the marginal likelihood for the GMM model, i.e. the likelihood of a variant sequence after marginalizing the latent variable that corresponds to the mixture assignment; the dashed blue and red lines represent the relative share of the marginal likelihood from the benign and pathogenic clusters respectively (*i.e.* the product of the marginal likelihood by each cluster).

Extended Data Fig. 4 EVE prediction for actionable genes and EVE comparison to other computational methods, including meta-predictors.

a, EVE AUCs versus ClinVar labels for set of ACMG “actionable genes”³³ that have 15 or more labels (shown in parentheses). AUCs are computed both for EVE scores of all variants (pale blue), and of the 75% variants with most confident scores (dark blue) ([Supplementary Methods](#)). **b**, Performance comparison of EVE to state-of-the-art computational variant effect predictors: 7 unsupervised, 8 supervised, and 8 supervised meta-prediction methods. Size of marker indicates how many genes for which the method would be relevant (on a per-protein basis validation) ([Supplementary Methods](#), [Supplementary Notes 2](#), Fig. 2, Supplementary Tables 3, 4).

Extended Data Fig. 5 Computational model EVE as good as high-throughput experiments for clinical labels.

(Companion to Fig. 3) **a**, Comparison of computational model predictions (upper panels EVE score) and experimental assay predictions (lower panels, experimental assay metric) to ClinVar labels (dots) and VUS (crosses) and where pale red and pale blue crosses indicate EVE assignments of VUS. Dashed red and blue lines correspond to EVE predictions after removing the 25% most uncertain variants (computed on all variants across all proteins; see [Supplementary Methods](#)). x-axes are position in protein. Experimental measurements data from deep mutational scans of P53¹⁴, from left (WT_Nutlin-3, A549_p53NULL_Nutlin-3, A549_p53NULL_Etoposide), SCN5A¹³, and BRCA1¹². **b**, Scatter plots of experiment scores (y-axis) against EVE scores (x-axis). Experimental measurements data from deep mutational scans same as **a** ([Supplementary Methods](#), Supplementary Table 6).

[Extended Data Fig. 6 Comparison of label policies, and comparison of EVE and experimental predictions of clinical labels.](#)

a, The y-axis is the subset of the ACMG actionable protein list with at least 5 benign and 5 pathogenic labels with at least a one-star review status in ClinVar, mean for the 3,219 proteins and mean for this subset. x-axis is AUCs computed using these labels (deep blue), labels with at least a two-star review status (light grey) and a more lenient labelling policy (sky blue), as defined in [Supplementary Methods](#). **b**, AUC of EVE predictions (blue circle) and experimental predictions (blue cross) computed on ClinVar labels. Whilst most of the papers that provide these experimental results refer to the goal of predicting association to human disease, the assays vary in their relevance to disease phenotype. Results use high-quality labels whenever they are sufficient for robust validation (MSH2, P53, BRCA1) and lenient labels for all other cases, and 2017-release ClinVar data whenever experimental results were used in defining labels reported in 2021 (P53 and BRCA1). Reported averages of all displayed AUC values, and of AUCs computed exclusively on 2017 and 2021-release high-quality labels ([Supplementary Methods](#), Supplementary Table 5,6).

Extended Data Fig. 7 EVE has many more genes that can be validated on, compared to supervised methods.

Mean number of genes, for EVE (dark blue) and a supervised method (light blue), that have sufficient labels for validation (5 (left), 10 (middle) and 20 labels (right)). We assume a 90% train 10% test random split of all labels in ClinVar for the supervised methods.

Extended Data Fig. 8 Data provided on our server evemodel.org.

Screenshot of evemodel.org for the example of KCNQ2. Our server provides information about each protein: aggregate AUC/Accuracy, performance curves (ROC & Precision-recall), variant-level EVE scores, classification and uncertainties, as well as the multiple sequence alignments used for training. All data is available to download both in bulk and for individual genes.

Extended Data Fig. 9 Fraction of genes per person with more than one variant.

Density function of the fraction of total genes per person with at least two variants, though not necessarily in the same chromosome. Data extracted from 50k genomes of the UK Biobank with self-reported ethnicity backgrounds ([Supplementary Methods](#)).

Extended Data Fig. 10 Performance as a function of alignment depth.

Average AUC of EVE scores as a function of N/L_{cov} for the subset of genes with at least 10 known clinical labels (5 benign and 5 pathogenic). For this subset of genes, the performance of the model can be carefully validated using AUCs. There is no strong correlation between alignment depth and performance: while models with very deep alignments tend to have good performance, models with very low N/L_{cov} can also have AUC close to 1.

Supplementary information

Supplementary Information

This file contains Supplementary Methods, Supplementary Note 1 on the limitations of supervised modeling methods and Supplementary Note 2 with comments on meta-predictors.

Reporting Summary

Supplementary Table 1

Statistics of multiple sequence alignments used in training.

Supplementary Table 2

Summary of class assignments and combination with other sources of evidence.

Supplementary Table 3

Comparison of performance of EVE and other computational models at predicting ClinVar labels.

Supplementary Table 4

Comparison of performance of EVE and other computational models at predicting results from high-throughput functional assays.

Supplementary Table 5

Sensitivity of predictions to label policy.

Supplementary Table 6

Comparison of performance of high-throughput experiments and EVE at predicting clinical labels.

Supplementary Table 7

Genes with at least 10 labels sorted by EVE performance.

Supplementary Table 8

Variants for which there is disagreement between EVE predictions and ClinVar labels.

Supplementary Table 9

All pairs of variants occurring in the same gene over the UK biobank population for the actionable genes defined by ACMG.

Source data

Source Data Fig. 2

Source Data Fig. 3

Source Data Fig. 4

Rights and permissions

Reprints and Permissions

About this article

Cite this article

Frazer, J., Notin, P., Dias, M. *et al.* Disease variant prediction with deep generative models of evolutionary data. *Nature* **599**, 91–95 (2021).

<https://doi.org/10.1038/s41586-021-04043-8>

- Received: 18 December 2020
- Accepted: 20 September 2021
- Published: 27 October 2021
- Issue Date: 04 November 2021
- DOI: <https://doi.org/10.1038/s41586-021-04043-8>

Share this article

Anyone you share the following link with will be able to read this content:

[Get shareable link](#)

Sorry, a shareable link is not currently available for this article.

[Copy to clipboard](#)

Provided by the Springer Nature SharedIt content-sharing initiative

This article was downloaded by **calibre** from <https://www.nature.com/articles/s41586-021-04043-8>

| [Section menu](#) | [Main menu](#) |

- Article
- [Published: 06 October 2021](#)

5-HT modulation of a medial septal circuit tunes social memory stability

- [Xiaoting Wu](#)¹,
- [Wade Morishita](#)¹,
- [Kevin T. Beier](#) [ORCID: orcid.org/0000-0002-4934-1338](#)²,
- [Boris D. Heifets](#) [ORCID: orcid.org/0000-0003-1474-0379](#)³ &
- [Robert C. Malenka](#) [ORCID: orcid.org/0000-0002-5428-5211](#)¹

Nature volume **599**, pages 96–101 (2021)

- 5630 Accesses
- 100 Altmetric
- [Metrics details](#)

Subjects

- [Hippocampus](#)
- [Social behaviour](#)

Abstract

Social memory—the ability to recognize and remember familiar conspecifics—is critical for the survival of an animal in its social group^{1,2}. The dorsal CA2 (dCA2)^{3,4,5} and ventral CA1 (vCA1)⁶ subregions of the

hippocampus, and their projection targets^{6,7}, have important roles in social memory. However, the relevant extrahippocampal input regions remain poorly defined. Here we identify the medial septum (MS) as a dCA2 input region that is critical for social memory and reveal that modulation of the MS by serotonin (5-HT) bidirectionally controls social memory formation, thereby affecting memory stability. Novel social interactions increase activity in dCA2-projecting MS neurons and induce plasticity at glutamatergic synapses from MS neurons onto dCA2 pyramidal neurons. The activity of dCA2-projecting MS cells is enhanced by the neuromodulator 5-HT acting on 5-HT_{1B} receptors. Moreover, optogenetic manipulation of median raphe 5-HT terminals in the MS bidirectionally regulates social memory stability. This work expands our understanding of the neural mechanisms by which social interactions lead to social memory and provides evidence that 5-HT has a critical role in promoting not only prosocial behaviours^{8,9}, but also social memory, by influencing distinct target structures.

Access options

Subscribe to Journal

Get full journal access for 1 year

\$199.00

only \$3.90 per issue

[Subscribe](#)

All prices are NET prices.

VAT will be added later in the checkout.

Tax calculation will be finalised during checkout.

Rent or Buy article

Get time limited or full article access on ReadCube.

from \$8.99

[Rent or Buy](#)

All prices are NET prices.

Additional access options:

- [Log in](#)
- [Access through your institution](#)
- [Learn about institutional subscriptions](#)

Fig. 1: Chemogenetic manipulation of the MS bidirectionally regulates social memory.

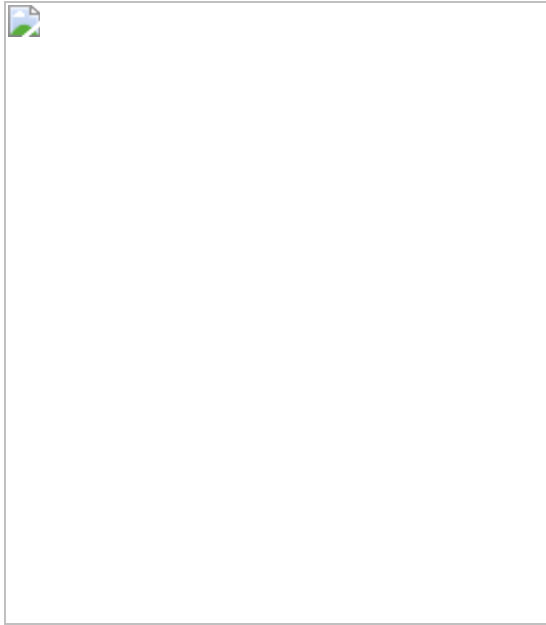


Fig. 2: Inhibition of MS to dorsal CA2 projection disrupts social memory.

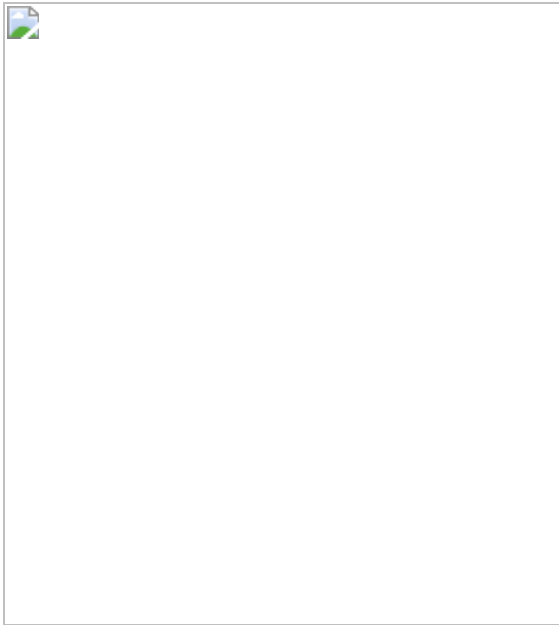


Fig. 3: Glutamatergic inputs from the MS to dCA2 have a crucial role in social memory formation.

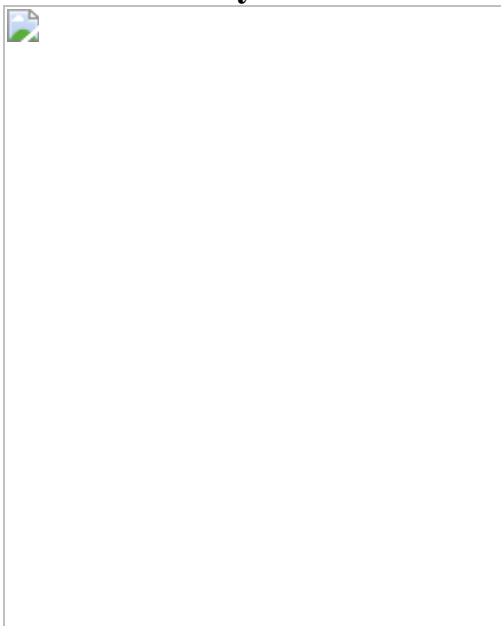


Fig. 4: Bidirectional modulation of social memory by MS 5-HT_{1B} receptors.

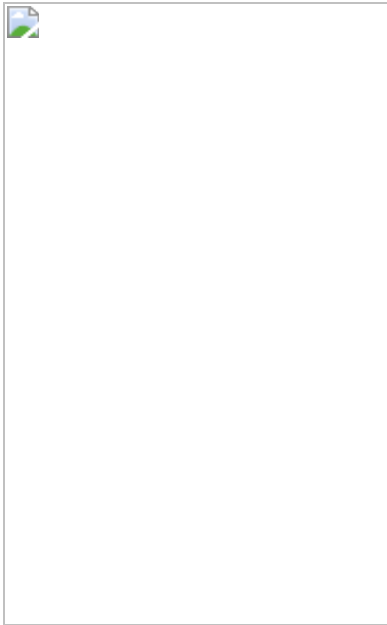
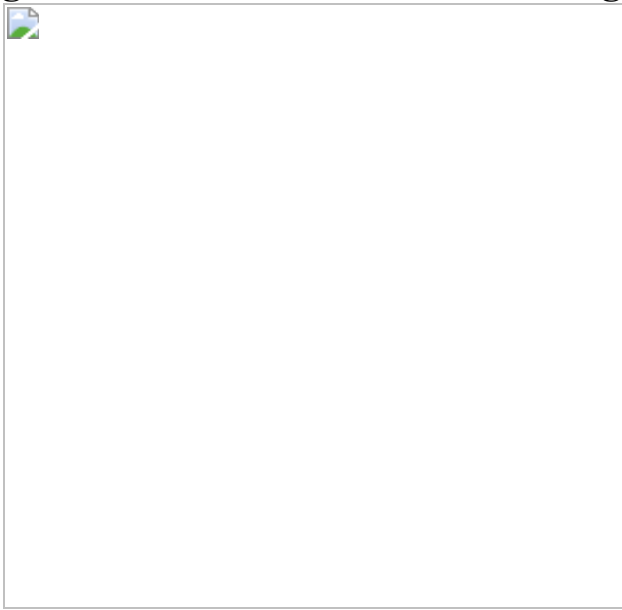


Fig. 5: MR 5-HT release in the MS regulates social memory.



Data availability

The datasets generated and analysed during this study are included in this published article and its supplementary information files. Any additional data generated during and/or analysed during this study are available from the corresponding author upon reasonable request. [Source data](#) are provided with this paper.

Code availability

Code used for data processing and analysis is available from the corresponding author upon reasonable request. The MATLAB code used for analyses of fibre photometry data is provided as a supplementary file.

References

1. 1.

McGraw, L. A. & Young, L. J. The prairie vole: an emerging model organism for understanding the social brain. *Trends Neurosci.* **33**, 103–109 (2010).

2. 2.

Okuyama, T. Social memory engram in the hippocampus. *Neurosci. Res.* **129**, 17–23 (2018).

3. 3.

Hitti, F. L. & Siegelbaum, S. A. The hippocampal CA2 region is essential for social memory. *Nature* **508**, 88–92 (2014).

4. 4.

Leroy, F., Brann, D. H., Meira, T. & Siegelbaum, S. A. Input-timing-dependent plasticity in the hippocampal CA2 region and its potential role in social memory. *Neuron* **95**, 1089–1102 (2017).

5. 5.

Meira, T. et al. A hippocampal circuit linking dorsal CA2 to ventral CA1 critical for social memory dynamics. *Nat. Commun.* **9**, 4163 (2018).

6. 6.

Okuyama, T., Kitamura, T., Roy, D. S., Itohara, S. & Tonegawa, S. Ventral CA1 neurons store social memory. *Science* **353**, 1536–1541 (2016).

7. 7.

Phillips, M. L., Robinson, H. A. & Pozzo-Miller, L. Ventral hippocampal projections to the medial prefrontal cortex regulate social memory. *Elife* **8**, e44182 (2019).

8. 8.

Walsh, J. J. et al. 5-HT release in nucleus accumbens rescues social deficits in mouse autism model. *Nature* **560**, 589–594 (2018).

9. 9.

Heifets, B. D. et al. Distinct neural mechanisms for the prosocial and rewarding properties of MDMA. *Sci Transl Med* **11**, eaaw6435 (2019).

10. 10.

Chiang, M. C., Huang, A. J. Y., Wintzer, M. E., Ohshima, T. & McHugh, T. J. A role for CA3 in social recognition memory. *Behav. Brain Res.* **354**, 22–30 (2018).

11. 11.

Leroy, F. et al. A circuit from hippocampal CA2 to lateral septum disinhibits social aggression. *Nature* **564**, 213–218 (2018).

12. 12.

Chandler, J. P. & Crutcher, K. A. The septohippocampal projection in the rat: an electron microscopic horseradish peroxidase study. *Neuroscience* **10**, 685–696 (1983).

13. 13.

Buzsaki, G. Theta oscillations in the hippocampus. *Neuron* **33**, 325–340 (2002).

14. 14.

Kaifosh, P., Lovett-Barron, M., Turi, G. F., Reardon, T. R. & Losonczy, A. Septo-hippocampal GABAergic signaling across multiple modalities in awake mice. *Nat. Neurosci.* **16**, 1182–1184 (2013).

15. 15.

Ciabatti, E., Gonzalez-Rueda, A., Mariotti, L., Morgese, F. & Tripodi, M. Life-long genetic and functional access to neural circuits using self-inactivating rabies virus. *Cell* **170**, 382–392 (2017).

16. 16.

Sans-Dublanc, A. et al. Septal GABAergic inputs to CA1 govern contextual memory retrieval. *Sci. Adv.* **6**, aba5003 (2020).

17. 17.

Zhang, G. W. et al. Transforming sensory cues into aversive emotion via septal-habenular pathway. *Neuron* **99**, 1016–1028 (2018).

18. 18.

Zhang, G. W. et al. A non-canonical reticular-limbic central auditory pathway via medial septum contributes to fear conditioning. *Neuron* **97**, 406–417 (2018).

19. 19.

Papouin, T., Dunphy, J. M., Tolman, M., Dineley, K. T. & Haydon, P. G. Septal cholinergic neuromodulation tunes the astrocyte-dependent gating of hippocampal NMDA receptors to wakefulness. *Neuron* **94**, 840–854 (2017).

20. 20.

Meng, X. et al. Manipulations of MeCP2 in glutamatergic neurons highlight their contributions to Rett and other neurological disorders. *Elife* **5**, e14199 (2016).

21. 21.

Kauer, J. A. & Malenka, R. C. Synaptic plasticity and addiction. *Nat. Rev. Neurosci.* **8**, 844–858 (2007).

22. 22.

Sharma, K. et al. Sexually dimorphic oxytocin receptor-expressing neurons in the preoptic area of the mouse brain. *PLoS One* **14**, e0219784 (2019).

23. 23.

Cloez-Tayarani, I. et al. Autoradiographic characterization of [³H]-5-HT-moduline binding sites in rodent brain and their relationship to 5-HT_{1B} receptors. *Proc. Natl Acad. Sci. USA* **94**, 9899–9904 (1997).

24. 24.

Elvander-Tottie, E., Eriksson, T. M., Sandin, J. & Ogren, S. O. 5-HT_{1A} and NMDA receptors interact in the rat medial septum and modulate hippocampal-dependent spatial learning. *Hippocampus* **19**, 1187–1198 (2009).

25. 25.

Sari, Y. Serotonin_{1B} receptors: from protein to physiological function and behavior. *Neurosci. Biobehav. Rev.* **28**, 565–582 (2004).

26. 26.

Leranth, C. & Vertes, R. P. Median raphe serotonergic innervation of medial septum/diagonal band of broca (MSDB) parvalbumin-containing neurons: possible involvement of the MSDB in the desynchronization of the hippocampal EEG. *J. Comp. Neurol.* **410**, 586–598 (1999).

27. 27.

Schwarz, L. A. et al. Viral-genetic tracing of the input-output organization of a central noradrenaline circuit. *Nature* **524**, 88–92 (2015).

28. 28.

Jiang, M. et al. Conditional ablation of neuroligin-1 in CA1 pyramidal neurons blocks LTP by a cell-autonomous NMDA receptor-independent mechanism. *Mol. Psychiatry* **22**, 375–383 (2017).

29. 29.

Bariselli, S. et al. Role of VTA dopamine neurons and neuroligin 3 in sociability traits related to nonfamiliar conspecific interaction. *Nat. Commun.* **9**, 3173 (2018).

30. 30.

Etherton, M. et al. Autism-linked neuroligin-3 R451C mutation differentially alters hippocampal and cortical synaptic function. *Proc. Natl Acad. Sci. USA* **108**, 13764–13769 (2011).

31. 31.

Wu, X. et al. Neuroligin-1 signaling controls LTP and NMDA receptors by distinct molecular pathways. *Neuron* **102**, 621–635 (2019).

32. 32.

Bunin, M. A. & Wightman, R. M. Quantitative evaluation of 5-hydroxytryptamine (serotonin) neuronal release and uptake: an investigation of extrasynaptic transmission. *J. Neurosci.* **18**, 4854–4860 (1998).

33. 33.

Jennings, K. A. A comparison of the subsecond dynamics of neurotransmission of dopamine and serotonin. *ACS Chem. Neurosci.* **4**, 704–714 (2013).

34. 34.

Liu, C., Goel, P. & Kaeser, P. S. Spatial and temporal scales of dopamine transmission. *Nat. Rev. Neurosci.* **22**, 345–358 (2021).

35. 35.

Nelson, R. J. & Trainor, B. C. Neural mechanisms of aggression. *Nat. Rev. Neurosci.* **8**, 536–546 (2007).

36. 36.

Nautiyal, K. M. et al. Distinct circuits underlie the effects of 5-HT_{1B} receptors on aggression and impulsivity. *Neuron* **86**, 813–826 (2015).

37. 37.

Okaty, B. W. et al. Multi-scale molecular deconstruction of the serotonin neuron system. *Neuron* **88**, 774–791 (2015).

38. 38.

Jensen, P. et al. Redefining the serotonergic system by genetic lineage. *Nat. Neurosci.* **11**, 417–419 (2008).

39. 39.

Baskin, B. M., Mai, J. J., Dymecki, S. M. & Kantak, K. M. Cocaine reward and memory after chemogenetic inhibition of distinct serotonin neuron subtypes in mice. *Psychopharmacology* **237**, 2633–2648 (2020).

40. 40.

Senft, R. A., Freret, M. E., Sturrock, N. & Dymecki, S. M. Neurochemically and hodologically distinct ascending VGLUT3 versus serotonin subsystems comprise the r2-*Pet1* median raphe. *J. Neurosci.* **41**, 2581–2600 (2021).

41. 41.

Ferguson, J. N. et al. Social amnesia in mice lacking the oxytocin gene. *Nat. Genet.* **25**, 284–288 (2000).

42. 42.

Raam, T., McAvoy, K. M., Besnard, A., Veenema, A. H. & Sahay, A. Hippocampal oxytocin receptors are necessary for discrimination of social stimuli. *Nat. Commun.* **8**, 2001 (2017).

43. 43.

Allen, W. E. et al. Thirst-associated preoptic neurons encode an aversive motivational drive. *Science* **357**, 1149–1155 (2017).

44. 44.

Beier, K. T. et al. Circuit architecture of VTA dopamine neurons revealed by systematic input-output mapping. *Cell* **162**, 622–634 (2015).

45. 45.

Kremer, E. J., Boutin, S., Chillon, M. & Danos, O. Canine adenovirus vectors: an alternative for adenovirus-mediated gene transfer. *J. Virol.* **74**, 505–512 (2000).

46. 46.

Hung, L. W. et al. Gating of social reward by oxytocin in the ventral tegmental area. *Science* **357**, 1406–1411 (2017).

47. 47.

Ferguson, J. N., Young, L. J. & Insel, T. R. The neuroendocrine basis of social recognition. *Front. Neuroendocrinol.* **23**, 200–224 (2002).

48. 48.

Cunningham, C. L., Gremel, C. M. & Groblewski, P. A. Drug-induced conditioned place preference and aversion in mice. *Nat. Protoc.* **1**, 1662–1670 (2006).

49. 49.

Wang, F. et al. RNAscope: a novel in situ RNA analysis platform for formalin-fixed, paraffin-embedded tissues. *J. Mol. Diagn.* **14**, 22–29 (2012).

50. 50.

Cardozo Pinto, D. F. et al. Characterization of transgenic mouse models targeting neuromodulatory systems reveals organizational principles of the dorsal raphe. *Nat. Commun.* **10**, 4633 (2019).

Acknowledgements

This work was supported by philanthropic funds donated to the Nancy Pritzker Laboratory at Stanford University. X.W. was supported by a NIH K99 Career Development Award (MH122697). K.T.B. was supported by NIH grant DP2 AG067666. B.D.H. was supported by a NIH K08 Career Development Award (MH110610). We thank B. S. Bentzley for providing assistance with the fear conditioning experiments; P. A. Neumann and S. R. Golf for providing mouse breeding pairs; and members of the Malenka

laboratory for discussions. Extended Data Fig. 10 schematic by Sci Stories, LLC.

Author information

Affiliations

1. Nancy Pritzker Laboratory, Department of Psychiatry and Behavioral Sciences, Stanford University, Stanford, CA, USA

Xiaoting Wu, Wade Morishita & Robert C. Malenka

2. Department of Physiology and Biophysics, University of California, Irvine, Irvine, CA, USA

Kevin T. Beier

3. Department of Anesthesiology, Perioperative and Pain Medicine, Stanford University, Stanford, CA, USA

Boris D. Heifets

Contributions

X.W. conceived the study and performed the majority of experiments. X.W. and R.C.M. designed the experiments, interpreted the results and wrote the paper, which was edited by all authors. W.M. and X.W. performed the ex vivo electrophysiology experiments. K.T.B. prepared and provided Flp-expressing rabies virus. B.D.H. contributed to the design and analysis of fibre photometry experiments, including hardware configuration and creating analysis scripts in MATLAB.

Corresponding author

Correspondence to Robert C. Malenka.

Ethics declarations

Competing interests

All protocols used during this study are freely available for non-profit use from the corresponding author upon reasonable request. R.C.M. is on the scientific advisory boards of MapLight Therapeutics and MindMed.

Additional information

Peer review information *Nature* thanks Susan Dymecki and the other, anonymous, reviewer(s) for their contribution to the peer review of this work.

Publisher's note Springer Nature remains neutral with regard to jurisdictional claims in published maps and institutional affiliations.

Extended data figures and tables

[Extended Data Fig. 1 MS cells show increased cFOS after a social experience.](#)

a, Schematic of experimental timeline, 4-OHT was administered via intraperitoneal injection. **b**, Quantification of tdTomato-positive cells in the median raphe (MR: $F_{2,12} = 4.681, P = 0.0314$), paraventricular nucleus of the hypothalamus (PVH: $F_{2,11} = 3.446, P = 0.0689$), nucleus of the diagonal band (NDB: $F_{2,12} = 4.423, P = 0.0364$), medial septum (MS: $F_{2,12} = 13.31, P = 0.0009$), lateral septum (LS: $F_{2,12} = 4.14, P = 0.0429$) in the social ($n = 7$), object ($n = 5$) and control ($n = 3$) conditions. Representative images of MS expressing tdTomato. Scale bar, 200 μm (right). **c**, Quantification of tdTomato-positive cells in the ventral CA1 (vCA1: $F_{2,8} = 1.478, P = 0.2842$) in social ($n = 5$), object ($n = 3$) and control ($n = 3$) conditions. **d**, Quantification of tdTomato-positive cells in the dorsal CA2 (dCA2: $F_{2,9} = 5.367, P = 0.0292$) in social ($n = 5$), object ($n = 4$) and control ($n = 3$)

conditions. Representative images of dCA2 expressing tdTomato. Scale bar, 200 μ m (right). **e**, Schematic of monosynaptic tracing experiment. **f**, Representative images of injection site in the dorsal hippocampus and presynaptic labelling in the MS (left), injection site in the ventral hippocampus and presynaptic labelling in the MS (right). Scale bar, 200 μ m, $n = 3$. **g**, Schematic of anterograde tracing experiment. **h**, Representative images of injection site in the MS (left) and axon terminals in the dorsal and ventral hippocampus (right). Statistical tests: **b–d**, One-way ANOVA with Tukey's post-hoc test, N.S. = not significant, * $P < 0.05$, ** $P < 0.01$, *** $P < 0.001$ (left). Scale bar, 200 μ m, $n = 3$. Error bars denote s.e.m.

[Source data](#)

[**Extended Data Fig. 2 Chemogenetic manipulation of the MS does not affect sociability and object memory.**](#)

a, Representative traces of subjects during three-chamber social memory test. **b**, Duration in chamber with novel object (no) or novel mouse (nm) (left) and discrimination scores (right) ($F_{2,40} = 0.2875$, $P = 0.7517$; mCh: $n = 19$, hM4Di: $n = 12$). **c**, Duration in chamber with familiar object (fo) or no (left) and discrimination scores (right) ($F_{2,40} = 0.04521$, $P = 0.9558$; mCh: $n = 19$, hM4Di: $n = 12$). **d**, Schematic and representative image of MS injection site showing hM3Dq expression. $n = 10$. Scale bar, 500 μ m. **e**, Duration in chamber with fm or nm (left) and discrimination scores (right) ($F_{2,27} = 6.689$, $P = 0.0044$, $n = 10$). **f**, Duration with no or nm (left) and discrimination scores (right) ($t_9 = 0.2358$, $P = 0.8189$; $n = 10$). **g**, Duration with familiar object (fo) or no (left) and discrimination scores (right) ($F_{2,27} = 0.3243$, $P = 0.9681$; $n = 10$). **h**, Schematic and representative image of hM4Di expression in the MS. $n = 8$. Scale bar, 500 μ m. **i**, Individual subjects from Fig. 1j. Statistical tests: **b, c, e, f, g**, duration: two-tailed paired Student's *t*-test. **b, c, e, g**, Discrimination scores: one-way ANOVA with Tukey's post-hoc test. **f**, Discrimination scores: two-tailed paired Student's *t*-test. N.S. = not significant, * $P < 0.05$, ** $P < 0.01$, *** $P < 0.001$. Error bars denote s.e.m.

[Source data](#)

Extended Data Fig. 3 Optogenetic MS cell body and chemogenetic terminal inhibition do not affect sociability and object memory.

a, Schematic of experimental set-up (left) and representative image of MS injection site showing NpHR expression (right). $n = 10$. Scale bar, 500 μm . **b**, Duration in chamber with no or nm (left) and discrimination scores (right) ($t_{18} = 0.9531$, $P = 0.3532$; $n = 10$). **c**, Duration in chamber with fo or no (left) and discrimination scores (right) ($t_{18} = 0.1348$, $P = 0.8943$; $n = 10$). **d**, Schematic of experimental set-up (left) and representative images of MS injection sites showing hM4Di expression and cannula implant sites (right). $n = 13$. Scale bar, 500 μm . **e**, Duration in chamber with no or nm (left) and discrimination scores (right) ($t_{26} = 0.2453$, $P = 0.8081$; mCh: $n = 15$, hM4Di: $n = 13$). **f**, Duration in chamber with fo or no (left) and discrimination scores (right) ($t_{22} = 0.6383$, $P = 0.5298$; $n = 12$). All data were assessed by two-tailed unpaired Student's t -test. N.S. = not significant, * $P < 0.05$, *** $P < 0.001$. Error bars denote s.e.m.

[Source data](#)

Extended Data Fig. 4 Inhibition of dCA2-projecting MS neurons has no effect on sociability, object memory, contextual fear memory and conditioned place preference.

a, Schematic of experimental set-up (left). Duration in chamber with fm or nm (middle) and discrimination scores (right) (hM4Di: $P = 0.5135$; female mCh: $n = 11$, hM4Di: $n = 10$, male mCh: $n = 4$, hM4Di: $n = 5$). **b**, Duration in chamber with no or nm (left) and discrimination scores (right) ($F_{2,42} = 0.4013$, $P = 0.6721$; $n = 15$, hM4Di+saline: $n = 14$). **c**, Duration with fo or no (left) and discrimination scores (right) ($t_{27} = 0.1384$, $P = 0.891$; mCh: $n = 15$, hM4Di: $n = 14$). **d**, Schematic of experimental set-up (top) and quantification of the percent freezing during shock and recall (bottom left) and fold increase in freezing time (bottom right) ($P = 0.2671$; $n = 15$). **e**,

Schematic of experimental set-up (top), quantification of the percent time spent on each surface after CNO and saline pairing (bottom left) and discrimination scores (bottom right) ($t_{28} = 0.2619$, $P = 0.7953$; $n = 15$). **f**, Schematic of virus injection, left. Representative images of MS injection site as well as the labelled axon in the dCA2, ventral CA1 (vCA1) and supramammillary nucleus (SUM), right ($n = 3$, scale bars = 500 μm above and 200 μm below; arrows point to mRuby puncta. Statistical tests: **a**, two-tailed Mann-Whitney test. **b**, **c**, Duration: two-tailed paired Student's *t*-test. **b**, Discrimination score: one-way ANOVA with Tukey's post-hoc test **c**, **e**, Discrimination scores: two-tailed unpaired Student's *t*-test. **d**, % freezing: Kruskal-Wallis with post-hoc Dunn's test, fold-increase in freezing: two-tailed Mann-Whitney test. **e**, % time on one side: one-way ANOVA with Tukey's post-hoc test. N.S. = not significant. * $P < 0.05$, ** $P < 0.01$, *** $P < 0.001$. Error bars denote s.e.m.

Source data

Extended Data Fig. 5 dCA2-projecting MS cells are primarily cholinergic and glutamatergic.

a, Schematic of monosynaptic rabies tracing set-up in *Amigo2-Cre* mice (left) and representative images of injection site in the dCA2 as well as *Gfp*-positive cells in the MS (right). Scale bar, 200 μm , $n = 3$. **b**, Representative images of *in-situ* hybridization. Scale bar, 200 μm (upper left panel), 40 μm . **c**, Quantification of *in-situ* hybridization, $n = 3$ subjects. **d**, Quantification of same *in-situ* hybridization data for percent of *Gfp*-positive cells colocalizing with *Chat* only, *Slc17a6* only, *Gad2* only or double-positive for *Slc17a6* and *Chat*, *Gad2* and *Chat* (right), $n = 3$ subjects. **e**, Quantification of colocalization with GFP-positive cells via immunohistochemistry (IHC) using either CHAT or CaMKII antibodies (left) and representative images (right, scale bar, 40 μm , $n = 3$). **f**, Schematic of experimental set-up and representative image of dCA2 infusion site filled with ink. **g**, Duration in chamber with no or nm (left) and discrimination scores (right) ($F_{2,36} = 1.702$, $P = 0.1967$; $n = 13$). **h**, Duration in chamber with fo or no (left) and discrimination scores (right) ($F_{2,36} = 3.259$, $P = 0.05$; $n = 13$). Statistical tests: **g**, **h**, duration: two-tailed paired Student's *t*-test; discrimination

scores: one-way ANOVA with Tukey's post-hoc test. N.S. = not significant, * $P < 0.05$, ** $P < 0.01$, *** $P < 0.001$. Error bars denote s.e.m.

[Source data](#)

Extended Data Fig. 6 MS synapses onto dCA2 pyramidal neurons are primarily glutamatergic and can express long-term depression ex vivo.

a, Top, pie charts of percentage of cells, in which the ChETA ($n = 20/9$) and ChR2 ($n = 22/6$) induced PSCs were >60% reduced by NBQX (10 μ M), picrotoxin (50 μ M) or Mecamylamine (5 μ M). Below, summary time course of ChETA-evoked PSCs from tdTomato-positive dCA2 pyramidal neurons, which were completely blocked (>90%) by bath-application of NBQX ($n = 13$). **b**, Representative traces of PSCs evoked by paired-pulse MS input activation in slices prepared from *Amigo2-Cre* mice exposed to a novel object or novel mouse (social). Scale bars, 50 pA, 100 ms. Quantification of paired-pulse ratios for mice (below) interacting with a novel object ($n = 17/3$, cells/mice) or novel mouse ($n = 24/4$) ($t_{39} = 1.589$, $P = 0.1201$), two-tailed unpaired Student's *t*-test. N.S. = not significant. **c**, Representative EPSCs from tdTomato-positive dCA2 pyramidal neurons before and after LTD induction protocol. Scale bars, 25 pA, 100 ms. Summary time-course of EPSCs with and without listed receptor antagonists in bath. With inhibitors: $n = 8/4$, without inhibitors: $n = 6/3$. **d**, Representative image of MS ChR2 injection site (above) and optical fibre implant site in the dCA2 (below). $n = 10$. Scale bars, 500 μ m. Error bars denote s.e.m.

[Source data](#)

Extended Data Fig. 7 Effects of in vivo optogenetic low frequency stimulation to induce LTD at MS to dCA2 synapses on sociability, social memory and object memory.

a, b, Duration in chambers with fm or nm (left) and discrimination scores (right), LTD stimulation (1 Hz for 10 min) was performed prior to sociability test, (**a**: $t_{13} = 2.898$, $P = 0.0125$; off: $n = 15$, 1 Hz: $n = 14$. **b**: $t_9 =$

0.9806, $P = 0.3524$; $n = 10$). **c, d**, Duration in chamber with no or nm, left and discrimination scores (right) in ChR2 and eYFP mice, LTD stimulation (1 Hz for 5 min) was performed after sociability test (**c**: $t_9 = 0.3201$, $P = 0.7563$; $n = 10$, **d**: $t_9 = 0.6328$, $P = 0.5426$; $n = 10$). **e**, Duration with fo or no (left) and discrimination scores (right) ($t_9 = 0.09968$, $P = 0.9228$; $n = 10$) in ChR2 mice. **f, g**, Duration in chamber with no or nm, left and discrimination scores (right) in ChR2 and eYFP mice (**f**: $t_{13} = 0.7717$, $P = 0.4540$; $n = 14$, **g**: $t_9 = 1.208$, $P = 0.2577$; $n = 10$). **h**, Duration with fo or no (left) and discrimination scores (right) ($t_{13} = 0.6186$, $P = 0.5469$; $n = 14$) in ChR2 mice. Two-tailed paired Student's t -test was performed on all data. N.S. = not significant, * $P < 0.05$, ** $P < 0.01$, *** $P < 0.001$. Error bars denote s.e.m.

Source data

Extended Data Fig. 8 Effects of CP93129 on dCA2-projecting MS neurons.

a, Sociability is not affected by MS infusion of indicated drugs. Duration in chamber with no or nm (left) and discrimination scores (right) ($F_{5,78} = 0.3144$, $P = 0.9029$; $n = 14$). **b**, Pie chart summarizing postsynaptic responses of EGFP-positive cells in CP93129 (2 or 5 μ M, $n = 42$). **c**, Pie chart illustrating action potential (AP) firing changes in CP93129 (left, $n = 15$). Representative traces -/+ CP93129 (right). V_m refers to unclamped resting membrane potential. Scale bars, 25 mV, 100 ms. **d**, Effects of CP93129 on MS neurons projecting to dCA2. Number of cells per current are indicated in parentheses ($t_{25} = 3.461$, $P = 0.002$; $n = 26$) (NOCHG, no change). **e**, Quantification of action potential firing as function of current injection for dCA2-projecting MS neurons with increased firing in CP93129 ($P = 0.001$; $n = 10$). **f**, Summary time course of IPSC responses in D-AP5 and NBQX with a pipette solution comprising CsMeSO₄+CsCl. Representative traces above shown at indicated time points. Scale bars, 100 pA, 50 ms, $n = 5/2$. **g**, Summary time course of EPSC responses in picrotoxin while recording with a pipette solution comprising CsMeSO₄. Representative traces above shown at indicated time points. Scale bars, 50

pA, 10 ms, $n = 5/3$. **h**, Amplitudes of IPSCs ($t_4 = 0.0285, P = 0.979, n = 5$) and EPSCs ($t_4 = 0.593, P = 0.585, n = 5$) averaged over the last 5 min of recording as a percentage of the first 3 min of baseline recording. **i, j**, Corresponding input resistance measurements for cells shown in **f** and **g**. **k**, R_N of IPSC ($t_4 = 0.058, P = 0.957, n = 5$) and EPSC ($t_4 = -1.409, P = 0.232, n = 5$) recordings averaged over the last 5 min of recording as a percentage of the first 3 min of baseline recording. **l**, Recordings of spontaneous inhibitory postsynaptic currents (sIPSCs) from EGFP-positive cells before and after bath-application of CP93129 (CP). Cumulative probability plot of sIPSC amplitudes with representative traces (above, scale bars, 15 pA, 15 ms, $n = 9/6$ (cells/mice)). Bar graph shows effect of CP93129 on mean IPSC amplitude. **m**, Cumulative probability plot of sIPSC inter-event intervals with representative traces (above, scale bars, 50 pA, 0.5 s, $n = 9/6$). Bar graph shows effect of CP93129 on mean IPSC frequency. Statistical tests: **a**, duration: two-tailed paired Student's *t*-test; discrimination scores: one-way ANOVA with Tukey's post-hoc test. **d, h, k**, Two-tailed paired Student's *t*-test. **e**, Repeated measures two-way ANOVA with Sidak's multiple comparison post-hoc test. **l, m**, Two-tailed Wilcoxon signed rank test. N.S. = not significant, * $P < 0.05$, ** $P < 0.01$, *** $P < 0.001$. Error bars and shading denote s.e.m.

Source data

Extended Data Fig. 9 Optogenetic inhibition or excitation of 5-HT inputs in the MS does not alter sociability and object memory.

a, Schematic of virus injection (left) and representative images of the injection site in the median raphe (MR) on the left and the EGFP-positive axons in the MS (right). $n = 5$. **b**, Schematic of virus injections to perform TRIO (left) and representative images of the injection site in the MS and the GFP-positive cells in the MR (right). $n = 3$. Scale bars = 500 μ m. **c, d**, Duration in chamber with no or nm (left) and discrimination scores (right) (**c**: $t_9 = 1.834; P = 0.0998; n = 10$. **d**: $P = 0.3750; n = 10$). **e, f**, Duration in chamber with fo or no (left) and discrimination scores (right) (**e**: $t_9 = 0.2418, P = 0.8143; n = 10$. **f**: $t_8 = 0.6029, P = 0.5632, n = 9$). **g, h**, Duration

in chamber with no or nm (left) and discrimination scores (right) (**g**: $t_{10} = 0.9294, P = 0.3746; n = 11$. **h**: $t_9 = 1.518, P = 0.1633; n = 10$). **i**, Duration in chamber with no or nm (left) and discrimination scores (right) ($t_{11} = 1.52, P = 0.152$; saline: $n = 12$, CP93129: $n = 14$). Statistical tests: **d**, eYFP on duration and discrimination score: two-tailed Wilcoxon signed rank test. All other data in this figure were analysed by two-tailed paired Student's *t*-test. N.S. = not significant, * $P < 0.05$, ** $P < 0.01$, *** $P < 0.001$. Error bars denote s.e.m.

[Source data](#)

[Extended Data Fig. 10 Model illustrating 5-HT action on dCA2-projecting MS neurons.](#)

During a novel social encounter, 5-HT diffuses away from its release sites to bind to 5-HT_{1B}Rs on the terminals of MS GABAergic interneurons thereby inhibiting GABA release onto the dCA2-projecting glutamatergic MS neurons. 5-HT also can bind to 5-HT_{1B}Rs on presynaptic glutamatergic terminals to inhibit glutamate release but a smaller proportion of glutamatergic inputs express 5-HT_{1B}Rs. The net effect of 5-HT is to reduce local inhibition of dCA2-projecting MS neurons to a greater extent than its reduction of excitatory drive, thereby resulting in increased activity in these neurons. The question mark indicates that there may also be a direct effect of 5-HT on dCA2-projecting MS neurons. The inset on the right depicts the circuitry investigated in this study from the median raphe (MR) to the medial septum (MS) to dorsal CA2 (dCA2).

Supplementary information

[Matlab code](#)

[Reporting Summary](#)

Source data

[**Source Data Fig. 1**](#)

[**Source Data Fig. 2**](#)

[**Source Data Fig. 3**](#)

[**Source Data Fig. 4**](#)

[**Source Data Fig. 5**](#)

[**Source Data Extended Data Fig. 1**](#)

[**Source Data Extended Data Fig. 2**](#)

[**Source Data Extended Data Fig. 3**](#)

[**Source Data Extended Data Fig. 4**](#)

[**Source Data Extended Data Fig. 5**](#)

[**Source Data Extended Data Fig. 6**](#)

[**Source Data Extended Data Fig. 7**](#)

[**Source Data Extended Data Fig. 8**](#)

[**Source Data Extended Data Fig. 9**](#)

Rights and permissions

[Reprints and Permissions](#)

About this article

Cite this article

Wu, X., Morishita, W., Beier, K.T. *et al.* 5-HT modulation of a medial septal circuit tunes social memory stability. *Nature* **599**, 96–101 (2021). <https://doi.org/10.1038/s41586-021-03956-8>

- Received: 11 February 2021
- Accepted: 25 August 2021
- Published: 06 October 2021
- Issue Date: 04 November 2021
- DOI: <https://doi.org/10.1038/s41586-021-03956-8>

Share this article

Anyone you share the following link with will be able to read this content:

[Get shareable link](#)

Sorry, a shareable link is not currently available for this article.

[Copy to clipboard](#)

Provided by the Springer Nature SharedIt content-sharing initiative

This article was downloaded by **calibre** from <https://www.nature.com/articles/s41586-021-03956-8>

- Article
- [Published: 06 October 2021](#)

Neurotoxic reactive astrocytes induce cell death via saturated lipids

- [Kevin A. Guttenplan](#) ORCID: [orcid.org/0000-0003-4242-4349^{1,2}](https://orcid.org/0000-0003-4242-4349),
- [Maya K. Weigel^{1 na1}](#),
- [Priya Prakash](#) ORCID: [orcid.org/0000-0003-2193-9669^{3 na1}](https://orcid.org/0000-0003-2193-9669),
- [Prageeth R. Wijewardhane](#) ORCID: [orcid.org/0000-0002-9781-3053³](https://orcid.org/0000-0002-9781-3053),
- [Philip Hasel](#) ORCID: [orcid.org/0000-0003-4378-3685⁴](https://orcid.org/0000-0003-4378-3685),
- [Uriel Rufen-Blanchette⁴](#),
- [Alexandra E. Münch](#) ORCID: [orcid.org/0000-0002-9609-3277¹](https://orcid.org/0000-0002-9609-3277),
- [Jacob A. Blum²](#),
- [Jonathan Fine³](#),
- [Mikaela C. Neal⁵](#),
- [Kimberley D. Bruce⁵](#),
- [Aaron D. Gitler](#) ORCID: [orcid.org/0000-0001-8603-1526²](https://orcid.org/0000-0001-8603-1526),
- [Gaurav Chopra](#) ORCID: [orcid.org/0000-0003-0942-7898^{3,6,7,8,9}](https://orcid.org/0000-0003-0942-7898),
- [Shane A. Liddelow](#) ORCID: [orcid.org/0000-0002-0840-1437^{4,10,11,12 na2}](https://orcid.org/0000-0002-0840-1437) &
- [Ben A. Barres^{1 na2}](#)

[Nature](#) volume 599, pages 102–107 (2021)

- 22k Accesses
- 466 Altmetric
- [Metrics details](#)

Subjects

- [Astrocyte](#)
- [Neurodegeneration](#)

Abstract

Astrocytes regulate the response of the central nervous system to disease and injury and have been hypothesized to actively kill neurons in neurodegenerative disease^{1,2,3,4,5,6}. Here we report an approach to isolate one component of the long-sought astrocyte-derived toxic factor^{5,6}. Notably, instead of a protein, saturated lipids contained in APOE and APOJ lipoparticles mediate astrocyte-induced toxicity. Eliminating the formation of long-chain saturated lipids by astrocyte-specific knockout of the saturated lipid synthesis enzyme ELOVL1 mitigates astrocyte-mediated toxicity in vitro as well as in a model of acute axonal injury in vivo. These results suggest a mechanism by which astrocytes kill cells in the central nervous system.

Access options

Subscribe to Journal

Get full journal access for 1 year

\$199.00

only \$3.90 per issue

[Subscribe](#)

All prices are NET prices.

VAT will be added later in the checkout.

Tax calculation will be finalised during checkout.

Rent or Buy article

Get time limited or full article access on ReadCube.

from \$8.99

[Rent or Buy](#)

All prices are NET prices.

Additional access options:

- [Log in](#)
- [Access through your institution](#)
- [Learn about institutional subscriptions](#)

Fig. 1: Proteins upregulated in reactive ACM.

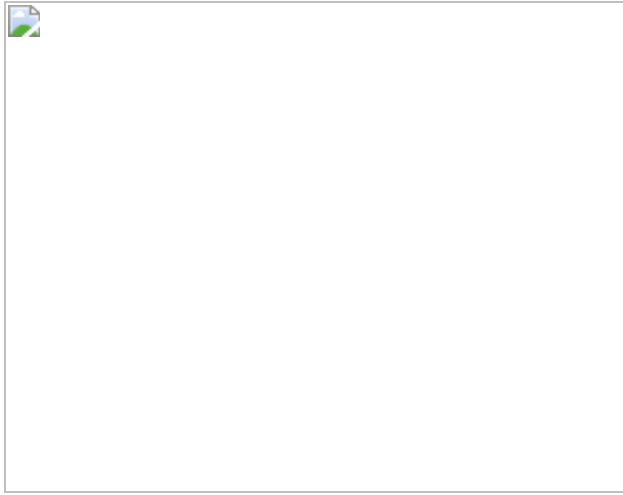


Fig. 2: Differentially regulated lipids in reactive astrocytes.



Fig. 3: Mechanism of cell death from reactive ACM.

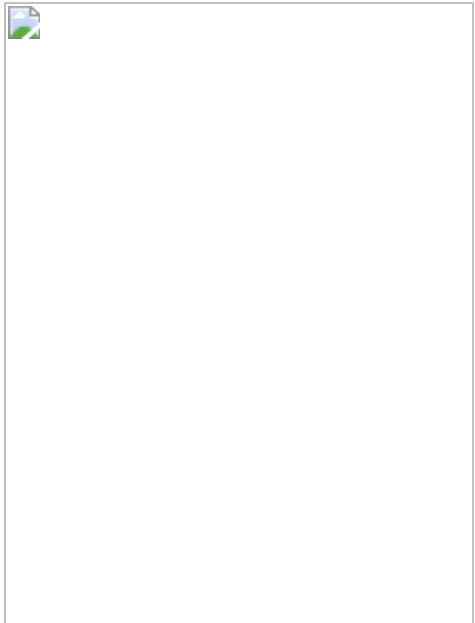
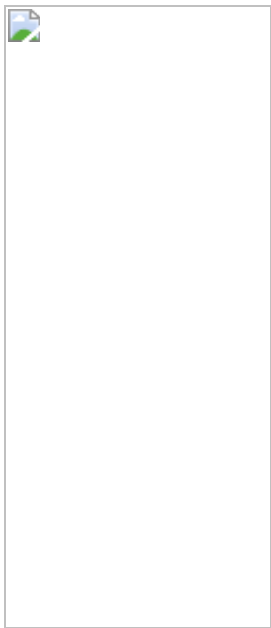


Fig. 4: Conditional knockout of the long-chain saturated lipid synthesis gene *Elovl1* reduces reactive astrocyte toxicity.



Data availability

Mass spectrometry data in Figs. 1, 2, 4 are publicly available at <http://gliaomics.com/> as well as the raw data in Supplementary Tables 1, 2. The accession information for raw protein mass spectrometry data is MassIVE MSV000087805

(<https://massive.ucsd.edu/ProteoSAFe/dataset.jsp?task=5f39b6cde74c4911951dbef1f2dac443>), and the accession information for raw lipid and metabolite mass spectrometry data is MassIVE MSV000087832 (<http://massive.ucsd.edu/ProteoSAFe/status.jsp?task=ca311727ff524e32868736d3d1b3cc0a>). Any other data are available from the corresponding author upon reasonable request.

Code availability

All mass spectrometry analysis code is available on the Chopra Lab Github (https://github.com/chopralab/reactive_astrocytes_omics).

References

1. 1.
Liddelow, S. A. & Barres, B. A. Reactive astrocytes: production, function, and therapeutic potential. *Immunity* **46**, 957–967 (2017).
2. 2.
Liddelow, S. A. et al. Neurotoxic reactive astrocytes are induced by activated microglia. *Nature* **541**, 481–487 (2017).
3. 3.
Guttenplan, K. A. et al. Neurotoxic reactive astrocytes drive neuronal death after retinal injury. *Cell Rep.* **31**, 107776 (2020).
4. 4.
Guttenplan, K. A. et al. Knockout of reactive astrocyte activating factors slows disease progression in an ALS mouse model. *Nat. Commun.* **11**, 3753 (2020).
5. 5.

Nagai, M. et al. Astrocytes expressing ALS-linked mutated SOD1 release factors selectively toxic to motor neurons. *Nat. Neurosci.* **10**, 615–622 (2007).

6. 6.

Giorgio, F., Carrasco, M. A., Siao, M. C., Maniatis, T. & Eggan, K. Non-cell autonomous effect of glia on motor neurons in an embryonic stem cell-based ALS model. *Nat. Neurosci.* **10**, 608–614 (2007).

7. 7.

Barres, B., Schmid, R., Sendnter, M. & Raff, M. Multiple extracellular signals are required for long-term oligodendrocyte survival. *Development* **118**, 283–295 (1993).

8. 8.

Banker, G. A. & Cowan, W. M. Rat hippocampal neurons in dispersed cell culture. *Brain Res.* **126**, 397–425 (1977).

9. 9.

Kucukdereli, H. et al. Control of excitatory CNS synaptogenesis by astrocyte-secreted proteins Hevin and SPARC. *Proc. Natl Acad. Sci. USA* **108**, E440–E449 (2011).

10. 10.

Bi, F. et al. Reactive astrocytes secrete lcn2 to promote neuron death. *Proc. Natl Acad. Sci. USA* **110**, 4069–4074 (2013).

11. 11.

Fagan, A. et al. Unique lipoproteins secreted by primary astrocytes from wild type, apoE^{-/-}, and human apoE transgenic mice. *J. Biol. Chem.* **274**, 30001–30007 (1999).

12. 12.

Folch, J., Lees, M. & Stanley, G. H. S. A simple method for the isolation and purification of total lipides from animal tissues. *J. Biol. Chem.* **226**, 497–509 (1957).

13. 13.

Sparks, D. L., Phillips, M. C. & Lund-Katz, S. The conformation of apolipoprotein A-I in discoidal and spherical recombinant high density lipoprotein particles. ¹³C NMR studies of lysine ionization behavior. *J. Biol. Chem.* **267**, 25830–25838 (1992).

14. 14.

DeMattos, R., Brendza, R. & Heuser, J. Purification and characterization of astrocyte-secreted apolipoprotein E and J-containing lipoproteins from wild-type and human apoE transgenic mice. *Neurochem. Int.* **39**, 415–425 (2001).

15. 15.

Cunha, D. A. et al. Death protein 5 and p53-upregulated modulator of apoptosis mediate the endoplasmic reticulum stress–mitochondrial dialog triggering lipotoxic rodent and human β-cell apoptosis. *Diabetes* **61**, 2763–2775 (2012).

16. 16.

Piccolis, M. et al. Probing the global cellular responses to lipotoxicity caused by saturated fatty acids. *Mol. Cell* **4**, 32–44 (2019).

17. 17.

Fanning, S. et al. Lipidomic analysis of α-synuclein neurotoxicity identifies stearoyl CoA desaturase as a target for Parkinson treatment. *Mol. Cell* **7**, 1001–1014 (2019).

18. 18.

Zhang, Y. et al. An RNA-sequencing transcriptome and splicing database of glia, neurons, and vascular cells of the cerebral cortex. *J. Neurosci.* **34**, 11929–11947 (2014).

19. 19.

Yan, P. et al. Palmitic acid triggers cell apoptosis in RGC-5 retinal ganglion cells through the Akt/FoxO1 signaling pathway. *Metab. Brain Dis.* **32**, 453–460 (2017).

20. 20.

Sterling, J. K. et al. GLP-1 receptor agonist NLY01 reduces retinal inflammation and neuron death secondary to ocular hypertension. *Cell Rep.* **33**, 108271 (2020).

21. 21.

Ioannou, M. S. et al. Neuron-astrocyte metabolic coupling protects against activity-induced fatty acid toxicity. *Cell* **177**, 1522–1535 (2019).

22. 22.

Legleiter, J., DeMattos, R. & Holtzman, D. In situ AFM studies of astrocyte-secreted apolipoprotein E-and J-containing lipoproteins. *J. Colloid Interface Sci.* **278**, 96–106 (2004).

23. 23.

Mishra, V. et al. Systematic elucidation of neuron-astrocyte interaction in models of amyotrophic lateral sclerosis using multi-modal integrated bioinformatics workflow. *Nat. Commun.* **11**, 5579 (2020).

24. 24.

Jovičić, A. & Gitler, A. D. Distinct repertoires of microRNAs present in mouse astrocytes compared to astrocyte-secreted exosomes. *PLoS One* **12**, e0171418 (2017).

25. 25.

Oishi, Y. et al. SREBP1 contributes to resolution of pro-inflammatory TLR4 signaling by reprogramming fatty acid metabolism. *Cell Metab.* **25**, 412–427 (2017).

26. 26.

Wurfel, M. M., Kunitake, S. T., Lichenstein, H., Kane, J. P. & Wright, S. D. Lipopolysaccharide (LPS)-binding protein is carried on lipoproteins and acts as a cofactor in the neutralization of LPS. *J. Exp. Med.* **180**, 1025–1035 (1994).

27. 27.

Nugent, A. A. et al. TREM2 regulates microglial cholesterol metabolism upon chronic phagocytic challenge. *Neuron* **105**, 837–854 (2020).

28. 28.

Foo, L. C. et al. Development of a method for the purification and culture of rodent astrocytes. *Neuron* **71**, 799–811 (2011).

29. 29.

Dugas, J. C. & Emery, B. Purification of oligodendrocyte precursor cells from rat cortices by immunopanning. *Cold Spring Harb. Protoc.* **2013**, pdb.prot070862 (2013).

30. 30.

Ullian, E. M., Sapperstein, S. K., Christopherson, K. S. & Barres, B. A. Control of synapse number by glia. *Science* **291**, 657–661 (2001).

31. 31.

Hedrick, V. E., LaLand, M. N., Nakayasu, E. S. & Paul, L. N. Digestion, purification, and enrichment of protein samples for mass

spectrometry. *Curr. Protoc. Chem. Biol.* **7**, 201–222 (2015).

32. 32.

Barabas, A. J., Aryal, U. K. & Gaskill, B. N. Proteome characterization of used nesting material and potential protein sources from group housed male mice, *Mus musculus. Sci Rep.* **9**, 17524 (2019).

33. 33.

McCarthy, D. J., Chen, Y. & Smyth, G. K. Differential expression analysis of multifactor RNA-seq experiments with respect to biological variation. *Nucleic Acids Res.* **40**, 4288–4297 (2012).

34. 34.

Robinson, M. D., McCarthy, D. J. & Smyth, G. K. edgeR: a Bioconductor package for differential expression analysis of digital gene expression data. *Bioinformatics* **26**, 139–140 (2010).

35. 35.

Bligh, E. G. & Dyer, W. J. A rapid method of total lipid extraction and purification. *Can. J. Biochem. Physiol.* **37**, 911–917 (1959).

36. 36.

Xie, Z., Ferreira, C. R., Virequ, A. A. & Cooks, R. G. Multiple reaction monitoring profiling (MRM profiling): small molecule exploratory analysis guided by chemical functionality. *Chem. Phys. Lipids* **235**, 105048 (2021).

37. 37.

Elias, J. E. & Gygi, S. P. Target-decoy search strategy for increased confidence in large-scale protein identifications by mass spectrometry. *Nat. Methods* **4**, 207–214 (2007).

Winzeler, A. & Wang, J. T. Purification and culture of retinal ganglion cells from rodents. *Cold Spring Harb. Protoc.* **2013**, 643–652 (2013).

Acknowledgements

On behalf of all his trainees and colleagues, this paper is dedicated to the memory of Ben Barres. We acknowledge Merck for allowing us to use the *Elovl1^{fl/fl}* mouse line for these experiments. This work used the Stanford Neuroscience Microscopy Service, which is supported by the grant award NIH NS069375. The Vincent Coates Foundation Mass Spectrometry Laboratory at Stanford University Mass Spectrometry contributed to this work. This work was supported in part by NIH P30 CA124435, using the Stanford Cancer Institute Proteomics/Mass Spectrometry Shared Resource. This work used the LTQ-Orbitrap mass spectrometer system that was purchased with funding from NIH Shared Instrumentation grant S10RR027425. Additional support was provided by the JPB Foundation, and Vincent and Stella Coates (to B.A.B.). K.A.G. was supported by the Wu Tsai Institute Interdisciplinary Scholar Award. S.A.L. was supported by the Cure Alzheimer's Fund, Anonymous Donors, the Blas Frangione Foundation and the MD Anderson Neurodegenerative Consortium. This work was also supported in part by an unrestricted grant from Research to Prevent Blindness (RPB). We thank C. Ferreira at the Purdue Metabolite Profiling Facility for assistance with lipid mass spectrometry; U. K. Aryal at the Purdue Proteomics Facility for help with protein mass spectrometry and deposition of data; and Agilent Technologies for their gift of the Triple Quadrupole LC/MS to the Chopra Laboratory. This work was supported, in part, by the United States Department of Defense USAMRAA award W81XWH2010665, NIH National Center for Advancing Translational Sciences ASPIRE Design Challenge awards, Purdue Integrative Data Science Institute award and a start-up package from the Department of Chemistry at Purdue University to G.C. Additional support, in part, by the Stark Neurosciences Research Institute; the Indiana Alzheimer Disease Center; Eli Lilly and Company; the Indiana Clinical and Translational Sciences Institute grant UL1TR002529 from the NIH, National Center for Advancing Translational Sciences; and the Purdue University Center for

Cancer Research funded by NIH grant P30 CA023168 is also acknowledged. The content is solely the responsibility of the authors and does not necessarily represent the official views of the National Institutes of Health. Select illustrations in figure subpanels were made using BioRender.

Author information

Author notes

1. These authors contributed equally: Maya K. Weigel, Priya Prakash
2. These authors jointly supervised this work: Shane A Liddelow, Ben A Barres

Affiliations

1. Department of Neurobiology, Stanford University, Stanford, CA, USA
Kevin A. Guttenplan, Maya K. Weigel, Alexandra E. Münch & Ben A. Barres
2. Department of Genetics, Stanford University, Stanford, CA, USA
Kevin A. Guttenplan, Jacob A. Blum & Aaron D. Gitler
3. Department of Chemistry, Purdue University, West Lafayette, IN, USA
Priya Prakash, Prageeth R. Wijewardhane, Jonathan Fine & Gaurav Chopra
4. Neuroscience Institute, NYU School of Medicine, New York, NY, USA
Philip Hasel, Uriel Rufen-Blanchette & Shane A. Liddelow
5. University of Colorado Anschutz Medical Campus, Aurora, CO, USA
Mikaela C. Neal & Kimberley D. Bruce

6. Purdue Institute for Integrative Neuroscience, Purdue University, West Lafayette, IN, USA

Gaurav Chopra

7. Purdue Institute for Drug Discovery, Purdue University, West Lafayette, IN, USA

Gaurav Chopra

8. Purdue Center for Cancer Research, Purdue University, West Lafayette, IN, USA

Gaurav Chopra

9. Purdue Institute of Inflammation, Immunology and Infectious Disease, Purdue University, West Lafayette, IN, USA

Gaurav Chopra

10. Department of Neuroscience and Physiology, NYU School of Medicine, New York, NY, USA

Shane A. Liddelow

11. Department of Ophthalmology, NYU School of Medicine, New York, NY, USA

Shane A. Liddelow

12. The Parekh Center for Interdisciplinary Neurology, NYU Grossman School of Medicine, New York, NY, USA

Shane A. Liddelow

Contributions

K.A.G., S.A.L., A.D.G. and B.A.B. designed the experiments. K.A.G. and S.A.L. wrote the paper. K.A.G., M.K.W. and A.E.M. performed

experiments and analysed data. P.P., P.R.W., J.F. and G.C. designed, performed and analysed mass spectrometry proteomics, lipidomics and metabolomics experiments and developed the web application. P.H., U.R.-B., J.A.B. and S.A.L. performed *Elovl1* cKO validation experiments. M.C.N. and K.D.B. performed HPLC and lipoparticle analysis experiments.

Corresponding author

Correspondence to Shane A. Liddelow.

Ethics declarations

Competing interests

A.D.G. has served as a consultant for Aquinnah Pharmaceuticals, Prevail Therapeutics and Third Rock Ventures, and is a scientific founder of Maze Therapeutics. S.A.L. is an academic founder of AstronauTx. B.A.B. is a co-founder of Annexon Biosciences, a company working to make new drugs for the treatment of neurological diseases. G.C. is the Director of the Merck-Purdue Center for Measurement Science funded by Merck Sharp & Dohme, a subsidiary of Merck. The remaining authors declare no competing interests.

Additional information

Peer review information *Nature* thanks Jeremy Kay, Robert Zorec and the other, anonymous, reviewer(s) for their contribution to the peer review of this work. Peer reviewer reports are available.

Publisher's note Springer Nature remains neutral with regard to jurisdictional claims in published maps and institutional affiliations.

Extended data figures and tables

Extended Data Fig. 1 Principal component analysis of protein mass spectrometry data.

a, Number of significant proteins and PCA variation based on number of replicates of protein mass spectrometry that were required to have a non-zero spectral count to be considered for analysis. 3660 total unique proteins detected in astrocytes and 183 total unique proteins detected in ACM. 4 of 10 (4x) was chosen for final analysis. **b**, PCA plots of cellular and ACM protein mass spectrometry of all proteins detected in at least 4 of 10 astrocytes samples see shows clear separation of the proteome and secretome of reactive versus control astrocytes. **c**, Quantification of differentially regulated proteins in reactive astrocytes and ACM (FDR < 0.1). **d**, 10 most upregulated and downregulated proteins in reactive versus control astrocytes (bold = known reactivity markers).

Extended Data Fig. 2 Testing the toxicity of various candidate toxic proteins.

a, Oligodendrocytes were treated with various doses of candidate toxic proteins found in our proteomics analysis or from previous literature but were not found to be toxic in our culture conditions. **b**, Reactive ACM, but not Lcn2, Lgals1, or complement component C3 family members, is toxic to retinal ganglion cell (RGC) neuron cultures. (all data represents N=3/4 independent samples from 2 separate primary cell isolations; presented as mean ± SEM).

Extended Data Fig. 3 Toxic factor enrichment.

a, Diagram of sequential toxic factor enrichment by various biochemical purification columns. **b**, Validation that sequentially enriched reactive ACM is more toxic than sequentially enriched control ACM. (data represents 3 independent samples from 3 separate primary cell isolations).

Extended Data Fig. 4 Astrocyte lipoparticle analysis.

a, Example control and reactive protein abundance traces for HPLC size exclusion column. **b**, ELISA shows an increase in APOJ concentration within fractions associated with astrocyte HDL. (individual data points represent independent samples from a single primary cell isolation; presented as mean \pm SEM) **c**, ELISA on concentrated control versus reactive HPLC fractions associated with HDL shows more APOE in reactive versus control. Control and reactive HDL fractions were combined and concentrated to achieve sufficient signal for APOE ELISA so only one sample for control versus reactive was analysed.

[Extended Data Fig. 5 Reconstituted HDL incorporation into cells.](#)

Example images of fluorescently labelled reconstituted HDL incorporation into oligodendrocyte, microglia, endothelial cells, oligodendrocyte precursor cells (OPCs), retinal ganglion cell neurons (RGCs), and astrocytes in vitro. Note that all cells incorporate reconstituted lipoparticles except for endothelial cells. (experiment performed on 2 separate primary cell isolations for each cell type; scale bar = 100 μm).

[Extended Data Fig. 6 Astrocyte metabolomics and lipidomics.](#)

a, Reactive (red) versus control (grey) astrocytes and ACM are somewhat separable in PCA space based on their metabolome, but less so than by their lipidome (Fig. 2). AFU, arbitrary fluorescence units. **b**, Distribution of MRM transitions selected for screening lipids. A total of 1547 transitions (used to ID lipid species) were organized into 11 MRM-based mass spectrometry methods (for lipid classes). **c**, Quantification of differentially regulated lipids and metabolites in reactive astrocytes and ACM (FDR < 0.1). **d**, Scatterplot of differentially regulated lipids in reactive versus control astrocytes and ACM highlights the overall abundance of differentially regulated lipids.

[Extended Data Fig. 7 Saturated free fatty acids and phosphatidylcholines are toxic to oligodendrocytes.](#)

a, Cultured oligodendrocytes (phase) incorporate fluorescent C16:0 free fatty acids (FFAs, green) upon treatment (0.5 μ M; scale bar = 150 μ m). **b**, Dose curve of oligodendrocyte survival following treatment with C16:0 and C18:0 saturated FFAs shows that saturated FFAs are toxic to oligodendrocytes with longer chain lengths leading to greater toxicity (curve fits performed using one-phase decay model). **c**, Long-chain saturated phosphatidylcholines (PC, 20:0) are toxic to oligodendrocytes in a dose-dependent fashion. (data, including representative image in subpanel a, represents N=4 independent samples from 3 separate primary cell isolations; presented as mean \pm SEM).

Extended Data Fig. 8 Further analysis of the mechanism of toxic-factor-induced cell death.

a, Various doses of ethoxyquin in DMSO was added to oligodendrocytes with or without 30 μ g/ml reactive ACM. Simple linear regression analysis on increasing doses of ethoxyquin without reactive ACM (Slope = -0.0000025, P value [slope \neq 0] = 0.1932) and with reactive ACM (Slope = -0.000001788, P value [slope \neq 0] = 0.4194) failed to show a significant relationship between ethoxyquin concentration and survival, suggesting that the free radical scavenger did not affect cell survival when treated in isolation and did not affect the toxicity of reactive ACM. This data, in addition to the data that Ferrostatin-1 has no effect on astrocyte toxicity², suggests that lipid peroxidation may not mediate the ACM toxicity. **b**, siRNAs potently knock down the lipoapoptosis sensitivity modulated genes *Scd1* and *Insig1* in oligodendrocytes in vitro. **c**, Knockdown of SCD and INSIG1, which bidirectionally modulate sensitivity to lipoapoptosis, bidirectionally modulate sensitivity of oligodendrocytes to toxic ACM. (data represents n=3 independent samples from 2 separate primary cell isolations; presented as mean \pm SEM).

Extended Data Fig. 9 *Elov11* cKO validation.

a, GFP expression (green) from NuTrap mice crossed to *Gfap*-Cre line used in this study shows efficient recombination in *Slc1a3*⁺ astrocytes (red, as identified by RNAscope in situ hybridization) of the ganglion cell layer

(GCL, identified by DAPI staining of nuclei, blue; ONL, outer nuclear layer; OPL, outer plexiform layer; INL, inner nuclear layer; IPL, inner plexiform layer). **b**, DNA gel following PCR amplification of *Elov11* and *Gfap* in the retina and optic nerve shows a decrease in *Elov11* expression relative to *Gfap* expression in the *Elov11* cKO mouse visual system. (white numbers indicate molecular weight markers) **c**, Quantification of the decrease in *Elov11* expression relative to *Gfap* expression in the *Elov11* cKO retina (top) and optic nerve (bottom) N=4 animals per group, bars represent s.e.m., two-tailed Student's t-test). **d**, Targeted lipidomics of *Elov11* cKO ACM shows dampened upregulation of the long-chain saturated lipids normally upregulated in WT reactive ACM. (black line indicates equal upregulation; red dots indicate lipids less upregulated in *Elov11* cKO versus WT ACM; black dot indicates a lipid less upregulated in WT ACM versus *Elov11* cKO ACM). **e**, Separation of *Elov11* cKO and WT cell and ACM lipidomes in PCA space.

Extended Data Fig. 10 Toxicity of *Elov11* cKO versus wild-type ACM over time.

Toxicity of oligodendrocytes in response to *Elov11* cKO versus wt control, reactive, and concentrated reactive ACM over 96 h (data represents mean ± SEM of 6 experimental replicates each from 3 independent samples from 3 separate primary cell isolations; presented as mean ± SEM).

Supplementary information

Supplementary Information

This file contains Supplementary Fig. 1 and Supplementary Tables 2 and 3. Supplementary Fig. 1 shows the uncropped western blots from Fig. 3. Supplementary Table 2 contains mass spectrometry data for lipoprotein pull-downs. Spectral counts of proteins detected in all replicates of APOE and APOJ antibody pull-downs of control and reactive ACM show little specificity between APOE and APOJ antibodies for detected lipoproteins. Supplementary Table 3 contains statistical details for all experimental comparisons including exact p-values.

Reporting Summary

Supplementary Table 1

Mass spectrometry data of purified ACM. Spectral counts from protein mass spectrometry of $n = 3$ control and $n = 6$ reactive ACM samples sequentially purified according to Extended Data Fig. 3.

Peer Review File

Rights and permissions

Reprints and Permissions

About this article

Cite this article

Guttenplan, K.A., Weigel, M.K., Prakash, P. *et al.* Neurotoxic reactive astrocytes induce cell death via saturated lipids. *Nature* **599**, 102–107 (2021). <https://doi.org/10.1038/s41586-021-03960-y>

- Received: 06 January 2021
- Accepted: 26 August 2021
- Published: 06 October 2021
- Issue Date: 04 November 2021
- DOI: <https://doi.org/10.1038/s41586-021-03960-y>

Share this article

Anyone you share the following link with will be able to read this content:

[Get shareable link](#)

Sorry, a shareable link is not currently available for this article.

[Copy to clipboard](#)

Provided by the Springer Nature SharedIt content-sharing initiative

This article was downloaded by **calibre** from <https://www.nature.com/articles/s41586-021-03960-y>.

| [Section menu](#) | [Main menu](#) |

- Article
- [Published: 22 September 2021](#)

Efficient and targeted COVID-19 border testing via reinforcement learning

- [Hamsa Bastani¹](#),
[ORCID: orcid.org/0000-0001-8288-5874²](#),
- [Kimon Drakopoulos](#) [ORCID: orcid.org/0000-0001-8288-5874²](#),
- [Vishal Gupta²](#),
- [Ioannis Vlachogiannis³](#),
- [Christos Hadjicristodoulou](#) [ORCID: orcid.org/0000-0002-4769-8376⁴](#),
- [Pagona Lagiou⁵](#),
- [Gkikas Magiorkinis⁵](#),
- [Dimitrios Paraskevis](#) [ORCID: orcid.org/0000-0001-6167-7152⁵](#) &
- [Sotirios Tsiodras](#) [ORCID: orcid.org/0000-0002-0463-4321⁶](#)

[Nature](#) volume 599, pages 108–113 (2021)

- 31k Accesses
- 474 Altmetric
- [Metrics details](#)

Subjects

- [Public health](#)
- [SARS-CoV-2](#)
- [Statistics](#)

Abstract

Throughout the coronavirus disease 2019 (COVID-19) pandemic, countries have relied on a variety of ad hoc border control protocols to allow for non-essential travel while safeguarding public health, from quarantining all travellers to restricting

entry from select nations on the basis of population-level epidemiological metrics such as cases, deaths or testing positivity rates^{1,2}. Here we report the design and performance of a reinforcement learning system, nicknamed Eva. In the summer of 2020, Eva was deployed across all Greek borders to limit the influx of asymptomatic travellers infected with severe acute respiratory syndrome coronavirus 2 (SARS-CoV-2), and to inform border policies through real-time estimates of COVID-19 prevalence. In contrast to country-wide protocols, Eva allocated Greece's limited testing resources on the basis of incoming travellers' demographic information and testing results from previous travellers. By comparing Eva's performance against modelled counterfactual scenarios, we show that Eva identified 1.85 times as many asymptomatic, infected travellers as random surveillance testing, with up to 2–4 times as many during peak travel, and 1.25–1.45 times as many asymptomatic, infected travellers as testing policies that utilize only epidemiological metrics. We demonstrate that this latter benefit arises, at least partially, because population-level epidemiological metrics had limited predictive value for the actual prevalence of SARS-CoV-2 among asymptomatic travellers and exhibited strong country-specific idiosyncrasies in the summer of 2020. Our results raise serious concerns on the effectiveness of country-agnostic internationally proposed border control policies³ that are based on population-level epidemiological metrics. Instead, our work represents a successful example of the potential of reinforcement learning and real-time data for safeguarding public health.

[Download PDF](#)

Main

In the first wave of the pandemic, many countries restricted non-essential travel to mitigate the spread of SARS-CoV-2. The restrictions crippled most tourist economies, with estimated losses of US\$1 trillion among European countries and 19 million jobs³. As conditions improved from April to July, countries sought to partially lift these restrictions, not only for tourists, but also for the flow of goods and labour.

Different countries adopted different border screening protocols, typically based on the origin country of the traveller. Despite the variety of the protocols, we group those used in early summer 2020 into four broad types: allowing unrestricted travel from designated 'white-list' countries; requiring travellers from designated 'grey-listed' countries to provide proof of a negative test by PCR with reverse transcription before arrival; requiring all travellers from designated 'red-listed' countries to quarantine on arrival; forbidding any non-essential travel from designated 'black-listed' countries.

Most nations employed a combination of all four strategies. However, the choice of which 'colour' to assign to a country differed across nations. For example, as of 1 July

2020, Spain designated the countries specified in ref. [1](#) as white-listed, whereas Croatia designated these countries as grey-listed or red-listed.

To the best of our knowledge, in all European nations except Greece, the above ‘colour designations’ were entirely based on population-level epidemiological metrics (for example, see refs. [1,2](#)) such as cases per capita, deaths per capita and/or positivity rates that were available in the public domain^{[4,5,6](#)}. (An exception is the UK, which engaged in small-scale testing at select airports that may have informed their policies.) However, such metrics are imperfect owing to under-reporting^{[7](#)}, symptomatic population biases^{[8,9](#)} and reporting delays.

These drawbacks motivated our design and nationwide deployment of Eva: the first fully algorithmic, real-time, reinforcement learning system for targeted COVID-19 screening with the dual goals of identifying asymptomatic, infected travellers and providing real-time information to policymakers for downstream decisions.

Overview of the Eva system

Eva as presented here was deployed across all 40 points of entry to Greece, including airports, land crossings and seaports from 6 August to 1 November 2020. Figure [1](#) schematically illustrates its operation; Supplementary Fig. [7](#) provides a more detailed schematic diagram of Eva’s architecture and data flow.

Fig. 1: A reinforcement learning system for COVID-19 testing (Eva).



Arriving passengers submit travel and demographic information 24 h before arrival. On the basis of these data and testing results from previous passengers, Eva selects a subset of passengers to test. Selected passengers self-isolate for 24–48 h while

laboratories process samples. Passengers testing positive are then quarantined and contact tracing begins; passengers testing negative resume normal activities. Results are used to update Eva to improve future testing and maintain high-quality estimates of prevalence across traveller subpopulations.

We next describe the main steps in processing a passenger.

Passenger locator form

All travellers must complete a passenger locator form (PLF; one per household) at least 24 h before arrival, containing (among other data) information on their origin country, demographics, and point and date of entry. Ref. [10](#) describes the exact fields and how these sensitive data were handled securely.

Estimating prevalence among traveller types

We estimate traveller-specific COVID-19 prevalence using recent testing results from previous travellers through Eva. Prevalence estimation entails two steps. First, we leverage LASSO (least absolute shrinkage and selection operator) regression from high-dimensional statistics^{[11](#)} to adaptively extract a minimal set of discrete, interpretable traveller types based on their demographic features (country, region, age and gender); these types are updated on a weekly basis using recent testing results. Second, we use an empirical Bayes method to estimate each type's prevalence daily. Empirical Bayes has previously been used in the body of literature on epidemiology to estimate prevalence across many populations^{[12,13](#)}. In our setting, COVID-19 prevalence is generally low (for example, ~2 in 1,000), and arrival rates differ substantively across countries. Combined, these features cause our testing data to be both imbalanced (few positive cases among those tested) and sparse (few arrivals from certain countries). Our empirical Bayes method seamlessly handles both challenges. Estimation details are provided in [Supplementary Methods 2.2](#).

Allocating scarce tests

Leveraging these prevalence estimates, Eva targets a subset of travellers for (group) PCR testing on arrival on the basis of their type alone, but no other personal information. The Greek National COVID-19 Committee of Experts approved group (Dorfman) testing^{[14](#)} in groups of five but eschewed larger groups and rapid testing owing to concerns over testing accuracy.

Eva's targeting must respect various port-level budget and resource constraints that reflect Greece's testing supply chain, which included 400 health workers staffing 40 points of entry, 32 laboratories across the country and delivery logistics for biological

samples. These constraints were (exogenously) defined and adjusted throughout the summer by the General Secretariat of Public Health.

The testing allocation decision is entirely algorithmic and balances two objectives. First, given current information, Eva seeks to maximize the number of infected asymptomatic travellers identified (exploitation). Second, Eva strategically allocates some tests to traveller types for which it does not currently have precise estimates to better learn their prevalence (exploration). This is a crucial feedback step. Today's allocations will determine the available data in the prevalence estimation step above when determining future prevalence estimates. Hence, if Eva simply (greedily) sought to allocate tests to types that currently had high prevalence, then, in a few days, it would not have any recent testing data about many other types that had moderate prevalence. Since COVID-19 prevalence can spike quickly and unexpectedly, this would leave a 'blind spot' for the algorithm and pose a serious public health risk. Such allocation problems can be formulated as multi-armed bandits^{15,16,17,18}—which are widely studied within the body of literature on reinforcement learning—and have been used in numerous applications such as mobile health¹⁹, clinical trial design²⁰, online advertising²¹ and recommender systems²².

Our application is a nonstationary^{23,24}, contextual²⁵, batched bandit problem with delayed feedback^{26,27} and constraints²⁸. Although these features have been studied in isolation, their combination and practical implementation poses unique challenges. One such challenge is accounting for information from 'pipeline' tests (allocated tests whose results have not yet been returned); we introduce a novel algorithmic technique of certainty-equivalent updates to model information we expect to receive from these tests, allowing us to effectively balance exploration and exploitation in nonstationary, batched settings. To improve interpretability, we build on the optimistic Gittins index for multi-armed bandits²⁹; each type is associated with a deterministic index that represents its current 'risk score', incorporating both its estimated prevalence and uncertainty. Algorithm details are provided in [Supplementary Methods 2.3](#).

Grey-listing recommendations

Eva's prevalence estimates are also used to recommend particularly risky countries to be grey-listed, in conjunction with the Greek COVID-19 taskforce and the Presidency of the Government. Grey-listing a country entails a tradeoff: requiring a PCR test reduces the prevalence among incoming travellers, but it also reduces non-essential travel significantly (approximately 39%; [Supplementary Methods 5](#)), because of the relative difficulty/expense in obtaining PCR tests in summer 2020. Hence, Eva recommends grey-listing a country only when necessary to keep the daily flow of (uncaught) infected travellers at a sufficiently low level to avoid overwhelming

contact-tracing teams³⁰. Ten countries were grey-listed over the summer of 2020 ([Supplementary Methods 5](#)).

Unlike testing decisions, our grey-listing decisions were not fully algorithmic, but instead involved human input. Indeed, while in theory, one might determine an ‘optimal’ cutoff for grey-listing to balance infected arrivals and reduced travel, in practice it is difficult to elicit such preferences from decision-makers directly. Rather, they preferred to retain some flexibility in grey-listing to consider other factors in their decisions.

Closing the loop

Results from the tests performed according to the test allocation step are logged within 24–48 h, and then used to update the prevalence estimates from the previous step.

To give a sense of scale, during peak season (August and September), Eva processed 41,830 ($\pm 12,784$) PLFs each day, and 16.7% ($\pm 4.8\%$) of arriving households were tested each day.

Value of targeted testing

We first present the number of asymptomatic, infected travellers caught by Eva relative to random surveillance testing (that is, where every arrival at a port of entry is equally likely to be tested). Random surveillance testing was Greece’s initial proposal and is very common, partly because it requires no information infrastructure to implement. However, we find that such an approach comes at a significant cost to performance (and therefore public health).

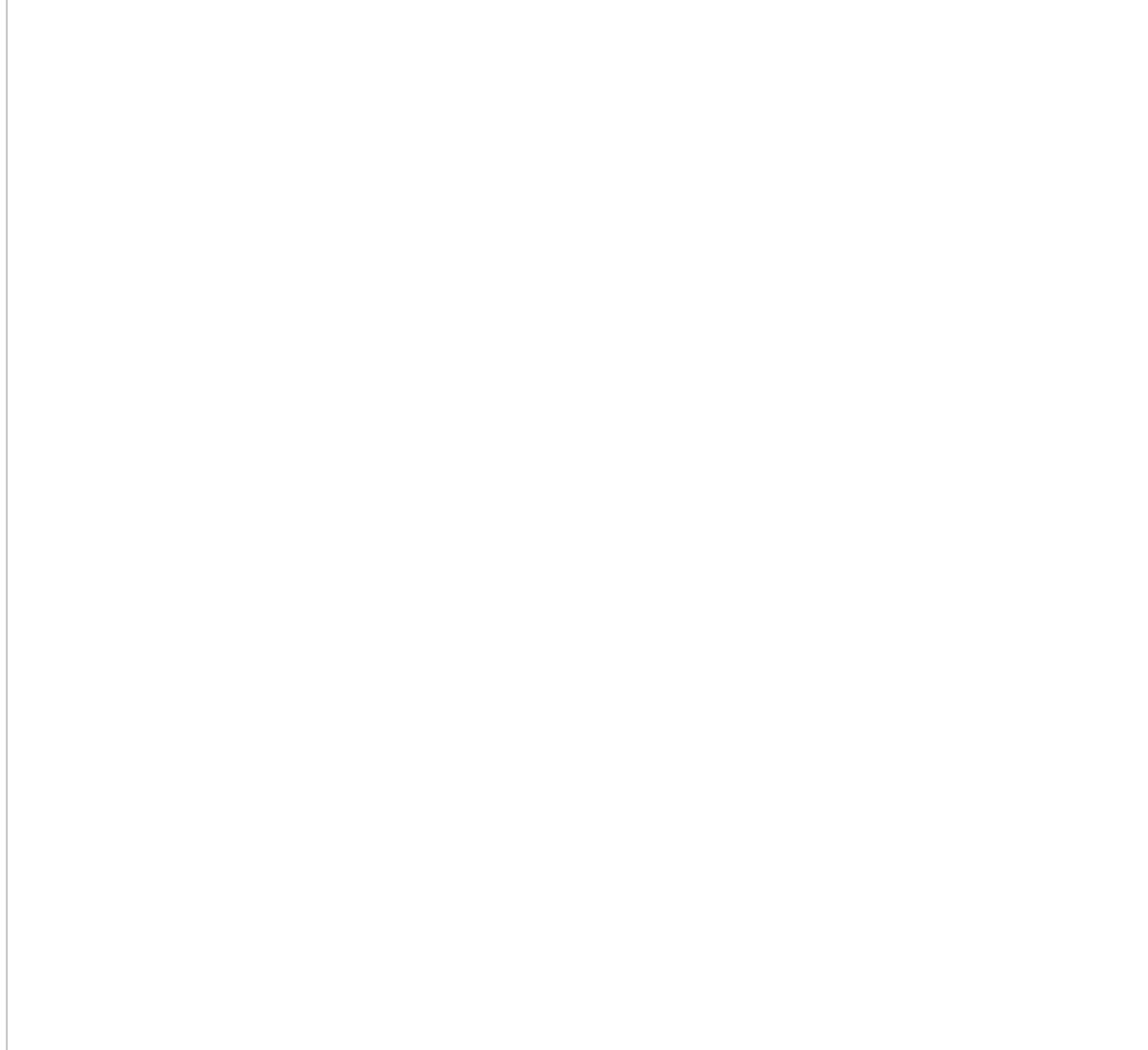
We perform counterfactual analysis using inverse propensity weighting^{31,32}, which provides a model-agnostic, unbiased estimate of the performance of random testing.

During the peak tourist season, we estimate that random surveillance testing would have identified 54.1% ($\pm 8.7\%$) of the infected travellers that Eva identified. (For anonymity, averages and standard deviations are scaled by a (fixed) constant, which we have taken without loss of generality to be the actual number of infections identified by Eva in the same period for ease of comparison.)

In other words, to achieve the same effectiveness as Eva, random testing would have required 85% more tests at each point of entry, a substantive supply chain investment. In October, when arrival rates dropped, the relative performance of random testing improved to 73.4% ($\pm 11.0\%$; Fig. 2). This difference is largely explained by the changing relative scarcity of testing resources (Fig. 3). As arrivals dropped, the

fraction of arrivals tested increased, thereby reducing the value of targeted testing. In other words, Eva's targeting is most effective when tests are scarce. In the extreme case of testing 100% of arrivals, targeted testing offers no value as both random and targeted testing policies test everyone. See [Supplementary Methods 3](#) for details.

Fig. 2: Comparing Eva versus randomized surveillance testing.



The number of infections caught by Eva (red) versus the estimated number of cases caught by random surveillance testing (teal). The peak (respectively, off-peak) season is 6 August to 1 October (respectively, 1 October to 1 November) and is denoted with triangular (respectively, circular) markers. Seasons are separated by the dashed line. The solid lines denote cubic-spline smoothing, with the 95% confidence intervals in grey.

Fig. 3: Relative efficacy of Eva over random surveillance versus fraction tested.

 figure3



The ratio of the number of infections caught by Eva relative to the number of (estimated) infections caught by random surveillance testing, as a function of the fraction of tested travellers. The short-dashed (respectively, long-dashed) line indicates the average fraction tested during the peak (respectively, off-peak) tourist season. Triangular (circular) markers denote estimates from peak (off-peak) days. The solid blue line denotes cubic-spline smoothing, with the 95% confidence interval in grey.

Value of reinforcement learning

We now compare the performance of Eva with that of policies that require similar infrastructure as Eva, namely PLF data, but instead target testing based on population-level epidemiological metrics (for example, as proposed by the European Union²) rather than reinforcement learning. The financial investments of such approaches are similar to those of Eva, and we show that these policies identify fewer cases. ([Supplementary Methods 3.2.3](#) highlights additional drawbacks of these policies, including poor data reliability and a mismatch in prevalence between the general population and the asymptomatic traveller population.)

We consider three separate policies that test passengers with probability proportional to cases per capita, deaths per capita or positivity rates for the passenger's country of origin^{4,5,6}, while respecting port budgets and arrival constraints. We again use inverse propensity weighting to estimate counterfactual performance (Fig. 4).

Fig. 4: Comparing Eva to policies based on epidemiological metrics.

 **figure4**

The lines represent cubic-spline smoothing of daily infections caught for each policy; raw points are shown only for Eva and the ‘Cases’ policy for clarity. The dashed line separates the peak (6 August to 1 October) and off-peak (1 October to 1 November) tourist seasons. The inset table shows the relative improvement of Eva over a policy based on the indicated epidemiological metric with the same testing budget for both the peak season and the off-peak season.

During the peak tourist season (August and September), we found that policies based on cases, deaths and positivity rates identified 69.0% ($\pm 9.4\%$), 72.7% ($\pm 10.6\%$) and 79.7% ($\pm 9.3\%$), respectively, of the infected travellers that Eva identified per test. In other words, Eva identified $1.25\times$ – $1.45\times$ more infections with the same testing budget and similar PLF infrastructure. In October, when arrival rates dropped, the relative performance of counterfactual policies based on cases, deaths and positivity rates

improved to 91.5% ($\pm 11.7\%$), 88.8% ($\pm 10.5\%$) and 87.1% ($\pm 10.4\%$), respectively. Like our results in the previous section, our findings show that the value of smart targeting is larger when testing resources are scarcer. In fact, Eva's relative improvement over these policies was highest in the second half of the peak season (when infection rates were much higher and testing resources were scarcer). See [Supplementary Methods 3](#) for details.

[Supplementary Methods 4](#) discusses possible reasons underlying the poor performance of simple policies based on population-level epidemiological metrics, including reporting delays and systematic differences between the general and asymptomatic traveller populations.

Poor predictive power of epidemiological metrics

Given the poor performance of simple policies based on population-level epidemiological metrics, a natural question is whether more sophisticated functions of these metrics would perform better. Although it is difficult to eliminate this possibility, we argue that this is probably not the case through a related analysis of the extent to which population-level epidemiological metrics can be used to predict COVID-19 prevalence among asymptomatic travellers as measured by Eva. Surprisingly, our findings suggest that widely used epidemiological data are generally ineffective in predicting the actual prevalence of COVID-19 among asymptomatic travellers (the group of interest for border control policies).

Specifically, we examine the extent to which these data can be used to classify a country as high risk (more than 0.5% prevalence) or low risk (less than 0.5% prevalence); such a classification informs whether a country should be grey- or black-listed. (A cutoff of 0.5% was typical for initiating grey-listing discussions with the Greek COVID-19 taskforce, but our results are qualitatively similar across a range of cutoffs.) We compute the true label for a country at each point in time on the basis of Eva's (real-time) estimates. We then train several models using a gradient boosted machine^{[33](#)} on different subsets of covariates derived from the 14-day time series of cases per capita, deaths per capita, testing rates per capita and testing positivity rates. Figure [5](#) summarizes their predictive accuracy; we obtained similar results for other state-of-the art machine learning algorithms.

Fig. 5: Predictive power of publicly reported epidemiological metrics.

 **figure5**

Each of the models 1–4 uses a different subset of features from: 14-day time series of cases per capita, deaths per capita, tests performed per capita and testing positivity rate. Model 5 additionally includes country fixed effects to model country-level idiosyncratic behaviour. Models 1–4 are essentially no better than random prediction, while model 5 achieves slightly better performance. See [Supplementary Methods 4.1](#) for details on model construction and features used in each model. AUROC, area under the receiver operating characteristic curve.

Note that a random model that uses no data has an area under the receiver operating characteristic curve of 0.5. Thus, models 1–4 offer essentially no predictive value, suggesting that these population-level epidemiological data are not informative of prevalence among asymptomatic travellers.

Model 5, which additionally uses country-level fixed effects, offers some improvement. These fixed effects collectively model country-specific idiosyncrasies representing aspects of their testing strategies, social distancing protocols and other non-pharmaceutical interventions that are unobserved in the public, epidemiological data. The improvement of model 5 suggests that these unobserved drivers are critical to distinguishing high- and low-risk countries.

Overall, this analysis raises concerns not only about travel protocols proposed by the European Union² based solely on widely used epidemiological metrics, but also about any protocol that treats all countries symmetrically. Indeed, the idiosyncratic effects of model 5 suggest that the threshold for deciding whether COVID-19 prevalence in travellers from country A is spiking may differ significantly from that of country B. See [Supplementary Methods 4.1](#) for details.

In [Supplementary Methods 4.3](#), we also study the information delay between a country's publicly reported cases (the most common metric) and prevalence among asymptomatic travellers from that country. We expect a lag because of the time taken for symptoms to manifest, and reporting delays induced by poor infrastructure. We find a modal delay of 9 days.

Value of grey-listing

Eva's measurements of COVID-19 prevalence were also used to provide early warnings for high-risk regions, in response to which Greece adjusted travel protocols by grey-listing these nations. We estimate that Eva prevented an additional 6.7% ($\pm 1.2\%$) infected travellers from entering the country through its early grey-listing decisions in the peak season; results in the off-peak season are similar. For privacy, we have expressed the benefit relative to the number of infected travellers identified by Eva. See [Supplementary Methods 5](#) for details.

Lessons learned from deployment and design

Eva is a large-scale data-driven system that was designed and deployed during the COVID-19 crisis. Leading up to and throughout deployment, we met twice a week with the COVID-19 Executive Committee of Greece, an interdisciplinary team of scientists and policymakers. Through those meetings, we gleaned several lessons that shaped Eva's design and contributed to its success.

Design the algorithm around data minimization

Data minimization (that is, requesting the minimum required information for a task) is a fundamental tenet of data privacy and the General Data Protection Regulation (GDPR). We met with lawyers, epidemiologists and policymakers before designing the algorithm to determine what data and granularity may legally and ethically be solicited by the PLF. Data minimization naturally entails a tradeoff between privacy and effectiveness. We limited requests to features thought to be predictive on the basis of the best available research at the time (origin, age and gender^{34,35}), but omitted potentially informative but invasive features (for example, occupation). We further designed our empirical Bayes estimation strategy around these data limitations.

Prioritize interpretability

For all parties to evaluate and trust the recommendations of a system, the system must provide transparent reasoning. An example from our deployment was the need to communicate the rationale for ‘exploration’ tests (that is tests for types with moderate but very uncertain prevalence estimates). Such tests may seem wasteful. Our choice of empirical Bayes allowed us to easily communicate that types with large confidence intervals may have significantly higher risk than their point estimate suggests, and thus require some tests to resolve uncertainty (see, for example, Supplementary Figs. 9 and 11, which were featured on policymakers’ dashboards).

A second example was our choice to use Gittins indices, which provide a simple, deterministic risk metric for each type that incorporates both estimated prevalence and corresponding uncertainty, driving intuitive test allocations. In contrast, using upper-confidence-bound or Thompson sampling with logistic regression^{36,37} would have made it more difficult to visualize uncertainty (a high-dimensional ellipsoid or posterior distribution), and test allocations would depend on this uncertainty through an opaque computation (a high-dimensional projection or stochastic sampling).

This transparency fostered trust across ministries of the Greek Government using our estimates to inform downstream policymaking, including targeting contact-tracing teams, staffing of mobile testing units and adjusting social distancing measures.

Design for flexibility

Finally, as these systems require substantial financial and technical investment, they need to be flexible to accommodate unexpected changes. We designed Eva in a modular manner disassociating type extraction, estimation and test allocation. Consequently, one module can easily be updated without altering the remaining modules. For example, had vaccine distribution begun in the summer of 2020, we could define new types based on passengers’ vaccination status without altering our procedure for prevalence estimates or test allocation. Similarly, if rapid testing were

approved, our allocation mechanism could be updated to neglect delayed feedback without affecting other components. This flexibility promotes longevity, as it is easier to get stakeholder buy-in for small adjustments to an existing system than for a substantively new approach.

Reporting summary

Further information on research design is available in the [Nature Research Reporting Summary](#) linked to this paper.

Data availability

To support further research, aggregated, anonymized data are available at https://github.com/kimondr/EVA_Public_Data. These data aggregate passenger arrival and testing information over pairs of consecutive days, country of origin and point of entry. The finer granularity data that support the (exact) findings of this study are protected by GDPR. These data are available from the Greek Ministry of Civil Protection, but restrictions apply to the availability of these data, which were used under licence for the current study, and so are not publicly available. Access to these data can be granted by the Greek Ministry of Civil Protection (info@gscp.gr) only for research that is conducted in the public interest for public health (GDPR Recital 159) and scientific purposes (GDPR Article 89). Finally, the population-level epidemiological metrics used in our analysis can be obtained freely from the Our World In Data COVID-19 dataset (<https://github.com/owid/covid-19-data/tree/master/public/data>).

Code availability

All code used in this paper was written in a combination of R and Python 3.7. The code for the deployment of the algorithm on a sample dataset is available at <https://github.com/vguptal/EvaTargetedCovid19Testing>. The code for reproducing the results of our counterfactual analysis is available at https://github.com/vguptal/Eva_CounterfactualAnalysis.

References

1. 1.

Council of the European Union. *Council Recommendation on the Temporary Restriction on Non-essential Travel into the EU and the Possible Lifting of Such*

Restrictionhttps://www.consilium.europa.eu/media/47592/st_9208_2020_init_en.pdf (30 June 2020).

2. 2.

European Commission. *Draft Council Recommendation on a Coordinated Approach to the Restriction of Free Movement in Response to the COVID-19 Pandemic* (12 October 2020).

3. 3.

World Travel and Tourism Council. *Recovery Scenarios 2020 & Economic Impact from COVID-19* <https://wttc.org/Research/Economic-Impact/Recovery-Scenarios> (November 2020).

4. 4.

Hasell, J. et al. A cross-country database of COVID-19 testing. *Sci. Data* **7**, 345 (2020).

5. 5.

Roser, M., Ritchie, H., Ortiz-Ospina, E. & Hasell, J. *Coronavirus Pandemic (COVID-19)* <https://ourworldindata.org/coronavirus> (OurWorldInData.org, 2020).

6. 6.

Dong, E., Du, H. & Gardner, L. An interactive web-based dashboard to track COVID-19 in real time. *Lancet Infect. Dis.* **20**, 533–534 (2020).

7. 7.

Wu, S. L. et al. Substantial underestimation of SARS-CoV-2 infection in the United States. *Nat. Commun.* **11**, 4507 (2020).

8. 8.

Cevik, M. et al. SARS-CoV-2, SARS-CoV, and MERS-CoV viral load dynamics, duration of viral shedding, and infectiousness: a systematic review and meta-analysis. *Lancet Microbe* **2**, e13–e22 (2021).

9. 9.

Phipps, S., Grafton, Q. & Kompas, T. Robust estimates of the true (population) infection rate for COVID-19: a backcasting approach. *R. Soc. Open Sci.* **7**, 200909 (2020).

10. 10.

Ministry of Civil Protection and Ministry of Tourism, Hellenic Republic. *Protocol for Arrivals in Greece* <https://travel.gov.gr/#/policy> (1 July 2020).

11. 11.

Tibshirani, R. Regression shrinkage and selection via the lasso. *J. R. Stat. Soc. B* **58.1**, 267–288 (1996).

12. 12.

Greenland, S. & Robins, J. Empirical-Bayes adjustments for multiple comparisons are sometimes useful. *Epidemiology* **2**, 244–251 (1991).

13. 13.

Devine, O. J., Louis, T. & Halloran, E. Empirical Bayes methods for stabilizing incidence rates before mapping. *Epidemiology* **5**, 622–630 (1994).

14. 14.

Dorfman, R. The detection of defective members of large populations. *Ann. Math. Stat.* **14**, 436–440 (1943).

15. 15.

Thompson, W. On the likelihood that one unknown probability exceeds another in view of the evidence of two samples. *Biometrika* **25.3/4**, 285–294 (1933).

16. 16.

Lai, T. L. & Robbins, H. Asymptotically efficient adaptive allocation rules. *Adv. Appl. Math.* **6.1**, 4–22 (1985).

17. 17.

Gittins, J. Bandit processes and dynamic allocation indices. *J. R. Stat. Soc. B* **41.2**, 148–164 (1979).

18. 18.

Auer, P. Using confidence bounds for exploitation-exploration trade-offs. *J. Mach. Learn. Res.* **3**, 397–422 (2002).

19. 19.

Tewari, A. & Murphy, S. A. In *Mobile Health—Sensors, Analytic Methods, and Applications* (eds Rehg, J. M., Murphy, S. A. & Kumar, S.) 495–517 (Springer, 2017).

20. 20.

Durand, A. et al. Contextual bandits for adapting treatment in a mouse model of de novo carcinogenesis. In *Proceedings of the 3rd Machine Learning for Healthcare Conference. Proc. Mach. Learn. Res.* **85**, 67–82 (2018).

21. 21.

Li, L., Chu, W., Langford, J. & Schapire, R. In *Proceedings of the 19th International Conference on World Wide Web* 6611–6670 (Association for Computing Machinery, 2010); <https://dl.acm.org/doi/10.1145/1772690.1772758>

22. 22.

Amat, F., Chandrashekhar, A., Jebara, T. & Basilico, J. In *Proceedings of the 12th ACM Conference on Recommender Systems* 487–488 (Association for Computing Machinery, 2018); <https://dl.acm.org/doi/10.1145/3240323.3241729>

23. 23.

Besbes, O., Gur Y. & Zeevi, A. In *Advances in Neural Information Processing Systems 27* (eds Ghahramani, Z., Welling, M., Cortes, C., Lawrence, N. & Weinberger, K. Q.) 199–207 (NIPS, 2014).

24. 24.

Luo, H., Wei, C.-Y., Agarwal, A. & Langford, J. Efficient contextual bandits in non-stationary worlds. In *Proceedings of the 31st Conference on Learning Theory. Proc. Mach. Learn. Res.* **75**, 1739–1776 (2018).

25. 25.

Bastani, H. & Bayati, M. Online decision making with high-dimensional covariates. *Oper. Res.* **68**.1, 276–294 (2020).

26. 26.

Gao, Z., Han, Y., Ren, Z. & Zhou, Z. In *Advances in Neural Information Processing Systems* 32 (eds Wallach, H. et al.) 503–514 (NeurIPS, 2019).

27. 27.

Perchet, V., Rigollet, P., Chassang, S. & Snowberg, E. Batched bandit problems. *Ann. Stat.* **44**.2, 660–681 (2016).

28. 28.

Agrawal, S. & Devanur, N. Bandits with concave rewards and convex knapsacks. In *Proceedings of the 15th ACM Conference on Economics and Computation* 989–1006 (Association for Computing Machinery, 2014);
<https://doi.org/10.1145/2600057.2602844>

29. 29.

Gutin, E. & Farias, V. In *Advances in Neural Information Processing Systems* 29 (eds Lee, D., Sugiyama, M., Luxburg, U., Guyon, I. & Garnett, R.) 3153–3161 (2016).

30. 30.

Hellewell, J. et al. Feasibility of controlling COVID-19 outbreaks by isolation of cases and contacts. *Lancet Glob. Health* **8**, e488–e496 (2020).

31. 31.

Imbens, W. G. & Rubin, B. D. *Causal Inference in Statistics, Social and Biomedical Sciences* (Cambridge Univ. Press, 2015).

32. 32.

Rosenbaum, P. & Rubin, D. The central role of the propensity score in observational studies for causal effects. *Biometrika* **70**, 41–55 (1983).

33. 33.

Friedman, J. H. Greedy function approximation: a gradient boosting machine. *Ann. Stat.* **29**, 1189–1232 (2001).

34. 34.

Davies, N. et al. Age-dependent effects in the transmission and control of COVID-19 epidemics. *Nat. Med.* **26**, 1205–1211 (2020).

35. 35.

Davies, S. E. & Bennet, B. A gendered human rights analysis of Ebola and Zika: locating gender in global health emergencies. *Int. Aff.* **92.5**, 1041–1060 (2016).

36. 36.

Agrawal S. & Goyal, N. Thompson sampling for contextual bandits with linear payoffs. In *Proceedings of the 30th International Conference on Machine Learning. Proc. Mach. Learn. Res.* **28**, 127–135 (2013).

37. 37.

Chu, W., Li, L., Reyzin, L. & Schapire, R. Contextual bandits with linear payoff functions. In *Proceedings of the 14th International Conference on Artificial Intelligence and Statistics. Proc. Mach. Learn. Res.* **15**, 208–214 (2011).

Acknowledgements

We thank all members of the Greek COVID-19 taskforce, the Greek Prime Minister K. Mitsotakis, the Ministry of Digital Governance, the General Secretariat for Civil Protection, the Ministry of Health, the National Public Health Organization, the development team from Cytech and the border control agents, doctors, nurses and laboratory personnel that contributed to Eva’s deployment. We also thank O. Bastani for discussions and analysis on constructing custom risk metrics from public data. V.G. was partially supported by the National Science Foundation through NSF grant CMMI-1661732.

Author information

Author notes

1. These authors contributed equally: Hamsa Bastani, Kimon Drakopoulos, Vishal Gupta

Affiliations

1. Department of Operations, Information and Decisions, Wharton School, University of Pennsylvania, Philadelphia, PA, USA

Hamsa Bastani

2. Department of Data Sciences and Operations, Marshall School of Business, University of Southern California, Los Angeles, CA, USA

Kimon Drakopoulos & Vishal Gupta

3. AgentRisk, Los Angeles, CA, USA

Ioannis Vlachogiannis

4. Department of Hygiene and Epidemiology, University of Thessaly, Larissa, Greece

Christos Hadjicristodoulou

5. Department of Hygiene, Epidemiology and Medical Statistics, School of Medicine, National and Kapodistrian University of Athens, Athens, Greece

Pagona Lagiou, Gkikas Magiorkinis & Dimitrios Paraskevis

6. Department of Internal Medicine, Attikon University Hospital, Medical School, National and Kapodistrian University of Athens, Athens, Greece

Sotirios Tsiodras

Contributions

H.B., K.D. and V.G. constructed the model, designed and coded the algorithm, and performed the analysis in this paper. I.V. designed the software architecture and application programming interfaces to communicate with the Central Database of the Ministry of Digital Governance. C.H., P.L., G.M., D.P. and S.T. contributed to and informed epidemiological modelling choices of the system. All authors coordinated Eva's operations and logistics throughout its deployment.

Corresponding author

Correspondence to Kimon Drakopoulos.

Ethics declarations

Competing interests

H.B., V.G. and I.V. declare no competing interests. K.D. declares a non-financial competing interest as an unpaid Data Science and Operations Advisor to the Greek Government from 1 May 2020 to 1 November 2020. C.H., P.L., G.M., D.P. and S.T. declare a non-financial competing interest as members of the Greek national COVID-19 taskforce.

Additional information

Peer review information *Nature* thanks Mark Jit, Ziad Obermeyer, Javier Sanchez-Monedero and the other, anonymous, reviewer(s) for their contribution to the peer review of this work.

Publisher's note Springer Nature remains neutral with regard to jurisdictional claims in published maps and institutional affiliations.

Supplementary information

Supplementary Information

This file contains Supplementary text, Supplementary Figs. 6–20, equations and references.

Reporting Summary

Rights and permissions

Reprints and Permissions

About this article

Cite this article

Bastani, H., Drakopoulos, K., Gupta, V. *et al.* Efficient and targeted COVID-19 border testing via reinforcement learning. *Nature* **599**, 108–113 (2021).

<https://doi.org/10.1038/s41586-021-04014-z>

- Received: 16 March 2021
- Accepted: 10 September 2021
- Published: 22 September 2021
- Issue Date: 04 November 2021
- DOI: <https://doi.org/10.1038/s41586-021-04014-z>

Share this article

Anyone you share the following link with will be able to read this content:

[Get shareable link](#)

Sorry, a shareable link is not currently available for this article.

[Copy to clipboard](#)

Provided by the Springer Nature SharedIt content-sharing initiative

[**A machine-learning algorithm to target COVID testing of travellers**](#)

- Ziad Obermeyer

News & Views 22 Sept 2021

[**Eva to the rescue**](#)

- Fernando Chirigati

Research Highlight 08 Oct 2021

This article was downloaded by **calibre** from <https://www.nature.com/articles/s41586-021-04014-z>

- Article
- Open Access
- [Published: 06 September 2021](#)

SARS-CoV-2 B.1.617.2 Delta variant replication and immune evasion

- [Petra Mlcochova](#)^{1,2} nat,
- [Steven A. Kemp](#)^{1,2,3} nat,
- [Mahesh Shanker Dhar](#)⁴ nat,
- [Guido Papa](#)⁵,
- [Bo Meng](#)^{1,2},
- [Isabella A. T. M. Ferreira](#)^{1,2},
- [Rawlings Datir](#)^{1,2},
- [Dami A. Collier](#)^{2,3},
- [Anna Albecka](#)⁵,
- [Sujeet Singh](#)⁴,
- [Rajesh Pandey](#)⁶,
- [Jonathan Brown](#)⁷,
- [Jie Zhou](#)⁷,
- [Niluka Goonawardane](#)⁷,
- [Swapnil Mishra](#)⁸,
- [Charles Whittaker](#)⁸,
- [Thomas Mellan](#)⁸,
- [Robin Marwal](#)⁴,
- [Meena Datta](#)⁴,
- [Shantanu Sengupta](#)⁶,
- [Kalaiarasan Ponnusamy](#)⁴,
- [Venkatraman Srinivasan Radhakrishnan](#)⁴,
- [Adam Abdullahi](#)^{1,2},
- [Oscar Charles](#)³,
- [Partha Chattopadhyay](#)⁶,
- [Priti Devi](#)⁶,
- [Daniela Caputo](#)⁹,
- [Tom Peacock](#)⁸,

- [Chand Wattal¹⁰](#),
- [Neeraj Goel¹⁰](#),
- [Ambrish Satwik¹⁰](#),
- [Raju Vaishya¹¹](#),
- [Meenakshi Agarwal¹²](#),
- [The Indian SARS-CoV-2 Genomics Consortium \(INSACOG\)](#),
- [The Genotype to Phenotype Japan \(G2P-Japan\) Consortium](#),
- [The CITIID-NIHR BioResource COVID-19 Collaboration](#),
- [Antranik Mavousian¹³](#),
- [Joo Hyeon Lee^{13,14}](#),
- [Jessica Bassi¹⁵](#),
- [Chiara Silacci-Fegni¹⁵](#),
- [Christian Saliba¹⁵](#),
- [Dora Pinto¹⁵](#),
- [Takashi Irie¹⁶](#),
- [Isao Yoshida¹⁷](#),
- [William L. Hamilton²](#),
- [Kei Sato^{18,19}](#),
- [Samir Bhatt^{4,20}](#),
- [Seth Flaxman²¹](#),
- [Leo C. James⁵](#),
- [Davide Corti¹⁵](#),
- [Luca Piccoli¹⁵](#),
- [Wendy S. Barclay⁸](#),
- [Partha Rakshit^{4 na1}](#),
- [Anurag Agrawal^{6 na1}](#) &
- [Ravindra K. Gupta ORCID: orcid.org/0000-0001-9751-1808^{1,2,22 na1}](#)

Nature volume 599, pages 114–119 (2021)

- 111k Accesses
- 1981 Altmetric
- [Metrics details](#)

Subjects

- [Infection](#)
- [SARS-CoV-2](#)

Abstract

The B.1.617.2 (Delta) variant of severe acute respiratory syndrome coronavirus 2 (SARS-CoV-2) was first identified in the state of Maharashtra in late 2020 and spread throughout India, outcompeting pre-existing lineages including B.1.617.1 (Kappa) and B.1.1.7 (Alpha)¹. In vitro, B.1.617.2 is sixfold less sensitive to serum neutralizing antibodies from recovered individuals, and eightfold less sensitive to vaccine-elicited antibodies, compared with wild-type Wuhan-1 bearing D614G. Serum neutralizing titres against B.1.617.2 were lower in ChAdOx1 vaccinees than in BNT162b2 vaccinees. B.1.617.2 spike pseudotyped viruses exhibited compromised sensitivity to monoclonal antibodies to the receptor-binding domain and the amino-terminal domain. B.1.617.2 demonstrated higher replication efficiency than B.1.1.7 in both airway organoid and human airway epithelial systems, associated with B.1.617.2 spike being in a predominantly cleaved state compared with B.1.1.7 spike. The B.1.617.2 spike protein was able to mediate highly efficient syncytium formation that was less sensitive to inhibition by neutralizing antibody, compared with that of wild-type spike. We also observed that B.1.617.2 had higher replication and spike-mediated entry than B.1.617.1, potentially explaining the B.1.617.2 dominance. In an analysis of more than 130 SARS-CoV-2-infected health care workers across three centres in India during a period of mixed lineage circulation, we observed reduced ChAdOx1 vaccine effectiveness against B.1.617.2 relative to non-B.1.617.2, with the caveat of possible residual confounding. Compromised vaccine efficacy against the highly fit and immune-evasive B.1.617.2 Delta variant warrants continued infection control measures in the post-vaccination era.

[Download PDF](#)

Main

India's first wave of SARS-CoV-2 infections in mid-2020 was relatively mild and was controlled by a nationwide lockdown. Following the easing of restrictions, India has seen expansion in cases of coronavirus disease 2019 since March 2021 with widespread fatalities and a death toll of more than 400,000. Cases of the B.1.1.7 Alpha variant, introduced by travel from the UK in late 2020, expanded in the north of India, and it is known to be more transmissible than previous versions of the virus bearing the D614G spike substitution, while maintaining sensitivity to vaccine-elicited neutralizing antibodies^{2,3}. The B.1.617 variant was first identified in the state of Maharashtra in late 2020⁴, spreading throughout India and to at least 90 countries.

The first sublineage to be detected was B.1.617.1 (ref. ¹), followed by B.1.617.2, both bearing the L452R spike receptor-binding motif (RBM) substitution also observed in

B.1.427/B.1.429 (refs. [1,5](#)). This alteration was previously reported to confer increased infectivity and a modest loss of susceptibility to neutralizing antibodies^{[6,7](#)}. The B.1.617.2 Delta variant has since dominated over B.1.617.1 (Kappa variant) and other lineages including B.1.1.7, although the reasons remain unclear.

Delta variant and neutralizing antibodies

We first plotted the relative proportion of variants in new cases of SARS-CoV-2 in India since the start of 2021. Although B.1.617.1 emerged earlier, the Delta variant B.1.617.2 has become more dominant (Fig. [1a](#)). We hypothesized that B.1.617.2 would exhibit immune evasion to antibody responses generated by previous SARS-CoV-2 infection. We used sera from 12 individuals infected during the first UK wave in mid-2020. These sera were tested for their ability to neutralize a B.1.617.2 viral isolate, in comparison with a B.1.1.7 variant isolate and a wild-type (WT) Wuhan-1 virus bearing D614G in spike. The Delta variant contains several spike alterations that are located at positions within the structure that are predicted to alter its function (Fig. [1b](#)). We found that the B.1.1.7 virus isolate was 2.3-fold less sensitive to the sera than the WT, and that B.1.617.2 was 5.7-fold less sensitive to the sera (Fig. [1c](#)).

Importantly, in the same assay, the B.1.351 Beta variant that was first identified in South Africa demonstrated an 8.2-fold loss of neutralization sensitivity relative to the WT.

Fig. 1: Rapid expansion of Delta variant B.1.617.2 cases in India and reduced sensitivity to neutralizing antibodies from sera derived following infection and vaccination.

 **figure1**

a, Proportion of lineages in incident cases of SARS-CoV-2 in India 2020–2021. **b**, Surface representation of the SARS-CoV-2 B.1.671.2 spike trimer (PDB: [6ZGE](#)). Red, L19R; green, del157/158; blue, L452R; yellow, T478K. The white dotted box indicates the location of the D950N substitution (orange). **c**, Neutralization of the Delta variant by convalescent human serum from mid-2020. Fold change in serum neutralization of 100 TCID₅₀ of B.1.17 (Alpha), B.1.351 (Beta) and B.1617.2 (Delta) variants relative to WT (IC19); $n = 12$. Shown is the ID₅₀, the serum dilution required for 50% virus inhibition, expressed as GMT (from technical replicates) with s.d. **d**, Neutralization of B.1617.2 live virus by sera from vaccinated individuals ($n = 10$ ChAdOx1 or $n = 10$ BNT12b2), compared with B.1.1.7 and Wuhan-1 WT. The graph presents the average of two independent experiments. **e**, Neutralization of B.1.617 spike PV and WT (Wuhan-1 D614G) by vaccine sera ($n = 33$ ChAdOx1 or $n = 32$ BNT162b2). The data are representative of two independent experiments each with two technical replicates. * $P < 0.05$, ** $P < 0.01$, *** $P < 0.0001$ (Wilcoxon matched-pairs signed rank test); NS, not significant.

We used the same B.1.617.2 live virus isolate to test susceptibility to vaccine-elicited serum neutralizing antibodies in individuals following vaccination with two doses of ChAdOx1 or BNT162b2. These experiments showed a loss of sensitivity for B.1.617.2 compared with WT Wuhan-1 bearing D614G of around eightfold for both sets of vaccine sera and reduction against B.1.1.7 that did not reach statistical significance (Fig. [1d](#)). We also used a pseudotyped virus (PV) system to test the neutralization

potency of a larger panel of 65 vaccine-elicited sera, this time against B.1.617.1 as well as B.1.617.2 spike compared with Wuhan-1 D614G spike (Fig. 1e). Comparison of demographic data for vaccinees showed similar characteristics (Extended Data Table 1). The mean geometric mean titre (GMT) against Delta variant spike PV was lower for ChAdOx1 than for BNT162b2 (GMT 654 versus 3,372, $P < 0.001$, Extended Data Table 1).

We investigated the role of the B.1.617.2 spike as an escape mechanism by testing 33 spike-specific monoclonal antibodies with an in vitro PV neutralization assay using Vero E6 target cells expressing transmembrane protease serine 2 (TMPRSS2) and the Wuhan-1 D614G SARS-CoV-2 spike or the B.1.617.2 spike (Extended Data Fig. 1 and Extended Data Table 2). We found that all three amino-terminal domain monoclonal antibodies (100%) and four out of nine (44%) non-RBM monoclonal antibodies completely lost neutralizing activity against B.1.617.2. Within the RBM-binding group, 16 out of 26 monoclonal antibodies (61.5%) showed a marked decrease (2- to 35-fold-change reduction) or complete loss (>40 -fold-change reduction) of neutralizing activity to B.1.617.2 (Extended Data Fig. 1). Among five clinical-stage RBM monoclonal antibodies tested, bamlanivimab did not neutralize B.1.617.2. Imdevimab, part of the REGN-COV2 therapeutic dual antibody cocktail⁸, displayed reduced neutralizing activity (Extended Data Fig. 1).

SARS-CoV-2 Delta variant replication

We first infected a lung epithelial cell line, Calu-3, comparing B.1.1.7 and B.1.617.2 (Fig. 2a–d). We observed a replication advantage for B.1.617.2 (Fig. 2a, b), as well as an increase in released virions from cells (Fig. 2c, d). Next we tested B.1.1.7 against two separate isolates of B.1.617.2 in a human airway epithelial (HAE) model⁹. In this system we again observed that both B.1.617.2 isolates had a significant replication advantage over B.1.1.7 (Fig. 2e, f). Finally, we infected primary three-dimensional airway organoids¹⁰ (Fig. 2g) with B.1.617.2 and B.1.1.7 virus isolates, noting a significant replication advantage for B.1.617.2 over B.1.1.7. These data clearly support the higher replication rate and therefore transmissibility of B.1.617.2 over B.1.1.7.

Fig. 2: Delta variant live virus replication kinetics and spike-mediated infectivity.

 **figure2**

a–d, Live virus replication comparing B.1.1.7 with B.1.617.2. Calu-3 cells were infected with variants at an MOI of 0.1. **a**, Viral loads measured by qPCR in cell lysates. **b**, Viral protein levels in cell lysates. **c, d**, Live virus produced from infected Calu-3 cell supernatants was collected and used to infect permissive Vero E6 ACE2/TMPRSS2 cells to measure viral loads (**c**) or TCID₅₀ ml⁻¹ (**d**). **e, f**, Virus replication kinetics in the HAE system. **g**, Live virus replication in airway epithelial organoid cultures. Airway epithelial organoids were infected with the SARS-CoV-2 variants B.1.1.7 and B.1.617.2 at an MOI of 1. Cells were lysed and total RNA was isolated. qPCR was used to determine the number of copies of the nucleoprotein gene in cells and the infectivity of cell-free virus measured by infection of Vero E6 ACE2/TMPRSS2 cells. The data are representative of two independent experiments.

dpi, days post-infection. **h, i**, Western blots of PV virions (**h**) and cell lysates (**i**) of 293T producer cells following transfection with plasmids expressing lentiviral vectors and SARS-CoV-2 S B.1.617.1 and Delta variant B.1.617.2 versus WT (Wuhan-1 with D614G), probed with antibodies to HIV-1 p24 and SARS-CoV-2 S2. **j**, Calu-3 cell entry by spike B.1.617.2 and B.1.617.1 versus WT D614G parental plasmid PVs. The data are representative of three independent experiments. **k**, Growth kinetics of B.1.617.1 and B.1.617.2 variants. Viral isolates of B.1.617.1 and B.1.617.2 were inoculated into Calu-3 cells, and viral RNA in the culture supernatant was quantified by real-time RT-PCR. The TCID₅₀ of released virus in supernatant was measured over time. Assays were performed in quadruplicate. NS, not significant; *P < 0.05, **P < 0.01, ***P < 0.001, ****P < 0.0001. The data are representative of two independent experiments. Uninfected cells are represented by a minus symbol. NP, nucleocapsid protein.

In the aforementioned experiments, we noted a higher proportion of intracellular B.1.617.2 spike in the cleaved state, compared with B.1.1.7 (Fig. 2b). We next ran western blots on purified virions probing for spike S2 and nucleoprotein, revealing B.1.617.2 spike predominantly in the cleaved form, in contrast to that in B.1 and B.1.1.7 (Extended Data Fig. 2a, b).

B.1.617.2 spike-mediated cell fusion

The plasma membrane route of entry, and indeed transmissibility in animal models, is critically dependent on the polybasic cleavage site between S1 and S2 (refs. 9,11,12) and cleavage of spike before virion release from producer cells. Alterations at P681 in the polybasic cleavage site have been observed in multiple SARS-CoV-2 lineages, most notably in the B.1.1.7 Alpha variant¹³. We previously showed that B.1.1.7 spike, bearing P681H, had significantly higher fusogenic potential than a D614G Wuhan-1 virus¹³. Here we tested B.1.617.1 and B.1.617.2 spike using a split GFP system to monitor cell-cell fusion (Extended Data Fig. 2c–g). The B.1.617.1 and B.1.617.2 spike proteins mediated higher fusion activity and syncytium formation than WT, probably mediated by P681R (Extended Data Fig. 2f, g). We next titrated sera from ChAdOx1 vaccinees and showed that indeed the cell-cell fusion could be inhibited in a manner that mirrored the neutralization activity of the sera against PV infection of cells (Extended Data Fig. 2h). Hence, B.1.617.2 may induce cell-cell fusion in the respiratory tract and possibly higher pathogenicity even in vaccinated individuals with neutralizing antibodies.

B.1.617.2 spike-mediated cell entry

We tested single-round viral entry of B.1.617.1 and B.1.617.2 spike (Fig. 2*h,i* and Extended Data Fig. 3*a,b*) using the PV system, infecting Calu-3 lung cells expressing endogenous levels of angiotensin-converting enzyme 2 (ACE2) and TMPRSS2 (Fig. 2*j*), as well as other cells transduced or transiently transfected with ACE2 and TMPRSS2 (Extended Data Fig. 3*b*). B.1.617 spike proteins were present predominantly in the cleaved form, in contrast to WT (Fig. 2*h,i* and Extended Data Fig. 3*c*). We observed 1 log increased entry efficiency for both B.1.617.1 and B.1.617.2 over WT (Extended Data Fig. 3*b*).

The B.1.617.1 variant was detected before B.1.617.2 in India, and the reasons for B.1.617.2 outcompeting B.1.617.1 are unknown. B.1.617.2 had an entry advantage compared with B.1.617.1 in Calu-3 cells bearing endogenous receptors (Fig. 2*j*). We confirmed higher infectivity of B.1.617.2 using live virus isolates in Calu-3 cells (Fig. 2*k*), offering a parsimonious explanation for the epidemiologic growth advantage of B.1.617.2.

B.1.617.2 vaccine breakthrough infection

We hypothesized that vaccine effectiveness against B.1.617.2 would be compromised relative to that against other circulating variants. Vaccination of health care workers (HCWs) started in early 2021 with the ChAdOx1 vaccine (Covishield). During the wave of infections in March and April, symptomatic SARS-CoV-2 was confirmed in 30 vaccinated staff members among a workforce of 3,800 at a single tertiary centre in Delhi. Genomic data from India and Delhi suggested B.1.1.7 dominance (Fig. 1*a* and Extended Data Fig. 4*a*), with growth of B.1.617 during March 2021. Short-read sequencing¹⁴ of symptomatic non-fatal infections in the HCW outbreak revealed that the majority were B.1.617.2 with a range of other B lineage viruses (Fig. 3*a*). Phylogenetic analysis demonstrated a group of highly related, and in some cases, genetically indistinct sequences that were sampled within 1 or 2 days of each other (Fig. 3*a* and Extended Data Fig. 4*b*). We next looked in greater detail at the vaccination history of affected individuals. Nearly all had received two doses at least 21 days previously. We obtained similar data on vaccine breakthrough infections in two other health facilities in Delhi with 1,100 and 4,000 HCW staff members, respectively (Fig. 3*b,c* and Extended Data Fig. 4*c,d*). In hospital 2, there were 118 sequences, representing more than 10% of the workforce over a 4-week period. After filtering, we reconstructed phylogenies using 66 with high-quality whole-genome coverage >95%. In hospital 3, there were 70 symptomatic infections, with 52 high-quality genomes used for inferring phylogenies after filtering.

Fig. 3: SARS-CoV-2 B.1.617.2 infection in vaccinated HCWs.



a–c, Maximum-likelihood phylogenies of vaccine breakthrough SARS-CoV-2 sequences among vaccinated HCWs at three centres. Phylogenies were inferred with IQTREE2 with 1,000 bootstrap replicates. SNPs, single nucleotide polymorphisms.

Across the three centres, we noted that the median age and duration of infection of those infected with B.1.617.2 versus non-B.1.617.2 were similar (Extended Data Table 3), with no evidence that B.1.617.2 was associated with higher risk of hospitalization (Extended Data Table 3). Next we evaluated the effect of B.1.617.2 on vaccine effectiveness against symptomatic infection in the HCWs, compared with other lineages. We used multivariable logistic regression to estimate the odds ratio of testing positive with B.1.617.2 versus non-B.1.617.2 in vaccinated relative to unvaccinated individuals¹⁵, adjusting for age, sex and hospital. The adjusted odds ratio for B.1.617.2 relative to non-B.1.617.2 was 5.45 (95% confidence interval 1.39–21.4, $P = 0.018$) for two vaccine doses (Extended Data Table 4).

Discussion

Here we have combined in vitro experimentation and molecular epidemiology to propose that increased replication fitness and reduced sensitivity of SARS-CoV-2 B.1.617.2 to neutralizing antibodies have contributed to the recent rapid increase of B.1.617.2, compared with B.1.1.7 and other lineages such as B.1.617.1, despite high vaccination rates in adults and/or high prevalence of prior infection¹⁶. These data are consistent with modelling analyses that support combination of immune evasion and higher transmissibility as likely drivers of the increase in Delta in Delhi¹⁷.

We demonstrate evasion of neutralizing antibodies by a B.1.617.2 live virus with sera from convalescent patients, as well as sera from individuals vaccinated with two different vaccines, one based on an adenovirus vector (ChAdOx1) and the other mRNA based (BNT162b2). The reduced efficacy for imedevimab against B.1.617.2 shown here could translate to compromised clinical efficacy or possible selection of escape variants where there is immune compromise and chronic SARS-CoV-2 infection with B.1.617.2 (ref. ¹⁸).

It is important to consider that increased infectivity at mucosal surfaces and cell–cell fusion and spread¹⁹ may also facilitate ‘evasion’ from antibodies²⁰. Indeed, our work also shows that B.1.617.2 had a fitness advantage compared with B.1.1.7 across physiologically relevant systems including HAE and three-dimensional airway organoids¹⁰ where cell-free and cell–cell infection are likely to be occurring together. These data support the notion of higher infectiousness of B.1.617.2, either due to higher viral burden or higher particle infectivity, resulting in higher probability of person-to-person transmission. We noted that B.1.617.2 live virus particles contained a higher proportion of cleaved spike than B.1.1.7, and postulated that this is involved in the mechanism of increased infectivity. This hypothesis was supported by our observation that PV particles bearing B.1.617.2 spike demonstrated significantly enhanced entry into a range of target cells.

Finally, we report ChAdOx1 vaccine breakthrough infections in HCWs at three Delhi hospitals, demonstrating reduced vaccine effectiveness against B.1.617.2. Therefore, strategies to boost vaccine responses against variants are warranted and attention to infection control procedures is needed in the post-vaccination era.

Methods

Serum samples and ethical approval

Ethical approval for the study of vaccine-elicited antibodies in sera from vaccinees was obtained from the East of England – Cambridge Central Research Ethics Committee Cambridge (REC ref. 17/EE/0025). Use of convalescent sera had ethical approval from the South Central - Berkshire B Research Ethics Committee (REC ref.

20/SC/0206; IRAS 283805). Studies involving HCWs (including testing and sequencing of respiratory samples) were reviewed and approved by The Institutional Human Ethics Committees of the National Centre for Disease Control (NCDC) and CSIR-IGIB(NCDC/2020/NERC/14 and CSIR-IGIB/IHEC/2020-21/01). Participants provided informed consent.

Sequencing quality control and phylogenetic analysis

Three sets of fasta consensus sequences were obtained from three separate hospitals in Delhi, India. Initially, all sequences were concatenated into a multi-fasta file and then aligned to the reference strain [MN908947.3](#) (Wuhan-Hu-1) with mafft v4.487 (ref. [21](#)) using the --keeplength and --addfragments options. Following this, all sequences were passed through Nextclade v0.15 (<https://clades.nextstrain.org/>) to determine the number of gap regions. This was noted and all sequences were assigned a lineage with Pangolin v3.1.5 (ref. [22](#)) and pangoLEARN (dated 15 June 2021). Sequences that could not be assigned a lineage were discarded. After assigning lineages, all sequences with more than 5% N regions were also excluded.

Phylogenies were inferred using maximum likelihood in IQTREE v2.1.4 (ref. [23](#)) using a GTR + R6 model with 1,000 rapid bootstraps. The inferred phylogenies were annotated in R v4.1.0 using ggtree v3.0.2 (ref. [24](#)) and rooted on the SARS-CoV-2 reference sequence ([MN908947.3](#)). Nodes were arranged in descending order and lineages were annotated on the phylogeny as coloured tips, alongside a heatmap defining the number of ChAdOx1 vaccine doses received by each patient.

Structural analyses

The PyMOL Molecular Graphics System v.2.4.0 (<https://github.com/schrodinger/pymol-open-source/releases>) was used to map the location of the mutations defining the Delta lineage (B.1.617.2) onto the closed-conformation spike protein (PDB: [6ZGE](#))²⁵.

Statistical analyses

Vaccine breakthrough infections in HCWs

Descriptive analyses of demographic and clinical data are presented as median and interquartile range or mean and standard deviation (s.d.) when continuous and as frequency and proportion (%) when categorical. The differences in continuous and categorical data were tested using the Wilcoxon rank sum test or *t*-test and chi-square test, respectively. The association between the Ct value and the SARS-CoV-2 variant

was examined using linear regression. Variants as the dependent variable were categorized into two groups: B.1.617.2 variant and non-B.1.617.2 variants. The following covariates were included in the model irrespective of confounding: age, sex, hospital and interval between symptom onset and nasal swab PCR testing.

Vaccine effectiveness

To estimate vaccine effectiveness for the B.1.617.2 variant relative to non-B.1.617.2 variants, we adopted a recently described approach¹⁵. This method is based on the premise that if the vaccine is equally effective against B.1.617.2 and non-B.1.617.2 variants, a similar proportion of cases with each variant would be expected in both vaccinated and unvaccinated cases. This approach overcomes the issue of higher background prevalence of one variant over the other. We determined the proportion of individuals with the B.1.617.2 variant relative to all other circulating variants by vaccination status. We then used logistic regression to estimate the odds ratio of testing positive with B.1.617.2 in vaccinated compared with unvaccinated individuals. The final regression model was adjusted for age as a continuous variable, and sex and hospital as categorical variables. Model sensitivity and robustness to inclusion of these covariates was tested by an iterative process of sequentially adding the covariates to the model and examining the impact on the odd ratios and confidence intervals until the final model was constructed (Extended Data Table 4). The R^2 measure, as proposed by McFadden²⁶, was used to test the fit of different specifications of the same model regression. This was performed by sequential addition of the variables adjusted for including age, sex and hospital until the final model was constructed. In addition, the absolute difference in the Bayesian information criterion was estimated. The McFadden R^2 measure of final model fitness was 0.11, indicating reasonable model fit. The addition of age, sex and hospital in the final regression model improved the measured fitness. However, the absolute difference in the Bayesian information criterion was 13.34 between the full model and the model excluding the adjusting variable, providing strong support for the parsimonious model. The fully adjusted model was nonetheless used as the final model as the sensitivity analyses (Extended Data Table 4) showed robustness to the addition of the covariates.

Neutralization titre analyses

The neutralization by vaccine-elicited antibodies after two doses of the BNT162b2 or ChadOx1 vaccines was determined by infections in the presence of serial dilutions of sera as described below. The ID₅₀ for each group was summarized as a GMT, and statistical comparisons between groups were performed with Mann–Whitney or Wilcoxon ranked sign tests. Statistical analyses were performed using Stata v13 and Prism v9.

PV experiments

Cells

HEK 293T CRL-3216, HeLa-ACE2 (gift from James Voss) and Vero CCL-81 cells were maintained in Dulbecco's modified Eagle medium (DMEM) supplemented with 10% fetal calf serum (FCS), 100 U ml⁻¹ penicillin and 100 mg ml⁻¹ streptomycin. All cells were regularly tested and found to be mycoplasma free. H1299 cells were a gift from Simon Cook. Calu-3 cells were a gift from Paul Lehner. A549 ACE2/TMPRSS2 (ref. 27) cells were a gift from Massimo Palmerini. Vero E6 ACE2/TMPRSS2 cells were a gift from Emma Thomson.

PV preparation for testing against vaccine-elicited antibodies and cell entry

Plasmids encoding the spike protein of SARS-CoV-2 D614 with a carboxy-terminal 19-amino-acid deletion with D614G were used. Mutations were introduced using the QuikChange Lightning Site-Directed Mutagenesis kit (Agilent) following the manufacturer's instructions. Preparation of the B.1.1.7 S-expressing plasmid was described previously, but in brief, it was generated by stepwise mutagenesis. Viral vectors were prepared by transfection of 293T cells by using Fugene HD transfection reagent (Promega). 293T cells were transfected with a mixture of 11 µl Fugene HD, 1 µg pCDNAΔ19 spike-HA, 1 µg p8.91 human immunodeficiency virus 1 (HIV-1) *gag-pol* expression vector and 1.5 µg pCSFLW (expressing the firefly luciferase reporter gene with the HIV-1 packaging signal). Viral supernatant was collected at 48 and 72 h after transfection, filtered through a 0.45-µm filter and stored at -80 °C as previously described. Infectivity was measured by luciferase detection in target 293T cells transfected with TMPRSS2 and ACE2, Vero E6 ACE2/TMPRSS2, Calu-3, A549 ACE2/TMPRSS2, H1299 and HeLa-ACE2 cells.

Standardization of virus input by SYBR Green-based product-enhanced PCR assay

The reverse transcriptase (RT) activity of virus preparations was determined by quantitative PCR (qPCR) using a SYBR Green-based product-enhanced PCR assay as previously described²⁸. In brief, tenfold dilutions of virus supernatant were lysed in a 1:1 ratio in a 2× lysis solution (made up of 40% glycerol (v/v), 0.25% Triton X-100 (v/v), 100 mM KCl, RNase inhibitor 0.8 U ml⁻¹, Tris HCl 100 mM, buffered to pH 7.4) for 10 min at room temperature.

A 12-µl volume of each sample lysate was added to 13 µl of a SYBR Green master mix (containing 0.5 µM MS2-RNA forward and reverse primers, 3.5 pmol ml⁻¹ MS2-

RNA and $0.125\text{ U}\mu\text{l}^{-1}$ Ribolock RNase inhibitor) and cycled in a QuantStudio. Relative amounts of RT activity were determined as the rate of transcription of bacteriophage MS2 RNA, with absolute RT activity calculated by comparing the relative amounts of RT activity with an RT standard of known activity.

Viral isolate comparison between B.1.617.1 and B.1.617.2

Cell culture

Vero E6 TMPRSS2 cells (an African green monkey (*Chlorocebus sabaeus*) kidney cell line; JCRB1819)²⁹ were maintained in DMEM (low glucose) (Wako, catalogue no. 041-29775) containing 10% FCS, G418 (1 mg ml $^{-1}$; Nacalai Tesque, catalogue no. G8168-10ML) and 1% antibiotics (penicillin and streptomycin (P/S)).

Calu-3 cells (a human lung epithelial cell line; ATCC HTB-55) were maintained in minimum essential medium Eagle (Sigma-Aldrich, catalogue no. M4655-500ML) containing 10% FCS and 1% PS.

SARS-CoV-2 B.1.617.1 versus B.1.617.2 experiment

Two viral isolates belonging to the B.1.617 lineage, B.1.617.1 (GISAID ID: EPI_ISL_2378733) and B.1.617.2 (GISAID ID: EPI_ISL_2378732), were isolated from SARS-CoV-2-positive individuals in Japan. Briefly, 100 μl of the nasopharyngeal swab obtained from SARS-CoV-2-positive individuals was inoculated into Vero E6 TMPRSS2 cells in a biosafety level 3 laboratory. After incubation at 37 °C for 15 min, a maintenance medium (Eagle's minimum essential medium (FUJIFILM Wako Pure Chemical Corporation, catalogue no. 056-08385) including 2% FCS and 1% PS) was added, and the cells were cultured at 37 °C under 5% CO₂. The cytopathic effect (CPE) was confirmed under an inverted microscope (Nikon), and the viral load of the culture supernatant in which CPE was observed was confirmed by real-time PCR with reverse transcription (RT-PCR). To determine viral genome sequences, RNA was extracted from the culture supernatant using the QIAamp viral RNA mini kit (Qiagen, catalogue no. 52906). A cDNA library was prepared using NEB Next Ultra RNA Library Prep Kit for Illumina (New England Biolab, catalogue no. E7530), and whole-genome sequencing was performed using a Miseq instrument (Illumina).

To prepare the working virus, 100 μl of the seed virus was inoculated into Vero E6 TMPRSS2 cells (5,000,000 cells in a T-75 flask). At 1 h after infection, the culture medium was replaced with DMEM (low glucose) (Wako, catalogue no. 041-29775) containing 2% FBS and 1% PS; at 2–3 days post-infection, the culture medium was collected and centrifuged, and the supernatants were collected as the working virus.

The titre of the prepared working virus was measured as 50% tissue culture infectious dose (TCID₅₀). Briefly, 1 day before infection, Vero E6 TMPRSS2 cells (10,000 cells per well) were seeded into a 96-well plate. Serially diluted virus stocks were inoculated onto the cells and incubated at 37 °C for 3 days. The cells were observed by microscopy to judge the CPE appearance. The TCID₅₀ ml⁻¹ value was calculated with the Reed–Muench method³⁰.

One day before infection, 20,000 Calu-3 cells were seeded into a 96-well plate. SARS-CoV-2 (200 TCID₅₀) was inoculated and incubated at 37 °C for 1 h. The infected cells were washed, and 180 µl of culture medium was added. The culture supernatant (10 µl) was collected at indicated time points and used for real-time RT–PCR to quantify the viral RNA copy number.

Real-time RT–PCR

Real-time RT–PCR was performed as previously described^{31,32}. In brief, 5 µl of culture supernatant was mixed with 5 µl of 2× RNA lysis buffer (2% Triton X-100, 50 mM KCl, 100 mM Tris HCl (pH 7.4), 40% glycerol, 0.8 U µl⁻¹ recombinant RNase inhibitor (Takara, catalogue no. 2313B)) and incubated at room temperature for 10 min. RNase-free water (90 µl) was added, and the diluted sample (2.5 µl) was used as the template for real-time RT–PCR performed according to the manufacturer’s protocol using the One Step TB Green PrimeScript PLUS RT–PCR kit (Takara, catalogue no. RR096A) and the following primers: forward *N*, 5'-AGCCTCTTCTCGTTCCATC AC-3'; and reverse *N*, 5'-CCGCCATTGCCAGCCATT C-3'. The copy number of viral RNA was standardized with a SARS-CoV-2 direct detection RT–qPCR kit (Takara, catalogue no. RC300A). The fluorescent signal was acquired using a QuantStudio 3 Real-Time PCR system (Thermo Fisher Scientific), a CFX Connect Real-Time PCR Detection System (Bio-Rad) or a 7500 Real Time PCR System (Applied Biosystems).

Virus growth kinetics in HAE cells

Primary nasal HAE cells at the air–liquid interface were purchased from Epithelix and the basal MucilAir medium (Epithelix) was changed every 2–3 days for maintenance of HAE cells. All dilution of viruses, wash steps and collection steps were carried out with OptiPRO serum-free medium (SFM; Life Technologies) containing 2× GlutaMAX (Gibco). All wash and collection steps were performed by addition of 200 µl SFM to the apical surface and incubation for 10 min at 37 °C before removing SFM. To infect cells, the basal medium was replaced, and the apical surface of the HAE cells was washed once with SFM to remove mucus before addition of virus to triplicate wells. Cells were infected at a multiplicity of infection (MOI) of 1 × 10⁴

genome copies of virus per cell based on E gene qRT–PCR. The cells were incubated with the inoculum for 1 h at 37 °C before washing their apical surface twice and retaining the second wash as the sample for 0 hpi. A single apical wash was performed to collect virus at 24, 48 and 71 h time points. Isolates used were B.1.617.2 isolate no. 60 hCoV-19/England/SHEF-10E8F3B/2021 (EPI_ISL_1731019), B.1.617.2 isolate no. 285 hCoV-19/England/PHEC-3098A2/2021 (EPI_ISL_2741645) and B.1.1.7 isolate no. 7540 SMH2008017540 (confirmed B.1.1.7 in-house but not yet available on GISAID).

Titration of outputs from HAE infections

For quantifying genome copies in the virus inputs and in the supernatant collected from HAE cells, RNA was extracted using the QIAsymphony DSP Virus/Pathogen Mini Kit on the QIAsymphony instrument (Qiagen). qRT–PCR was then performed using the AgPath RT–PCR (Life Technologies) kit on a QuantStudio(TM) 7 Flex System with the primers for SARS-CoV-2 E gene used previously³³. A standard curve was also generated using dilutions of viral RNA of known copy number to allow quantification of E gene copies in the samples from Ct values. E gene copies per millilitre of original virus supernatant were then calculated.

For measuring infectious virus in samples collected from HAE cells, plaque assays were carried out by performing serial log dilutions of supernatant in DMEM, 1% NEAA and 1% P/S and inoculating onto PBS-washed Vero cells, incubating for 1 h at 37 °C, removing inoculum and overlaying with 1× MEM, 0.2% (w/v) BSA, 0.16% (w/v) NaHCO₃, 10 mM HEPES, 2 mM l-glutamine, 1× P/S, 0.6% (w/v) agarose. Plates were incubated for 3 days at 37 °C before the overlay was removed and cells were stained for 1 h at room temperature in crystal violet solution.

Lung organoid infection by replication-competent SARS-CoV-2 isolates

Airway epithelial organoids were prepared as previously reported¹⁰. For viral infection, primary organoids were passaged and incubated with SARS-CoV-2 in suspension at an MOI of 1 for 2 h. Subsequently, the infected organoids were washed twice with PBS to remove the viral particles. Washed organoids were plated in 20-μl Matrigel domes, cultured in organoid medium and collected at different time points.

Cells were lysed 24 and 48 h post-infection and total RNA was isolated. cDNA was synthesized and qPCR was used to quantify copies of the nucleoprotein gene in samples. A standard curve was prepared using SARS-CoV-2 Positive Control plasmid encoding full nucleocapsid protein (N gene; NEB) and used to quantify copies of the N gene in organoid samples. 18S ribosomal RNA was used as a housekeeping gene to normalize sample-to-sample variation.

Western blotting

Cells were lysed and supernatants were collected 48 h post transfection. Purified virions were prepared by collecting supernatants and passing them through a 0.45- μm filter. Clarified supernatants were then loaded onto a thin layer of 8.4% OptiPrep density gradient medium (Sigma-Aldrich) and placed in a TLA55 rotor (Beckman Coulter) for ultracentrifugation for 2 h at 20,000 r.p.m. The pellet was then resuspended for western blotting. Cells were lysed with cell lysis buffer (Cell Signaling), treated with Benzonase nuclease (70664 Millipore) and boiled for 5 min. Samples were then run on 4–12% Bis Tris gels and transferred onto nitrocellulose or polyvinylidene fluoride membranes using an iBlot or semidry system (Life Technologies and Bio-Rad, respectively).

Membranes were blocked for 1 h in 5% non-fat milk in PBS + 0.1% Tween-20 (PBST) at room temperature with agitation, incubated in primary antibody (anti-SARS-CoV-2 spike, which detects the S2 subunit of SARS-CoV-2 S (Invitrogen, PA1-41165), anti-GAPDH (Proteintech) or anti-p24 (NIBSC)) diluted in 5% non-fat milk in PBST for 2 h at 4 °C with agitation, washed four times in PBST for 5 min at room temperature with agitation and incubated in secondary antibodies anti-rabbit HRP (1:10,000, Invitrogen 31462) and anti- β -actin HRP (1:5,000; sc-47778) diluted in 5% non-fat milk in PBST for 1 h with agitation at room temperature. Membranes were washed four times in PBST for 5 min at room temperature and imaged directly using a ChemiDoc MP imaging system (Bio-Rad).

Virus infection for virion western blotting

Vero E6 ACE2/TMPRSS2 cells were infected with an MOI of 1 and incubated for 48 h. Supernatant was cleared by a 5-min spin at 300g and then precipitated with 10% PEG6000 (4 h at room temperature). Pellets were resuspended directly in Laemmli buffer with 1 mM dithiothreitol, treated with Benzonase nuclease (70664 Millipore) and sonicated before loading for gel electrophoresis

Serum pseudotype neutralization assay

Spike pseudotype assays have been shown to have similar characteristics to neutralization testing using fully infectious WT SARS-CoV-2 (³⁴). Virus neutralization assays were performed on 293T cells transiently transfected with ACE2 and TMPRSS2 using SARS-CoV-2 spike PV expressing luciferase³⁵. PV was incubated with serial dilutions of heat-inactivated human serum samples or convalescent plasma in duplicate for 1 h at 37 °C. Virus- and cell-only controls were also included. Then, freshly trypsinized 293T ACE2/TMPRSS2-expressing cells were added to each well.

Following a 48-h incubation in a 5% CO₂ environment at 37 °C, the luminescence was measured using the Steady-Glo Luciferase assay system (Promega).

Neutralization assays for convalescent plasma

Convalescent serum samples from HCWs at St Mary's Hospital at least 21 days since PCR-confirmed SARS-CoV-2 infection were collected in May 2020 as part of the REACT2 study.

Convalescent human serum samples were inactivated at 56 °C for 30 min, and replicate serial twofold dilutions ($n = 12$) were mixed with an equal volume of SARS-CoV-2 (100 TCID₅₀; total volume 100 µl) at 37 °C for 1 h. Vero E6

ACE2/TMPRSS2 cells were subsequently infected with serial fold dilutions of each sample for 3 days at 37 °C. Virus neutralization was quantified via crystal violet staining and scoring for CPE. Each run included 1:5 dilutions of each test sample in the absence of virus to ensure virus-induced CPE in each titration. Back titrations of SARS-CoV-2 infectivity were performed to demonstrate infection with ~100 TCID₅₀ in each well.

Vaccinee serum neutralization, live virus assays

Vero E6 ACE2/TMPRSS2 cells were seeded at a cell density of 2×10^4 per well in a 96-well plate 24 h before infection. Serum was titrated starting at a final 1:10 dilution, with WT (SARS-CoV-2/human/Liverpool/REMRQ0001/2020), B.1.1.7 or B.1.617.2 virus isolates being added at an MOI of 0.01. The mixture was incubated for 1 h before adding to cells. The plates were fixed with 8% PFA 72 h post-infection and stained with Coomassie blue for 20 min. The plates were washed in water and dried for 2 h. 1% SDS solution was then added to wells and the staining intensity was measured using FLUOstar Omega (BMG Labtech). The percentage of cell survival was determined by comparing the intensity of staining with that in an uninfected well. A nonlinear sigmoidal 4PL model (Graphpad Prism 9.1.2) was used to determine the ID₅₀ for each serum.

Vesicular stomatitis virus pseudovirus generation for monoclonal antibody assays

Replication-defective vesicular stomatitis virus (VSV) pseudovirus expressing SARS-CoV-2 spike proteins corresponding to the different variants of concern were generated as previously described with some modifications³⁶. Lenti-X 293T cells (Takara, 632180) were seeded in 10-cm² dishes at a density of 5×10^6 cells per dish and the following day transfected with 10 µg of WT or B.1.617.2 spike expression

plasmid with TransIT-Lenti (Mirus, 6600) according to the manufacturer's instructions. One day post-transfection, cells were infected with VSV–luc (VSV G) with an MOI of 3 for 1 h, rinsed three times with PBS containing $\text{Ca}^{2+}/\text{Mg}^{2+}$, and then incubated for an additional 24 h in complete medium at 37 °C. The cell supernatant was clarified by centrifugation, filtered (0.45 µm), aliquoted and frozen at –80 °C.

PV neutralization assay for monoclonal antibody

Vero E6 cells expressing TMPRSS2 or not were grown in DMEM supplemented with 10% FBS and seeded into white 96-well plates (PerkinElmer, 6005688) at a density of 20 thousand cells per well. The next day, monoclonal antibodies were serially diluted in pre-warmed complete medium, mixed with WT or B.1.617.2 pseudoviruses and incubated for 1 h at 37 °C in round-bottom polypropylene plates. Medium from cells was aspirated and 50 µl of virus–monoclonal antibody complexes was added to cells and then incubated for 1 h at 37 °C. An additional 100 µl of pre-warmed complete medium was then added on top of complexes, and cells were incubated for an additional 16–24 h. Conditions were tested in duplicate wells on each plate and at least six wells per plate contained untreated infected cells (defining the 0% of neutralization, MAX relative light unit (RLU) value) and infected cells in the presence of S2E12 and S2X259 at 25 µg ml⁻¹ each (defining the 100% of neutralization, MIN RLU value). Medium containing virus–monoclonal antibody complexes was then aspirated from cells and 50 µl of a 1:2 dilution of SteadyLite Plus (Perkin Elmer, 6066759) in PBS with Ca^{2+} and Mg^{2+} was added to cells. Plates were incubated for 15 min at room temperature and then analysed on the Synergy-H1 (Biotek). The average RLU value for untreated infected wells ($\text{MAX RLU}_{\text{ave}}$) was subtracted by the average MIN RLU ($\text{MIN RLU}_{\text{ave}}$) value and used to normalize the percentage of neutralization of individual RLU values of experimental data according to the following formula: $(1 - (\text{RLU}_x - \text{MIN RLU}_{\text{ave}})/(\text{MAX RLU}_{\text{ave}} - \text{MIN RLU}_{\text{ave}})) \times 100$. Data were analysed and visualized with Prism (Version 9.1.0). IC₅₀ values were calculated from the interpolated value from the log[inhibitor] versus response, using variable slope (four parameters) nonlinear regression with an upper constraint of ≤ 100 , and a lower constraint equal to 0. Each neutralization assay was conducted on two independent experiments (that is, biological replicates), with each biological replicate containing a technical duplicate. IC₅₀ values across biological replicates are presented as arithmetic mean ± s.d. The loss or gain of neutralization potency across spike variants was calculated by dividing the variant IC₅₀ by the WT IC₅₀ within each biological replicate, and then visualized as arithmetic mean ± s.d.

Plasmids for split GFP system to measure cell–cell fusion

pQCXIP-BSR-GFP11 and pQCXIP-GFP1–10 were from Yutaka Hata³⁷ (Addgene plasmid no. 68716; <http://n2t.net/addgene:68716>; RRID: Addgene_68716 and Addgene plasmid no. 68715; <http://n2t.net/addgene:68715>; RRID: Addgene_68715).

Generation of GFP1–10 or GFP11 lentiviral particles

Lentiviral particles were generated by co-transfection of Vero cells with pQCXIP-BSR-GFP11 or pQCXIP-GFP1–10 as previously described³⁸. Supernatant containing virus particles was collected after 48 and 72 h, 0.45-μm filtered, and used to infect 293T or Vero cells to generate stable cell lines. 293T and Vero cells were transduced to stably express GFP1–10 or GFP11, respectively, and were selected with 2 μg ml⁻¹ puromycin.

Cell–cell fusion assay

The cell–cell fusion assay was carried out as previously described^{38,39} but using a split GFP system. Briefly, Vero GFP1–10 and Vero-GFP11 cells were seeded at 80% confluence in a 1:1 ratio in a 24-well plate the day before. Cells were co-transfected with 0.5 μg of spike expression plasmids in pCDNA3 using Fugene 6 following the manufacturer’s instructions (Promega). Cell–cell fusion was measured using an Incucyte and determined as the proportion of green area to total phase area. Data were then analysed using Incucyte software. Graphs were generated using Prism 8 software.

Reporting summary

Further information on research design is available in the [Nature Research Reporting Summary](#) linked to this paper.

Data availability

All SARS-CoV-2 fasta consensus sequence files used in this analysis are available from <https://gisaid.org> (with accession numbers: hospital 1, EPI_ISIL_1970102–EPI_ISIL_17010116; hospital 2, EPI_ISIL_2461070–EPI_ISIL_2955768; hospital 3, EPI_ISL_2955782–EPI_ISL_3066853) or https://github.com/Steven-Kemp/hospital_india/tree/main/consensus_fasta. All consensus sequence data have also been submitted to NCBI GenBank and can be found with the accession numbers [MZ724413–MZ724540](#).

References

1. 1.
Ferreira, I. et al. SARS-CoV-2 B.1.617 mutations L452 and E484Q are not synergistic for antibody evasion. *J. Infect. Dis.* <https://doi.org/10.1093/infdis/jiab368> (2021).
2. 2.
Volz, E. et al. Assessing transmissibility of SARS-CoV-2 lineage B.1.1.7 in England. *Nature* <https://doi.org/10.1038/s41586-021-03470-x> (2021).
3. 3.
Collier, D. A. et al. SARS-CoV-2 B.1.1.7 sensitivity to mRNA vaccine-elicited, convalescent and monoclonal antibodies. *Nature* **593**, 136–141 (2021).
4. 4.
Cherian, S. et al. Convergent evolution of SARS-CoV-2 spike mutations, L452R, E484Q and P681R, in the second wave of COVID-19 in Maharashtra, India. Preprint at <https://doi.org/10.1101/2021.04.22.440932> (2021).
5. 5.
Deng, X. et al. Transmission, infectivity, and antibody neutralization of an emerging SARS-CoV-2 variant in California carrying a L452R spike protein mutation. Preprint at <https://doi.org/10.1101/2021.03.07.21252647> (2021).
6. 6.
McCallum, M. et al. SARS-CoV-2 immune evasion by variant B.1.427/B.1.429. Preprint at <https://doi.org/10.1101/2021.03.31.437925> (2021).
7. 7.
Motozono, C. et al. An emerging SARS-CoV-2 mutant evading cellular immunity and increasing viral infectivity. Preprint at <https://doi.org/10.1101/2021.04.02.438288> (2021).
8. 8.
Weinreich, D. M. et al. REGN-COV2, a neutralizing antibody cocktail, in outpatients with Covid-19. *N. Engl. J. Med.* **384**, 238–251 (2020).

9. 9.

Peacock, T. P. et al. The furin cleavage site in the SARS-CoV-2 spike protein is required for transmission in ferrets. *Nat. Microbiol.* <https://doi.org/10.1038/s41564-021-00908-w> (2021).

10. 10.

Youk, J. et al. Three-dimensional human alveolar stem cell culture models reveal infection response to SARS-CoV-2. *Cell Stem Cell* **27**, 905–919 (2020).

11. 11.

Papa, G. et al. Furin cleavage of SARS-CoV-2 Spike promotes but is not essential for infection and cell–cell fusion. *PLoS Pathog.* **17**, e1009246 (2021).

12. 12.

Cattin-Ortolá, J. et al. Sequences in the cytoplasmic tail of SARS-CoV-2 Spike facilitate expression at the cell surface and syncytia formation. Preprint at <https://doi.org/10.1101/2020.10.12.335562> (2021).

13. 13.

Meng, B. et al. Recurrent emergence and transmission of a SARS-CoV-2 spike deletion H69/V70 and role in Alpha variant B.1.1.7. *Cell Rep.* <https://doi.org/10.1016/j.celrep.2021.109292> (2021).

14. 14.

Bhoyar, R. C. et al. High throughput detection and genetic epidemiology of SARS-CoV-2 using COVIDSeq next-generation sequencing. *PLoS ONE* **16**, e0247115 (2021).

15. 15.

Lopez Bernal, J. et al. Effectiveness of Covid-19 vaccines against the B.1.617.2 (Delta) variant. *N. Engl. J. Med.* <https://doi.org/10.1056/NEJMoa2108891> (2021).

16. 16.

Bernal, J. L. et al. Effectiveness of COVID-19 vaccines against the B.1.617.2 variant. Preprint at <https://doi.org/10.1101/2021.05.22.21257658> (2021).

17. 17.
Dhar, M. S. et al. Genomic characterization and epidemiology of an emerging SARS-CoV-2 variant in Delhi, India. *Science* <https://www.science.org/doi/10.1126/science.abj9932> (2021).
18. 18.
Kemp, S. A. et al. SARS-CoV-2 evolution during treatment of chronic infection. *Nature* **592**, 277–282 (2021).
19. 19.
Zeng, C. et al. SARS-CoV-2 spreads through cell-to-cell transmission. Preprint at *bioRxiv* <https://doi.org/10.1101/2021.06.01.446579> (2021).
20. 20.
Jackson, L. et al. SARS-CoV-2 cell-to-cell spread occurs rapidly and is insensitive to antibody neutralization. Preprint at <https://doi.org/10.1101/2021.06.01.446516> (2021).
21. 21.
Katoh, K. & Standley, D. M. MAFFT multiple sequence alignment software version 7: improvements in performance and usability. *Mol. Biol. Evol.* **30**, 772–780 (2013).
22. 22.
Rambaut, A. et al. A dynamic nomenclature proposal for SARS-CoV-2 lineages to assist genomic epidemiology. *Nat. Microbiol.* **5**, 1403–1407 (2020).
23. 23.
Minh, B. Q. et al. IQ-TREE 2: new models and efficient methods for phylogenetic inference in the genomic era. Preprint at <https://doi.org/10.1101/849372> (2019).
24. 24.
Yu, G., Smith, D. K., Zhu, H., Guan, Y. & Lam, T. T. Y. ggtree: an R package for visualization and annotation of phylogenetic trees with their covariates and other associated data. *Methods Ecol. Evol.* **8**, 28–36 (2017).

25. 25.

Wrobel, A. G. et al. SARS-CoV-2 and bat RaTG13 spike glycoprotein structures inform on virus evolution and furin-cleavage effects. *Nat. Struct. Mol. Biol.* **27**, 763–767 (2020).

26. 26.

McFadden, D. in *Frontiers in Econometrics* 105–142 (ed. Zarembka, P.) (Academic, 1974).

27. 27.

Rihn, S. J. et al. A plasmid DNA-launched SARS-CoV-2 reverse genetics system and coronavirus toolkit for COVID-19 research. *PLoS Biol.* **19**, e3001091 (2021).

28. 28.

Vermeire, J. et al. Quantification of reverse transcriptase activity by real-time PCR as a fast and accurate method for titration of HIV, lenti- and retroviral vectors. *PLoS ONE* **7**, e50859 (2012).

29. 29.

Matsuyama, S. et al. Enhanced isolation of SARS-CoV-2 by TMPRSS2-expressing cells. *Proc. Natl Acad. Sci. USA* **117**, 7001–7003 (2020).

30. 30.

Reed, L. J. & Muench, H. A simple method of estimating fifty percent endpoints. *Am. J. Hyg.* **27**, 493–497 (1938).

31. 31.

Motozono, C. et al. SARS-CoV-2 spike L452R variant evades cellular immunity and increases infectivity. *Cell Host Microbe* <https://doi.org/10.1016/j.chom.2021.06.006> (2021).

32. 32.

Shema Mugisha, C. et al. A simplified quantitative real-time PCR assay for monitoring SARS-CoV-2 growth in cell culture. *mSphere* <https://doi.org/10.1128/mSphere.00658-20> (2020).

33. 33.

Corman, V. M. et al. Detection of 2019 novel coronavirus (2019-nCoV) by real-time RT-PCR. *Euro Surveill.* **25**, 2000045 (2020).

34. 34.

Schmidt, F. et al. Measuring SARS-CoV-2 neutralizing antibody activity using pseudotyped and chimeric viruses. Preprint at <https://doi.org/10.1101/2020.06.08.140871> (2020).

35. 35.

Mlcochova, P. et al. Combined point of care nucleic acid and antibody testing for SARS-CoV-2 following emergence of D614G Spike variant. *Cell Rep. Med.* <https://doi.org/10.1016/j.xcrm.2020.100099> (2020).

36. 36.

Ou, X. et al. Characterization of spike glycoprotein of SARS-CoV-2 on virus entry and its immune cross-reactivity with SARS-CoV. *Nat. Commun.* **11**, 1620 (2020).

37. 37.

Kodaka, M. et al. A new cell-based assay to evaluate myogenesis in mouse myoblast C2C12 cells. *Exp. Cell Res.* **336**, 171–181 (2015).

38. 38.

Papa, G. et al. Furin cleavage of SARS-CoV-2 Spike promotes but is not essential for infection and cell-cell fusion. *PLoS Pathog.* **17**, e1009246 (2021).

39. 39.

Buchrieser, J. et al. Syncytia formation by SARS-CoV-2-infected cells. *EMBO J.* **39**, e106267 (2020).

Acknowledgements

We thank the Department of Biotechnology, NCDC, for coordination of the HCW aspect of the study. R.K.G. is supported by a Wellcome Trust Senior Fellowship in Clinical Science (WT108082AIA). This study was supported by the Cambridge

NIHRB Biomedical Research Centre. We also thank A. Mutreja for discussions. We thank T. de Silva for the Delta isolate and K. Kimelian for discussions. S.A.K. is supported by the Bill and Melinda Gates Foundation via PANGEA grant OPP1175094. I.A.T.M.F. is funded by a SANTHE award (DEL-15-006). S. Flaxman acknowledges theEPSRC (EP/V002910/1). We thank P. Lehner, J. Voss, S. Cook, M. Palmerini and E. Thomson for Calu-3 cells, HeLa ACE2, H1299, A549 ACE2/TMPRSS2 and Vero E6 ACE2/TMPRSS2 cells, respectively. We thank C. Lloyd and S. Saglani for providing the primary airway epithelial cultures . We thank the Geno2pheno UK consortium. We acknowledge support from the G2P-UK National Virology consortium funded by MRC/UKRI (grant ref. MR/W005611/1). This study was also supported by The Rosetrees Trust and the Geno2pheno UK consortium. K. Sato is supported by the AMED Research Program on Emerging and Re-emerging Infectious Diseases (20fk0108270 and 20fk0108413), JST SICORP (JPMJSC20U1 and JPMJSC21U5) and JST CREST (JPMJCR20H4).

Author information

Author notes

1. These authors contributed equally: Petra Mlcochova, Steven Kemp, Mahesh Shanker Dhar, Partha Rakshit, Anurag Agrawal, Ravindra K. Gupta

Affiliations

1. Cambridge Institute of Therapeutic Immunology & Infectious Disease (CITIID), Cambridge, UK

Petra Mlcochova, Steven A. Kemp, Bo Meng, Isabella A. T. M. Ferreira, Rawlings Datir, Adam Abdullahi, Stephen Baker, Gordon Dougan, Paul J. Lehner, Paul A. Lyons, Nicholas J. Matheson, Ben Bullman & Ravindra K. Gupta

2. Department of Medicine, University of Cambridge, Cambridge, UK

Petra Mlcochova, Steven A. Kemp, Bo Meng, Isabella A. T. M. Ferreira, Rawlings Datir, Dami A. Collier, Adam Abdullahi, Stephen Baker, Gordon Dougan, Christoph Hess, Paul J. Lehner, Paul A. Lyons, Nicholas J. Matheson, Charlotte Summers, James E. D. Thaventhiran, Mark Toshner, Michael P. Weekes, Benjamin J. Dunmore, Stefan Gräf, Kelvin Hunter, Ekaterina Legchenko, Cecilia Matara, Jennifer Martin, Federica Mescia, Ciara O'Donnell, Linda Pointon, Nicole Pond, Joy Shih, Rachel Sutcliffe, Tobias Tilly, Carmen Treacy, Zhen Tong, Jennifer Wood, Marta

Wylot, Laura Bergamaschi, Ariana Betancourt, Georgie Bower, Chiara Cossetti, Aloka De Sa, Madeline Epping, Stuart Fawke, Nick Gleadall, Richard Grenfell, Andrew Hinch, Sarah Jackson, Isobel Jarvis, Ben Krishna, Ommar Omarjee, Marianne Perera, Martin Potts, Nathan Richoz, Veronika Romashova, Luca Stefanucci, Mateusz Strezlecki, Lori Turner, Eckart M. D. D. De Bie, Katherine Bunclark, Masa Josipovic, Michael Mackay, William L. Hamilton & Ravindra K. Gupta

3. University College London, London, UK

Steven A. Kemp, Dami A. Collier, Oscar Charles & Georgina Okecha

4. National Centre for Disease Control, Delhi, India

Mahesh Shanker Dhar, Sujeet Singh, Robin Marwal, Meena Datta, Kalaiarasan Ponnusamy, Venkatraman Srinivasan Radhakrishnan, Himanshu Chauhan, Tenzin Dikid, Hema Gogia, Hemlata Lall, Kaptan Verma, Mahesh Shanker Dhar, Manoj K. Singh, Namita Soni, Namonarayan Meena, Preeti Madan, Priyanka Singh, Ramesh Sharma, Rajeev Sharma, Sandhya Kabra, Sattender Kumar, Swati Kumari, Uma Sharma, Urmila Chaudhary, Josh Hodgson, Christopher Huang, Daniel Lewis, Joe Marsden, Natalia Savinykh Yarkoni, Rahul Sharma, Mayurun Selvan, Samir Bhatt & Partha Rakshit

5. MRC – Laboratory of Molecular Biology, Cambridge, UK

Guido Papa, Anna Albecka & Leo C. James

6. CSIR Institute of Genomics and Integrative Biology, Delhi, India

Rajesh Pandey, Shantanu Sengupta, Partha Chattopadhyay, Priti Devi, Sridhar Sivasubbu, Vinod Scaria & Anurag Agrawal

7. Department of Infectious Diseases, Imperial College London, London, UK

Jonathan Brown, Jie Zhou & Niluka Goonawardane

8. Medical Research Council (MRC) Centre for Global Infectious Disease Analysis, Jameel Institute, School of Public Health, Imperial College London, London, UK

Swapnil Mishra, Charles Whittaker, Thomas Mellan, Tom Peacock & Wendy S. Barclay

9. NIHR Bioresource, Cambridge, UK

Daniela Caputo, Nathalie Kingston, John Allison, Helen Butcher, Daniela Caputo, Debbie Clapham-Riley, Eleanor Dewhurst, Anita Furlong, Barbara Graves, Jennifer Gray, Tasmin Ivers, Mary Kasanicki, Emma Le Gresley, Rachel Linger, Sarah Meloy, Francesca Muldoon, Nigel Ovington, Sofia Papadia, Isabel Phelan, Hannah Stark & Jennifer Webster

10. Sri Ganga Ram Hospital, New Delhi, India

Chand Wattal, Neeraj Goel, Ambrish Satwik, J. K. Oberoi, Reena Raveendran & S. Datta

11. Indraprastha Apollo Hospital, New Delhi, India

Raju Vaishya

12. Northern Railway Central Hospital, New Delhi, India

Meenakshi Agarwal & Kathleen E. Stirrups

13. Wellcome-MRC Cambridge Stem Cell Institute, Cambridge, UK

Antranik Mavousian & Joo Hyeon Lee

14. Department of Physiology, Development and Neuroscience, University of Cambridge, Cambridge, UK

Joo Hyeon Lee

15. Humabs Biomed SA, a subsidiary of Vir Biotechnology, Bellinzona, Switzerland

Sarah Spencer, Jessica Bassi, Chiara Silacci-Fegni, Christian Saliba, Dora Pinto, Davide Corti & Luca Piccoli

16. Institute of Biomedical and Health Sciences, Hiroshima University, Hiroshima, Japan

Ryoko Kawabata, Nanami Morizako & Takashi Irie

17. Tokyo Metropolitan Institute of Public Health, Tokyo, Japan

Kenji Sadamasu, Hiroyuki Asakura, Mami Nagashima, Kazuhisa Yoshimura & Isao Yoshida

18. Division of Systems Virology, The Institute of Medical Science, The University of Tokyo, Tokyo, Japan

Jumpei Ito, Izumi Kimura, Keiya Uriu, Yusuke Kosugi, Mai Suganami, Akiko Oide, Miyabishara Yokoyama, Mika Chiba & Kei Sato

19. CREST, Japan Science and Technology Agency, Saitama, Japan

Kei Sato

20. Section of Epidemiology, Department of Public Health, University of Copenhagen, Copenhagen, Denmark

Samir Bhatt

21. Department of Computer Science, University of Oxford, Oxford, UK

Caroline Saunders & Seth Flaxman

22. Africa Health Research Institute, Durban, South Africa

Willem H. Owehand, Jonathan Stephens, Kathleen E. Stirrups & Ravindra K. Gupta

23. National Institute of Biomedical Genomics, Kalyani, India

Saumitra Das, Arindam Maitra, Sreedhar Chinnaswamy & Nidhan Kumar Biswas

24. Institute of Life Sciences (ILS), Bhubaneswar, India

Ajay Parida, Sunil K. Raghav & Punit Prasad

25. InSTEM/ NCBS, Bangalore, India

Apurva Sarin, Satyajit Mayor, Uma Ramakrishnan, Dasaradhi Palakodeti & Aswin Sai Narain Seshasayee

26. Centre for DNA Fingerprinting and Diagnostics, Hyderabad, India

K. Thangaraj, Murali Dharan Bashyam & Ashwin Dalal

27. National Centre for Cell Science, Pune, India

Manoj Bhat, Yogesh Shouche & Ajay Pillai

28. National Institute of Virology, Pune, India

Priya Abraham, Varsha Atul Potdar & Sarah S. Cherian

29. National Institute of Mental Health and Neuroscience, Bangalore, India

Anita Sudhir Desai, Chitra Pattabiraman, M. V. Manjunatha, Reeta S. Mani & Gautam Arunachal Udupi

30. Centre for Cellular and Molecular Biology, Hyderabad, India

Vinay Nandicoori, Karthik Bharadwaj Tallapaka, Divya Tej Sowpati & Mary Kasanicki

31. University of Miyazaki, Miyazaki, Japan

Akatsuki Saito, Erika P. Butlertanaka, Yuri L. Tanaka & Emma Jones

32. Kumamoto University, Kumamoto, Japan

Terumasa Ikeda, Chihiro Motozono, Hesham Nasser, Ryo Shimizu, Yue Yuan, Kazuko Kitazato & Haruyo Hasebe

33. Tokai University, Tokyo, Japan

So Nakagawa, Jiaqi Wu & Miyoko Takahashi

34. Hokkaido University, Sapporo, Japan

Takasuke Fukuhara, Kenta Shimizu, Kana Tsushima & Haruko Kubo

35. Kyoto University, Kyoto, Japan

Kotaro Shirakawa, Yasuhiro Kazuma, Ryosuke Nomura, Yoshihito Horisawa & Akifumi Takaori-Kondo

36. National Institute of Infectious Diseases, Tokyo, Japan

Kenzo Tokunaga & Seiya Ozono

37. Cambridge University Hospitals NHS Trust, Cambridge, UK

Patrick Maxwell, Ashley Shaw, Sabrina Rossi & Cissy Yong

38. Cambridge Clinical Research Centre, NIHR Clinical Research Facility,
Cambridge University Hospitals NHS Foundation Trust, Addenbrooke's Hospital,
Cambridge, UK

Ashlea Bucke, Jo Calder, Laura Canna, Jason Domingo, Anne Elmer, Stewart
Fuller, Julie Harris, Sarah Hewitt, Jane Kennet, Sherly Jose, Jenny
Kourampa, Anne Meadows, Criona O'Brien, Jane Price, Cherry Publico, Rebecca
Rastall, Carla Ribeiro, Jane Rowlands, Valentina Ruffolo & Hugo Tordesillas

39. Department of Biochemistry, University of Cambridge, Cambridge, UK

Stuart Fawke & Oisin Huhn

40. University of Cambridge, Cambridge Biomedical Campus, Cambridge, UK

Francesca Nice, Helen Butcher, Daniela Caputo, Debbie Clapham-Riley, Eleanor
Dewhurst, Anita Furlong, Barbara Graves, Jennifer Gray, Tasmin Ivers, Emma Le
Gresley, Rachel Linger, Sarah Meloy, Francesca Muldoon, Sofia Papadia, Isabel
Phelan, Hannah Stark, Paul Townsend, Neil Walker, Jennifer Webster, Ingrid
Scholtes, Sabine Hein & Rebecca King

Consortia

The Indian SARS-CoV-2 Genomics Consortium (INSACOG)

- , Himanshu Chauhan
- , Tanzin Dikid
- , Hema Gogia
- , Hemlata Lall
- , Kalaiarasan Ponnusamy
- , Kaptan Verma
- , Mahesh Shanker Dhar
- , Manoj K. Singh
- , Meena Datta
- , Namita Soni
- , Namonarayan Meena
- , Preeti Madan
- , Priyanka Singh
- , Ramesh Sharma
- , Rajeev Sharma
- , Sandhya Kabra
- , Sattender Kumar
- , Swati Kumari

- , Uma Sharma
- , Urmila Chaudhary
- , Sridhar Sivasubbu
- , Vinod Scaria
- , Chand Wattal
- , J. K. Oberoi
- , Reena Raveendran
- , S. Datta
- , Saumitra Das
- , Arindam Maitra
- , Sreedhar Chinnaswamy
- , Nidhan Kumar Biswas
- , Ajay Parida
- , Sunil K. Raghav
- , Punit Prasad
- , Apurva Sarin
- , Satyajit Mayor
- , Uma Ramakrishnan
- , Dasaradhi Palakodeti
- , Aswin Sai Narain SeshaSAYEE
- , K. Thangaraj
- , Murali Dharan Bashyam
- , Ashwin Dalal
- , Manoj Bhat
- , Yogesh Shouche
- , Ajay Pillai
- , Priya Abraham
- , Varsha Atul Potdar
- , Sarah S. Cherian
- , Anita Sudhir Desai
- , Chitra Pattabiraman
- , M. V. Manjunatha
- , Reeta S. Mani
- , Gautam Arunachal Udupi
- , Vinay Nandicoori
- , Karthik Bharadwaj Tallapaka
- & Divya Tej Sowpati

The Genotype to Phenotype Japan (G2P-Japan) Consortium

- Ryoko Kawabata
- , Nanami Morizako

- , Kenji Sadamasu
- , Hiroyuki Asakura
- , Mami Nagashima
- , Kazuhisa Yoshimura
- , Jumpei Ito
- , Izumi Kimura
- , Keiya Uriu
- , Yusuke Kosugi
- , Mai Suganami
- , Akiko Oide
- , Miyabishara Yokoyama
- , Mika Chiba
- , Akatsuki Saito
- , Erika P. Butlertanaka
- , Yuri L. Tanaka
- , Terumasa Ikeda
- , Chihiro Motozono
- , Hesham Nasser
- , Ryo Shimizu
- , Yue Yuan
- , Kazuko Kitazato
- , Haruyo Hasebe
- , So Nakagawa
- , Jiaqi Wu
- , Miyoko Takahashi
- , Takasuke Fukuhara
- , Kenta Shimizu
- , Kana Tsushima
- , Haruko Kubo
- , Kotaro Shirakawa
- , Yasuhiro Kazuma
- , Ryosuke Nomura
- , Yoshihito Horisawa
- , Akifumi Takaori-Kondo
- , Kenzo Tokunaga
- & Seiya Ozono

The CITIID-NIHR BioResource COVID-19 Collaboration

- Stephen Baker
- , Gordon Dougan
- , Christoph Hess

- , Nathalie Kingston
- , Paul J. Lehner
- , Paul A. Lyons
- , Nicholas J. Matheson
- , Willem H. Owehand
- , Caroline Saunders
- , Charlotte Summers
- , James E. D. Thaventhiran
- , Mark Toshner
- , Michael P. Weekes
- , Patrick Maxwell
- , Ashley Shaw
- , Ashlea Bucke
- , Jo Calder
- , Laura Canna
- , Jason Domingo
- , Anne Elmer
- , Stewart Fuller
- , Julie Harris
- , Sarah Hewitt
- , Jane Kennet
- , Sherly Jose
- , Jenny Kourampa
- , Anne Meadows
- , Criona O'Brien
- , Jane Price
- , Cherry Publico
- , Rebecca Rastall
- , Carla Ribeiro
- , Jane Rowlands
- , Valentina Ruffolo
- , Hugo Tordesillas
- , Ben Bullman
- , Benjamin J. Dunmore
- , Stuart Fawke
- , Stefan Gräf
- , Josh Hodgson
- , Christopher Huang
- , Kelvin Hunter
- , Emma Jones
- , Ekaterina Legchenko
- , Cecilia Matara

- , Jennifer Martin
- , Federica Mescia
- , Ciara O'Donnell
- , Linda Pointon
- , Nicole Pond
- , Joy Shih
- , Rachel Sutcliffe
- , Tobias Tilly
- , Carmen Treacy
- , Zhen Tong
- , Jennifer Wood
- , Marta Wylot
- , Laura Bergamaschi
- , Ariana Betancourt
- , Georgie Bower
- , Chiara Cossetti
- , Aloka De Sa
- , Madeline Epping
- , Stuart Fawke
- , Nick Gleadall
- , Richard Grenfell
- , Andrew Hinch
- , Oisin Huhn
- , Sarah Jackson
- , Isobel Jarvis
- , Ben Krishna
- , Daniel Lewis
- , Joe Marsden
- , Francesca Nice
- , Georgina Okecha
- , Ommar Omarjee
- , Marianne Perera
- , Martin Potts
- , Nathan Richoz
- , Veronika Romashova
- , Natalia Savinykh Yarkoni
- , Rahul Sharma
- , Luca Stefanucci
- , Jonathan Stephens
- , Mateusz Strezlecki
- , Lori Turner
- , Eckart M. D. D. De Bie

- , Katherine Bunclark
- , Masa Josipovic
- , Michael Mackay
- , Federica Mescia
- , Sabrina Rossi
- , Mayurun Selvan
- , Sarah Spencer
- , Cissy Yong
- , John Allison
- , Helen Butcher
- , Daniela Caputo
- , Debbie Clapham-Riley
- , Eleanor Dewhurst
- , Anita Furlong
- , Barbara Graves
- , Jennifer Gray
- , Tasmin Ivers
- , Mary Kasanicki
- , Emma Le Gresley
- , Rachel Linger
- , Sarah Meloy
- , Francesca Muldoon
- , Nigel Ovington
- , Sofia Papadia
- , Isabel Phelan
- , Hannah Stark
- , Kathleen E. Stirrups
- , Paul Townsend
- , Neil Walker
- , Jennifer Webster
- , Ingrid Scholtes
- , Sabine Hein
- & Rebecca King

Contributions

Conceived study: A.A., P.R., S.A.K., D.C., S. Bhatt, S. Flaxman, S. Mishra, R.K.G., K. Sato, D.A.C., L. Piccoli, J.B., D. Pinto, D.C. Designed study and experiments: B.M., P. Mlcochova, R.K.G., J.B., N.G., L.C.J., G.P., K. Sato, I.A.T.M. Performed experiments: P. Mlcochova, B.M., D.A.C., A. Abdullahi, R.D., I.A.T.M.F., G.P., C.S.-F., C. Saliba, R.M., M.D., D. Pinto, T. Irie, I.Y., L.C.G., J.B., J.Z., N.G., G.B.M. Patient data collection and analysis: M.S.D., S.S., R.P., N. Goel, A. Satwik, R.V.,

M.A., A. Mavousian, J.H.L., P.D., P.C., D.C., S. Sengupta, K.P., V.S.R. Performed bioinformatic analyses: W.L.H., M.S.D., S.A.K., O.C. Performed statistical analyses: D.A.C., S. Flaxman, S. Bhatt, C.W., T.M., S.P. Interpreted data: R.K.G., S.A.K., A.A., S.S., J.B., N.G., R.P., P.C., P.D., K.P., V.S.R., S.S., D.C., T.P., O.C., K. Sato, G.P., T. Irie, I.Y., L.C.J., W.S.B., G.P., S. Flaxman, S. Bhatt, D.A.C., B.M., R.D., I.A.T.M.F., P.R., J.B., K.G.C.S., S. Mishra, C. Wattal, M.S.D., T.M., S. Bhatt, L. Piccoli, D.C., C. Saliba, W.L.H., C.S.-F. and S. Flaxman.

Corresponding authors

Correspondence to Partha Rakshit, Anurag Agrawal or Ravindra K. Gupta.

Ethics declarations

Competing interests

J.B., C.S.-F., C. Saliba, D. Pinto, D.C. and L. Piccoli are employees of Vir Biotechnology and may hold shares in Vir Biotechnology. R.K.G. has received consulting fees from Johnson and Johnson and GSK. The remaining authors declare no competing interests.

Additional information

Peer review information *Nature* thanks Natalie Dean and the other, anonymous, reviewer(s) for their contribution to the peer review of this work. Peer reviewer reports are available.

Publisher's note Springer Nature remains neutral with regard to jurisdictional claims in published maps and institutional affiliations.

Extended data figures and tables

[Extended Data Fig. 1 Delta variant B.1.617.2 shows reduced sensitivity to monoclonal antibodies.](#)

Neutralisation by a panel of NTD- and RBD-specific mAbs against WT and B.1.617.2 mutant SARS-CoV-2 pseudotyped viruses. **a.** Neutralisation of WT D614 (black) and B.1.617.2 mutant (blue) pseudotyped SARS-CoV-2-VSV by 6 selected mAbs from one representative experiment out of 2 independent experiments. S2X333 is an NTD-specific mAb, S2D97, S2E12 and S2X58 are RBM-specific mAbs, while S2X35 and

S2X305 are non-RBM mAbs. **b.** Neutralisation of WT and B.1.617.2 VSV by 38 mAbs targeting NTD ($n = 3$), RBM ($n = 26$, including 5 clinical stage mAb) and non-RBM ($n = 9$). Shown are the mean IC₅₀ values (ng/ml) from 2 independent experiments. Non-neutralising IC₅₀ titers were set at 10⁴ ng/ml. **c.** Neutralisation shown as mean IC₅₀ values (upper panel) and average fold change of B.1.617.2 relative to WT (lower panel) of 38 mAbs tested in 2 independent experiments (including 5 clinical-stage mAbs), tested using Vero E6 cells expressing TMPRSS2. **d–e.** Neutralisation of WT D614 (black) and B.1.617.2 mutant (blue/red) pseudotyped SARS-CoV-2-VSV by 5 clinical-stage mAbs using Vero E6 cells expressing TMPRSS2 (d) or not (e). Shown is one representative experiment out of 2 independent experiments.

Extended Data Fig. 2 Spike cleavage in B.1.617.2 virions compared to B.1.1.7. and spike mediated cell-cell fusion.

a. Representative western blot analysis of spike and nucleoprotein present in SARS-CoV-2 particles from the indicated viruses produced in Vero E6 ACE2/TMPRSS2 cells 48 h post infection. The arrowhead identifies the S2 subunit. **b.** Quantification of cleaved and full-length spike of the indicated viruses. **c.** Schematic of cell-cell fusion assay. **d.** Reconstructed images at 10 h of GFP positive syncytia formation. Scale bars represent 400 mm. **e.** western blot of cell lysates 48 h after transfection of spike plasmids. **f,g.** Quantification of cell-cell fusion kinetics showing percentage of green area to total cell area over time. Mean is plotted with error bars representing SEM. **h.** Comparison of impact of post vaccine sera ($n = 2$) on PV neutralisation (top) and cell-cell fusion (bottom), comparing WT and Delta variant B.1.671.2. Data are representative of at least two independent experiments.

Extended Data Fig. 3 B.1.617.2 spike confers increased cell entry.

a. diagram showing mutations present in spike plasmids used for cell entry PV experiments **b.** Single round infectivity on different cell targets by spike B.1.617.1 and B.1.617.1 versus WT (Wuhan-1 D614G) PV produced in 293T cells. Data are representative of three independent experiments. Statistics were performed using unpaired Student t test. **c.** Western blotting of supernatants from transfected 293T probing for S2 and p24 in PV and showing no spike control.

Extended Data Fig. 4 Breakthrough SARS-CoV-2 infections amongst vaccinated health care workers (HCW).

a. Case frequencies of five most commonly occurring SARS CoV-2 lineages over a six week period from March to April 2021 for Delhi **b,c,d.** case frequency graph for

hospital 1, 2 and 3 respectively by date of testing. e. Comparison of IgG antibody titres between a control group of vaccinated individuals receiving two doses of ChAdOx-1 who have not been infected with SARS-CoV-2, with vaccinated healthcare workers who had received two doses and subsequently tested positive for SARS-CoV-2. f. Ct values in nose/throat swabs from HCW testing positive by hospital. Bars represent Mean and 95% CI. Ct values were compared using the Student t test.

Extended Data Table 1 Demographic information for individuals undergoing two dose SARS-CoV-2 vaccination with ChAdOx-1 or BNT162b2

Extended Data Table 2 Monoclonal antibodies used in neutralisation assays against pseudotyped virus bearing spike from WT (Wuhan-1 D614) or B.1.617.2
Extended Data Table 3 Data on SARS-CoV-2 infections in three hospitals with near universal staff vaccination during first half of 2021

Extended Data Table 4 Relative receipt vaccine effectiveness against B1.617.2 v non- B1.617.2: Upper Table: Odds ratios for detection of B.1.617.2 relative to non-B.1.617.2 in vaccinated compared to unvaccinated individuals in multi-variable logistic regression

Supplementary information

Supplementary Information

This file contains acknowledgements to individuals from the originating laboratories responsible for obtaining the specimens, as well as the submitting laboratories where the genome data were generated and shared via GISAID, on which this research is based.

Reporting Summary

Peer Review File

Rights and permissions

Open Access This article is licensed under a Creative Commons Attribution 4.0 International License, which permits use, sharing, adaptation, distribution and reproduction in any medium or format, as long as you give appropriate credit to the original author(s) and the source, provide a link to the Creative Commons license, and indicate if changes were made. The images or other third party material in this article are included in the article's Creative Commons license, unless indicated otherwise in a credit line to the material. If material is not included in the article's Creative Commons license and your intended use is not permitted by statutory regulation or exceeds the

permitted use, you will need to obtain permission directly from the copyright holder.
To view a copy of this license, visit <http://creativecommons.org/licenses/by/4.0/>.

[Reprints and Permissions](#)

About this article

Cite this article

Mlcochova, P., Kemp, S.A., Dhar, M.S. *et al.* SARS-CoV-2 B.1.617.2 Delta variant replication and immune evasion. *Nature* **599**, 114–119 (2021).
<https://doi.org/10.1038/s41586-021-03944-y>

- Received: 18 June 2021
- Accepted: 23 August 2021
- Published: 06 September 2021
- Issue Date: 04 November 2021
- DOI: <https://doi.org/10.1038/s41586-021-03944-y>

Share this article

Anyone you share the following link with will be able to read this content:

[Get shareable link](#)

Sorry, a shareable link is not currently available for this article.

[Copy to clipboard](#)

Provided by the Springer Nature SharedIt content-sharing initiative

This article was downloaded by **calibre** from <https://www.nature.com/articles/s41586-021-03944-y>.

- Article
- [Published: 13 October 2021](#)

Unravelling the collateral damage of antibiotics on gut bacteria

- [Lisa Maier](#) [ORCID: orcid.org/0000-0002-6473-4762](#)^{1,2,3} na1,
- [Camille V. Goemans](#) [ORCID: orcid.org/0000-0002-5564-1644](#)¹ na1,
- [Jakob Wirbel](#) [ORCID: orcid.org/0000-0002-4073-3562](#)⁴,
- [Michael Kuhn](#) [ORCID: orcid.org/0000-0002-2841-872X](#)⁴,
- [Claudia Eberl](#)^{5,6},
- [Mihaela Pruteanu](#)¹ nAff12,
- [Patrick Müller](#) [ORCID: orcid.org/0000-0003-3290-8251](#)^{2,3},
- [Sarela Garcia-Santamarina](#) [ORCID: orcid.org/0000-0002-0611-7918](#)¹,
- [Elisabetta Cacace](#) [ORCID: orcid.org/0000-0001-8239-0353](#)¹,
- [Boyao Zhang](#) [ORCID: orcid.org/0000-0002-2856-9376](#)⁴,
- [Cordula Gekeler](#) [ORCID: orcid.org/0000-0001-9041-6672](#)^{2,3},
- [Tisya Banerjee](#) [ORCID: orcid.org/0000-0003-1842-9350](#)¹ nAff13,
- [Exene Erin Anderson](#)¹ nAff14,
- [Alessio Milanese](#) [ORCID: orcid.org/0000-0002-7050-2239](#)⁴,
- [Ulrike Löber](#) [ORCID: orcid.org/0000-0001-7468-9531](#)^{7,8},
- [Sofia K. Forslund](#) [ORCID: orcid.org/0000-0003-4285-6993](#)^{4,7,8},
- [Kiran Raosaheb Patil](#) [ORCID: orcid.org/0000-0002-6166-8640](#)^{4,9},
- [Michael Zimmermann](#) [ORCID: orcid.org/0000-0002-5797-3589](#)⁴,
- [Bärbel Stecher](#) [ORCID: orcid.org/0000-0002-7445-5193](#)^{5,6},
- [Georg Zeller](#) [ORCID: orcid.org/0000-0003-1429-7485](#)⁴,
- [Peer Bork](#) [ORCID: orcid.org/0000-0002-2627-833X](#)^{4,8,10,11} &
- [Athanasios Typas](#) [ORCID: orcid.org/0000-0002-0797-9018](#)^{1,4}

Nature volume 599, pages 120–124 (2021)

- 11k Accesses
- 412 Altmetric
- [Metrics details](#)

Subjects

- [Antibiotics](#)
- [Microbiome](#)

Abstract

Antibiotics are used to fight pathogens but also target commensal bacteria, disturbing the composition of gut microbiota and causing dysbiosis and disease¹. Despite this well-known collateral damage, the activity spectrum of different antibiotic classes on gut bacteria remains poorly characterized. Here we characterize further 144 antibiotics from a previous screen of more than 1,000 drugs on 38 representative human gut microbiome species². Antibiotic classes exhibited distinct inhibition spectra, including generation dependence for quinolones and phylogeny independence for β -lactams. Macrolides and tetracyclines, both prototypic bacteriostatic protein synthesis inhibitors, inhibited nearly all commensals tested but also killed several species. Killed bacteria were more readily eliminated from in vitro communities than those inhibited. This species-specific killing activity challenges the long-standing distinction between bactericidal and bacteriostatic antibiotic classes and provides a possible explanation for the strong effect of macrolides on animal^{3,4,5} and human^{6,7} gut microbiomes. To mitigate this collateral damage of macrolides and tetracyclines, we screened for drugs that specifically antagonized the antibiotic activity against abundant *Bacteroides* species but not against relevant pathogens. Such antidotes selectively protected *Bacteroides* species from erythromycin treatment in human-stool-derived communities and gnotobiotic mice. These findings illuminate the activity spectra of antibiotics in commensal bacteria and suggest strategies to circumvent their adverse effects on the gut microbiota.

Access options

Subscribe to Journal

Get full journal access for 1 year

\$199.00

only \$3.90 per issue

[Subscribe](#)

All prices are NET prices.

VAT will be added later in the checkout.

Tax calculation will be finalised during checkout.

Rent or Buy article

Get time limited or full article access on ReadCube.

from \$8.99

[Rent or Buy](#)

All prices are NET prices.

Additional access options:

- [Log in](#)
- [Access through your institution](#)
- [Learn about institutional subscriptions](#)

Fig 1: Activity spectrum of antibiotic classes on human gut commensals.

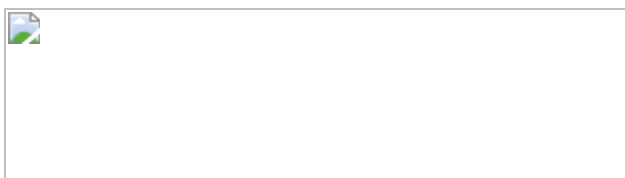


Fig 2: Macrolides and tetracyclines kill some human gut commensal species.

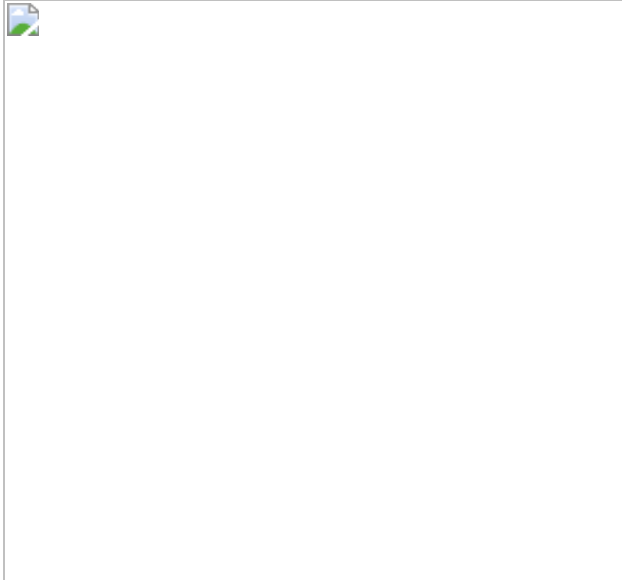
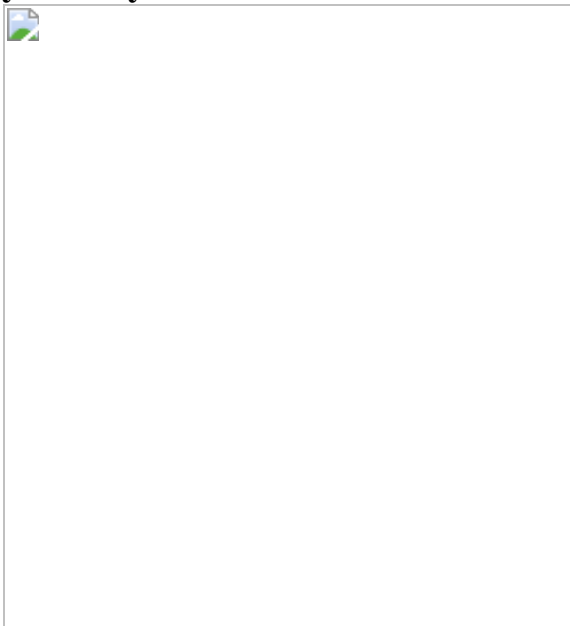


Fig 3: Dicumarol selectively protects *Bacteroides* species from erythromycin in microbial communities.



Data availability

All primary data generated in this study are in the Article and its Supplementary Information and are available from Zenodo: (<https://doi.org/10.5281/zenodo.3527540>). Clinical breakpoints (Fig. 1c)

were retrieved from the EUCAST database:
https://eucast.org/clinical_breakpoints/. Source data are provided with this paper.

Code availability

Code for analysing data and generating the figures (except Fig. 2 and Extended Data Figs. 5, 6) is available at <https://git.embl.de/maier/abxbug>.

References

1. 1.
Blaser, M. J. Antibiotic use and its consequences for the normal microbiome. *Science* **352**, 544–545 (2016).
2. 2.
Maier, L. et al. Extensive impact of non-antibiotic drugs on human gut bacteria. *Nature* **555**, 623–628 (2018).
3. 3.
Cho, I. et al. Antibiotics in early life alter the murine colonic microbiome and adiposity. *Nature* **488**, 621–626 (2012).
4. 4.
Cox, L. M. et al. Altering the intestinal microbiota during a critical developmental window has lasting metabolic consequences. *Cell* **158**, 705–721 (2014).
5. 5.
Ruiz, V. E. et al. A single early-in-life macrolide course has lasting effects on murine microbial network topology and immunity. *Nat. Commun.* **8**, 518 (2017).

6. 6.

Korpela, K. et al. Intestinal microbiome is related to lifetime antibiotic use in Finnish pre-school children. *Nat. Commun.* **7**, 10410 (2016).

7. 7.

Parker, E. P. K. et al. Changes in the intestinal microbiota following the administration of azithromycin in a randomised placebo-controlled trial among infants in south India. *Sci. Rep.* **7**, 9168 (2017).

8. 8.

Falony, G. et al. Population-level analysis of gut microbiome variation. *Science* **352**, 560–564 (2016).

9. 9.

Rothschild, D. et al. Environment dominates over host genetics in shaping human gut microbiota. *Nature* **555**, 210–215 (2018).

10. 10.

Zimmermann, M., Patil, K. R., Typas, A. & Maier, L. Towards a mechanistic understanding of reciprocal drug–microbiome interactions. *Mol. Syst. Biol.* **17**, e10116 (2021).

11. 11.

Vich Vila, A. et al. Impact of commonly used drugs on the composition and metabolic function of the gut microbiota. *Nat. Commun.* **11**, 362 (2020).

12. 12.

Kuhn, M., Letunic, I., Jensen, L. J. & Bork, P. The SIDER database of drugs and side effects. *Nucleic Acids Res.* **44**, D1075–D1079 (2016).

13. 13.

Dethlefsen, L. & Relman, D. A. Incomplete recovery and individualized responses of the human distal gut microbiota to repeated antibiotic perturbation. *Proc. Natl Acad. Sci. USA* **108**, 4554–4561 (2011).

14. 14.

Uzan-Yulzari, A. et al. Neonatal antibiotic exposure impairs child growth during the first six years of life by perturbing intestinal microbial colonization. *Nat. Commun.* **12**, 443 (2021).

15. 15.

Nagy, E., Boyanova, L., Justesen, U. S. & ESCMID Study Group of Anaerobic Infections. How to isolate, identify and determine antimicrobial susceptibility of anaerobic bacteria in routine laboratories. *Clin. Microbiol. Infect.* **24**, 1139–1148 (2018).

16. 16.

European Committee on Antimicrobial Susceptibility Testing. Breakpoint tables for interpretation of MICs and zone diameters. v.; http://www.eucast.org/clinical_breakpoints/ (2019).

17. 17.

Bullman, S. et al. Analysis of *Fusobacterium* persistence and antibiotic response in colorectal cancer. *Science* **358**, 1443–1448 (2017).

18. 18.

Manfredo Vieira, S. et al. Translocation of a gut pathobiont drives autoimmunity in mice and humans. *Science* **359**, 1156–1161 (2018).

19. 19.

Gaulton, A. et al. The ChEMBL database in 2017. *Nucleic Acids Res.* **45**, D945–D954 (2017).

20. 20.

Slimings, C. & Riley, T. V. Antibiotics and hospital-acquired *Clostridium difficile* infection: update of systematic review and meta-analysis. *J. Antimicrob. Chemother.* **69**, 881–891 (2014).

21. 21.

Baron, S., Diene, S. & Rolain, J.-M. Human microbiomes and antibiotic resistance. *Hum. Microb. J.* **10**, 43–52 (2018).

22. 22.

Tramontano, M. et al. Nutritional preferences of human gut bacteria reveal their metabolic idiosyncrasies. *Nat. Microbiol.* **3**, 514–522 (2018).

23. 23.

Habib, G. et al. 2015 ESC Guidelines for the management of infective endocarditis: the Task Force for the Management of Infective Endocarditis of the European Society of Cardiology (ESC). Endorsed by: European Association for Cardio-Thoracic Surgery (EACTS), the European Association of Nuclear Medicine (EANM). *Eur. Heart J.* **36**, 3075–3128 (2015).

24. 24.

Kasper, D.L., F. A., Hauser S. L. & Longo D. L. *Harrison's Principles of Internal Medicine* (McGraw-Hill, 2012).

25. 25.

Lobritz, M. A. et al. Antibiotic efficacy is linked to bacterial cellular respiration. *Proc. Natl Acad. Sci. USA* **112**, 8173–8180 (2015).

26. 26.

French, G. L. Bactericidal agents in the treatment of MRSA infections—the potential role of daptomycin. *J. Antimicrob. Chemother.* **58**, 1107–111 (2006).

27. 27.

Jelic, D. & Antolovic, R. From erythromycin to azithromycin and new potential ribosome-binding antimicrobials. *Antibiotics (Basel)* **5**, 29 (2016).

28. 28.

Nemeth, J., Oesch, G. & Kuster, S. P. Bacteriostatic versus bactericidal antibiotics for patients with serious bacterial infections: systematic review and meta-analysis. *J. Antimicrob. Chemother.* **70**, 382–395 (2015).

29. 29.

Wald-Dickler, N., Holtom, P. & Spellberg, B. Busting the myth of “static vs cidal” a systemic literature review. *Clin. Infect. Dis.* **66**, 1470–1474 (2018).

30. 30.

Brochado, A. R. et al. Species-specific activity of antibacterial drug combinations. *Nature* **559**, 259–263 (2018).

31. 31.

Brugiroux, S. et al. Genome-guided design of a defined mouse microbiota that confers colonization resistance against *Salmonella enterica* serovar Typhimurium. *Nat. Microbiol.* **2**, 16215 (2016).

32. 32.

Palleja, A. et al. Recovery of gut microbiota of healthy adults following antibiotic exposure. *Nat. Microbiol.* **3**, 1255–1265 (2018).

33. 33.

Schmidt, T. S. B., Raes, J. & Bork, P. The human gut microbiome: from association to modulation. *Cell* **172**, 1198–1215 (2018).

34. 34.

Milanese, A. et al. Microbial abundance, activity and population genomic profiling with mOTUs2. *Nat. Commun.* **10**, 1014 (2019).

35. 35.

Feng, Q. et al. Gut microbiome development along the colorectal adenoma-carcinoma sequence. *Nat. Commun.* **6**, 6528 (2015).

36. 36.

Vogtmann, E. et al. Colorectal cancer and the human gut microbiome: reproducibility with whole-genome shotgun sequencing. *PLoS ONE* **11** (2016).

37. 37.

Wirbel, J. et al. Meta-analysis of fecal metagenomes reveals global microbial signatures that are specific for colorectal cancer. *Nat. Med.* **25**, 679–689 (2019).

38. 38.

Yu, J. et al. Metagenomic analysis of faecal microbiome as a tool towards targeted non-invasive biomarkers for colorectal cancer. *Gut* **66**, 70–78 (2017).

39. 39.

Zeller, G. et al. Potential of fecal microbiota for early-stage detection of colorectal cancer. *Mol. Syst. Biol.* **10**, 766 (2014).

40. 40.

Kultima, J. R. et al. MOCAT2: a metagenomic assembly, annotation and profiling framework. *Bioinformatics* **32**, 2520–2523 (2016).

41. 41.

Schneider, C. A., Rasband, W. S. & Eliceiri, K. W. NIH Image to ImageJ: 25 years of image analysis. *Nat. Methods* **9**, 671–675 (2012).

42. 42.

Schindelin, J. et al. Fiji: an open-source platform for biological-image analysis. *Nat. Methods* **9**, 676–682 (2012).

43. 43.

Frostegård, A. et al. Quantification of bias related to the extraction of DNA directly from soils. *Appl. Environ. Microbiol.* **65**, 5409–5420 (1999).

44. 44.

Caporaso, J. G. et al. Global patterns of 16S rRNA diversity at a depth of millions of sequences per sample. *Proc. Natl Acad. Sci. USA* **108**, 4516–4522 (2011).

45. 45.

Callahan, B. J. et al. DADA2: high-resolution sample inference from Illumina amplicon data. *Nat. Methods* **13**, 581–583 (2016).

46. 46.

Altschul, S. F., Gish, W., Miller, W., Myers, E. W. & Lipman, D. J. Basic local alignment search tool. *J. Mol. Biol.* **215**, 403–410 (1990).

47. 47.

Matias Rodrigues, J. F., Schmidt, T. S. B., Tackmann, J. & von Mering, C. MAPseq: highly efficient k-mer search with confidence

estimates, for rRNA sequence analysis. *Bioinformatics* **33**, 3808–3810 (2017).

48. 48.

Nawrocki, E. P. & Eddy, S. R. Infernal 1.1: 100-fold faster RNA homology searches. *Bioinformatics* **29**, 2933–2935 (2013).

49. 49.

Matias Rodrigues, J. F. & von Mering, C. HPC-CLUST: distributed hierarchical clustering for large sets of nucleotide sequences. *Bioinformatics* **30**, 287–288 (2014).

50. 50.

Schmidt, T. S. B., Matias Rodrigues, J. F. & von Mering, C. Limits to robustness and reproducibility in the demarcation of operational taxonomic units. *Environ. Microbiol.* **17**, 1689–1706 (2015).

51. 51.

Love, M. I., Huber, W. & Anders, S. Moderated estimation of fold change and dispersion for RNA-seq data with DESeq2. *Genome Biol.* **15**, 550 (2014).

52. 52.

McMurdie, P. J. & Holmes, S. Waste not, want not: why rarefying microbiome data is inadmissible. *PLoS Comput. Biol.* **10**, e1003531 (2014).

53. 53.

Benjamini, Y. & Hochberg, Y. Controlling the false discovery rate: a practical and powerful approach to multiple testing. *J. R. Stat. Soc. B* **57**, 289–300 (1995).

54. 54.

Chen, M. et al. Inhibition of renal NQO1 activity by dicoumarol suppresses nitroreduction of aristolochic acid I and attenuates its nephrotoxicity. *Toxicol. Sci.* **122**, 288–296 (2011).

55. 55.

Cai, H. Y. et al. Benzbromarone, an old uricosuric drug, inhibits human fatty acid binding protein 4 in vitro and lowers the blood glucose level in db/db mice. *Acta Pharmacol. Sin.* **34**, 1397–1402 (2013).

56. 56.

Herp, S. et al. *Mucispirillum schaedleri* antagonizes *Salmonella* virulence to protect mice against colitis. *Cell Host Microbe* **25**, 681–694 (2019).

57. 57.

Zimmermann, M., Zimmermann-Kogadeeva, M., Wegmann, R. & Goodman, A. L. Mapping human microbiome drug metabolism by gut bacteria and their genes. *Nature* **570**, 462–467 (2019).

58. 58.

Sunagawa, S. et al. Metagenomic species profiling using universal phylogenetic marker genes. *Nat. Methods* **10**, 1196–1199 (2013).

59. 59.

Huerta-Cepas, J., Serra, F. & Bork, P. ETE 3: reconstruction, analysis, and visualization of phylogenomic data. *Mol. Biol. Evol.* **33**, 1635–1638 (2016).

60. 60.

Sievers, F. et al. Fast, scalable generation of high-quality protein multiple sequence alignments using Clustal Omega. *Mol. Syst. Biol.* **7**, 539 (2011).

61. 61.

Nguyen, L. T., Schmidt, H. A., von Haeseler, A. & Minh, B. Q. IQ-TREE: a fast and effective stochastic algorithm for estimating maximum-likelihood phylogenies. *Mol. Biol. Evol.* **32**, 268–274 (2015).

62. 62.

Cani, P. D. & de Vos, W. M. Next-generation beneficial microbes: the case of *Akkermansia muciniphila*. *Front. Microbiol.* **8**, 1765 (2017).

63. 63.

Routy, B. et al. Gut microbiome influences efficacy of PD-1-based immunotherapy against epithelial tumors. *Science* **359**, 91–97 (2018).

Acknowledgements

We thank S. Göttig and members of the Typas lab for feedback on the manuscript; A. R. Brochado for help with experimental design; and EMBL GeneCore and Flow Cytometry Core Facilities for services and experimental advice. We acknowledge EMBL, JPIAMR grant combinatorials and ERC grant uCARE (ID 819454) for funding. L.M., S.G.-S. and M.P. were supported by the EMBL Interdisciplinary Postdoc programme under the Marie Skłodowska Curie Actions COFUND (grant numbers 291772 and 664726). L.M. is supported by the DFG (CMFI Cluster of Excellence EXC 2124 and Emmy Noether Program). C.V.G. is the recipient of an EMBO long-term postdoctoral fellowship and an add-on fellowship from the Christiane Nüsslein-Volhard-Stiftung. U.L. is supported by JPIAMR grant EMBARK. K.R.P. is supported by the UK Medical Research Council (MC_UU_00025/11). B.S. is supported by DFG CRC1371, ERC grant EVOGUTHEALTH (ID 865615), DZIF and CEGIMIR.

Author information

Author notes

1. Mihaela Pruteanu

Present address: Department of Biology, Humboldt University Berlin, Berlin, Germany

2. Tisya Banerjee

Present address: Department of Chemistry, TU Munich, Munich, Germany

3. Exene Erin Anderson

Present address: NYU School of Medicine, New York, NY, USA

4. These authors contributed equally: Lisa Maier, Camille V. Goemans

Affiliations

1. Genome Biology Unit, European Molecular Biology Laboratory, Heidelberg, Germany

Lisa Maier, Camille V. Goemans, Mihaela Pruteanu, Sarela Garcia-Santamarina, Elisabetta Cacace, Tisya Banerjee, Exene Erin Anderson & Athanasios Typas

2. Interfaculty Institute of Microbiology and Infection Medicine, University of Tübingen, Tübingen, Germany

Lisa Maier, Patrick Müller & Cordula Gekeler

3. Cluster of Excellence ‘Controlling Microbes to Fight Infections’, University of Tübingen, Tübingen, Germany

Lisa Maier, Patrick Müller & Cordula Gekeler

4. Structural and Computational Biology Unit, European Molecular Biology Laboratory, Heidelberg, Germany

Jakob Wirbel, Michael Kuhn, Boyao Zhang, Alessio Milanese, Sofia K. Forslund, Kiran Raosaheb Patil, Michael Zimmermann, Georg Zeller, Peer Bork & Athanasios Typas

5. Max-von-Pettenkofer Institute, LMU Munich, Munich, Germany

Claudia Eberl & Bärbel Stecher

6. German Center for Infection Research (DZIF), partner site LMU Munich, Munich, Germany

Claudia Eberl & Bärbel Stecher

7. Experimental and Clinical Research Center, a cooperation of Charité - Universitätsmedizin Berlin and Max-Delbrück-Center for Molecular Medicine, Berlin, Germany

Ulrike Löber & Sofia K. Forslund

8. Max-Delbrück-Center for Molecular Medicine, Berlin, Germany

Ulrike Löber, Sofia K. Forslund & Peer Bork

9. The Medical Research Council Toxicology Unit, University of Cambridge, Cambridge, UK

Kiran Raosaheb Patil

10. Yonsei Frontier Lab (YFL), Yonsei University, Seoul, South Korea

Peer Bork

11. Department of Bioinformatics, Biocenter, University of Würzburg, Würzburg, Germany

Peer Bork

Contributions

This study was conceived by K.R.P., P.B. and A.T.; designed by L.M., C.V.G., M.P. and A.T.; and supervised by L.M., M.Z., B.S., G.Z., P.B. and A.T. L.M., M.P., T.B. and E.E.A. conducted MIC measurements. C.V.G. performed the bactericidal/bacteriostatic experiments. L.M., C.V.G., C.E., P.M., S.G.S., E.C., B.Z. and C.G. performed the antidote experiments (L.M., P.M., E.C. and C.G. the screen and in vitro validation; C.V.G., P.M. and S.G.-S. the community experiments; and L.M., C.E. and B.Z. the mouse experiments). Data pre-processing, curation and comparisons to databases were performed by J.W., M.K., A.M., U.L. and S.K.F. Data interpretation was performed by L.M., C.V.G., J.W., M.Z., B.S., G.Z. and A.T. L.M., C.V.G. and A.T. wrote the manuscript with feedback from all authors. L.M., C.V.G., J.W. and M.K. designed the figures with input from G.Z. and A.T. All authors approved the final version for publication.

Corresponding authors

Correspondence to Lisa Maier or Athanasios Typas.

Ethics declarations

Competing interests

EMBL has filed a patent on using the antidotes identified in this study for prevention and/or treatment of dysbiosis and for microbiome protection (European patent application no. EP19216548.8). L.M., C.V.G., E.C. and A.T. are listed as inventors.

Additional information

Peer review information *Nature* thanks Gerry Wright and the other, anonymous, reviewer(s) for their contributions to the peer review of this work.

Publisher's note Springer Nature remains neutral with regard to jurisdictional claims in published maps and institutional affiliations.

Extended data figures and tables

Extended Data Fig. 1 Effects of 144 antibiotics on 40 human gut commensals.

Heat map according to sensitivity or resistance of each strain to the respective antibiotic at a concentration of 20 µM. Antibiotics are grouped according to drug classes and species are clustered according to their responses across the 144 antibiotics tested. Data is replotted from². Of note, *Akkermansia muciniphila*, a species associated with protection against different diseases and dysbiotic states⁶², and even positive responses to immunotherapy⁶³, is resistant to nearly all quinolone antibiotics (red box). We consolidated this finding by MIC determination for Ciprofloxacin (>32 µg/ml), Gatifloxacin (>32 µg/ml), Moxifloxacin (>32 µg/ml), Norfloxacin (>256 µg/ml) and Ofloxacin (>32 µg/ml).

[Source data](#)

Extended Data Fig. 2 MICs for 20 species/27 strains on 35 antimicrobials.

Heat map depicts MICs for each drug-strain pair in µg/ml. Heat map color gradient is adjusted to the MICs concentration range tested on the respective MIC test strip. Black depicts sensitivity and light grey resistance. Mean values across two biological replicates are shown (Suppl. Table 4). The species/strains from the screen are shown in black, additional strains to investigate intraspecies and intragenus variation within the *Bacteroides* genus are shown in blue. The grey background indicates that several strains per species were tested. Of note, *C. difficile* is particularly resistant to all tested macrolides and clindamycin (red box).

[Source data](#)

Extended Data Fig. 3 MIC dataset validates antibiotic sensitivity profiles from the screen and is consistent with

publicly available MICs.

a. Receiver operating characteristic (ROC) curve analysis was performed to evaluate sensitivity and specificity of the screen² using the MIC dataset. Results from the screen were considered as validated if MICs were below/above the 20 µM antibiotic concentration that was tested in the screen (allowing a twofold error margin). N is the number of antibiotics that we tested both in the screen and determined MICs for; AUROC is the area under the characteristic ROC. TN denotes true negatives, FP false positives, TP true positives, FN false negatives. **b.** Comparison including Spearman correlation coefficients of the MICs from this study to MICs from the ChEMBL¹⁹ and EUCAST¹⁶ databases. Panels in the upper row: comparison between all MICs that are shared between the two indicated datasets. Panels in the lower row: comparison of the 69 MICs that are shared across all three datasets. Despite experimental differences, our MICs correlate well with available EUCAST/ ChEMBL data. **c.** Number of the sum of new (this study) and already available MICs (EUCAST/ ChEMBL) per drug according to antibiotic class and prevalence/virulence of the bacterial species. The new dataset expands MICs across the board and specifically fills the knowledge gap on non-pathogenic species.

Source data

Extended Data Fig. 4 Antibiotic classes exhibit distinct behaviours in gut bacterial species.

a. Number of inhibited strains per antibiotic class (number of tested drugs per class in brackets). In total 40 strains were tested at a 20 µM antibiotic concentration. Boxes span the IQR and whiskers extend to the most extreme data points up to a max of 1.5 times the IQR. **b.** Number of inhibited strains per (fluoro-)quinolone drug generation. Number of tested drugs per generation is indicated in brackets - boxplots as in **a**. **c-d.** Overview of the number of drugs tested per β-lactam subclasses on *Bacteroides* species (*spp*) in screen (**c**) and for MICs (**d**). **e.** Heat map of phylogenetic relationship between *Bacteroides spp* (upper triangular matrix) ordered by phylogeny and their resistance profiles across β-lactam antibiotics (lower triangular matrix). Colors represent the pairwise

phylogenetic distance and the Euclidean distance on the log₂ transformed MICs for β -lactams. Examples of strains from the same species (*B. fragilis* / *B. uniformis*) that respond differently to β -lactam antibiotics, are highlighted.

[Source data](#)

Extended Data Fig. 5 Selective killing of macrolides and tetracyclines.

- a. Time-kill curves. The survival of 12 abundant gut microorganisms was assessed over a 5 h-treatment with either erythromycin, azithromycin or doxycycline. The graph shows the mean \pm SD of 3 independent experiments.
- b. Live/dead staining of macrolide or tetracycline-treated *E. coli* ED1a and *B. vulgatus*. The left panel shows an overlay of phase contrast and fluorescence microscopy images of propidium iodide (PI)-stained *E. coli* ED1a or *B. vulgatus* before and 5 h after erythromycin, azithromycin or doxycycline treatment. Cultures were concentrated before imaging; the scale bar is 10 μ m. The right panel shows the corresponding quantification of live/dead-stained cells by flow cytometry with Syto9 on the x-axis (live cells) and PI on the y-axis (dead cells). As *E. coli* ED1a cells stain poorly with Syto9, we only quantified PI stained cells in this case. Both the total number of measured events (n) and the percentage of cells found in each region of the graph are indicated.

[Source data](#)

Extended Data Fig. 6 Assessing potential confounding factors for the killing capacities of erythromycin, azithromycin and doxycycline.

- a. Scatter plot of individual bacterial specific growth rates (μ - hr $^{-1}$) and percentage survival after a 5-hour treatment with 5-fold MIC of erythromycin, azithromycin or doxycycline. r is the Spearman correlation coefficient. Tested species are color-coded here and, in all panels thereafter as indicated at the bottom of this figure. b. *B. fragilis* (blue), *F. nucleatum*

(beige), *P. copri* (pink) and *E. coli* ED1a (grey) survival was assessed after a 5h erythromycin and azithromycin treatment (5-fold MIC) at 30 °C (slow growth) and 37 °C (fast growth) - mean ± SD of three independent experiments. No monotonic trend was observed. **c.** Scatter plot of MICs and % survival after a 5h treatment with 5-fold MIC of erythromycin, azithromycin or doxycycline. *r* is the Spearman correlation coefficient. Doxycycline exhibited a significant (*P* value = 0.0015) anti-correlation, i.e. more sensitive species to doxycycline (lower MIC) survived better when treated with antibiotic. Therefore, we tested further whether increasing the drug concentration in sensitive strains increased killing (panel d). **d.** *B. fragilis* (blue) and *F. nucleatum* (beige) survival after a 5-hour treatment as function of increasing doxycycline concentrations (mean ± SD of three independent experiments). No significant differences observed. In all cases doxycycline remained bacteriostatic. Significance calculated by unpaired two-sided t-test here and in all panels thereafter. **e.** To evaluate whether outgrowth from stationary phase affected our results, we selected two slow-growing strains, *E. rectale* (green) and *R. intestinalis* (orange) and grew them for 2 or 3h after diluting from an overnight culture to an of OD₅₇₈ 0.01. Both strains were then treated for 5h with 5-fold MIC of erythromycin, azithromycin or doxycycline and their survival was assessed (mean ± SD of three independent experiments). Although 3h grown cultures were killed slightly more effectively (difference is not statistically significant due to low number of replicates), this did not change the bactericidal or bacteriostatic characteristic of antibiotics. If anything, this means that we underestimate the killing for slow-growers, since all other experiments were performed with 2 h outgrowth. Nd: not detected (detection limit: 1 CFU/ml.). **f–g.** The survival of 8 selected gut microorganisms was measured after treating cells in exponential phase (E – 2h after dilution from an overnight culture) or in stationary phase (S – overnight growth) with 5-fold MIC of erythromycin (**f**) or doxycycline (**g**) for 5h (mean ± SD of three independent experiments). Consistent with the knowledge that antibiotic killing requires active growth, survival is higher in stationary phase for most strains (but not all – see *F. nucleatum*) that erythromycin or doxycycline kills. ns = non-significant; *, ** and *** denote *P* value <0.05, <0.01 and <0.001, respectively. nd as in e. **h.** *E. coli* ED1a survival was assessed after 5h treatment with 5-fold MIC of

doxycycline in the presence or absence of oxygen. Killing was similar in both conditions.

[Source data](#)

Extended Data Fig. 7 Identification and validation of macrolide and tetracycline antagonists (antidotes) in *B. vulgatus* and *B. uniformis*.

a. Schematic illustration of combinatorial screen concept: searching for antidote compounds that antagonize the antibacterial effect of erythromycin or doxycycline on commensal but not on pathogenic bacteria. **b.** Z-scores on bacterial growth for combinatorial drug exposure with antibiotic and 1197 FDA-approved drugs of Prestwick library (2 replicates). Compounds that successfully protected *B. vulgatus* and/or *B. uniformis* in the presence of antibiotic ($z\text{-score} > 3$) are indicated in gray. The strongest hits (circles) were validated in concentration-dependent assays (**c–d**). Box plots as in Fig. [1c](#). **c.** Validation of the strongest antagonistic interactions in independent experiments. Erythromycin and doxycycline concentrations were kept constant for each species and concentration ranges were tested for antagonists. Asterisks indicate that at least 25% of the bacterial growth (compared to no drug controls) could be rescued by the antagonist at a given concentration. Heat map depicts median growth across triplicates. **d.** For 10 of the validated antagonists, 8×8 checkerboard assays were performed to define better the range of the antagonistic interaction. Heat maps depict bacterial growth based on normalized median of AUCs of 3–4 replicates. Antagonistic interactions are framed in red (all). **e.** Percentage of surviving *B. vulgatus* cells were determined after 5h incubation with either erythromycin ($3.25 \mu\text{M}$) or doxycycline ($0.4 \mu\text{M}$) alone or in presence of benzboromarone ($40 \mu\text{M}$), dicumarol ($20 \mu\text{M}$), tolafenamic acid ($40 \mu\text{M}$) or diflunisal ($80 \mu\text{M}$). Data is based on three independent experiments. Boxplots are plotted as in Fig. [1c](#).

[Source data](#)

Extended Data Fig. 8 Schematic overview of screen for microbiome-protective antibiotic antidotes.

Workflow with decision process on which erythromycin and doxycycline antagonists to move to next evaluation step.

Extended Data Fig. 9 Antidotes work on further gut commensals, but do not compromise antibiotic efficacy on relevant pathogens.

a. 8×8 checkerboard assays to investigate if antidote is also protective for additional gut commensals. All combinations were tested in MGAM medium under anaerobic conditions. Heat map depicts bacterial growth based on median AUCs from 2–3 independent replicates. Concentrations are stated in μM . **b.** 8×8 checkerboard assays to evaluate antidote effects on the activity of erythromycin and doxycycline in relevant pathogenic species. The gastrointestinal pathogens *E. faecalis* and *E. faecium* were tested under anaerobic conditions. *S. aureus*, a cause of extra-intestinal infections, such as bacteremia and infective endocarditis, was tested under aerobic conditions. Heatmaps depict mean normalized AUCs of three biological replicates. Antidotes exhibit either neutral or even slight synergistic effects with antibiotics. **c.** Dicumarol rescues commensal growth ($n = 2$, anaerobic conditions) in a concentration-dependent manner. Erythromycin still retains its activity against pertinent pathogens such as *E. faecium*, *E. faecalis* ($n = 3$, anaerobic conditions) and *S. aureus* ($n = 3$, aerobic conditions) - see Suppl. Table 1 for strains used. $0.65 \mu\text{M}$ ($\sim 0.5 \mu\text{g/ml}$) erythromycin is within range of the MIC breakpoints for *Staphylococcus* ($1 \mu\text{g/ml}$) and *Streptococci* groups A, B, C & G ($0.25 \mu\text{g/ml}$). Error bars depict standard deviation.

[Source data](#)

Extended Data Fig. 10 The antidote benzboromarone selectively protects *Bacteroides* species from erythromycin in microbial communities.

a. The same 7-member synthetic gut microbial community as in Fig. 3a can be protected from erythromycin by the antidote benzboromarone. Heatmaps depict median bacterial growth based on normalized AUCs of the

community of three replicates. **b.** Community compositions in selected erythromycin-benzbromarone concentration combinations (1–4 referring to checkerboard tiles in **a**) demonstrate that benzbrumarone alone does not alter the community structure, but rescues some *Bacteroides* species and largely the community composition from erythromycin treatment. Depicted as in Fig. [3b](#) - control and erythromycin alone experiments same as in Fig. [3b](#). **c.** When the Bacteroidales community contains the pathogen *E. faecalis*, benzbrumarone rescues community growth upon erythromycin treatment, but enhances the ability of erythromycin to target *E. faecalis*. Plotted as in Fig. [3c](#). **d–f.** In complex human-stool derived communities from nine healthy donors (column #1 – 9), benzbrumarone protects 65% of Bacteroidales OTUs from erythromycin, and at least one sensitive Bacteroidales OTU per individual (2 biological \times 2 technical replicates). Plotted as in Fig. [3d](#). The fractions of rescued OTUs per order (**e**) and for Bacteroidales OTUs per genus (**f**) across all nine donors indicate that primarily *Bacteroides* species are rescued. **g.** In gnotobiotic mice colonized with a defined 12-member mouse microbiome^{[31](#)} and *B. vulgatus*, administration of benzbrumarone slightly (albeit not significantly, two-sided Mann-Whitney U test) mitigates the temporal decrease in fecal *B. vulgatus* counts that erythromycin causes. Mice received a single oral dose of erythromycin ($N = 9$) or erythromycin + benzbrumarone ($N = 9$) in two independent experiments. Data of the erythromycin-treated group is partially overlapping with data shown in Fig. [3g](#) as experiments were conducted in parallel. Boxes are plotted as in Fig. [1c](#). **h.** Both groups of mice show similar faecal erythromycin concentrations over the course of the experiment shown in **g**.

Source data

Extended Data Fig. 11 The antidote tolafenamic acid protects *Bacteroides* species from erythromycin in microbial communities.

a. Tolafenamic acid rescues commensal growth (based on median AUCs, $N = 2$) at clinical relevant erythromycin concentrations in a concentration-dependent manner (anaerobic conditions). Erythromycin still retains its activity against pertinent pathogens such as *E. faecium*, *E. faecalis* (based

on median AUCs, N = 3, anaerobic conditions) and *S. aureus* ([erythromycin] = 0.14 μM, N = 3, aerobic conditions). Error bars depict standard deviation. **b.** The same 7-member synthetic gut microbial community as in Fig. 3a can be protected from erythromycin by the tolfenamic acid. Heat maps depict median bacterial growth based on normalized AUCs of the community of 3 replicates. **c.** Community compositions in selected erythromycin-tolfenamic acid concentration combinations (1–4 referring to checkerboard tiles in **b**) demonstrate that tolfenamic acid alone does not alter the community structure, but rescues some *Bacteroides* species and largely the community composition from erythromycin treatment. Depicted as in Fig. 3b – control and erythromycin alone experiments same as in Fig. 3b. **d–f.** In complex human-stool derived communities from 9 healthy donors (column #1 – 9), tolfenamic acid can rescue 42% of the erythromycin-sensitive Bacteroidales OTUs (2 biological × 2 technical replicates). Data is plotted as in Fig. 3d. Bars depict the absolute numbers of erythromycin-sensitive OTUs and the percentage of rescued OTUs per order (**e**) or genus (**f**) across all nine individuals.

[Source data](#)

Supplementary information

[Supplementary Fig. 1](#)

This file contains an illustration of the flow cytometry gating strategy.

[Reporting Summary](#)

[Supplementary Tables 1–6](#)

This file contains Supplementary Tables 1–6.

[Supplementary Video 1](#)

Time-lapse of *B. vulgatus* growing on mGAM-agarose 1% pad.

Supplementary Video 2

Time-lapse of *B. vulgatus* growing on mGAM-agarose 1% pad containing fivefold MIC of erythromycin.

Supplementary Video 3

Time-lapse of *B. uniformis* growing on mGAM-agarose 1% pad.

Supplementary Video 4

Time-lapse of *B. uniformis* growing on mGAM-agarose 1% pad containing fivefold MIC of erythromycin.

Source data

Source Data Fig. 1

Source Data Fig. 2

Source Data Fig. 3

Source Data Extended Data Fig. 1

Source Data Extended Data Fig. 2

Source Data Extended Data Fig. 3

Source Data Extended Data Fig. 4

Source Data Extended Data Fig. 5

Source Data Extended Data Fig. 6

Source Data Extended Data Fig. 7

[**Source Data Extended Data Fig. 9**](#)

[**Source Data Extended Data Fig. 10**](#)

[**Source Data Extended Data Fig. 11**](#)

Rights and permissions

[Reprints and Permissions](#)

About this article

Cite this article

Maier, L., Goemans, C.V., Wirbel, J. *et al.* Unravelling the collateral damage of antibiotics on gut bacteria. *Nature* **599**, 120–124 (2021).
<https://doi.org/10.1038/s41586-021-03986-2>

- Received: 06 November 2019
- Accepted: 01 September 2021
- Published: 13 October 2021
- Issue Date: 04 November 2021
- DOI: <https://doi.org/10.1038/s41586-021-03986-2>

Share this article

Anyone you share the following link with will be able to read this content:

[Get shareable link](#)

Sorry, a shareable link is not currently available for this article.

[Copy to clipboard](#)

Provided by the Springer Nature SharedIt content-sharing initiative

This article was downloaded by **calibre** from <https://www.nature.com/articles/s41586-021-03986-2>

| [Section menu](#) | [Main menu](#) |

- Article
- [Published: 20 October 2021](#)

Regulation of intestinal immunity and tissue repair by enteric glia

- [Fränze Progatzky](#) [ORCID: orcid.org/0000-0003-0784-1323¹](#),
- [Michael Shapiro^{1,2 nA1}](#),
- [Song Hui Chng](#) [ORCID: orcid.org/0000-0003-1872-1626^{1 nA1 nAff7}](#),
- [Bethania Garcia-Cassani¹](#),
- [Cajsa Helena Classon](#) [ORCID: orcid.org/0000-0002-1638-4550¹](#),
- [Selin Sevgi¹](#),
- [Anna Laddach¹](#),
- [Ana Carina Bon-Frauches](#) [ORCID: orcid.org/0000-0001-7325-6021^{1 nAff8}](#),
- [Reena Lasrado¹](#),
- [Maryam Rahim¹](#),
- [Eleni-Maria Amaniti^{1,2 nAff9}](#),
- [Stefan Boeing³](#),
- [Kathleen Shah²](#),
- [Lewis J. Entwistle^{2 nAff10}](#),
- [Alejandro Suárez-Bonnet](#) [ORCID: orcid.org/0000-0003-0296-5896^{4,5}](#),
- [Mark S. Wilson](#) [ORCID: orcid.org/0000-0003-1737-1281⁶](#),
- [Brigitta Stockinger](#) [ORCID: orcid.org/0000-0001-8781-336X²](#) &
- [Vassilis Pachnis](#) [ORCID: orcid.org/0000-0001-9733-7686¹](#)

[Nature](#) volume 599, pages 125–130 (2021)

- 6855 Accesses
- 164 Altmetric

- [Metrics details](#)

Subjects

- [Glial biology](#)
- [Parasitic infection](#)

Abstract

Tissue maintenance and repair depend on the integrated activity of multiple cell types¹. Whereas the contributions of epithelial^{2,3}, immune^{4,5} and stromal cells^{6,7} in intestinal tissue integrity are well understood, the role of intrinsic neuroglia networks remains largely unknown. Here we uncover important roles of enteric glial cells (EGCs) in intestinal homeostasis, immunity and tissue repair. We demonstrate that infection of mice with *Heligmosomoides polygyrus* leads to enteric gliosis and the upregulation of an interferon gamma (IFN γ) gene signature. IFN γ -dependent gene modules were also induced in EGCs from patients with inflammatory bowel disease⁸. Single-cell transcriptomics analysis of the tunica muscularis showed that glia-specific abrogation of IFN γ signalling leads to tissue-wide activation of pro-inflammatory transcriptional programs. Furthermore, disruption of the IFN γ –EGC signalling axis enhanced the inflammatory and granulomatous response of the tunica muscularis to helminths. Mechanistically, we show that the upregulation of *Cxcl10* is an early immediate response of EGCs to IFN γ signalling and provide evidence that this chemokine and the downstream amplification of IFN γ signalling in the tunica muscularis are required for a measured inflammatory response to helminths and resolution of the granulomatous pathology. Our study demonstrates that IFN γ signalling in enteric glia is central to intestinal homeostasis and reveals critical roles of the IFN γ –EGC–CXCL10 axis in immune response and tissue repair after infectious challenge.

Access options

Subscribe to Journal

Get full journal access for 1 year

\$199.00

only \$3.90 per issue

[Subscribe](#)

All prices are NET prices.

VAT will be added later in the checkout.

Tax calculation will be finalised during checkout.

Rent or Buy article

Get time limited or full article access on ReadCube.

from \$8.99

[Rent or Buy](#)

All prices are NET prices.

Additional access options:

- [Log in](#)
- [Access through your institution](#)
- [Learn about institutional subscriptions](#)

Fig. 1: Inflammatory injury induces IFN γ signature in EGCs.

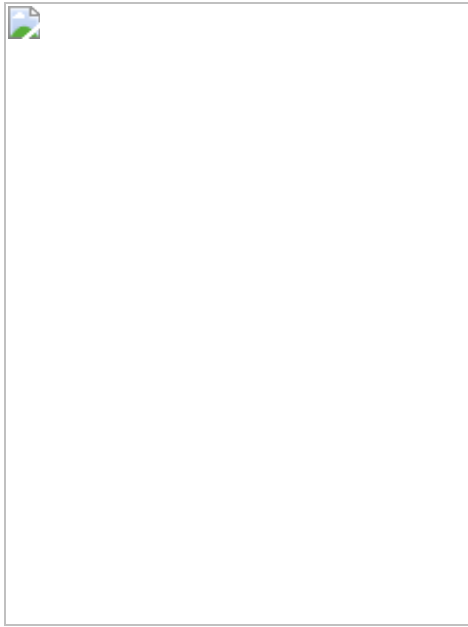


Fig. 2: IFN γ signalling in EGCs promotes intestinal tissue repair after helminth infection.

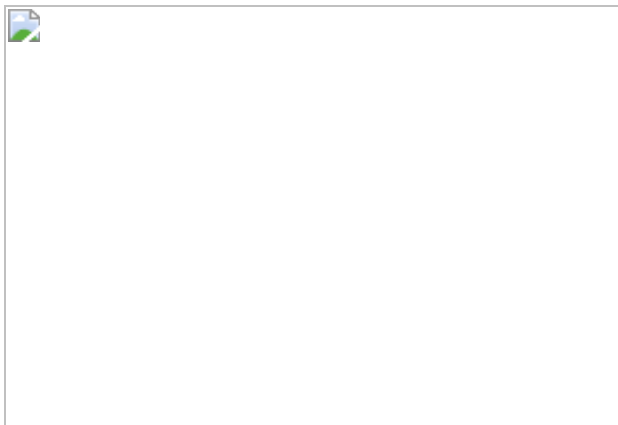
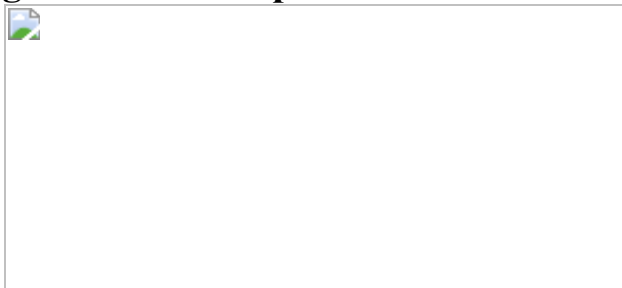


Fig. 3: Tissue-wide regulation of immune homeostasis and immune responses in the TM by the IFN γ –EGC signalling axis.



Fig. 4: Early activation of the IFN γ -EGC-Cxcl10 signalling axis regulates tissue repair after helminth infection.



Data availability

The .fastq files, Seurat objects, count matrices and associated meta data are publicly available at the GEO repository under accession number [GSE185412](#) ([GSE182708](#) and [GSE182715](#) for the bulk and scRNA-seq analysis of naive and *H. polygyrus*-infected EGCs, respectively, and [GSE182506](#) for the scRNA-seq of the naive and *H. polygyrus*-infected TM of *Ifngr2*^{control} and *Ifngr2*^{ΔEGC} mice). All datasets are available to search online (<https://biologic.crick.ac.uk/ENS/EGCinflammation>). Data for all graphs associated with the scRNA-seq analysis are available at GitHub (<https://github.com/michaeldshapiro/RegulationOfIntestinalImmuneHomeostasis>). [Source data](#) are provided with this paper.

Code availability

The code used for all scRNA-seq analysis is available at GitHub (<https://github.com/michaeldshapiro/RegulationOfIntestinalImmuneHomeostasis>).

References

1. 1.

Kotas, M. E. & Medzhitov, R. Homeostasis, inflammation, and disease susceptibility. *Cell* **160**, 816–827 (2015).

2. 2.

Turner, J. R. Intestinal mucosal barrier function in health and disease. *Nat. Rev. Immunol.* **9**, 799–809 (2009).

3. 3.

Abreu, M. T. Toll-like receptor signalling in the intestinal epithelium: how bacterial recognition shapes intestinal function. *Nat. Rev. Immunol.* **10**, 131–144 (2010).

4. 4.

Maloy, K. J. & Powrie, F. Intestinal homeostasis and its breakdown in inflammatory bowel disease. *Nature* **474**, 298–306 (2011).

5. 5.

Klose, C. S. & Artis, D. Innate lymphoid cells as regulators of immunity, inflammation and tissue homeostasis. *Nat. Immunol.* **17**, 765–774 (2016).

6. 6.

Roulis, M. & Flavell, R. A. Fibroblasts and myofibroblasts of the intestinal lamina propria in physiology and disease. *Differentiation* **92**, 116–131 (2016).

7. 7.

Koliaraki, V., Prados, A., Armaka, M. & Kollias, G. The mesenchymal context in inflammation, immunity and cancer. *Nat. Immunol.* **21**, 974–982 (2020).

8. 8.

Kinchen, J. et al. Structural remodeling of the human colonic mesenchyme in inflammatory bowel disease. *Cell* **175**, 372–386 (2018).

9. 9.

Laranjeira, C. et al. Glial cells in the mouse enteric nervous system can undergo neurogenesis in response to injury. *J. Clin. Invest.* **121**, 3412–3424 (2011).

10. 10.

Reynolds, L. A., Filbey, K. J. & Maizels, R. M. Immunity to the model intestinal helminth parasite *Heligmosomoides polygyrus*. *Semin. Immunopathol.* **34**, 829–846 (2012).

11. 11.

Boesmans, W., Lasrado, R., Vanden Berghe, P. & Pachnis, V. Heterogeneity and phenotypic plasticity of glial cells in the mammalian enteric nervous system. *Glia* **63**, 229–241 (2015).

12. 12.

Heanue, T. A. & Pachnis, V. Prospective identification and isolation of enteric nervous system progenitors using Sox2. *Stem Cells* **29**, 128–140 (2011).

13. 13.

Lasrado, R. et al. Lineage-dependent spatial and functional organization of the mammalian enteric nervous system. *Science* **356**, 722–726 (2017).

14. 14.

Bach, E. A., Aguet, M. & Schreiber, R. D. The IFN γ receptor: a paradigm for cytokine receptor signaling. *Annu. Rev. Immunol.* **15**, 563–591 (1997).

15. 15.

Lee, H. M. et al. IFN γ signaling endows DCs with the capacity to control type I inflammation during parasitic infection through promoting T-bet $^+$ regulatory T cells. *PLoS Pathog.* **11**, e1004635 (2015).

16. 16.

Huang, S. et al. Immune response in mice that lack the interferon- γ receptor. *Science* **259**, 1742–1745 (1993).

17. 17.

Gentile, M. E. et al. NK cell recruitment limits tissue damage during an enteric helminth infection. *Mucosal Immunol.* **13**, 357–370 (2020).

18. 18.

Nusse, Y. M. et al. Parasitic helminths induce fetal-like reversion in the intestinal stem cell niche. *Nature* **559**, 109–113 (2018).

19. 19.

Roulis, M. et al. Paracrine orchestration of intestinal tumorigenesis by a mesenchymal niche. *Nature* **580**, 524–529 (2020).

20. 20.

Rinkevich, Y. et al. Identification and prospective isolation of a mesothelial precursor lineage giving rise to smooth muscle cells and fibroblasts for mammalian internal organs, and their vasculature. *Nat. Cell Biol.* **14**, 1251–1260 (2012).

21. 21.

Mutsaers, S. E. et al. Mesothelial cells in tissue repair and fibrosis. *Front. Pharmacol.* **6**, 113 (2015).

22. 22.

Stetson, D. B. et al. Constitutive cytokine mRNAs mark natural killer (NK) and NK T cells poised for rapid effector function. *J. Exp. Med.* **198**, 1069–1076 (2003).

23. 23.

Dufour, J. H. et al. IFN- γ -inducible protein 10 (IP-10; CXCL10)-deficient mice reveal a role for IP-10 in effector T cell generation and trafficking. *J. Immunol.* **168**, 3195–3204 (2002).

24. 24.

Mills Ko, E. et al. Deletion of astroglial CXCL10 delays clinical onset but does not affect progressive axon loss in a murine autoimmune multiple sclerosis model. *J. Neuroinflammation* **11**, 105 (2014).

25. 25.

Ostvik, A. E. et al. Enhanced expression of CXCL10 in inflammatory bowel disease: potential role of mucosal Toll-like receptor 3 stimulation. *Inflamm. Bowel Dis.* **19**, 265–274 (2013).

26. 26.

Wang, L. et al. An atlas of genetic variation linking pathogen-induced cellular traits to human disease. *Cell Host Microbe* **24**, 308–323 (2018).

27. 27.

Sasselli, V. et al. Planar cell polarity genes control the connectivity of enteric neurons. *J. Clin. Invest.* **123**, 1763–1772 (2013).

28. 28.

Schindelin, J. et al. Fiji: an open-source platform for biological-image analysis. *Nat. Methods* **9**, 676–682 (2012).

29. 29.

Tavares, G. et al. Employing an open-source tool to assess astrocyte tridimensional structure. *Brain Struct. Funct.* **222**, 1989–1999 (2017).

30. 30.

Martin, M. Cutadapt removes adapter sequences from high-throughput sequencing reads. *EMBnet J.* **17**, 10–12 (2011).

31. 31.

Dobin, A. et al. STAR: ultrafast universal RNA-seq aligner. *Bioinformatics* **29**, 15–21 (2013).

32. 32.

Butler, A., Hoffman, P., Smibert, P., Papalexi, E. & Satija, R. Integrating single-cell transcriptomic data across different conditions, technologies, and species. *Nat. Biotechnol.* **36**, 411–420 (2018).

33. 33.

Su, S. et al. CellBench: R/Bioconductor software for comparing single-cell RNA-seq analysis methods. *Bioinformatics* **36**, 2288–2290 (2020).

34. 34.

Finak, G. et al. MAST: a flexible statistical framework for assessing transcriptional changes and characterizing heterogeneity in single-cell RNA sequencing data. *Genome Biol.* **16**, 278 (2015).

35. 35.

Reimand, J. et al. g:Profiler—a web server for functional interpretation of gene lists (2016 update). *Nucleic Acids Res.* **44**, W83–W89 (2016).

36. 36.

Sergushichev, A. An algorithm for fast preranked gene set enrichment analysis using cumulative statistic calculation. Preprint at <https://doi.org/10.1101/060012> (2016).

37. 37.

NCBI Resource Coordinators Database resources of the national center for biotechnology information. *Nucleic Acids Res.* **46**, D8–D13 (2018).

38. 38.

R Core Team *R: A Language and Environment for Statistical Computing* (R Foundation for Statistical Computing, 2019).

39. 39.

Stuart, T. et al. Comprehensive integration of single-cell data. *Cell* **177**, 1888–1902 (2019).

40. 40.

Wickham, H. *ggplot2: Elegant Graphics for Data Analysis*. (Springer, 2016).

41. 41.

ggsignif: significance brackets for 'ggplot2'. Preprint at <https://doi.org/10.31234/osf.io/7awm6> (2019).

42. 42.

ggrepel: automatically position non-overlapping text labels with 'ggplot2'. R package version 0.9.1; <https://CRAN.R-project.org/package=ggrepel> (2020).

43. 43.

ggsci: scientific journal and sci-fi themed color palettes for 'ggplot2'. R package version 2.9; <https://CRAN.R-project.org/package=ggsci>

(2018).

Acknowledgements

We thank staff at the Crick Science Technology Platforms (STPs) for expert support, in particular, the Biological Research Facility (R. Subramaniam, A. Vanderplank, M. Miah, S. Cooper), the Flow Cytometry STP (D. Das, K. Bartolovic), the Advanced Sequencing Facility (R. Goldstone, D. Jackson, A. Edwards, M. Costa) and the Experimental Histopathology Laboratory (E. Nye). We also thank C. Minutti and all members of the Pachnis laboratory for useful advice, discussions and insightful comments on the manuscript. We thank W. Müller for providing the *Ifngr2* floxed mice and R. Locksley and A. Luster for giving us permission to use the Yeti and *Cxcl10*^{-/-} mice, respectively. *Ifngr2* This work was supported by the Francis Crick Institute, which receives its core funding from Cancer Research UK (FC001128, FC001159), the UK Medical Research Council (FC001128, FC001159) and the Wellcome Trust (FC001128, FC001159). V.P. acknowledges additional funding from BBSRC (BB/L022974) and the Wellcome Trust (212300/Z/18/Z). B.S. was also funded by the Wellcome Trust (210556/Z/18/Z).

Author information

Author notes

1. Song Hui Chng

Present address: Roche Innovation Center Shanghai, Shanghai, China

2. Ana Carina Bon-Frauches

Present address: Department of Pathology, GROW-School for Oncology and Developmental Biology, Maastricht University Medical Centre, Maastricht, The Netherlands

3. Eleni-Maria Amaniti

Present address: Sainsbury Wellcome Centre, London, UK

4. Lewis J. Entwistle

Present address: Adaptive Immunity Research Unit, GSK, Stevenage, UK

5. These authors contributed equally: Michael Shapiro and Song Hui Chng

Affiliations

1. Development and Homeostasis of the Nervous System Laboratory, The Francis Crick Institute, London, UK

Fränze Progatzky, Michael Shapiro, Song Hui Chng, Bethania Garcia-Cassani, Cajsa Helena Classon, Selin Sevgi, Anna Laddach, Ana Carina Bon-Frauches, Reena Lasrado, Maryam Rahim, Eleni-Maria Amaniti & Vassilis Pachnis

2. AhRImmunity Laboratory, The Francis Crick Institute, London, UK

Michael Shapiro, Eleni-Maria Amaniti, Kathleen Shah, Lewis J. Entwistle & Brigitta Stockinger

3. Bioinformatics & Biostatistics STP, The Francis Crick Institute, London, UK

Stefan Boeing

4. Department of Pathobiology & Population Sciences, The Royal Veterinary College, Hatfield, UK

Alejandro Suárez-Bonnet

5. Experimental Histopathology STP, The Francis Crick Institute, London, UK

Alejandro Suárez-Bonnet

6. Immunology Discovery, Genentech Inc, South San Francisco, CA,
USA

Mark S. Wilson

Contributions

F.P. and V.P. conceived the study and, together with B.S. and M.S.W., designed the experiments. S.H.C., C.H.C., S.S., M.R., E.-M.A., A.C.B.-F., R.L. and L.J.E. helped with the experiments. S.H.C. performed cell culture of primary EGCs. M.S. and A.L. performed scRNA-seq bioinformatics analysis. S.B. performed bulk RNA-seq bioinformatics analysis. A.C.B.-F., S.S. and B.G.-C. performed immunohistochemistry analysis of the TM. B.G.-C. and C.H.C. designed, performed and analysed immunophenotyping experiments. K.S. designed some of the immunophenotyping experiments. A.S.-B. performed the histopathology examination. V.P. and F.P. wrote the manuscript with help from B.S. and contributions from all of the authors.

Corresponding authors

Correspondence to Fränze Progatzky or Vassilis Pachnis.

Ethics declarations

Competing interests

The authors declare no competing interests.

Additional information

Peer review information *Nature* thanks Isaac Chiu and the other, anonymous, reviewer(s) for their contribution to the peer review of this work. Peer reviewer reports are available.

Publisher's note Springer Nature remains neutral with regard to jurisdictional claims in published maps and institutional affiliations.

Extended data figures and tables

Extended Data Fig. 1 Intestinal helminth infection induces ENS injury and gliosis.

(**a–i**) TM preparations (**a–d, f–i**) and cross-section (**e**) from the duodenum of SOX10|tdT mice immunostained for CD45 (**a**), CD31 (**b**), PDGFRA (**c**), C-KIT (**d**), EPCAM(**e**), SOX10 (**f, h**) and HuC/D (**f, i**). Indicated are cells negative for tdT (empty arrowheads), tdT⁺ EGCs (asterisks) and neurons (arrowheads). **g, h** and **i** show single spectrum images of **f**. $n = 3$. (**j**) Quantification of tdT⁺ cells expressing SOX10 (EGCs) and HuC/D (neurons) ($n = 11$ field of views, representative of 3 experiments). (**k**) Schematic of intestinal cross-section illustrating the organization of the EGC-network and the life-cycle of *H. polygyrus*. Third-stage *H. polygyrus* larvae penetrate the duodenum mucosa and settle in the TM, eliciting local tissue damage, inflammation and formation of granulomatous infiltrates. 10 days later they emerge as adult worms into the lumen where they mate and produce eggs. (**l, m**) Cross-section (**l**) and whole-mount view (**m**) of the duodenum of *H. polygyrus*-infected SOX10|tdT mice (7 d.p.i.). Schematics (top left) show the orientation of the images. Arrowheads point to *H. polygyrus* settlement sites. $n = 4$. (**n, o, q, r**) TM preparations from the duodenum of naive and *H. polygyrus*-infected (7 dpi **n, o**; 10 dpi **q, r**) animals immunostained for GFAP and SOX10 (**n, o**) and S100 (**q, r**). $n = 5$. (**p**) Quantification (RT-qPCR) of *Gfap* transcripts in the TM of naive and *H. polygyrus*-infected mice (7 d.p.i.). $n=8$ (naive), $n = 6$ (*H. polygyrus*). 2 experiments. (**s–u**) Quantification of S100⁺ type III EGC morphology including total process length (**s**) $n = 10$, process thickness (**t**) ($n = 10$) and Scholl analysis for EGC process branching (**u**) $n = 5$. 2 experiments. Two-tailed Mann-Whitney test (**p, t**), unpaired two-tailed t-test (**s**), Two-way ANOVA with multiple comparisons (**u**). Mean ± s.e.m. Scale bars: **a–i**: 50 μm ; **l, m, n, o, q, r**: 100 μm , insets: 12.5 μm .

[Source data](#)

Extended Data Fig. 2 Transcriptomic analysis of *H. polygyrus*-infected TM.

(a) Experimental design for bulk RNA-seq of EGCs from the TM of naive and *H. polygyrus*-infected (7 d.p.i.) SOX10|tdT mice. tdT⁺ and tdT⁻ cell populations of dissociated TM were separated using FACS and subjected to RNA-seq. **(b)** Sorting strategy for tdT⁺ EGCs and tdT⁻ non-glia cells. **(c, d)** Volcano plot showing mean log₂-transformed fold change (x-axis) and significance ($-\log_{10}[P_{\text{adj}}]$) of differentially expressed genes between tdT⁻ and tdT⁺ cells from naive mice **(c)** and in tdT⁻ cells from naive and *H. polygyrus*-infected animals **(d)**. Coloured dots in **(c)** indicate genes specific to EGCs (*Sox10*, *Plp1*, *S100b*, *Foxd3*, *Erbb3*, *Sox2*; red), enteric neurons (*Ret*, *Tubb3*, *Sst*, *Elavl3*, *Elavl4*; green), immune cells (*Ptprc*; cyan), interstitial cells of Cajal (*Kit*; orange), smooth muscle cells (*Actg2*; pink), fibroblasts (*Pdgfra*; purple) and in **(d)** genes specific to type II immune response (*Arg1*, *Retnla*, *Chil3*) and T_H2 cytokines (*Il13*). $n = 4$. **(e)** Quantification of IFNγ in the TM of naive and *H. polygyrus*-infected animals (7 d.p.i.). Mean±SD; $n=6$. Two-tailed Mann-Whitney test. **(f)** UMAP of sequenced EGCs from the TM of naive and *H. polygyrus* infected mice. Cells are colour-coded according to experimental batches. **(g)** Violin plots showing normalized expression of representative EGC marker genes in EGC1 and EGC2 clusters in Fig. [1g](#). **(h, i)** Top 20 up-regulated and top 20 down-regulated genes in EGCs from *H. polygyrus*-infected mice **(h)** and in EGC2 relative to EGC1 **(i)**. IFNγ-target genes shown in bold **(h)**. Dot size indicates proportion of expressing cells and fill colour indicates mean normalized, centred and scaled expression level. **(j, k)** GO terms significantly enriched among the differentially expressed genes in EGC1 and EGC2 clusters shown in Fig. [1g](#) **(j)** and in hEGC1 and hEGC2 clusters shown in Fig. [1j](#) **(k)**.

[Source data](#)

[Extended Data Fig. 3 Cell autonomous activation of EGCs by IFNγ.](#)

(a, b) RT-qPCR analysis of *Ifngr1* (a) and *Ifngr2* (b) transcript levels from spleen cells and FACS-isolated EGCs (tdT⁺) and non-glia cells (tdT⁻) from SOX10|tdT mice. $n = 3$. **(c, d)** Cultures of FACS-isolated EGCs from SOX10|tdT mice in the absence **(c)** or presence **(d)** of IFNγ immunostained

for pH3 (green) and labelled with EdU (blue). Scale bars: 100 µm. (e, f) Quantification of pH3⁺ (e) and EdU⁺ (f) EGCs (tdT⁺ cells) in the cultures shown in c and d, respectively. n=8 field of views from each of 3 experiments. (g) RT-qPCR analysis of *Ifngr2* transcript levels in muscularis macrophages, fibroblasts, endothelial cells and EGCs FACS-isolated from the TM of *Ifngr2*^{control} and *Ifngr2*^{ΔEGC} mice. n = 3. (h) Images of IFNγ-treated (1 h) myenteric plexus preparations from the duodenum of *Ifngr2*^{control} and *Ifngr2*^{ΔEGC} mice immunostained for pStat1, SOX10 and HuC/D and counterstained for DAPI. Indicated are pStat1⁺ EGCs (empty arrowheads), pStat1⁻ EGCs (filled arrowheads). Scale bar = 10 µm. (i) Quantification of pStat1⁺ muscularis macrophages, fibroblasts, neurons and EGCs in IFNγ-treated (1 h) TM preparations from *Ifngr2*^{control} and *Ifngr2*^{ΔEGC} mice. n = 8. (j-l) RT-qPCR analysis of *Ifngr2*, *Cxcl10* and *Gbp10* transcript levels from rIFNγ treated EGCs isolated from *Ifngr2*^{control} and *Ifngr2*^{ΔEGC} mice. n = 4. (m) Quantification of Ki67⁺ EGCs in the TM of *H. polygyrus*-infected *Ifngr2*^{control} and *Ifngr2*^{ΔEGC} mice at 7 d.p.i. (n = 10). (n) Quantification of Ki67⁺ EGCs in the TM of wild-type and *Ifngr1*^{-/-} mice (n = 8). 2 experiments (m, n). Two-tailed Mann-Whitney test (e, f, n), unpaired two-tailed t-test (g, i, j, k, l, m). Mean±SEM.

[Source data](#)

Extended Data Fig. 4 Characterization of mice with glia-specific deletion of IFNγ signalling.

(a) Quantification of granulomas in the small intestine at 28 d.p.i. (n = 10) and 80 d.p.i. (n = 5) WT and *Ifngr1*^{-/-} mice (2 experiments). (b) Representative images of *H. polygyrus* settlement sites in *Ifngr2*^{control} and *Ifngr2*^{ΔEGC} gut at 7 d.p.i. Note bleeding in *Ifngr2*^{ΔEGC} mice (65.2±3.14 versus 31.8±1.56 in *Ifngr2*^{control} mice). n = 20 animals analysed. (c, d, f) Flow cytometry gating strategy to immunophenotype the TM of naive and *H. polygyrus*-infected *Ifngr2*^{control} and *Ifngr2*^{ΔEGC} mice showing debris exclusion and doublet discrimination, selection of live immune cells (c), followed by gating of myeloid cells (d) or NK-/ T cells (f). (e) Flow cytometry quantification of neutrophils in the TM of naive *Ifngr2*^{control} and

Ifngr2^{ΔEGC} mice. $n = 5$ (*Ifngr2*^{control}), $n = 6$ (*Ifngr2*^{ΔEGC}). (g–i) Flow cytometry quantification of CD4 and $\gamma\delta$ T cells and NK cells at indicated time-points after *H. polygyrus* infection within the TM of *Ifngr2*^{control} and *Ifngr2*^{ΔEGC} mice. ($n = 4$, data from 1 experiment). (j) Quantification of worms in the TM at 7 d.p.i. ($n = 8$) or recovered from the intestinal tract at 28 ($n = 11$) and 60 d.p.i. ($n = 15$). Two-way Anova. (k) *H. polygyrus* egg burden at 14 ($n_{control} = 15$, $n_{\Delta EGC} = 16$), 28 ($n = 11$) and 60 d.p.i. ($n = 9$). Two-tailed Mann-Whitney Test (e), Two-way Anova (a, g–k). Mean±SD (a, j, k), Mean±SEM (e, g–i).

Source data

Extended Data Fig. 5 Cellular atlas of small intestine TM.

(a) Mean normalized expression of representative marker genes and proportion of expressing cells (indicated by dot size) in the cell clusters shown in (c). Clusters are labelled with post facto annotation based on known markers. (b) Sorting strategy for live TM cells. (c) UMAP of all sequenced cells from small intestine TM. The numbers of clusters in c correspond to the numbers in a. (d) UMAP analysis of integrated scRNA-seq datasets of mesenchymal cells from the lamina propria (GSE142431)¹⁹ and the TM (present study; Fig. 3a, b). Annotation of cellular clusters matches those reported by Roulis et al¹⁹ on the basis of respective marker genes. Note that cell populations from the TM overlap with those from the lamina propria. (e) Violin plot quantification of *Pdgfra* expression per single cell highlighting that, similar to those in the lamina propria¹⁹, TM fibroblasts are divided into *Pdgfra*^{high} and *Pdgfra*^{low} cells. (f–i) Representative images of cross-section (f) or TM preparations (g–i) from the small intestine of SOX10|tdT (f and h), SOX10|YFP (g) and wild type (i) mice immunostained for PDPN to identify mesothelial cells (, arrowhead) and lymphatic endothelial cells (g), VEGFR2 and PDGFRB to identify endothelial cells and pericytes (arrowhead), respectively (h), and CD3 and IBA1 to identify T cells and macrophages, respectively (i). Note the small number of T cells in TM relative to macrophages. Scale bars: 50 μ m, insets: 25 μ m. Images representative of $n = 5$ animals analysed.

Extended Data Fig. 6 Glia-specific ablation of IFN γ signalling induces a tissue-wide pro-inflammatory state of TM at steady state and modulates the response to *H. polygyrus* infection.

(a–c) UMAP representation of mesothelial cells (**a**), fibroblasts (**b**) and muscularis macrophages (**c**) from naive *Ifngr2*^{control} (black) and *Ifngr2*^{ΔEGC} (orange) mice. **(d)** RT-qPCR analysis of *Lcn2*, *Il1b*, *Saa3* and *Il6* transcript levels in the TM from naive *Ifngr2*^{control} and *Ifngr2*^{ΔEGC} mice. $n_{\text{control}} = 12$, $n_{\Delta\text{EGC}} = 11$. **(e)** Representative haematoxylin and eosin stained intestinal cross-sections from naive *Ifngr2*^{control} and *Ifngr2*^{ΔEGC} mice. Empty and filled arrowheads in inset highlight reactive mesothelial cells and eosinophils, respectively. Scale bars = 50 μm , insets: 20 μm . Shown also is histology severity score (right) assessing inflammation in the lamina propria and tunica muscularis from naive *Ifngr2*^{control} and *Ifngr2*^{ΔEGC} mice. $n = 8$. 2 experiments. **(f)** Intestinal paracellular permeability in naive *Ifngr2*^{control} and *Ifngr2*^{ΔEGC} mice. $n_{\text{control}} = 8$, $n_{\Delta\text{EGC}} = 7$ (2 independent experiments). **(g)** Whole intestinal transit time in naive *Ifngr2*^{control} and *Ifngr2*^{ΔEGC} mice. $n_{\text{control}} = 9$, $n_{\Delta\text{EGC}} = 8$. **(h)** Fraction of cells per cluster in naive and *H. polygyrus*-infected *Ifngr2*^{control} and *Ifngr2*^{ΔEGC} mice. **(i)** Violin plot visualization of *Ifng* expression levels per single cell in indicated cell clusters. **(j)** Dot plot quantification of expression levels of *Ifng* vs *Cd8a* (left panel) and *Ifng* vs *Cd4* (right panel) in the Other lymphoid cells, NK cells, T Cells 1, T Cells 2 and T Cells 3 clusters, indicating that *Cd8a* T cells are a major source of *Ifng* in the TM of *H. polygyrus*-infected mice at 7 dpi. Two-tailed Mann-Whitney test (**d**, **f**). Unpaired two-tailed t-test (**g**). Mean±SEM.

[Source data](#)

Extended Data Fig. 7 Activation of the IFN γ -CXCL10 axis in TM precedes type II immune response and promotes tissue repair after helminth infection.

(a, b) RT-qPCR analysis of *Il4* and *Il13* transcripts in TM (a; $n_{\text{naive}} = 8$, $n_{3 \text{ d.p.i.}, 7 \text{ d.p.i.}, 10 \text{ d.p.i.}, 14 \text{ d.p.i.}} = 6$, $n_{5 \text{ d.p.i.}, 28 \text{ d.p.i.}} = 7$, $n_{7 \text{ d.p.i.}} = 9$, $n_{21 \text{ d.p.i.}} = 3$)

and *Ifng*, *Il4*, *Il13* and *Arg1* transcripts in mucosa (b; $n_{\text{naive}, 7 \text{ dpi}, 10 \text{ dpi}} = 6$, $n_{3 \text{ dpi}, 5 \text{ dpi}, 14 \text{ dpi}, 21 \text{ dpi}, 28 \text{ dpi}} = 3$) of small intestine following *H. polygyrus* infection. 2 experiments. (c, d) qRT-PCR time-course analysis of *Gbp6* (c) and *Gbp10* (d) transcript levels in TM after *H. polygyrus* infection. $n_{\text{naive}} = 8$, $n_{3 \text{ d.p.i.}, 7 \text{ d.p.i.}, 10 \text{ d.p.i.}, 14 \text{ d.p.i.}} = 6$, $n_{5 \text{ d.p.i.}, 28 \text{ d.p.i.}} = 7$, $n_{21 \text{ d.p.i.}} = 3$. 2 experiments. (e) Flow cytometric quantification of IFN γ -producing cells in the TM of *H. polygyrus*-infected WT mice (3 d.p.i.). $n_{\text{naive}} = 7$, $n_{3 \text{ d.p.i.}} = 9$. 2 experiments. (f) RT-qPCR analysis of *Cxcl10* transcripts in TM from *H. polygyrus*-infected (7 dpi) WT and *Ifngr1*^{-/-} mice. $n = 10$. 2 experiments. (g) Quantification of granulomas in the small intestine *H. polygyrus*-infected (28 d.p.i.) *Ifngr1*^{-/-} and *Cxcl10*^{-/-} mice. $n = 9$. 2 experiments. (h) RT-qPCR analysis of *Cxcl10* transcripts from rIFN γ -treated cultures (24 h) of EGCs from *Cxcl10*^{control} and *Cxcl10* ^{Δ EGC} mice. $n_{\text{Control}} = 2$, $n_{\text{rIFN}\gamma} = 3$. (i) *In situ* hybridization for *Cxcl10* in IFN γ -treated (1 h) myenteric plexus from the duodenum of *Cxcl10*^{control} and *Cxcl10* ^{Δ EGC} mice. CXCL10 $^+$ EGCs indicated by empty arrowhead. Scale bar = 10 μm . (j) Quantification of CXCL10 $^+$ EGCs in IFN γ -treated (1 h) TM preparations from *Cxcl10*^{control} and *Cxcl10* ^{Δ EGC} mice. $n_{\text{control}} = 3$, $n_{\Delta\text{EGC}} = 4$. (k) Quantification of CXCL10 $^+$ EGCs in the TM of *H. polygyrus*-infected *Cxcl10*^{control} and *Cxcl10* ^{Δ EGC} mice (3 d.p.i.). $n_{\text{control}} = 3$, $n_{\Delta\text{EGC}} = 6$. (l, m) Quantification of adult worms (l) and eggs (m) in small intestine from *H. polygyrus*-infected *Cxcl10*^{control} and *Cxcl10* ^{Δ EGC} mice (28 d.p.i.). $n_{\text{control}} = 12$, $n_{\Delta\text{EGC}} = 13$. 2 experiments. (n) Dot plot analysis of *Cxcr3* vs *Cd8a* expression indicating that Cd8 $^+$ T cells in TM express *Cxcr3*. Two-tailed Mann-Whitney test (f, j, k). Kruskal-Wallis test (g). Unpaired two-tailed t-test (e, h). Mean \pm SEM.

[Source data](#)

Supplementary information

[Reporting Summary](#)

[Peer Review File](#)

Source data

[Source Data Fig. 1](#)

[Source Data Fig. 2](#)

[Source Data Fig. 3](#)

[Source Data Fig. 4](#)

[Source Data Extended Data Fig. 1](#)

[Source Data Extended Data Fig. 2](#)

[Source Data Extended Data Fig. 3](#)

[Source Data Extended Data Fig. 4](#)

[Source Data Extended Data Fig. 6](#)

[Source Data Extended Data Fig. 7](#)

Rights and permissions

[Reprints and Permissions](#)

About this article

Cite this article

Progatzky, F., Shapiro, M., Chng, S.H. *et al.* Regulation of intestinal immunity and tissue repair by enteric glia. *Nature* **599**, 125–130 (2021).
<https://doi.org/10.1038/s41586-021-04006-z>

- Received: 21 October 2020
- Accepted: 07 September 2021
- Published: 20 October 2021
- Issue Date: 04 November 2021
- DOI: <https://doi.org/10.1038/s41586-021-04006-z>

Share this article

Anyone you share the following link with will be able to read this content:

[Get shareable link](#)

Sorry, a shareable link is not currently available for this article.

[Copy to clipboard](#)

Provided by the Springer Nature SharedIt content-sharing initiative

[Immunoregulatory role of enteric glia](#)

- Katrina Ray

Research Highlight 01 Nov 2021

This article was downloaded by **calibre** from <https://www.nature.com/articles/s41586-021-04006-z>

- Article
- [Published: 13 October 2021](#)

Oestrogen engages brain MC4R signalling to drive physical activity in female mice

- [William C. Krause](#)¹,
- [Ruben Rodriguez](#) ORCID: orcid.org/0000-0001-8174-2556¹,
- [Bruno Gegenhuber](#)^{2,3},
- [Navneet Matharu](#)^{4,5},
- [Andreas N. Rodriguez](#)¹,
- [Adriana M. Padilla-Roger](#) ORCID: orcid.org/0000-0003-4858-8221⁶,
- [Kenichi Toma](#)^{7,8},
- [Candice B. Herber](#)¹,
- [Stephanie M. Correa](#) ORCID: orcid.org/0000-0002-6221-689X¹ nAff⁹,
- [Xin Duan](#) ORCID: orcid.org/0000-0001-5260-8972^{7,8},
- [Nadav Ahituv](#) ORCID: orcid.org/0000-0002-7434-8144^{4,5},
- [Jessica Tollkuhn](#) ORCID: orcid.org/0000-0001-5991-7620³ &
- [Holly A. Ingraham](#) ORCID: orcid.org/0000-0001-6739-2967¹

Nature volume **599**, pages 131–135 (2021)

- 8158 Accesses
- 255 Altmetric
- [Metrics details](#)

Subjects

- [Neuroendocrinology](#)
- [Neuroscience](#)

Abstract

Oestrogen depletion in rodents and humans leads to inactivity, fat accumulation and diabetes^{1,2}, underscoring the conserved metabolic benefits of oestrogen that inevitably decrease with age. In rodents, the preovulatory surge in 17 β -oestradiol (E2) temporarily increases energy expenditure to coordinate increased physical activity with peak sexual receptivity. Here we report that a subset of oestrogen-sensitive neurons in the ventrolateral ventromedial hypothalamic nucleus (VMHvl)^{3,4,5,6,7} projects to arousal centres in the hippocampus and hindbrain, and enables oestrogen to rebalance energy allocation in female mice. Surges in E2 increase melanocortin-4 receptor (MC4R) signalling in these VMHvl neurons by directly recruiting oestrogen receptor- α (ER α) to the *Mc4r* gene. Sedentary behaviour and obesity in oestrogen-depleted female mice were reversed after chemogenetic stimulation of VMHvl neurons expressing both MC4R and ER α . Similarly, a long-term increase in physical activity is observed after CRISPR-mediated activation of this node. These data extend the effect of MC4R signalling — the most common cause of monogenic human obesity⁸ — beyond the regulation of food intake and rationalize reported sex differences in melanocortin signalling, including greater disease severity of MC4R insufficiency in women⁹. This hormone-dependent node illuminates the power of oestrogen during the reproductive cycle in motivating behaviour and maintaining an active lifestyle in women.

Access options

Subscribe to Journal

Get full journal access for 1 year

\$199.00

only \$3.90 per issue

Subscribe

All prices are NET prices.
VAT will be added later in the checkout.
Tax calculation will be finalised during checkout.

Rent or Buy article

Get time limited or full article access on ReadCube.

from \$8.99

Rent or Buy

All prices are NET prices.

Additional access options:

- [Log in](#)
- [Access through your institution](#)
- [Learn about institutional subscriptions](#)

Fig. 1: VMHvl neurons are sensitive to oestrogen and maintain energy expenditure in adult female mice.

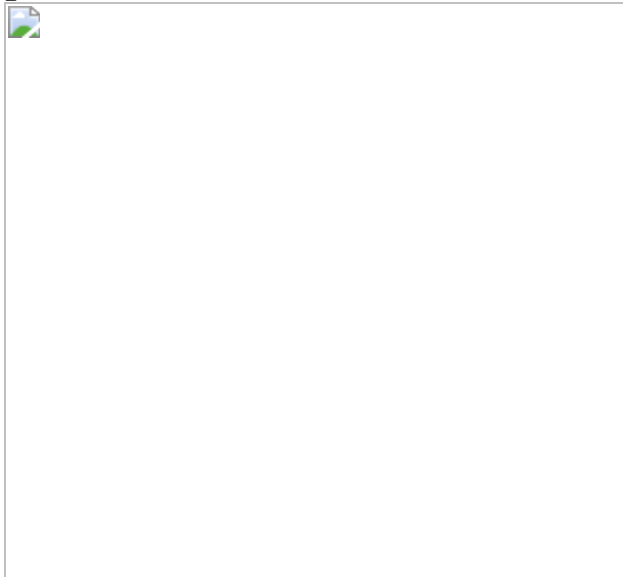


Fig. 2: VMHvl^{MC4R} neurons are a molecularly and anatomically distinct subset of VMHvl^{ER α} neurons.



Fig. 3: VMHvl^{MC4R} neurons control physical activity levels and when stimulated reverse inactivity and hypometabolism in obese OVX female mice.

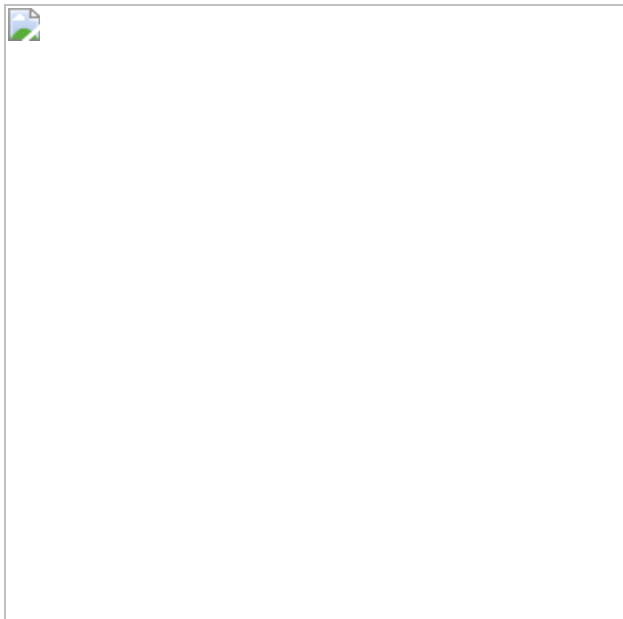
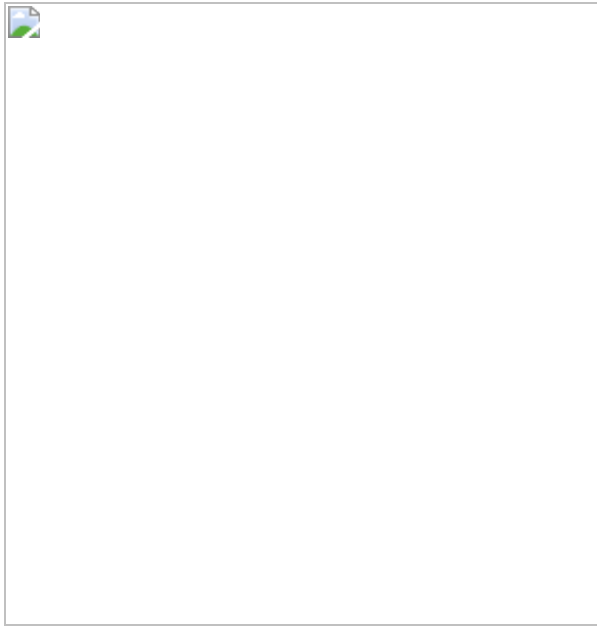


Fig. 4: Sex-specific role for MC4R signalling in the VMHvl can be bypassed using CRISPRa.



Data availability

RNA-sequencing and CUT&RUN datasets are available through the NCBI Gene Expression Omnibus⁵³ and are identified under the GEO accession numbers [GSE181204](#) and [GSE141434](#), respectively. Other supporting data are available upon request from the corresponding authors.

References

1. 1.

Mauvais-Jarvis, F., Clegg, D. J. & Hevener, A. L. The role of estrogens in control of energy balance and glucose homeostasis. *Endocr. Rev.* **34**, 309–338 (2013).

2. 2.

Carr, M. C. The emergence of the metabolic syndrome with menopause. *J. Clin. Endocrinol. Metab.* **88**, 2404–2411 (2003).

3. 3.

Correa, S. M. et al. An estrogen-responsive module in the ventromedial hypothalamus selectively drives sex-specific activity in females. *Cell Rep.* **10**, 62–74 (2015).

4. 4.

Herber, C. B. et al. Estrogen signaling in arcuate *Kiss1* neurons suppresses a sex-dependent female circuit promoting dense strong bones. *Nat. Commun.* **10**, 163 (2019).

5. 5.

Martinez de Morentin, P. B. et al. Estradiol regulates brown adipose tissue thermogenesis via hypothalamic AMPK. *Cell Metab.* **20**, 41–53 (2014).

6. 6.

Xu, Y. et al. Distinct hypothalamic neurons mediate estrogenic effects on energy homeostasis and reproduction. *Cell Metab.* **14**, 453–465 (2011).

7. 7.

van Veen, J. E. et al. Hypothalamic estrogen receptor alpha establishes a sexually dimorphic regulatory node of energy expenditure. *Nat. Metab.* **2**, 351–363 (2020).

8. 8.

Farooqi, I. S. et al. Dominant and recessive inheritance of morbid obesity associated with melanocortin 4 receptor deficiency. *J. Clin. Invest.* **106**, 271–279 (2000).

9. 9.

Qi, L., Kraft, P., Hunter, D. J. & Hu, F. B. The common obesity variant near *MC4R* gene is associated with higher intakes of total energy and

dietary fat, weight change and diabetes risk in women. *Hum. Mol. Genet.* **17**, 3502–3508 (2008).

10. 10.

Thammacharoen, S., Lutz, T. A., Geary, N. & Asarian, L. Hindbrain administration of estradiol inhibits feeding and activates estrogen receptor- α -expressing cells in the nucleus tractus solitarius of ovariectomized rats. *Endocrinology* **149**, 1609–1617 (2008).

11. 11.

Villanueva, E. C. et al. Complex regulation of mammalian target of rapamycin complex 1 in the basomedial hypothalamus by leptin and nutritional status. *Endocrinology* **150**, 4541–4551 (2009).

12. 12.

Mountjoy, K. G., Mortrud, M. T., Low, M. J., Simerly, R. B. & Cone, R. D. Localization of the melanocortin-4 receptor (MC4-R) in neuroendocrine and autonomic control circuits in the brain. *Mol. Endocrinol.* **8**, 1298–1308 (1994).

13. 13.

Ste Marie, L., Miura, G. I., Marsh, D. J., Yagaloff, K. & Palmiter, R. D. A metabolic defect promotes obesity in mice lacking melanocortin-4 receptors. *Proc. Natl Acad. Sci. USA* **97**, 12339–12344 (2000).

14. 14.

Chen, A. S. et al. Role of the melanocortin-4 receptor in metabolic rate and food intake in mice. *Transgenic Res.* **9**, 145–154 (2000).

15. 15.

Huszar, D. et al. Targeted disruption of the melanocortin-4 receptor results in obesity in mice. *Cell* **88**, 131–141 (1997).

16. 16.

Sina, M. et al. Phenotypes in three pedigrees with autosomal dominant obesity caused by haploinsufficiency mutations in the melanocortin-4 receptor gene. *Am. J. Hum. Genet.* **65**, 1501–1507 (1999).

17. 17.

Skene, P. J., Henikoff, J. G. & Henikoff, S. Targeted in situ genome-wide profiling with high efficiency for low cell numbers. *Nat. Protoc.* **13**, 1006–1019 (2018).

18. 18.

Lin, C. Y. et al. Whole-genome cartography of estrogen receptor α binding sites. *PLoS Genet.* **3**, e87 (2007).

19. 19.

Lo, L. et al. Connectional architecture of a mouse hypothalamic circuit node controlling social behavior. *Proc. Natl Acad. Sci. USA* **116**, 7503–7512 (2019).

20. 20.

Fuhrmann, F. et al. Locomotion, theta oscillations, and the speed-correlated firing of hippocampal neurons are controlled by a medial septal glutamatergic circuit. *Neuron* **86**, 1253–1264 (2015).

21. 21.

Góis, Z. H. T. D. & Tort, A. B. L. Characterizing speed cells in the rat hippocampus. *Cell Rep.* **25**, 1872–1884 (2018).

22. 22.

Evans, D. A. et al. A synaptic threshold mechanism for computing escape decisions. *Nature* **558**, 590–594 (2018).

23. 23.

Tovote, P. et al. Midbrain circuits for defensive behaviour. *Nature* **534**, 206–212 (2016).

24. 24.

Carter, M. E. et al. Tuning arousal with optogenetic modulation of locus coeruleus neurons. *Nat. Neurosci.* **13**, 1526–1533 (2010).

25. 25.

Coimbra, B. et al. Role of laterodorsal tegmentum projections to nucleus accumbens in reward-related behaviors. *Nat. Commun.* **10**, 4138 (2019).

26. 26.

Balthasar, N. et al. Divergence of melanocortin pathways in the control of food intake and energy expenditure. *Cell* **123**, 493–505 (2005).

27. 27.

Matharu, N. et al. CRISPR-mediated activation of a promoter or enhancer rescues obesity caused by haploinsufficiency. *Science* **363**, eaau0629 (2019).

28. 28.

Slonaker, J. R. The effect of pubescence, oestruation and menopause on the voluntary activity in the albino rat. *Am. J. Physiol.* **68**, 294–315 (1924).

29. 29.

Lotta, L. A. et al. Human gain-of-function *MC4R* variants show signaling bias and protect against obesity. *Cell* **177**, 597–607 (2019).

30. 30.

Pfau, J. G., Shadiack, A., Van Soest, T., Tse, M. & Molinoff, P. Selective facilitation of sexual solicitation in the female rat by a melanocortin receptor agonist. *Proc. Natl Acad. Sci. USA* **101**, 10201–10204 (2004).

31. 31.

Clayton, A. H. et al. Bremelanotide for female sexual dysfunctions in premenopausal women: a randomized, placebo-controlled dose-finding trial. *Womens Health* **12**, 325–337 (2016).

32. 32.

Chandler, D. J. et al. Redefining noradrenergic neuromodulation of behavior: impacts of a modular locus coeruleus architecture. *J. Neurosci.* **39**, 8239–8249 (2019).

33. 33.

Duval, K. et al. Effects of the menopausal transition on energy expenditure: a MONET Group Study. *Eur. J. Clin. Nutr.* **67**, 407–411 (2013).

34. 34.

O’Neal, T. J., Friend, D. M., Guo, J., Hall, K. D. & Kravitz, A. V. Increases in physical activity result in diminishing increments in daily energy expenditure in mice. *Curr. Biol.* **27**, 423–430 (2017).

35. 35.

Duggal, N. A., Niemiro, G., Harridge, S. D. R., Simpson, R. J. & Lord, J. M. Can physical activity ameliorate immunosenescence and thereby reduce age-related multi-morbidity? *Nat. Rev. Immunol.* **19**, 563–572 (2019).

36. 36.

Garfield, A. S. et al. A neural basis for melanocortin-4 receptor-regulated appetite. *Nat. Neurosci.* **18**, 863–871 (2015).

37. 37.

Dhillon, H. et al. Leptin directly activates SF1 neurons in the VMH, and this action by leptin is required for normal body-weight homeostasis. *Neuron* **49**, 191–203 (2006).

38. 38.

Krashes, M. J. et al. Rapid, reversible activation of AgRP neurons drives feeding behavior in mice. *J. Clin. Invest.* **121**, 1424–1428 (2011).

39. 39.

Cai, D., Cohen, K. B., Luo, T., Lichtman, J. W. & Sanes, J. R. Improved tools for the Brainbow toolbox. *Nat. Methods* **10**, 540–547 (2013).

40. 40.

Hu, Y. et al. Differential effects of unfolded protein response pathways on axon injury-induced death of retinal ganglion cells. *Neuron* **73**, 445–452 (2012).

41. 41.

Nagai, Y. et al. Deschloroclozapine, a potent and selective chemogenetic actuator enables rapid neuronal and behavioral modulations in mice and monkeys. *Nat. Neurosci.* **23**, 1157–1167 (2020).

42. 42.

Kim, D., Langmead, B. & Salzberg, S. L. HISAT: a fast spliced aligner with low memory requirements. *Nat. Methods* **12**, 357–360 (2015).

43. 43.

Anders, S., Pyl, P. T. & Huber, W. HTSeq—a Python framework to work with high-throughput sequencing data. *Bioinformatics* **31**, 166–169 (2015).

44. 44.

Love, M. I., Huber, W. & Anders, S. Moderated estimation of fold change and dispersion for RNA-seq data with DESeq2. *Genome Biol.* **15**, 550 (2014).

45. 45.

Mo, A. et al. Epigenomic signatures of neuronal diversity in the mammalian brain. *Neuron* **86**, 1369–1384 (2015).

46. 46.

Martin, M. Cutadapt removes adapter sequences from high-throughput sequencing reads. *EMBnet J.* **17**, 10–12 (2011).

47. 47.

Langmead, B. & Salzberg, S. L. Fast gapped-read alignment with Bowtie 2. *Nat. Methods* **9**, 357–359 (2012).

48. 48.

Li, H. et al. The Sequence Alignment/Map format and SAMtools. *Bioinformatics* **25**, 2078–2079 (2009).

49. 49.

Ramirez, F. et al. deepTools2: a next generation web server for deep-sequencing data analysis. *Nucleic Acids Res.* **44**, W160–W165 (2016).

50. 50.

Zhang, Y. et al. Model-based analysis of ChIP-seq (MACS). *Genome Biol.* **9**, R137.

51. 51.

Hahne, F. & Ivanek, R. Visualizing genomic data using Gviz and Bioconductor. *Methods Mol. Biol.* **1418**, 335–351 (2016).

52. 52.

Crane, J. D., Mottillo, E. P., Farncombe, T. H., Morrison, K. M. & Steinberg, G. R. A standardized infrared imaging technique that specifically detects UCP1-mediated thermogenesis in vivo. *Mol Metab.* **3**, 490–494 (2014).

53. 53.

Edgar, R., Domrachev, M. & Lash, A. E. Gene Expression Omnibus: NCBI gene expression and hybridization array data repository. *Nucleic Acids Res.* **30**, 207–210 (2002).

Acknowledgements

We thank C. Paillart and T. McMahon for technical assistance with the running and data acquisition for the CLAMS and ANY-maze systems; all members of the Ingraham laboratory for their comments and discussions; O. Yabut for expertise in imaging; and C. Vaisse for insights on MC4R signalling. This work was supported by funding to H.A.I. (R01DK121657, R01AG062331, UCSF Women's Reproductive Health RAP Award and GCRLE Senior Scholar Award 0320), to W.C.K. (American Heart Association Postdoctoral Fellowship 16POST27260361), to R.R. (K12GM081266 IRACDA Program), to B.G. (2T32GM065094, F31MH124365), to N.M. (UCSF Mary Ann Koda-Kimble Innovation Seed Award, UCSF Catalyst Program), to X.D. (R01EY030138, Research to Prevent Blindness and Klingenstein-Simons Neuroscience Fellowship), to S.M.C. (K01 DK098320, UCLA Women's Health Center, UL1TR001881), to C.B.H. (F32 DK107115-01A1, AHA Postdoctoral Fellowship)

16POST29870011), to N.A. (R01CA197139, R01 MH109907), to J.T. (R01MH113628, SFARI600568). We acknowledge the mouse metabolic core funded by P30 DK098722-01.

Author information

Author notes

1. Stephanie M. Correa

Present address: Department of Integrative Biology and Physiology,
University of California Los Angeles, Los Angeles, CA, USA

Affiliations

1. Department of Cellular and Molecular Pharmacology, School of
Medicine, University of California San Francisco, San Francisco, CA,
USA

William C. Krause, Ruben Rodriguez, Andreas N. Rodriguez, Candice
B. Herber, Stephanie M. Correa & Holly A. Ingraham

2. School of Biological Sciences, Cold Spring Harbor Laboratory, Cold
Spring Harbor, NY, USA

Bruno Gegenhuber

3. Cold Spring Harbor Laboratory, Cold Spring Harbor, NY, USA

Bruno Gegenhuber & Jessica Tollkuhn

4. Department of Bioengineering and Therapeutic Sciences, University of
California San Francisco, San Francisco, CA, USA

Navneet Matharu & Nadav Ahituv

5. Institute for Human Genetics, University of California San Francisco,
San Francisco, CA, USA

Navneet Matharu & Nadav Ahituv

6. Graduate Program in Neuroscience, University of California San Francisco, San Francisco, USA

Adriana M. Padilla-Roger

7. Department of Ophthalmology, University of California San Francisco, San Francisco, CA, USA

Kenichi Toma & Xin Duan

8. Department of Physiology, University of California San Francisco, San Francisco, CA, USA

Kenichi Toma & Xin Duan

Contributions

W.C.K. designed experiments, analysed data and wrote the manuscript. R.R. performed thermal and glucose homeostasis analyses in mice. B.G. optimized, performed and analysed the CUT&RUN method for ER α binding in neurons. N.M. provided CRISPRa viral vectors and expert advice. A.N.R. performed histology experiments and quantification of expression data. A.M.P.-R. aided with chemogenetic data acquisition and analyses. C.B.H. analysed bone and plasma lipid data. S.M.C. designed experiments, provided animal models and analysed data. K.T. and X.D. provided the AAV-DIO-mYFP vector. N.A. provided key unpublished reagents related to CRISPRa constructs and helped to guide studies. J.T. optimized CUT&RUN method for ER α binding in neurons, performed analyses and wrote the manuscript. H.A.I. designed experiments, analysed data and wrote the manuscript.

Corresponding authors

Correspondence to Jessica Tollkuhn or Holly A. Ingraham.

Ethics declarations

Competing interests

The authors declare no competing interests.

Additional information

Peer review information Nature thanks Miguel López and the other, anonymous, reviewer(s) for their contribution to the peer review of this work.

Publisher's note Springer Nature remains neutral with regard to jurisdictional claims in published maps and institutional affiliations.

Extended data figures and tables

[Extended Data Fig. 1 VMHvl^{ERαKO} does not affect energy intake or physical activity during the light phase but does decrease iBAT thermogenic gene expression.](#)

a, Representative image of a successful hit confirmed post-mortem by loss of ER α expression (red) in the VMHvl (white arrow) with corresponding expression of GFP driven by the AAV2-Cre viral vector. Scale bars, 100 μ m. **b**, Food intake and X-ambulatory parameters obtained in light period for VMHvl^{ERαKO} ($n = 10$) and ARC^{ERαKO} ($n = 12$) female cohorts compared to controls ($n = 7$ and 5). **c, d**, Equivalent fat mass in VMHvl^{ERαKO} ($n = 9$), ARC^{ERαKO} ($n = 11$), and control ($n = 7$ and 6) (**c**) and oxygen consumption rates in VMHvl^{ERαKO} ($n = 12$), ARC^{ERαKO} ($n = 11$), and control ($n = 6$ and 6) (**d**) female mice measured by EchoMRI and indirect calorimetry in CLAMS, respectively. **e**, Quantification of BAT thermogenic gene expression levels by qPCR in VMHvl^{ERαKO} ($n = 6$), ARC^{ERαKO} ($n = 7$), and control ($n = 6$ and 3) female mice (VMHvl^{ERαKO} *Ucp1*: unpaired two-tailed Student's *t*-test, $t_9 = 2.599$, $P = 0.0288$).

Extended Data Fig. 2 Induction of pS6 and *Mc4r* in the VMHvl depends on oestrogen signalling through ER α .

a, Immunofluorescence microscopy images of ER α and pS6(S244/S247) in the VMHvl (left panels) and ARC (right panels) of *Esr1*^{fl/fl} and OVX female mice 4 h post oestradiol benzoate treatment. **b**, Immunofluorescence microscopy images of ER α (red) and pS6(S244/S247) (green) in the VMHvl in conditional knockout (*Esr1*^{Nkx2-1Cre}) 4OVX female mice following 4 h after oestradiol benzoate treatment. **c**, Immunofluorescence microscopy images of ER α (red) and pS6(S244/S247) (green) in the VMHvl of intact adult male mice following 4 h post vehicle or oestradiol benzoate treatment. Bar graph to the right shows increased number of pS6(S244/S247)-positive neurons in the VMHvl of male mice after oestradiol benzoate treatment as done for OVX female mice (unpaired two-tailed *t*-test, $t_6 = 8.569$, $P = 0.0001$). **d**, Mammalian Phenotype Ontology terms most significantly enriched and top five significantly enriched Reactome Pathways among DEGs in the VMHvl (vehicle versus oestradiol benzoate). **e**, qPCR analysis of the indicated target genes in VMHvl from oestrus female mice, proestrus female mice, and male mice; data points represent values from individual mice (one-way ANOVA *Nmur2*: $F_{2,15} = 8.469$, $P = 0.0035$, post hoc: oestrus (E) versus proestrus (P) $P = 0.0454$, proestrus versus male $P = 0.0030$, and oestrus versus male $P = 0.1438$; *Esr1*: $F_{2,11} = 10.18$, $P = 0.0031$, post hoc: oestrus versus proestrus $P = 0.1650$, proestrus versus male $P = 0.0374$, and oestrus versus male $P = 0.0033$). Holm–Šidák multiple comparisons test. **f**, *Mc4r* expression levels in VMHvl from OVX oestradiol-benzoate-treated ($n = 6$) female mice normalized to vehicle treatment ($n = 3$) (unpaired two-tailed Student's *t*-test $t_6 = 6.519$, $P = 0.0006$). **g**, ISH showing *Mc4r* expression (red arrows) in the VMHvl of an oestrus female, a proestrus female, and an intact male. **h**, Representative ISH (*Mc4r*, red arrows) and immunofluorescent (pS6, yellow arrows) staining in the VMHvl (dashed circle) from OVX female mice treated with vehicle for 4 h, oestradiol benzoate for 2 h, or oestradiol benzoate for 4 h. **i**, Full size images showing bilateral expression of *Mc4r* and *Rprm* in intact female mice staged for oestrus and proestrus. *Rprm* expression is unchanged in both oestrous stages. Data presented as box

plots (see Fig. 1c legend for description). Micrographs are representative of data from 5 mice.

Extended Data Fig. 3 ER α -binding sites in oestradiol-benzoate-sensitive target genes contain conserved ERE consensus sequences.

CUT&RUN CPM-normalized coverage track showing oestradiol-benzoate-specific ER α binding sites containing EREs (pink boxes) within the *Greb1* locus (**a**; 3/3 replicates) and *Pgr* locus (**b**; 3/3 replicates), and in the *Mc4r* promoter (**c**; 1 of 3 replicates) in 400,000 sub-cortical brain nuclei collected from vehicle and oestradiol benzoate (5 μ g) treated gonadectomized mice. Below each track the location and sequence conservation of full (**a, b**) ERE and half (**c**) SP1/ERE consensus sites in target gene loci indicated by pink and green boxes. **d, e**, Location and sequence conservation of ERE consensus sites within *Mc4r* and *Nmur2* loci corresponding to ER α binding sites presented in Fig 1g. For all panels the genomic intervals containing ERE/SP1 sites are located within the ER α binding sites identified by CUT&RUN.

Extended Data Fig. 4 Limited induction of *Mc4r* expression in the MeA by ER α signalling, and additional neuroanatomical targets of VMHvl^{MC4R} neurons.

a, Representative coronal brain images of *Ai14^{Mc4r}* female mice stained for ER α (green) and Ai14 (magenta) in the MeA used for quantification shown in Fig 2a. **b**, Additional ISH comparing *Mc4r* induction in the VMHvl and MEA in oestrus and proestrus female mice. **c**, Representative mYFP reporter expression in additional neuroanatomical regions. Scale bars, 200 μ m. **d**, Heat map from Fig. 2d rearranged to compare VMHvl^{MC4R} and VMHvl^{ER α} projection intensity in target regions along the anterior-posterior axis. **e**, VMHvl^{MC4R} projections to the PAG preferentially target the PAGdl/l and PAGdm. Scale bars, 200 μ m.

Extended Data Fig. 5 VMHvl^{MC4R} neurons function specifically to drive physical activity.

a, Distance travelled over time in female and male mice following a single injection of CNO (repeated-measures two-way ANOVA interaction effect female: $F_{39,312} = 11.96, P < 0.0001$; male: $F_{39,312} = 6.898, P < 0.0001$). Holm–Šidák multiple comparisons test. **b**, Total time spent immobile in intact female and male VMHvl^{Cre-} controls ($n = 5/4$) and VMHvl^{MC4R::hM3Dq} mice ($n = 5/5$) (repeated-measures two-way ANOVA female interaction effect $F_{1,8} = 33.89, P = 0.0004$, post hoc $P < 0.0001$ and male interaction effect $F_{1,8} = 96.79, P = 0.0005$, post hoc $P < 0.0001$). Holm–Šidák multiple comparisons test. **c**, Thermal imaging of BAT surface temperatures for VMHvl^{Cre-} (left mouse) and VMHvl^{MC4R:: hM3Dq} (right mouse) female mice treated with CL-316,243. **d**, No differences were observed in *Ucp1* mRNA in the BAT from VMHvl^{Cre-} and VMHvl^{MC4R::hM3Dq} mice collected 1.5 h after a single CNO injection. **e**, Body weights for female VMHvl^{Cre-} ($n = 5$) and VMHvl^{MC4R::hM3Dq} ($n = 6$, baseline measurement includes 1 mouse with mistargeted injection) mice prior to glucose tolerance test (GTT). **f**, GTT glucose levels for intact female cohorts treated with saline or CNO and total area under the curve (AUC) (unpaired two-tailed Student's *t*-test $t_8 = 2.824, P = 0.0223$). **g**, Body weight normalized food consumption in female mice ($n = 5/5$) following Sal/CNO injection during light dark period (ZT12–ZT17) (repeated-measures two-way ANOVA Dark period interaction effect $F_{1,8} = 3.502, P = 0.0982$, post hoc $P = 0.0489$). Holm–Šidák multiple comparisons test. **h**, Sustained physical activity increase across light/dark periods in VMHvl^{MC4R::hM3Dq} ($n = 5$) female mice administered CNO-H₂O as compared to VMHvl^{Cre-} female mice ($n = 5$) or during exposure to plain drinking water (H₂O). **i, j**, Cumulative distance travelled (**i**) and number of rearing events (**j**) during light/dark periods following administration of CNO or water during the light stage (**i** repeated-measures two-way ANOVA $F_{1,8} = 15.8, P = 0.0041$, post hoc $P = 0.0006$ and **j**, repeated-measures two-way ANOVA $F_{1,8} = 15.8, P = 0.0041$, post hoc $P = 0.0006$). Holm–Šidák multiple comparisons test. **k**, Starting body weights and weight change

during continuous administration of CNO-H₂O for intact female mice. **l**, ERα and mCherry expression in the VMHvl following targeted injection of Cre-dependent AAV-hM4Di-mCherry into a female *Mc4r-t2a-cre* mouse. **m**, Number of rearing episodes during the dark period in VMHvl^{MC4R::hM4Di} ($n = 8$) and VMHvl^{Cre-} ($n = 4$) intact female mice following administration of plain or DCZ-laden drinking water. Data are mean ± s.e.m. or box plots (described in Fig. [1c](#) legend).

Extended Data Fig. 6 Increased physical activity and improvement in metabolic health markers in OVX VMHvl^{MC4R::hM3Dq} female mice in response to acute and chronic CNO.

a, Distance travelled over time in OVX female VMHvl^{Cre-} ($n = 5$) and VMHvl^{MC4R::hM3Dq} ($n = 5$) mice during administration of plain H₂O or CNO-H₂O (repeated-measures two-way ANOVA interaction effect $F_{11,88} = 5.265, P < 0.0001$). **b**, Total dark period rearing events in intact and OVX female mice administered plain H₂O or CNO-H₂O drinking water (repeated-measures two-way ANOVA interaction effect $F_{1,8} = 60.31, P < 0.0001$ post hoc $P < 0.0001$). **c**, Body weights (repeated-measures two-way ANOVA time effect $F_{2,24} = 49.51, P < 0.0001$; genotype effect $F_{2,24} = 33.50, P < 0.0001$) and fasting glucose levels (repeated-measures two-way ANOVA time effect $F_{2,26} = 6.456, P = 0.0053$; genotype effect $F_{1,26} = 10.11, P = 0.0038$) in female mice after OVX and subsequent HFD feeding. **d**, Blood glucose (left) and AUC (right) during ITT in chow-fed OVX female mice following 6-hour fast and saline/CNO treatment. **e**, Blood glucose (left, repeated-measures two-way ANOVA interaction effect $F_{1,8} = 7.791, P = 0.0235$, post hoc: VMHvl^{MC4R::hM3Dq} saline versus CNO, T15 $P = 0.0009$ and T60 $P = 0.0318$) and AUC (right, repeated-measures ANOVA with mixed-effects model, note: one *cre*⁺ female with missed injection was included in saline but not CNO treated groups, interaction effect $F_{1,8} = 7.791, P = 0.0235$, post hoc: VMHvl^{MC4R::hM3Dq} saline versus CNO $P = 0.0007$) values during 90 min ITT test on HFD-fed OVX female mice performed 6 hours post fasting and post injection with saline or CNO. **f**,

Blood glucose levels following a 6 h fast in OVX female mice maintained on Chow/HFD following a single saline or CNO injection (repeated-measures ANOVA with mixed-effects model, note: one *cre*⁺ female with missed injection was included in saline but not CNO treated groups, Chow: treatment effect $F_{1,17} = 5.038, P = 0.0384$, post hoc $P = 0.0179$; and HFD: interaction effect $F_{1,17} = 20.47, P = 0.0019$, post hoc $P = 0.0073$). **g**, Percentage change in body weight in HFD-fed OVX female mice ($n = 5/5$) continuously administered CNO-laden drinking water (repeated-measures two-way ANOVA interaction effect $F_{7,64} = 4.583, P = 0.0003$. **h**, Fasting blood glucose levels in OVX/HFD mice before and after 8 days of chronic CNO (repeated-measures ANOVA with mixed-effects model, note: one *cre*⁺ female with missed injection was included in saline but not CNO treated groups, interaction effect $F_{1,17} = 5.180, P = 0.0361$ post hoc: VMHvl^{MC4R::hM3Dq} Pre versus Post $P = 0.0156$). **i**, Plasma cholesterol levels before (Pre) and after (Post) 8 days of continuous CNO-H₂O exposure (repeated-measures ANOVA with mixed-effects model, note: one *cre*⁺ female with missed injection was included in saline- but not CNO-treated groups, interaction effect $F_{1,8} = 5.502, P = 0.0470$, post hoc $P = 0.0203$). **j**, Average daily food intake during 8 days of continuous CNO-H₂O exposure (points represent separate daily measurements of average consumption per mouse). Data are mean \pm s.e.m. or box plots (described in Fig. [1c](#) legend). **a–h**, ANOVA with Holm–Šidák multiple comparisons test.

[Extended Data Fig. 7 Additional metabolic and expression data for conditional *Mc4r*-rescue mice.](#)

a, FOS expression (arrows) in the VMHvl and PVH of female mice treated with oestradiol benzoate \pm MT-II. **b**, FOS⁺ cells in oestradiol benzoate + MT-II ($n = 5$) compared to vehicle (Veh) + MT-II ($n = 3$, ** $P = 0.0037$) and oestradiol benzoate + vehicle ($n = 4$, ** $P = 0.0046$) treated female mice (one-way ANOVA $F_{2,9} = 14.00, P = 0.0017$). **c**, *Mc4r* and *Sf1* expression patterns from Genotype-Tissue Expression Project intersect specifically in the hypothalamus (blue arrows) and not in peripheral tissues (red arrows). Transcripts/million (TPM) expression presented as box plots with centre line at median, box edges are 25th and 75th percentiles, and whiskers are

1.5x interquartile range. **d**, Equivalent body weights within cohorts of female and male $Mc4r^{+/+}$, $Mc4r^{loxTB}$ and $Mc4r^{Sfl-cre}$ mice at weaning. **e**, Percentage lean (one-way ANOVA $F_{2,31} = 101.4$, $P < 0.0001$, post hoc: $Mc4r^{+/+}$ versus $Mc4r^{loxTB}$ $P < 0.0001$, $Mc4r^{+/+}$ versus $Mc4r^{Sfl-cre}$ $P < 0.0001$, and $Mc4r^{Sfl-cre}$ versus $Mc4r^{loxTB}$ $P = 0.0720$) and % fat (one-way ANOVA $F_{2,31} = 104.2$, $P < 0.0001$, post hoc: $Mc4r^{+/+}$ versus $Mc4r^{loxTB}$ $P < 0.0001$, $Mc4r^{+/+}$ versus $Mc4r^{Sfl-cre}$ $P < 0.0001$, and $Mc4r^{Sfl-cre}$ versus $Mc4r^{loxTB}$ $P = 0.0769$) body composition analysis (EchoMRI) in adult female mice of each genotype. **f**, Oxygen consumption (VO_2) as a function of body weight in adult female mice. **g**, Body weights in 13-week-old $Mc4r^{+/+}$, $Mc4r^{loxTB}$, and $Mc4r^{Sfl-cre}$ female mice (one-way ANOVA $F_{2,32} = 226.6$, post hoc: $Mc4r^{+/+}$ versus $Mc4r^{loxTB}$ $P < 0.0001$, $Mc4r^{+/+}$ versus $Mc4r^{Sfl-cre}$ $P < 0.0001$, and $Mc4r^{Sfl-cre}$ versus $Mc4r^{loxTB}$ $P = 0.0029$). Data presented as mean \pm s.e.m. or scatterplots of values from individual mice. Number of mice analysed are indicated on each bar. **b, d-g**, Holm–Šidák multiple comparisons test.

Extended Data Fig. 8 Expression and physical activity levels in male and female $Mc4r^{CRISPRa}$ mice.

a, mCherry expression in $Mc4r^{CRISPRa}$ female hypothalamus. **b**, Fluorescent ISH images from $Mc4r^{CRISPRa}$ female (left) and male (right) showing *Esr1* and *Mc4r* expression. Images are reproduced and expanded from Fig. 4g to show limited induction of *Mc4r* outside of the VMHvl target region. **c**, Dark phase (ZT12–ZT24) physical activity levels (distance per 12 h) as a function of *Mc4r* or *mCherry* mRNA expression in microdissected VMHvl from control and $Mc4r^{CRISPRa}$ female mice. **d**, Home-cage activity in $Mc4r^{CRISPRa}$ ($n = 4$) and control ($n = 3$) male mice. **e**, Time spent immobile during the 12 hour dark phase in control and $Mc4r^{CRISPRa}$ female (unpaired two-tailed Student's *t*-test, $t_9 = 2.015$, $P = 0.0747$) and male $Mc4r^{CRISPRa}$ mice (see Fig. 4 for number of mice per group) (unpaired two-tailed Student's *t*-test, $t_5 = 3.245$, $P = 0.0228$). **f**, $Mc4r^{CRISPRa}$ ($n = 6$) and control ($n = 7$) female body weights during ad lib feeding. **g**, Normalized daily food intake in $Mc4r^{CRISPRa}$ ($n = 6$) and control ($n = 7$) female mice (unpaired

two-tailed Student's *t*-test, $t_{11} = 2.409$, * $P = 0.0347$). **h**, BAT surface temperatures in female control ($n = 4$) and $Mc4r^{CRISPRa}$ ($n = 5$) mice, repeated measurements at 30- and 60-min post-anaesthesia. **i**, Cortical bone thickness for female cohorts (unpaired two-tailed *t*-test, $t_6 = 2.957$, $P = 0.0254$). **j**, Body weights in control ($n = 4$) and $Mc4r^{CRISPRa}$ ($n = 6$) female mice at wk 9 and at wk 17 after eight weeks of OVX. **k**, Distance travelled over 24 hours in OVX control and OVX $Mc4r^{CRISPRa}$ compared to intact female mice (blue). **l**, Total dark phase distance in intact ($n = 5$), OVX control ($n = 7$), and OVX $Mc4r^{CRISPRa}$ ($n = 8$) female mice. Data are presented as scatterplots of values from individual mice, mean \pm s.e.m., or as box plots (described in the legend of Fig. [1c](#)).

Extended Data Table 1 Brain region abbreviations

Extended Data Table 2 Statistical tests and results

Supplementary information

[Supplementary Video 1](#)

CNO administered in the drinking water stimulates VMHvl^{MC4R} neurons to increase physical activity. Video recording of VMHvl^{MC4R::hM3dq} (top) and VMHvl^{Cre-} (bottom) female mice following addition of CNO-laden drinking water (0.25 mg ml⁻¹) during the inactive, lights-on period. Recordings have been sped up 20×.

[Reporting Summary](#)

Rights and permissions

[Reprints and Permissions](#)

About this article

[Cite this article](#)

Krause, W.C., Rodriguez, R., Gegenhuber, B. *et al.* Oestrogen engages brain MC4R signalling to drive physical activity in female mice. *Nature* **599**, 131–135 (2021). <https://doi.org/10.1038/s41586-021-04010-3>

- Received: 06 November 2019
- Accepted: 09 September 2021
- Published: 13 October 2021
- Issue Date: 04 November 2021
- DOI: <https://doi.org/10.1038/s41586-021-04010-3>

Share this article

Anyone you share the following link with will be able to read this content:

[Get shareable link](#)

Sorry, a shareable link is not currently available for this article.

[Copy to clipboard](#)

Provided by the Springer Nature SharedIt content-sharing initiative

[A two-step hormone-signalling mechanism that drives physical activity](#)

- Stephanie L. Padilla

News & Views 13 Oct 2021

This article was downloaded by **calibre** from <https://www.nature.com/articles/s41586-021-04010-3>

- Article
- [Published: 27 October 2021](#)

SLC25A39 is necessary for mitochondrial glutathione import in mammalian cells

- [Ying Wang¹](#) na1,
- [Frederick S. Yen](#) [ORCID: orcid.org/0000-0001-7300-9370](#)¹ na1,
- [Xiphias Ge Zhu¹](#) na1,
- [Rebecca C. Timson¹](#) na1,
- [Ross Weber¹](#),
- [Changrui Xing²](#),
- [Yuyang Liu¹](#),
- [Benjamin Allwein](#) [ORCID: orcid.org/0000-0002-8756-4786](#)²,
- [Hanzhi Luo³](#),
- [Hsi-Wen Yeh¹](#),
- [Søren Heissel⁴](#),
- [Gokhan Unlu](#) [ORCID: orcid.org/0000-0002-2704-2724](#)¹,
- [Eric R. Gamazon](#) [ORCID: orcid.org/0000-0003-4204-8734](#)^{5,6},
- [Michael G. Kharas](#) [ORCID: orcid.org/0000-0002-1165-6991](#)³,
- [Richard Hite](#) [ORCID: orcid.org/0000-0003-0496-0669](#)² &
- [Kıvanç Birsoy](#) [ORCID: orcid.org/0000-0002-7579-9895](#)¹

[Nature](#) volume **599**, pages 136–140 (2021)

- 13k Accesses
- 187 Altmetric
- [Metrics details](#)

Subjects

- [Cancer metabolism](#)
- [Metabolomics](#)
- [Mitochondria](#)

Abstract

Glutathione (GSH) is a small-molecule thiol that is abundant in all eukaryotes and has key roles in oxidative metabolism¹. Mitochondria, as the major site of oxidative reactions, must maintain sufficient levels of GSH to perform protective and biosynthetic functions². GSH is synthesized exclusively in the cytosol, yet the molecular machinery involved in mitochondrial GSH import remains unknown. Here, using organellar proteomics and metabolomics approaches, we identify SLC25A39, a mitochondrial membrane carrier of unknown function, as a regulator of GSH transport into mitochondria. Loss of SLC25A39 reduces mitochondrial GSH import and abundance without affecting cellular GSH levels. Cells lacking both SLC25A39 and its parologue SLC25A40 exhibit defects in the activity and stability of proteins containing iron–sulfur clusters. We find that mitochondrial GSH import is necessary for cell proliferation in vitro and red blood cell development in mice. Heterologous expression of an engineered bifunctional bacterial GSH biosynthetic enzyme (GshF) in mitochondria enables mitochondrial GSH production and ameliorates the metabolic and proliferative defects caused by its depletion. Finally, GSH availability negatively regulates SLC25A39 protein abundance, coupling redox homeostasis to mitochondrial GSH import in mammalian cells. Our work identifies SLC25A39 as an essential and regulated component of the mitochondrial GSH-import machinery.

Access options

Subscribe to Journal

Get full journal access for 1 year

\$199.00

only \$3.90 per issue

[Subscribe](#)

All prices are NET prices.

VAT will be added later in the checkout.

Tax calculation will be finalised during checkout.

Rent or Buy article

Get time limited or full article access on ReadCube.

from \$8.99

[Rent or Buy](#)

All prices are NET prices.

Additional access options:

- [Log in](#)
- [Access through your institution](#)
- [Learn about institutional subscriptions](#)

Fig. 1: Global analysis of mitochondrial proteome under GSH depletion.

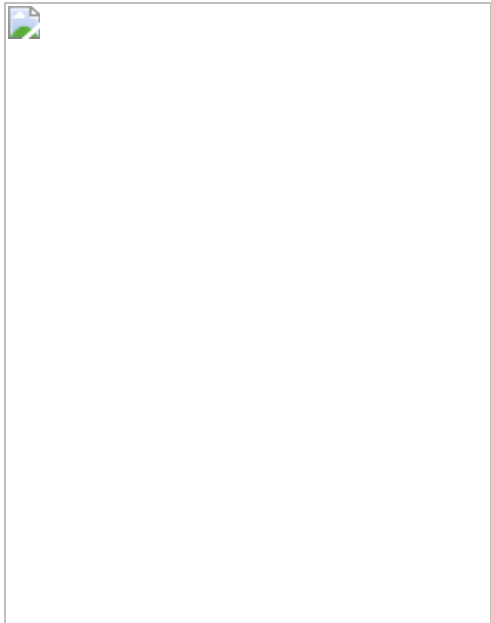


Fig. 2: SLC25A39 is required for mitochondrial GSH import.

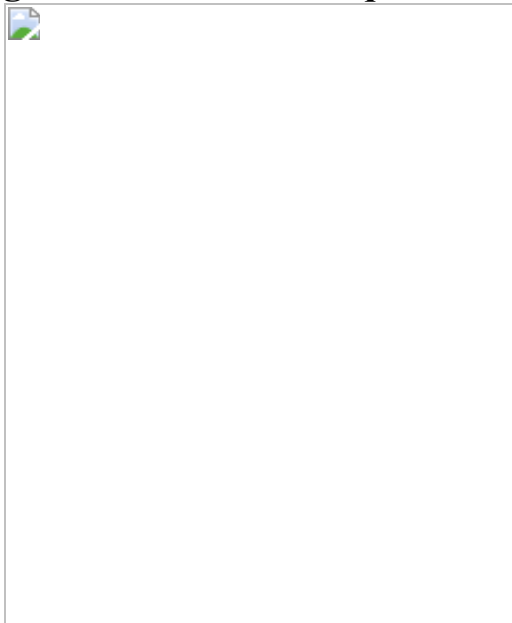


Fig. 3: Mitochondrial GSH import is essential for cell proliferation.

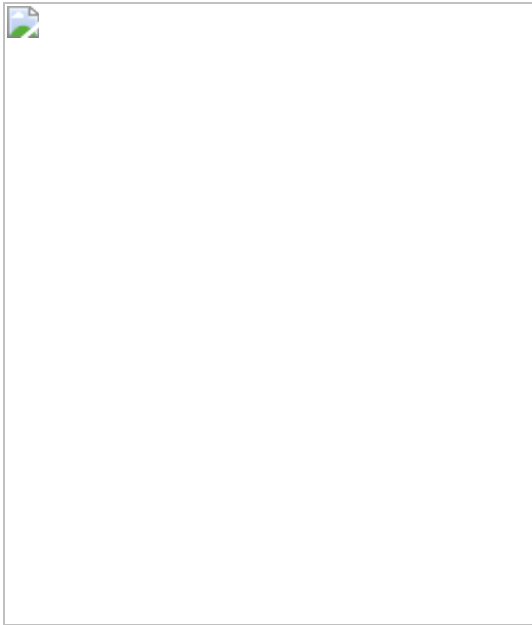
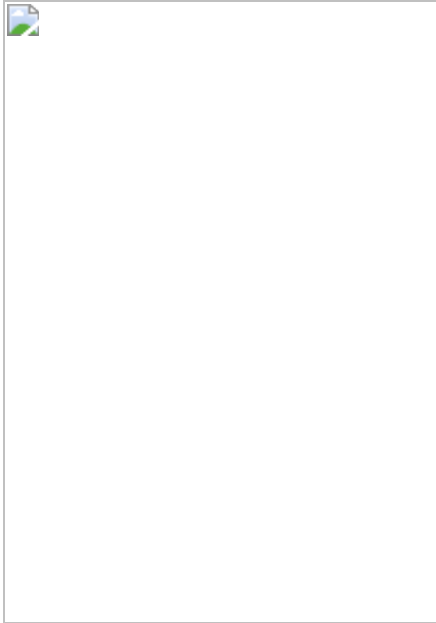


Fig. 4: Mitochondrial GSH depletion impairs erythropoiesis and iron-sulfur cluster proteins.



Data availability

Proteomics data have been deposited to the ProteomeXchange Consortium with the dataset identifier [PXD027673](#). Other data generated are available from the corresponding author upon reasonable request. [Source data](#) are provided with this paper.

References

1. 1.

Meister, A. & Anderson, M. E. Glutathione. *Annu. Rev. Biochem.* **52**, 711–760 (1983).

2. 2.

Mårtensson, J., Lai, J. C. & Meister, A. High-affinity transport of glutathione is part of a multicomponent system essential for mitochondrial function. *Proc. Natl Acad. Sci. USA* **87**, 7185–7189 (1990).

3. 3.

Deponte, M. The incomplete glutathione puzzle: just guessing at numbers and figures? *Antioxid. Redox Signal.* **27**, 1130–1161 (2017).

4. 4.

Griffith, O. W. & Meister, A. Origin and turnover of mitochondrial glutathione. *Proc. Natl Acad. Sci. USA* **82**, 4668–4672 (1985).

5. 5.

Hwang, C., Sinskey, A. J. & Lodish, H. F. Oxidized redox state of glutathione in the endoplasmic reticulum. *Science* **257**, 1496–1502 (1992).

6. 6.

Meredith, M. J. & Reed, D. J. Status of the mitochondrial pool of glutathione in the isolated hepatocyte. *J. Biol. Chem.* **257**, 3747–3753 (1982).

7. 7.

Deneke, S. M. & Fanburg, B. L. Regulation of cellular glutathione. *Am. J. Physiol. Lung Cell. Mol. Physiol.* **257**, L163–L173 (1989).

8. 8.

Jones, D. P. Redox potential of GSH/GSSG couple: assay and biological significance. *Methods Enzymol.* **348**, 93–112 (2002).

9. 9.

Kurosawa, K., Hayashi, N., Sato, N., Kamada, T. & Tagawa, K. Transport of glutathione across the mitochondrial membranes. *Biochem. Biophys. Res. Commun.* **167**, 367–372 (1990).

10. 10.

Griffith, O. W. & Meister, A. Potent and specific inhibition of glutathione synthesis by buthionine sulfoximine (*S*-n-butyl homocysteine sulfoximine). *J. Biol. Chem.* **254**, 7558–7560 (1979).

11. 11.

Münch, C. & Harper, J. W. Mitochondrial unfolded protein response controls matrix pre-RNA processing and translation. *Nature* **534**, 710–713 (2016).

12. 12.

Lee, H.-R. et al. Adaptive response to GSH depletion and resistance to l-buthionine-(*S,R*)-sulfoximine: involvement of Nrf2 activation. *Mol. Cell. Biochem.* **318**, 23–31 (2008).

13. 13.

Sun, X. et al. Activation of the p62–Keap1–NRF2 pathway protects against ferroptosis in hepatocellular carcinoma cells. *Hepatology* **63**, 173–184 (2016).

14. 14.

Booty, L. M. et al. Selective disruption of mitochondrial thiol redox state in cells and in vivo. *Cell Chem. Biol.* **26**, 449-461.e8 (2019).

15. 15.

Ruprecht, J. J. & Kunji, E. R. S. The SLC25 mitochondrial carrier family: structure and mechanism. *Trends Biochem. Sci.* **45**, 244–258 (2020).

16. 16.

Pebay-Peyroula, E. et al. Structure of mitochondrial ADP/ATP carrier in complex with carboxyatractyloside. *Nature* **426**, 39–44 (2003).

17. 17.

Zhu, X. G. et al. CHP1 regulates compartmentalized glycerolipid synthesis by activating GPAT4. *Mol. Cell* **74**, 45–58.e7 (2019).

18. 18.

Zhang, H., Go, Y.-M. & Jones, D. P. Mitochondrial thioredoxin-2/peroxiredoxin-3 system functions in parallel with mitochondrial GSH system in protection against oxidative stress. *Arch. Biochem. Biophys.* **465**, 119–126 (2007).

19. 19.

Seelig, G. F., Simondsen, R. P. & Meister, A. Reversible dissociation of gamma-glutamylcysteine synthetase into two subunits. *J. Biol. Chem.* **259**, 9345–9347 (1984).

20. 20.

Li, W., Li, Z., Yang, J. & Ye, Q. Production of glutathione using a bifunctional enzyme encoded by gshF from *Streptococcus thermophilus* expressed in *Escherichia coli*. *J. Biotechnol.* **154**, 261–268 (2011).

21. 21.

Chen, W. W., Freinkman, E., Wang, T., Birsoy, K. & Sabatini, D. M. Absolute quantification of matrix metabolites reveals the dynamics of mitochondrial metabolism. *Cell* **166**, 1324–1337.e11 (2016).

22. 22.

Slabbaert, J. R. et al. Shawn, the *Drosophila* homolog of SLC25A39/40, is a mitochondrial carrier that promotes neuronal survival. *J. Neurosci.* **36**, 1914–1929 (2016).

23. 23.

Usaj, M. et al. TheCellMap.org: a web-accessible database for visualizing and mining the global yeast genetic interaction network. *Genes Genomes Genet.* **7**, 1539–1549 (2017).

24. 24.

Luk, E., Carroll, M., Baker, M. & Culotta, V. C. Manganese activation of superoxide dismutase 2 in *Saccharomyces cerevisiae* requires MTM1, a member of the mitochondrial carrier family. *Proc. Natl Acad. Sci. USA* **100**, 10353–10357 (2003).

25. 25.

Nilsson, R. et al. Discovery of genes essential for heme biosynthesis through large-scale gene expression analysis. *Cell Metab.* **10**, 119–130 (2009).

26. 26.

Biederbick, A. et al. Role of human mitochondrial Nfs1 in cytosolic iron–sulfur protein biogenesis and iron regulation. *Mol. Cell. Biol.* **26**, 5675–5687 (2006).

27. 27.

Mayr, J. A., Feichtinger, R. G., Tort, F., Ribes, A. & Sperl, W. Lipoic acid biosynthesis defects. *J. Inherit. Metab. Dis.* **37**, 553–563 (2014).

28. 28.

Chen, Z. & Lash, L. H. Evidence for mitochondrial uptake of glutathione by dicarboxylate and 2-oxoglutarate carriers. *J. Pharmacol. Exp. Ther.* **285**, 608–618 (1998).

29. 29.

Booty, L. M. et al. The mitochondrial dicarboxylate and 2-oxoglutarate carriers do not transport glutathione. *FEBS Lett.* **589**, 621–628 (2015).

30. 30.

Kumar, C. et al. Glutathione revisited: a vital function in iron metabolism and ancillary role in thiol-redox control. *EMBO J.* **30**, 2044–2056 (2011).

31. 31.

Rodríguez-Manzaneque, M. T., Tamarit, J., Bellí, G., Ros, J. & Herrero, E. Grx5 is a mitochondrial glutaredoxin required for the activity of iron/sulfur enzymes. *Mol. Biol. Cell* **13**, 1109–1121 (2002).

32. 32.

Almusafri, F. et al. Clinical and molecular characterization of 6 children with glutamate–cysteine ligase deficiency causing hemolytic anemia. *Blood Cells. Mol. Dis.* **65**, 73–77 (2017).

33. 33.

Wessel, D. & Flügge, U. I. A method for the quantitative recovery of protein in dilute solution in the presence of detergents and lipids. *Anal. Biochem.* **138**, 141–143 (1984).

34. 34.

McAlister, G. C. et al. MultiNotch MS3 enables accurate, sensitive, and multiplexed detection of differential expression across cancer cell line proteomes. *Anal. Chem.* **86**, 7150–7158 (2014).

35. 35.

Tyanova, S. et al. The Perseus computational platform for comprehensive analysis of (prote)omics data. *Nat. Methods* **13**, 731–740 (2016).

36. 36.

Birsoy, K. et al. An essential role of the mitochondrial electron transport chain in cell proliferation is to enable aspartate synthesis. *Cell* **162**, 540–551 (2015).

37. 37.

Concordet, J.-P. & Haeussler, M. CRISPOR: intuitive guide selection for CRISPR/Cas9 genome editing experiments and screens. *Nucleic Acids Res.* **46**, W242–W245 (2018).

38. 38.

Shola, D. T. N., Yang, C., Han, C., Norinsky, R. & Peraza, R. D. in *Mouse Genetics: Methods and Protocols* (eds. Singh, S. R., Hoffman, R. M. & Singh, A.) 1–27 (Springer US, 2021).

39. 39.

Murgha, Y. E., Rouillard, J.-M. & Gulari, E. Methods for the preparation of large quantities of complex single-stranded oligonucleotide libraries. *PLoS ONE* **9**, e94752 (2014).

40. 40.

Sadreyev, I. R., Ji, F., Cohen, E., Ruvkun, G. & Tabach, Y. PhyloGene server for identification and visualization of co-evolving proteins using

normalized phylogenetic profiles. *Nucleic Acids Res.* **43**, W154–W159 (2015).

41. 41.

Ruan, J. et al. TreeFam: 2008 update. *Nucleic Acids Res.* **36**, D735–D740 (2008).

42. 42.

Thomas, P. D. et al. PANTHER: a library of protein families and subfamilies indexed by function. *Genome Res.* **13**, 2129–2141 (2003).

43. 43.

Studer, G. et al. ProMod3—a versatile homology modelling toolbox. *PLOS Comput. Biol.* **17**, e1008667 (2021).

44. 44.

Pebay-Peyroula, E. et al. Structure of mitochondrial ADP/ATP carrier in complex with carboxyatractyloside. *Nature* **426**, 39–44 (2003).

45. 45.

Robinson, A. J. & Kunji, E. R. S. Mitochondrial carriers in the cytoplasmic state have a common substrate binding site. *Proc. Natl. Acad. Sci.* **103**, 2617–2622 (2006).

46. 46.

Pettersen, E. F. et al. UCSF Chimera—a visualization system for exploratory research and analysis. *J. Comput. Chem.* **25**, 1605–1612 (2004).

47. 47.

Bycroft, C. et al. The UK Biobank resource with deep phenotyping and genomic data. *Nature* **562**, 203–209 (2018).

48. 48.

Barbeira, A. N. et al. Integrating predicted transcriptome from multiple tissues improves association detection. *PLoS Genet.* **15**, e1007889 (2019).

49. 49.

Zhou, D. et al. A unified framework for joint-tissue transcriptome-wide association and Mendelian randomization analysis. *Nat. Genet.* **52**, 1239–1246 (2020).

50. 50.

Unlu, G. et al. Phenome-based approach identifies RIC1-linked Mendelian syndrome through zebrafish models, biobank associations and clinical studies. *Nat. Med.* **26**, 98–109 (2020).

51. 51.

Aguet, F. et al. Genetic effects on gene expression across human tissues. *Nature* **550**, 204–213 (2017).

Acknowledgements

We thank all members of the Birsoy laboratory for helpful suggestions. Y.W. is supported by UL1 TR001866 from the National Center for Advancing Translational Sciences (NCATS, National Institutes of Health (NIH) Clinical and Translational Science Award (CTSA) programme. F.S.Y. and R.W. are supported by a Medical Scientist Training Program grant from the National Institute of General Medical Sciences of the NIH under award number T32GM007739 to the Weill Cornell/Rockefeller/Sloan Kettering Tri-Institutional MD-PhD Program. G.U. is a Damon Runyon Fellow supported by the Damon Runyon Cancer Research Foundation (DRG-2431-21). E.R.G. was supported by NIH/NHGRI R01HG011138 and R35HG010718. H.L. is funded by NIH K99 DK128602-01. M.G.K. is a Scholar of the Leukemia and Lymphoma Society and is supported by the

US NIH NIDDK R01-DK101989-01A1; NCI 1R01CA193842-01, 1R01CA193842-06A1, 5R01CA186702-07, 1R01DK1010989-06A1, R01HL135564 and R01CA225231-01; NYSTEM 0266-A121-4609, the Alex's Lemonade Stand A Award. R.H. is supported by NIH/NCI Cancer Center Support Grant (P30 CA008748) and the Searle Scholars Program. We thank R. Vaughan, Director of Biostatistics at the Rockefeller University for his assistance with statistics used in this manuscript. K.B. is supported by the NIH/NCI (DP2 OD024174-01), NIH/NIDDK (R01 DK123323-01), Pershing Square Sohn Foundation and Mark Foundation Emerging Leader Award; and is a Searle and Pew-Stewart Scholar.

Author information

Author notes

1. These authors contributed equally: Ying Wang, Frederick S. Yen, Xiphias Ge Zhu, Rebecca C. Timson

Affiliations

1. Laboratory of Metabolic Regulation and Genetics, The Rockefeller University, New York, NY, USA

Ying Wang, Frederick S. Yen, Xiphias Ge Zhu, Rebecca C. Timson, Ross Weber, Yuyang Liu, Hsi-Wen Yeh, Gokhan Unlu & Kivanç Birsoy

2. Structural Biology Program, Memorial Sloan Kettering Cancer Center, New York, NY, USA

Changrui Xing, Benjamin Allwein & Richard Hite

3. Molecular Pharmacology Program, Memorial Sloan Kettering Cancer Center, New York, NY, USA

Hanzhi Luo & Michael G. Kharas

4. The Proteomics Resource Center, The Rockefeller University, New York, NY, USA

Søren Heissel

5. Division of Genetic Medicine, Department of Medicine, Vanderbilt University Medical Center, Nashville, TN, USA

Eric R. Gamazon

6. Clare Hall and MRC Epidemiology Unit, University of Cambridge, Cambridge, UK

Eric R. Gamazon

Contributions

K.B. conceived the project and K.B., Y.W., F.S.Y., X.G.Z., R.C.T. and R.W. designed the experiments. Y.W., F.S.Y., X.G.Z. and R.C.T. performed most of the experiments with the assistance of H.-W.Y., R.W. and Y.L. R.C.T. and R.W. designed and engineered GshF constructs. H.L. and M.G.K. characterized the mouse phenotypes. C.X., B.A. and R.H. assisted with the substrate mutant experiments. G.U. and E.R.G. performed the human genetic and transcriptome analysis. S.H. performed proteomics analysis. K.B. wrote the manuscript.

Corresponding author

Correspondence to Kivanç Birsoy.

Ethics declarations

Competing interests

K.B. is scientific advisor to Nanocare Pharmaceuticals and Barer Institute.

Additional information

Peer review information *Nature* thanks Michael Murphy, Tracey Rouault and the other, anonymous, reviewer(s) for their contribution to the peer review of this work. Peer reviewer reports are available.

Publisher's note Springer Nature remains neutral with regard to jurisdictional claims in published maps and institutional affiliations.

Extended data figures and tables

[Extended Data Fig. 1 SLC25A39 protein levels are directly regulated by cellular GSH availability.](#)

a, Gene enrichment analysis (Gorilla) for proteomics data from the immunopurified mitochondria of HeLa cells (top). Gene ontology analysis of proteins altered by BSO treatment (bottom). Log (FDR), log false discovery rate (bottom). Statistical significance was determined by Fisher's exact or binomial distribution test. **b**, Immunoblot of SLC25A39, SLC25A12 and CS in HeLa cells treated with the indicated doses of BSO for 24 h. CS was used as the loading control. **c**, Immunoblot of indicated proteins in HEK-293T (top) and K562 (bottom) cells treated with BSO (1 mM; 10 µM, respectively) for the indicated days. CS and GAPDH were used as loading controls. **d**, Immunofluorescence analysis of indicated proteins in HeLa cells treated with vehicle or BSO (1 mM) for 24 h. Micrographs are representative images. Scale bar, 10 µm (top). Immunofluorescence analysis of SLC25A39 in parental and SLC25A39 knockout HeLa cells treated with BSO (1 mM) and erastin (5 uM) for 24 h (bottom). Micrographs are representative images of three independent experiments. Scale bar, 20 µm. **e**, Relative abundance of *SLC25A39*, *GCLM* and *SLC25A40* transcripts in HEK-293T cells treated with BSO (1 mM) for the indicated days using quantitative reverse transcription PCR (RT-qPCR), normalized to transcripts of *β-ACTIN*. Error bars represent mean ± s.d.; *n* = 3 biologically independent samples. Statistical significance was determined by one-way ANOVA followed by Bonferroni post-hoc analysis. **f**, Immunoblot of indicated proteins in HEK-293T *SLC25A39* knockout cells expressing a

vector control or *SLC25A39* cDNA treated with BSO (1 mM) for the indicated times. GAPDH was used as the loading control. **g**, The design of 3xFLAG- *SLC25A39*-P2A-RFP construct (top). Immunoblot of indicated proteins in HEK-293T cells expressing 3xFLAG- *SLC25A39*-P2A-RFP treated with BSO (1 mM) and erastin (5 μ M) for 48 h (bottom). $\backslash(\alpha\backslash)$ -Tubulin was used as the loading control. **h**, Immunoblot of indicated proteins in HeLa cells treated with indicated doses of H₂O₂ for 24 h. CS and GAPDH were used as loading controls. **i**, Immunoblot of indicated proteins in HeLa cells treated with erastin (5 μ M) or indicated doses of KI696 (NRF2 activator) for 24 h. GAPDH were used as loading controls. **j**, Immunoblot of indicated proteins in HeLa cells treated with erastin (5 μ M) or indicated doses of RSL-3, an inhibitor of glutathione peroxidase 4 (GPX4), for 24 h. CS was used as a loading control. **k**, Immunoblot of *SLC25A39* and ATF4 proteins in HeLa cells treated with indicated doses of mitoCDNB, diamide and BSO (1 mM)/erastin (5 μ M) for 24 h. GAPDH was used as loading control. **l**, Immunoblot of indicated proteins in HeLa cells treated with erastin (5 μ M) and co-treated with either GSH (10 mM), GSHee (10 mM), Trolox (50 μ M) or Ferrostatin-1 (5 μ M) for 48 h. CS was used as a loading control. GSHee, glutathione ethyl ester.

[Source data](#)

[Extended Data Fig. 2 Mitochondrial GSH import is mediated by SLC25A39.](#)

a, Volcano plots showing the fold change in mitochondrial metabolite abundance (\log_2) versus *P* values (-log) from K562 and HEK-293T *SLC25A39* knockout cell lines expressing a vector control or *SLC25A39* cDNA. Red data points highlight GSH and GSSG. The dotted line represents *P* = 0.05. Statistical significance was determined by multiple two-tailed unpaired *t*-tests with correction for multiple comparisons using the Holm-Šídák method. **b**, Immunoblot of indicated proteins in whole cell lysates and mitochondria isolated from HEK-293T (top) and HeLa (bottom) *SLC25A39* knockout cells expressing a vector control or *SLC25A39* cDNA. **c**, Mitochondrial GSH and GSSG abundance (top and middle panels) and total intracellular GSH levels in HEK-293T parental or *SLC25A39* knockout cells expressing a vector control or *SLC25A39* cDNA. Data are

normalized by citrate synthase (CS) protein levels. **d**, Uptake of indicated concentrations of [$^{13}\text{C}_2, ^{15}\text{N}$]-GSH into mitochondria isolated from parental HEK-293T mitotag cells for 10 min. Data are normalized to the NAD⁺ abundance. **e**, Uptake of indicated concentrations of [$^{13}\text{C}_2, ^{15}\text{N}$]-GSH or GSH into mitochondria isolated from parental HEK-293T mitotag cells for 10 min. Data are normalized to the NAD⁺ abundance. **f**, Uptake of [$^{13}\text{C}_2, ^{15}\text{N}$]-GSH (5 mM, top) or [$^{13}\text{C}_4, ^{15}\text{N}_2$]-GSSG (0.5 mM, bottom) into mitochondria isolated from HEK-293T *SLC25A39* knockout cells expressing a vector control or *SLC25A39* cDNA for 10 min. Data are normalized by citrate synthase (CS) protein levels. **g**, Uptake of [$^{13}\text{C}_2, ^{15}\text{N}$]-GSH (5 mM) into mitochondria isolated from HEK-293T *SLC25A39* knockout cells expressing *SLC25A39* cDNA for 10 min in the presence or absence of DTT (100 mM). Data are normalized by citrate synthase (CS) protein levels. **h**, Mitochondrial GSH abundance in HeLa *SLC25A39* knockout cells expressing indicated cDNAs (top). Data are normalized by citrate synthase (CS) protein levels. Immunoblot of indicated proteins in HeLa *SLC25A39* knockout cells expressing indicated cDNAs (bottom). α -Tubulin was used as a loading control. **c, d, e, f, g, h**, Bars represent mean \pm s.d.; **a, c, d, e, f, g, h**, $n = 3$ biologically independent samples. Statistical significance in **c, d, f, g and h** was determined by one-way ANOVA followed by Bonferroni post-hoc analysis; **a, e** by two-tailed unpaired *t*-test.

Source data

Extended Data Fig. 3 *SLC25A40*, the mammalian paralog for *SLC25A39* can compensate *SLC25A39* loss.

a, Individual sgRNA scores of *SLC25A40* and *TXNRD2* from the CRISPR screens in indicated cell lines from Fig. [3b](#). **b**, CRISPR gene scores in indicated *SLC25A39* knockout HEK-293T cells expressing a vector control or *SLC25A39* cDNA. *SLC25A40* data point is highlighted in blue (top). Top 15 scoring genes differentially required for the proliferation of HEK-293T *SLC25A39* knockout cells (bottom). **c**, Phylogenetic tree of *SLC25A39* homologs across model organisms. **d**, Top ranked (z-scores) co-evolved genes with *SLC25A40* across species. **e**, Relative conservation of *SLC25A40* and *SLC25A39* in different species compared to their human

homologs. **f**, Representative bright-field micrographs of Jurkat *SLC25A39* knockout cells transduced with the indicated sgRNA at the end of the cell proliferation assay. Scale bar, 50 μ m (right). **g**, Relative fold change in cell number of the indicated HEK-293T *SLC25A39* knockout cells expressing a vector control or *SLC25A39* cDNA transduced with the indicated sgRNAs. Cells were cultured for 4 days (mean \pm SD, n = 3). Cell doublings were normalized to the average of the *SLC25A39* knockout cells expressing *SLC25A39* cDNA. Statistical significance was determined by one-way ANOVA followed by Bonferroni post-hoc analysis. **h**, Volcano plots of the fold change in mitochondrial metabolite abundance (\log_2) versus P values (-log) from HEK-293T *SLC25A39* knockout cell line expressing a vector control or *SLC25A40* cDNA. Red data points highlight GSH and GSSG. The dotted line represents P = 0.05. **i**, Immunoblot of indicated proteins in HEK-293T cells expressing an *SLC25A40* cDNA in the presence or absence of BSO. CS and β -actin were used as loading controls.

[Source data](#)

Extended Data Fig. 4 Expression of *S.thermophilus* *GshF* can modulate cellular GSH levels in mammalian cells.

a, Mitochondrial abundance of GSH in HEK-293T *SLC25A39* knockout cells expressing a vector control or *SLC25A39* cDNA treated with GSH (5 mM) or GSHee (5 mM) for 24 h. Data are normalized by CS protein levels. **b**, Relative cell number of indicated *SLC25A39* knockout Jurkat cells transduced with indicated sgRNAs. Cells were cultured for 4 days with or without GSHee (10 mM). Cell numbers were normalized to the average of the *SLC25A39* knockout cells in each treatment condition. **c**, Immunofluorescence analysis of GshF (FLAG, red) and CS (green) in HeLa cells. Micrographs are representative images. Scale bar, 20 μ m. **d**, Immunoblots of indicated proteins in HEK-293T cells expressing a vector control or *GshF* cDNA. GAPDH was used as the loading control. **e**, Schematic of engineered *GshF* construct for mammalian expression and the domains of the protein with GCL and GS function (top). Whole cell GSH abundance (bottom left) and fold change in cell number (\log_2) of HEK-293T cells expressing a vector control or engineered *GshF* cDNA treated with indicated BSO concentrations for 5 days (bottom right). **f**, Immunoblot

analysis of indicated proteins in whole-cell lysates and mitochondria isolated from *SLC25A39* knockout HEK-293T cells expressing a vector control, mito-GshF or *SLC25A39* cDNA. **g**, Mitochondrial abundance of GSSG in HEK-293T *SLC25A39* knockout cells transduced with the indicated cDNAs. Data are normalized by CS protein levels. **a, b, e, g** Bars represent mean \pm s.d.; **a, b, e, g** $n = 3$ biologically independent samples. Statistical significance in **a, g** were determined by one-way ANOVA followed by Bonferroni post-hoc analysis; **b, e** were determined by two-way ANOVA followed by Bonferroni post-hoc analysis.

[Source data](#)

Extended Data Fig. 5 Mitochondrial GSH depletion sensitizes cells to BSO treatment.

a, Scheme of the in vitro sgRNA competition assay performed in HEK-293T *SLC25A39* knockout cells expressing a vector control or *SLC25A39* cDNA transduced with a pool of 5 control sgRNAs (sgControl, gray) and sgRNAs targeting *TXNRD2* (pink) and *SLC25A40* (green) (left). Differential guide scores in the indicated cell lines upon treatment with 20 μ M BSO (right). Bars represent mean \pm s.d. **b**, Synthetic lethal genetic interactions of *mtm1* with other genes in *S. cerevisiae*.

[Source data](#)

Extended Data Fig. 6 *Slc25a39* is essential for embryonic development and red cell differentiation *in vivo*.

a, Targeting scheme for *Slc25a39* knockout mice. **b**, Gross appearance of E12.5 embryos of the indicated genotypes. Genotyping of *Slc25a39* E12.5 embryos from heterozygous mating. PCR of wild type allele and targeted allele result in \sim 1,500bp and \sim 800bp bands, respectively (left). The number of viable pups with indicated genotypes is shown (right). **c**, Targeting scheme for *Slc25a39* conditional knockout (*Slc25a39^{f/f}*) mice in which two loxp sites were inserted in the indicated intronic regions. The resultant *Slc25a39^{f/f}* mice were mated with erythroid-lineage specific Cre-recombinase (*ErGFP-cre*) mice to generate an erythroid-specific

conditional knockout mice. **d**, The number of viable pups with indicated genotypes is shown resulting from the indicated mating. **e**, Representative images of H&E staining of fetal liver cells from E12.5 *Slc25a39^{f/f}* and *ErGFP-cre^{+/−} Slc25a39^{f/f}* embryos. The bottom images are the boxed area of the top images. Arrows show that many haematopoietic cells in the fetal liver display nuclear fragmentation and cellular shrinkage. Bars, 50 µm (top panel), 12.5 µm (bottom panel). **f**, Percent of Prussian blue positive peripheral blood cells from indicated E12.5 embryos (top). Representative images of Prussian blue staining of indicated E12.5 whole embryo sections (bottom). Blue and orange arrows indicate blood cells in developing heart with negative or positive staining, respectively. Bar, 360 µm. **g**, Gating strategy and quantification of erythroblast populations at different differentiation stages using surface markers: Ter119 and CD44, and FSC (size). Percentage of cells of indicated populations among total fetal liver cells (left). Gating strategy (right). $n = 3$, *ErGFP-cre^{+/−} Slc25a39^{f/f}*; $n = 4$ *Slc25a39^{f/f}* embryos. **h**, Profiling of cells of myeloid lineage (top), myeloid progenitor cells (middle) and lymphoid lineage (bottom). Data are presented as the population among total fetal liver cells. E12 embryos: $n = 12$ *Slc25a39^{f/f}* or *Slc25a39^{f/f}*, $n = 7$ *ErGFP-cre^{+/−} Slc25a39^{f/f}*, $n = 4$ *ErGFP-cre^{+/−} Slc25a39^{f/f}*. **i**, Relative RPKM values of SLC25A39, FTL and HBB genes in human erythroblasts at differing stages of terminal differentiation. **f**, **g** and **h**, Bars represent mean ± s.d.; statistical significance in **f** and **h** was determined by one-way ANOVA followed by Bonferroni post-hoc analysis; **g** was determined by two-tailed unpaired *t*-test.

Source data

Extended Data Fig. 7 Loss of SLC25A39/40 decreases the steady state levels of iron-sulfur containing proteins and phenocopies iron-sulfur cluster deficiency.

a, Comparison of proteomics data from BSO treated HeLa cells and *SLC25A39/40* double knockout Jurkat cells. The criteria are indicated on the Venn diagram. **b**, Gene ontology analysis of significantly downregulated genes in *SLC25A39/40* double knockout Jurkat cells. FDR, false discovery rate. **c**, Immunoblot of indicated proteins in the indicated HEK-293T

SLC25A39 knockout cells expressing a vector control or *SLC25A39* cDNA transduced with the indicated sgRNA. β -ACTIN was used as a loading control. **d**, Immunoblot of indicated proteins in indicated HEK-293T cells transduced with shRNA targeting either *GFP* as a control or *NFS1* (two different shRNAs). Proteins were extracted from cells 6 days after transduction. GAPDH was used as a loading control. **e**, Schematic showing how the iron-sulfur cluster-containing protein LIAS enables OGDH and PDH activity by transferring lipoic acid as a cofactor to their enzyme complexes (left). Heatmap showing fold change in metabolite levels (\log_2) of the indicated cell lines relative to the average of those in *SLC25A39* knockout cells complemented with *SLC25A39* cDNA (middle). Metabolites were extracted 5 days after transduction with indicated sgRNAs. Values were normalized to the protein concentration of each cell line (left). Relative ratios of pyruvate to citrate metabolite levels of each indicated cell line from the metabolomics analysis in Fig. 4e (middle). Ratios were normalized to the average of the *SLC25A39* knockout cells expressing *SLC25A39* cDNA. Immunoblot with antibody against lipoic acid in the indicated Jurkat *SLC25A39* knockout cells expressing a vector control or *SLC25A39* cDNA transduced with the indicated sgRNA. Arrows indicate E2 complexes of PDH and OGDH containing lipoic acid (right). **f**, Representative bright-field micrographs of Jurkat *SLC25A39* knockout cells transduced with the indicated sgRNA at the end of the cell proliferation assay. Scale bar, 50 μ m. **g**, Relative cell number of the indicated Jurkat *SLC25A39* knockout cells expressing a vector control or *SLC25A39* cDNA transduced with the indicated sgRNA. Cells were cultured for 4 days with or without hemin (1 μ M) and pyruvate (1 mM). Cell numbers were normalized to the average of the *SLC25A39* knockout cells in each treatment condition. **e, g**, Bars represent mean \pm s.d.; **e, g**, $n = 3$ biologically independent samples. Statistical significance in **e** was determined by one-way ANOVA followed by Bonferroni post-hoc analysis; **g** was determined by two-way ANOVA followed by Bonferroni post-hoc analysis.

[Source data](#)

[**Extended Data Fig. 8 Expression of DIC/OGC does not complement the decrease of mitochondrial GSH availability in *SLC25A39* knockout cells.**](#)

a, Uptake of [$^{13}\text{C}_2, ^{15}\text{N}$]-GSH into mitochondria isolated from HEK-293T *SLC25A39* knockout cells expressing a vector control, *SLC25A39* cDNA, *SLC25A10* (DIC, mitochondrial dicarboxylate carrier) or *SLC25A11* (OGC, mitochondrial oxoglutarate carrier) cDNA at 5 s and 10 min. Bars represent mean \pm s.d.; $n = 3$ biologically independent samples. Statistical significance was determined by two-way ANOVA followed by Bonferroni post-hoc analysis. **b**, PrediXcan-based TWAS design in UK biobank and summary graph of *SLC25A39*-associated phenotypes. Bonferroni-adjusted p -values are reported.

[Source data](#)

Supplementary information

[Supplementary Figure](#)

This file contains Supplementary Fig. 1, the unprocessed Western blots and/or gels associated with the data presented in the figures and extended data figures.

[Reporting Summary](#)

[Supplementary Table 1](#)

Global analysis of mitochondrial proteome of HeLa cells in response to cellular GSH depletion. Statistical significance was determined by two-tailed unpaired t -test.

[Supplementary Table 2](#)

Metabolism focused CRISPR genetic screens in *SLC25A39*-knockout Jurkat and HEK 293T cells.

[Supplementary Table 3](#)

Whole-cell proteomic analysis of Jurkat cells in response to mitochondrial GSH depletion.

Supplementary Table 4 SLC25A39 variants and their effect sizes on genetically determined expression.

Peer Review File

Source data

Source Data Fig. 1

Source Data Fig. 2

Source Data Fig. 3

Source Data Fig. 4

Source Data Extended Data Fig. 1

Source Data Extended Data Fig. 2

Source Data Extended Data Fig. 3

Source Data Extended Data Fig. 4

Source Data Extended Data Fig. 5

Source Data Extended Data Fig. 6

Source Data Extended Data Fig. 7

Source Data Extended Data Fig. 8

Rights and permissions

[Reprints and Permissions](#)

About this article

Cite this article

Wang, Y., Yen, F.S., Zhu, X.G. *et al.* SLC25A39 is necessary for mitochondrial glutathione import in mammalian cells. *Nature* **599**, 136–140 (2021). <https://doi.org/10.1038/s41586-021-04025-w>

- Received: 26 March 2021
- Accepted: 09 September 2021
- Published: 27 October 2021
- Issue Date: 04 November 2021
- DOI: <https://doi.org/10.1038/s41586-021-04025-w>

Share this article

Anyone you share the following link with will be able to read this content:

[Get shareable link](#)

Sorry, a shareable link is not currently available for this article.

[Copy to clipboard](#)

Provided by the Springer Nature SharedIt content-sharing initiative

| [Section menu](#) | [Main menu](#) |

- Article
- [Published: 06 October 2021](#)

Whole-cell organelle segmentation in volume electron microscopy

- [Larissa Heinrich](#) [ORCID: orcid.org/0000-0003-2852-6664](#)¹,
- [Davis Bennett](#) [ORCID: orcid.org/0000-0001-7579-2848](#)¹,
- [David Ackerman](#)¹,
- [Woohyun Park](#)¹,
- [John Bogovic](#)¹,
- [Nils Eckstein](#) [ORCID: orcid.org/0000-0003-2226-8174](#)^{1,2},
- [Alyson Petruncio](#)¹,
- [Jody Clements](#)¹,
- [Song Pang](#) [ORCID: orcid.org/0000-0002-7231-4151](#)¹,
- [C. Shan Xu](#) [ORCID: orcid.org/0000-0002-8564-7836](#)¹,
- [Jan Funke](#) [ORCID: orcid.org/0000-0003-4388-7783](#)¹,
- [Wyatt Korff](#) [ORCID: orcid.org/0000-0001-8396-1533](#)¹,
- [Harald F. Hess](#) [ORCID: orcid.org/0000-0003-3000-1533](#)¹,
- [Jennifer Lippincott-Schwartz](#)¹,
- [Stephan Saalfeld](#) [ORCID: orcid.org/0000-0002-4106-1761](#)¹,
- [Aubrey V. Weigel](#) [ORCID: orcid.org/0000-0003-1694-4420](#)¹ &
- [COSEM Project Team](#)

[Nature](#) volume 599, pages 141–146 (2021)

- 12k Accesses
- 1 Citations
- 396 Altmetric

- [Metrics details](#)

Subjects

- [Cellular imaging](#)
- [Data mining](#)
- [Image processing](#)
- [Machine learning](#)
- [Organelles](#)

Abstract

Cells contain hundreds of organelles and macromolecular assemblies. Obtaining a complete understanding of their intricate organization requires the nanometre-level, three-dimensional reconstruction of whole cells, which is only feasible with robust and scalable automatic methods. Here, to support the development of such methods, we annotated up to 35 different cellular organelle classes—ranging from endoplasmic reticulum to microtubules to ribosomes—in diverse sample volumes from multiple cell types imaged at a near-isotropic resolution of 4 nm per voxel with focused ion beam scanning electron microscopy (FIB-SEM)¹. We trained deep learning architectures to segment these structures in 4 nm and 8 nm per voxel FIB-SEM volumes, validated their performance and showed that automatic reconstructions can be used to directly quantify previously inaccessible metrics including spatial interactions between cellular components. We also show that such reconstructions can be used to automatically register light and electron microscopy images for correlative studies. We have created an open data and open-source web repository, ‘OpenOrganelle’, to share the data, computer code and trained models, which will enable scientists everywhere to query and further improve automatic reconstruction of these datasets.

Access options

Subscribe to Journal

Get full journal access for 1 year

\$199.00

only \$3.90 per issue

[Subscribe](#)

All prices are NET prices.

VAT will be added later in the checkout.

Tax calculation will be finalised during checkout.

Rent or Buy article

Get time limited or full article access on ReadCube.

from \$8.99

[Rent or Buy](#)

All prices are NET prices.

Additional access options:

- [Log in](#)
- [Access through your institution](#)
- [Learn about institutional subscriptions](#)

Fig. 1: Training data and machine learning.

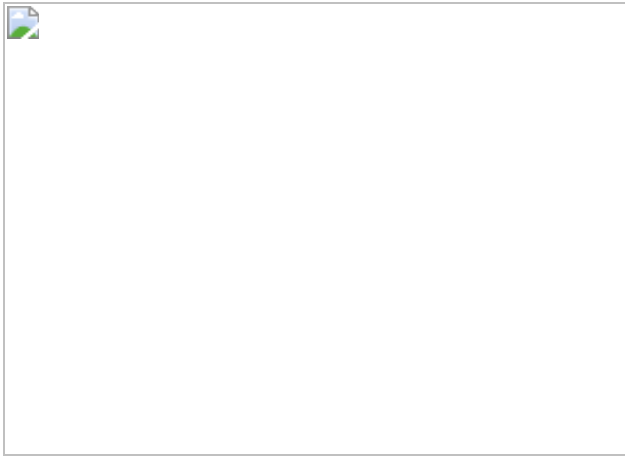


Fig. 2: Network evaluations and refined predictions.

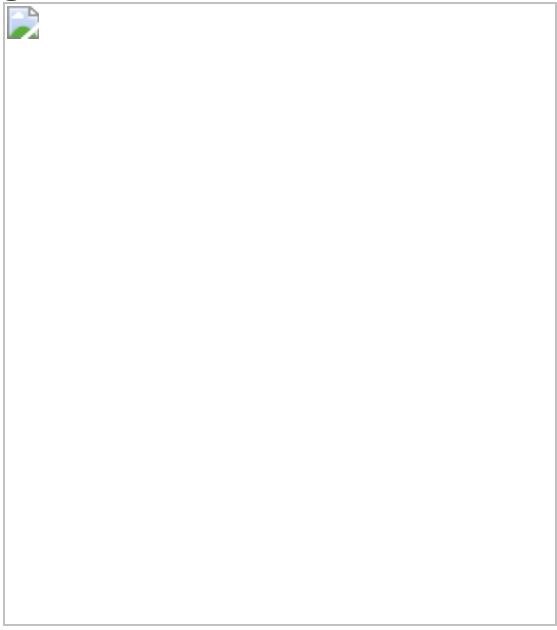


Fig. 3: Analysis and biological insight.

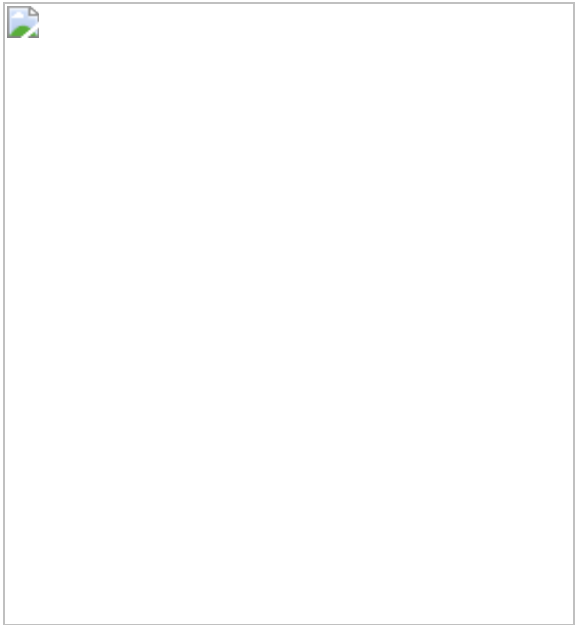


Fig. 4: Scaling predictions and CLEM auto-registration.



Data availability

All data generated and analysed during this study can be found and explored through <https://openorganelle.janelia.org/>. For queries and feedback on the project, please email cosemdata@janelia.hhmi.org. [Source data](#) are provided with this paper.

Code availability

All software and source code generated during this study can be found at <https://github.com/janelia-cosem/heinrich-2021a/tree/dff2e07>.

References

1. 1.

Xu, C. S. et al. An open-access volume electron microscopy atlas of whole cells and tissues. *Nature* <https://doi.org/10.1038/s41586-021-03992-4> (2021).

2. 2.

Valm, A. M. et al. Applying systems-level spectral imaging and analysis to reveal the organelle interactome. *Nature* **546**, 162–167 (2017).

3. 3.

Turaga, S. C. et al. Convolutional networks can learn to generate affinity graphs for image segmentation. *Neural Comput.* **22**, 511–538 (2010).

4. 4.

Ciresan, D., Giusti, A., Gambardella, L. M. & Schmidhuber, J. Deep neural networks segment neuronal membranes in electron microscopy images. In *Proc. 25th International Conference on Neural Information Processing Systems* (eds Pereira, F., Burges, C. J. C., Bottou, L. & Weinberger, K. Q.) 2843–2851 (Curran Associates, 2012).

5. 5.

Januszewski, M. et al. High-precision automated reconstruction of neurons with flood-filling networks. *Nat. Methods* **15**, 605–610 (2018).

6. 6.

Funke, J. et al. Large scale image segmentation with structured loss based deep learning for connectome reconstruction. *IEEE Trans. Pattern Anal. Mach. Intell.* **41**, 1669–1680 (2019).

7. 7.

Kreshuk, A. et al. Automated detection and segmentation of synaptic contacts in nearly isotropic serial electron microscopy images. *PLoS ONE* **6**, e24899 (2011).

8. 8.

Becker, C., Ali, K., Knott, G. & Fua, P. Learning context cues for synapse segmentation in EM volumes. In *Medical Image Computing and Computer-Assisted Intervention—MICCAI 2012* (eds Ayache, N., Delingette, H., Golland, P. & Mori, K.) 585–592 (Springer, 2012).

9. 9.

Dorkenwald, S. et al. Automated synaptic connectivity inference for volume electron microscopy. *Nat. Methods* **14**, 435–442 (2017).

10. 10.

Heinrich, L., Funke, J., Pape, C., Nunez-Iglesias, J. & Saalfeld, S. Synaptic cleft segmentation in non-isotropic volume electron microscopy of the complete *Drosophila* brain. In *Medical Image Computing and Computer Assisted Intervention—MICCAI 2018* (eds Frangi, A. et al.) 317–325 (Springer, 2018).

11. 11.

Buhmann, J. et al. Automatic detection of synaptic partners in a whole-brain *Drosophila* EM dataset. *Nat. Methods* **18**, 771–774 (2021)

12. 12.

Lucchi, A., Li, Y., Smith, K. & Fua, P. Structured image segmentation using kernelized features. In *Computer Vision—ECCV 2012* (eds

Fitzgibbon, A. et al.) 400–413 (Springer, 2012).

13. 13.

Kasthuri, N. et al. Saturated reconstruction of a volume of neocortex. *Cell* **162**, 648–661 (2015).

14. 14.

Lucchi, A. et al. Learning structured models for segmentation of 2-D and 3-D imagery. *IEEE Trans. Med. Imaging* **34**, 1096–1110 (2015).

15. 15.

Márquez Neila, P. et al. A fast method for the segmentation of synaptic junctions and mitochondria in serial electron microscopic images of the brain. *Neuroinformatics* **14**, 235–250 (2016).

16. 16.

Oztel, I., Yolcu, G., Ersoy, I., White, T. & Bunyak, F. Mitochondria segmentation in electron microscopy volumes using deep convolutional neural network. In *2017 IEEE International Conference on Bioinformatics and Biomedicine (BIBM)* 1195–1200 (IEEE, 2017).

17. 17.

Cetina, K., Buenaposada, J. M. & Baumela, L. Multi-class segmentation of neuronal structures in electron microscopy images. *BMC Bioinformatics* **19**, 298 (2018).

18. 18.

Casser, V., Kang, K., Pfister, H. & Haehn, D. Fast mitochondria detection for connectomics. In *Proceedings of Machine Learning Research (PMRL)*. (Eds Arbel, T. et al.) **121**, 111–120 (2020).

19. 19.

Wei, D. et al. MitoEM dataset: large-scale 3D mitochondria instance segmentation from EM images. In *Medical Image Computing and Computer Assisted Intervention—MICCAI 2020* (eds Martel, A. L. et al.) 66–76 (Springer, 2020).

20. 20.

Perez, A. J. et al. A workflow for the automatic segmentation of organelles in electron microscopy image stacks. *Front. Neuroanat.* **8**, 126 (2014).

21. 21.

Tek, F. B., Boray Tek, F., Kroeger, T., Mikula, S. & Hamprecht, F. A. Automated cell nucleus detection for large-volume electron microscopy of neural tissue. In *2014 IEEE 11th International Symposium on Biomedical Imaging (ISBI)* 69–72 (IEEE, 2014).

22. 22.

Narasimha, R., Ouyang, H., Gray, A., McLaughlin, S. W. & Subramaniam, S. Automatic joint classification and segmentation of whole cell 3D images. *Pattern Recognit.* **42**, 1067–1079 (2009).

23. 23.

Rigamonti, R., Lepetit, V. & Fua, P. *Beyond KernelBoost*.
https://infoscience.epfl.ch/record/200378/files/rigamonti_tr14a_1.pdf (2014).

24. 24.

Karabağ, C. et al. Segmentation and modelling of the nuclear envelope of HeLa cells imaged with serial block face scanning electron microscopy. *J. Imaging* **5**, 75 (2019).

25. 25.

Spiers, H. et al. Deep learning for automatic segmentation of the nuclear envelope in electron microscopy data, trained with volunteer segmentations. *Traffic* **22**, 240–253 (2021).

26. 26.

Žerovnik Mekuč, M. et al. Automatic segmentation of mitochondria and endolysosomes in volumetric electron microscopy data. *Comput. Biol. Med.* **119**, 103693 (2020).

27. 27.

Liu, J. et al. Automatic reconstruction of mitochondria and endoplasmic reticulum in electron microscopy volumes by deep learning. *Front. Neurosci.* **14**, 599 (2020).

28. 28.

Eckstein, N., Buhmann, J., Cook, M. & Funke, J. Microtubule tracking in electron microscopy volumes. In *Medical Image Computing and Computer Assisted Intervention—MICCAI 2020* (eds Martel, A. L. et al.) 99–108 (Springer, 2020).

29. 29.

Ronneberger, O., Fischer, P. & Brox, T. U-Net: convolutional networks for biomedical image segmentation. In *Medical Image Computing and Computer-Assisted Intervention—MICCAI 2015* (eds Navab, N., Hornegger, J., Wells, W. & Frangi, A.) 234–241 (Springer, 2015).

30. 30.

Çiçek, Ö., Abdulkadir, A., Lienkamp, S. S., Brox, T. & Ronneberger, O. 3D U-Net: learning dense volumetric segmentation from sparse annotation. In *Medical Image Computing and Computer-Assisted Intervention—MICCAI 2016* (eds Ourselin, S. et al.) 424–432 (Springer, 2016).

31. 31.

Funke, J., Wu, J., Barnes, C. Waterz—simple watershed and agglomeration library for affinity graphs. *GitHub* <https://github.com/funkey/waterz/tree/7c530ac> (2020).

32. 32.

Zlateski, A. & Seung, H. S. Image segmentation by size-dependent single linkage clustering of a watershed basin graph. Preprint at <https://arxiv.org/abs/1505.00249> (2015).

33. 33.

Barlan, K. & Gelfand, V. I. Microtubule-based transport and the distribution, tethering, and organization of organelles. *Cold Spring Harb. Perspect. Biol.* **9**, a025817 (2017).

34. 34.

Goyal, U. & Blackstone, C. Untangling the web: mechanisms underlying ER network formation. *Biochim. Biophys. Acta Mol. Cell Res.* **1833**, 2492–2498 (2013).

35. 35.

Blackstone, C. Cellular pathways of hereditary spastic paraplegia. *Annu. Rev. Neurosci.* **35**, 25–47 (2012).

36. 36.

Descoteaux, M., Audette, M., Chinzei, K. & Siddiqi, K. Bone enhancement filtering: application to sinus bone segmentation and simulation of pituitary surgery. *Comput. Aided Surg.* **11**, 247–255 (2006).

37. 37.

Nixon-Abell, J. et al. Increased spatiotemporal resolution reveals highly dynamic dense tubular matrices in the peripheral ER. *Science* **354**, aaf3928 (2016).

38. 38.

Terasaki, M. et al. Stacked endoplasmic reticulum sheets are connected by helicoidal membrane motifs. *Cell* **154**, 285–296 (2013).

39. 39.

Coulter, M. E. et al. The ESCRT-III protein CHMP1A mediates secretion of sonic hedgehog on a distinctive subtype of extracellular vesicles. *Cell Rep.* **24**, 973–986 (2018).

40. 40.

Hoffman, D. P. et al. Correlative three-dimensional super-resolution and block-face electron microscopy of whole vitreously frozen cells. *Science* **367**, eaaz5357 (2020).

41. 41.

Xu, C. S. et al. Enhanced FIB-SEM systems for large-volume 3D imaging. *Elife* **6**, e25916 (2017).

42. 42.

Saalfeld, S., Cardona, A., Hartenstein, V. & Tomančák, P. As-rigid-as-possible mosaicking and serial section registration of large ssTEM datasets. *Bioinformatics* **26**, i57–i63 (2010).

43. 43.

Saalfeld, S., Pisarev, I. Hanslovsky, P., Bogovic, J.A., Champion, A., Rueden, C., Kirkham, J.A. N5—a scalable Java API for hierarchies of chunked n-dimensional tensors and structured meta-data. *GitHub* <https://github.com/saalfeldlab/n5/tree/n5-2.5.1> (2021)

44. 44.

Pavelka, M. & Roth, J. *Functional Ultrastructure: Atlas of Tissue Biology and Pathology* (Springer, 2015).

45. 45.

Saalfeld, S., Funke, J., Pietzsch T., Nunez-Iglesias, J., Hanslovsky, P., Bogovic, J., Wolny, A., Melnikov, E. BigCAT. *GitHub* <https://github.com/saalfeldlab/bigcat/tree/0.0.3-beta-1> (2018).

46. 46.

Kingma, D. P. & Ba, J. Adam: a method for stochastic optimization. Preprint at <https://arxiv.org/abs/1412.6980> (2014).

47. 47.

Rueden, C., Schindelin, J., Hiner, M., Arganda-Carreras, I., Skeletonize3D. GitHub https://github.com/fiji/Skeletonize3D/tree/Skeletonize3D_2.1.1 (2017).

48. 48.

Lee, T. C., Kashyap, R. L. & Chu, C. N. Building skeleton models via 3-D medial surface axis thinning algorithms. *CVGIP Graph. Models Image Process.* **56**, 462–478 (1994).

49. 49.

Klein, S., Staring, M., Murphy, K., Viergever, M. A. & Pluim, J. P. W. elastix: a toolbox for intensity-based medical image registration. *IEEE Trans. Med. Imaging* **29**, 196–205 (2010).

50. 50.

Maitin-Shepard, J. et al. Neuroglancer. *GitHub* <https://github.com/google/neuroglancer/tree/v2.22> (2021).

51. 51.

Abramov, D. et al. React. *GitHub* <https://github.com/facebook/react/tree/v17.0.2> (2021).

52. 52.

Perlman, E. Visualizing and interacting with large imaging data. *Microsc. Microanal.* **25**, 1374–1375 (2019).

53. 53.

Hubbard, P. M. et al. Accelerated EM connectome reconstruction using 3D visualization and segmentation graphs. Preprint at <https://doi.org/10.1101/2020.01.17.909572> (2020).

54. 54.

Schindelin, J. et al. Fiji: an open-source platform for biological-image analysis. *Nat. Methods* **9**, 676–682 (2012).

55. 55.

Pietzsch, T., Saalfeld, S., Preibisch, S. & Tomancak, P. BigDataViewer: visualization and processing for large image data sets. *Nat. Methods* **12**, 481–483 (2015).

56. 56.

Bogovic, J.A., Saalfeld, S., Hulbert, C., Pisarev, I., Rueden, C., Moon, H.K., Preibisch, S. N5-IJ. *GitHub* <https://github.com/saalfeldlab/n5-ij/tree/n5-ij-3.0.0> (2021).

57. 57.

Amazon Web Services. What is the AWS Command Line Interface? <https://docs.aws.amazon.com/cli/latest/userguide/cli-chap-welcome.html> (2021).

Acknowledgements

This work is part of the COSEM Project Team at Janelia Research Campus, Howard Hughes Medical Institute. The COSEM Project Team consisted of:

R. Ali, R. Arruda, R. Bahtra, D. Bennett, D. Nguyen, W. Park and A. Petruncio, led by A. Weigel with Steering Committee of J. Funke, H. Hess, W. Korff, J. Lippincott-Schwartz and S. Saalfeld. We thank R. Ali, R. Arruda and D. Nguyen for their work generating training data; R. Bahtra for his work generating masks of datasets and providing manual annotations; A. Aziz for his work correcting mitochondria overmerging; G. Ihrke and Project Technical Resources for management and coordination and staff support; the Janelia Scientific Computing Shared Resource, especially T. Dolafi and S. Berg, for their help generating the database and visualization tools; C. Pape and J. Nunez-Iglesias for their work on the inference pipeline; V. Custard for administrative support; S. van Engelenburg, H. Hoffman, E. Betzig, D. Hoffman, C. Walsh and M. Coulter for providing their data; Amazon Web Services for free hosting of our data through their open data program; G. Shtengel for providing FIB-SEM data attributes and for his early work manually segmenting organelles and aligning CLEM datasets, which motivated the need for more automated approaches; and G. Meissner for critical reading of the manuscript. This work was supported by Howard Hughes Medical Institute, Janelia Research Campus.

Author information

Affiliations

1. Janelia Research Campus, Howard Hughes Medical Institute, Ashburn, VA, USA

Larissa Heinrich, Davis Bennett, David Ackerman, Woohyun Park, John Bogovic, Nils Eckstein, Alyson Petruncio, Jody Clements, Song Pang, C. Shan Xu, Jan Funke, Wyatt Korff, Harald F. Hess, Jennifer Lippincott-Schwartz, Stephan Saalfeld, Aubrey V. Weigel, Riasat Ali, Rebecca Arruda, Rohit Bahtra & Destiny Nguyen

2. Institute of Neuroinformatics UZH/ETHZ, Zurich, Switzerland

Nils Eckstein

Consortia

COSEM Project Team

- Riasat Ali
- , Rebecca Arruda
- , Rohit Bahtra
- , Davis Bennett
- , Destiny Nguyen
- , Woohyun Park
- , Alyson Petruncio
- , Jan Funke
- , Harald F. Hess
- , Wyatt Korff
- , Jennifer Lippincott-Schwartz
- , Stephan Saalfeld
- & Aubrey V. Weigel

Contributions

The COSEM Project Team, S.S., A.V.W., W.K., J.L.-S., H.F.H. and J.F. conceptualized and supervised the project. C.S.X. and H.F.H. provided the FIB-SEM data and preprocessing. D.B., S.P. and C.S.X. organized FIB-SEM data and data attributes. W.P., A.P. and A.V.W. provided manual annotations, evaluations and proofreading. D.B. built the data management infrastructure. L.H. and S.S. developed machine learning algorithms. L.H. performed network training and automatic evaluations. N.E. and J.F. developed MT modelling algorithms. N.E. performed MT modelling. D.A. and S.S. developed refinement and analysis algorithms. D.A. analysed data. J.B. and S.S. developed automated CLEM registration algorithms. J.B. performed automated CLEM registration. D.B., J.C. and A.V.W. developed, D.B. and J.C. implemented and A.V.W., D.B. and S.P. proofread and contributed data to the data portal, OpenOrganelle. L.H., A.V.W., S.S., D.B., D.A., J.B., N.E. and A.P. wrote the manuscript with input from all co-authors. J.L.-S. provided critical review, commentary and revision in the writing process of the manuscript.

Corresponding authors

Correspondence to Stephan Saalfeld or Aubrey V. Weigel.

Ethics declarations

Competing interests

The authors declare no competing interests.

Additional information

Peer review information *Nature* thanks Robert Murphy, Jason Swedlow and the other, anonymous, reviewer(s) for their contribution to the peer review of this work. Peer reviewer reports are available.

Publisher's note Springer Nature remains neutral with regard to jurisdictional claims in published maps and institutional affiliations.

Extended data figures and tables

Extended Data Fig. 1 Organelle classification.

Examples of each class used for training input from multiple datasets. Organelles were manually identified using morphological features established in the literature. A description of each class can be found in the [Supplementary Methods](#). Scale bars are 100 nm.

Extended Data Fig. 2 Class frequencies and holdout block.

a, 37 different classes are used to classify all intracellular structures. These classes are combined into 35, potentially overlapping semantic categories (see [Supplementary Methods](#), Extended Data Fig. 1). Classes in bold depict these super classes. As an example, the ER object class is expanded in the subpanel. In green are classes that are predicted jointly by type ‘many’ networks. Denoted with a dot are the super classes, with a few additional classes, used in the type ‘few’ networks. The type ‘all’ networks train

jointly on all 35 classes. **b**, Annotated volume according to datasets. Reported are the percentage of the total cell that is annotated. **c, d**, 3D rendering of thresholded predictions (**c**) and ground truth (**d**) in a $4 \mu\text{m} \times 4 \mu\text{m} \times 4 \mu\text{m}$ holdout block in jrc_hela-3. Shown are the nucleus (magenta), plasma membrane (grey), ER and NE (green), mitochondria (orange), vesicles (red), lysosomes (yellow), endosomes (blue), and microtubules (white).

[Source data](#)

Extended Data Fig. 3 Network evaluations and refined predictions.

a, Validation and test performance measured by F_1 score for thresholded predictions on holdout blocks from four datasets. Manual validation refers to F_1 score of inferences with settings optimized manually on the whole dataset. Labels sorted by average test score. **b**, Comparison of networks using different multi-class strategies. Each data point represents the F_1 score (test performance) on a holdout block with the colour denoting the multi-class strategy ('all'/'many'/'few'). **c**, 3D rendering of refined predictions for each dataset. Classes shown are plasma membrane (grey), ER (green), mitochondria (orange), nucleus (purple), endosomal system (blue), and vesicles (red).

[Source data](#)

Extended Data Fig. 4 Evaluation metrics and comparison of manual and automatic hyperparameter tuning.

a, F_1 scores on holdout blocks from four datasets comparing manual and automatic hyperparameter tuning. Data includes all results we collected using the manual comparison of thresholded predictions on whole cells, i.e., comparisons across iterations only as well as comparisons across the best iterations of different network types. For automatic validation scores equivalent queries were made against the database. **b**, F_1 scores on holdout regions from four datasets comparing F_1 score and Mean False Distance as

the metric used for hyperparameter tuning. Data points are equivalent to those from **a**.

[Source data](#)

Extended Data Fig. 5 Effect of prediction refinements on evaluation metrics.

a–c, F₁ score (**a**), precision (**b**) and recall (**c**) on holdout blocks from four datasets before (raw) and after (refined) refinements described in the [Supplementary Methods](#). Network type and iterations represented here are listed in Supplementary Table 1 and are optimized manually with a bias towards potential improvement through the refinement process.

[Source data](#)

Extended Data Fig. 6 Mitochondria overmerging corrections.

a, Whole cell, 3D rendering of mitochondria in jrc_hela-2 segmented using naive connected component analysis method. Scale bar is 4 μm. **b**, FIB-SEM and raw mitochondria predictions thresholded at 127 ($d = 0$ nm) for the boxed region in **(a)**, shown for one 2D slice. **c**, Naive connected component segmentation of mitochondria for the region in **(a)**, performed on smoothed, thresholded predictions at 127 and followed by size filtering and hole-filling. **d**, To alleviate overmerging of mitochondria, we smooth the predictions and perform watershed segmentation on all voxels greater than or equal to 127. Shown are the resultant watershed fragments. **e**, To create the improved mitochondria segmentations, we agglomerate adjacent fragments in **d** based on parameters that best optimize the resultant segmentations, as chosen by an expert user. **f**, Final whole-cell rendering of corrected mitochondria predictions. Scale bar is 4 μm.

Extended Data Fig. 7 Microtubule refinement.

a, 3D renderings of the ground truth (red) and reconstructed microtubules (cyan) in a selected 2 μm cube test block on jrc_hela-2. Note the close correlation between ground-truth-based versus automatically reconstructed

microtubules. **b**, Comparison of the accuracy of MT reconstruction after refinement for four different cells, measured over two densely traced 2 μm cubes for each dataset. Accuracy is measured on individual edges, where an edge is correct if the edge connects two reconstruction vertices that are matched to the same ground truth microtubule track. **c, d**, Comparison of the baseline microtubule refinement and the method described in Eckstein et al.²⁸. Shown is the accuracy in terms of topological errors on full tracks (**c**) and precision and recall on individual edges (**d**). Each column shows the accuracy of both methods, acquired via 6-fold cross validation over 4 ground truth annotation blocks, where we used two blocks for validation and the remaining two for testing for each run. Numbers above each column in (**c**) are the median value of the 6 cross-validation runs. **e–g**, 2D FIB-SEM slice with ground truth and reconstructed microtubules in the plane, 3D renderings of the ground truth (red) and reconstructed microtubules (cyan) in selected 2 μm cube test blocks on jrc_hela-3 (**e**), jrc_jurkat-1 (**f**) and jrc_makrophage-3 (**g**). Plots show the topological errors normalized by ground-truth microtubule cable length for each cell respectively. See Supplementary Table 4 for a complete listing of evaluation results. Standard box plots are used showing the minima and maxima (whiskers), outliers (points), the first and third quartile (box), and median (line). For each dataset $n = 4$ samples over 6 experiments in 1 cell.

Source data

Extended Data Fig. 8 Measurements in holdout regions.

a, b, Surface area (**a**) and volume (**b**) deviations from the ground truth for sample organelles in the holdout regions. Analysis was performed on both raw predictions thresholded at 127 (dark shade), and refined predictions (light shade). To get some sense of reliability, we divide each holdout region in half in 3 dimensions resulting in 6 regions. The measurements within these 6 regions are shown (circles), as well as the measurements for the entire holdout region (bar).

Source data

Extended Data Fig. 9 Analysis and biological insight.

a, Relative volume occupied by each predicted organelle, per cell. MT volume only shown for jrc_hela-2. **b**, ER predictions in jrc_macrophage-2. Left panel is a 2D FIB-SEM slice with overlaid ER predictions in green, the middle panel shows a 3D rendering of the ER predictions, and the right panel shows the ER medial surface partitioned into planar and tubular structures and corresponding tubule thicknesses (colour bar). Scale bar is 500 nm. **c**, ER predictions in jrc_hela-2. Left panel is a 2D FIB-SEM slice with overlaid ER predictions in green and mitochondria predictions in orange (bottom), the middle panel shows a 3D rendering of the ER predictions and mitochondria predictions (bottom), and the right panel shows the ER medial surface partitioned into planes and tubes along with tubule thicknesses (colour bar). Also shown in the bottom right panel are the contact site regions (blue) where ER and mitochondria are within 10 nm of each other. Scale bars are 500 nm. **d**, Quantification of the peripheral ER curvature and surface area compared between jrc_hela-2 and jrc_macrophage-2. **e**, Quantification of the peripheral ER curvature at contact sites between peripheral ER and mitochondria, for jrc_hela-2 and jrc_macrophage-2.

[Source data](#)

[Extended Data Fig. 10 Organelle contact sites, planarity and skeletons.](#)

a, ER (reconstructed, green) and mitochondria (orange) dense regions of jrc_hela-2 chosen for comparison, with 2D FIB-SEM slice also displayed. **b**, 2D FIB-SEM slice shown in **a** displays ER predictions (green), mitochondria predictions (orange), naive contact sites (magenta) and refined contact sites (blue), which are subsets of the naive contact sites. Scale bar is 1 μ m. **c**, 3D rendering of mitochondria (orange) and simple contact sites (magenta). **d**, 3D rendering of mitochondria (orange) and refined contact sites (blue). **e**, 3D rendering of refined ER segmentation in an example region of jrc_hela-2. Scale bar is 200 nm. **f**, Medial surface (black) produced from iterative topological thinning of the ER segmentation (grey). Scale bar is 200 nm. **g**, A planar metric (colour) is calculated for each voxel in the medial surface based on the ER's Hessian matrix eigenvalues at that voxel; higher values correspond to more planar regions.

Scale bar is 200 nm. **h**, The planarity metric medial surface in (**c**) is used to reconstruct a curvature-labelled ER which is thresholded at 0.6, above which voxels are considered planes (blue) and below which voxels are considered non-planar (red). Scale bar is 200 nm. **i**, Topological thinning is used to produce skeletons. Shown is a 3D rendering of an example mitochondria (grey), skeleton (red), pruned skeleton (blue), and longest shortest path (green) from jrc_hela-2. Scale bar is 1 μm . **j**, Unpruned skeleton used as a starting point. Scale bar is 1 μm . **k**, Repetitive pruning produced a final skeleton such that no remaining branch was shorter than 80 nm. Scale bar is 1 μm . **l**, Mitochondrial length and average radius were calculated using the longest shortest path within the pruned skeleton. Scale bar is 1 μm . See [Supplementary Methods](#) for in depth description.

[Extended Data Fig. 11 Scaling predictions and CLEM auto-registration.](#)

a, Comparison of networks trained with 4 nm and simulated 8 nm raw data of all samples. Each data point represents the F_1 score (test performance) on one of the four holdout blocks, similar to Fig. [2b](#). **b**, Qualitative comparison of automated and manual registration for the region marked with the dashed box in **c**. PALM images show ER (magenta) and mitochondria (green). Landmarks were placed at corresponding points in the ER light channel and ER predictions of the electron microscopy image that were not used for automatic registration. This unbiased measurement enables us to measure errors in an unbiased way, with respect to the true underlying transformation, not only the "part" of the transformation that can be inferred from the mitochondria membrane channel. White glyphs show human-human error (vertical) and human-automatic error (horizontal). Scale bar is 2 μm . **c**, A single slice of the Jacobian determinant map for the transformation registering electron microscopy to PALM for jrc_cos7-11. Red (blue) indicates local increase (decrease) in volume. Dotted area shows the approximate location of cells. Scale bar is 10 μm . **d**, Histogram of Jacobian determinant over the whole volume. **e**, Error map showing differences for automatic registrations using PALM or SIM as the target image. Dotted area shows the approximate location of cells. Scale bar is 10 μm . **f**, Histogram of PALM versus SIM errors over the area where a cell is

present (white dotted line in e). All statistics from a single cell in a single dataset as specified.

[Source data](#)

Supplementary information

[41586_2021_3977_MOESM1_ESM.pdf](#)

Supplementary Information This file contains Supplementary Note, Supplementary Methods, Supplementary Discussion and Supplementary References.

[Reporting Summary](#)

[Peer Review File](#)

[Supplementary Tables](#)

This file contains Supplementary Tables 1–5.

[Supplementary Video 1](#)

FIB-SEM, training data, and predictions. Showcase of the processing pipeline, using jrc_hela-2 as an example. We begin with the electron microscopy data. Then skilled annotators classify every voxel within a volume; shown here are 15 of these training blocks. These segmentations are fed into machine learning algorithms as training data. The prediction outputs from these algorithms are refined. Once the predicted, whole-cell segmentations are achieved, quantitative analytics of subcellular distributions, interactions, sizes and morphologies can be acquired as shown in Supplementary Video 2.

[Supplementary Video 2](#)

Three analysis examples. Three analysis examples in jrc_hela-2. The first example is from Fig. 3a, a microtubule contacting multiple different organelles. The second example is from Extended Data Fig. 9b, displaying the relationship between ER morphology and mitochondria contact sites. The third example is from Fig. 3c, showing the distribution of ribosomes bound to the ER.

Supplementary Video 3

CLEM registration. FIB-SEM and correlative light microscopy automatically registered using whole-cell mitochondria membrane predictions. Displayed are PALM images of mitochondria membrane marker Halo/JF525-TOMM20 and ER luminal marker mEmerald-ER3, predictions for mitochondria membrane and ER, as well as the corresponding (8 nm × 8 nm × 8 nm) FIB-SEM. A ‘warping’ from affine-only to the full-deformable transformation is also shown.

Source data

[**Source Data Fig. 2**](#)

[**Source Data Fig. 3**](#)

[**Source Data Extended Data Fig. 2**](#)

[**Source Data Extended Data Fig. 3**](#)

[**Source Data Extended Data Fig. 4**](#)

[**Source Data Extended Data Fig. 5**](#)

[**Source Data Extended Data Fig. 7**](#)

[**Source Data Extended Data Fig. 8**](#)

[Source Data Extended Data Fig. 9](#)

[Source Data Extended Data Fig. 11](#)

Rights and permissions

[Reprints and Permissions](#)

About this article

Cite this article

Heinrich, L., Bennett, D., Ackerman, D. *et al.* Whole-cell organelle segmentation in volume electron microscopy. *Nature* **599**, 141–146 (2021). <https://doi.org/10.1038/s41586-021-03977-3>

- Received: 13 November 2020
- Accepted: 31 August 2021
- Published: 06 October 2021
- Issue Date: 04 November 2021
- DOI: <https://doi.org/10.1038/s41586-021-03977-3>

Share this article

Anyone you share the following link with will be able to read this content:

[Get shareable link](#)

Sorry, a shareable link is not currently available for this article.

[Copy to clipboard](#)

Provided by the Springer Nature SharedIt content-sharing initiative

Nanometre-scale imaging and AI reveal the interior of whole cells

- Jason R. Swedlow
- Lucy Collinson

News & Views 25 Oct 2021

This article was downloaded by **calibre** from <https://www.nature.com/articles/s41586-021-03977-3>

| [Section menu](#) | [Main menu](#) |

- Article
- [Published: 06 October 2021](#)

An open-access volume electron microscopy atlas of whole cells and tissues

- [C. Shan Xu](#) ORCID: [orcid.org/0000-0002-8564-7836¹](https://orcid.org/0000-0002-8564-7836),
- [Song Pang](#) ORCID: [orcid.org/0000-0002-7231-4151^{1 nA1}](https://orcid.org/0000-0002-7231-4151),
- [Gleb Shtengel](#) ORCID: [orcid.org/0000-0001-6830-640X^{1 nA1}](https://orcid.org/0000-0001-6830-640X),
- [Andreas Müller^{2,3,4}](#),
- [Alex T. Ritter⁵](#),
- [Huxley K. Hoffman^{6 nAff12}](#),
- [Shin-ya Takemura](#) ORCID: [orcid.org/0000-0003-2400-6426¹](https://orcid.org/0000-0003-2400-6426),
- [Zhiyuan Lu¹](#),
- [H. Amalia Pasolli](#) ORCID: [orcid.org/0000-0003-3899-3530^{1 nAff13}](https://orcid.org/0000-0003-3899-3530),
- [Nirmala Iyer¹](#),
- [Jeeyun Chung^{7,8}](#),
- [Davis Bennett](#) ORCID: [orcid.org/0000-0001-7579-2848¹](https://orcid.org/0000-0001-7579-2848),
- [Aubrey V. Weigel](#) ORCID: [orcid.org/0000-0003-1694-4420¹](https://orcid.org/0000-0003-1694-4420),
- [Melanie Freeman^{1 nAff14}](#),
- [Schuyler B. van Engelenburg](#) ORCID: [orcid.org/0000-0003-2100-3617⁶](https://orcid.org/0000-0003-2100-3617),
- [Tobias C. Walther](#) ORCID: [orcid.org/0000-0003-1442-1327^{7,8,9,10}](https://orcid.org/0000-0003-1442-1327),
- [Robert V. Farese Jr.](#) ORCID: [orcid.org/0000-0001-8103-2239^{7,8}](https://orcid.org/0000-0001-8103-2239),
- [Jennifer Lippincott-Schwartz¹](#),
- [Ira Mellman⁵](#),
- [Michele Solimena](#) ORCID: [orcid.org/0000-0002-3653-8107^{2,3,4,11}](https://orcid.org/0000-0002-3653-8107) &
- [Harald F. Hess](#) ORCID: [orcid.org/0000-0003-3000-1533¹](https://orcid.org/0000-0003-3000-1533)

[Nature](#) volume **599**, pages 147–151 (2021)

- 6888 Accesses
- 1 Citations
- 106 Altmetric
- [Metrics details](#)

Subjects

- [Cell biology](#)
- [Electron microscopy](#)
- [Imaging](#)
- [Neuroscience](#)

A [Publisher Correction](#) to this article was published on 03 November 2021

This article has been [updated](#)

Abstract

Understanding cellular architecture is essential for understanding biology. Electron microscopy (EM) uniquely visualizes cellular structures with nanometre resolution. However, traditional methods, such as thin-section EM or EM tomography, have limitations in that they visualize only a single slice or a relatively small volume of the cell, respectively. Focused ion beam-scanning electron microscopy (FIB-SEM) has demonstrated the ability to image small volumes of cellular samples with 4-nm isotropic voxels¹. Owing to advances in the precision and stability of FIB milling, together with enhanced signal detection and faster SEM scanning, we have increased the volume that can be imaged with 4-nm voxels by two orders of magnitude. Here we present a volume EM atlas at such resolution

comprising ten three-dimensional datasets for whole cells and tissues, including cancer cells, immune cells, mouse pancreatic islets and *Drosophila* neural tissues. These open access data (via OpenOrganelle²) represent the foundation of a field of high-resolution whole-cell volume EM and subsequent analyses, and we invite researchers to explore this atlas and pose questions.

Access options

Subscribe to Journal

Get full journal access for 1 year

\$199.00

only \$3.90 per issue

[Subscribe](#)

All prices are NET prices.

VAT will be added later in the checkout.

Tax calculation will be finalised during checkout.

Rent or Buy article

Get time limited or full article access on ReadCube.

from \$8.99

[Rent or Buy](#)

All prices are NET prices.

Additional access options:

- [Log in](#)
- [Access through your institution](#)
- [Learn about institutional subscriptions](#)

Fig. 1: Enhanced FIB-SEM configuration, operation, and resolution.



Fig. 2: Interphase HeLa cell.

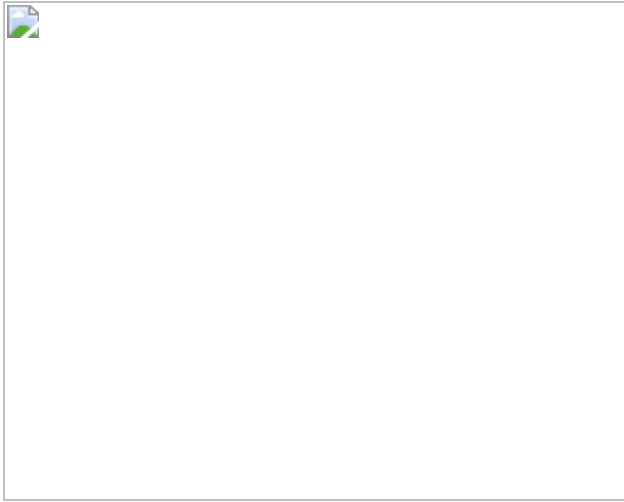


Fig. 3: Mouse CTL engaging an ovarian cancer cell.

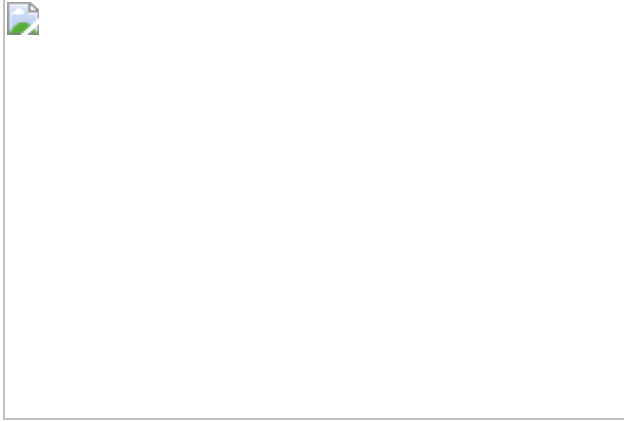
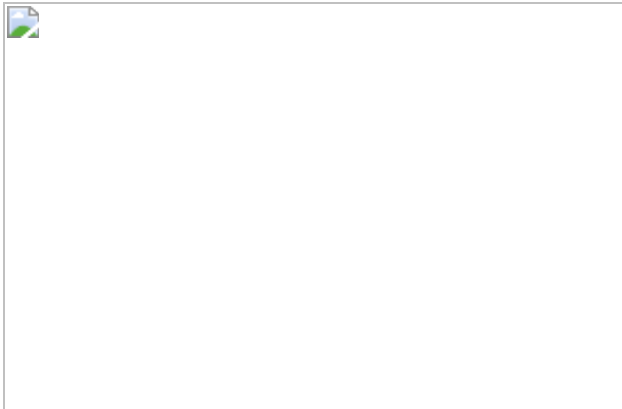


Fig. 4: Tissue sample datasets.



Data availability

All FIB-SEM datasets in this work have been deposited to OpenOrganelle repository (<https://openorganelle.janelia.org>) and made publicly available with DOIs: wild-type interphase HeLa cell 2017-06-21 (<https://doi.org/10.25378/janelia.13114211>), wild-type interphase HeLa cell 2017-08-09 (<https://doi.org/10.25378/janelia.13114244>), wild-type mitotic HeLa cell 2019-05-30 (<https://doi.org/10.25378/janelia.13114472>), wild-type THP-1 macrophage 2018-11-11 (<https://doi.org/10.25378/janelia.13114343>), wild-type immortalized T-cells (Jurkat) 2018-08-10 (<https://doi.org/10.25378/janelia.13114259>), wild-type immortalized breast cancer cell 2017-11-21 (<https://doi.org/10.25378/janelia.13114352>), killer T-cell attacking cancer cell 2020-02-04 (<https://doi.org/10.25378/janelia.13114454>), isolated murine pancreatic islets 2019-03-01 (<https://doi.org/10.25378/janelia.13114499>), *Drosophila* fan-shaped body from a 5-day-old male 2019-09-14 (<https://doi.org/10.25378/janelia.13114529>), *Drosophila* accessory calyx from a 5-day old male 2019-12-06 (<https://doi.org/10.25378/janelia.13114514>). Source data are provided with this paper.

Code availability

FIB-SEM image acquisition LabVIEW code used in this work is available from. https://github.com/cshanxu/Enhanced_FIB-SEM. Python code for

resolution characterizations using ribosomes is available from.
https://github.com/gleb-shtengel/FIB-SEM_resolution_evaluation.

Change history

- **03 November 2021**

A Correction to this paper has been published:
<https://doi.org/10.1038/s41586-021-04132-8>

References

1. 1.
Xu, C. S. et al. Enhanced FIB-SEM systems for large-volume 3D imaging. *eLife* **6**, e25916 (2017).
2. 2.
Heinrich, L. et al. Whole cell organelle segmentation in volumetric electron microscopy. *Nature* <https://doi.org/10.1038/s41586-021-03977-3> (2021).
3. 3.
Lodish, H. et al. *Molecular Cell Biology* 8th edn (W. H. Freeman, 2016).
4. 4.
Porter, K. R., Claude, A., & Fullam, E. F. A study of tissue culture cells by electron microscopy: methods and preliminary observations. *J. Exp. Med.* **81**, 233–246 (1945).
5. 5.

Denk, W., & Horstmann, H. Serial block-face scanning electron microscopy to reconstruct three-dimensional tissue nanostructure. *PLoS Biol.* **2**, e329 (2004).

6. 6.

Titze, B. *Techniques to Prevent Sample Surface Charging and Reduce Beam Damage Effects for SBEM Imaging*. Dissertation, Heidelberg University (2013).

7. 7.

Xu, C. S., Hayworth, K. J., & Hess, H. F. Enhanced FIB-SEM systems for large-volume 3D imaging. US Patent 10, 600, 615 (2020).

8. 8.

Xu, C. S., Pang, S., Hayworth, K. J., & Hess, H. F. in: *Volume Microscopy Neuromethods* vol. 155 (eds Wacker, I. et al.) (Humana, 2020).

9. 9.

Xu, C. S. et al. A connectome of the adult *Drosophila* central brain. Preprint at <https://doi.org/10.1101/2020.01.21.911859> (2020).

10. 10.

Wu, Y. et al. Contacts between the endoplasmic reticulum and other membranes in neurons. *Proc. Natl Acad. Sci. USA* **114**, E4859–E4867 (2017).

11. 11.

Stinchcombe, J. C., Bossi, G., Booth, S., & Griffiths, G. M. The immunological synapse of CTL contains a secretory domain and membrane bridges. *Immunity* **15**, 751–761 (2001).

12. 12.

Kupfer, A. & Dennert, G. Reorientation of the microtubule-organizing center and the Golgi apparatus in cloned cytotoxic lymphocytes triggered by binding to lysable target cells. *J. Immunol.* **133**, 2762–2766 (1984).

13. 13.

Stinchcombe, J. C., Majorovits, E., Bossi, G., Fuller, S. & Griffiths, G. M. Centrosome polarization delivers secretory granules to the immunological synapse. *Nature*. **443**, 462–465 (2006); correction **444**, 236 (2006).

14. 14.

Noske, A. B., Costin, A. J., Morgan, G. P. & Marsh, B. J. Expedited approaches to whole cell electron tomography and organelle mark-up *in situ* in high-pressure frozen pancreatic islets. *J. Struct. Biol.* **161**, 298–313 (2008).

15. 15.

Müller, A. et al. 3D FIB-SEM reconstruction of microtubule–organelle interaction in whole primary mouse β cells. *J. Cell Biol.* **220**, e202010039 (2021).

16. 16.

Takemura, S. Y. et al. A connectome of a learning and memory center in the adult *Drosophila* brain. *eLife* **6**, e26975 (2017).

17. 17.

Aso, Y. et al. Nitric oxide acts as a cotransmitter in a subset of dopaminergic neurons to diversify memory dynamics. *eLife* **8**, e49257 (2019).

18. 18.

Bullen, A. et al. Inner ear tissue preservation by rapid freezing: Improving fixation by high-pressure freezing and hybrid methods. *Hear. Res.* **315**, 49–60 (2014).

19. 19.

Sartori, N., Richter, K., & Dubochet, J. Vitrification depth can be increased more than 10-fold by high-pressure freezing. *J. Microsc.* **172**, 55–61 (1993).

20. 20.

National Research Council. *Guide for the Care and Use of Laboratory Animals* Eighth Edition (National Academies Press, 2011).

21. 21.

Gotoh, M., Maki, T., Kiyoizumi, T., Satomi, S., & Monaco, A. P. An improved method for isolation of mouse pancreatic islets. *Transplantation* **40**, 437–438 (1985).

22. 22.

Müller, A. et al. A global approach for quantitative super resolution and electron microscopy on cryo and epoxy sections using self-labeling protein tags. *Sci Rep.* **7**, 23 (2017).

23. 23.

Kremer, J. R., Mastronarde, D. N., & McIntosh, J. R., Computer visualization of three-dimensional image data using IMOD. *J. Struct. Biol.* **116**, 71–76 (1996).

24. 24.

Lu, Z. et al. En bloc preparation of *Drosophila* brains enables high-throughput FIB-SEM connectomics. Preprint at <https://doi.org/10.1101/855130> (2019).

25. 25.

Saalfeld, S., Cardona, A., Hartenstein, V. & Tomančák, P. As-rigid-as-possible mosaicking and serial section registration of large ssTEM datasets. *Bioinformatics* **26**, i57–i63 (2010).

26. 26.

van der Walt, S. et al. scikit-image: image processing in Python. *PeerJ*. **2**, e453 (2014).

Acknowledgements

We thank K.J. Hayworth and W. Qiu at Howard Hughes Medical Institute (HHMI) Janelia Research Campus (JRC) for invaluable discussions and data collection support; P.K. Rivlin, S.M. Plaza and I.A. Meinertzhagen for the JRC EM shared resource; the FlyEM project team support for staining protocols development; the electron microscopy facility of MPI-CBG and of the CMCB Technology Platform at TU Dresden for their services; Y. Wu from the laboratory of P. De Camilli at Yale for advice. C.S.X., S.P., G.S., S.T., Z.L., H.A.P., N.I., D.B., A.V.W., M.F., T.C.W., J.L.-S. and H.F.H. are funded by Howard Hughes Medical Institute (HHMI). A.M. received support from the Carl Gustav Carus Faculty of Medicine at TU Dresden via a MeDDrive GRANT. A.M. and M.S. were supported with funds from the German Center for Diabetes Research (DZD e.V.) by the German Ministry for Education and Research (BMBF), from the German-Israeli Foundation for Scientific Research and Development (GIF) (grant I-1429-201.2/2017) and from the German Research Foundation (DFG) jointly with the Agence nationale de la recherche (ANR) (grant SO 818/6-1) to M.S. A.T.R. and I.M. are funded by Genentech/Roche. H.K.H and S.B.v.E. are funded by NIAID grant R01AI138625. R.V.F. is supported by NIH R01GM124348. T.C.W. is supported by NIH R01GM097194. J.C. is a fellow of the Damon Runyon Cancer Research Foundation.

Author information

Author notes

1. Huxley K. Hoffman

Present address: Department of Cell and Developmental Biology,
University of Colorado Anschutz Medical Campus, Aurora, CO, USA

2. H. Amalia Pasolli

Present address: Electron Microscopy Resource Center, The
Rockefeller University, New York, NY, USA

3. Melanie Freeman

Present address: Advanced Bio-imaging Center, Department of
Molecular and Cell Biology, University of California, Berkeley, CA,
USA

4. These authors contributed equally: Song Pang, Gleb Shtengel

Affiliations

1. Janelia Research Campus, Howard Hughes Medical Institute, Ashburn, VA, USA

C. Shan Xu, Song Pang, Gleb Shtengel, Shin-ya Takemura, Zhiyuan
Lu, H. Amalia Pasolli, Nirmala Iyer, Davis Bennett, Aubrey V.
Weigel, Melanie Freeman, Jennifer Lippincott-Schwartz & Harald F.
Hess

2. Molecular Diabetology, University Hospital and Faculty of Medicine Carl Gustav Carus, TU Dresden, Dresden, Germany

Andreas Müller & Michele Solimena

3. Paul Langerhans Institute Dresden (PLID) of the Helmholtz Center Munich at the University Hospital Carl Gustav Carus and Faculty of Medicine of the TU Dresden, Dresden, Germany

Andreas Müller & Michele Solimena

4. German Center for Diabetes Research (DZD e.V.), Neuherberg,
Germany

Andreas Müller & Michele Solimena

5. Genentech, South San Francisco, CA, USA

Alex T. Ritter & Ira Mellman

6. Molecular and Cellular Biophysics Program, Department of Biological Sciences, University of Denver, Denver, CO, USA

Huxley K. Hoffman & Schuyler B. van Engelenburg

7. Department of Molecular Metabolism, Harvard T.H. Chan School of Public Health, Boston, MA, USA

Jeeyun Chung, Tobias C. Walther & Robert V. Farese Jr.

8. Department of Cell Biology, Harvard Medical School, Boston, MA, USA

Jeeyun Chung, Tobias C. Walther & Robert V. Farese Jr.

9. Howard Hughes Medical Institute, Boston, MA, USA

Tobias C. Walther

10. Broad Institute of Harvard and MIT, Cambridge, MA, USA

Tobias C. Walther

11. Max-Planck Institute of Molecular Cell Biology and Genetics, Dresden, Germany

Michele Solimena

Contributions

C.S.X. and H.F.H. supervised the project; C.S.X., S.P., G.S. and H.F.H. wrote the manuscript with input from all co-authors; C.S.X. developed the enhanced FIB-SEM platform for large-volume high-resolution imaging and optimized imaging conditions; C.S.X., S.P. and G.S. conducted FIB-SEM experiments; C.S.X. and S.P. performed image post-processing; S.P., G.S., A.M., A.T.R., H.K.H., S.B.v.E., Z.L., H.A.P., N.I., J.C., A.V.W. and M.F. prepared samples; G.S., A.M., A.T.R. and S.T. analysed data; D.B. prepared and uploaded data to the OpenOrganelle website; S.B.v.E., T.C.W., R.V.F., J.L.-S., I.M. and M.S. proposed biological questions and provided samples.

Corresponding authors

Correspondence to C. Shan Xu or Harald F. Hess.

Ethics declarations

Competing interests

Portions of the technology described here are covered by U.S. Patent 10,600,615 titled ‘Enhanced FIB-SEM systems for large-volume 3D imaging’, which was issued to C.S.X., K.J.H. and H.F.H. and assigned to Howard Hughes Medical Institute on 24 March 2020. The other authors declare no competing interests.

Additional information

Peer review information *Nature* thanks Robert Murphy, Jason Swedlow and the other, anonymous, reviewer(s) for their contribution to the peer review of this work. Peer reviewer reports are available.

Publisher’s note Springer Nature remains neutral with regard to jurisdictional claims in published maps and institutional affiliations.

Extended data figures and tables

Extended Data Fig. 1 Isotropic voxel (representing the minimal voxel size dictated by the worst-case axial resolution) vs. volume for comparing different volume EM methods.

The light green space represents the Resolution-Volume regime accessible with enhanced FIB-SEM technology through long term imaging. The present work of whole cell volumes colored in yellow matches the resolutions at 4-nm isotropic voxels shown in Fig. 1b, compared to the prior work of smaller volumes colored in red. Adopted from ref. 1 with modifications.

Extended Data Fig. 2 Murine CTL engaging an ovarian cancer cell.

Zooms on regions showing different immunological synapse topology features. **a**, Interdigitation. **b**, Flat apposition. **c**, Filopodia caught between cells. Scale bars, 0.5 μ m.

Extended Data Fig. 3 Edge transition distributions determined from ribosomes in cultured cells datasets.

a, Distributions of 37%–63% transition distances in X-, Y- (left), Z_{top} - (center), and Z_{bot} - (right) directions. **b**, Distributions of 20%–80% transition distances in X-, Y- (left), Z_{top} -(center), and Z_{bot} - (right) directions.

Source data

Extended Data Fig. 4 Cross-sections of the example of ribosomes from the dataset Interphase HeLa Cell 2017-06-21 and the profiles with the transition analysis.

The top three rows are the brightest ribosomes and the bottom three rows are the dimmest ribosomes.

[Source data](#)

Extended Data Fig. 5 Cross-sections of the example of ribosomes from the dataset Interphase HeLa Cell 2017-08-09 and the profiles with the transition analysis.

The top three rows are the brightest ribosomes and the bottom three rows are the dimmest ribosomes.

[Source data](#)

Extended Data Fig. 6 Cross-sections of the example of ribosomes from the dataset Wild-type THP-1 Macrophage 2018-11-11 and the profiles with the transition analysis.

The top three rows are the brightest ribosomes and the bottom three rows are the dimmest ribosomes.

[Source data](#)

Extended Data Fig. 7 Cross-sections of the example of ribosomes from the dataset Immortalized T-cells (Jurkat) 2018-08-10 and the profiles with the transition analysis.

The top three rows are the brightest ribosomes and the bottom three rows are the dimmest ribosomes.

[Source data](#)

Extended Data Fig. 8 Cross-sections of the example of ribosomes from the dataset Immortalized breast cancer cell (SUM159) 2017-11-21 and the profiles with the transition analysis.

The top three rows are the brightest ribosomes and the bottom three rows are the dimmest ribosomes.

[Source data](#)

Extended Data Fig. 9 Cross-sections of the example of ribosomes from the dataset Killer T-cell attacking cancer cell 2020-02-04 on Cancer Cell and the profiles with the transition analysis.

The top three rows are the brightest ribosomes and the bottom three rows are the dimmest ribosomes.

[Source data](#)

Extended Data Table 1 Descriptions of exemplary datasets with imaging conditions and estimated z-scaling factors

Supplementary information

Supplementary Information

This file contains Supplementary Methods, legends for Supplementary Videos 1 and 2, and Supplementary References.

Reporting Summary

Peer Review File

Supplementary Video 1

A new paradigm of high-resolution whole-cell imaging enabled by enhanced FIB-SEM.

Supplementary Video 2

T cell attacking cancer cell revealed by FIB-SEM with 4-nm voxels.

Source data

[Source Data Fig. 1](#)

[Source Data Extended Data Fig. 3](#)

[Source Data Extended Data Fig. 4](#)

[Source Data Extended Data Fig. 5](#)

[Source Data Extended Data Fig. 6](#)

[Source Data Extended Data Fig. 7](#)

[Source Data Extended Data Fig. 8](#)

[Source Data Extended Data Fig. 9](#)

Rights and permissions

[Reprints and Permissions](#)

About this article

Cite this article

Xu, C.S., Pang, S., Shtengel, G. *et al.* An open-access volume electron microscopy atlas of whole cells and tissues. *Nature* **599**, 147–151 (2021).
<https://doi.org/10.1038/s41586-021-03992-4>

- Received: 13 November 2020

- Accepted: 02 September 2021
- Published: 06 October 2021
- Issue Date: 04 November 2021
- DOI: <https://doi.org/10.1038/s41586-021-03992-4>

Share this article

Anyone you share the following link with will be able to read this content:

[Get shareable link](#)

Sorry, a shareable link is not currently available for this article.

[Copy to clipboard](#)

Provided by the Springer Nature SharedIt content-sharing initiative

Further reading

- [**Whole-cell organelle segmentation in volume electron microscopy**](#)
 - Larissa Heinrich
 - , Davis Bennett
 - , David Ackerman
 - , Woohyun Park
 - , John Bogovic
 - , Nils Eckstein
 - , Alyson Petruncio
 - , Jody Clements
 - , Song Pang
 - , C. Shan Xu
 - , Jan Funke
 - , Wyatt Korff

- , Harald F. Hess
- , Jennifer Lippincott-Schwartz
- , Stephan Saalfeld
- , Aubrey V. Weigel
- , Riasat Ali
- , Rebecca Arruda
- , Rohit Bahtra
- & Destiny Nguyen

Nature (2021)

Nanometre-scale imaging and AI reveal the interior of whole cells

- Jason R. Swedlow
- Lucy Collinson

News & Views 25 Oct 2021

This article was downloaded by **calibre** from <https://www.nature.com/articles/s41586-021-03992-4>

| [Section menu](#) | [Main menu](#) |

- Article
- [Published: 13 October 2021](#)

Systems-level effects of allosteric perturbations to a model molecular switch

- [Tina Perica](#) [ORCID: orcid.org/0000-0003-3152-8425](#)^{1,2,3} na1,
- [Christopher J. P. Mathy](#) [ORCID: orcid.org/0000-0002-5546-9733](#)^{1,2,4} na1,
- [Jiewei Xu](#)^{2,5,6},
- [Gwendolyn M. Jang](#)^{2,5,6},
- [Yang Zhang](#)^{1,2},
- [Robyn Kaake](#)^{2,5,6},
- [Noah Ollikainen](#)^{1,2,7},
- [Hannes Braberg](#) [ORCID: orcid.org/0000-0002-7070-2257](#)^{2,5,6},
- [Danielle L. Swaney](#) [ORCID: orcid.org/0000-0001-6119-6084](#)^{2,5,6},
- [David G. Lambright](#)^{8,9},
- [Mark J. S. Kelly](#)¹⁰,
- [Nevan J. Krogan](#) [ORCID: orcid.org/0000-0003-4902-337X](#)^{2,5,6} &
- [Tanja Kortemme](#) [ORCID: orcid.org/0000-0002-8494-680X](#)^{1,2,4,7,11}

[Nature](#) volume 599, pages 152–157 (2021)

- 3711 Accesses
- 63 Altmetric
- [Metrics details](#)

Subjects

- [GTP-binding protein regulators](#)
- [Molecular conformation](#)
- [Networks and systems biology](#)
- [Proteomic analysis](#)
- [Regulatory networks](#)

Abstract

Molecular switch proteins whose cycling between states is controlled by opposing regulators^{1,2} are central to biological signal transduction. As switch proteins function within highly connected interaction networks³, the fundamental question arises of how functional specificity is achieved when different processes share common regulators. Here we show that functional specificity of the small GTPase switch protein Gsp1 in *Saccharomyces cerevisiae* (the homologue of the human protein RAN)⁴ is linked to differential sensitivity of biological processes to different kinetics of the Gsp1 (RAN) switch cycle. We make 55 targeted point mutations to individual protein interaction interfaces of Gsp1 (RAN) and show through quantitative genetic⁵ and physical interaction mapping that Gsp1 (RAN) interface perturbations have widespread cellular consequences. Contrary to expectation, the cellular effects of the interface mutations group by their biophysical effects on kinetic parameters of the GTPase switch cycle and not by the targeted interfaces. Instead, we show that interface mutations allosterically tune the GTPase cycle kinetics. These results suggest a model in which protein partner binding, or post-translational modifications at distal sites, could act as allosteric regulators of GTPase switching. Similar mechanisms may underlie regulation by other GTPases, and other biological switches. Furthermore, our integrative platform to determine the quantitative consequences of molecular perturbations may help to explain the effects of disease mutations that target central molecular switches.

Access options

Subscribe to Journal

Get full journal access for 1 year

\$199.00

only \$3.90 per issue

[Subscribe](#)

All prices are NET prices.

VAT will be added later in the checkout.

Tax calculation will be finalised during checkout.

Rent or Buy article

Get time limited or full article access on ReadCube.

from \$8.99

[Rent or Buy](#)

All prices are NET prices.

Additional access options:

- [Log in](#)
- [Access through your institution](#)
- [Learn about institutional subscriptions](#)

Fig. 1: GI profiles of Gsp1 interface point mutants cluster by biological processes but not by targeted interfaces.

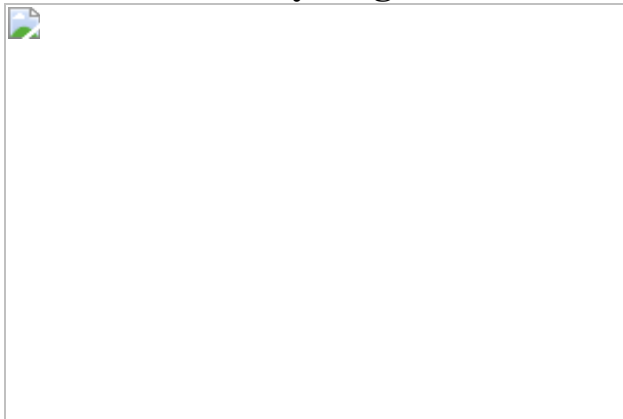


Fig. 2: Gsp1 interface point mutations rewire the physical interaction network of Gsp1, including interactions with the switch regulators GEF (Srm1) and GAP (Rna1).

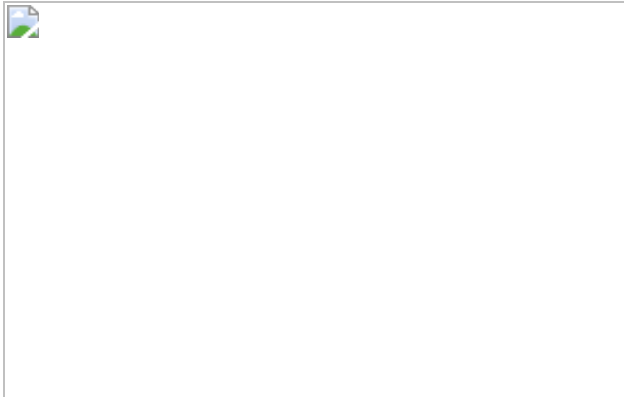


Fig. 3: Point mutations in Gsp1 interfaces allosterically modulate GTPase cycle parameters by tuning active site conformational distributions.

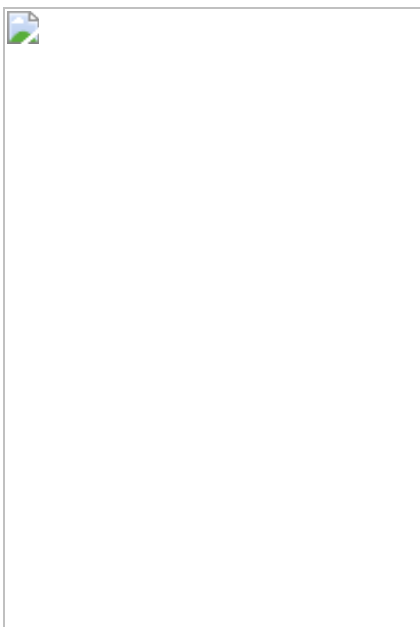
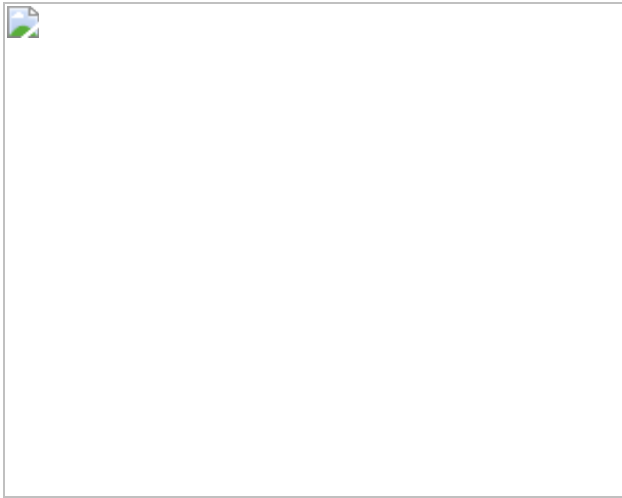


Fig. 4: Cellular effects of interface mutations group by their effect on GTPase cycle kinetics.



Data availability

The mass spectrometry proteomics data have been deposited to the PRIDE proteomics data repository with the dataset identifier [PXD016338](#) and are available as Supplementary Tables. Raw biophysics data (cycle kinetics, circular dichroism spectroscopy and NMR), and E-MAP S-scores, scaled SGA scores and their correlations are available from https://github.com/tinaperica/Gsp1_manuscript/tree/master/Data. All other data that support the findings of this study are available within the paper and its supplementary files. [Source data](#) are provided with this paper.

Code availability

Custom written R and Python scripts are available without restrictions at https://github.com/tinaperica/Gsp1_manuscript.

References

1. 1.

- Ferrell, J. E. & Ha, S. H. Ultrasensitivity part I: Michaelian responses and zero-order ultrasensitivity. *Trends Biochem. Sci* **39**, 496–503 (2014).

2. 2.

Goldbeter, A. & Koshland, D. E. An amplified sensitivity arising from covalent modification in biological systems. *Proc. Natl Acad. Sci. USA* **78**, 6840–6844 (1981).

3. 3.

Eisenberg, D., Marcotte, E. M., Xenarios, I. & Yeates, T. O. Protein function in the post-genomic era. *Nature* **405**, 823–826 (2000).

4. 4.

Rush, M. G., Drivas, G. & D'Eustachio, P. The small nuclear GTPase Ran: how much does it run? *BioEssays* **18**, 103–112 (1996).

5. 5.

Collins, S. R., Schuldiner, M., Krogan, N. J. & Weissman, J. S. A strategy for extracting and analyzing large-scale quantitative epistatic interaction data. *Genome Biol.* **7**, R63 (2006).

6. 6.

Braberg, H. et al. Genetic interaction mapping informs integrative structure determination of protein complexes. *Science* **370**, eaaz4910 (2020).

7. 7.

Braberg, H. et al. From structure to systems: high-resolution, quantitative genetic analysis of RNA polymerase II. *Cell* **154**, 775–788 (2013).

8. 8.

Dasso, M. The Ran GTPase: theme and variations. *Curr. Biol.* **12**, R502–R508 (2002).

9. 9.

Bischoff, F. R. & Ponstingl, H. in *The Small GTPase Ran* Vol. 1 (eds Rush, M. & D'Eustachio, P.) 163–176 (Springer, 2001);
https://doi.org/10.1007/978-1-4615-1501-2_9

10. 10.

Moore, M. S. & Blobel, G. The GTP-binding protein Ran/TC4 is required for protein import into the nucleus. *Nature* **365**, 661–663 (1993).

11. 11.

Köhler, A. & Hurt, E. Exporting RNA from the nucleus to the cytoplasm. *Nat. Rev. Mol. Cell Biol.* **8**, 761–773 (2007).

12. 12.

Arnaoutov, A. & Dasso, M. The Ran GTPase regulates kinetochore function. *Dev. Cell* **5**, 99–111 (2003).

13. 13.

Ren, M. et al. Separate domains of the Ran GTPase interact with different factors to regulate nuclear protein import and RNA processing. *Mol. Cell. Biol.* **15**, 2117–2124 (1995).

14. 14.

Costanzo, M. et al. A global genetic interaction network maps a wiring diagram of cellular function. *Science* **353**, aaf1420 (2016).

15. 15.

Geyer, M. et al. Conformational states of the nuclear GTP-binding protein Ran and its complexes with the exchange factor RCC1 and the effector protein RanBP1. *Biochemistry* **38**, 11250–11260 (1999).

16. 16.

Henriksen, P. et al. Proteome-wide analysis of lysine acetylation suggests its broad regulatory scope in *Saccharomyces cerevisiae*. *Mol. Cell. Proteomics* **11**, 1510–1522 (2012).

17. 17.

de Boor, S. et al. Small GTP-binding protein Ran is regulated by posttranslational lysine acetylation. *Proc. Natl Acad. Sci. USA* **112**, E3679–E3688 (2015).

18. 18.

Besray Unal, E. et al. Systems level expression correlation of Ras GTPase regulators. *Cell Commun. Signal.* **16**, 46 (2018).

19. 19.

Görlich, D., Seewald, M. J. & Ribbeck, K. Characterization of Ran-driven cargo transport and the RanGTPase system by kinetic measurements and computer simulation. *EMBO J.* **22**, 1088–1100 (2003).

20. 20.

Barr, F. A. Review series: Rab GTPases and membrane identity: causal or inconsequential? *J. Cell Biol.* **202**, 191–199 (2013).

21. 21.

Levy, E. D. A simple definition of structural regions in proteins and its use in analyzing interface evolution. *J. Mol. Biol.* **403**, 660–670 (2010).

22. 22.

Rojas, A. M., Fuentes, G., Rausell, A. & Valencia, A. The Ras protein superfamily: evolutionary tree and role of conserved amino acids. *J.*

Cell Biol. **196**, 189–201 (2012).

23. 23.

Collins, S. R., Roguev, A. & Krogan, N. J. Quantitative genetic interaction mapping using the E-MAP approach. *Methods Enzymol.* **470**, 205–231 (2010).

24. 24.

Schuldiner, M. et al. Exploration of the function and organization of the yeast early secretory pathway through an epistatic miniarray profile. *Cell* **123**, 507–519 (2005).

25. 25.

Giaever, G. et al. Functional profiling of the *Saccharomyces cerevisiae* genome. *Nature* **418**, 387–391 (2002).

26. 26.

Collins, S. R. et al. Functional dissection of protein complexes involved in yeast chromosome biology using a genetic interaction map. *Nature* **446**, 806–810 (2007).

27. 27.

Cherry, J. M. et al. SGD: *Saccharomyces* Genome Database. *Nucleic Acids Res.* **26**, 73–79 (1998).

28. 28.

Benjamini, Y. & Hochberg, Y. Controlling the false discovery rate—a practical and powerful approach to multiple testing. *J. R. Stat. Soc. B* **57**, 289–300 (1995).

29. 29.

Benjamini, Y. & Yekutieli, D. The control of the false discovery rate in multiple testing under dependency. *Ann. Stat.* **29**, 1165–1188, 1124 (2001).

30. 30.

Jäger, S. et al. Global landscape of HIV–human protein complexes. *Nature* **481**, 365–370 (2011).

31. 31.

Jäger, S. et al. Purification and characterization of HIV–human protein complexes. *Methods* **53**, 13–19 (2011).

32. 32.

Cox, J. & Mann, M. MaxQuant enables high peptide identification rates, individualized p.p.b.-range mass accuracies and proteome-wide protein quantification. *Nat. Biotechnol.* **26**, 1367–1372 (2008).

33. 33.

Cox, J. et al. Accurate proteome-wide label-free quantification by delayed normalization and maximal peptide ratio extraction, termed MaxLFQ. *Mol. Cell. Proteomics* **13**, 2513–2526 (2014).

34. 34.

Teo, G. et al. SAINTexpress: improvements and additional features in Significance Analysis of INTERactome software. *J. Proteomics* **100**, 37–43 (2014).

35. 35.

Choi, M. et al. MSstats: an R package for statistical analysis of quantitative mass spectrometry-based proteomic experiments. *Bioinformatics* **30**, 2524–2526 (2014).

36. 36.

Studier, F. W. Protein production by auto-induction in high density shaking cultures. *Protein Expression Purif.* **41**, 207–234 (2005).

37. 37.

Markley, J. L. et al. Recommendations for the presentation of NMR structures of proteins and nucleic acids—IUPAC-IUBMB-IUPAB Inter-Union Task Group on the Standardization of Data Bases of Protein and Nucleic Acid Structures Determined by NMR Spectroscopy. *J. Biomol. NMR* **12**, 1–23 (1998).

38. 38.

Mishra, A. K. & Lambright, D. G. High-throughput assay for profiling the substrate specificity of Rab GTPase-activating proteins. *Methods Mol. Biol.* **1298**, 47–60 (2015).

39. 39.

Goudar, C. T., Sonnad, J. R. & Duggleby, R. G. Parameter estimation using a direct solution of the integrated Michaelis–Menten equation. *Biochim. Biophys. Acta* **1429**, 377–383 (1999).

40. 40.

Malaby, A. W. et al. Methods for analysis of size-exclusion chromatography–small-angle X-ray scattering and reconstruction of protein scattering. *J. Appl. Crystallogr.* **48**, 1102–1113 (2015).

41. 41.

Klebe, C., Bischoff, F. R., Ponstingl, H. & Wittinghofer, A. Interaction of the nuclear GTP-binding protein Ran with its regulatory proteins RCC1 and RanGAP1. *Biochemistry* **34**, 639–647 (1995).

Acknowledgements

We thank R. Ordonez for contributions to the design of mutations; C. Melero, D. Jeon, S. Mathur, R. D. Kim and K. Kundert for technical help; M. Jaime Garza for contributions to the conformational analysis by NMR; C. Ryan for advice on E-MAP analysis; and D. Agard, G. Narlikar, J. Fraser and J. M. Thornton for discussions. This work was supported by a grant from the National Institutes of Health (R01-GM117189) to T.K. and a Sir Henry Wellcome Postdoctoral Fellowship (101614/Z/13/Z) to T.P. C.J.P.M. is a UCSF Discovery Fellow. T.K. is a Chan Zuckerberg Biohub investigator.

Author information

Author notes

1. These authors contributed equally: Tina Perica, Christopher J. P. Mathy

Affiliations

1. Department of Bioengineering and Therapeutic Sciences, University of California San Francisco, San Francisco, CA, USA

Tina Perica, Christopher J. P. Mathy, Yang Zhang, Noah Ollikainen & Tanja Kortemme

2. Quantitative Biosciences Institute (QBI), University of California San Francisco, San Francisco, CA, USA

Tina Perica, Christopher J. P. Mathy, Jiewei Xu, Gwendolyn M. Jang, Yang Zhang, Robyn Kaake, Noah Ollikainen, Hannes Braberg, Danielle L. Swaney, Nevan J. Krogan & Tanja Kortemme

3. European Molecular Biology Laboratory, European Bioinformatics Institute (EMBL-EBI), Cambridge, UK

Tina Perica

4. The UC Berkeley–UCSF Graduate Program in Bioengineering,
University of California San Francisco, San Francisco, CA, USA

Christopher J. P. Mathy & Tanja Kortemme

5. Department of Cellular and Molecular Pharmacology, University of
California San Francisco, San Francisco, CA, USA

Jiewei Xu, Gwendolyn M. Jang, Robyn Kaake, Hannes
Braberg, Danielle L. Swaney & Nevan J. Krogan

6. The J. David Gladstone Institutes, San Francisco, CA, USA

Jiewei Xu, Gwendolyn M. Jang, Robyn Kaake, Hannes
Braberg, Danielle L. Swaney & Nevan J. Krogan

7. Graduate Program in Bioinformatics, University of California San
Francisco, San Francisco, California, USA

Noah Ollikainen & Tanja Kortemme

8. Program in Molecular Medicine, University of Massachusetts Medical
School, Worcester, MA, USA

David G. Lambright

9. Department of Biochemistry and Molecular Pharmacology, University
of Massachusetts Medical School, Worcester, MA, USA

David G. Lambright

10. Department of Pharmaceutical Chemistry, University of California San
Francisco, San Francisco, CA, USA

Mark J. S. Kelly

11. Chan Zuckerberg Biohub, San Francisco, CA, USA

Tanja Kortemme

Contributions

T.P., C.J.P.M., N.J.K. and T.K. identified and developed the core questions. T.P. and C.J.P.M. performed the majority of the experiments and data analysis. J.X. and T.P. performed the E-MAP screens. G.M.J. performed the pull-down experiments. D.L.S. and R.K. performed the mass spectrometry experiments and together with T.P. analysed the data. N.O. contributed to the design of Gsp1 mutants. H.B. contributed to E-MAP analysis. M.J.S.K. suggested the NMR studies. C.J.P.M. and M.J.S.K. performed the NMR experiments and analysed the data. T.P. performed the kinetics experiments. D.G.L. contributed to the analysis of the kinetics data. T.P., C.J.P.M. and Y.Z. purified the proteins. Y.Z. performed the western blot experiments. T.P., C.J.P.M. and T.K. wrote the manuscript with contributions from the other authors. N.J.K. and T.K. oversaw the project.

Corresponding authors

Correspondence to Nevan J. Krogan or Tanja Kortemme.

Ethics declarations

Competing interests

The authors declare no competing interests.

Additional information

Peer review information *Nature* thanks Katrin Rittinger and the other, anonymous, reviewer(s) for their contribution to the peer review of this work.

Publisher's note Springer Nature remains neutral with regard to jurisdictional claims in published maps and institutional affiliations.

Extended data figures and tables

Extended Data Fig. 1 Design of interface point mutations in *S. cerevisiae* Gsp1.

Interface residues are categorized as interface core, rim, and support positions (see [Supplementary Methods](#)) and provided in Supplementary Table 2. **a–f**, Structures of RAN (Gsp1) in partner-bound conformations with interface residues coloured by partner protein. All mutated Gsp1 residues are shown as spheres.: **a**, Srm1 (GEF) interface core (dark teal) and interface rim and support (light teal) PDB 1I2M; **b**, Rna1 (GAP) interface core (dark orange) and interface rim and support (light orange) PDB 1K5D; **c**, Ntf2 interface core (dark purple) and interface rim and support (light purple) PDB 1A2K; **d**, Residues that are in both the core of the Yrb1 and Yrb2 interfaces (dark yellow), and in only one of the two interfaces (light yellow) PDB 1K5D; **e**, Srp1 interface core (dark pink) and interface rim and support (light pink) PDB 1WA5; **f**, Residues that are in the core of four or more (dark green), two to three (green) and one (light green) karyopherin interface. Karyopherins are: Kap95, Crm1, Los1, Kap104, Msn5, Cse1, Mtr10. PDB 2BKU. **g**, Location of Gsp1 residues in partner interfaces. Residues within 5 Å of the nucleotide, in the canonical P-loop, or in the switch I or II regions²² were not mutated. Residues belonging to the switch I, switch II, and C-terminal α helix are indicated by dark navy bars. Chosen Gsp1 point mutation substitutions are provided in Supplementary Table 3.

[Source data](#)

Extended Data Fig. 2 Endogenous expression levels of Gsp1 in *S. cerevisiae* strains with genomically integrated *GSP1* point mutations profiled by western blot.

a, Expression data for strong mutants, defined as mutants with nine or more significant GIs. **b**, Expression data for weak mutants, defined as mutants with fewer than nine significant GIs. In **a**, and **b**, bar heights indicate averages over two or more biological replicates (n) grown on separate days (except for T34D which has only one biological replicate), with error bars indicating one standard deviation for n >= 3. Overlaid points indicate individual biological replicates (each an average over at least 12 technical

replicates per biological replicate for wild-type and MAT: α strains, and between one and six technical replicates per biological replicate for mutant strains). Expression levels are relative to the expression levels of wild-type Gsp1 protein with clonNAT resistance marker (WT) shown as red dashed lines (relative expression of 1). MAT: α is the starting *S. cerevisiae* strain (see [Supplementary Methods](#)). **c**, Distributions of average relative expression levels for strong and weak mutants. Each point is as in **a** and **b**. Horizontal pink bars indicate the mean of the point distributions.

[Source data](#)

Extended Data Fig. 3 GI profiles of the 56 *GSP1* strains (wild-type *GSP1* with clonNAT cassette and 55 point mutants).

Negative S-score (blue) represents synthetic sick or synthetic lethal GIs, positive S-score (yellow) represents suppressive or epistatic GIs; neutral S-scores (no significant GI) are shown in black. Gsp1 point mutants and *S. cerevisiae* genes are hierarchically clustered by Pearson correlation. *GSP1* mutants fall into two clusters: a cluster of 23 strong mutants with nine or more significant GIs and 32 weak mutants with fewer than nine significant GIs.

[Source data](#)

Extended Data Fig. 4 Functional profiles of *GSP1* mutants cannot be explained solely by the positions of mutations in interfaces.

a, Locations of mutated residues in structurally characterized interfaces. $\Delta rASA$ is the difference in accessible surface area of a residue upon binding, relative to an empirical maximum for the solvent accessible surface area of each amino acid residue type (see [Supplementary Methods](#)). **b**, GI profiles of *GSP1* mutants group *S. cerevisiae* genes by biological processes and complexes, such as the dynein/dynactin pathway, SWR1 complex, the Hog1 signalling pathway, mRNA splicing, mitochondrial proteins, and the Rpd3L histone deacetylase complex. **c**, Distributions of Pearson correlations between the GI profiles of strong *GSP1* mutants and

alleles of Gsp1 direct interaction partners with available co-complex crystal structures (left) and strong *GSP1* mutants and alleles of all other *S. cerevisiae* genes (right). **d**, Distributions of Pearson correlations between the GI profiles of Gsp1 interaction partners and strong and weak *GSP1* mutants if mutation is (black and light purple) or is not (grey and dark purple) in the interface with that partner. Teal violin plot on the right represents the distribution of all other Pearson correlations between *GSP1* mutants and *S. cerevisiae* genes. In **c** and **d**, point size indicates the false discovery rate adjusted one-sided (positive) p-value of Pearson correlation, and pink bars indicate the mean of the point distributions; n denotes the number of *GSP1* point mutant-gene GI profile correlations in each category. Data for strong mutants are also shown in Fig. 1e and included here for comparison.

[Source data](#)

[Extended Data Fig. 5 Interface point mutations in Gsp1 rewire its physical interaction network.](#)

a, Schematic representation of the affinity purification mass spectrometry (AP-MS) experiment to determine the abundance of pulled-down protein interaction partners of wild type and mutant Gsp1. The change in abundance of partner proteins pulled down with Gsp1 mutants in **b**, **c**, and **d** is represented as log₂-transformed fold change (FC) between abundance of a partner pulled-down with a Gsp1 mutant versus pulled-down with wild-type Gsp1 ($\log_2(\text{abundance(PREY})^{\text{MUT}}/\text{abundance(PREY})^{\text{WT}})$). To account for possible tag effects, the fold change in prey abundance was always computed relative to the wild-type protein with the corresponding tag. Decreased abundance compared to pull-down with wild-type Gsp1 is annotated in red and increased abundance in blue. The log₂-transformed fold change values are capped at +/- 4. **b**, Amino- and **c**, -carboxy terminally 3xFLAG-tagged Gsp1 point mutants (rows) and prey proteins identified by AP-MS (columns) hierarchically clustered by the log₂-transformed fold change in prey abundance. **d**, Prey proteins pulled down by both amino- and carboxy-terminal tagged constructs. Left semi-circle represents an amino-terminal 3xFLAG-tagged Gsp1 point mutant, and right semi-circle represents carboxy-terminal 3xFLAG-tagged Gsp1 point

mutant. Semi-circle size is proportional to the significance of the log₂-transformed fold change (false discovery rate adjusted p-value) of the prey abundance in pulled-down complexes with a Gsp1 mutant compared to complexes with the wild-type Gsp1. Overall we identified 316 high-confidence prey partner proteins, with the amino- and carboxy-terminally tagged Gsp1 mutants pulling down 264 and 103 preys, respectively, including 51 overlapping preys. The difference in preys identified by experiments with N- or C-terminal tags illustrates the sensitivity of the interaction network to perturbation of Gsp1.

Source data

Extended Data Fig. 6 Gsp1 interface mutations rewire interactions with the core regulators Srm1 and Rna1.

a, b, Protein-protein interactions between interface mutants of Gsp1 and Gsp1 partners for which there are co-complex X-ray crystal structures (core regulators Srm1 and Rna1, and effectors Yrb1, Kap95, Pse1, and Srp1). Change in pulled-down prey partner abundance is expressed as log2(PREY abundanceMUT/PREY abundanceWT)). N-3xFL and C-3xFL labelled mutants are tagged with an amino- or carboxy-terminal triple FLAG tag, respectively, and partners are coloured as indicated. **a**, Bar plot depicting changes in pulled-down prey partner abundance when the point mutation is in the core of the Gsp1 interface with the prey partner. **b**, Bar plot depicting all changes in pulled-down prey partner abundance for core regulators Srm1 and Rna1, and effectors Yrb1, Kap95, Pse1, and Srp1, regardless whether the mutation is directly in the interface core with the partner or not. **c**, Distribution showing the variation in log₂-transformed fold change in abundance of all prey proteins pulled down with the Gsp1 mutants, as defined by interquartile range (IQR) across mutants. Values for core partners shown as arrows (Rna1 orange, Srm1 teal, Yrb1 yellow, Kap95 green, Pse1 light green, Srp1 pink). Mean and +1 standard deviation of IQR values are highlighted with a dark grey and a light grey arrow, respectively. The extent to which the abundance of the two cycle regulators Rna1 and Srm1 changed across the Gsp1 point mutants is larger than the change for an average prey protein. All IQR values are provided in Supplementary Table 5. **d**, Position of T34 with respect to the interfaces with Rna1 (GAP,

orange surface, PDB 1K5D), Srm1 (GEF, teal surface, PDB 2I1M), and Yrb1 (yellow surface, PDB 1K5D). As the coordinates for T34 are not resolved in the 2I1M structure, in all three structures the pink spheres show the residue location in the aligned 1K5D structure. Gsp1: navy cartoon; GTP nucleotide: stick representation. Residues that were mutated in the Rna1 and Srm1 interfaces are shown in sphere representation and are coloured in orange (Rna1, left) or teal (Srm1, middle).

[Source data](#)

Extended Data Fig. 7 Effect of Gsp1 point mutations on the in vitro efficiency of GAP-mediated GTP hydrolysis and GEF-mediated nucleotide exchange.

a, k_{cat} and **b**, K_m values of GAP-mediated GTP hydrolysis of wild-type and point mutant Gsp1. Error bars represent the standard deviation of the k_{cat} and the K_m parameters from the integrated Michaelis-Menten fit for $n \geq 3$ replicates. **c**, k_{cat} and **d**, K_m of GEF-mediated nucleotide exchange of wild-type and point mutant Gsp1. Inset shows the K_m bar plot for all but the four mutants with the highest K_m (K101R, R108L, R108I, and R108Y). Error bars represent the value plus/minus the standard error of the Michaelis-Menten fit to data from $n \geq 17$ measurements at different substrate concentrations. **a**, **b**, **c**, **d**, Dotted lines indicate the wild-type values. Dark blue bar denotes the wild-type Gsp1, and orange and teal bars highlight the residues that are in the core of the interface with the GAP and GEF, respectively. **e**, Comparison of relative change in catalytic efficiencies of GAP-mediated GTP hydrolysis (orange bars) and GEF-mediated nucleotide exchange (teal bars) defined as $k_{\text{cat}}^{\text{MUT}}/K_m^{\text{MUT}} / k_{\text{cat}}^{\text{WT}}/K_m^{\text{WT}}$. Grey line indicates a three-fold increase compared to wild type and black line indicates a three-fold decrease compared to wild type. Error bars represent the added standard error of the mean (for GAP) or standard error of the fit (for GEF) values of the mutant and the wild-type efficiency (k_{cat}/K_m) values. Mutations not in the interface core with the GAP both increased (3-fold, R108G mutant) and decreased (3 to 10-fold, T34E/Q/A/G, R78K, D79S/A, R108I, and R112S mutants) the catalytic efficiency k_{cat}/K_m of

GAP-mediated GTP hydrolysis, compared to wild-type Gsp1. As expected, mutations in the interface core with the GEF (K101, and R108) decreased the catalytic efficiency of GEF-mediated nucleotide exchange >40-fold. However, other mutations not in the GEF interface core (R78K, R112S, Y157A) also decreased the efficiency notably (3- to 10-fold).

[Source data](#)

Extended Data Fig. 8 Gsp1 interface mutations act allosterically to modulate the rate of GTP hydrolysis.

a, Annotated 1D ^{31}P NMR spectrum of wild-type Gsp1 loaded with GTP. Peak areas are computed over intervals shown and normalized to the GTP β bound peak. The peaks from left to right correspond to: free phosphate (Pi), β phosphate of GDP bound to Gsp1 (GDP β bound), β phosphate of free (unbound) GDP (GDP β free), γ phosphate of GTP bound to Gsp1 in conformation 1 (γ 1), γ phosphate of GTP bound to Gsp1 in conformation 2 (γ 2), α phosphate of bound or unbound GDP or GTP, β phosphate of GTP bound to Gsp1 (GTP β bound), β phosphate of free (unbound) GTP (GTP β free). **b**, Rate of intrinsic GTP hydrolysis of wild-type Gsp1 and mutants. Dotted line indicates wild-type value. Error bars represent the standard deviations from $n \geq 3$ replicates (dots). **c**, Natural log-transformed exchange equilibrium constant between the γ 2 and γ 1 conformations plotted against the relative rate of intrinsic GTP hydrolysis represented as a natural logarithm of the ratio of the rate for the mutant over the rate of the wild type. The pink line is a linear fit. Error bars represent the standard deviation from $n \geq 3$ replicates of intrinsic GTP hydrolysis measurements. **d**, Location of Y157, H141, and Q147 (pink spheres) in the Crm1 interface (grey surface, PDB 3M1I). Gsp1: navy cartoon; GTP nucleotide: yellow stick representation. **e**, Location of T34 (pink spheres) in the interface with Yrb1 (grey surface, PDB 1K5D). Distances from the γ phosphate of GTP to the residue α -carbon are indicated below the residue numbers in **d** and **e**.

[Source data](#)

Extended Data Fig. 9 Relative prey protein abundance overlaid onto the effects of each mutation on relative in vitro efficiencies

of GAP-mediated GTP hydrolysis and GEF-mediated nucleotide exchange.

Relative GAP-mediated hydrolysis and GEF-mediated exchange efficiencies are plotted as $\ln(k_{\text{cat}}^{\text{MUT}}/K_m^{\text{MUT}}/k_{\text{cat}}^{\text{WT}}/K_m^{\text{WT}})$. Mutants that affect the efficiency (k_{cat}/K_m) of GEF-catalysed nucleotide exchange more than the efficiency of GAP-catalysed GTP hydrolysis are above the diagonal, and the mutants that affect the GAP-catalysed hydrolysis are below the diagonal. Left semi-circle represents an amino-terminal 3xFLAG-tagged Gsp1 point mutant, and right semi-circle represents a carboxy-terminal 3xFLAG-tagged Gsp1 point mutant, relative to wild-type Gsp1 with the corresponding tag. **a**, Colour represents \log_2 -transformed ratio of GAP and GEF abundance fold change for each Gsp1 point mutant compared to wild type defined as

$\log_2((\text{abundance}(\text{Rna1})^{\text{MUT}}/\text{abundance}(\text{Rna1})^{\text{WT}})/(\text{abundance}(\text{Srm1})^{\text{MUT}}/\text{abundance}(\text{Srm1})^{\text{WT}}))$. Orange coloured mutants pull-down relatively less Rna1 (GAP) and teal mutants less Srm1 (GEF). **b-f**, Colour represents the log-transformed ratio of mutant and wild type pulled-down prey protein represented as $\log_2(\text{PREY abundance}^{\text{MUT}}/\text{PREY abundance}^{\text{WT}})$. Log-transformed relative abundance values are capped at $+/- 4$. Decreased prey abundance from AP-MS in pulled-down complexes with a mutant Gsp1 compared to complexes with the wild-type Gsp1 is represented in red and increased abundance in blue. Prey proteins: **b**, Rna1 (GAP); **c**, Srm1 (GEF); **d**, Yrb1; **e**, Kap95, and **f**, Vps71. Yrb1 follows a pattern similar to that of Rna1 (GAP), whereas Kap95 and Vps71 are similar to Srm1 (GEF).

[Source data](#)

Extended Data Fig. 10 Sets of *S. cerevisiae* genes grouped by biological functions.

Heat maps of the false discovery rate adjusted one-sided (positive) p-values of the Pearson correlations between the GI profiles of 22 strong *GSP1* point mutants and GI profiles of knock-outs or knock-downs of *S. cerevisiae* genes from Ref. ¹⁴. The p-value is represented as a white to grey range as in

Fig. 4a. Genes are organized in gene sets based on their biological function (Methods). The line plots above the heat maps are the same as in Fig. 4c. **a**, *GSP1* point mutants and alleles of Gsp1 binding partners with available co-complex X-ray crystal structures, and *S. cerevisiae* genes involved in nuclear transport of RNA and proteins. **b**, *GSP1* point mutants and *S. cerevisiae* genes involved in transcription regulation or 5' mRNA capping. **c**, *GSP1* point mutants and *S. cerevisiae* genes involved in the cytoplasm-to-vacuole targeting (CVT) pathway, and actin, tubulin, and cell polarity.

[Source data](#)

Supplementary information

[Supplementary Information](#)

This file contains the Supplementary Discussion, Supplementary Methods, Supplementary Figures 1–16, Supplementary Tables 1–9 and Supplementary References.

[Reporting Summary](#)

[Supplementary Data 1](#)

Genetic interaction (GI) data from the E-MAP screens. This file contains genetic interaction (GI) scores (S-scores) from the E-MAP screens of 56 *S. cerevisiae* strains (wild type and 55 *GSP1* point mutants).

[Supplementary Data 2](#)

Pairwise Pearson correlations of profiles between SGA genes and *GSP1* point mutants, with associated *P* values. This file contains the Pearson correlation coefficients and accompanying *P* values for correlations between genetic interaction profiles of *GSP1* point mutants and the genetic interaction profiles of *S. cerevisiae* alleles from the CellMap SGA dataset published in ref. 14.

Supplementary Data 3

Affinity purification mass spectrometry (AP-MS) data reported as fold change and significance value, as well as a list of significant interaction hits. This file contains two tables. Table 1 contains the affinity purification mass spectrometry (AP-MS) data for Gsp1 point mutants. The data in the table are the output from MSstats35 (see Supplementary Methods) and report on the abundance of the pulled-down protein, the log-transformed fold change of the abundance compared to the wild type with the appropriate 3×Flag tag, and the accompanying FDR-adjusted *P* value. The data are provided for both the global and equalized median normalization methods available. Table 2 contains the list of high-confidence interaction partners of Gsp1 from our AP-MS experiments (as determined by SAINTexpress (ref. 34), see Supplementary Methods).

41586_2021_3982_MOESM6_ESM.xlsx

Supplementary Data 4 *S. cerevisiae* genes from the SGA data with significant positive correlations with *GSP1* mutants organized by biological functions into gene sets. This file provides a list of *S. cerevisiae* alleles from the SGA dataset whose GI profiles have significant correlations with the GI profiles of *GSP1* mutants (see Methods). The genes were manually grouped into ‘gene sets’ according to their biological function (as annotated in the *Saccharomyces* Genome Database, <https://www.yeastgenome.org>).

Source data

Source Data Fig. 1

Source Data Fig. 2

Source Data Fig. 3

Source Data Fig. 4

Source Data Extended Data Fig. 1

[**Source Data Extended Data Fig. 2**](#)

[**Source Data Extended Data Fig. 3**](#)

[**Source Data Extended Data Fig. 4**](#)

[**Source Data Extended Data Fig. 5**](#)

[**Source Data Extended Data Fig. 6**](#)

[**Source Data Extended Data Fig. 7**](#)

[**Source Data Extended Data Fig. 8**](#)

[**Source Data Extended Data Fig. 9**](#)

[**Source Data Extended Data Fig. 10**](#)

Rights and permissions

[Reprints and Permissions](#)

About this article

Cite this article

Perica, T., Mathy, C.J.P., Xu, J. *et al.* Systems-level effects of allosteric perturbations to a model molecular switch. *Nature* **599**, 152–157 (2021). <https://doi.org/10.1038/s41586-021-03982-6>

- Received: 01 January 2020
- Accepted: 01 September 2021
- Published: 13 October 2021

- Issue Date: 04 November 2021
- DOI: <https://doi.org/10.1038/s41586-021-03982-6>

Share this article

Anyone you share the following link with will be able to read this content:

[Get shareable link](#)

Sorry, a shareable link is not currently available for this article.

[Copy to clipboard](#)

Provided by the Springer Nature SharedIt content-sharing initiative

This article was downloaded by **calibre** from <https://www.nature.com/articles/s41586-021-03982-6>

| [Section menu](#) | [Main menu](#) |

- Article
- Open Access
- [Published: 22 September 2021](#)

Structural basis of gating modulation of Kv4 channel complexes

- [Yoshiaki Kise](#) [ORCID: orcid.org/0000-0002-1840-5028¹](#) nA¹,
- [Go Kasuya](#) [ORCID: orcid.org/0000-0003-1756-5764²](#) nA¹,
- [Hiroyuki H. Okamoto¹](#),
- [Daichi Yamanouchi¹](#),
- [Kan Kobayashi¹](#) nAff³,
- [Tsukasa Kusakizako](#) [ORCID: orcid.org/0000-0002-6186-6647¹](#),
- [Tomohiro Nishizawa](#) [ORCID: orcid.org/0000-0001-7463-8398¹](#) nAff⁴,
- [Koichi Nakajo](#) [ORCID: orcid.org/0000-0003-0766-7281²](#) &
- [Osamu Nureki](#) [ORCID: orcid.org/0000-0003-1813-7008¹](#)

Nature volume **599**, pages 158–164 (2021)

- 6580 Accesses
- 21 Altmetric
- [Metrics details](#)

Subjects

- [Cryoelectron microscopy](#)
- [Patch clamp](#)

Abstract

Modulation of voltage-gated potassium (Kv) channels by auxiliary subunits is central to the physiological function of channels in the brain and heart^{1,2}. Native Kv4 tetrameric channels form macromolecular ternary complexes with two auxiliary β-subunits—intracellular Kv channel-interacting proteins (KChIPs) and transmembrane dipeptidyl peptidase-related proteins (DPPs)—to evoke rapidly activating and

inactivating A-type currents, which prevent the backpropagation of action potentials^{1,2,3,4,5}. However, the modulatory mechanisms of Kv4 channel complexes remain largely unknown. Here we report cryo-electron microscopy structures of the Kv4.2–DPP6S–KChIP1 dodecamer complex, the Kv4.2–KChIP1 and Kv4.2–DPP6S octamer complexes, and Kv4.2 alone. The structure of the Kv4.2–KChIP1 complex reveals that the intracellular N terminus of Kv4.2 interacts with its C terminus that extends from the S6 gating helix of the neighbouring Kv4.2 subunit. KChIP1 captures both the N and the C terminus of Kv4.2. In consequence, KChIP1 would prevent N-type inactivation and stabilize the S6 conformation to modulate gating of the S6 helices within the tetramer. By contrast, unlike the reported auxiliary subunits of voltage-gated channel complexes, DPP6S interacts with the S1 and S2 helices of the Kv4.2 voltage-sensing domain, which suggests that DPP6S stabilizes the conformation of the S1–S2 helices. DPP6S may therefore accelerate the voltage-dependent movement of the S4 helices. KChIP1 and DPP6S do not directly interact with each other in the Kv4.2–KChIP1–DPP6S ternary complex. Thus, our data suggest that two distinct modes of modulation contribute in an additive manner to evoke A-type currents from the native Kv4 macromolecular complex.

[Download PDF](#)

Main

Voltage-gated ion channels often form macromolecular complexes that consist of a pore-forming α -subunit and auxiliary subunits^{1,6,7}. Auxiliary subunits not only regulate subcellular localization, but also modulate the gating properties of the α -subunit for the physiological functions of channels in neurons and muscle cells. However, the mechanisms of modulation by auxiliary subunits remain mostly unknown, whereas the ion selectivity and voltage-dependent activation and inactivation mechanisms have been extensively studied^{8,9}.

Among 12 subfamilies of Kv channels, Kv4 (Kv4.1–Kv4.3) channels mediate the transient outward A-type current, which is characterized by fast activation at subthreshold membrane potentials, fast inactivation and fast recovery from the inactivated state^{3,4}. In neurons, Kv4 is localized at the soma and dendrites, where it controls the frequency of slow repetitive spike firing and attenuates the backpropagation of action potentials^{2,3,4}. In cardiomyocytes, Kv4 controls the early repolarization phase of the action potential¹⁰. Kv4s exhibit a unique inactivation process called closed-state inactivation (CSI), which is mechanistically distinct from open-state inactivation (OSI) as characterized by the ‘N-type inactivation’ observed in Shaker-related Kv1 channels^{11,12,13,14,15,16,17,18} (Extended Data Fig. 1). After depolarization and S6 gate opening, Kv1 enters the N-type inactivation state in which

the N-terminal ‘inactivation ball’ of the α -or β -subunit occludes the pore^{13,19} (Extended Data Fig. 1). Although the N terminus of Kv4 reportedly serves as the inactivation ball when Kv4 is expressed alone²⁰, Kv4s close the gate immediately with unknown mechanisms and end up in a closed inactivated state irrespective of the magnitude of depolarization (that is, CSI), from which they recover with fast kinetics^{12,21,22} (Extended Data Fig. 1).

Kv4s require both of two auxiliary β -subunits—cytoplasmic KChIPs and single-pass transmembrane DPPs—to achieve the native A-type current, particularly with the unique voltage dependence of inactivation kinetics characteristic of CSI and fast recovery from inactivation^{5,23}. KChIPs reportedly inhibit N-type inactivation, but accelerate CSI and recovery^{11,24,25}. Previous crystal structures of the Kv4.3 N-terminal domain (tetramerization 1 (T1) domain) in complex with KChIP1 revealed a cross-shaped octamer, in which four KChIP1 molecules are attached on the lateral side of the Kv4.3 T1 tetramer and interact with the N-terminal inactivation ball^{26,27}. These studies support the model that KChIP prevents N-type inactivation through sequestering the N terminus of Kv4s²⁰ (Extended Data Fig. 1b). However, it remains unknown how KChIP modulates other gating properties of CSI and recovery. DPP6 has been shown to accelerate the ‘gating charge’ movement of Kv4.2, suggesting that DPP6 expedites the movement of the S4 voltage-sensing helix directly or indirectly²⁸. However, the structure of the Kv4–DPP complex has not been reported, which hinders our understanding of the modulatory mechanisms. To gain insight into the mechanisms of gating modulation of Kv4s by KChIPs and DPPs, we determined the structures of full-length Kv4.2 alone, the Kv4.2–KChIP1 and Kv4.2–DPP6S binary complexes, and the Kv4.2–DPP6S–KChIP1 macromolecular ternary complex by single-particle cryo-electron microscopy (cryo-EM) (Fig. 1).

Fig. 1: Structures of Kv4.2 alone and the Kv4.2–KChIP1, Kv4.2–DPP6S and Kv4.2–DPP6S–KChIP1 complexes.

 **figure1**

a, Overall structures of the Kv4.2-alone tetramer, Kv4.2–KChIP1 octamer, Kv4.2–DPP6S octamer and Kv4.2–DPP6S–KChIP1 dodecamer (left to right). Four Kv4.2 subunits are coloured blue, four KChIP1 subunits are coloured yellow and four DPP6S subunits are coloured magenta. **b**, Structural comparison of the Kv4.2 N and C termini in the presence (right) and absence (left) of KChIP1. Protomers of Kv4.2 alone and three complexes are shown. Although both N and C termini are disordered in Kv4.2 alone and in the Kv4.2–DPP6S complex (left), both termini are resolved in the Kv4.2–KChIP1 and the Kv4.2–DPP6S–KChIP1 complexes (right). **c**, The intracellular S6 helix of Kv4.2 alone bends at the interface on the T1–S1 linker (dashed ellipse) and is subsequently disordered. By contrast, the S6 helix of the Kv4.2–KChIP1 complex extends straight toward KChIP1. **d**, Close-up view of the superimposed image in the dashed ellipse in **c**. The intracellular S6 of Kv4.2 starts bending from A419 and extend away from the T1–S1 linker in Kv4.2 alone and in the Kv4.2–DPP6S complex. However, it keeps a close distance to the T1–S1 linker without bending in the Kv4.2–KChIP1 and the Kv4.2–DPP6S–KChIP1 complexes.

Structures of Kv4.2 alone and Kv4.2–KChIP1

We first determined the cryo-EM structures of human Kv4.2 alone and the Kv4.2–KChIP1 complex (Fig. 1a, Extended Data Table 1). The fourfold symmetrical structures of both Kv4.2 alone and the Kv4.2–KChIP1 complex were determined to an overall resolution of 2.9 Å by single-particle cryo-EM analysis with *C*4 symmetry

imposed (Fig. 1a, Extended Data Figs. 2–4, Supplementary Figs. 1–4). The structure of Kv4.2 alone is compact with dimensions of around 75 Å × 75 Å × 100 Å and both N- and C-terminal regions (amino acids 1–39 and 437–630) are disordered (Fig. 1a, b, Supplementary Fig. 2a). The structure of the Kv4.2–KChIP1 complex has dimensions of around 105 Å × 105 Å × 100 Å (Fig. 1a, Supplementary Fig. 2b), which are consistent with the previous negative-stain electron microscopy structure of Kv4.2–KChIP2 at 21 Å resolution²⁹. As observed in the previous crystal structures of the Kv4.3 T1 domain–KChIP1 complex^{26,27}, the full-length Kv4.2–KChIP1 complex forms an octamer that consists of four Kv4.2s and four KChIP1s (Fig. 1a, Supplementary Fig. 2b). As compared to the structure of Kv4.2 alone, the N terminus (amino acids 2–39) and part of the C terminus (437–450 and 473–495) of Kv4.2 are resolved and captured by KChIP1 (Figs. 1a–c, 2a, b, e, f).

Fig. 2: Tripartite interactions of the Kv4.2 N terminus, Kv4.2 C terminus and KChIP1.



a, Overall structure of the Kv4.2–KChIP1 complex. The two neighbouring Kv4.2 subunits and one KChIP1 subunit are coloured yellow, red and blue, respectively. The C-terminal cytoplasmic S6 helix stops at S450 when it reaches the bottom of the complex. The interaction site of Kv4.2 and KChIP1 is highlighted by a dotted box. A magnified view from the direction of the arrow is presented in **b**. **b, c**, Comparison of the Kv4–KChIP1 complex with (**b**) or without (**c**) the Kv4 C terminus. Bottom views of the Kv4.2 (full-length)–KChIP1 complex (**b**) and the Kv4.3(T1)–KChIP1 complex (**c**; Protein Data Bank (PDB) code: 2NZ0) are shown. The neighbouring Kv4 subunits are coloured red and yellow. The Kv4.2 S6 helix (Kv4.2-S6) extends downward to the

bottom of the complex (S450) and is further followed by the C-terminal segment (Kv4.2-C) consisting of a short helix and a loop (S472–D495), which occupies the hydrophobic space generated by the Kv4.2 N terminus (Kv4.2-N) and KChIP1 (**b**). **d**, Inter-subunit interaction of the Kv4.2 N and C termini. Residues involved in the interaction are shown. Two neighbouring Kv4.2 subunits are coloured red and yellow. **e**, Interaction of the Kv4.2 C terminus (red) and KChIP1 (blue). Residues involved in the interaction are shown. **f**, The Kv4.2 intracellular S6 helix is captured by KChIP1 and the Kv4.2 C terminus. Residues involved in the interaction are shown.

The structures of Kv4.2–KChIP1 show that the Kv4.2 protomer comprises an N-terminal cytoplasmic domain with an N-terminal hydrophobic segment of approximately 40 residues in length (referred to as the inactivation ball), the T1 domain, a transmembrane domain with six transmembrane helices S1–S6, and the C-terminal cytoplasmic domain (Fig. [1b](#), Extended Data Fig. [5a](#)). The transmembrane domain of Kv4.2 adopts the Shaker-type topology, with the S1–S4 voltage-sensing domain and the S5–S6 channel pore forming helices composing a homo-tetramer in a domain-swapped manner, whereby the S1–S4 voltage sensor interacts with S5 of the pore domain from the neighbouring subunit^{[30,31](#)} (Supplementary Fig. [2b](#), Extended Data Fig. [5a,b](#)). It adopts a depolarized S4 up and S6 open conformation in both Kv4.2 alone and Kv4.2–KChIP1^{[30,31,32](#)} (Extended Data Figs. [5b,6](#)). The C-terminal intracellular S6 helix continuously extends from the transmembrane S6 helix toward KChIP1 (Figs. [1a,c,2a](#), Extended Data Fig. [5a](#)), which was not observed in previous studies. In addition, the intracellular S6 helix interacts with the T1–S1 linker in the structure of the Kv4.2–KChIP1 complex (Fig. [1b–d](#), Extended Data Fig. [5c–e](#)). By contrast, the intracellular S6 helix bends at A419 in the structure of Kv4.2 alone, which results in a partial loss of interaction between the intracellular S6 helix and the T1–S1 linker (Fig. [1d](#), Extended Data Fig. [5d,e](#)), suggesting a key mechanism of Kv4 gating modulation by KChIPs. The last 130 or so C-terminal amino acid residues of Kv4.2 (residues 496–630) are not resolved and are thus predicted to lack secondary structure (Fig. [1b](#), Extended Data Fig. [5a,f](#)), suggesting their flexibility. As in the Kv1.2 structure^{[30,31](#)}, the tetrameric T1 domain of Kv4.2 is located under the tetrameric channel pore domains at a distance of 25 Å—provided by the long T1–S1 linker and the long intracellular S6 helix—thus creating sufficient space for K⁺ ions to laterally enter the channel pore (Fig. [1a](#), Extended Data Fig. [5a](#)). However, it should be noted that, within the protomer of both Kv4.2 alone and the Kv4.2–KChIP1 complex, the topological relationship between the T1 and transmembrane domains is different from that in Kv1.2, owing to the distinct orientation of the T1–S1 linker following the T1 domain (Extended Data Fig. [5b,g–i](#)). The Kv4-specific topology of the T1 domain would facilitate the proper interaction between the intracellular S6 helix and KChIP1 (Extended Data Fig. [5j](#)).

Kv4.2–KChIP1 interaction

KChIP1s are laterally anchored next to the T1 domains of Kv4.2, consistent with the previous crystal structures of the Kv4.3 T1 domain–KChIP1 complex^{26,27} (Fig. 2a–c). The N-terminal hydrophobic segment (A2–R35) of Kv4.2, referred to as the inactivation ball, was captured by KChIP1 (Fig. 2b), which may explain why Kv4.2 exhibits a closed inactivated (CSI) mechanism, rather than an open inactivated (OSI) mechanism like Kv1.2, as previously discussed for Kv4.3^{26,27}. The present structure of the full-length Kv4.2–KChIP1 complex reveals that the C terminus of Kv4.2 tightly interacts with both KChIP1 and the N terminus of Kv4.2 (Figs. 1a,c, 2b,d–f). The C-terminal cytoplasmic S6 helix continuously extends from the transmembrane S6 helix and terminates at S450, which is localized at the bottom of the complex (Fig. 2a,b, Extended Data Fig. 5a). Although the residues from G451 to G471 are disordered, the following second cytoplasmic helix with a short loop (C-terminal segment: S472–D495) fits into the hydrophobic crevice formed by KChIP1 and the Kv4.2 N-terminal segment (A2–R35) from the neighbouring Kv4.2 subunit (Fig. 2b). In addition, the cytoplasmic S6 helix (around S450) is captured by KChIP1 directly and indirectly, through the hydrophobic interactions between Kv4.2 (Y444), Kv4.2 (H479-L482-F493) and KChIP1 (H84) and the electrostatic interactions of Kv4.2 (Y444–K448) with Kv4.2 (H483–E486), respectively (Fig. 2f). Together, these interactions suggest that KChIPs modulate the inactivation and recovery of the Kv4 channel by directly regulating S6 gating, and are consistent with a previous study that suggested that the Kv4 C-terminal region is involved in modulation by KChIPs³³. The amino acid sequence of the C-terminal helix segment (S473–T489) perfectly matches the dendritic targeting motif that is conserved in the Shal family of potassium channels—including Kv4—suggesting that this motif has a dual function as a KChIP-binding site and a dendrite localization signal³⁴.

To examine how the interaction of KChIP1 with the C terminus of Kv4 (S472–D495) affects Kv4 modulation, four alanine-substituted mutant versions of Kv4 were generated (F474A/H478A, H480A, L482A/L485A and H491A/F493A/V494A) on the basis of the hydrophobic interactions with KChIP1 (Fig. 2e). Using two-electrode voltage clamp (TEVC) recording in *Xenopus* oocytes, we assessed the effects of these mutations on activation, inactivation and recovery (Fig. 3, Extended Data Figs. 7, 8, Supplementary Fig. 5, Supplementary Table 1). KChIP1 decelerates the inactivation of wild type Kv4.2 at the early phase of depolarization (OSI), but accelerates inactivation during the late phase (CSI)^{11,24,35} (Fig. 3a, Extended Data Fig. 7a). When expressed alone, all of the Kv4.2 mutants exhibited similar current-time traces to those of the wild type, and the H480A and H491A/F493A/V494A mutants exhibited slightly faster inactivation than the wild type (Fig. 3a, Extended Data Fig. 8, Supplementary Fig. 5a, b, Supplementary Table 1). However, all of the Kv4.2 C-terminal mutants were inactivated more slowly than the wild type in the presence of KChIP1 (Fig. 3a, Extended Data Fig. 8, Supplementary Fig. 5a, b, Supplementary Table 1). In addition, whereas KChIP1 produced a negative voltage shift to activate wild type Kv4.2 in the

conductance–voltage relation, as described in previous reports²⁴, it produced a positive voltage shift to activate all of the Kv4.2 C-terminal mutants (Extended Data Figs. 7b–e, 8, Supplementary Table 1).

Fig. 3: Influence of Kv4.2–KChIP1 interface mutations on KChIP1 modulation.

 figure3

a, Normalized and superposed current traces of wild-type Kv4.2 (WT) (grey) and each mutant (black) with (right) or without (left) KChIP1 elicited by test pulses of 40 mV for the qualitative comparisons of inactivation kinetics ($n = 8$ independent experiments). **b–e**, Comparisons of the recovery rate from inactivation in wild-type Kv4.2 with (black) or without (black and dashed) KChIP1, and in each mutant Kv4.2 (F474A/H478A (**b**), H480A (**c**), L482A/L485A (**d**) and H491A/F493A/V494A (**e**)) with (coloured) or without (coloured and dashed) KChIP1. The currents were elicited by a two-pulse protocol (inset) using prepulses (500 ms) and test pulses (100 ms) at 40 mV with an interpulse interval (Δt) of the duration from 10 to 490 ms at –100 mV. The fractional recovery at each point was determined by normalizing the peak current amplitude of the test pulse by the amplitude of the prepulse. Symbols and bars represent mean \pm s.e.m. ($n = 8$). Lines represent single-exponential fits. For the Kv4.2(F474A/H478A) with KChIP1 and Kv4.2(H480A) with KChIP1 conditions, only data obtained using prepulses from 10 ms to 90 ms were used for single-exponential fits, owing to reduced fractional recovery at longer prepulses.

Next, we assessed the effects of these mutations on voltage-dependent inactivation. KChIP1 shifted the inactivation curve of the wild type to the positive direction, indicating a relative destabilization of the inactivated state³⁵ (Extended Data Figs. 7f–i, 8). Although KChIP1 shifted the inactivation curve of F474A/H478A, H480A and H491A/F493A/V494A mutants to the positive direction, as for the wild type, it shifted that of the L482A/L485A mutant to the negative direction, suggesting that the Kv4.2

C terminus is important for the modulation of steady-state inactivation by KChIP1 (Extended Data Figs. 7f–i, 8, Supplementary Fig. 5c).

Finally, we assessed the effects of the mutations on recovery from inactivation, as KChIP1 reportedly accelerates the recovery from inactivation of Kv4s²⁴. In the absence of KChIP1, all of the Kv4.2 C-terminal mutants exhibited quite similar recovery rates to that of the wild type (Fig. 3b–e, Supplementary Fig. 5d, Extended Data Fig. 8). However, each mutant received a different modulatory effect on the recovery rate by KChIP1 (Fig. 3b–e, Supplementary Fig. 5d, Extended Data Fig. 8). KChIP1 accelerated the recovery rate of the L482A/L485A mutant, but more weakly compared to the wild type (Fig. 3d, Extended Data Fig. 8), whereas it did not affect the recovery rate of the H491A/F493A/V494A mutant (Fig. 3e, Extended Data Fig. 8). KChIP1 accelerated the recovery rate of the F474A/H478A and H480A mutants even more strongly than the wild type, together with an ‘overshoot’ current^{36,37} (Fig. 3b, c, Extended Data Fig. 8). Altogether, these results indicate that the interaction of the Kv4.2 C-terminal segment with KChIP1 affects the gating modulation of Kv4.2.

Structures of Kv4.2–DPP6S and Kv4.2–DPP6S–KChIP1

DPP6 and DPP10 are single-pass transmembrane proteins with a large extracellular domain and a short intracellular segment^{38,39}. DPPs reportedly accelerate the activation, inactivation and recovery of Kv4s^{38,39}. DPPs modulate Kv4s through their single transmembrane helices and short intracellular segments^{40,41}, suggesting that they have modulatory mechanisms that are distinct from those of KChIPs. To investigate how DPPs modulate the properties of Kv4, we solved the structures of the human Kv4.2–DPP6S binary and Kv4.2–DPP6S–KChIP1 ternary complexes (Fig. 1a, Supplementary Fig. 2c, d, Extended Data Table 1). During 3D classification with C1 symmetry, two different classes of structures were obtained, with two or four DPP6S molecules integrated in the complex (Extended Data Figs. 9, 10), which is consistent with the previous stoichiometric analysis of the Kv4–DPP complex⁴². The 3D classes that contained four DPP6S molecules were selected for further 3D refinement with C2 symmetry imposed, because two DPP6S dimers were integrated with C2 symmetry in the complexes (Extended Data Figs. 9, 10, Supplementary Figs. 6, 7). Owing to the flexible position of the large extracellular domains of DPP6S floating above Kv4.2, the overall resolutions are 4.2 Å and 4.5 Å for the Kv4.2–DPP6S and Kv4.2–DPP6S–KChIP1 complexes, respectively (Extended Data Figs. 9, 10). However, the focused refinement improved the resolutions of the transmembrane and intracellular regions to 3.4 Å and 3.9 Å for the Kv4.2–DPP6S and Kv4.2–DPP6S–KChIP1 complexes, respectively (Extended Data Figs. 9, 10). The dimeric crystal structure of the DPP6S extracellular domain⁴³ was used as a guide to construct the atomic models of the Kv4.2–DPP6S and Kv4.2–DPP6S–KChIP1 structures (Fig. 1a, Supplementary Fig. 2c, d). The structures revealed that one DPP6S binds to one Kv4.2 in both complexes

through their transmembrane domains, forming an octamer for Kv4.2–DPP6S and a dodecamer for Kv4.2–DPP6S–KChIP1 (Fig. 1a, Supplementary Fig. 2c,d). In the extracellular region, two DPP6S dimers float above the channel core. Within the intracellular part, most of the N-terminal intracellular segment of DPP6S (around 30 amino acids) is not resolved, indicating its flexibility.

Structures of the Kv4.2–DPP6S and Kv4.2–DPP6S–KChIP1 complexes adopt the S4 up and S6 open conformation, like those of Kv4.2 alone and Kv4.2–KChIP1 (Fig. 1b, Extended Data Figs. 6a, 11). Structural comparisons of Kv4.2–DPP6S and Kv4.2–DPP6S–KChIP1 as well as that of Kv4.2 alone and Kv4.2–KChIP1 further support the role of KChIP1 as a modulator of the Kv4.2 S6 helix by stabilizing the conformations of the Kv4.2 N and C termini as well as the intracellular S6 helix (Fig. 1b,d, Extended Data Fig. 11a–c).

Kv4.2–DPP6S interaction

In the structures of the Kv4.2–DPP6S and Kv4.2–DPP6S–KChIP1 complexes, the DPP6S transmembrane helix hydrophobically interacts with the voltage-sensing domain of Kv4.2, specifically at the lower half of S1 and the upper half of S2 (Fig. 4a, b). This is consistent with a previous domain-swapping study, which suggested that DPP10 interacts with S1 and/or S2 of Kv4.3⁴⁰. Recently, two potassium channel structures (Kv7.1 and Slo1) in complex with a modulatory transmembrane β -subunit have been reported^{44,45}. In both the Kv7.1–KCNE3 and Slo1– β 4 complexes, the β -subunit associates with the transmembrane interface between neighbouring α -subunits (Extended Data Fig. 12). The structure of the Kv4.2–DPP6S complex therefore represents a distinct interaction mode among the potassium channel complexes reported thus far. The interaction of the Kv4.2–DPP6S complex somewhat resembles that of voltage-gated sodium channels, such as the Nav1.4– β 1 and Nav1.7– β 1 complexes, in which the β 1 transmembrane helix interacts with S0 and S2 of Nav (Extended Data Fig. 12), and therefore their modulation mechanisms could be similar^{46,47}. However, the specific involvement of S1 in the Kv4.2–DPP6S interaction suggests the unique modulatory mechanisms of Kv4.

Fig. 4: The interaction of Kv4.2–DPP6S and the influence of Kv4.2–DPP6S interface mutations on DPP6S modulation.

 **figure4**

a, Side and top views of the Kv4.2–DPP6S complex, focused on a single voltage-sensing domain. DPP6S interacts with S1 and S2 of the Kv4.2 voltage sensor. **b**, Residues in Kv4.2 S1–S2 facing the interface on DPP6S are shown. **c–e**, Normalized and superposed current traces of wild-type Kv4.2 (grey) and each mutant Kv4.2 (black) (V190W (**c**), A228W (**d**) and C231W (**e**)) with (right) or without (left) DPP6S elicited by test pulses of 40 mV for the qualitative comparisons of inactivation kinetics ($n = 8$ independent experiments). **f–h**, Comparison of the recovery rate from inactivation in wild-type Kv4.2 with (black circle) or without (white circle) DPP6S, and in each mutant Kv4.2 (V186W (**f**), V190W (**g**) and C231W (**h**)) with (coloured symbol) or without (coloured open symbol) DPP6S, obtained from Supplementary Fig. 11. The fractional recovery at each point was determined by normalizing the peak current amplitude of the test pulse by the amplitude of the prepulse. Symbols and bars represent mean \pm s.e.m. ($n = 8$). Lines represent single-exponential fits.

Although the side chains of the DPP6S transmembrane helix could not be easily assigned owing to the lack of characteristic density (Supplementary Figs. 6–8), the Kv4.2–DPP6S structure revealed seven hydrophobic residues in S1 and S2 of Kv4.2 that face and potentially interact with DPP6S (Fig. 4b). To examine the importance of these residues in the modulation of Kv4.2 by DPP6S, we generated a series of Kv4.2–DPP6S interface mutants by substituting each residue in S1–S2 with tryptophan residue to physically interfere with their potential interaction. When expressed alone, the wild type and all Kv4.2 S1–S2 mutants exhibited similar current-time traces and voltage-dependent activation curves. (Fig. 4c–e, Supplementary Fig. 9). As reported previously³⁸, DPP6S accelerates activation and inactivation and also shifts the voltage-dependent activation curve to more negative membrane potentials (Fig. 4c–e, Extended Data Figs. 8, 13a–g, Supplementary Fig. 9). Although the quite rapid

activation mediated by DPP6S made it difficult to evaluate the effects of the mutations on the activation kinetics, three mutants (V190W in S1; and A228W and C231W in S2) were inactivated more slowly than the wild type in the presence of DPP6S (Fig. 4c–e, Extended Data Fig. 8, Supplementary Fig. 9, Supplementary Table 1). In addition, in the presence of DPP6S these three mutants exhibited smaller negative voltage shifts for channel activation, as compared to the wild type (Extended Data Figs. 8, 13c, e, f).

We next assessed the mutational effects on voltage-dependent inactivation (Extended Data Figs. 8, 13h–n, Supplementary Fig. 10). DPP6S shifted the inactivation curves of the wild type to the negative direction with the steeper voltage dependence, indicating relative stabilization of the inactivated state³⁸ (Extended Data Figs. 8, 13h–n). Five mutants (T182W, V186W, F194W, A228W and C231W) showed a similar negative voltage shift in the presence of DPP6S to that of the wild type (Extended Data Figs. 8, 13h, i, k–m). By contrast, DPP6S shifted the inactivation curves of V190W in S1 and A235W in S2 mutants to the positive direction (Extended Data Figs. 8, 13j, n), suggesting that the S1 and S2 helices of Kv4.2 are important for the modulation of steady-state inactivation by DPP6S.

DPP6S reportedly accelerates the recovery of Kv4.2 from inactivation³⁸ (Fig. 4f–h, Extended Data Figs. 8, 13o–u, Supplementary Fig. 11). However, the V190W and C231W mutants exhibited slower recovery rates than the wild type in the presence of DPP6S, even though the V190W mutant alone recovered faster than the wild type in the absence of DPP6S (Fig. 4g, h, Extended Data Fig. 8). The V186W mutant alone recovered faster than the wild type, which made it difficult to evaluate the effect of DPP6S on this mutant (Fig. 4f, Extended Data Fig. 8). Together, all these results indicate that DPP6S modulates the activation, inactivation and recovery of Kv4.2 through interactions with the S1 and S2 helices of the Kv4.2 voltage-sensing domain.

Conclusions

The structures we present here, combined with complementary electrophysiological analyses, suggest that KChIP1 stabilizes the S6 conformation to modulate synchronized and accelerated gating of the S6 helices within the tetramer, preventing N-type inactivation but promoting fast CSI and recovery. On the other hand, DPP6S may accelerate the voltage-dependent movement of the S4 helices by stabilizing the S1–S2 conformation. KChIP1 and DPP6S do not directly interact with each other, and they interact with distinct structures of Kv4.2 to modulate its gating kinetics in different manners. Therefore, our results suggest that these two distinct modes of modulation additively contribute to evoking A-type currents from the native Kv4 macromolecular complex by eliminating OSI, and accelerating CSI and fast recovery from CSI ('Discussion' in [Methods](#)).

Methods

Data reporting

No statistical methods were used to predetermine sample size. The experiments were not randomized and the investigators were not blinded to allocation during experiments and outcome assessment.

Cloning, expression and purification of Kv4.2–KChIP1, Kv4.2–DPP6S and Kv4.2–KChIP1–DPP6S

The DNAs encoding human Kv4.2, KChIP1 and DPP6S were PCR-amplified from a human brain cDNA library (Zyagen). The C-terminally GFP–8×His-tagged Kv4.2, C-terminally Flag-tagged Kv4.2, N-terminally 8×His–GFP-tagged KChIP1, N-terminally Flag-tagged KChIP1 and C-terminally 8×His-tagged DPP6S were subcloned into the pEG BacMam expression vector. Recombinant baculoviruses of Kv4.2, KChIP1 and DPP6S were generated in *Spodoptera frugiperda* Sf9 cells (American Type Culture Collection, CRL-1711), using the Bac-to-Bac system (Invitrogen). Cultures (3.2 l) of HEK293S GnTI[−] cells (1×10^6 – 1.5×10^6 cells per ml) in Freestyle 293 medium (Gibco) supplemented with 2% FBS were infected with 320 ml of P2 virus mixtures of Kv4.2–GFP–8×His only, Kv4.2–Flag:8×His–GFP–KChIP1 (1:2), Kv4.2–GFP–8×His:DPP6S–8xHis (1:1), or Kv4.2–GFP–8×His:Flag–KChIP1:DPP6S–8×His (1:1:1) for 18–24 h at 37 °C. After adding 10 mM sodium butyrate, the cells were cultured at 30 °C for another 36 h to induce protein expression. The cells expressing Kv4.2–KChIP1, Kv4.2–DPP6S or Kv4.2–DPP6S–KChIP1 complexes were collected and resuspended in 80 ml of buffer consisting of 50 mM Tris, pH 7.4, 150 mM KCl and 2 mM CaCl₂ with protease inhibitor cocktails (Roche), sonicated, and centrifuged at 10,000g for 10 min. The supernatant was further ultracentrifuged at 40,000 rpm for 1 h to precipitate the membrane fraction. The membrane fraction was solubilized by an incubation at 4 °C for 1 h in 50 mM Tris buffer, pH 7.4, containing 150 mM KCl, 2 mM CaCl₂ and 1.5% DDM-0.3% CHS with protease inhibitor cocktails. The cells expressing Kv4.2 alone were collected and directly solubilized by an incubation at 4 °C for 1 h in 50 mM Tris buffer, pH 7.4, containing 150 mM KCl, 2 mM CaCl₂ and 1.5% DDM-0.3% CHS with protease inhibitor cocktails. The cell lysate was cleared by ultracentrifugation at 40,000 rpm for 30 min, and the supernatant was incubated with GFP minimizer nanobody resin for 1 h. The resin was washed with 50 mM Tris buffer, pH 7.4, containing 500 mM KCl, 2 mM CaCl₂ and 0.03% GDN. The GFP tag was cleaved by TEV protease overnight at 4 °C in wash buffer. The Kv4.2 alone and Kv4.2 complexes were further purified by size-exclusion chromatography on a Superose 6 10/300 GL increase column (GE Healthcare) equilibrated with 50 mM Tris

buffer, pH 7.4, 150 mM KCl, 2 mM CaCl₂ and 0.03% GDN. Peak fractions were pooled, concentrated to 1.5–2 mg ml⁻¹ using a 100-kDa MWCO centrifugal device (Amicon), and ultracentrifuged at 4,000g for 10 min before grid preparation.

Grid preparation, data collection and data processing

Quantifoil R1.2/1.3 holey carbon Au grids (Quantifoil) were glow-discharged for 2 min. Afterwards, 3-μl portions of protein samples were applied on the grids, blotted for 4 s with blot force 10 at 100% humidity, and frozen in liquid ethane cooled with liquid nitrogen by using a Vitrobot Mark IV (FEI). Grids were first subjected to Talos Arctica (FEI) with a K2 direct electron detector (Gatan) to screen good ones for data collection using EPU (v.1.19) (FEI). Then, grids were subjected to Titan Krios (FEI) microscopy with a K3 direct electron detector (Gatan). Datasets of Kv4.2–KChIP1, Kv4.2–DPP6S and Kv4.2–DPP6S–KChIP1 complexes were collected with a total dose of around 50 electrons per Å² per 48 frames by the standard mode and datasets of Kv4.2 alone were collected with a total dose of around 50 electrons per Å² per 64 frames by the CDS mode, using SerialEM (v.3.7.10)⁴⁸ in the counting mode with a pixel size of 0.83 Å and defocus range of 0.8 to 1.6 μm. Data were processed and structures were determined with RELION v.3.0 or 3.1. For data processing details, see Extended Data Figs. 3, 4, 9, 10.

Model building

Models were built with Coot⁴⁹. Models for Kv4.2 and KChIP1 were manually built with reference to the crystal structures of the Kv1.2-2.1 chimera (PDB code: 2R9R) and KChIP1 (2I2R). Owing to its flexibility and low-resolution map, modelling for DPP6S was performed by fitting to the crystal structure of DPPX (1XFD), using MOLREP (v.11.7). The structural models were refined with phenix.real_space_refine⁵⁰. The pore radius was calculated with HOLE (v.2.2.004)⁵¹. Graphics were prepared using UCSF Chimera (v.1.14) and CueMol2 (v.2.2.3.443) (<http://www.cuemol.org/>).

Protein expression in *Xenopus laevis* oocytes

The human Kv4.2 (NP_036413.1; wild type and mutants), human KChIP1 (NP_055407.1; wild type), and human DPP6S (NP_001927.3; wild type) genes were cloned into the pGEMHE expression vector⁵². The cRNAs were transcribed using a mMESSAGE mMACHINE T7 Transcription Kit (Thermo Fisher Scientific). Oocytes were surgically taken from female *Xenopus laevis* anaesthetized in water containing 0.15% tricaine (Sigma-Aldrich, E10521) for 15–30 min. They were treated with collagenase (Sigma-Aldrich, C0130) for 6–7 h at room temperature to remove the

follicular cell layer. Defolliculated oocytes of a similar size at stage V or VI were selected and microinjected with 50 nl of cRNA solution. They were then incubated for 1–2 days at 18 °C in MBSH buffer, containing 88 mM NaCl, 1 mM KCl, 2.4 mM NaHCO₃, 10 mM HEPES, 0.3 mM Ca(NO₃)₂, 0.41 mM CaCl₂, and 0.82 mM MgSO₄, pH 7.6, supplemented with 0.1% penicillin–streptomycin solution (Sigma-Aldrich, P4333)^{25,42}. All experiments were approved by the Animal Care Committee of Jichi Medical University and were performed following the institutional guidelines.

Two-electrode voltage clamp recordings

Ionic currents were recorded under two-electrode voltage clamp with an OC-725C amplifier (Warner Instruments) at room temperature. The bath chamber was perfused with ND-96 buffer, containing 96 mM NaCl, 2 mM KCl, 1.8 mM CaCl₂, 1 mM MgCl₂ and 5 mM HEPES, pH 7.5. The microelectrodes were drawn from borosilicate glass capillaries (Harvard Apparatus, GC150TF-10) using a P-1000 micropipette puller (Sutter Instrument) to a resistance of 0.2–0.5 MΩ and filled with 3 M KCl. Generation of voltage-clamp protocols and data acquisition were performed using a Digidata 1550 interface (Molecular Devices) controlled by the pClampex 10.7 software (Molecular Devices). Data were sampled at 10 kHz and filtered at 1 kHz by the pClampfit 10.7 software (Molecular Devices).

Data analysis

For the voltage-dependent activation

The holding potential was −80 mV. After 500 ms of hyperpolarization at −110 mV to remove inactivation, currents were elicited by 400-ms test pulses to membrane potentials from −80 to 40 mV with 10-mV increments. Conductance values were calculated from peak current amplitudes by normalizing to the maximum current amplitude obtained in the experiment, assuming a linear open channel current–voltage relationship and a reversal potential of −98 mV (normalized chord conductance). Normalized peak conductance was plotted versus voltage and fitted with single Boltzmann functions to estimate the half-activation voltage ($V_{1/2,\text{act}}$) and the effective charge (z_{act}) in Extended Data Fig. 8.

Recovery from inactivation

The currents were elicited by a two-pulse protocol using the prepulse (500 ms) and the test pulses (100 ms) at 40 mV with an interpulse interval of the duration from 10 to 490 ms at −100 mV. The fractional recovery at each point was determined by normalizing the peak current amplitude of the test pulse by the amplitude of the

prepulse and fitted with single exponential functions to estimate the recovery time constant (τ_{rec}) in Extended Data Fig. 8. For the Kv4.2 (F474A/H478A) with KChIP1 and Kv4.2 (H480A) with KChIP1 conditions, only data obtained using prepulses from 10 ms to 90 ms were used for single-exponential fits owing to reduced fractional recovery at longer prepulses.

Voltage-dependent prepulse inactivation

The holding potential was -100 mV. After 5 s of prepulses from -120 mV to 0 mV with 10-mV increments, currents were elicited by 250-ms test pulses at 60 mV. The fractional recovery at each point was determined by normalizing the peak current amplitude of the test pulse by the test pulse after the prepulse of -120 mV and fitted with single Boltzmann functions to estimate the half-inactivation voltage ($V_{1/2,\text{inact}}$) and the effective charge (z_{inact}) in Extended Data Fig. 8.

Statistical analysis

The electrophysiological data were expressed as mean \pm s.e.m. ($n = 8$). Differences between wild type and mutants, between wild type with KChIP1 and mutants with KChIP1, and between wild type with DPP6S and mutants with DPP6S were evaluated by Dunnett's test with EZR software⁵³.

Discussion

Modulation by KChIP1

KChIPs reportedly prevent OSI and accelerate CSI and recovery from inactivation^{11,24,35} (Fig. 3, Extended Data Fig. 7a, Supplementary Fig. 5). The structural comparison between Kv4.2 alone and the Kv4.2–KChIP1 complex provides insight into how KChIPs modulate the gating of Kv4s. In the Kv4.2–KChIP1 complex, KChIP1s bind and sequester the both N-terminal inactivation ball and the C terminus (amino acids 472–495) of Kv4.2, which would therefore result in preventing N-type inactivation. Moreover, while S6 gating helices adopt a more flexible conformation with weaker interaction with T1–S1 linkers in the structure of Kv4.2 alone, KChIP1 stabilizes these structures and enhances their interactions in the structure of Kv4.2–KChIP1. These structural changes mediated by KChIPs, together with the following three observations and reports, might explain how KChIPs accelerate the S6 gating of Kv4s, including CSI and recovery from inactivation. First, one KChIP1 stabilizes the S6 conformation as well as the N terminus from the neighbouring subunit of Kv4.2. Second, one KChIP1 also interacts with two T1 domains from neighbouring subunits^{26,27} (Fig. 2b). Third, previous functional studies have suggested that the T1–

S1 linker of Kv4 dodecameric channels undergoes major conformational shifts tightly coupled to movements of the S6 tail^{54,55}, although we do not know what the T1 conformational change is. Together, these structural features mediated by KChIP1 may allow synchronized and accelerated S6 gating to enable fast CSI and recovery (Extended Data Fig. 14a).

Modulation by DPP6

DPP6S reportedly accelerates the activation, inactivation, and recovery of K4 channels³⁸. In the Kv4.2–DPP6S complexes, the single-spanning transmembrane helix of DPP6S apparently stabilizes the structure of S1 and S2 helices because it simultaneously interacts with the lower half of S1 and the upper half of S2 (Fig. 4a, b). DPP6S reportedly accelerates both the outward and the inward movements of the Kv4.2 gating charge after depolarization and repolarization, respectively²⁸. Among the hypotheses to explain the voltage dependency in voltage-gated channels, the hypothesis that S4 slides on the surface formed by S1 and S2 depending on the membrane potential might be most likely¹³. Therefore, the stabilization of the S1–S2 conformation may facilitate the movement of the S4 helices upon depolarization and repolarization, which could explain the fast kinetics of activation and recovery from the closed inactivated state (Extended Data Fig. 14b).

Previous studies suggest that DPP6S accelerates both OSI and CSI of Kv4s^{39,56} (Extended Data Fig. 14b). The acceleration of OSI by DPP6S could involve the N-terminal intracellular domain of DPP6S and the N terminus of Kv4s³⁹; however, both regions are disordered in the structure of Kv4.2–DPP6S and further investigations are required. Previous studies suggest that the dynamic interaction of the S4–S5 linker and the S6 gate is the molecular basis of CSI^{12,22}. Therefore, the acceleration of CSI by DPP6S could be, at least in part, attributed to the accelerated conformational change of S4 as discussed above (Extended Data Fig. 14b).

Modulation in the Kv4 macromolecular ternary complex

Native Kv4s form macromolecular ternary complex with KChIPs and DPPs. The structure of the Kv4.2–DPP6S–KChIP1 dodecameric complex (Fig. 1a) supports the additive contribution of KChIPs and DPPs to the modulation of Kv4s in the ternary complex. KChIP1 and DPP6S interact with distinct structures of Kv4.2 to modulate its gating kinetics in different manners (Figs. 1a, 2, 4a). In addition, KChIP1 and DPP6S do not interact with each other. Overall, the modulatory mechanisms of Kv4.2 by KChIP1 and DPP6S are different, and therefore, native Kv4s form ternary macromolecular complexes with both KChIPs and DPPs to exhibit eliminated OSI, accelerated CSI and fast recovery rate from CSI⁵ (Extended Data Fig. 14c).

Structurally mechanistic elucidations of CSI will further clarify the mechanisms of modulation by KChIPs and DPPs.

Insight into closed-state inactivation of Kv4.2

The structural correlates of Kv4 in closed-state inactivation (CSI) remain unknown. Previous studies have proposed that the interaction between the S4–S5 linker and S6 in Kv4s, which couples the S4 movement to S6 gating in Kv1, might be lost following the upshifted movement of S4 during depolarization^{12,21,22} (Extended Data Fig. 1b). Indeed, the amino acid sequences of Kv4 around the S4–S5 linker and S6 on the intracellular side are unique among the Shaker-related Kv subfamilies (Kv1–Kv4) (Supplementary Fig. 12a), and mutations of these regions affect the CSI kinetics of Kv4^{21,22} (Supplementary Fig. 12b). In addition, the open conformation of Kv4.2 complexes revealed several Kv4-specific residues involved in the intra-subunit interactions between the S4–S5 linker and S6, as well as the inter-subunit interactions between the S4–S5 linker and S5 (Supplementary Fig. 12a,c,d). Further study of this ‘pre-closing’ conformation may lead to elucidating the mechanism of CSI. Together, future structural studies of the resting and closed inactivated states will provide more mechanistic insights into Kv4 channel gating, CSI and modulation by auxiliary subunits.

Reporting summary

Further information on research design is available in the [Nature Research Reporting Summary](#) linked to this paper.

Data availability

The cryo-EM density maps and atomic coordinates have been deposited in the Electron Microscopy Data Bank (EMDB). The accession codes for the maps are [EMD-31433](#) (Kv4.2–KChIP1-whole (map A)), [EMD-31009](#), (Kv4.2–KChIP1-whole (map A)), [EMD-31005](#) (Kv4.2–KChIP1-TM (map B)), [EMD-31013](#) (Kv4.2–DPP6S-whole (map E)), [EMD-31011](#) (Kv4.2–DPP6S-TM and cyto (map F)), [EMD-31012](#) (Kv4.2–DPP6S-TM and EC (map G)), [EMD-31019](#) (Kv4.2–DPP6S–KChIP1-whole (map H)), [EMD-31016](#) (Kv4.2–DPP6S–KChIP1 (TM and cyto (map I)), [EMD-31018](#) (Kv4.2–DPP6S–KChIP1-TM and EC (map J)) and [EMD-31399](#) (Kv4.2 alone (map X)). The PDB accession codes for the coordinates are [7F3F7E84](#) (Kv4.2–KChIP1-whole), [7E83](#) (Kv4.2–KChIP1-cyto), [7E7Z](#) (Kv4.2–KChIP1-TM), [7E8B](#) (Kv4.2–DPP6S-whole), [7E87](#) (Kv4.2–DPP6S-TM and cyto), [7E89](#) (Kv4.2–DPP6S-EC), [7E8H](#) (Kv4.2–DPP6S–KChIP1-whole), [7E8E](#) (Kv4.2–DPP6S–KChIP1-TM and cyto), [7E8G](#)

(Kv4.2–DPP6S–KChIP1-EC) and [7F0J](#) (Kv4.2 alone). For detail, see also Extended Data Table [1](#), Extended Data Figs. [3](#), [4](#), [9](#), [10](#).

References

1. 1.

Li, Y., Um, S. Y. & McDonald, T. V. Voltage-gated potassium channels: regulation by accessory subunits. *Neuroscientist* **12**, 199–210 (2006).

2. 2.

Coetzee, W. A. et al. Molecular diversity of K⁺ channels. *Ann. N. Y. Acad. Sci.* **868**, 233–285 (1999).

3. 3.

Zemel, B. M., Ritter, D. M., Covarrubias, M. & Muqeem, T. A-type Kv channels in dorsal root ganglion neurons: diversity, function, and dysfunction. *Front. Mol. Neurosci.* **11**, 253 (2018).

4. 4.

Covarrubias, M. et al. The neuronal Kv4 channel complex. *Neurochem. Res.* **33**, 1558–1567 (2008).

5. 5.

Amarillo, Y. et al. Ternary Kv4.2 channels recapitulate voltage-dependent inactivation kinetics of A-type K⁺ channels in cerebellar granule neurons. *J. Physiol.* **586**, 2093–2106 (2008).

6. 6.

O’Malley, H. A. & Isom, L. L. Sodium channel β subunits: emerging targets in channelopathies. *Annu. Rev. Physiol.* **77**, 481–504 (2015).

7. 7.

Catterall, W. A. Voltage-gated calcium channels. *Cold Spring Harb. Perspect. Biol.* **3**, a003947 (2011).

8. 8.

Catterall, W. A., Wisedchaisri, G. & Zheng, N. The chemical basis for electrical signaling. *Nat. Chem. Biol.* **13**, 455–463 (2017).

9. 9.

McCoy, J. G. & Nimigean, C. M. Structural correlates of selectivity and inactivation in potassium channels. *Biochim. Biophys. Acta* **1818**, 272–285 (2012).

10. 10.

Dixon, J. E. et al. Role of the Kv4.3 K⁺ channel in ventricular muscle. A molecular correlate for the transient outward current. *Circ. Res.* **79**, 659–668 (1996).

11. 11.

Jerng, H. H., Pfaffinger, P. J. & Covarrubias, M. Molecular physiology and modulation of somatodendritic A-type potassium channels. *Mol. Cell. Neurosci.* **27**, 343–369 (2004).

12. 12.

Bähring, R. & Covarrubias, M. Mechanisms of closed-state inactivation in voltage-gated ion channels. *J. Physiol.* **589**, 461–479 (2011).

13. 13.

Blunck, R. & Batulan, Z. Mechanism of electromechanical coupling in voltage-gated potassium channels. *Front. Pharmacol.* **3**, 166 (2012).

14. 14.

Bähring, R., Barghaan, J., Westermeier, R. & Wollberg, J. Voltage sensor inactivation in potassium channels. *Front. Pharmacol.* **3**, 100 (2012).

15. 15.

Fineberg, J. D., Szanto, T. G., Panyi, G. & Covarrubias, M. Closed-state inactivation involving an internal gate in Kv4.1 channels modulates pore blockade by intracellular quaternary ammonium ions. *Sci. Rep.* **6**, 31131 (2016).

16. 16.

Fineberg, J. D., Ritter, D. M. & Covarrubias, M. Modeling-independent elucidation of inactivation pathways in recombinant and native A-type Kv channels. *J. Gen. Physiol.* **140**, 513–527 (2012).

17. 17.

Dougherty, K., Santiago-Castillo, J. A. & Covarrubias, M. Gating charge immobilization in Kv4.2 channels: the basis of closed-state inactivation. *J. Gen. Physiol.* **131**, 257–273 (2008).

18. 18.

Kaulin, Y. A., Santiago-Castillo, J. A., Rocha, C. A. & Covarrubias, M. Mechanism of the modulation of Kv4:KChIP-1 channels by external K⁺. *Biophys. J.* **94**, 1241–1251 (2008).

19. 19.

Vardanyan, V. & Pongs, O. Coupling of voltage-sensors to the channel pore: a comparative view. *Front. Pharmacol.* **3**, 145 (2012).

20. 20.

Gebauer, M. et al. N-type inactivation features of Kv4.2 channel gating. *Biophys. J.* **86**, 210–223 (2004).

21. 21.

Barghaan, J. & Bähring, R. Dynamic coupling of voltage sensor and gate involved in closed-state inactivation of kv4.2 channels. *J. Gen. Physiol.* **133**, 205–224 (2009).

22. 22.

Wollberg, J. & Bähring, R. Intra- and intersubunit dynamic binding in Kv4.2 channel closed-state inactivation. *Biophys. J.* **110**, 157–175 (2016).

23. 23.

Kaulin, Y. A. et al. The dipeptidyl-peptidase-like protein DPP6 determines the unitary conductance of neuronal Kv4.2 channels. *J. Neurosci.* **29**, 3242–3251 (2009).

24. 24.

An, W. F. et al. Modulation of A-type potassium channels by a family of calcium sensors. *Nature* **403**, 553–556 (2000).

25. 25.

Kitazawa, M., Kubo, Y. & Nakajo, K. The stoichiometry and biophysical properties of the Kv4 potassium channel complex with K⁺ channel-interacting protein (KChIP) subunits are variable, depending on the relative expression level. *Biol. Chem.* **289**, 17597–17609 (2014).

26. 26.

Pioletti, M., Findeisen, F., Hura, G. L. & Minor, D. L. Jr. Three-dimensional structure of the KChIP1–Kv4.3 T1 complex reveals a cross-shaped octamer. *Nat. Struct. Mol. Biol.* **13**, 987–995 (2006).

27. 27.

Wang, H. et al. Structural basis for modulation of Kv4 K⁺ channels by auxiliary KChIP subunits. *Nat. Neurosci.* **10**, 32–39 (2007).

28. 28.

Dougherty, K. & Covarrubias, M. A dipeptidyl aminopeptidase-like protein remodels gating charge dynamics in Kv4.2 channels. *J. Gen. Physiol.* **128**, 745–753 (2006).

29. 29.

Kim, L. A. et al. Three-dimensional structure of I_{to}; Kv4.2–KChIP2 ion channels by electron microscopy at 21 Å resolution. *Neuron* **41**, 513–519 (2004).

30. 30.

Long, S. B., Campbell, E. B. & Mackinnon, R. Crystal structure of a mammalian voltage-dependent Shaker family K⁺ channel. *Science* **309**, 897–903 (2005).

31. 31.

Long, S. B., Tao, X., Campbell, E. B. & MacKinnon, R. Atomic structure of a voltage-dependent K⁺ channel in a lipid membrane-like environment. *Nature* **450**, 376–382 (2007).

32. 32.

Tao, X., Lee, A., Limapichat, W., Dougherty, D. A. & MacKinnon, R. A gating charge transfer center in voltage sensors. *Science* **328**, 67–73 (2010).

33. 33.

Callsen, B., et al. Contribution of N- and C-terminal Kv4.2 channel domains to KChIP interaction. *J. Physiol.* **568**, 397–412 (2005).

34. 34.

Rivera, J. F., Ahmad, S., Quick, M. W., Liman, E. R. & Arnold, D. B. An evolutionarily conserved dileucine motif in Shal K⁺ channels mediates dendritic targeting. *Nat. Neurosci.* **6**, 243–250 (2003).

35. 35.

Beck, E. J., Bowlby, M., An, W. F., Rhodes, K. J. & Covarrubias, M. Remodelling inactivation gating of Kv4 channels by KChIP1, a small-molecular-weight calcium-binding protein. *J. Physiol.* **538**, 691–706 (2002).

36. 36.

Wettwer, E., Amos, G. J., Posival, H. & Ravens, U. Transient outward current in human ventricular myocytes of subepicardial and subendocardial origin. *Circ. Res.* **75**, 473–482 (1994).

37. 37.

Radicke, S. et al. Functional modulation of the transient outward current Ito by KCNE beta-subunits and regional distribution in human non-failing and failing hearts. *Cardiovasc. Res.* **71**, 695–703 (2006).

38. 38.

Nadal, M. S. et al. The CD26-related dipeptidyl aminopeptidase-like protein DPPX is a critical component of neuronal A-type K⁺ channels. *Neuron* **37**, 449–461 (2003).

39. 39.

Jerng, H. H., Qian, Y. & Pfaffinger, P. J. Modulation of Kv4.2 channel expression and gating by dipeptidyl peptidase 10 (DPP10). *Biophys. J.* **87**, 2380–2396 (2004).

40. 40.

Ren, X., Hayashi, Y., Yoshimura, N. & Takimoto, K. Transmembrane interaction mediates complex formation between peptidase homologues and Kv4 channels. *Mol. Cell. Neurosci.* **29**, 320–332 (2005).

41. 41.

Dougherty, K., Tu, L., Deutsch, C. & Covarrubias, M. The dipeptidyl-aminopeptidase-like protein 6 is an integral voltage sensor-interacting β-subunit of neuronal Kv4.2 channels. *Channels* **3**, 122–128 (2009).

42. 42.

Kitazawa, M., Kubo, Y. & Nakajo, K. Kv4.2 and accessory dipeptidyl peptidase-like protein 10 (DPP10) subunit preferentially form a 4:2 (Kv4.2:DPP10) channel complex. *J. Biol. Chem.* **290**, 22724–22733 (2015).

43. 43.

Strop, P., Bankovich, A. J., Hansen, K. C., Garcia, K. C. & Brunger, A. T. Structure of a human A-type potassium channel interacting protein DPPX, a member of the dipeptidyl aminopeptidase family. *J. Mol. Biol.* **343**, 1055–1065 (2004).

44. 44.

Sun, J. & MacKinnon, R. Structural basis of human KCNQ1 modulation and gating. *Cell* **180**, 340–347 (2020).

45. 45.

Tao, X. & MacKinnon, R. Molecular structures of the human Slo1 K⁺ channel in complex with β4. *eLife* **8**, e51409 (2019).

46. 46.

Pan, X. et al. Structure of the human voltage-gated sodium channel Nav1.4 in complex with β1. *Science* **362**, eaau2486 (2018).

47. 47.

Shen, H., Liu, D., Wu, K., Lei, J. & Yan, N. Structures of human Nav1.7 channel in complex with auxiliary subunits and animal toxins. *Science* **363**, 1303–1308

(2019).

48. 48.

Mastronarde, D. N. Automated electron microscope tomography using robust prediction of specimen movements. *J. Struct. Biol.* **152**, 36–51 (2005).

49. 49.

Emsley, P., Lohkamp, B., Scott, W. G. & Cowtan, K. Features and development of Coot. *Acta Crystallogr. D* **66**, 486–501 (2010).

50. 50.

Afonine, P. V., Grosse-Kunstleve, R. W., Adams, P. D. & Urzhumtsev, A. Bulk-solvent and overall scaling revisited: faster calculations, improved results. *Acta Crystallogr. D* **69**, 625–634 (2013).

51. 51.

Smart, O. S., Neduvvelil, J. G., Wang, X., Wallace, B. A. & Sansom, M. S. HOLE: a program for the analysis of the pore dimensions of ion channel structural models. *J. Mol. Graph.*, **14**, 354–360 (1996).

52. 52.

Liman, E., Tytgat, J. & Hess, P. Subunit stoichiometry of a mammalian K⁺ channel determined by construction of multimeric cDNAs. *Neuron* **9**, 861–871 (1992).

53. 53.

Kanda, Y. Investigation of the freely available easy-to-use software ‘EZR’ for medical statistics. *Bone Marrow Transplant.* **48**, 452–458 (2013).

54. 54.

Wang, G. et al. Functionally active t1–t1 interfaces revealed by the accessibility of intracellular thiolate groups in kv4 channels. *J. Gen. Physiol.* **126**, 55–69 (2005).

55. 55.

Wang, G. & Covarrubias, M. Voltage-dependent gating rearrangements in the intracellular T1–T1 interface of a K⁺ channel. *J. Gen. Physiol.* **127**, 391–400 (2006).

56. 56.

Barghaan, J., Tozakidou, M., Ehmke, H. & Bähring, R. Role of N-terminal domain and accessory subunits in controlling deactivation-inactivation coupling of Kv4.2 channels. *Biophys. J.* **94**, 1276–1294 (2008).

57. 57.

Lee, C. H. & MacKinnon, R. Voltage sensor movements during hyperpolarization in the HCN channel. *Cell* **179**, 1582–1589 (2019).

Acknowledgements

We thank the members of the O.N. laboratory and the staff scientists at the University of Tokyo's cryo-EM facility, especially Y. Sakamaki, H. Yanagisawa, A. Tsutsumi, M. Kikkawa and R. Danev. This work was supported by a MEXT Grant-in-Aid for Specially Promoted Research (grant number 16H06294) and JST Core Research for Evolutional Science and Technology (CREST) (grant number 20344981) to O.N.; by KAKENHI (grant numbers 18K06207 to Y.K. and 20H03200 to G.K.); and by the Platform Project for Supporting Drug Discovery and Life Science Research (Basis for Supporting Innovative Drug Discovery and Life Science Research) from AMED under grant number JP19am01011115 (support number 1110). Y.K. was also supported by Uchang Cho Institute of Science.

Author information

Author notes

1. Kan Kobayashi

Present address: Peptidream, Kawasaki, Japan

2. Tomohiro Nishizawa

Present address: Graduate School of Medical Life Science, Yokohama City University, Yokohama, Japan

3. These authors contributed equally: Yoshiaki Kise, Go Kasuya

Affiliations

1. Department of Biological Sciences, Graduate School of Science, The University of Tokyo, Tokyo, Japan

Yoshiaki Kise, Hiroyuki H. Okamoto, Daichi Yamanouchi, Kan Kobayashi, Tsukasa Kusakizako, Tomohiro Nishizawa & Osamu Nureki

2. Division of Integrative Physiology, Department of Physiology, Jichi Medical University, Shimotsuke, Japan

Go Kasuya & Koichi Nakajo

Contributions

Y.K. designed the whole study. Y.K. performed the cryo-EM analyses, with sample preparation assistance from H.H.O. and D.Y. Y.K., K.K., T.K. and T.N. performed cryo-EM data collection and processing. Y.K., G.K. and K.N. designed and G.K performed the electrophysiological experiments, and G.K. and K.N. analysed the data. Y.K. performed model building and model refinement with assistance from T.N. and T.K. Y.K. wrote the initial manuscript. Y.K., G.K., K.N. and O.N. edited the manuscript with help from all of the other authors. Y.K., G.K. and O.N. supervised all of the research.

Corresponding authors

Correspondence to Yoshiaki Kise, Go Kasuya or Osamu Nureki.

Ethics declarations

Competing interests

The authors declare no competing interests.

Additional information

Peer review information *Nature* thanks Manuel Covarrubias and the other, anonymous, reviewer(s) for their contribution to the peer review of this work. Peer reviewer reports are available.

Publisher's note Springer Nature remains neutral with regard to jurisdictional claims in published maps and institutional affiliations.

Extended data figures and tables

Extended Data Fig. 1 Kv4-specific gating mechanism.

Comparison of the inactivation mechanisms between Kv4 and Kv1. R: resting state; C: closed activated state; O: open activated state; OSI: open inactivated state (open state inactivation); CSI: closed inactivated state (closed state inactivation). Upon depolarization, Kv4 adopts CSI to become inactivated. CSI involves the closure of the S6 gate. OSI plays a minor role in Kv4 inactivation, although it is the main pathway to become inactivated in Kv1. Upon repolarization, Kv4 returns to the resting state (R) from CSI with the milliseconds order of the fast recovery rate whereas Kv1 returns to the resting state from OSI with the tens of seconds of the slow recovery rate. For a detailed schematic explanation, please see (b) below. **a.** Gating model of Kv4 without auxiliary subunits. Upon depolarization, the S4 (green) adopts the “up” conformation (closed activated: C), and then the S6 gate opens via the interaction with the S4-S5 linker (orange) to form the open activated conformation (O). After activation, Kv4 takes two distinct inactivation pathways. Open activated Kv4 (O) goes to an open inactivated state (OSI) through the occlusion of the pore by its own N-terminus (N-ball), which is characterized by fast inactivation kinetics and called N-type inactivation or open state inactivation (OSI). However, the open inactivated state of Kv4 (OSI) is not stable, and Kv4 reverts to a closed activated state (C) and then goes to a closed inactivated state (CSI). This process is characterized by slower inactivation kinetics than OSI and referred to as closed state inactivation (CSI) through the S6 closing and S4 conformational change. It should be noted that CSI is still a fast millisecond-order process. As a result, during depolarization Kv4 accumulates in a closed inactivated state (CSI). Upon repolarization, Kv4 recovers from CSI to the resting state (R) through the sliding down of S4 and the conformational change of S6.

Extended Data Fig. 2 Expression and purification of Kv4.2 alone and the Kv4.2–KChIP1, Kv4.2–DPP6S and Kv4.2–DPP6S–KChIP1 complexes.

a. Fluorescence-detection size exclusion chromatography (FSEC) analyses of the Kv4.2 α -subunit alone or in complex with KChIP1 or DPP6S. The human full-length Kv4.2 alone showed a relatively broad but still monodisperse peak. When co-expressed with KChIP1 or DPP6S, Kv4.2 showed a monodisperse and sharp peak with high expression. **b.** FSEC analyses of the Kv4.2–KChIP1, Kv4.2–DPP6S, and Kv4.2–DPP6S–KChIP1 complexes. **c.** Representative size-exclusion chromatography (SEC) profile of the Kv4.2 alone (left) and SDS-PAGE of the SEC peak fractions stained by

Coomassie Brilliant Blue (CBB) (right). Fractions indicated by red bars were pooled for cryo-EM grid preparation. **d**. Representative SEC profile of the Kv4.2–KChIP1 complex (left) and SDS-PAGE of the SEC peak fractions stained by CBB (right). Fractions indicated by red bars were pooled for cryo-EM grid preparation. **e**. Representative SEC profile of the Kv4.2–DPP6S complex (left) and SDS-PAGE of the SEC peak fractions stained by CBB (right). **f**. Representative SEC profile of Kv4.2–DPP6S–KChIP1 complex (left) and SDS-PAGE of the SEC peak fractions stained by CBB (right).

Extended Data Fig. 3 Cryo-EM micrograph, data processing and electron microscopy map of Kv4.2 alone.

Each step of data processing leading to the final structure of Kv4.2 alone and representative images of cryo-EM micrograph and 2D classes are shown.

Extended Data Fig. 4 Cryo-EM micrograph, data processing and electron microscopy map of the Kv4.2–KChIP1 complex.

Each step of data processing leading to the final structure of Kv4.2–KChIP1 complex and representative images of cryo-EM micrograph and 2D classes are shown.

Extended Data Fig. 5 Structures of the Kv4.2 α -subunit protomer in the presence and absence of KChIP1 and comparison with the Kv1.2-2.1 chimera.

- a.** Structure of the Kv4.2 α -subunit protomer in the Kv4.2–KChIP1 complex. The T1 domain is located beneath the transmembrane domain at a distance of 25 Å. Note that the transmembrane S6_{TM} helix further extends toward the intracellular region, as indicated by the S6_{cyto} (to S450) and C-terminal segment (S472-D495). Residues 496–630 are disordered and most of this region is predicted to lack secondary structure (**f**).
- b.** Structural comparison of Kv4.2–KChIP1 with the Kv1.2-2.1 chimera, superimposed by transmembrane domains. The overall structure of the transmembrane domain of Kv4.2 is similar to the structures of the Kv1.2-2.1 paddle chimera. Note that the two T1 domains do not superimpose on each other. The Kv1.2-2.1 chimera does not have an intracellular S6 helix.
- c.** The intracellular S6 helix of Kv4.2 alone bends at the interface on the T1-S1 linker (dashed ellipse) and is subsequently disordered. In contrast, the S6 helix of Kv4.2–KChIP1 complex extends straight toward KChIP1.
- d.** Close-up view of the superimposed image in the dashed ellipse in (**c**). The intracellular S6 of Kv4.2 starts bending from A419 and extend away from the T1-S1 linker in the Kv4.2 alone. However, it keeps a close distance to T1-S1 linker without bending in the Kv4.2–KChIP1 complex.
- e.** In the Kv4.2–KChIP1 complex, the intracellular S6 and

T1-S1 linker interact via electrostatic interactions (right). In the Kv4.2 alone, the intracellular S6 largely dissociates from the T1-S1 linker (left). **f**. Prediction of the secondary structure of Kv4.2 by PSIPRED. Most of the region consisting of residues 496-630 is predicted to lack secondary structure. **g**. Structural comparison of Kv4.2–KChIP1 with the Kv1.2-2.1 chimera, superimposed by the T1 domains. The two T1 domains fit very well, but the transmembrane domains do not. **h**. Different directions of the C-terminal part of T1 domains, resulting in distinct topologies between Kv4.2 and the Kv1.2-2.1 chimera. Side (left) and top (right) views of the T1 domains are shown. **i**. Superimposition of the protomers of Kv4.2 alone and the Kv4.2-KChIP1 complex shows that the T1 domains of Kv4.2 overlap and retain the same topology in the presence and absence of KChIP1. **j**. When the Kv4.2-T1 domain is aligned with the Kv1.2-T1 topology (shown by translucent structure), the Kv4.2 S6 helix clashes with KChIP1 and does not interact with a T1-S1-linker.

Extended Data Fig. 6 Kv4.2 adopts the S4 up and S6 open conformation.

a. Structures of the voltage sensors (S1-S4) from Kv1.2-2.1, Kv4.2 alone, Kv4.2–KChIP1, Kv4.2–DPP6S, and Kv4.2–DPP6S–KChIP1. S4 helices are coloured. Arg/Lys gating charges as well as other key residues are shown with side chains. The positions of positively charged amino acid residues in the S4 helix relative to a phenylalanine residue in the S2 helix indicates that the present S4 helix of Kv4.2 adopts the depolarized “up” conformation in all of four structures. **b**. Alignment of S4 amino acid sequences among the closely related Kv1 to Kv4. **c**. Radii of the pores of Kv4.2 alone, Kv4.2–KChIP1, and the Kv1.2-2.1 chimera, calculated using the HOLE program. **d**. The density map of the Kv4.2–KChIP1 complex at the selectivity filter shows the averaged densities of potassium ions and water. The S6 helix forming the pore adopts an open conformation, with the selectivity filter occupied by dehydrated K⁺ ions and water molecules, through the close interaction with the S4-S5 linker, as observed in the Kv1.2 structure³⁰ (Extended Data Figs. [5a](#),[b](#)). The previous electrophysiological studies reported that upon depolarization, Kv4s adopt the closed conformation (i.e. CSI) at all physiologically relevant membrane potentials within a cell^{[11](#),[12](#),[13](#),[14](#),[15](#),[16](#),[17](#),[18](#)} (Extended Data Fig. [1](#)). This discrepancy could be attributed to the micelle which is likely to facilitate the open conformation. Similar inconsistent example was observed in the cryo-EM structure of the HCN channel in a hyperpolarized conformation in which the pore is closed while it is open within a cell^{[57](#)}.

Extended Data Fig. 7 Influence of Kv4.2–KChIP1 interface mutations on KChIP1 modulation of activation and inactivation.

a. Normalized and superposed current traces of WT with (black) or without (gray) KChIP1 elicited by test pulses of 40 mV for the qualitative comparisons of inactivation kinetics ($n = 8$ independent experiments). **b–e.** Peak conductance-Voltage (G_p-V) relationships of WT with (black circle) or without (white circle) KChIP1, and each mutant with (coloured symbol) or without (coloured open symbol) KChIP1 obtained from Supplementary Fig. 5a. Symbols and bars represent means \pm s.e.m. ($n = 8$). **f–i.** Comparison of the voltage-dependent prepulse inactivation for WT with (black circle) or without (white circle) KChIP1, and each mutant with (coloured symbol) or without (coloured open symbol) KChIP1 obtained from Supplementary Fig. 5c.

Extended Data Fig. 8 Summary of parameters for wild-type Kv4.2 and Kv4.2 mutants and inactivation kinetics obtained at 40 mV.

a. The number of the half-activation voltage ($V_{1/2,\text{act}}$) and effective charge (z_{act}) of the voltage-dependent activation experiments obtained by single Boltzmann fittings, the inactivation voltage ($V_{1/2,\text{inact}}$) and effective charge (z_{inact}) of the recovery from inactivation experiments obtained by single Boltzmann fittings, and the recovery time constant (τ_{rec}) of the recovery from inactivation experiments obtained by single exponential fittings are listed as average \pm s.e.m. Statistical significance was determined by Dunnett's test. *, **, and *** denote $P < 0.05$, $P < 0.01$, and $P < 0.001$ for each mutant compared to WT, for each mutant with KChIP1 compared to WT with KChIP1, and each mutant with DPP6S compared to WT with DPP6S. For Kv4.2 F474A/H478A with KChIP1 and Kv4.2 H480A with KChIP1 conditions, only data obtained using prepulses from 10 ms to 90 ms were used for single-exponential fits to calculate the recovery time constant owing to reduced fractional recovery at longer prepulses (marked as #). **b.** Fractional contribution of the slow inactivation component ($A_{\text{slow}}/(A_{\text{slow}} + A_{\text{fast}})$) at 40 mV. **c.** The slow (τ_{slow} ; white) and fast (τ_{fast} ; gray) inactivation time constants at 40 mV. Bars represent means \pm s.e.m. ($n = 8$). Inactivation time constants (τ_{slow} and τ_{fast}) and the corresponding amplitude (A_{slow} and A_{fast}) were obtained by fitting the inactivation time course to a sum of two exponentials.

Extended Data Fig. 9 Cryo-EM micrograph, data processing and electron microscopy map of the Kv4.2–DPP6S complex.

Focused refinement at TM-intracellular part and TM-extracellular part was applied to improve the resolution of each part. The local resolutions of each density map and model building at TM region are shown in Supplementary Fig. 6.

Extended Data Fig. 10 Cryo-EM micrograph, data processing and electron microscopy map of the Kv4.2–DPP6S–KChIP1 complex.

Focused refinement at TM-intracellular part and TM-extracellular part was applied to improve the resolution of each part. Model building at TM region is shown in Supplementary Fig. 7.

Extended Data Fig. 11 Structural comparison of N- and C-terminal conformations in the presence and absence of KChIP1.

a. Structural comparison of the Kv4.2 protomers from Kv4.2 alone, Kv4.2–KChIP1, Kv4.2–DPP6S, and Kv4.2–DPP6S–KChIP1, showing that both the N- and C-terminal regions are disordered in the absence of KChIP1 as observed in the structure of Kv4.2–DPP6S and Kv4.2 alone. Both terminal regions are resolved in the structure of Kv4.2–DPP6S–KChIP1 and Kv4.2–KChIP1. **b.** Comparison of the Kv4.2 S6 conformations. The intracellular S6 helices of Kv4.2–DPP6S and Kv4.2 alone bend at the interface on the T1-S1 linker (dashed ellipse in the superimposed image) and is subsequently disordered. By contrast, the S6 helices of Kv4.2–DPP6S–KChIP1 and Kv4.2–KChIP1 complexes extend straight toward KChIP1. **c.** Close-up view of the superimposed image in the dashed box in (b). The intracellular S6 of Kv4.2 bend and extend away from the T1-S1 linker in the Kv4.2–DPP6S complex and Kv4.2 alone. However, it keeps a close distance to T1-S1 linker without bending in the Kv4.2–DPP6S–KChIP1 and Kv4.2–KChIP1 complexes. **d.** Superimposition of the four Kv4.2 structures reveals that the S6 helices adopt an open conformation in all structures.

Extended Data Fig. 12 Kv4-specific interaction with the transmembrane β-subunit revealed by structural comparisons with other potassium and sodium channel complexes.

Side and top views (without extracellular domain) of the Kv4.2–DPP6S–KChIP1, Kv7.1-KCNE3-CaM, Slo1-β4, and Nav1.7-β1-β2 complexes are shown from left to right. EC: extracellular region; TM: transmembrane region; IC: intracellular region. Dotted boxes in the side views highlight the interface of the channel α subunits and β subunits, and close-up views are shown (bottom). Note that a single DPP6S interacts with S1-S2 of a single voltage-sensing domain (VSD), whereas KCNE3 and β4 interact with the interface between two neighbouring α subunits in the Kv7.1 and Slo1 complexes, respectively. The interaction of Nav1.7 and β1 is rather similar to that of Kv4.2–DPP6S, in that a single β subunit interacts with a single VSD. However, the interaction of Kv4.2 and DPP6S is unique, because S1 of Nav1.7 is not involved in the interaction with β1.

Extended Data Fig. 13 Influence of Kv4.2–DPP6S interface mutations on DPP6S modulation.

a-g. Peak conductance-Voltage (G_p-V) relationships of WT with (black circle) or without (white circle) DPP6S, and each mutant with (coloured symbol) or without (coloured open symbol) DPP6S obtained from Supplementary Fig. 9a. Symbols and bars represent means \pm s.e.m. ($n = 8$). **h-n.** Comparison of the voltage-dependent prepulse inactivation for WT with (black circle) or without (white circle) DPP6S, and each mutant with (coloured symbol) or without (coloured open symbol) DPP6S obtained from Supplementary Fig. 10. The fractional recovery at each point was determined by normalizing the peak current amplitude of the test pulse by the test pulse after the prepulse of -120 mV and fitted with single Boltzmann functions. Symbols and bars represent means \pm s.e.m. ($n = 8$). **o-u.** Comparison of the recovery rate from inactivation among WT with (black circle) or without (white circle) DPP6S and each mutant with (coloured symbol) or without (coloured open symbol) DPP6S, obtained from Supplementary Fig. 11. The fractional recovery at each point was determined by normalizing the peak current amplitude of the test pulse by the amplitude of the prepulse. Symbols and bars represent means \pm s.e.m. ($n = 8$). Lines represent single-exponential fits.

Extended Data Fig. 14 Model for Kv4 modulation by KChIP and DPP.

a. Model for Kv4 modulation by KChIP. KChIPs capture the Kv4 N- and C-termini, thereby inhibiting open state inactivation (OSI). On the other hand, KChIPs stabilize the S6 conformation and might enable synchronized movement of the four S6 gating helices, thereby accelerating closed state inactivation and recovery. **b.** Model for Kv4 modulation by DPP. DPPs might stabilize the conformation of Kv4 S1-S2 and facilitate S4 conformational change, including S4 sliding up and down, thereby accelerating activation, inactivation, and recovery. **c.** Model for Kv4 modulation in the Kv4–DPP–KChIP ternary complex. KChIPs capture the Kv4 N- and C-termini of two adjacent subunits, thereby prevent open state inactivation (OSI). As a result, Kv4 ternary complex preferentially inactivates from a closed activated state (CSI). In addition, KChIPs stabilize the S6 conformation and accelerates S6 gating. DPPs stabilize the conformation of Kv4 S1-S2 and accelerates S4 conformation change including S4 movement upon membrane voltage shift. All together additive modulations by KChIPs and DPPs confer A-type current characterized as fast activation, fast closed state inactivation, and fast recovery.

Extended Data Table 1 Cryo-EM data collection, refinement and validation statistics

Supplementary information

Supplementary Information

This file contains Supplementary Discussion, Supplementary Figures 1–12 and Supplementary Table 1.

Reporting Summary

Peer Review File

Rights and permissions

Open Access This article is licensed under a Creative Commons Attribution 4.0 International License, which permits use, sharing, adaptation, distribution and reproduction in any medium or format, as long as you give appropriate credit to the original author(s) and the source, provide a link to the Creative Commons license, and indicate if changes were made. The images or other third party material in this article are included in the article's Creative Commons license, unless indicated otherwise in a credit line to the material. If material is not included in the article's Creative Commons license and your intended use is not permitted by statutory regulation or exceeds the permitted use, you will need to obtain permission directly from the copyright holder. To view a copy of this license, visit <http://creativecommons.org/licenses/by/4.0/>.

Reprints and Permissions

About this article

Cite this article

Kise, Y., Kasuya, G., Okamoto, H.H. *et al.* Structural basis of gating modulation of Kv4 channel complexes. *Nature* **599**, 158–164 (2021). <https://doi.org/10.1038/s41586-021-03935-z>

- Received: 02 March 2021
- Accepted: 19 August 2021
- Published: 22 September 2021
- Issue Date: 04 November 2021

- DOI: <https://doi.org/10.1038/s41586-021-03935-z>

Share this article

Anyone you share the following link with will be able to read this content:

[Get shareable link](#)

Sorry, a shareable link is not currently available for this article.

[Copy to clipboard](#)

Provided by the Springer Nature SharedIt content-sharing initiative

This article was downloaded by **calibre** from <https://www.nature.com/articles/s41586-021-03935-z>

| [Section menu](#) | [Main menu](#) |

Amendments & Corrections

- [**Author Correction: Mapping the emergence of molecular vibrations mediating bond formation**](#) [14 October 2021]
Author Correction •
- [**Publisher Correction: A pan-serotype dengue virus inhibitor targeting the NS3–NS4B interaction**](#) [20 October 2021]
Publisher Correction •

- Author Correction
- [Published: 14 October 2021](#)

Author Correction: Mapping the emergence of molecular vibrations mediating bond formation

- [Jong Goo Kim^{1,2,3},](#)
- [Shunsuke Nozawa^{4,5},](#)
- [Hanui Kim^{1,2,3},](#)
- [Eun Hyuk Choi^{1,2,3},](#)
- [Tokushi Sato^{6,7},](#)
- [Tae Wu Kim^{1,2,3},](#)
- [Kyung Hwan Kim⁸,](#)
- [Hosung Ki^{1,2,3},](#)
- [Jungmin Kim^{1,2,3},](#)
- [Minseo Choi^{1,2,3},](#)
- [Yunbeom Lee^{1,2,3},](#)
- [Jun Heo^{1,2,3},](#)
- [Key Young Oang⁹,](#)
- [Kouhei Ichiyanagi⁴,](#)
- [Ryo Fukaya⁴,](#)
- [Jae Hyuk Lee¹⁰,](#)
- [Jaeku Park¹⁰,](#)
- [Intae Eom¹⁰,](#)
- [Sae Hwan Chun¹⁰,](#)
- [Sunam Kim¹⁰,](#)
- [Minseok Kim¹⁰,](#)
- [Tetsuo Katayama^{11,12},](#)
- [Tadashi Togashi^{11,12},](#)

- [Sigeki Owada](#)^{11,12},
- [Makina Yabashi](#)^{11,12},
- [Sang Jin Lee](#)^{1,2,3},
- [Seonggon Lee](#)^{1,2,3},
- [Chi Woo Ahn](#)^{1,2,3},
- [Doo-Sik Ahn](#)^{1,2,3},
- [Jiwon Moon](#)¹³,
- [Seungjoo Choi](#)¹⁴,
- [Joonghan Kim](#)¹³,
- [Taiha Joo](#)⁸,
- [Jeongho Kim](#)¹⁴,
- [Shin-ichi Adachi](#)^{4,5} &
- [Hyotcherl Ihee](#) ^{1,2,3}

[Nature](#) volume **599**, page E1 (2021)

- 406 Accesses
- 2 Altmetric
- [Metrics details](#)

Subjects

- [Excited states](#)
- [Reaction kinetics and dynamics](#)

The [Original Article](#) was published on 24 June 2020

[Download PDF](#)

Correction to: *Nature* <https://doi.org/10.1038/s41586-020-2417-3> Published online 24 June 2020

In the Supplementary Information originally published with this Article, there were errors in Eq. (S1) and Supplementary Table S1. Specifically, “ $\langle \text{vec}\{\{\boldsymbol{q}\}\} \rangle$ ” was presented as a vector in Eq. (S1) in three instances and nine times in the paragraph immediately following Eq. (S1). The vector should instead have appeared in scalar form, “ q .” The scalar “ q ” now appears in Eq. (S1) three times and also replaces “ $\langle \text{vec}\{\{\boldsymbol{q}\}\} \rangle$ ” in the subsequent paragraph.

In the first three sections of Supplementary Table S1 (Asymmetric S_0 , Symmetric S_0 , T_1') where “Debye-Waller factor for R_{AB} and R_{BC} , $\sigma_1^2 (\text{\AA}^2)$ ” and “Debye-Waller factor for R_{AC} , $\sigma_2^2 (\text{\AA}^2)$ ” originally appeared in the fourth and fifth rows of the three sections, they have been amended to read “Mean-squared displacement of Debye-Waller factor for R_{AB} and R_{BC} , $\sigma_1^2 (\text{\AA}^2)$ ” and “Mean-squared displacement of Debye-Waller factor for R_{AC} , $\sigma_2^2 (\text{\AA}^2)$.” The Supplementary Information has been corrected online.

Author information

Affiliations

1. Department of Chemistry, KAIST, Daejeon, Republic of Korea

Jong Goo Kim, Hanui Kim, Eun Hyuk Choi, Tae Wu Kim, Hosung Ki, Jungmin Kim, Minseo Choi, Yunbeom Lee, Jun Heo, Sang Jin Lee, Seonggon Lee, Chi Woo Ahn, Doo-Sik Ahn & Hyotcherl Ihee

2. KI for the BioCentury, KAIST, Daejeon, Republic of Korea

Jong Goo Kim, Hanui Kim, Eun Hyuk Choi, Tae Wu Kim, Hosung Ki, Jungmin Kim, Minseo Choi, Yunbeom Lee, Jun Heo, Sang Jin Lee, Seonggon Lee, Chi Woo Ahn, Doo-Sik Ahn & Hyotcherl Ihee

3. Center for Nanomaterials and Chemical Reactions, Institute for Basic Science (IBS), Daejeon, Republic of Korea

Jong Goo Kim, Hanui Kim, Eun Hyuk Choi, Tae Wu Kim, Hosung Ki, Jungmin Kim, Minseo Choi, Yunbeom Lee, Jun Heo, Sang Jin Lee, Seonggon Lee, Chi Woo Ahn, Doo-Sik Ahn & Hyotcherl Ihee

4. Photon Factory, Institute of Materials Structure Science, High Energy Accelerator Research Organization (KEK), Tsukuba, Japan

Shunsuke Nozawa, Kouhei Ichiyangagi, Ryo Fukaya & Shin-ichi Adachi

5. Department of Materials Structure Science, School of High Energy Accelerator Science, The Graduate University for Advanced Studies, Tsukuba, Japan

Shunsuke Nozawa & Shin-ichi Adachi

6. Center for Free-Electron Laser Science (CFEL), Deutsches Elektronen-Synchrotron (DESY), Hamburg, Germany

Tokushi Sato

7. European XFEL, Schenefeld, Germany

Tokushi Sato

8. Department of Chemistry, Pohang University of Science and Technology (POSTECH), Pohang, Republic of Korea

Kyung Hwan Kim & Taiha Joo

9. Radiation Center for Ultrafast Science, Quantum Optics Division, Korea Atomic Energy Research Institute (KAERI), Daejeon, Republic of Korea

Key Young Oang

10. Pohang Accelerator Laboratory, Pohang, Republic of Korea

Jae Hyuk Lee, Jaeku Park, Intae Eom, Sae Hwan Chun, Sunam Kim & Minseok Kim

11. Japan Synchrotron Radiation Research Institute (JASRI), Sayo, Japan

Tetsuo Katayama, Tadashi Togashi, Sigeaki Owada & Makina Yabashi

12. RIKEN SPring-8 Center, Sayo, Japan

Tetsuo Katayama, Tadashi Togashi, Sigeaki Owada & Makina Yabashi

13. Department of Chemistry, The Catholic University of Korea, Bucheon, Republic of Korea

Jiwon Moon & Joonghan Kim

14. Department of Chemistry, Inha University, Incheon, Republic of Korea

Seungjoo Choi & Jeongho Kim

Corresponding author

Correspondence to Hyotcherl Ihee.

Rights and permissions

[Reprints and Permissions](#)

About this article

Cite this article

Kim, J.G., Nozawa, S., Kim, H. *et al.* Author Correction: Mapping the emergence of molecular vibrations mediating bond formation. *Nature* **599**, E1 (2021). <https://doi.org/10.1038/s41586-021-04036-7>

- Published: 14 October 2021

- Issue Date: 04 November 2021
- DOI: <https://doi.org/10.1038/s41586-021-04036-7>

Share this article

Anyone you share the following link with will be able to read this content:

[Get shareable link](#)

Sorry, a shareable link is not currently available for this article.

[Copy to clipboard](#)

Provided by the Springer Nature SharedIt content-sharing initiative

This article was downloaded by **calibre** from <https://www.nature.com/articles/s41586-021-04036-7>

| [Section menu](#) | [Main menu](#) |

- Publisher Correction
- [Published: 20 October 2021](#)

Publisher Correction: A pan-serotype dengue virus inhibitor targeting the NS3–NS4B interaction

- [Suzanne J. F. Kaptein](#) ORCID: [orcid.org/0000-0002-7935-0219¹](https://orcid.org/0000-0002-7935-0219),
- [Olivia Goethals²](#),
- [Dominik Kiemel³](#),
- [Arnaud Marchand⁴](#),
- [Bart Kesteleyn⁵](#),
- [Jean-François Bonfanti](#) ORCID: [orcid.org/0000-0002-2107-8857^{6 nAff11}](https://orcid.org/0000-0002-2107-8857),
- [Dorothée Bardiot⁴](#),
- [Bart Stoops⁵](#),
- [Tim H. M. Jonckers⁵](#),
- [Kai Dallmeier](#) ORCID: [orcid.org/0000-0002-8117-9166¹](https://orcid.org/0000-0002-8117-9166),
- [Peggy Geluykens^{5 nAff12}](#),
- [Kim Thys⁵](#),
- [Marjolein Crabbe⁵](#),
- [Laurent Chatel-Chaix](#) ORCID: [orcid.org/0000-0002-7390-8250^{3 nAff13}](https://orcid.org/0000-0002-7390-8250),
- [Max Münster³](#),
- [Gilles Querat⁷](#),
- [Franck Touret](#) ORCID: [orcid.org/0000-0002-4734-2249⁷](https://orcid.org/0000-0002-4734-2249),
- [Xavier de Lamballerie⁷](#),
- [Pierre Raboisson^{5 nAff14}](#),

- [Kenny Simmen⁵](#),
- [Patrick Chalton^{4,8}](#),
- [Ralf Bartenschlager](#) ORCID: [orcid.org/0000-0001-5601-9307^{3,9}](https://orcid.org/0000-0001-5601-9307),
- [Marnix Van Loock](#) ORCID: [orcid.org/0000-0003-4151-4588²](https://orcid.org/0000-0003-4151-4588) &
- [Johan Neyts](#) ORCID: [orcid.org/0000-0002-0033-7514^{1,10}](https://orcid.org/0000-0002-0033-7514)

[Nature](#) volume **599**, page E2 (2021)

- 666 Accesses
- 3 Altmetric
- [Metrics details](#)

Subjects

- [Dengue virus](#)
- [Target identification](#)

The [Original Article](#) was published on 06 October 2021

[Download PDF](#)

Correction to: *Nature* <https://doi.org/10.1038/s41586-021-03990-6>
 Published online 30 June 2021

In this version of this Article originally published, there were errors in Fig. 2 and in the references list. Specifically, in the Fig. 2c colour key, the middle cyan key now reading “JNJ-A07, 10 mg per kg, b.i.d” was missing the number of units, “10,” in the originally published version. Further, refs. [27](#) and [28](#) were swapped in the references list; their correct order appears below. The original Article has been corrected online.

References

1. 27.

Low, J. G., Ooi, E. E. & Vasudevan, S. G. Current status of dengue therapeutic research and development. *J. Infect. Dis.* **215**, S96–S102 (2017).

2. 28.

Unlocking the Potential of Preventive Therapies for Malaria. World Health Organization, <https://www.who.int/malaria/media/preventive-therapies/en/> (7 April 2017).

Author information

Author notes

1. Jean-François Bonfanti

Present address: Galapagos, Romainville, France

2. Peggy Geluykens

Present address: Charles River Beerse, Discovery, Beerse, Belgium

3. Laurent Chatel-Chaix

Present address: Institut National de la Recherche Scientifique, Centre Armand-Frappier Santé Biotechnologie, Quebec, Quebec, Canada

4. Pierre Raboisson

Present address: Aligos, Leuven, Belgium

Affiliations

1. Laboratory of Virology and Chemotherapy, Department of Microbiology, Immunology and Transplantation, Rega Institute for Medical Research, KU Leuven, Leuven, Belgium

Suzanne J. F. Kaptein, Kai Dallmeier & Johan Neyts

2. Janssen Global Public Health, Janssen Pharmaceutica, Beerse, Belgium

Olivia Goethals & Marnix Van Loock

3. Department of Infectious Diseases, Molecular Virology, Heidelberg University, Heidelberg, Germany

Dominik Kiemel, Laurent Chatel-Chaix, Max Münster & Ralf Bartenschlager

4. Cistim Leuven, Leuven, Belgium

Arnaud Marchand, Dorothée Bardiot & Patrick Chaltn

5. Janssen Research & Development, Janssen Pharmaceutica, Beerse, Belgium

Bart Kesteleyn, Bart Stoops, Tim H. M. Jonckers, Peggy Geluykens, Kim Thys, Marjolein Crabbe, Pierre Raboisson & Kenny Simmen

6. Janssen Infectious Diseases Discovery, Janssen-Cilag, Val de Reuil, France

Jean-François Bonfanti

7. Unité des Virus Émergents (UVE), Aix-Marseille Univ, IRD 190 Inserm 1207, IHU Méditerranée Infection, Marseille, France

Gilles Querat, Franck Touret & Xavier de Lamballerie

8. Centre for Drug Design and Discovery (CD3), KU Leuven, Leuven, Belgium

Patrick Chaltn

9. German Center for Infection Research, Heidelberg Partner Site,
Heidelberg, Germany

Ralf Bartenschlager

10. Global Virus Network (GVN), Baltimore, MD, USA

Johan Neyts

Corresponding authors

Correspondence to Marnix Van Loock or Johan Neyts.

Rights and permissions

[Reprints and Permissions](#)

About this article

Cite this article

Kaptein, S.J.F., Goethals, O., Kiemel, D. *et al.* Publisher Correction: A pan-serotype dengue virus inhibitor targeting the NS3–NS4B interaction. *Nature* **599**, E2 (2021). <https://doi.org/10.1038/s41586-021-04123-9>

- Published: 20 October 2021
- Issue Date: 04 November 2021
- DOI: <https://doi.org/10.1038/s41586-021-04123-9>

Share this article

Anyone you share the following link with will be able to read this content:

[Get shareable link](#)

Sorry, a shareable link is not currently available for this article.

[Copy to clipboard](#)

Provided by the Springer Nature SharedIt content-sharing initiative

This article was downloaded by **calibre** from <https://www.nature.com/articles/s41586-021-04123-9>

| [Section menu](#) | [Main menu](#) |